



HAL
open science

Thermo-mechanical modelling of the Wire Arc Additive Manufacturing process (WAAM)

Sami Hilal

► **To cite this version:**

Sami Hilal. Thermo-mechanical modelling of the Wire Arc Additive Manufacturing process (WAAM). Mechanics of materials [physics.class-ph]. Université Paris sciences et lettres, 2022. English. NNT : 2022UPSLM021 . tel-03868998

HAL Id: tel-03868998

<https://pastel.hal.science/tel-03868998>

Submitted on 24 Nov 2022

HAL is a multi-disciplinary open access archive for the deposit and dissemination of scientific research documents, whether they are published or not. The documents may come from teaching and research institutions in France or abroad, or from public or private research centers.

L'archive ouverte pluridisciplinaire **HAL**, est destinée au dépôt et à la diffusion de documents scientifiques de niveau recherche, publiés ou non, émanant des établissements d'enseignement et de recherche français ou étrangers, des laboratoires publics ou privés.



THÈSE DE DOCTORAT

DE L'UNIVERSITÉ PSL

Préparée à MINES ParisTech

**Thermo-mechanical modelling of the Wire Arc Additive
Manufacturing process (WAAM)**

**Simulation thermo-mécanique du procédé de fabrication
additive par dépôt-fil WAAM**

Soutenue par

Sami HILAL

Le 03 mai 2022

Ecole doctorale n° 621

**Ingénierie des Systèmes,
Matériaux, Mécanique,
Energétique (ISMME)**

Spécialité

Mécanique

Composition du jury :

Cyril BORDREUIL Professeur, Université de Montpellier	<i>Président</i>
Mike C. SMITH Professeur, The University of Manchester	<i>Rapporteur</i>
Eric FEULVARCH Professeur, ENISE	<i>Rapporteur</i>
Muriel CARIN Professeure, Université Bretagne-Sud	<i>Examinatrice</i>
Pierre KERFRIDEN Assistant Professeur, Mines ParisTech	<i>Examineur</i>
Djamel MISSOUM-BENZIANE Ingénieur de recherche, Mines ParisTech	<i>Examineur</i>
Sofiane HENDILI Ingénieur de recherche, EDF R&D	<i>Examineur</i>
Matthieu MAZIERE Professeur, Mines ParisTech	<i>Directeur de thèse</i>

Acknowledgements

C'est avec émotion que se clôt ce chapitre de ma vie, mes 3 années de thèse, qui, malgré des hauts et des bas, restera très certainement un des moments les plus marquants dans ma vie.

Je tiens tout d'abord à remercier les professeurs Muriel Carin, Cyril Bordreuil, Mike C. Smith, Eric Feulvach ainsi que Xavier Gostiaux d'avoir accepté de faire partie de mon jury. Merci d'avoir pris le temps de lire mes travaux, et merci pour les échanges à la fois enrichissants et agréables que nous avons eus.

Je tiens également à te remercier, Matthieu. Tu as toujours été d'une clairvoyance et d'un avis très percutant, avec des remarques et observations qui permettaient de mettre en évidence des points cruciaux. Tes conseils ont très souvent été décisifs tout le long de la thèse et je t'en remercie profondément.

Pierre, je tiens à te remercier pour ton encadrement, ton dynamisme, ta dévotion et ta passion à l'idée de révolutionner le domaine dans lequel tu évolues; toute cette ardeur transparaît au quotidien. Tu m'as aidé à sortir de ma zone de confort à plusieurs reprises et à explorer des domaines qui m'étaient jusque-là inconnus.

Djamel ! Quel personnage ! Sache que j'ai toujours été impressionné par ton incroyable et in-tarissable savoir, avec une large culture scientifique dont je n'ai pour l'instant pas réussi à entrevoir les limites. Nos très nombreuses discussions, cafés et repas étaient un réel plaisir. Je te dois d'ailleurs de très nombreux cafés.... Malgré les innombrables débats qu'on a eus, les multiples désaccords (même si, comme tu l'as toi-même reconnu, j'ai eu quelques fois raison !) tu as été un super encadrant, auprès de qui j'ai vraiment évolué. Je t'en serai toujours reconnaissant.

Pour ce qui est de l'équipe encadrante à EDF, je tiens tout particulièrement à te remercier, Sofiane (ou l'autre "SH"). Je n'oublierai jamais nos nombreuses sessions de travail ensemble en début de thèse, nos innombrables discussions sur le balcon et tes multiples conseils toujours très judicieux. Merci pour ta patience, je sais comme ça a dû être parfois fatigant de m'avoir comme doctorant ... Merci aussi pour la confiance indéfectible que tu as eue en moi à de très nombreuses reprises. Sache que pour moi, ça a été un réel bonheur de t'avoir comme encadrant (scientifiquement et humainement). A vrai dire, tu as été plus qu'un encadrant pendant cette thèse, tu as été et tu resteras toujours un mentor et un ami.

Mon ami Josselin ! Comment pourrais-je t'oublier dans ces remerciements. Merci pour ta gentillesse et ta bienveillance. Ta bonne humeur communicative et ton humour toujours au rendez-vous rendent le travail à tes côtés terriblement plaisant. Sache, néanmoins, que je me vengerais pour le coup du post-it.

Je veux également vous remercier, Alexandre, Damien et Laurent pour les nombreuses discussions le matin autour d'un café au labo. Vous m'avez vraiment beaucoup apporté pendant la thèse, tant humainement que professionnellement.

Je souhaite exprimer ma reconnaissance à tous les membres de la compétence PSPS: Vincent, Rafael, Salma, Alexandre, Jules, Audrey, David, Laurent et surtout sans oublier Sylvie. Parmi les nombreuses personnes avec qui j'ai pu travailler, je souhaite tout particulièrement te remercier Mickael. J'aurais aimé avoir la chance de travailler plus avec toi pendant la thèse, mais sache que les quelques moments passés ensemble étaient à la fois très enrichissants et incroyablement plaisants.

Pendant ces trois ans, j'ai fait de magnifiques rencontres. Je tiens dans un premier à remercier la team fantastique des thésards et des stagiaires. Merci à Jérôme et Thomas de nous avoir si bien accueilli. Merci à vous, Clément (Clémzouze pour les intimes) que je vois plus souvent à EDF que certaines personnes depuis la pandémie, Mathilde, Pierre et tous les autres stagiaires avec qui j'ai partagé tellement de bons moments que ce soit pendant la première année et même après. Paul et Alvaro, partager ces 3 années de thèse avec vous était un réel plaisir. Merci pour ces très longues discussions qui pouvaient aussi bien porter sur la thèse ou nos problèmes administratifs, que sur l'hydrodynamique dans une tasse de café. Merci infiniment à toi Paul, grace à toi j'ai pu me convaincre que je n'étais pas tout seul à être coincé dans le tourbillon infernal des trucs administratifs à faire ! Je tiens tout particulièrement à te remercier, Vanessa, pour ta gentillesse, ta bienveillance et ta présence. Malgré le fait que tu aies déménagé à Toulouse (nos pauses me manquent déjà), tu pourras toujours compter sur moi, y compris pour tes futurs déménagements ! Merci Antoine pour tous ces moments partagés et ces rires. "Etre archi incroyable !". On s'est quand même vachement bien amusé pendant ces 3 années. Azénor, merci pour tous ces moments passés ensemble, ces navettes prises ensemble, et ces taquineries constantes (qui très souvent, je l'admets, viennent de moi) et surtout pour ta confiance. Tu es une de mes plus belles rencontres.

Je veux également remercier les membres fondateurs du bureau de la chance, Théo et Pablo. On a vraiment tout traversé ensemble pendant cette thèse, y compris le Covid (la Covid c'est pas très beau je trouve). On a passé des moments inoubliables, des fous rire aux moments difficiles allant du coup de mou aux ordinateurs/disques durs/clusters qui crament. Merci Pablo pour ces 3 ans à se soutenir mutuellement en tant que co-bureau, co-thésard de PSPS, co-thésard du CdM et très certainement pour encore plusieurs années ! Et Théo, je te l'ai déjà dit de nombreuses fois, c'est un vrai bonheur d'avoir fait ta connaissance. La "HiBou" est loin d'avoir fini de tout casser. Bien entendu, je ne t'oublie pas Nicolas. Tu es une super rencontre, une personne aussi brillante que gentille. J'espère que tu t'épanouiras complètement dans la réalisation de ta thèse.

Marouane, quel plaisir de faire ces très longues pauses du matin quand on arrive tôt. Merci pour ces moments. Merci Laura pour ta bonne humeur quasiment imperturbable, les très nombreuses petites pauses de fin d'après-midi qui rendent la journée tellement plus sympathique. Merci également à Bilal, ainsi que Elias, Pauline, Claire, Thibault, Vincent, Joseph, etc ... ainsi que tous les autres personnes du bâtiment S, P17, P12, etc.... (la liste est très longue....). Je tiens tous à vous remercier pour ces nombreuses discussions à la salle convivialité, les très nombreux cafés et afterworks. Cette aventure n'aurait pas eu la même saveur sans vous. Vous avez tous contribué au fait que je ne prenne que très peu de vacances, tellement l'environnement de travail était incroyable (sans aucune exagération, tout le monde connaît bien entendu ma modération légendaire) !

Enfin, je souhaite remercier ma famille, tout particulièrement mes parents, mon frère Marwane et Ixi, que j'aime du fond du coeur. Sans vous, je ne serais très certainement pas la personne que je suis aujourd'hui. Quand on repense au 23 mars 2016, ça fait bizarre de se dire qu'on en est là aujourd'hui. Je tiens également à te remercier Nargisse, avec qui j'ai eu le plaisir de traverser cette épreuve. Pendant ces trois ans, tu m'as épaulé pendant toute cette aventure, tu m'as soutenu, supporté et inspiré. Sans toi, cette thèse n'aurait pas ressemblé à ça d'autant plus que c'est toi qui as trouvé l'offre à la base ...

Enfin je voudrais dédier cette thèse à ma chienne, ma petite sœur, Dida, avec qui j'ai grandi. Je n'ai malheureusement pas pu te revoir avant la fin, mais sache que je ne t'oublierai jamais.

C'est avec une grande émotion que je réalise à l'écriture de ces mots que cette magnifique expérience se termine, et que je souhaite aux personnes motivées une très bonne lecture des pages qui suivent !

Encore merci à tous

Sami HILAL

Contents

Acknowledgements	iii
List of Figures	xix
List of Tables	xxi
1 Introduction	1
1.1 Industrial context: EDF & AFH consortium	2
1.1.1 Growing interest for additive manufacturing at EDF	2
1.1.2 The AFH consortium	3
1.1.3 WAAM process at EDF	3
1.2 Problem statement	6
1.3 Framework	7
1.3.1 Main objective	7
1.3.2 Thesis outline	8
I The fundamentals of WAAM mesoscopic thermo-mechanical modeling	9
2 State of the art & Modelisation hypothesis	10
2.1 Introduction	11
2.2 Additive manufacturing processes & WAAM	11
2.2.1 Main AM processes	11
2.2.2 Presentation of the WAAM process	13
2.3 Review of WAAM modeling approaches	16
2.3.1 Microscopic scale	17
2.3.2 Mesoscopic scale	19
2.3.3 Macroscopic scale	20
2.4 Mesoscopic scale modeling	26
2.4.1 Physical aspects & assumptions	26
2.4.2 Material deposition approaches	28
2.4.3 Mesoscopic thermal model	30
2.4.4 Mesoscopic mechanical model	37
2.5 Conclusion & perspectives	41

3	Proposed mesoscopic thermo-mechanical model	42
3.1	Introduction	43
3.2	Material deposition approach	43
3.2.1	Material progressive deposition modeling	44
3.2.2	Mesh generation tool	45
3.3	Thermal model	49
3.3.1	Equivalent heat source developed: Adaptive Goldak with heat flux correction	49
3.3.2	Boundary conditions	54
3.3.3	Material deposition	56
3.3.4	Synthesis of the thermal model parameters	56
3.3.5	Examples	57
3.4	Mechanical model	59
3.4.1	Plasticity model	60
3.4.2	Hardening annealing	66
3.4.3	Material deposition	67
3.4.4	Molten pool mechanical reset	68
3.4.5	Reference temperature change	68
3.4.6	Cut-off temperature	69
3.4.7	Examples	72
3.5	Conclusion & perspectives	73
3.6	In a nutshell	74
4	Digital twinning for mesoscopic model calibration	75
4.1	Introduction	76
4.2	Problem description	76
4.3	State of the art	77
4.4	Surrogate model approach: Sparse Polynomial Chaos Expansion	78
4.4.1	Theoretical presentation of chaos polynomials	79
4.4.2	Construction steps	81
4.4.3	Sensitivity analysis	84
4.4.4	Conclusion	85
4.5	Bayesian parameter estimation	86
4.5.1	Introduction	86
4.5.2	Bayesian inference	86
4.5.3	Monte Carlo Markov Chain (MCMC) sampling	87
4.5.4	Inverse problem step-by-step instructions	89
4.6	Example for the application of the method	90
4.7	Conclusion & perspectives	92
4.8	In a nutshell	93
5	Validation cases and numerical results	94
5.1	Introduction	95
5.2	1 st use case: high displacement "Zigzag" wall test case	96

5.2.1	Introduction and objectives	96
5.2.2	Description of the experimental setup	96
5.2.3	Thermal model parameters calibration	98
5.2.4	Numerical results	100
5.2.5	Conclusion of the study	104
5.3	2 nd use case: " <i>Zigzag</i> " & " <i>Raster</i> " walls	106
5.3.1	Introduction and objectives	106
5.3.2	Description of the experimental setup	106
5.3.3	Thermal model parameters calibration	111
5.3.4	Numerical results	114
5.3.5	Conclusion of the study	126
5.4	3 rd use case: NET Network consortium Task Group 9 (TG9)	127
5.4.1	Introduction and objectives	127
5.4.2	Description of the experimental setup	127
5.4.3	Thermal model parameters calibration	131
5.4.4	Numerical results	133
5.4.5	Conclusion of the study	142
5.5	4 th use case: AFH block with cooling devices and idle time	145
5.5.1	Introduction and objectives	145
5.5.2	Description of the experimental setup	146
5.5.3	Thermal model parameters calibration	149
5.5.4	Numerical results	153
5.5.5	Conclusion of the study	157
5.6	Thermal parameters sensitivity analysis	158
5.7	Conclusion & perspectives	160
5.8	In a nutshell	162

II Computationally efficient approaches 163

6 Macro-deposition & local meso-resolution methods 164

6.1	Introduction	165
6.2	Description of the macro-deposition method	166
6.2.1	Main concepts behind macro-deposition	166
6.2.2	Problematic	167
6.3	Calibration of the macro-deposition method	167
6.3.1	Introduction	167
6.3.2	Presentation of the study cases	168
6.3.3	1 st case study: " <i>Raster</i> " using TIG process	171
6.3.4	2 nd case study: " <i>Raster</i> " using CMT process	174
6.3.5	3 rd case study: " <i>Zigzag</i> " using TIG process	177
6.3.6	4 th case study: " <i>Raster</i> " using TIG process	179
6.3.7	5 th case study: Kaplan blade representative bloc using TIG process	181

6.3.8	Conclusion on the five study cases	183
6.3.9	Perspectives and possible applications for macro-deposition	184
6.4	Mixed approach: macro-deposition with "local meso-resolution"	187
6.4.1	Overview of the "local meso-resolution" approach	187
6.4.2	Application to the 5 th case study	187
6.5	Conclusion & perspectives	190
6.6	In a nutshell	192
7	Data-driven inherent strain prediction	193
7.1	Introduction	194
7.2	Inherent strain field calibration step	195
7.2.1	Problem description	195
7.2.2	Inherent strain field results	196
7.3	Inherent strain prediction by Deep Learning	200
7.3.1	Introduction	200
7.3.2	MultiLayer Perceptron (MLP) using prior feature extraction: Isothermal values	201
7.3.3	Full temperature profiles: Convolutional Neural Network (CNN)	204
7.3.4	Full temperature profiles: Recurrent Neural Network (RNN)	205
7.3.5	Discussion on the use of Deep Learning to investigate inherent strains	207
7.4	Conclusion & perspectives	208
7.4.1	Conclusion	208
7.4.2	Perspectives: residual stress prediction by inherent strain	209
7.5	In a nutshell	210
8	Conclusion	211
8.1	Mesoscopic thermo-mechanical model	212
8.2	Digital twinning assisted calibration	214
8.3	Computationally efficient approaches	216
8.4	Final words	218
	Bibliography	233
A	Additional data from the 2nd test case of Chapter 5	234
A.1	Calibration steps of the "Zigzag" and of the "Raster"	234
A.2	Validation of the thermal model calibration methodology on a cylinder	235
B	Extra study: Inverse problem using macrographies	238
C	Extra study: Sensitivity analysis	240
D	Extra study: Thermal dissipation model selection	244
D.1	Presentation of the study	244
D.2	Models & Results	245
E	Constitutive behavior models monotonic response to a tensile loading	247

F	Extra study: Thermal model calibration using stress experimental data	249
G	Data-driven inherent strain field calibration method	253
G.1	Introduction	253
G.1.1	Overview of the problem	253
G.1.2	Proposed model	254
G.2	Data deviation term	255
G.3	Regularization term	258
G.3.1	Jump model	258
G.3.2	Neo-Hook term	258
G.4	Overview of the method	259
H	Neural network architectures	261
H.1	MLP model description	261
H.2	CNN model description	263
H.3	RNN model description	265

List of Figures

1.1	Industrial Adoption of additive manufacturing (AM) [3].	2
1.2	Schematic illustration of the WAAM process.	4
1.3	Schematic illustration of nozzle manufacturing on an existing pipe.	5
1.4	Workpieces of interest for at EDF using WAAM process: a) Kaplan pale in the hydraulic field (reduced scale), b) PPB in the nuclear field.	5
1.5	Illustration of the steps for the prediction of the residual state for a nozzle.	8
2.1	Metal Additive Manufacturing Market in 2020 [3].	11
2.2	Schematic illustration of (a) PBF and (b) DED processes [22].	12
2.3	Overview of the most used metal arc welding technologies, Metal arc welding technologies: a) Gas Tungsten Arc Welding (GTAW), b) Gas Metal Arc Welding (GMAW) [28].	14
2.4	Influence of voltage and current on the metal transfer mode in GMAW welding using Argon Shielding [30].	15
2.5	Schematic illustration of the main physical phenomena involved a) in the molten pool, b) and in the solid phase.	17
2.6	a) Decomposition of a single powder layer into several fractions to be heated consecutively, b) Treatment of layer fractions and illustration of the laser scan overlay coefficient [76].	22
2.7	Couplings between thermal, metallurgical and mechanical modeling aspects.	27
2.8	Illustration of the material deposition approaches: a) Geometry, b) "Quiet element" method, c) "Inactive element" method.	29
2.9	Representation of the latent heat of fusion phenomenon.	30
2.10	Surface heat source, with constant or gaussian flux distribution.	34
2.11	Half-spherical heat source with gaussian flux distribution.	34
2.12	Goldak heat source: double ellipsoid heat source with gaussian flux distribution.	35
2.13	Montevecchi heat source: double ellipsoid heat source with gaussian flux distribution, with filler constant flux distribution.	35
2.14	Conical heat source with gaussian flux distribution.	36
2.15	Double cylindrical heat source with gaussian flux distribution.	37

2.16	Hardening model: a) Isotropic hardening model showing the expansion of the yield surface with plastic strain, b) kinematic hardening model showing the translation of the yield surface with plastic strain, c) mixed isotropic–kinematic hardening model showing the expansion and translation of the yield surface with plastic strain, d) resulting stress–strain curves showing different yield stress in compression as predicted by different plasticity models: C – kinematic hardening, D – mixed hardening, and E – isotropic hardening [125].	39
3.1	Illustration of the material deposition methodology.	44
3.2	Generation tools of the geometry with a simplified rectangular cross-section bead.	46
3.3	Geometry and mesh generation tools of a block, for three different deposition patterns.	47
3.4	Geometry and mesh generation from a 3D scan of the Kaplan blade.	47
3.5	Geometry and mesh generation tools for cylinders: a) Cylinder on a flat substrate with a circular deposition pattern, b) Cylinder on a pipe substrate with a scanning deposition pattern, c) Multiple cylinders on a pipe substrate with a circular deposition pattern.	48
3.6	Geometry and mesh generation for the PPB.	48
3.7	Goldak integral as a function of spatial and temporal discretization.	50
3.8	Comparison between the Goldak heat source and the new adaptive Goldak heat source developed.	52
3.9	Schematic illustration of the Adaptive Goldak heat source on a simple example.	53
3.10	Comparison of the heat losses model (in $\text{W}\cdot\text{mm}^{-2}$): in blue the constant heat coefficients model, in green the linear heat coefficients model, in red the tanh combined model, in cyan the value for $h = 15e - 6$ ($\text{W}\cdot\text{mm}^{-2}\cdot\text{K}^{-1}$) & $\varepsilon = 0.35$ (usually used in literature).	55
3.11	Schematic illustration of the clamping heat loss.	56
3.12	Thermal simulations of two pipes made with different deposition patterns at three instants (32 s, 1497 s and 3152 s): a) Scanning deposition pattern, b) Circular deposition pattern.	58
3.13	Thermal simulation of the PPB at 1:5 scale at four instants (62 s, 831 s, 1660 s and 2254 s).	58
3.14	Hardening annealing coefficient as a function of temperature: below 600 °C, no hardening annealing and above 1000 °C complete hardening annealing.	67
3.15	Reference temperature: a) configuration with a reference temperature of 1400 °C on the elements of the deposited material, b) configuration where all the elements that passed the melting temperature threshold have a reference temperature of 1400 °C.	69
3.16	Thermo-mechanical simulations performed using the "mesh cut-off" method for different temperature isotherms: on the left column the temperature field on the cut mesh on which the resolution of the nonlinear mechanical problem is performed, on the right column the residual stress field after complete cooling of the workpiece.	71
3.17	Evolution of the residual stress error (Von Mises mean absolute error) and the reduction of the computational time of the simulations with temperature mesh "cut-off" with respect to the reference simulation presented in Figure 3.16.	72

3.18	Thermo-mechanical simulations of two pipes made with different deposition patterns after cooling to ambient temperature: a) Scanning deposition pattern, b) Circular deposition pattern.	72
4.1	Design Of Experiment examples using Monte Carlo sampling method and the Sobol's sequences. The input parameters \mathcal{X} are independent random variables ($p = 3$) uniformly distributed: $\mathcal{X} = (\mathcal{X}_1, \mathcal{X}_2, \mathcal{X}_3)$, $\mathcal{X}_i \sim \mathcal{U}(0, 1)$, $i = 1, \dots, 3$	83
4.2	Illustration of the digital twinning bayesian calibration method.	91
5.1	Illustration of the 1 st test case: a) Schematic illustration of the wall, b) Thermocouples locations, c) The final part.	96
5.2	Temperature profiles during the 32 beads wall use case using type K thermocouples . . .	97
5.3	3D scan of the 32 beads wall use case, and free end displacement measurement.	98
5.4	Corner plot of the posterior distribution resulting from the calibration step. The MAP is represented in blue.	100
5.5	Displacement field for the 32 beads wall, using the VMIS_ISOT_TRAC model, without the linear elastic computation at the activation of the elements.	101
5.6	Displacement field for the 32 beads wall, using the VMIS_ISOT_TRAC model, with the linear elastic computation at the activation of the elements.	102
5.7	Displacement field for the 32 beads wall, using the VMIS_ISOT_TRAC model, with the linear elastic computation when activating the elements and with a boundary condition representing the welding torch position.	102
5.8	Material deposition methodology.	103
5.9	Benchmark of constitutive behavior models for the "Zigzag" test case.	104
5.10	Schematic illustration of the "Zigzag" and "Raster" deposition pattern.	106
5.11	"Zigzag" and "Raster" experimental test cases presentation.	107
5.12	Thermal camera FLIR Orion SC7500-BB.	108
5.13	a) Stereo-correlation device, b) Displacement measurement of a marker during the "Zigzag" wall test case	110
5.14	3D scan of the "Zigzag" and "Raster" 50 beads walls	110
5.15	Thermocouple curves of the "Zigzag" and "Raster" 50 beads walls, and the experimental data used for the calibration step.	111
5.16	Corner plot of the posterior distribution resulting from the calibration step of the "Zigzag" & "Raster" tests cases. The MAP $\theta_{z\&r}^*$ is represented in blue.	113
5.17	Comparison of the thermocouples profiles of the "Zigzag" wall test with the temperature profiles for the 3 MAP: in red the experimental data, in blue the computed thermal profiles for the calibration on the "Zigzag" test, in green the computed thermal profiles for the calibration on the "Raster" test, and in black computed thermal profiles for the calibration on both tests.	115

5.18	Comparison of the thermocouples profiles of the " <i>Raster</i> " wall test with the temperature profiles for the 3 MAP: in red the experimental data, in blue the computed thermal profiles for the calibration on the " <i>Zigzag</i> " test, in green the computed thermal profiles for the calibration on the " <i>Raster</i> " test, and in black computed thermal profiles for the calibration on both tests.	115
5.19	Evolution of the molten pool length during the 50 beads " <i>Zigzag</i> " wall test: in red the computed estimation, and in blue, the experimental measurements.	117
5.20	Evolution of the molten pool length during the 50 beads " <i>Raster</i> " wall test: in red the computed estimation, and in blue, the experimental measurements.	117
5.21	Evolution of the inter-layer temperature of the " <i>Zigzag</i> " wall.	118
5.22	Evolution of the inter-layer temperature of the " <i>Raster</i> " wall.	118
5.23	Displacement field of the " <i>Zigzag</i> " and " <i>Raster</i> ".	119
5.24	Experimental (in blue) and computed (in green) deflection profiles evolution of the " <i>Zigzag</i> " wall: a) Displacement along the z-axis, b) Displacement along the x-axis. . .	120
5.25	Experimental (in blue) and computed (in green) deflection profiles evolution of the " <i>Raster</i> " wall: a) Displacement along the z-axis, b) Displacement along the x-axis. . .	121
5.26	Residual stress fields of the 3 stress components σ_{xx} , σ_{yy} , and σ_{zz} for the two tests: a) " <i>Zigzag</i> ", b) " <i>Raster</i> ".	123
5.27	Residual stress profiles of the 3 stress components σ_{xx} , σ_{yy} , and σ_{zz} for the two tests on 3 sections: a) " <i>Zigzag</i> ", b) " <i>Raster</i> ".	124
5.28	Standard deviation of the residual stress fields of the 3 stress components σ_{xx} , σ_{yy} , and σ_{zz} for the two tests: a) " <i>Zigzag</i> ", b) " <i>Raster</i> ".	125
5.29	Macrograph of the "five-beads" test at different sections. Images from the PhD thesis of Cambon et al. [100].	128
5.30	TG9 "five-beads" full test: wall dimensions.	129
5.31	TG9 "five-bead" test: thermocouples locations.	130
5.32	a) TG9 nominal "single-bead" test: residual stress measurement profiles S1, S2, S3 and S4 are shown in green, and the displacement measurement location during the test is indicated with the blue arrow, b) TG9 full "five-beads" test: residual stress measurement profile S5 are shown in green, and the displacement measurement location during the test is indicated with the blue arrow.	131
5.33	Corner plot of the posterior distribution resulting from the calibration step of the TG9 test case. The MAP is represented in blue.	132
5.34	In black the experimental data, in blue the surrogate model estimation using the MAP, with the 95% confidence interval.	133
5.35	Comparison of computed and experimental temperature profiles of the thermocouple 2.	134
5.36	Comparison of computed and experimental temperature profiles of the thermocouples 3-4.	134
5.37	"Five-beads" test residual stress fields using the VMIS_CINE_LINE behavior model with hardening annealing.	135

5.38	Evolution of the free end displacement along the z-axis during the complete TG9 nominal "single-bead" test. In blue, the experimental measurements, and in solid line the numerical predictions for different constitutive behaviors.	136
5.39	Longitudinal stress profile on the S1 section for the TG9 "single-bead" test: in blue the experimental measurements, in solid line the numerical predictions for different constitutive behaviors, and in bold, the curve closest to the experimental data.	137
5.40	Transverse stress profile on the S1 section for the TG9 "single-bead" test: in blue the experimental measurements, in solid line the numerical predictions for different constitutive behaviors, and in bold, the curve closest to the experimental data.	137
5.41	Longitudinal stress profile on the S2 section for the TG9 "single-bead" test: in blue, the experimental measurements, in solid line, the numerical predictions for different constitutive behaviors and in bold the curve closest to the experimental data.	138
5.42	Transverse stress profile on the S2 section for the TG9 "single-bead" test: in blue, the experimental measurements, in solid line, the numerical predictions for different constitutive behaviors, and in bold the curve closest to the experimental data.	138
5.43	Longitudinal stress profile on the S3 section for the TG9 "single-bead" test: in blue, the experimental measurements, and in solid line, the numerical predictions for different constitutive behaviors. In bold is represented the curve closest to the experimental data.	139
5.44	Transverse stress profile on the S3 section for the TG9 "single-bead" test: in blue, the experimental measurements, and in solid line, the numerical predictions for different constitutive behaviors. In bold is represented the curve closest to the experimental data.	139
5.45	Longitudinal stress profile on the S4 section for the TG9 "single-bead" test: in blue, the experimental measurements, and in solid line, the numerical predictions for different constitutive behaviors. In bold is represented the curve closest to the experimental data.	140
5.46	Transverse stress profile on the S4 section for the TG9 "single-bead" test: in blue, the experimental measurements, and in solid line, the numerical predictions for different constitutive behaviors. In bold is represented the curve closest to the experimental data.	140
5.47	Evolution of the free end displacement along the z-axis during the complete TG9 test (5 beads). In blue are represented the experimental measurements, and in solid line, the numerical predictions for different constitutive behaviors.	141
5.48	Longitudinal stress profile on the S5 section for the TG9 "five-beads" full test. In blue are represented the experimental measurements, and in solid line, the numerical predictions for different constitutive behaviors. In bold is shown the curve closest to the experimental data.	142
5.49	Transverse stress profile on the S5 section for the TG9 "five-bead" full test. In blue are represented the experimental measurements, and in solid line, the numerical predictions for different constitutive behaviors. In bold is shown the curve closest to the experimental data.	142
5.50	Comparison of residual stress measurements and computational results for the material behavior that gives the closest results, using the kinematic hardening model VMIS_CINE_LINE with hardening annealing on the "single-bead" and the "five-beads" tests.	144

5.51	Schematic illustration of the inter-layer temperature.	145
5.52	Calibration bloc test, with the associated deposition strategy.	147
5.53	Schematic illustration of the used cooling devices: in green cylinder device around the welding torch, and in yellow high-pressure compressed air on the base plate.	148
5.54	a) Thermocouples during all the duration of the "calibration test", b) Part of the thermocouple data selected for the calibration of the cooling parameters, c) Part of the thermocouple data selected for the calibration without cooling devices.	149
5.55	Corner plot of the posterior distribution resulting from the calibration step of the 10 th to 18 th layer of the calibration bloc test case. The MAP is represented in blue.	151
5.56	Results of the calibration step: in black, the experimental data used for the calibration, in blue and dotted line, the curve predicted by the surrogate model using the MAP, and in light blue the 95% confidence interval of the posterior distribution.	151
5.57	Corner plot of the posterior distribution resulting from the calibration step of the 10 th to 18 th layer of the calibration bloc test case. The MAP is represented in blue.	152
5.58	Results of the calibration step: in black, the experimental data used for the calibration, in blue and dotted line, the curve predicted by the surrogate model using the MAP, and in light blue the 95% confidence interval of the posterior distribution.	153
5.59	Comparison of computed and experimental temperature curves for the first 9 th layers (manufacturing with cooling devices).	154
5.60	Comparison of computed and experimental temperature curves for the last 9 th layers (manufacturing without cooling devices).	154
5.61	100 layers "repeatability block" deposition pattern	155
5.62	Inter-layer cooling time required for different inter-layer temperatures criteria (12 th first layers).	156
5.63	Thermal parameters sensitivity analysis results (first-order Sobol indices) of the four test cases presented previously: a) 1 st test case, b) 2 nd test case, c) 3 rd test case, d) 4 th test case.	158
5.64	Comparison of aggregated first-order Sobol indices obtained from the calibration using residual stress data (blue) and from the calibration using temperature data at thermocouple points (red). The parameters are ranked in descending order according to the aggregated first-order Sobol indices using residual stress data.	159
6.1	Schematic representation of the macro-deposition approach: the mesoscopic approach on the left, and the corresponding macro-deposition approach on the right.	166
6.2	Presentation of the geometry and the deposition pattern of the first 4 study cases: a) 1 st and 2 nd 2 layers full "Raster" study case, b) 3 rd 2 layers "Zigzag" study case, c) 4 th 8 layers full "Raster" study case.	169
6.3	Illustration of the management of the material deposition in macro-deposition method for the 1 st use case.	171
6.4	Sampling presentation for the parametric study of the macro-deposition method for the test case 1: a) Sampling using l_d and t_d^{heat} , b) Sampling using the fraction parameter f_{l_d} and $f_{t_d^{heat}}$	172

6.5	Macro-deposition displacement prediction for the 1 st case study: a) 3D displacement error response surface, b) Response surface of the displacement error with a "threshold" value (maximum error accepted), c) Response surface predicting the computation time of the macro-deposition simulation as a percentage of reference simulation computation time, d) Response surface of the calculation time on the domain where the error on the displacements is lower than the defined "threshold" value and the associated computation time for the "optimal" parameter set.	172
6.6	Macro-deposition stress prediction for the 1 st case study.	173
6.7	1 st test case results of the reference and macro-deposition simulations for the optimal displacement and stress configurations θ_{displ} and θ_{stress} : a) Von Mises stress field, b) Displacement field.	174
6.8	Macro-deposition displacement prediction for the 2 nd case study.	175
6.9	Macro-deposition stress prediction for the 2 nd case study.	176
6.10	2 nd test case results of the reference and macro-deposition simulations for the optimal displacement and stress configurations θ_{displ} and θ_{stress} : a) Von Mises stress field, b) Displacement field.	176
6.11	Macro-deposition displacement prediction for the 3 rd case study.	177
6.12	Macro-deposition stress prediction for the 3 rd case study.	178
6.13	3 rd test case results of the reference and macro-deposition simulations for the optimal displacement and stress configurations θ_{displ} and θ_{stress} : a) Von Mises stress field, b) Displacement field.	178
6.14	Macro-deposition displacement prediction for the 4 th case study	179
6.15	Macro-deposition stress prediction for the 4 th case study.	180
6.16	4 th test case results of the reference and macro-deposition simulations for the optimal displacement and stress configurations θ_{displ} and θ_{stress} : a) Von Mises stress field, b) Displacement field.	181
6.17	The Kaplan blade geometry and the representative bloc: a) In orange the full Kaplan blade and in gray the 8 first layers, b) In gray the 8 th layer deposition pattern and in blue the simplified deposition pattern for the 5 th test case.	182
6.18	Macro-deposition stress prediction for the 5 th case study: a) 3D stress error response surface, b) Response surface of the stress error.	182
6.19	Macro-deposition displacement prediction for the 5 th case study: a) 3D displacement error response surface, b) Response surface of the displacement error.	183
6.20	Kaplan blade macro-deposition simulation: a) Kaplan blade mesh with the 68 layers, b) Von Mises residual stress field after cooling to ambient temperature.	185
6.21	PPB macro-deposition simulation: a) Geometry of the 10 first layer of the PPB, b) Experimental test, c) Von Mises residual stress field, d) Magnitude displacement field.	186
6.22	Illustration of the mixed approach macro-deposition / local zoom for the block of the 5 th study case: a) reference configuration, b) configuration with macro-deposition and full thermo-mechanical simulation on 12 beads of each layer in the middle of the block.	187

6.23	5 th Case study: Evolution of the temperature profile at the same location: a) Mesh and in red the point location, b) Mesoscopic approach in red, c) Macro-deposition approach in green, d) Local meso-resolution approach in blue, with the zones highlighted in blue correspond to the mesoscopic local focus.	188
6.24	5 th Case study: Von-Mises equivalent stress field: a) Reference thermo-mechanical simulation, b) Macro-deposition, c) Macro-deposition and local meso-resolution.	189
6.25	Goldak integration along welding torch path: a) Uniform heat source on a full layer, b) Integrated spherical heat source on a full layer.	191
7.1	Comparison of the "ideal" geometry of the Kaplan blade resulting from the manufacturing paths and the 3D scan of the Kaplan blade after manufacturing.	194
7.2	a) Deformed mesh obtained for the "Zigzag" wall using the calibration algorithm, b) Quality of the initial mesh, c) "Zigzag" wall mesh quality evolution.	196
7.3	a) Deformed mesh obtained for the "Raster" wall using the calibration algorithm, b) Quality of the initial mesh, c) "Raster" wall mesh quality evolution.	197
7.4	Deformed mesh obtained for the "Zigzag" & "Raster" wall using the calibration algorithm.	198
7.5	Relationship between the inter-layer temperatures at each element activation and the resulting wall shape.	199
7.6	Computed temperature profiles at the ($x = -0.75$, $y = 49.0$, $z = 6.03$) coordinate point for the "Raster" and "Zigzag" walls.	200
7.7	Histogram of the time spent under each temperature for node located at ($x = -0.75$, $y = 49.$, $z = 6.03$)	202
7.8	Deformation with the isotherm model. In red: the predicted deformation, In green: the theoretical deformation, In grey: the initial mesh, In blue: the test used for training.	203
7.9	Neural network structure for the convolutional model.	204
7.10	Deformation with the isotherm model. In red: the predicted deformation, in green: the theoretical deformation, in grey: the initial mesh, In blue: the test used for training.	205
7.11	Neural network structure for the recurrent model.	206
7.12	Deformation with the isotherm model. In red: the predicted deformation, In green: the theoretical deformation, In grey: the initial mesh, In blue: the test used for training.	207
8.1	Deformed mesh obtained for the "Raster" wall using the calibration algorithm.	214
A.1	Corner plot of the posterior distribution resulting from the calibration step of the "Zigzag" test case. The MAP θ_z^* is represented in blue.	234
A.2	Corner plot of the posterior distribution resulting from the calibration step of the "Raster" test case. The MAP θ_r^* is represented in blue.	235
A.3	Cylinder experimental test.	236
A.4	Validation of the temperature profiles for the thermocouples of the cylinder test on the first 25 beads with the parameters $\theta_{z\&r}^*$	237
A.5	Validation of the temperature profiles for the thermocouples of the cylinder test on the first 25 beads with the parameters $\theta_{z\&r}^*$ and an adaptation of $h_{cl} = 200$ (W.m ⁻² .K ⁻¹).	237
B.1	Example of calibration of the thermal source on a molten zone profile.	239

C.1	"Zigzag" test case: Sensitivity analysis field	242
C.2	"Zigzag" test case: Sensitivity analysis field aggregated on time	242
C.3	"Raster" test case: Sensitivity analysis field	243
C.4	"Raster" test case: Sensitivity analysis field aggregated on time	243
E.1	Constitutive behavior models monotonic response to a tensile loading for multiple temperatures: 20°C, 100°C, 200°C, 300°C, 400°C, 500°C, 600°C, 700°C, 800°C, 900°C, 1000°C.	248
F.1	All the experimental data with the 512 stress curves used for the metamodel construction	250
F.2	All the concatenate experimental data with the 512 stress curves concatenate used for the metamodel construction	250
F.3	Corner plot of the posterior distribution resulting from the calibration step.	251
F.4	Comparison of aggregated first-order Sobol indices obtained from the calibration using residual stress data (blue) and from the calibration using temperature data at thermocouple points (red). The parameters are ranked in descending order according to the aggregated first-order Sobol indices using residual stress data.	251
F.5	Experimental and MAP metamodel estimation with the confidence interval	252
G.1	Diagram illustrating the choice of correspondence between the skin of the mesh and the target: in green the points of the target point cloud, in blue the skin nodes of the mesh, in red the correspondences following the mesh-to-target strategy, in black the centroids associated with the target-to-mesh method, in purple the correspondences of the target-to-mesh method.	256
G.2	Orientation of the normal between two elements T^+ and T^- for the definition of the gradient jump.	258
H.1	a) Example of linear regression, b) Neuron with N inputs and 1 output.	261
H.2	Schematic of a N input and 1 output neuron with the ϕ activation function.	262
H.3	Example of a neural network with 3 inputs, 2 hidden layers with respectively 9 and 14 neurons, and 1 layer of 3 outputs.	263
H.4	a) Illustration of a convolution by a Sobel filter, b) Illustration of max pooling.	264
H.5	Schematic illustration of a recurrent network.	265

List of Tables

3.1	Evolution of the thermal parameters of 316L SS as a function of temperature: a) The thermal conductivity $\lambda(T)$ ($\text{W}\cdot\text{m}^{-1}\cdot\text{K}^{-1}$), b) The enthalpy $H(T)$ ($\text{J}\cdot\text{m}^{-3}$).	49
3.2	Evolution of Young's modulus, Poisson ratio, yield strength, and thermal dilation coefficient with temperature.	60
3.3	Linear & Piecewise linear isotropic hardening elasto-plastic model.	61
3.4	Linear isotropic hardening parameter E_T as a function of the temperature.	62
3.5	Piecewise linear isotropic hardening parameter: stress (MPa) depending on temperature ($^{\circ}\text{C}$) and cumulative plastic strain (%).	62
3.6	Linear kinematic hardening elasto-plastic model.	63
3.7	Kinematic hardening constitutive behavior parameters as a function of the temperature (VMIS_CINE_LINE): the Prager coefficient C	63
3.8	Mixed isotropic hardening elasto-plastic model.	64
3.9	Mixed hardening constitutive behavior parameters as a function of the temperature (VMIS_ECMI_LINE): the Prager coefficient C	64
3.10	Chaboche hardening elasto-plastic & elasto-viscoplastic model.	65
3.11	Elastoplastic Chaboche constitutive behavior parameters as a function of the temperature (VMIS_CIN1_CHAB), $\gamma_1^0 = 727.6$, $b = 2.74$, $k = 1$, $w = 0$, $a_{\infty} = 0$	66
3.12	Elasto-viscoplastic Chaboche constitutive behavior parameters as a function of the temperature (VISC_CIN1_CHAB), with $k = 1$, $w = 0$, $a_{\infty} = 1$	66
5.1	Process parameters used for the 1 st test case.	97
5.2	Parameters to be calibrated, with the sampling distribution for the PCE surrogate model training and the prior distribution for the MCMC algorithm calibration step. . .	98
5.3	Identified MAP from the thermal inverse problem.	99
5.4	Process parameters used for the 50 beads " <i>Zigzag</i> " and " <i>Raster</i> " walls.	107
5.5	Parameters to be calibrated, with the sampling distribution for the PCE surrogate model training and the prior distribution for the MCMC algorithm calibration step. . .	112
5.6	Identified MAP for each 3 thermal inverse problems.	113
5.7	Evolution of the yield strength with temperature [188].	114
5.8	Mean standard deviation of the residual stress fields of the 3 stress components σ_{xx} , σ_{yy} , and σ_{zz} for the two tests (MPa).	122
5.9	Process parameters used for the TG9 test case.	128
5.10	Parameters to be calibrated, with the sampling distribution for the PCE surrogate model training and the prior distribution for the MCMC algorithm calibration step. . .	131

5.11	Identified MAP for the TG9 test case.	133
5.12	Process parameters used for the AFH block test case.	148
5.13	Parameters to be calibrated, with the sampling distribution for the PCE surrogate model training and the prior distribution for the MCMC algorithm calibration step. . .	150
5.14	Identified MAP of the 10 th to 18 th layer of the calibration bloc test case.	150
5.15	Parameters to be calibrated, with the sampling distribution for the PCE surrogate model training and the prior distribution for the MCMC algorithm calibration step. . .	152
5.16	Identified MAP of the 1 st to 9 th layer of the calibration bloc test case.	152
5.17	Estimation of the manufacturing time according to the inter-layer temperature to be respected.	156
6.1	Stress field error criteria.	168
6.2	Displacement field error criteria.	168
6.3	Macro-deposition calibration results summary for the 1 st case study.	174
6.4	Macro-deposition calibration results summary for the 2 nd case study.	175
6.5	Summary of the 3 rd case study macro-deposition calibration results.	179
6.6	Macro-deposition calibration results summary for the 4 th case study.	180
6.7	Macro-deposition calibration results summary for the 5 th case study.	183
7.1	Numerical results of the deformation prediction using isothermal values model	202
7.2	Numerical results of the deformation prediction using CNN	205
7.3	Numerical results of the deformation prediction using Recurrent Neural Network model.	206
7.4	Parameters sets comparisons of the different models.	207
A.1	Thermocouples locations.	236
D.1	Parameters range for the 1 st model.	245
D.2	Parameters range for the 2 nd model.	245
D.3	Parameters range for the 3 rd model.	246
D.4	ABC results: Acceptance rate for the 3 models.	246

Chapter 1

Introduction

Contents

1.1 Industrial context: EDF & AFH consortium	2
1.1.1 Growing interest for additive manufacturing at EDF	2
1.1.2 The AFH consortium	3
1.1.3 WAAM process at EDF	3
1.2 Problem statement	6
1.3 Framework	7
1.3.1 Main objective	7
1.3.2 Thesis outline	8

1.1 Industrial context: EDF & AFH consortium

1.1.1 Growing interest for additive manufacturing at EDF

EDF ("*Electricité de France*") is responsible for the safety of its energy production plants, and must therefore carefully control the components manufacturing quality, particularly for large parts. To date, the majority of the components manufactured for EDF are forged or molded. Yet, EDF is currently looking at different manufacturing processes to have alternative supply solutions. Such alternatives would eventually allow for more agility and reactivity during maintenance operations. For instance, for the nuclear industry, the objective of these new processes would be to reduce the duration of the shutdown of the power plants needed for maintenance. Among the various processes considered, EDF is investigating several additive manufacturing (AM) methods.

Contrary to the more conventional methods of manufacturing by material removal (machining) or shaping (forging and casting), additive manufacturing corresponds to all the processes allowing manufacturing objects by stacking layers of materials subsequently. The parts are first modeled using a computer-aided design (CAD) software, and then the deposition patterns are derived. The interest for AM has increased in recent years in many fields such as the medical [1], automotive, aeronautical [2], naval, and energy production sectors (Figure 1.1).

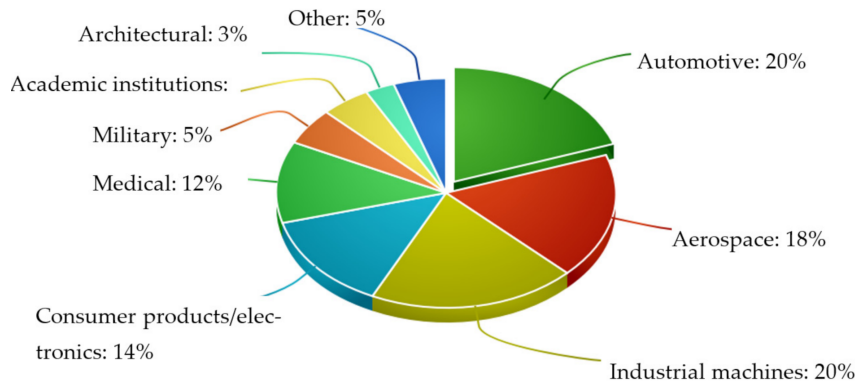


Figure 1.1 – Industrial Adoption of additive manufacturing (AM) [3].

Its use is no longer limited to creating model parts or prototypes but is gradually opening up to industrial components [4]. This growing interest is motivated by the many advantages of the AM processes. Indeed, additive manufacturing offers great freedom of design and enables the production of complex geometries. This versatility allows carrying out topological optimizations to redesign and alleviate components. For example, AM can reduce the weight of certain parts by 80% in the aeronautics industry, which is a critical issue in this sector to reduce aircraft fuel consumption. In addition, the ability to produce complex geometry components in a single step eliminates the need for welding, bolting, or riveting. Among the many advantages associated with the additive manufacturing processes, one of the most important is the saving of material, characterized by the "*buy-to-fly*" ratio, which is the percentage of material "lost" during manufacturing. In fact, contrary to the manufacturing by material removal, such as machining, the finishing machining operation in additive manufacturing is limited to the finishing of the surface state, thus reducing the material waste. This advantage can be of first importance given the high cost of certain materials (such as titanium for instance). It also has a

strong ecological interest. Finally, for some conventional manufacturing processes, the manufacturing of the components requires specific molds, making the modification or the improvement of the designs complicated and costly. This limitation does not apply to additive manufacturing processes, which on the contrary, provide very flexible designs.

Additive manufacturing processes are of particular interest to EDF for dealing with part obsolescence problems. Indeed, the nuclear park was built about forty years ago, and many manufacturers no longer exist. AM makes possible the reproduction of existing parts scanned in 3D that the manufacturers can no longer produce, and even optimize them if necessary. Indeed, as mentioned earlier, additive manufacturing allows creating highly complex parts (making possible their alleviation) as well as preserving materials, while ensuring a mechanical behavior equivalent to that obtained with conventional manufacturing processes.

1.1.2 The AFH consortium

This PhD thesis is part of the French consortium "*Additive Factory Hub*" (AFH) (<https://www.additivefactoryhub.com/>). This platform is a grouping of skills from major French industrial groups (EDF, Air Liquide, Safran, Vallourec, etc.), research centers (CEA, Onera, CNRS, etc.), and academic laboratories (Arts et Métiers, Mines ParisTech). The main objective of AFH is to integrate and develop additive manufacturing technologies and, more particularly, two AM processes: the Laser Beam Melting (LBM) and the Wire Arc Additive Manufacturing (WAAM). In addition, AFH aims to be an international showcase of knowledge in terms of the control and optimization of the process, the metallurgical properties, as well as the residual mechanical properties of industrial components.

1.1.3 WAAM process at EDF

Given the applications and industrial needs of EDF, one of the alternative processes identified for the manufacture of large components by the R&D of EDF is the WAAM process.

The WAAM process, directly derived from welding, makes possible the manufacturing of metallic components of large dimensions by stacking successive layers of metal using arc welding technologies (GTAW, GMAW, CMT, PAW, etc.). To do this, the filler material, which is in the form of a metal wire, is melted using an electric arc, as illustrated in Figure 1.2.

WAAM seems promising for many reasons. First, it is a process derived from welding, and therefore uses welding equipment that is well known and mastered. Moreover, unlike many other processes, the equipment needed and the filler material in the form of a metallic wire are inexpensive. The WAAM process is also less restrictive from a safety point of view in comparison with the AM processes that use metal powders. Moreover, it has a reasonable deposition rate [5] (generally between 2 and 4 kg per hour) without the constraint of a controlled atmosphere, allowing for the manufacture of large industrial parts. Moreover, the flexibility of this process opens up a wide range of design possibilities and technical solutions. Indeed, in addition to being able to optimize the shape, geometry, and manufacturing strategy of newly fabricated parts, this process enables the carrying out of repair operations on parts [5, 6], eventually already on-site. All these characteristics would allow EDF to optimize the supply chain, thus reducing the delays and ultimately the maintenance costs.

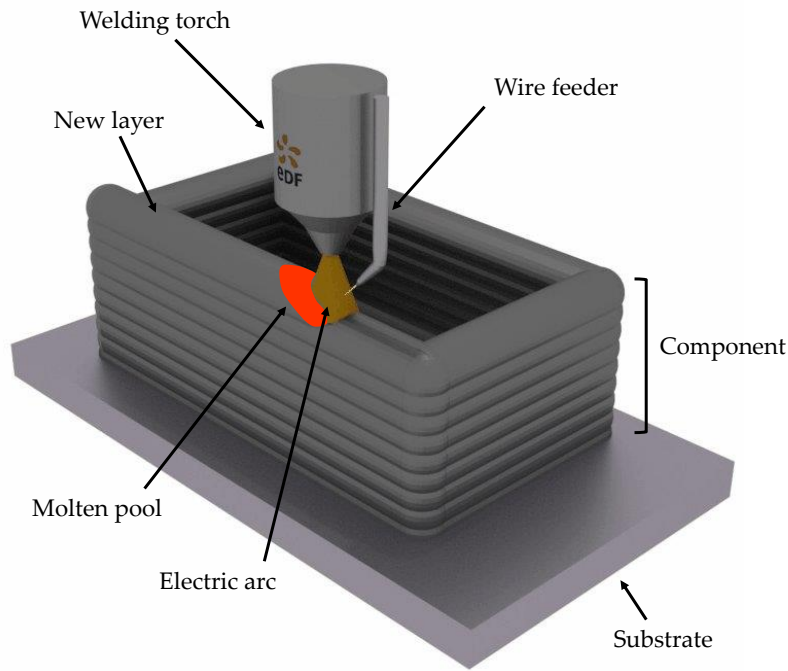


Figure 1.2 – Schematic illustration of the WAAM process.

Several workpieces have been identified as being of interest for the use of WAAM. First, the function addition on existing workpieces, by adding nozzles for instance, are of particular interest to EDF (Figure 1.3). Indeed, they could be considered as alternatives to critical welds. Their technological relevance is currently under study at EDF R&D.

Other specific workpieces are also identified (Figure 1.4). The PPB, for the "*Pièce de Préhension du Bouchon*", is one the workpieces of interest for EDF (Figure 1.4-b). This part, used in the nuclear field, is employed to handle the plug of spent fuel packages. The interest of WAAM for the manufacture of the PPB is the reduction of material waste during the manufacture (approximately 75% of the raw material used for forging is removed by machining). In addition, switching the current process to the WAAM process would allow dividing by three the total supply time: from 5 months of manufacturing (supply time needed for forging and machining operations) to a few weeks.

Moreover, EDF Hydro, the branch of EDF that deals with the hydraulic production facilities, has identified the Kaplan blade as a workpiece of interest to be manufactured using the WAAM process. This blade is presented in Figure 1.4-a. The benefit of the WAAM for this workpiece is the fact that it is a unitary part produced in small series with different possible dimensions depending on the application. Furthermore, due to its complex shape, the predicted gain in the amount of machined material is significant.

The WAAM process has, however, some drawbacks [7]. First, it can lead to a high surface roughness that requires machining after the manufacture. In addition, the components produced are subjected to deformations and residual stresses generated during the deposition process. This comes as a result of the thermal cycles and the very high-temperature gradients, and can affect the integrity of the part, its mechanical strength, and the subsequent machining operations.

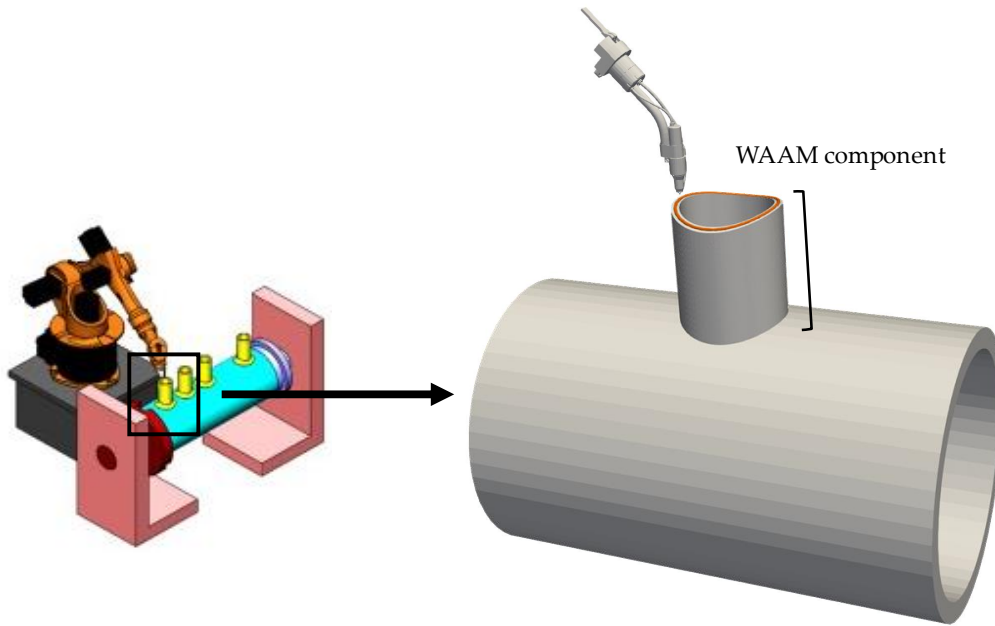


Figure 1.3 – Schematic illustration of nozzle manufacturing on an existing pipe.

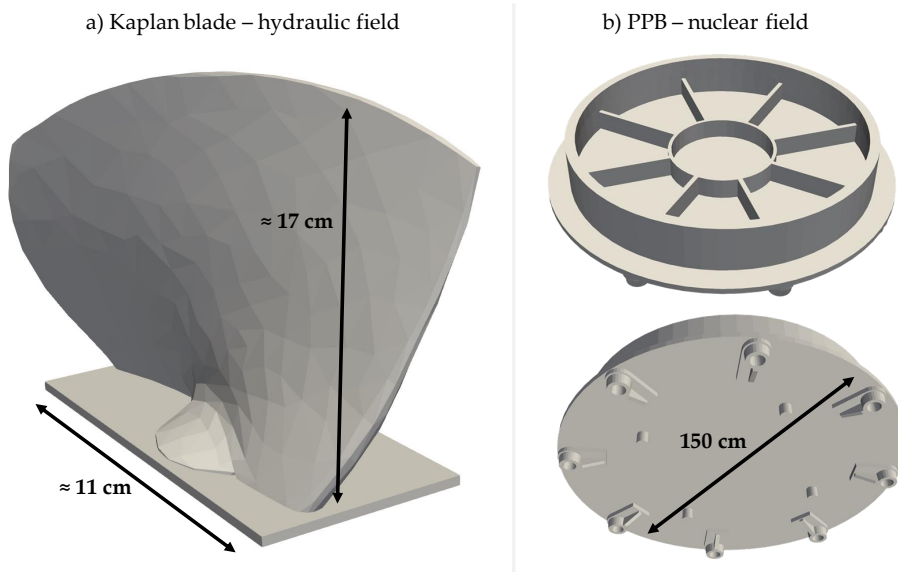


Figure 1.4 – Workpieces of interest for at EDF using WAAM process: a) Kaplan pale in the hydraulic field (reduced scale), b) PPB in the nuclear field.

The critical point for the deployment of the WAAM process in an industrial context is the control of the quality of the manufactured components. Indeed, as for other additive manufacturing processes, the obstacle to its industrialization is the need to ensure the control of the process and its repeatability. Therefore, since EDF must ensure the reliability of the components in service and their lifespan, a good control of the quality of the parts is critical for the implementation of the process on the different energy production plants.

1.2 Problem statement

The main issues identified at the moment for the industrialization of the WAAM process are the control of the process, the residual mechanical state of the components, and the repeatability of the process.

As previously mentioned, welding processes and their derivatives suffer from an intense heat input that generates high thermal gradients [8], leading to large distortion, microstructural changes, and residual stresses and deformations. This can affect the quality of the components, which must respect dimensional criteria and a target mechanical resistance.

The estimation of residual stresses is of primary interest [9] since it can help ascertain the resistance of the components to different types of solicitations, such as fatigue, and often causes stress corrosion cracking and brittle fracture of the components fabricated. Post-manufacturing heat treatments at high-temperature are thus sometimes needed to induce the partial or total relaxation of the residual stresses. However, this stress-relieving step is not always feasible, usually due to the size of the component.

In order to control and optimize the WAAM process, there is a need to increase the understanding of the impact of the process parameters on the final properties of the part. Indeed, the mechanical properties and the microstructure of the WAAM manufactured parts directly depend on the process parameters, such as the nature of the material, the wire feed speed, the parameters of the electric arc, the deposition strategy, or the cooling time between beads.

However, studying the impact of the process parameters, the choice of deposition strategies, and the influence of the thermal history during the manufacturing process would require numerous experimental tests, which can be costly time-wise and resource-wise. Moreover, some physical quantities are hard to access experimentally. It is the case, for instance, for the temperature evolution of the components during the manufacturing process, as well as for the distribution of the residual stresses at the component scale. Indeed, the latter are usually measured on small-scale samples or require destructive tests.

As a result, the modeling of the manufacturing process appears to be an attractive alternative to heavy experimental campaigns. Indeed, it allows for the prediction of the distribution of temperature, residual stresses, and distortions [10]. Furthermore, as the maturity of this manufacturing process gradually begins to be proven and operationalized in the industry, the implementation of these models would allow for a better understanding of the physical phenomena involved and a more widespread use of the WAAM process. However, since one of the main objectives is to simulate the manufacturing of large parts, modeling assumptions are required to provide results in reasonable computational times. A major challenge of this thesis is thus to calibrate the modeling parameters introduced carefully. Moreover, the models developed must be robust to be applied in the largest possible number of configurations.

As EDF is not a component manufacturer but has a responsibility for the quality control of the components of its energy production plants, the simulation can also help for the implementation of component specifications. Indeed, having expertise in the control of the process and the operating parameters would help accompany the manufacturers during the component production process. Finally, the numerical tools to be developed also aim at supporting the qualification process of WAAM manufactured parts in the nuclear [11] and hydraulic fields.

1.3 Framework

1.3.1 Main objective

The presentation of the industrial context highlighted issues of the first order for the deployment of the WAAM process for the manufacturing of large components. Indeed, the manufacturing process is a critical step that governs the quality of the finished product.

In this perspective, this PhD project aims to develop a finite element (FE) thermo-mechanical model at the mesoscopic scale to simulate the WAAM manufacturing of components and obtain the residual state (Figure 1.5). All the modeling work within the framework of this PhD thesis is carried out with the open-source finite element code Code_Aster [12] developed by EDF.

This main objective can be subdivided into four sub-objectives:

- **Development of a thermo-mechanical modeling methodology at the mesoscopic scale of the WAAM process** on Code_Aster, as well as the parametric tools for the geometry and the mesh generation. Indeed, the objective of the thesis is to implement a robust simulation methodology applicable to the larger possible number of configurations, either from a geometrical point of view or from a deposition strategy point of view. Therefore, it is inconceivable to implement the geometries and meshes manually and case by case.
- **Development of a robust calibration methodology** for the unknown parameters of the model set up, with the help of instrumented experimental tests. This methodology relies on a digital twinning strategy in order to optimize the duration of the calibration step, thus eventually allowing for the in-situ calibration of each new WAAM manufacturing configuration.
- **Validation of the developed thermo-mechanical model**, as well as the associated calibration steps. This objective is also accompanied by the identification of quantities of interest that the simulation can predict in order to help with the implementation and optimization of the manufacturing process.
- **Prospection of different approaches for computational time reduction**. Indeed, the objective is to simulate industrial parts of very large dimensions in reasonable times. Therefore, it is necessary to propose methods that ensure a good compromise between the accuracy of the results on targeted physical quantities and the computation time.

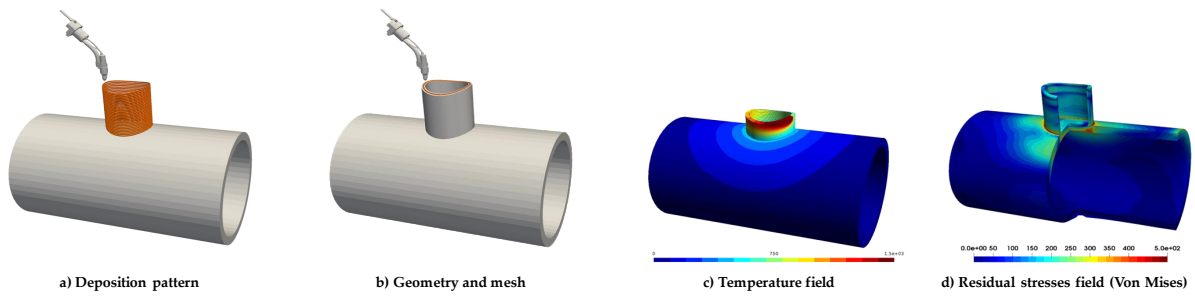


Figure 1.5 – Illustration of the steps for the prediction of the residual state for a nozzle.

1.3.2 Thesis outline

This manuscript is divided into 8 chapters, which are organized into two main axes. The first axis focuses on the modeling of the WAAM process at the mesoscopic scale. In **Chapter 2**, a state of the art of welding, additive manufacturing processes and WAAM numerical simulations is performed. From this state of the art, modeling choices are presented. In **Chapter 3**, a description of the material deposition approach, the geometry and mesh generation tools proposed is made. Following this, the thermal and mechanical models are presented in detail: the formulation of the thermal and mechanical problem is introduced, along with some discussions on the aspects related to the modeling of the process, such as the heat source, the material constitutive law, or the management of the deposition material. **Chapter 4** deals with the implementation of a calibration methodology for the thermal model parameters by solving a bayesian inverse problem using a digital twinning approach. The **5th Chapter** deals with the validation of the developed thermo-mechanical models. In this chapter, the proposed models are tested for four experimental studies. Each of these studies has a different objective, aiming at validating the models in multiple configurations: different processes, process parameters, deposition pattern, physical quantities of interest, etc.

The second axis of this work is composed of the last two chapters, **Chapter 6** and **Chapter 7** of this manuscript. They are dedicated to the reduction of the computation time. This axis aims at investigating different approaches or simplified methods, allowing for the prediction of quantities of interest in reasonable computational times. In **Chapter 6**, the macro-deposition method, as well as the structural zoom methods, are implemented and discussed. **Chapter 7** deals with the prediction of the deformation field by data assimilation. Finally, this manuscript ends with a conclusion to summarize the work done and present the many prospects identified to be explored in future work.

Part I

The fundamentals of WAAM mesoscopic thermo-mechanical modeling

Chapter 2

State of the art & Modelisation hypothesis

Contents

2.1	Introduction	11
2.2	Additive manufacturing processes & WAAM	11
2.2.1	Main AM processes	11
2.2.2	Presentation of the WAAM process	13
2.3	Review of WAAM modeling approaches	16
2.3.1	Microscopic scale	17
2.3.2	Mesosopic scale	19
2.3.3	Macroscopic scale	20
2.4	Mesosopic scale modeling	26
2.4.1	Physical aspects & assumptions	26
2.4.2	Material deposition approaches	28
2.4.3	Mesosopic thermal model	30
2.4.4	Mesosopic mechanical model	37
2.5	Conclusion & perspectives	41

2.1 Introduction

This chapter presents the scientific context of this PhD thesis, with a specific focus on the a state of the art of the numerical simulation of the WAAM process.

The first part of this chapter briefly describes the additive manufacturing processes and how the WAAM process falls within these processes. After a concise presentation of the physical phenomena involved in arc manufacturing processes, the different modeling scales for welding, additive manufacturing processes and specifically the WAAM, are detailed: the microscopic scale, the mesoscopic scale, and the macroscopic scale. A review of the studies found in the literature is carried out, and the advantages and disadvantages of each modeling scale are discussed. The last part of this chapter will focus on the finite element thermo-mechanical models, which is the mesoscopic modeling scale identified as the most relevant to meet the industrial objectives of EDF.

Following this literature review, the mesoscopic modeling scale is identified as the most relevant to meet the industrial objectives of EDF. Therefore, it will be the subject of the last part, which deals with the modeling choices and associated modeling assumptions within the framework of this thesis, with a description of the different aspects of FE thermo-mechanical modeling.

2.2 Additive manufacturing processes & WAAM

2.2.1 Main AM processes

Many types of additive manufacturing processes for metallic components have gradually emerged [13, 14]. They differ in the nature of the input material, the method for material feed stock (powder bed, powder feed systems, or wire feed systems, etc.), or the energy source used [14]. They can be classified into two main families as represented in Figure 2.1: processes by "*Powder Bed Fusion*" (PBF) and processes by "*Direct Energy Deposition*" (DED). Other families of processes exist, such as "*Binder Jetting*" or "*Sheet Lamination*", but they will not be presented here.

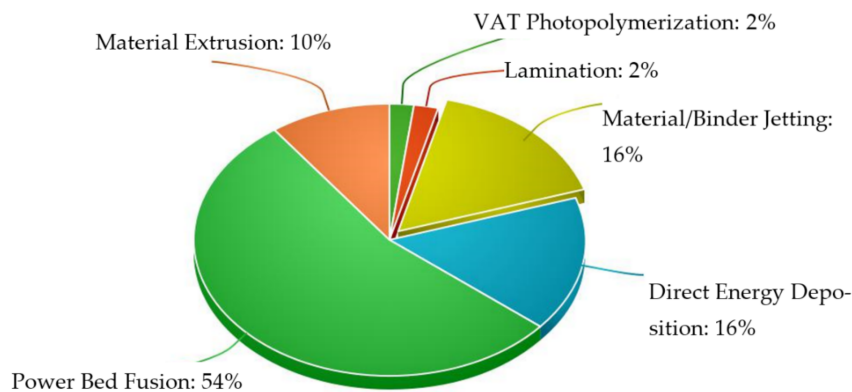


Figure 2.1 – Metal Additive Manufacturing Market in 2020 [3].

■ ***Powder Bed Fusion (PBF)***: The principle behind the powder bed fusion processes is to use a thermal source to induce the local fusion of the powder [15, 16]. These processes can be subdivided into different processes, the most widespread being the following: Laser Beam Melting (LBM), Selective

Laser Sintering (SLS) [17], and Electron Beam Melting (EBM) [18]. In the case of LBM, a high-power laser is used to melt the powder according to a scanning pattern [19]. SLS is very similar to LBM, but the laser is used to sinter the metal powder selectively [20]. EBM is also very similar to LBM [21]. The difference is that the energy source used for the fusion of the powder is an electron laser beam. This difference means that the beads can be smaller and more precise, but the chamber in which the part is manufactured must be under a vacuum.

These PBF processes produce of extremely precise parts with very complex geometries and structures that could not be achieved with other processes. This high precision also allows reaching excellent surface finishes [15]. Nevertheless, the main disadvantage of these processes is the limit in component dimensions. Indeed, PBF processes require controlled atmosphere chambers. The size of the components is thus limited by the size of the chamber. Therefore, these processes are mainly adapted for components with complex geometries and reduced dimensions of the order of ten centimeters.

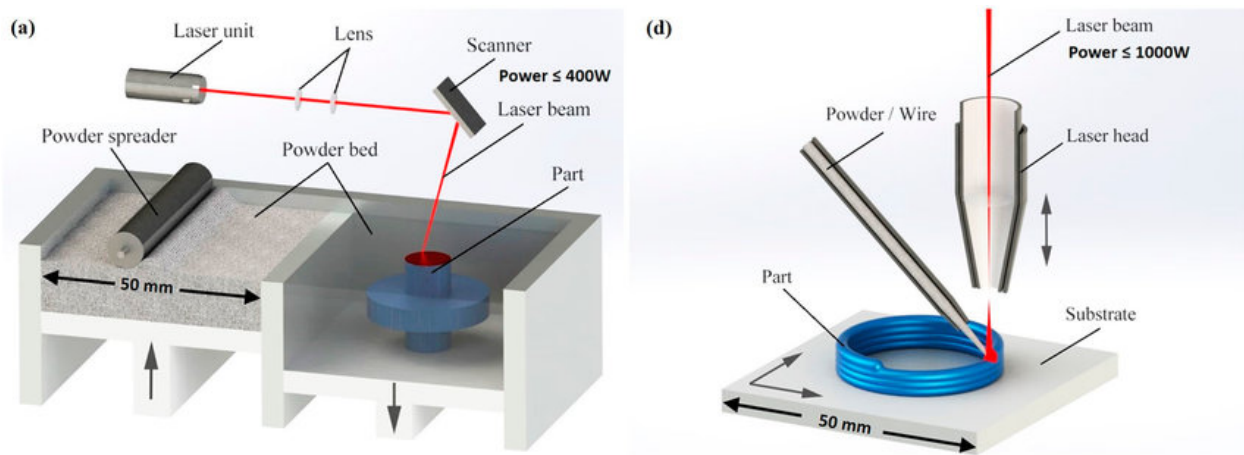


Figure 2.2 – Schematic illustration of (a) PBF and (b) DED processes [22].

■ **Direct Energy Deposition (DED):** For the Direct Energy Deposition processes, concentrated thermal energy is used to melt the feedstock material [23]. The feedstock material can be of various natures. It can be in the form of metal powders as, for instance, the "*Laser Metal Deposition*" (LMD). It can also be in the form of a wire filler material, as is the case for the "*Wire Laser Additive Manufacturing*" (WLAM), the "*Electron Beam FreeForm Fabrication*" (EBF3), or the "*Wire Arc Additive Manufacturing*" (WAAM). The wire feed is melted using a heat source, which varies according to the process: laser, electron beam, or electric arc. The LMD process is a process for which the input material is in the form of a metallic powder projected by a powder nozzle [24]. The projected powders are thus melted by a laser (coaxial with the nozzle of projection), and a gas shielding protects the whole. The wire-based DED processes differ mainly by the source of energy used to melt the input material. For the WLAM process, the energy source used is a laser [25]. In addition, the fabrication must be performed in an enclosure with a controlled atmosphere, usually using argon. For the WAAM process, the source of energy used is an electric arc [26]. Contrary to the WLAM process, the controlled atmosphere is not mandatory. Instead, a gas shielding around the electric arc is used to protect the molten pool zone.

In general, the DED processes are used to manufacture parts of significant dimensions, of the order

of ten centimeters to several meters. Another advantage of these processes is that they can be used to manufacture parts on non-flat substrates, to perform, for instance, part functionalization or carry out repair operations [5, 6]. However, one of the disadvantages of these processes is that the "relatively large" beads generated result in a wavy surface, thus inducing the need for machining after fabrication.

The two families of processes (PBF and DED) are very different. All the DED processes allow manufacturing parts of large dimensions (superior to 1 m). Their deposition rates (between 1.0 and 4.0 kg h⁻¹) are larger than those of the PBF processes (about 0.1-0.2 kg h⁻¹). However, they do not provide the same precision and finesse of manufacturing, as well as the same complexity of component geometries as PBF processes. Indeed, a high deposition rate is accompanied by larger welding beads. The applications targeted by these two families of processes are therefore very different. For the applications desired at EDF, the DED processes seem more suitable, and more specifically, the wire-deposition processes. Indeed, the use of powders induces significant safety constraints. Among the wire deposition processes, the WLAM provides the higher precision but has the lower deposition rate, while, on the contrary, the EBF3 allows for larger deposition rates. The WAAM deposition rates lie between the two other DED processes. Moreover, unlike the WAAM process, the WLAM and EBF3 processes require a controlled atmosphere which is a limitation in terms of part dimensions due to the size of the enclosure used and the manufacturing complexity. This feature makes the WAAM process more suitable for EDF applications.

2.2.2 Presentation of the WAAM process

This thesis focuses specifically on the WAAM process. In this section, a more technical introduction of the WAAM process is carried out, and the technical issues needed to be addressed to deploy this process at the industrial level are presented.

This process, directly derived from welding, makes possible the manufacture of metallic components of large dimensions by stacking successive layers of metal using arc welding technologies (GTAW, GMAW, CMT, PAW, etc.). To this end, the filler material, which is in the form of a metal wire, is melted using an electric arc.

As stated previously, in comparison with the processes using metal powders, the WAAM process has many advantages. It has a high deposition rate (generally between 2 and 4 kg h⁻¹), allows to produce large parts with a good material efficiency ("buy to fly ratio"), and relies on very well-known and inexpensive welding equipment. Therefore, the WAAM process is one of the most promising additive manufacturing processes for manufacturing large metal components. Several welding processes can be used for WAAM. In the following, a brief presentation of these processes is given.

■ ***Gas Tungsten Arc Welding (GTAW)***: Gas Tungsten Arc Welding uses a refractory electrode to create an electrical arc between the electrode and the workpiece [27]. The electric arc is protected from the ambient air by an inert gas (which can be of various natures: argon, helium, or others...). The protective gas prevents the oxidation of the deposited metal during the cooling and keeps the arc stable. The material is fed in from the side of the arc as illustrated in Figure 2.3-a. The orientation of the material deposition is, therefore, a parameter that must be controlled. It can be, for example, according to the manufacturing direction, or always in the same direction. In both cases, the programming of the deposition pattern can become complex.

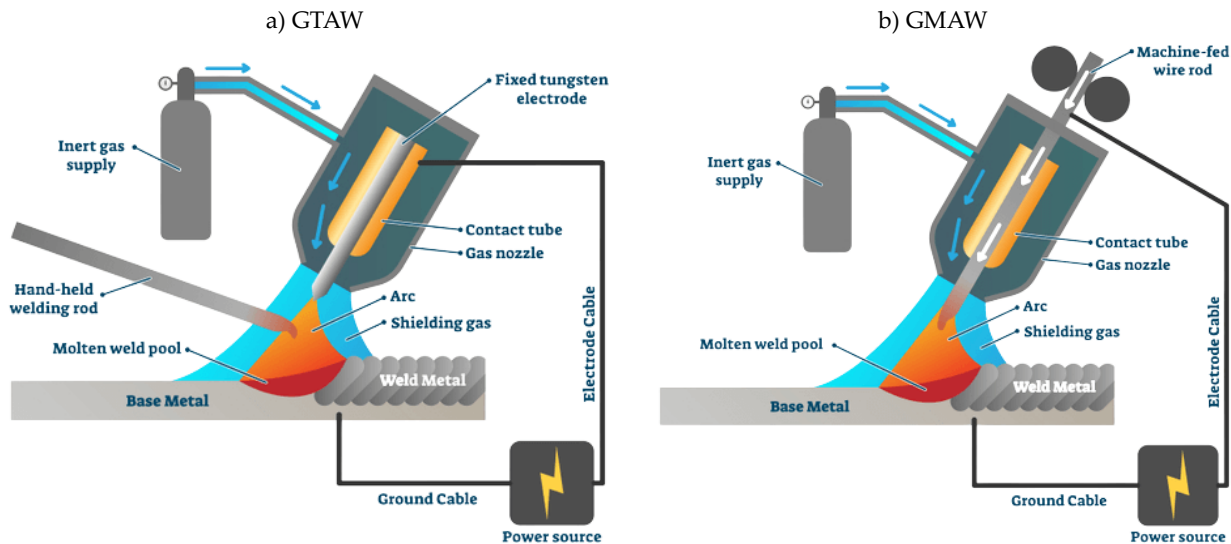


Figure 2.3 – Overview of the most used metal arc welding technologies, Metal arc welding technologies: a) Gas Tungsten Arc Welding (GTAW), b) Gas Metal Arc Welding (GMAW) [28].

■ **Plasma Arc Welding (PAW):** Plasma Arc Welding (PAW) is very similar to GTAW. The difference comes from the plasma gas circulating in the nozzle, which will create a constriction of the arc. This adaptation allows concentrating the deposited energy on a reduced surface. Moreover, as for the GTAW, a gas shielding ensures the protection of the molten pool.

■ **Gas Metal Arc Welding (GMAW):** Contrary to the GTAW, the GMAW (Gas Metal Arc Welding) uses the wire as a consumable electrode to both create the arc and bring the material (Figure 2.3-b). This implies that the wire is fed coaxially to the torch. This feature is particularly interesting, as the orientation of the wire feed is no longer a parameter. Also, it allows deposition rate 2 or 3 times higher than the GTAW or PAW processes. This welding process is currently one of the most widely used in the industry, including in the nuclear field.

■ **Cold Metal Transfer (CMT):** The CMT is a process derived from the GMAW process. It was developed to improve the quality of the deposition significantly. It is a short-circuit transfer process coupled with a forward and backward movement of the wire feed [29]. These movements of the wire (filler material and consumable electrode) cause the ignition and extinction of the arc. This methodology allows for a lower energy input, which results in a better regularity of the beads. Because of its lower energy input, the CMT process is very interesting for additive manufacturing operations, where heat accumulation is often problematic [29].

The WAAM process depends on several operating parameters that have a first order influence on the residual state of the workpiece. These main deposition parameters are the same as for welding. First, the voltage U (V) and the current I (A) (can be combined into one parameter which is the power ($U \times I$ in W)) highly influence the metal transfer mode (and the molten pool shape as illustrated in Figure 2.4),

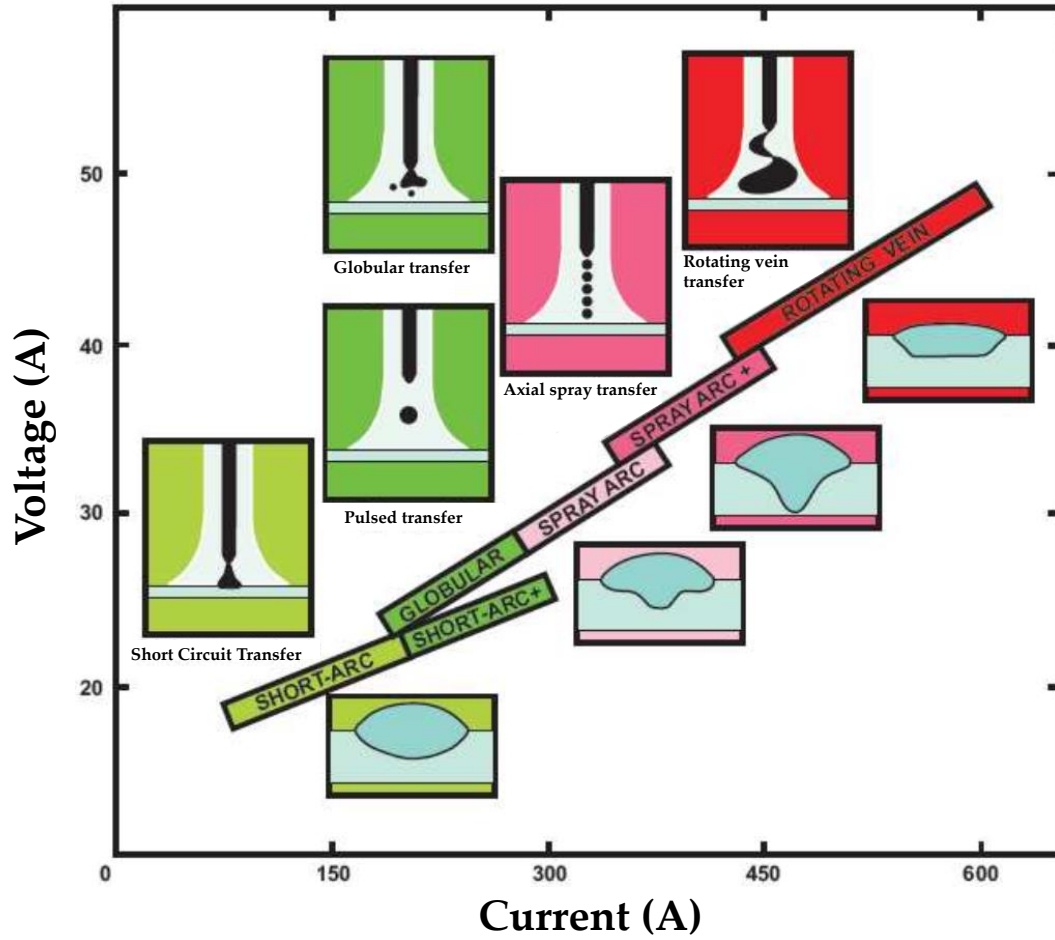


Figure 2.4 – Influence of voltage and current on the metal transfer mode in GMAW welding using Argon Shielding [30].

the energy delivered to the part, the temperature and the residual shape of the beads. Moreover, the wire feed speed v_w (in m s^{-1}) coupled with the wire diameter d_w (in m) define the quantity of material deposited, and, therefore, strongly affect the size of the resulting bead. Furthermore, the welding torch speed v_t (in m s^{-1}) significantly impacts on the energy supplied and the flow of deposited material. Indeed, for a fixed power and a fixed wire feed speed, if the welding torch speed is increased, the bead will be smaller and less collapsed due to a lower material input and a lower linear energy E_l (in J m^{-1}), defined Equation 2.1.

$$E_l = \frac{UI}{v_t}. \quad (2.1)$$

Other parameters involved, such as the angle of inclination of the torch or of the material input, can influence the resulting bead, especially since the paths can be very complex during WAAM manufacturing. The shielding gas and its flow rate can also affect the material feed rate, as well as the heat transfers, the arc height, etc.

2.3 Review of WAAM modeling approaches

There are numerous approaches to model welding and additive manufacturing processes, including the WAAM process. In this section, a brief discussion is performed on the physical phenomena involved in the process, after what the different modeling scales found in the literature are introduced [31]. This literature review will allow identifying the best approaches in view of the objectives of the thesis.

The physical phenomena occurring during the WAAM process are widely described [27, 30, 32, 33]. There are of a very complex nature due to the strong multi-scale and multi-physics aspects involved. Indeed, there are electromagnetic and hydrodynamic phenomena in the electric arc and the molten pool. Moreover, there are thermal, metallurgical, and mechanical transfer phenomena in the solid phase of the manufactured part. These phenomena are briefly presented in the following.

■ **Phenomena in the molten pool:** Complex phenomena occur between the electrode, the electric arc, and the molten pool. In addition to the electromagnetic phenomena at the electrode, several phenomena occur in the molten pool, such as the fluid flows (Figure 2.5-a). The electromagnetic phenomena induced by the Lorentz forces can strongly impact the fluid flows within the molten pool and, more specifically, the penetration of the molten pool. Moreover, one of the most influential phenomena in the molten pool is the Marangoni effect, which is caused by the surface tension gradients. This phenomenon has a significant influence on the shape of the molten pool. Furthermore, due to the density gradient in the molten pool generated by the temperature, the presence of different chemical elements, as well as the gravity, Buoyancy forces can be generated. These forces induce convective flows that tend to enlarge the molten pool. Compared to the Lorentz and Marangoni forces, the Buoyancy forces effects are generally of the second order. Finally, the surface of the molten pool is also subject to the pressure of the arc and the shielding gas. This leads to the generation of centrifugal currents that tend to deepen and widen the free surface of the molten pool. In addition to all these physical phenomena, the progressive deposition of molten metal complexes even further the convective movements in the molten pool.

■ **Phenomena in the solid phase:** In the solid part, three aspects are involved in a coupled way (Figure 2.5-b). First, the thermal aspect involves the different modes of transfer by convection, radiation, and conduction. In addition, metallurgical grain growth phenomena occur at the solidification interface of the molten pool (between the liquid and the solid zone). Several phase transformations also take place in the Heat Affected Zone (HAZ), which corresponds to the zone whose temperature is higher than a defined material-dependent threshold, according to different kinetics, depending on the temperature, cooling rate, and mechanical state. Finally, the high-temperature gradients generate residual stresses [8, 34] (local heating and following cooling generates a local thermal shrinkage inducing residual stresses and strains) that depend on the material behavior of the metallurgical phases involved. It should be noted that the thermal, metallurgical, and mechanical phenomena occurring in the solid phase are coupled and influence each other at different levels (see Section 2.4.1 for more details).

Many studies focus on the general presentation of the modeling scales of WAAM [35]. In this section, the different scales for the modeling of WAAM are examined. They can be divided in three:

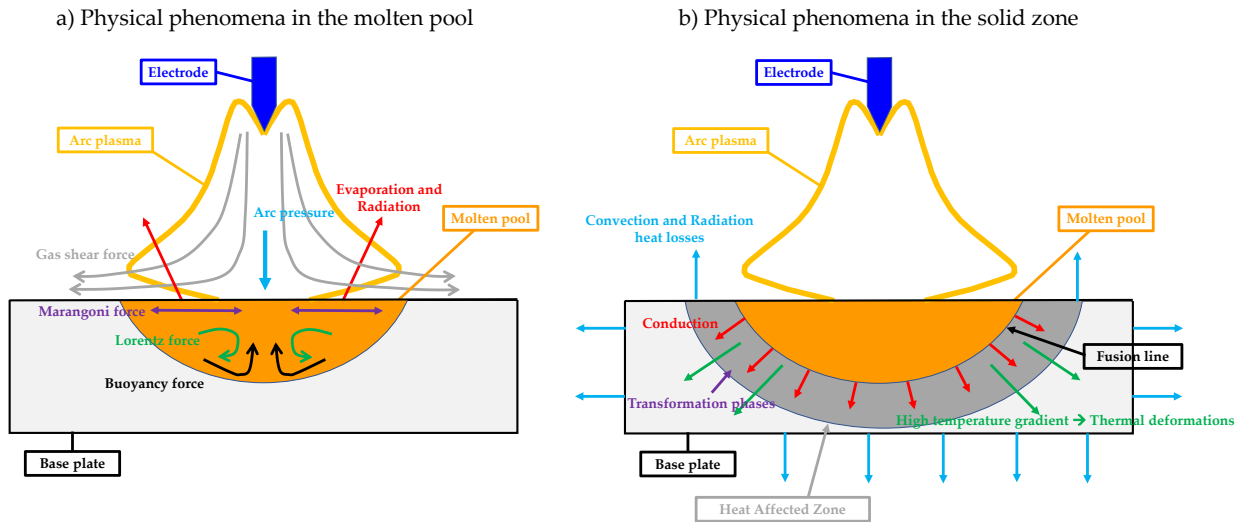


Figure 2.5 – Schematic illustration of the main physical phenomena involved a) in the molten pool, b) and in the solid phase.

multi-physics microscopic scale, solid thermo-mechanics mesoscopic scale and simplified macroscopic scale simulations. Due to the fact that the physics of welding and WAAM are similar, and given that some modeling assumptions are alike for several types of additive manufacturing processes, not all of the studies presented in this chapter concern the WAAM process.

2.3.1 Microscopic scale

This section focuses on the detailed simulation of the WAAM process, taking into account the electro-magneto-thermo-hydraulic phenomena occurring in the molten pool [36, 37, 38]. The objective of these micro-scale models is to model as well as possible all the physical phenomena occurring during the process. In general, these models are based on the coupled resolution of the equations of mass continuity, momentum conservation, energy conservation, and Maxwell's equations in the electrode, the droplet (wire feed), the electric arc (plasma), and the molten pool. These models are generally used to improve the knowledge of the process. Indeed, they allow to explore and improve in a local and very precise way the interaction of the physical phenomena at stake, understand the influence of the operating parameters and their effect on the residual behavior of the simulated workpiece (defect, resulting shape of the beads etc.). Nonetheless, there is a graduation in the complexity of the microscopic models developed in the literature according to the physical phenomena modeled. Indeed, in order to reduce the computation time while ensuring the prediction of identified quantities of interest, the models can be simplified. These simplifications consist either in discarding a negligible physical phenomenon or in adopting a simplified modeling based on an empirical approach or on an experimental calibration. For instance, the simplified phenomena can be the pressure of the electric arc on the molten pool, the heat input, or the material feed.

Cadiou et al. [37] propose a 2D axisymmetric model to simulate the pulsed WAAM to investigate the heat and mass transfer mechanisms. The proposed model allows predicting the detachment of the droplet but also its impingement into the molten pool to predict the resulting bead shape. In

its model, all the main physical phenomena are modeled, with the least simplification and numerical calibration to be performed. For this purpose, the authors consider fluid, electromagnetic, and heat transfer phenomena in the arc, the molten pool, and the workpiece. They were able to highlight the interest of taking into account the modeling of the input on the molten pool and the temperature field. Fan et al. [39] also set up a 2D axisymmetric model for the GMAW process to predict droplet formation, droplet detachment, and droplet impingement in the melt for another welding regime, which is the globular one.

Cadiou et al. [40] then proposed a new 3D model for the simulation of the CMT process. As in their previous study, the developed 3D multi-physics model takes into account electromagnetism, fluid flows, and heat transfer in the wire feed, the electric arc, the molten pool, and the substrate. The model also considers also the forward and backward movement of the wire feed. Ogino et al. [38] developed a 3D model taking into account the interaction between the material input and the electric arc in a weakly coupled way. The physics of the electric arc is solved for a configuration of droplet shape state at a given time step, which is then updated by performing a calculation with the electric arc as a boundary condition. They studied the impact of physical phenomena on the transfer mode as a function of the current. Other studies also focus on the influence of the shielding gas on the droplet and the effect of the welding regime [41]. Zhou et al. [42] also proposed a weakly coupled 3D model. As a first step, a simulation of the arc is performed. From this simulation, the electromagnetic force, arc pressure, plasma shear stress, and heat flux are applied as boundary conditions for the metal transport model.

One approach is not to model the metal deposition but to use a simplified material input method coupled with an equivalent heat source instead of the electric arc. For example, the study by Unnikrishnakurup et al. [43] focuses on 2D multi-physics modeling of static GTAW process, with the heat flux, current, and drag force of the arc on the free surface are spatially distributed and modeled using Gaussian expressions. The objectives of the study are to calibrate the equivalent heat source and to study the heat exchange between the arc and the workpiece. Bai et al. [44] developed a multi-layer deposition model to accurately investigate the fluid flows and thermal transfers and predict the bead geometry. They consider a simplified material input by adding a source term in the mass conservation equation (which is nevertheless accompanied by the determination of some parameters such as the position of the material input). The thermal input is also simplified by using a volume equivalent heat source which is calibrated on thermal camera images. Similarly, Ogino et al. [45] set up 3D model of the CMT process for the prediction of part shape. As for the previous study, the heat input and arc pressure are simplified. The model developed allows obtaining similar trends as in experiments for the shapes of the parts (wall and cylinder) for various configurations: different welding paths and idle time between beads. Their numerical results also highlight the importance of a good temperature and welding path management to control the shape of the part.

Overall, microscopic models are valuable for understanding the influence of the process parameters. They allow predicting various quantities such as the temperature, velocity, and pressure fields, as well as the resulting bead shapes. They are used to investigate the influence of quantities of interest on the residual shape of the beads and eventually to understand the occurrence of defects.

Nevertheless, these models are very complex to set up and very expensive in computation resources. They are thus limited to very short "physical times" of the order of a few seconds. Therefore, these models are only applicable at the scale of the bead. In addition, only a few studies are made on the

juxtaposition or superposition / overlapping of the beads. Therefore, this modeling approach does not seem to be the most suitable given the purpose of this thesis project.

2.3.2 Mesoscopic scale

What is referred to as mesoscopic models are models at the scale of several beads, or even a whole part, that do not consider the electric arc / molten pool interaction. At this modeling scale, the phenomena related to the energy input, the molten pool, and the material input are not modeled. The interaction between the electric arc, the molten pool, and all the physical phenomena involved are simplified by an equivalent thermal source. The shape of the beads is thus not a result of the calculation, as it is the case for microscopic simulations. Moreover, the material input is also represented in a simplified way. The models developed in the literature at this scale are, for the most part, based on Finite Element (FE) method, which model the thermal, possibly metallurgical, and mechanical phenomena of a solid at the scale of the part.

Concerning the thermal aspects, different modeling choices can be found in the literature, such as the equivalent thermal source [46] or the thermal dissipations [47]. Kik et al. [48] studied multiples equivalent heat source models and their impact on the stresses for laser welding. Winczek et al. [49] compared the shapes and sizes of thermally affected zones generated by different heat source models (volumetric source, bimodal volumetric/surface source, and bimodal volumetric/volumetric source).

Moreover, many studies use the numerical simulation to optimize the process. These studies investigate the impact of the process parameters on the global thermal field during the manufacturing of a part. Montevecchi et al. [50] studied the impact of inter-layer cooling on the temperature field and the size of the molten pool. In the study performed by Oyama et al. [46], a method is implemented to optimize the manufacturing process based on a modification of the process parameters for each deposited layer. To do this, the authors monitored the change in the size of the molten pool (isothermal at the fusion temperature) during the manufacturing of a wall. Different demonstrators have been set up, both experimentally and through modeling, to compare different process parameters and deposition strategies and provide guidelines to optimize the manufacturing process. In particular, the total distortion and the residual stresses were selected as indicators.

Other studies have focused on predicting microstructural evolutions from the transient thermal field obtained during manufacturing. This is the case of [51] which uses a cellular automaton approach (called CAFE method) to account for grain growth and derive the metallurgical field for austenitic steels based on a temperature field obtained by finite element simulation at a mesoscopic scale. Other studies investigated other materials using metallurgical models [52].

Furthermore, there are several studies on the prediction and validation of residual stresses [53, 54]. More specifically, in welding, many studies focus on the impact of the mechanical behavior law selected on the residual stresses. Indeed, the choice of a constitutive model [55, 56, 57], the consideration of viscous phenomena, thermal creep, or a restoration of the hardening [58] at high temperature can strongly influence the residual stress fields. Therefore, the thermo-mechanical models implemented are often confronted with experimental measurements of residual stresses [59]. Furthermore, these studies often highlight that a material behavior adapted to cyclic loading is imperative for the numerical simulation of multipass welding [56] or WAAM.

Other mechanical studies are more specifically focused on the influence of specific process parameters or are used to optimize the process. For example, when simulating several beads, the influence of the manufacturing path on the residual state of the part has been investigated [60, 61, 62, 63, 64]. This is the case of the study by Israr et al. [61], which models a block fabricated in WAAM with different fabrication strategies and analyzes the residual stress profiles and strains.

Moreover, Chiumenti et al. [65] set up AM simulations to identify areas of possible crack initiation. On another note, Wang et al. [66] evaluated the residual stress generated by the tightening of the substrate. Furthermore, the influence of the preheating temperature on the fabricated workpiece has been addressed by Xiong et al. [67]. These models can also be used to study the evolution of thermal gradients in a part, as well as the influence of the preheating of the base plate.

In conclusion, mesoscopic models allow carrying out simulations at the scale of several beads or even a complete part of several tens of centimeters. These models give access to the precise transient temperature field, the metallurgical field, and the stress, strain, and displacement residual states. These models are often used to investigate the first-order process parameters influence on the thermo-mechanical quantities at the part scale. Nonetheless, these models can be computationally expensive, thus limiting the size of the parts modeled to a few tens of centimeters. A more macroscopic approach is thus necessary for the simulation of larger industrial parts.

2.3.3 Macroscopic scale

Modeling the WAAM process is an effective tool to investigate and have better control of the manufacturing process, as well as to make predictions. However, one of the main issues in the simulation of the manufacturing of industrial-scale parts is the computational time. In the case of the additive manufacturing of large components with complex geometry that would contain many thousands of beads, a complete simulation of all the beads is not feasible from a resource and computation time point of view. Indeed, in addition to the size of the mesh that becomes larger as the size of the component to be modeled increases, the simulations include many iterations of non-linear thermal and mechanical calculations and many operations. These operations are of various natures: the manipulations on the mesh for the progressive activation of the meshes, the adjustment of the contributed energy, as well as the possible post-processing operations during the simulation. All these aspects increase the computational costs of the simulations.

Therefore, specific modeling strategies are necessary to reduce the computational time while maintaining relevant and accurate simulation results in order to apply the developed tools to industrial problems. Several simplified methodologies exist for the modeling of the WAAM process at an industrial scale level with as objective the prediction of distortions and residual stresses. These methods are either based on a further simplification of the models, on a reduction of the model size (mesh adaptation), or on model reduction.

2.3.3.1 2D modeling approach

A first way of reducing the computational time of WAAM simulations is the implementation of 2D models. Indeed, several studies in the field of multi-pass welding simulation use a 2D modeling approach [68] (use of 2D plane-strain model, 2D axis-symmetric model or 3D shell model). This is the case, for

example, in the work of Depradeux et al. [54] or Rossillon et al. [69], in which the hypothesis of axisymmetry is assumed. Moreover, Cambon et al. [70] implemented a 2D thermo-mechanical model under plane stress assumption, to analyze the residual stresses and the distortions generated by the WAAM process.

Unfortunately, 2D modeling is only valid for a limited number of configurations (axisymmetric configuration or configuration of plane deformations), making the model very inflexible for an additive manufacturing process with complex deposition patterns and part geometries.

2.3.3.2 Adaptive meshing method

Several studies implement mesh refinement and coarsening approaches to reduce computation time [71, 72, 73]. For example, Montevecchi et al. [74] developed an alternative technique to reduce the number of elements of the mesh. The proposed technique divides the substrate into several zones, discretized separately, and then connected using adapted boundary conditions. This strategy reduces significantly the number of elements required while having an accurate temperature prediction. The effectiveness of the proposed method was proven using experimental validation tests. However, one of the drawbacks of such a method is that it induces many manipulations on the mesh. Indeed, the existing conventional mesh adaptation techniques used to reduce computational costs significantly do not seem well suited for additive manufacturing simulations due to the continuous modification of the studied mesh group.

The method developed by Martukanitz et al. [75] is based on the introduction of discretized geometries updated at regular intervals during the simulation process. As new elements are added for each layer, elements from previous layers are coarsen so that the total number of elements considered during simulation is kept constant, even when modeling very large parts. In addition, layers close to the active layer are refined while elements farther away are enlarged. This approach significantly improves the computation times compared to the standard configuration (from 176 hours to approximately 3 hours).

Jayanath et al. [72] implemented a similar approach. As the simulation progresses, the mesh is gradually coarsen far from the source so that the number of meshes remains almost constant throughout the simulation. The model is evaluated by simulating a wall, and a thin-walled cylinder by DMD process. They show that the results obtained (residual stresses and strains) by conventional simulations and reduced computation time simulations (about 50%) show excellent agreement.

2.3.3.3 Macro-deposition approach

The principle of the macro-deposition method is widely explained in the literature [76, 77]. Instead of bringing the elements progressively, this method consists in the deposition of several beads or layer-by-layer deposition at a time. The macro-deposited part can vary from an increment of element as in a mesoscopic thermo-mechanical simulations to a full layer at once. The method could be used for the deposition of multiple lumped layers [78]. This method is commonly used for LBM simulation where the number of layers is huge.

The simplification of the material deposition goes along with a simplification of the heat input distribution. As a result, the heat input distribution is simplified: the input can be applied as an imposed temperature [79, 80, 78] chosen by expertise or as a volume flux on the input [76]. Indeed,

rather than modeling the moving equivalent heat source, each layer fraction is entirely heated. Even if the heat input is simplified, the equivalent heat source still has a ηUI power distribution. Nevertheless, despite simplifying the modeling of the material input and the energy input, the manufacturing time must be respected. If the manufacturing time of the activated macro-deposit is t_d (s), the total energy to be supplied is $\eta UI \times t_d$.

This simplified heat input is also characterized by a parameter: its temporal distribution. The key point of this modeling aspect is to define the heating time t_d^{heat} during which the layer fraction is heated and $t_d^{cool} = t_d - t_d^{heat}$ a cooling time after the heating step [76] as illustrated in Figure 2.6. The total energy of a layer fraction can therefore be supplied over a very short period of time, which will result in very high temperature peaks, or over a very long period of time, which will result in a very gradual increase in temperature and lower temperature peaks. Therefore, the heating time parameter is crucial, as it influences the temperature of the workpiece (especially on the local maximum temperature reached) and thus on the mechanical residual state.

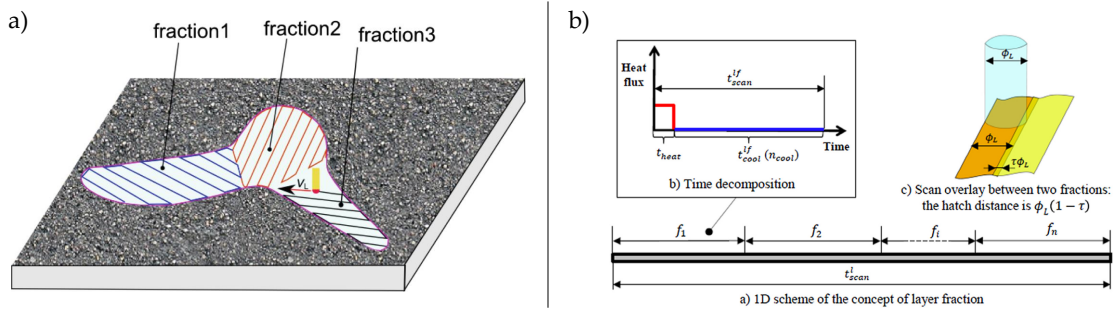


Figure 2.6 – a) Decomposition of a single powder layer into several fractions to be heated consecutively, b) Treatment of layer fractions and illustration of the laser scan overlay coefficient [76].

In the work presented by Zhang et al. [76], this heating time is defined as the time during which a point is exposed to the equivalent thermal source. For a surface or half-spherical thermal source with a radius r (s), it can be equal to: $t_d^{heat} = 2r/v_t$. On the other hand, it can be defined as being equal to the complete deposition time of the layer fraction: $t_d^{heat} = t_d$ and $t_d^{cool} = 0$.

In their study, Kiran et al. [78] present a layer-by-layer input method with an imposed temperature cycle for DED process simulation. The temperature cycle is defined in such a way as to have a conservation of the input energy with respect to mesoscopic simulations with progressive material deposition, according to the manufacturing time and the volume of material deposited. The parameters of the input are defined according to the melting temperature of the material, but no indication is given on the choice of the cycle to apply. Moreover, the cycle defined for a configuration is not necessarily transposable to other configurations. Finally, the authors show that it is also possible to group the layers to bring several at the same time.

The macro-deposition method has many advantages. First, this method makes possible the elimination of a large part of the mesh manipulation operations, some of which are not optimized in the standard mesoscopic simulations and increase the calculation time significantly. Moreover, the concatenation of several beads allows for coarser elements. Indeed, in the case of the standard model, the size of the element is constrained by the dimensions of the beads. Mesh creation by grouping the beads beforehand makes it possible to get rid of this constraint, and thus to use larger elements. Finally, a

clear advantage of this modeling method is the considerable reduction in the number of time steps. When the macro-deposit is brought in, a relatively fine time step is used, and then, during the cooling step, a progressive reduction of the number of time steps is performed. The limitation of this method is that, for a layer-by-layer approach, the deposition pattern and the associated anisotropic behavior will not be taken into account. Therefore, the purpose of the macro-deposition method is to have a general estimation of the stress distribution in the workpiece, but not to study the deposition pattern on the stress field.

2.3.3.4 Inherent strain approach

Among the most computationally efficient methodology to predict distortions is the so-called inherent strain method (or sometimes referred to as the applied plastic inherent strain method). This method has originally been introduced by Ueda et al. [81] in the context of numerical welding simulation. After that, it was first used for welding [82], and then extended to AM processes.

This empirical method is based on the fact that the residual stresses in a workpiece originate from the inelastic deformation field. This inherent deformation field can thus be produced by the plastic deformation field, thermal deformation, deformations arising from phase transformation, and all other inelastic deformation contributions. The total strain ε can be decomposed into the sum of elastic strain ε^e , plastic strain ε^p , thermal strain ε^{th} , creep strain ε^c , and that produced through phase transformation ε^t such as:

$$\varepsilon = \varepsilon^e + \varepsilon^p + \varepsilon^{th} + \varepsilon^c + \varepsilon^t. \quad (2.2)$$

Noting that the deformation and the stress are produced by the total strain and elastic strain, the previous equation can be rearranged to:

$$\varepsilon - \varepsilon^e = \varepsilon^p + \varepsilon^{th} + \varepsilon^c + \varepsilon^t = \varepsilon^*. \quad (2.3)$$

The general principle of the method is thus to replace the transient FE thermo-mechanical mesoscopic simulations by a FE linear-elastic computation with the inherent strain as input data in order to predict distortion and residual stress fields.

$$\underline{\underline{\sigma}} = \underline{\underline{C}} : (\underline{\underline{\varepsilon}} - \underline{\underline{\varepsilon}}^*). \quad (2.4)$$

with $\underline{\underline{C}}$ the 4th order stiffness tensor.

In many studies, in many studies on materials without phase transformations such as austenitic steels, the inherent strain field is defined as the plastic deformation field. However, one of the main critical points of this method is to define the inherent strain responsible for the residual stresses and the distortions which, assuming symmetry of ε^* , consist of 6 components: $(\varepsilon_{xx}^*, \varepsilon_{yy}^*, \varepsilon_{zz}^*, \varepsilon_{xy}^*, \varepsilon_{yz}^*, \varepsilon_{xz}^*, \varepsilon_{yx}^*)$. This is often simplified by neglecting the shearing strain components [83]. Therefore, only 3 independent components must be identified: $(\varepsilon_{xx}^*, \varepsilon_{yy}^*, \varepsilon_{zz}^*)$.

The inherent strains generated in the manufactured components can be obtained in two ways: by experimental measurement or by numerical mesoscopic thermo-elastoplastic computation [84]. By experimental measurement, the springback after cutting the base plates is due to the stress relaxation generated in the part during its manufacture. Indeed, the residual stress is itself a consequence of the

inherent deformation generated in the material. In the study of Setien et al. [85], the calibration of the tensor is performed by the iterative comparison between the displacement of an experimental part and the calculated displacement. Several studies on the LBM process have shown that the optimization in an iterative way, between the numerical deformation field and the experimental test, allows predicting reasonable inherent deformation values while guaranteeing a good accuracy compared to the experiments. Nevertheless, this method may be time-consuming and costly since many samples need to be manufactured, in addition to the computation time required for the numerical optimization process.

The second approach, which is the numerical approach, consists in carrying out a transient thermo-mechanical simulation at a mesoscopic scale. This simulation can, for example, be carried out on an elementary volume in order to extract the inherent deformations. The plastic deformation field is thus obtained, once the whole domain has cooled to ambient temperature (vanishing of the thermal deformation). In the study of Liang et al. [86] and the work of Lu et al. [83], they consider that only a small representative volume needs to be fully simulated to look into the accumulation of the inelastic strains. From the plastic field obtained, the average values of the 3 diagonal terms of the plastic deformations are calculated (averaged over the representation volume). For both approaches, it is important to calibrate the inherent strain on a test representative of the case to be simulated, i.e., with the same material, the same manufacturing parameters, and a sufficiently representative volume.

The extracted mean inherent strain vector will then be applied to a part-scale model layer-by-layer in order to simulate the accumulation of the residual deformation by static linear elastic finite element analysis and predict the residual stress field. The application layer-by-layer allows having an inherent strain for each layer if their deposition patterns is different (such a difference must be considered). Some studies consider configurations more complicated than plastic deformation for the definition of their inherent strain. This is the case of Liang et al. [63, 87] which considers that the melting of the previously deposited layer strongly affects the redistribution of the elastic and plastic strain in the deposited layers.

2.3.3.5 Review of other macroscopic approaches

Many other methods exist for reducing calculation times for welding and additive manufacturing. Among them, Malmelöv et al. [77] have developed a thermo-mechanical FE model and experimentally validated (of the directed energy deposition process). The studied test case is a block test with a "Raster" manufacturing strategy (the beads are always deposited in the same direction). In order to reduce the computation time, the authors propose an approach that consists in merging the beads, according to the height while keeping the moving equivalent heat source with material deposition. An adaptation of the speed is made to respect the manufacturing time and thus the energy brought (to keep the same linear energy). This method, as for the macro-deposition, is not adapted to perform metallurgical calculations given the poor estimation of the temperature field, but allows for a good first prediction of the stresses. For the case illustrated in the study, the calculation time can be decreased from 80 to 97%. This method has several limitations, the first of which is that it is only applicable to wall, block, or cylinder configurations where the beads are perfectly aligned and deposited in the same direction.

Maekawa et al. [88] use the ISM method (for Iterative Substructure Method). This method is based on the assumption that only the region around the thermal source has a nonlinear mechanical

behavior. The general idea of the ISM method is thus to perform the numerical simulation by combining the large-scale problem with constant stiffness with a small-scale problem with nonlinear mechanical behavior on the area around the molten pool and the heat source. The authors showed that this type of method can reduce the calculation time by twenty.

Finally, in their work, Li et al. [89] developed a multi-scale approach for fast prediction of the distortions and residual stress field of LBM manufactured parts. An equivalent thermal source is considered (micro-scale simulation). From this simulation, a temperature cycle is defined, and applied as imposed thermal input to predict the local residual stress field at the meso-scale layer fraction (equivalent to the macro-deposition method). Finally, the stresses obtained at the meso-scale are mapped to the layer (macro-scale).

The different scales highlight several key conclusions. The microscopic models allow for fine and precise predictions in the molten pool and the electric arc. They allow, for example, studying the influence of physical phenomena on the shape of the arc at a very local scale. However, these models have very high computational costs. On the other hand, mesoscopic models enable the prediction of the thermal field, the displacements, and the residual stresses in an accurate way for small to medium-size workpieces. These models take into account the phenomena in the arc and in the molten pool, as well as the material deposition in a simplified form. They can thus be used to predict the thermo-mechanical residual state as a function of the process parameters. Finally, the macroscopic scale models allow estimating / approximating the mechanical residual state using even more simplified methods. These simplified methods are generally implemented from experimental data or simulations at the mesoscopic scale.

2.4 Mesoscopic scale modeling

In the previous state of the art, the various scales and approaches of the WAAM modeling are identified. The simulations are classified into three classes: micro-scale, meso-scale and macro-scale. Simulations at different scales are characterized according to the physical phenomenon modeled and their degree of accuracy. Given the complexity of the process and the objectives of this thesis project, it is imperative to simplify the models while representing the process as accurately as possible.

The most suitable modeling scales to fulfill the industrial objectives of EDF are the mesoscopic and macroscopic approaches. Most of the work in this manuscript will focus on implementing and validating of a mesoscopic model. Then, based on this model, some macroscopic approaches will be undertaken.

In this section, the mesoscopic modeling scale and the associated assumptions are presented. Indeed, the choice of this scale of modeling is accompanied by the selection of the physical aspects considered and modeled, as well as of the representation of specific modeling aspects of the process, such as the material deposition or heat input and the formulation of the physical problems to be solved.

2.4.1 Physical aspects & assumptions

Simulations at the mesoscopic and macroscopic scales, where the phenomena present in the electric arc and molten pool are not modeled, seem more appropriate in the context of this thesis. Indeed, it is not needed to give a full account of the hydrodynamic phenomena in the molten pool to provide accurate estimates for the stresses and strains of a part. Instead, these complex multi-physical phenomena are replaced by the definition of an equivalent heat source and a material deposition strategy.

Moreover, in order to obtain the temperature distribution, the residual stresses, and distortions during the manufacturing process, it is necessary to model the thermal, metallurgical, and mechanical phenomena in the workpiece [90, 52]. These phenomena intervene in a coupled way, as illustrated in Figure 2.7.

The interactions are the following:

- **Thermal** \Rightarrow **Metallurgical**: The temperature variations are at the origin of the evolution of the microstructure of the material during the manufacturing process.
- **Metallurgical** \Rightarrow **Thermal**: Metallurgical transformations generate latent heat phenomena of phase change which can influence the thermal field. Moreover, the phases involved do not necessarily have the same thermal parameters.
- **Metallurgical** \Rightarrow **Mechanical**: There are several effects of the metallurgy on the mechanical behavior. For instance, volume variations during phase transformations generate deformations of metallurgical origin. Moreover, each phase has its own mechanical behavior. Depending on the phases in presence, the mechanical behavior can thus be different.
- **Mechanical** \Rightarrow **Metallurgical**: The effect of the stress on the transformation phases.
- **Mechanical** \Rightarrow **Thermal**: The viscous effects can be accompanied by a release of heat which can eventually influence the temperature. For the WAAM process, another effect can also appear. The workpiece is manufactured following a defined path, but if the workpiece or base plate is subjected to strong deformations, the temperature field is affected.

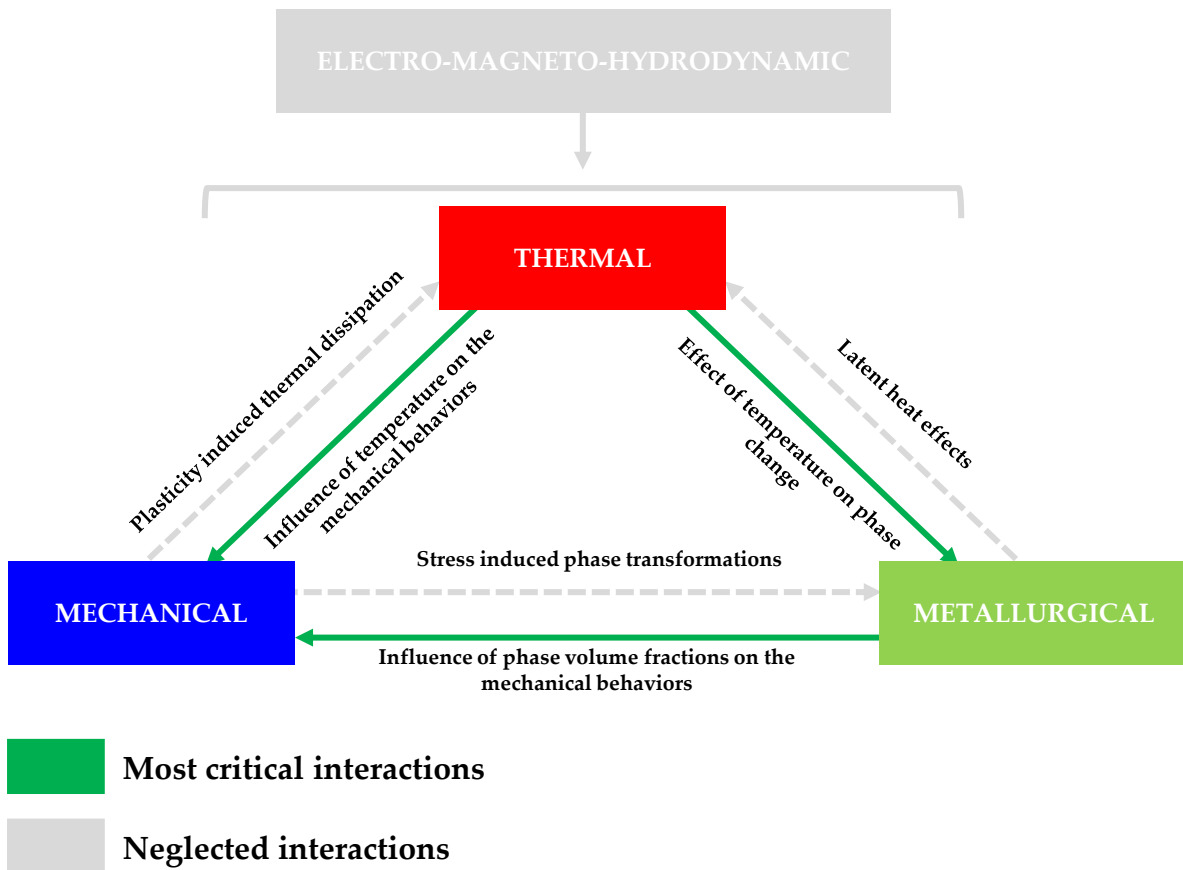


Figure 2.7 – Couplings between thermal, metallurgical and mechanical modeling aspects.

- **Thermal \Rightarrow Mechanical:** The temperature affects the mechanical properties of the material. Moreover, the deformations of thermal origin induce stresses.

Only the strongest interactions are taken into account to simplify the physical problem to be modeled. The objective is to select a limited number of relevant physical phenomena. Figure 2.7 presents the couplings between the thermal, metallurgical, and mechanical aspects: the most critical couplings, which will be considered for the study, are represented in green, while the couplings generally neglected because of their weak influence are represented in gray. As indicated in Chapter 1, the metallurgical aspect is not taken into account. Indeed, for austenitic stainless steels such as 316L SS, the hypothesis can be made that there are no metallurgical transformations [33]. The phenomena of phase transformations latent heat are thus not considered. Nevertheless, the effect of latent heat by change of solid/liquid state is taken into account (Sections 2.4.3.1 and 3.3).

Moreover, the mechanical properties of the material are considered to evolve with temperature. Indeed, the WAAM process involves a large range of temperatures between the ambient and the melting temperatures. The models implemented are highly nonlinear due to both the material behavior used and the thermal and mechanical properties of the material, which are temperature-dependent (Young's modulus, thermal expansion coefficient, yield strength, etc.). Nevertheless, the effects of the mechanical aspect on the thermal aspect are not taken into account.

Based on these assumptions, the simulations can be carried out sequentially: for each time step, the transient thermal calculation is first carried out, then, from the results of this calculation, the metallurgical post-processing can be derived if necessary. Finally, a non-linear mechanical calculation can be achieved to determine the stresses and displacement fields.

2.4.2 Material deposition approaches

One of the main aspects of this type of process is the fact that the material is deposited in a progressive way. Different methodologies are classically used to manage the material input.

■ **Non-conforming mesh methods based on the evolution of a moving interface in a mesh, either explicitly by defining a Level Set or implicitly by Volume of Fluid method:** This interface represents the boundary between two phases: the gas and the metal. The material input is managed by evolving this boundary/interface over time. The Level Set (LS) approach [91] is also often used for multiphysics microscopic or mesoscopic scale simulations. This approach is used, for example, by Cadiou et al.[92] who set up a numerical model to simulate the material input and the thermal field for a WAAM operation with the CMT process. The moving interface between the shielding gas and the metal phase is tracked. Moreover, the wire, the base plate, and the molten metal are treated as a single metal phase. The level set method allows simulating the dynamic shape of the wire tip, the detachment of the droplet during wire retraction, and the dynamic shape of the deposited material during material addition.

For multiphysics simulations, the method used is generally the "Volume Of Fluid" method (VOF). Unlike the Level Set method, the VOF method is not an interface method but can be used to track the molten pool surface. This eulerian approach is used in general for the representation of two-phase flows. Nevertheless, in the present case, the medium is treated as a single fluid whose material properties are averaged by the volume fraction in each cell without modifying the mesh. This approach is used by Hu et al.[93] to simulate the transport phenomena occurring during a welding process. In the developed model, the authors considered the coupling between the plasma, the electrode, the droplet generation, and molten pool hydrodynamics. This method is exclusively used with finite volume discretization.

The VOF and LS methods are mainly used for simulations at the microscopic scale [37, 40, 38, 42]. Indeed, these methods are difficult to implement for mesoscopic and macroscopic scale simulations (but possible [76]).

■ **Conforming mesh methods based on the Quiet elements / Inactive elements:** Two methods are currently predominant in FE simulations: the "Quiet element" [61] method (also referred as the "Silent element" method) and the "Inactive element" [94] method (also known as the "Element birth and death" method). A detailed comparison of these two methods can be found in the work of Michaleris et al. [95]. In the "Quiet element" method, the properties of the material yet to be deposited are defined as "transparent" to the thermal and mechanical calculation: the thermal conductivity λ (in $\text{W m}^{-1} \text{K}^{-1}$) and the specific heat C_p (in $\text{J kg}^{-1} \text{K}^{-1}$), the Young's modulus E (in MPa), as illustrated in Figure 2.8-b. For example, if the conductivity λ is zero (or close to zero), the temperature of the quiet elements should not change. These elements are then activated progressively according to the deposition pattern. Once they are activated, they recover their nominal properties. The advantage of

this method is its simplicity of implementation and the fact that the mesh is not scalable. Nevertheless, choosing the material parameters assigned to the quiet elements is not easy, and this method can lead to convergence problems or numerical oscillations at the interfaces between the elements with artificial conductivity and the activated elements. For the "Inactive element" method, contrary to the "Quiet element" method, the elements representing the material to be deposited are completely deactivated as represented in Figure 2.8-a, although they are part of the mesh. They do not intervene at all in the calculation until their progressive activation according to the deposition pattern.

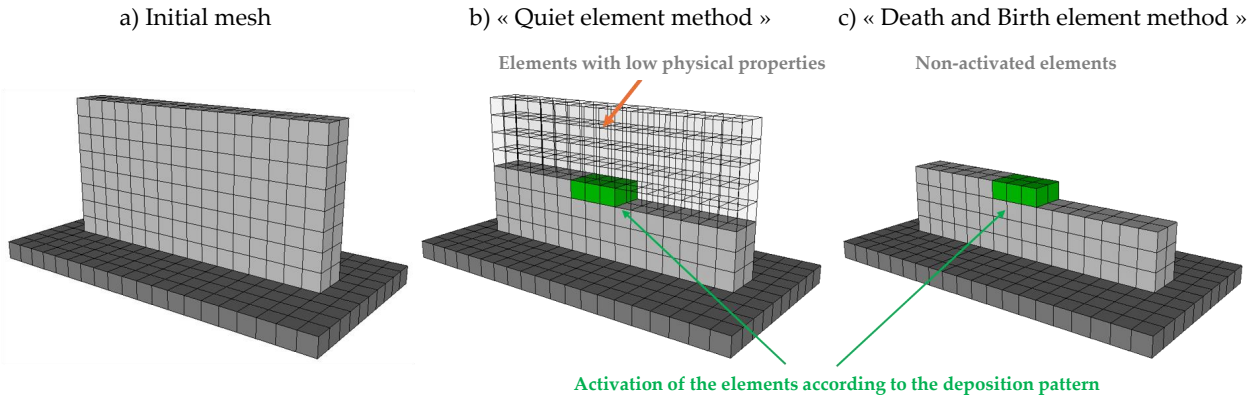


Figure 2.8 – Illustration of the material deposition approaches: a) Geometry, b) "Quiet element" method, c) "Inactive element" method.

According to Michaleris et al. [95], these two methods lead to similar results. A new hybrid "Inactive & Quiet element" method is also proposed. In this approach, the elements corresponding to the metal deposition are initially all inactive. The "Inactive element" method is used to activate the layers one after the other, and the "Quiet element" method is applied to each layer. In other words, when a layer is being deposited, the entire layer is added to the calculation, and the yet "non-deposited" elements of the layer are assigned weak thermo-mechanical properties. For large workpiece simulation, this approach allows having shorter computation times.

A more simplified method has been considered by Tuan et al. [96]. The authors used the "Element Birth and Death" method to bring the beads one after the other, without making "Quiet element" the yet non-deposited elements of the bead. Given the high speed of the torch, the conduction in the "not brought" elements of the bead can be disregarded.

Other less common methods exist. For example, in their study on the laser metal deposition, Peyre et al. [97] represent the material deposition as a free surface motion of the mesh, dependent on the powder-feed rate. The primary interest of such a model is that it allows for the estimation of the workpiece shape. The authors applied this method to a wall configuration. However, its application would be much more difficult for more complex-shaped parts. Moreover, this approach does not take into account the evolution of the shape of the beads with the progressive accumulation of heat in the part in order to predict potential drifts, defects and collapses. Therefore, the part shape can only be predicted for small parts that do not accumulate too much heat.

Because of the modeling scale and the finite element code used, the two most suitable candidates are the "Inactive element" and the "Quiet element" method.

2.4.3 Mesoscopic thermal model

2.4.3.1 Thermal conduction equation

The establishment of the thermal model is a critical step because it will condition the results of the mechanical (and metallurgical, if applicable) calculations. In the thermal model implemented, three modes of heat transfer are considered: conduction, convection, and radiation. The calculation of the temperature field is made through the non-linear and transient resolution of the heat equation [98, 99, 100]:

$$\rho C_p \frac{\partial T}{\partial t} - \text{div}(\lambda \vec{\text{grad}} T) = G \quad \forall (\underline{x}, t) \in \Omega_i \times [0, t_{last}], \quad (2.5)$$

with:

- $\rho(T)$ (kg.m^{-3}), the density,
- $C_p(T)$ ($\text{J.kg}^{-1}.\text{K}^{-1}$), the specific heat,
- $\lambda(T)$ ($\text{W.m}^{-1}.\text{K}^{-1}$), the thermal conductivity,
- G ($\text{J.s}^{-1}.\text{m}^{-3}$), the volume contribution of heat.

When the melting temperature is reached, the thermal capacity, which represents the energy needed to induce a change in phase, is discontinuous, resulting in a latent heat of fusion. Figure 2.9 illustrates this phenomenon.

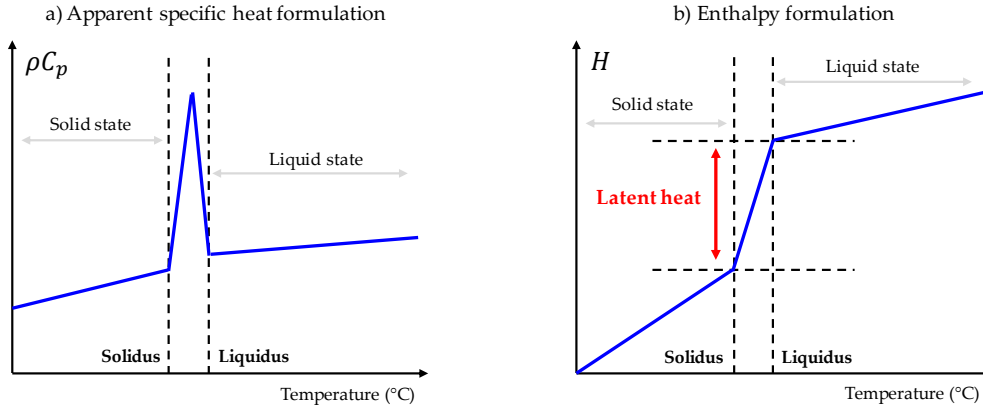


Figure 2.9 – Representation of the latent heat of fusion phenomenon.

To prevent this from affecting the simulation results, an enthalpy formulation of the heat equation can be considered. Indeed, if the time steps are not sufficiently small, the formulation in capacity risks missing this transformation. The enthalpy formulation, which overcomes this problem, can be expressed as follows:

$$\frac{\partial H}{\partial t} - \text{div}(\lambda \vec{\text{grad}} T) = G \quad \forall (\underline{x}, t) \in \Omega_i \times [0, t_{last}], \quad (2.6)$$

with $H(T)$ (Jm^{-3}), the enthalpy.

2.4.3.2 Thermal boundary conditions

Initial and boundary conditions are also needed. The latter are either imposed temperature, flux, or exchanges by radiation and convection with the external environment. During the additive manufacturing process, heat losses of different nature can occur: free convection, thermal radiation, forced convection, or conduction between the part and its clamp.

Therefore, the conduction is the dominant phenomenon. For the WAAM process, the manufacturing times are much longer, and the thermal heat accumulation is larger. The thermal losses can thus become significant. Moreover, the longer the manufacturing process and the larger the manufactured part, the more heat the part accumulates, and the larger the exchange surfaces (external surfaces of the component) become. In addition, as the height of the components increases, it becomes harder for the thermal heat to be dissipated by conduction towards the substrate. Moreover, as the part heats up, the substrate also heats up. Thus, the effect of the thermal transfer at the clamped zones will gradually be observed.

Finally, the temperatures determined at a given time step are used as a basis for the next time step. As a result, fuzzy modeling of these boundary conditions can increasingly generate a divergence compared to the actual behavior. The different transfer modes presented above must therefore be modeled as precisely as possible in order to have a predictive thermal modeling.

■ **Convection and radiation:** The thermal limit conditions are defined as follows:

$$-\lambda(T)\frac{\partial T}{\partial n} = h(T - T_{amb}) + \varepsilon\sigma(T^4 - T_{amb}^4) + q, \quad (2.7)$$

with:

- n , the external normal,
- h ($\text{W.m}^{-2}.\text{K}^{-1}$), the convective exchange coefficient,
- σ ($\text{W.m}^{-2}.\text{K}^{-4}$), the Stefan-Boltzman constant,
- ε , the emissivity of the material,
- q (W.m^{-2}), the external surface heat source,
- T_{amb} (K), the reference temperature, which corresponds to the ambient temperature in general.

The 1st term of Equation 2.7 represents the resultant heat transport by conduction that is normal to the workpiece surface $\partial\Omega_i$ at each time step. The 2nd and 3rd terms represent the heat loss by convection and radiation from the workpiece external surface at each time step, respectively. And finally, the 4th term represents an imposed surface heat flux.

The convection and radiation boundary conditions can be defined in various ways. Most studies consider the convection coefficient h and the emissivity coefficient ε to be constant [70, 101]. In some studies, they may also be neglected. This is the case in the study of Zinoviev et al. [51], which only considers convection, as for Jiang et al. [102]. However, it is also common to use a convection coefficient that changes with temperature in order to represent the different phenomena within the molten pool or to consider the forced convection generated by the shielding gas occurring during the passage of the torch [98]. The convection and emissivity coefficients can also be taken as temperature-dependent due to the fact that, during a WAAM operation, there is a gradual accumulation of temperature,

thus inducing a variation of these coefficients [47]. Other studies prefer to model the heat losses in a combined way in order to have only one coefficient of loss [103, 104]. Indeed, rather than model the losses separately, a lumped heat loss coefficient, which combines the radiation and convective heat losses, can be defined to get rid of potential non-linearity.

■ **Clamped zone and contact surface heat losses:** Before the manufacturing process, the base plate is held using screws, bolts or jaws. During manufacture, the temperature of the part rises, which causes heat exchange by conduction. In the literature, these thermal losses are very often not taken into account in thermal models. This modeling choice is usually correct and justified when the heat transfer to the contact is considered to be limited. Indeed, when the test is of limited duration, if the volume of the substrate is significant, and/or if the embedding is far from the manufacturing zone, the temperature near the contact clamped zone does not increase, which implies that the heat exchanges are very low, and can thus be neglected. Several methods exist to model this heat loss [90]. The most practical method is to simulate the conduction by introducing a factor that depends on the roughness of the surfaces in contact. This leads to a reduction in the heat transfer rate between two touching surfaces and to an effect called contact resistance. Nonetheless, a more straightforward method is to model these losses considering an increased convection zone as follows:

$$q_{cl} = h_{cl}(T - T_{amb}), \quad (2.8)$$

with:

- q_{cl} (W.m^{-2}), the heat flux dissipated at the clamped zone,
- h_{cl} ($\text{W.m}^{-2}.\text{K}^{-1}$), the equivalent convective heat exchange coefficient at the clamped zone,
- T (K), the temperature,
- T_{amb} (K), the reference temperature, which corresponds to the ambient temperature in general.

2.4.3.3 Equivalent heat source

One of the most critical aspects of the thermal model is the heat input modeling. As previously stated, the interaction of the complex thermo-physical phenomena of the molten pool during manufacturing, and thus the heat input, are modeled using an equivalent thermal source [105, 106]. In the following, some reminders are made regarding the definition of the heat input in the numerical simulation of welding, multi-pass welding, and additive manufacturing. In the case of electric arc welding/additive manufacturing, the energy emitted per unit of time is:

$$Q = UI, \quad (2.9)$$

with:

- Q (W or J.s^{-1}), the power or energy emitted per unit of time,
- U (V), the voltage,
- I (A), the current.

However, only part of this energy is transferred to the filler material to melt it. The remainder is exchanged with the outside by convection and radiation around the arc column and the molten pool

[107]. In the current simulations, these losses are represented by introducing an efficiency factor η (unitless) ranging between 0 and 1:

$$Q_{real} = \eta Q = \eta UI. \quad (2.10)$$

The value of this parameter can vary significantly from one welding process to another. This parameter is complicated to quantify or measure, but it is one of the most influential parameters. Moreover, the thermal source can be introduced in different ways: external boundary conditions or internal heat sources. In all cases, this source is a function of space and time. It can be applied as an imposed temperature or a flux defined by a geometry and a distribution. The use of a flux is widely favored in the literature [48].

■ **Imposed temperature:** The heat source can be modeled quite simply by imposing temperature cycles on the deposited material / on the elements activated at each time step. The disadvantage of this method is the fact that, in general, the imposed temperature cycle is identified beforehand and is the same during the whole manufacturing process, which makes this method more suitable for simple trajectories and short manufacturing times like welding (low heat accumulation in the component), and unsuitable for complex 3D trajectories. In general, this approach can be used in 2D in multi-pass welding.

■ **Input flux - Punctual heat source:** Moreover, internal heat sources can also be considered. One of the first heat source developed is the point source model of Rosenthal et al. [108]. This model is mainly used for analytical resolutions of the thermal field.

■ **Input flux - Surface heat source:** Internal heat source models with more complex distributions can also be selected, either on the surface (essentially considering the energy contribution of the covering plasma), or in volume on the mesh (considering the molten pool), or both (surface and volume) with a uniform or a gaussian distribution heat flux. For instance, Eagar et al. [109] proposed a surface thermal source in the form of a disk, with a Gaussian distribution of the heat flux:

$$q(x, y) = \frac{3Q_{real}}{\pi r_0^2} \exp\left(-\frac{3(x^2 + y^2)}{r_0^2}\right), \quad (2.11)$$

with r_0 (m) the source radius.

■ **Input flux - Volume heat source:** For welding and additive manufacturing simulations at the WAAM scale, volume equivalent heat sources are generally used.

Semi-spherical heat source: The half-spherical source is presented in Figure 2.11. It can be considered as a particular case of the following source, the equivalent thermal source proposed by Goldak et al. [110].

Goldak heat source: In most studies in the literature related to the simulation of multi-pass welding or WAAM, the Goldak model is used. Goldak et al. [110] proposed a double ellipsoid (non-axisymmetric) volume source with a gaussian heat flux distribution. The advantage of this source lies

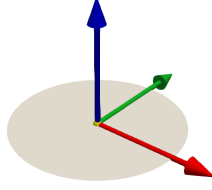


Figure 2.10 – Surface heat source, with constant or gaussian flux distribution.

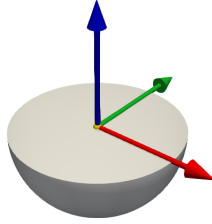


Figure 2.11 – Half-spherical heat source with gaussian flux distribution.

in its versatility and flexibility, which allows it to be used for different processes. Moreover, the Goldak shape can approach the shape of the molten pool and the thermally affected zone that can be observed experimentally. The following equations describe this volume model of heat flux:

$$\text{for } x > 0 : \quad q(x, y, z) = \frac{Q_{real} f_f 6\sqrt{3}}{a_f b c \pi^{3/2}} \exp\left(\frac{-3x^2}{a_f^2} + \frac{-3y^2}{b^2} + \frac{-3z^2}{c^2}\right), \quad (2.12)$$

$$\text{for } x < 0 : \quad q(x, y, z) = \frac{Q_{real} f_r 6\sqrt{3}}{a_r b c \pi^{3/2}} \exp\left(\frac{-3x^2}{a_r^2} + \frac{-3y^2}{b^2} + \frac{-3z^2}{c^2}\right), \quad (2.13)$$

$$\text{with: } f_f = \frac{2a_f}{a_f + a_r} \quad \text{and} \quad f_f + f_r = 2, \quad (2.14)$$

with:

- a_r and a_f (m), the back and front lengths of the double ellipsoid,
- f_r and f_f , the ratios of the heat flux at the front and the rear of the source,
- b (m), the width of the double ellipsoid,
- c (m), the depth of the double ellipsoid,
- η , the efficiency.

Montevecchi heat source: In the literature, one can find a few studies that compare and critique these models. For example, Winczek et al. [49] compared the shapes and sizes of thermally affected zones generated by different heat source models: volume source, bimodal volume/surface source, and

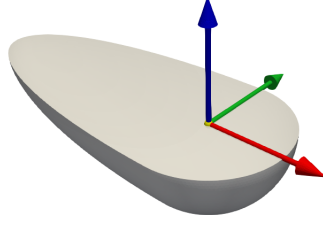


Figure 2.12 – Goldak heat source: double ellipsoid heat source with gaussian flux distribution.

bimodal volume/volume source. Moreover, Montevecchi et al. [50] considered that the Goldak source does not account for the proper heat distribution. Indeed, according to Dupont et al. [111], not all the power is delivered to the part but only 50%, the rest is being used to melt the wire feed. Montevecchi et al. [50] thus proposed a new definition of the heat source, which is a modified version of the Goldak source, in order to have a more realistic heat flux distribution. The Montevecchi heat source is defined as:

$$q_{molten\ pool}(x, y, z) = \frac{Q_{molten\ pool} f_{f,r} 6\sqrt{3}}{a_{f,r} b c \pi^{3/2}} \exp\left(\frac{-3x^2}{a_{f,r}^2} + \frac{-3y^2}{b^2} + \frac{-3z^2}{c^2}\right). \quad (2.15)$$

Similarly, the heat flux that corresponds to the influence of the deposited material can be expressed as follows:

$$q_{wire\ feed}(x, y, z) = \frac{Q_{wire\ feed}}{V_{wire\ feed}}, \quad (2.16)$$

$$Q_{real} = \eta UI = Q_{molten\ pool} + Q_{wire\ feed}. \quad (2.17)$$

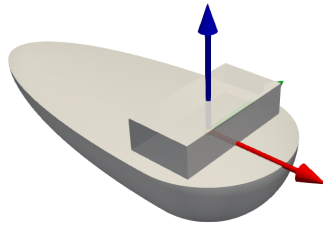


Figure 2.13 – Montevecchi heat source: double ellipsoid heat source with gaussian flux distribution, with filler constant flux distribution.

Conical or double cylindrical heat source: One of the disadvantages of the sources presented previously is the fact that generally, they will consider the molten pool of circular or elliptical shape. This is very often the case for the GTAW process. However, for processes such as laser, plasma, or sometimes CMT, molten pools with a more penetrating shape can be observed, such as "keyhole". For

instance, Figure 2.4 represents the fusion line profile for different metal transfer modes. Therefore, equivalent thermal sources with other shapes might be needed for a more accurate representation of the melted zone [112, 113, 114].

Figure 2.14 represents the general shape of a conical heat source, and its formulation is described as follows [115]:

$$q(x, y, z) = \frac{6Q_{real}}{\pi (r_e^2 + r_e r_i + r_i^2) |z_e - z_i|} \exp\left(-\frac{3(x^2 + y^2)}{r_0(z)^2}\right), \quad (2.18)$$

$$r_0(z) = r_e + \frac{r_i - r_e}{z_i - z_e} (z - z_e), \quad (2.19)$$

with:

- r_e and r_i (m), respectively the upper and lower radius of the conical heat source,
- z_e and z_i (m), respectively the position of the upper and lower section along the z-axis,
- z and $r_0(z)$ (m), respectively the position along the z-axis of the associated radius.

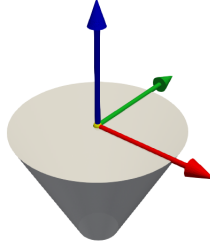


Figure 2.14 – Conical heat source with gaussian flux distribution.

For cylindrical sources, Figure 2.15 presents an example of a double cylindrical heat source. They are expressed as [116]:

$$q(x, y, z) = \frac{3Q_{real}}{\pi r_0^2 |z_1 - z_0|} \exp\left(-\frac{3(x^2 + y^2)}{r_0^2}\right), \quad (2.20)$$

with:

- z_0 and z_1 (m), respectively the position of the upper and lower section along the z-axis,
- r_0 (m), the cylinder radius.

Many other thermal source variations exist depending on the modeling needs, such as mixtures of the previously introduced sources [117, 118, 119].

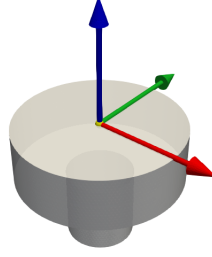


Figure 2.15 – Double cylindrical heat source with gaussian flux distribution.

2.4.4 Mesoscopic mechanical model

2.4.4.1 General mechanical formulation

As presented in Section 2.4, there is a weak coupling between the thermal and the mechanical calculations. Generally, the non-linear mechanical calculation is performed at each time step by solving the static equilibrium equations from the transient temperature field obtained by the thermal calculation [33, 96, 65, 61, 59, 56, 52, 120]. The simulation is quasi-static, which means that the acceleration terms are neglected:

$$\operatorname{div} \underline{\underline{\sigma}} + \rho \underline{\underline{f}} = 0 \quad \forall (\underline{\underline{x}}, t) \in \Omega_i \times [0, t_{last}]. \quad (2.21)$$

Mechanical simulations usually assume a small deformation hypothesis (the current configuration at the time t_i is considered very close to the initial one). This choice is justified. Indeed, in the WAAM (in the framework of a FE simulation), the deformations are of thermally induced origin. For a coefficient of thermal expansion of the order of $1.5 \times 10^{-5} \text{ K}^{-1}$ with a ΔT of up to 2×10^3 , the thermal deformation (Equation 2.24) is of the order of $\alpha \times \Delta T = 3 \times 10^{-2}$. The deformation values will generally be in the range 0 – 5%. Therefore, the linearized strain tensor $\underline{\underline{\varepsilon}}^{tot}$ is defined based on the displacement $\underline{\underline{u}}$ as:

$$\underline{\underline{\varepsilon}}^{tot} = \frac{1}{2}(\underline{\underline{\nabla}}\underline{\underline{u}} + \underline{\underline{\nabla}}^T\underline{\underline{u}}) \quad \forall (\underline{\underline{x}}, t) \in \Omega_i \times [0, t_{last}]. \quad (2.22)$$

This tensor can be decomposed in different deformation terms as follows:

$$\underline{\underline{\varepsilon}}^{tot} = \underline{\underline{\varepsilon}}^e + \underline{\underline{\varepsilon}}^{th} + \underline{\underline{\varepsilon}}^p \text{ (or } vp) \quad \forall (\underline{\underline{x}}, t) \in \Omega_i \times [0, t_{last}], \quad (2.23)$$

with:

- $\underline{\underline{\varepsilon}}^e$, the elastic strain,
- $\underline{\underline{\varepsilon}}^{th}$, the thermal strain,
- $\underline{\underline{\varepsilon}}^p$, the plastic strain,
- $\underline{\underline{\varepsilon}}^{vp}$, the viscoplastic strain.

The strain induced by thermal expansion is:

$$\underline{\underline{\varepsilon}}^{th} = \alpha(T)(T - T_{ref})\underline{\underline{1}} \quad \forall (\underline{\underline{x}}, t) \in \Omega_i \times [0, t_{last}], \quad (2.24)$$

with:

- $\alpha(T)$ (K^{-1}), the thermal expansion coefficient (temperature-dependent),
- T_{ref} (K), the reference temperature at which the thermal deformation is equal to zero (ambient temperature for the base plate and fusion temperature for the deposited material).

The elastic strain is related to the stress tensor through Hooke's law:

$$\underline{\underline{\sigma}} = \underline{\underline{C}} : \underline{\underline{\epsilon}}^e = \underline{\underline{C}} : (\underline{\underline{\epsilon}}^{tot} - \underline{\underline{\epsilon}}^{th} - \underline{\underline{\epsilon}}^p) \quad \forall (\underline{x}, t) \in \Omega_i \times [0, t_{last}], \quad (2.25)$$

with $\underline{\underline{C}}$ the 4th order stiffness tensor.

These equations, in addition to the boundary conditions, form the mechanical model. The boundary conditions can be split in Dirichlet and Neumann. The Dirichlet boundary conditions can be considered to model the embedding of the base plate of the parts to be simulated by constraining the displacements. They are defined as follows:

$$\underline{u} = \underline{u}^d \quad \forall (\underline{x}, t) \in \partial\Omega^u \times [0, t_{last}]. \quad (2.26)$$

The Neumann boundary conditions correspond to the imposed forces. They can be expressed as:

$$\underline{\underline{\sigma}} \cdot \underline{n} = \underline{F} \quad \forall (\underline{x}, t) \in \partial\Omega^F \times [0, t_{last}]. \quad (2.27)$$

All the material properties are temperature-dependent and must be characterized, ideally, from room temperature to melting temperature.

2.4.4.2 Material mechanical behavior modeling

Now that a general presentation of the mechanical problem has been carried out, the focus is made on the material behavior, which is an essential input in most mechanical studies. The constitutive behavior is required to define the elastic and inelastic domains and depend on parameters which may evolve strongly with temperature. This implies that all the parameters associated with the material behavior, such as the thermal expansion coefficient α , the elastic behavior of the material, and even the parameters involved in the modeling of the plastic behavior, must be characterized for a range of temperatures going ideally from the ambient temperature to the melting temperature of the material.

The definition of $\underline{\underline{\epsilon}}^p$ requires additional plasticity/hardening evolution equations. Regarding the non-linear aspect of the material behavior, the choice of the constitutive behavior model used depends on the material, on the type of loading to which the material is subjected, and on the desired accuracy of the simulation. In other words, the more physical phenomena are taken into account in the models, the larger is the complexity of the models.

To describe the plastic behavior, three components are needed:

- a **yield function**, which is the criterion that defines if the material is in the plastic state or not,
- a **flow function** describing the plastic strain rate and providing the evolution of $\dot{\underline{\underline{\epsilon}}}_p$,
- a **hardening function**.

Several types of non-linear elasto-plastic behavior associated with different hardening model can be considered. For the large majority of FE mechanical simulation, the plastic behavior is considered

through Von Mises criterion. Moreover, the choice of the type of hardening representation is a key modeling point [121]. The different approaches used in the literature are presented below.

Some authors, such as Lee et al. [122], do not take hardening into account, and estimate the residual stress considering perfect plasticity. This type of behavior means that there is no evolution of the yield surface.

Isotropic hardening model allow modeling a uniform increase in the size of the yield surface with the same plastic deformation in all directions (Figure 2.16-a), while maintaining its center. A linear isotropic hardening approach is, for instance, used by Ogawa et al. [68] and by Prajadhama et al. [123]. These types of constitutive behaviors are generally valid for global monotonic loading and are not recommended for cyclic loading. Indeed, there is a risk of overestimating the stresses for high deformations because nothing limits the hardening profile. One way to reduce this overestimation is to use a non-linear or piecewise linear isotropic hardening. For instance, in the study of Hu et al. [124], piecewise linear approximations of measured monotonic uni-axial tensile stress-strain data were considered. Nevertheless, an overestimation of the stresses can mean that the simulations are conservative, which may be not problematic depending the application.

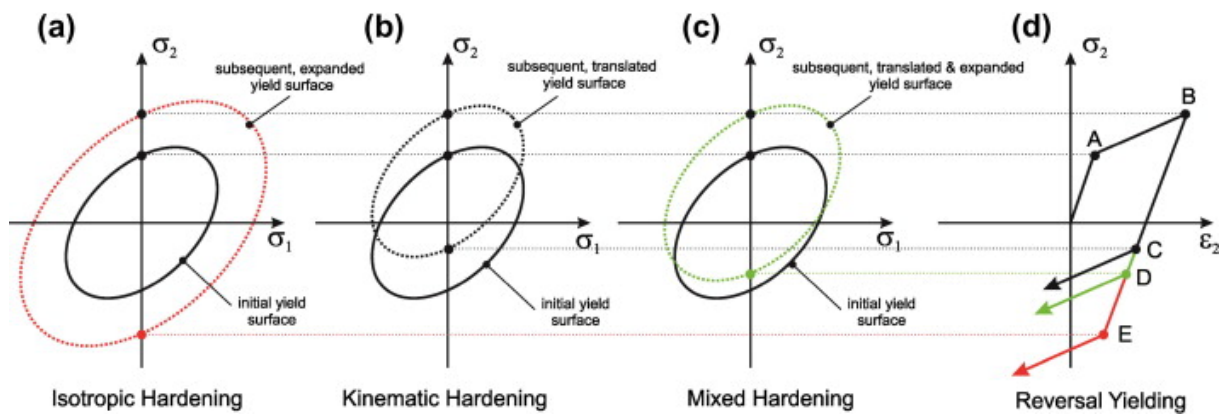


Figure 2.16 – Hardening model: a) Isotropic hardening model showing the expansion of the yield surface with plastic strain, b) kinematic hardening model showing the translation of the yield surface with plastic strain, c) mixed isotropic–kinematic hardening model showing the expansion and translation of the yield surface with plastic strain, d) resulting stress–strain curves showing different yield stress in compression as predicted by different plasticity models: C – kinematic hardening, D – mixed hardening, and E – isotropic hardening [125].

The kinematic hardening model are adapted to models in which the loading is cyclic. It takes into account the Baushinger effect [126], which is the softening in compression following a tensile hardening. Thus, contrary to the isotropic hardening, the kinematic hardening corresponds to the displacement of the yield surface, without change in size, as illustrated Figure 2.16-b. This approach was, for instance considered in the study of Gilles et al. [127] for welding, and Israr et al. [61] for WAAM simulations. However, using such a hardening model can lead to a possible under-estimation of the residual stresses, especially in configurations where the number of cycles is high.

Finally, the last approach described here is the mixed isotropic-kinematic hardening which allows both a uniform size variation and a translation of the yield surface. This allows taking into account the Baushinger effect and the isotropic part of the hardening. Several models of mixed hardening exist [128, 126, 129, 130]. Among these models, the Prager-type mixed hardening models and Chaboche-

type models constitutive behaviors seem to be efficient to take into account the cyclic effects. For instance, Cambon et al. [70] used a elasto-plastic Chaboche constitutive behavior model.

In addition to the choice of the hardening model, the impact of the temperature on the mechanical behavior (and more specifically on the inelastic strains) can also be introduced. In a first step, instead of considering an elasto-plastic behavior, it is possible to take into account the viscosity, which will have an impact for high temperatures. The material behavior constitutive models are thus elasto-viscoplastic. For instance, constitutive behaviors of the Lemaître-Chaboche elasto-viscoplastic can be relevant for the WAAM process. Indeed, unlike welding operations which are much shorter, there is an intense heat accumulation in the component during a WAAM manufacturing operation. Moreover, the longer the operation, the more heat the part can accumulate, thus increasing the influence of creep and viscous phenomena. It is therefore essential to study the influence of these phenomena for the WAAM.

Furthermore, at high temperatures, the diffusion phenomena in the material lead to a reduction of the hardening of the material. This can be introduced using "annealing" models, in which the equivalent plastic strain is eliminated either fully or progressively according to the temperature [131].

Finally, various studies have focused on the investigation of the impact of the material behavior on the residual stresses, mostly for welding, and very few for additive manufacturing processes. In the field of welding, previous studies conducted by the European consortium NET (European Network on Neutron Techniques Standardisation for Structural Integrity) [132] have illustrated the importance of the material hardening laws on the prediction of the residual stresses in finite element simulation through multiple "Task Groups" studies, in particular for the 316L SS. Numerical simulation results are compared to experimental data to validate the accuracy of the different models [133, 134, 135, 125, 136, 137, 138, 139, 140, 141].

A detailed presentation of the constitutive behavior models used in the present work for the 316L SS material is provided in Chapter 3.

2.5 Conclusion & perspectives

In this chapter, the AM manufacturing processes were introduced, with a specific focus on the WAAM process. After that, the physical phenomena occurring during the WAAM process were described. Three modeling scales can be considered to investigate the WAAM process according to the objectives considered: the micro-scale, the meso-scale, and the macro-scale.

The mesoscopic scale has been identified as the one that best responds to the objectives of the present work. Therefore, in the second part of this chapter, a more detailed description of the mesoscopic simulations have been performed. First, the modeling hypothesis were presented, among which the fact that there are no metallurgical transformations given the material considered (316L SS) and the weak thermo-mechanical coupling. Then, a state of the art of welding and WAAM modeling was presented:

- The different material deposition methods were introduced, and the "Quiet element" and "Inactive element" methods were identified as the best suiting for FE simulations.
- The general formulation of the thermal problem was presented, with a specific focus on the different possible approaches for the modeling of thermal dissipation and equivalent thermal sources.
- The general formulation of the mechanical problem was described with a specific focus on the different material behavior models.

In the next chapter, the thermo-mechanical model proposed in the context of this PhD is presented.

Chapter 3

Proposed mesoscopic thermo-mechanical model

Contents

3.1	Introduction	43
3.2	Material deposition approach	43
3.2.1	Material progressive deposition modeling	44
3.2.2	Mesh generation tool	45
3.3	Thermal model	49
3.3.1	Equivalent heat source developed: Adaptive Goldak with heat flux correction	49
3.3.2	Boundary conditions	54
3.3.3	Material deposition	56
3.3.4	Synthesis of the thermal model parameters	56
3.3.5	Examples	57
3.4	Mechanical model	59
3.4.1	Plasticity model	60
3.4.2	Hardening annealing	66
3.4.3	Material deposition	67
3.4.4	Molten pool mechanical reset	68
3.4.5	Reference temperature change	68
3.4.6	Cut-off temperature	69
3.4.7	Examples	72
3.5	Conclusion & perspectives	73
3.6	In a nutshell	74

3.1 Introduction

The first part of this chapter presents the methodology developed to numerically solve the equations describing the thermal behavior. The main objective is to present the mathematical description of the thermal problem, the physical phenomena modeled, the modeling assumptions considered, and the numerous parameters involved in the simulations. The modeling approach presented is general and can be applied to different finite element codes as well as other additive manufacturing processes. After this general presentation, the modeling choices made and the different developments achieved are described and presented. In particular, an adaptive equivalent thermal source, coupled with a heat flux correction during the simulation, is developed.

The second part of this chapter focuses on the presentation of the quasi-static non-linear mechanical problem. The mechanical behavior of 316L austenitic SS is presented. Several constitutive behaviors associated with different hardening models are described and discussed. The constitutive behaviors of the 316L austenitic SS used in this work have been previously characterized at EDF and Mines Paristech for the numerical simulation of welding. Therefore, the calibration of the parameters of the constitutive behaviors is not performed in the framework of this PhD thesis. Finally, several aspects related to the process modeling that affect the mechanical simulations are described, such as the management of the material deposition modeling.

The main points covered in this chapter are therefore:

- Presentation of the transient thermal model formulation,
- Development of an adaptive equivalent heat source with a flux correction,
- Consideration of temperature dependant heat losses coefficients,
- Presentation of the formulation of the quasi-static non-linear mechanical problem,
- Description and discussion of the constitutive behaviors considered,
- Presentation of the mechanical modeling aspects related to the process:
 - Progressive material input,
 - Molten pool reset and annealing hardening,
 - Reference temperature change,
 - "Cut-off" temperature.

3.2 Material deposition approach

In this first section, the material deposition management methodology is presented. In order to be able to perform simulations on a large variety of components and deposition pattern strategies, geometry and mesh generation tools are developed using Salome-Meca software [142]. These are presented in this section.

3.2.1 Material progressive deposition modeling

In this thesis, the deposition strategy selected is the "Inactive element" method (more details can be found in Section 2.4.2). There are two main reasons for this choice. First, using the "Quiet element" method can lead to possible convergence and oscillation problems at the interface of the "activated" and "non-activated" elements [61]. Moreover, in Code_Aster, there is a fundamental concept, named MODELE, which allows selecting only on a group of meshes and not on the whole mesh, and thus carrying out a simulation only on a restricted part of the mesh. Combined with the material deposition methodology, a procedure for updating the external surface of the mesh is implemented in the current work in order to redefine at each time step the group of surface meshes on which the convection and radiation boundary conditions are applied. The methodology is illustrated in Figure 3.1-b.

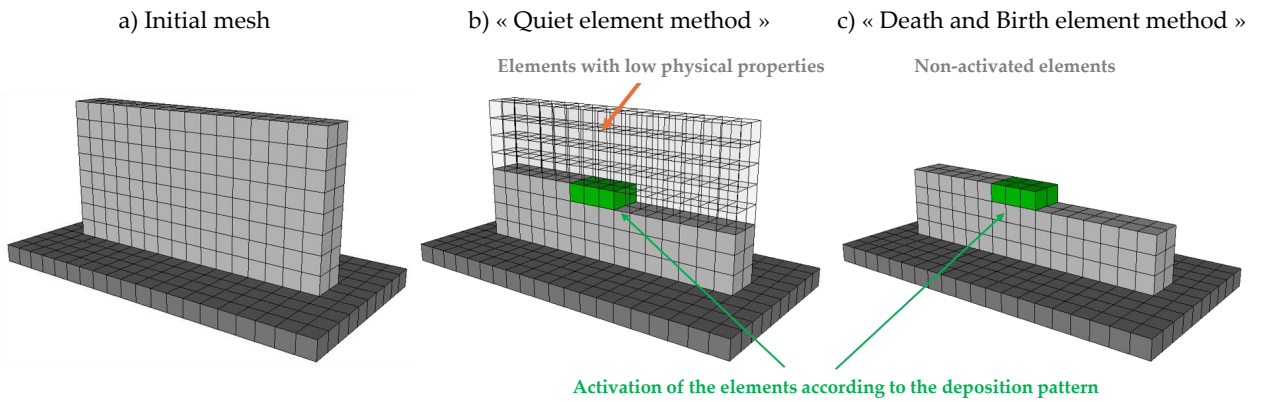


Figure 3.1 – Illustration of the material deposition methodology.

The mesh is constructed before the simulation. The domain corresponding to the complete manufactured part along with the base plate is denoted Ω . At each time step, the elements of the part are progressively activated according to the manufacturing path. The domain of elements activated at each instant is noted Ω_i and the group of elements activated at instant i is $\Delta\Omega_i = \Omega_i - \Omega_{i-1}$. Moreover, the group corresponding to the external surface of the mesh at time i to which the thermal dissipation boundary conditions are applied is noted $\partial\Omega_i$.

The evolution of the elements at each time step is associated with field manipulations during the simulation. In general, during a quasi-static transient simulation without material deposition, the final state obtained for the time step i is used as the initial state of the time step $i + 1$. The realization of a calculation with the addition of new elements during the manufacturing process requires some intermediate operations. Indeed, the final state i must be adapted to correspond to the initial state at time step $i + 1$ in the resolution operator. To do so, from the calculation performed at time step i , the displacements, constraints, and internal variables fields are extracted. These thermal and mechanical fields are then carefully extended at each activation of new elements. The strategies developed to manage and extend the initial thermal and mechanical states are presented in Sections 3.3 and 3.4.

3.2.2 Mesh generation tool

One of the specificities of additive manufacturing processes is the large variety of possible shapes. Therefore, one of the objectives of this work is to set up models that can be transposed to many configurations. To be able to implement the most generic simulation methodology possible, mesh and geometry generation tools are set up. The developed tools generate a mesh from the welding path provided to the welding robot or from a programmatically generated welding path file. The mesh generation tools are developed using the "opensource" software Salome-Meca [142].

It should be noted that Code_Aster [12] is a finite element software that allows manipulating existing 1D, 2D, and 3D elements of the mesh, but not creating them (unlike other finite element codes). Therefore, when generating the mesh before the simulation, it is necessary to create the groups of volume and surface meshes associated with each bead. The definition of these groups enables managing the elements of the mesh during the simulation, and thus the evolution of the external surface $\partial\Omega_i$ during the material deposition.

3.2.2.1 Bead morphology

For the morphological aspect of the beads, it is essential to respect the volume of material supplied and the volume of the part. This volume can easily be deduced from the path (more specifically the travel length of the welding path l_{scan} (m)), the speed of the wire v_w (m s^{-1}), the diameter of the wire d_w (m), and the welding speed v_t (m s^{-1}) such that:

$$V = \pi d_w^2 \times v_w \times \frac{l_{scan}}{v_t} \quad (3.1)$$

The dimensions and the shape of the beads are not predicted by the thermo-mechanical model, but can be deduced from either experimental data or multiphysics calculations, if available. Several methods exist to model the beads. In some studies, arc-shaped beads more or less representative of the real shape of the beads are used [143, 62, 144, 104, 94]. Although realistic, this method has several drawbacks. First, the resulting mesh is complex, with numerous elements [123, 94]. Moreover, this method requires a complicated mesh generation step due to the superposition and juxtaposition of the beads for multi-pass configurations [62].

Therefore, in the vast majority of studies performed at the mesoscopic and macroscopic scales, a simplified geometry using a rectangular cross-section is preferred [52, 61, 65]. Indeed, this approach significantly reduces the complexity of the mesh built-up, without affecting the prediction of temperature, residual stresses, or displacements [123]. In this case, Equation 3.1 becomes:

$$\pi d_w^2 \times v_w \times \frac{l_{scan}}{v_t} = e \times l \times l_{scan} \quad (3.2)$$

with e (m) the thickness and l (m) the width of the bead, whose ratio is still yet to be determined as illustrated in Figure 3.2.

Some studies propose the implementation of models to predict the bead size according to the welding process parameters. It is the case, for example, of Sreeraj et al. [145], which developed a neural network model from experimental data in order to derive the desired size geometry of the bead with reasonable accuracy. Xiong et al. [146] also proposed a model to predict bead geometry from the process parameters for welding-based additive manufacturing.

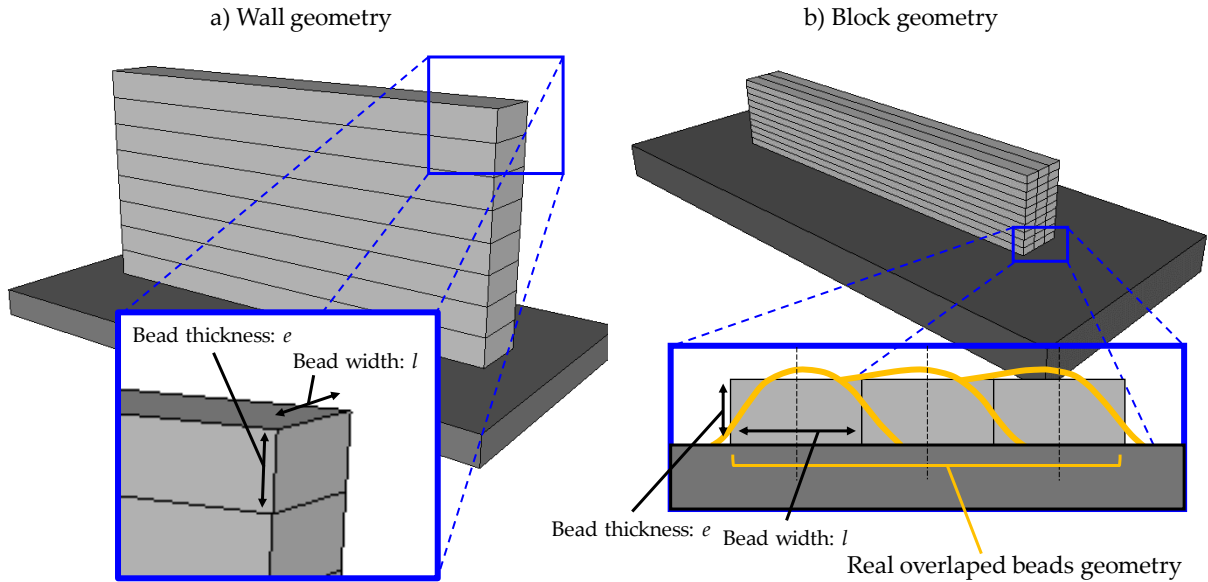


Figure 3.2 – Generation tools of the geometry with a simplified rectangular cross-section bead.

The implementation of such a model seems much more appropriate for welding than for a WAAM operation. In fact, in the simple case of a wall, the thickness or width can be fixed. These dimensions can be chosen either by expertise, through measurements on an experimental test to be simulated, or by using a bead size prediction model. However, in more complex cases where many beads are placed side by side (as for a block), the width of the beads l is fixed by the deposition pattern, and it is equivalent to the space between the beads. The thickness e can thus be explicitly defined from Equation 3.2.

3.2.2.2 Workpiece geometry & mesh

In the thesis, several mesh generation tools are implemented to produce the various part configurations required to meet the possible needs of EDF or AFH for WAAM applications. The method used is not a voxelization method as often used, for example, in the framework of finite element simulations of parts in LBM and LMD [147].

The first configuration, which is the most encountered, consists of workpieces with straight beads. In this case, the deposition pattern, defined by a script with the same architecture as for the robot, is subdivided into segments, and each of these segments represents a bead.

The welding path is essential for the generation of the mesh. This path can be in two forms. The path can be generated using parametric scripts, knowing the geometry of the part to be produced and the desired deposition strategy. The other approach is to directly take the scanning path file provided to the welding robot as input. The main difference between the two approaches is that, in the latter, all the points through which the robot passes are recorded, regardless of whether the welding is being carried out. This state is controlled by a variable that takes 1 if the electric arc is activated and 0 if the robot moves without an electric arc. Figure 3.3 shows an example of a path for a block, whose geometry and mesh are generated automatically.

This methodology can also be applied to any other complex configuration with straight beads. For

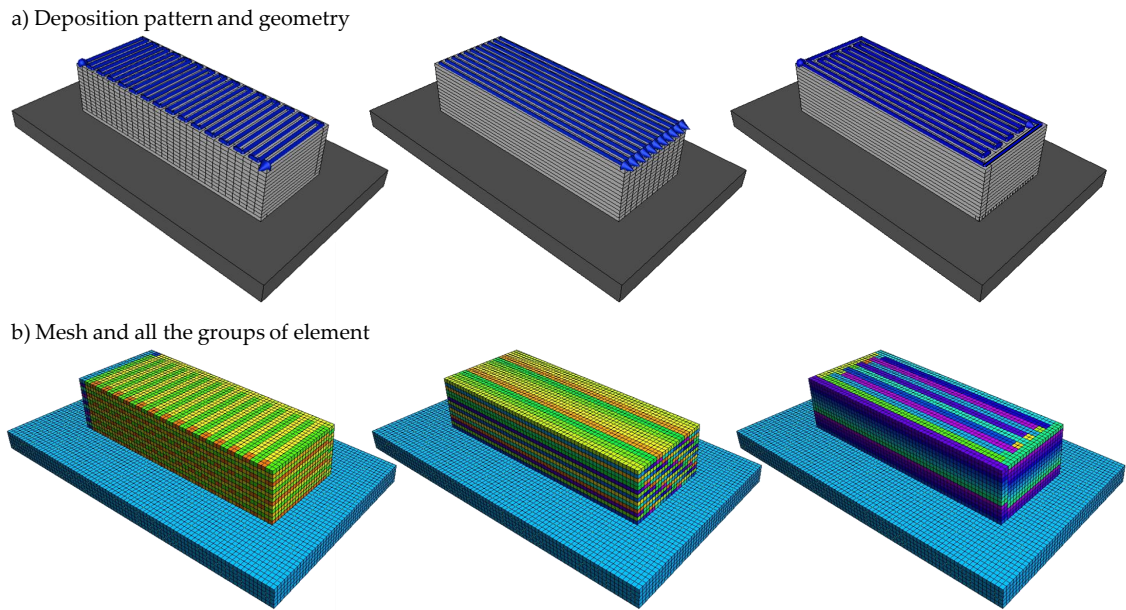


Figure 3.3 – Geometry and mesh generation tools of a block, for three different deposition patterns.

example, this methodology is extended to the generation of the mesh of a Kaplan Blade, which is a part of interest for the hydraulic park of EDF. In this case, the original part is scanned in 3D, to derive the geometry, and then generate the deposition pattern, as shown in Figure 3.4.

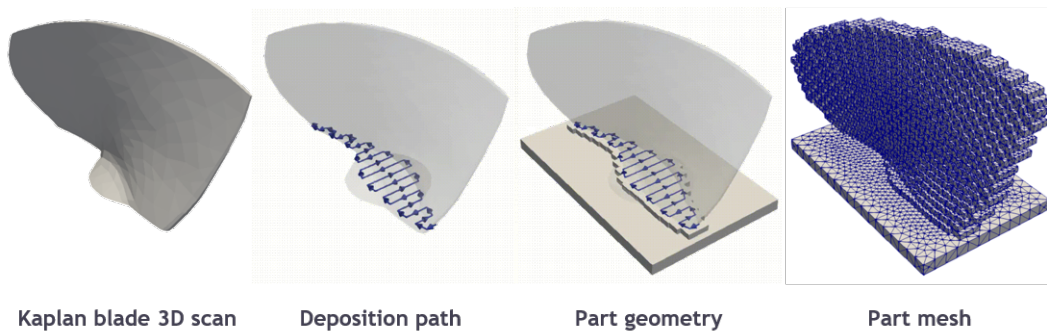


Figure 3.4 – Geometry and mesh generation from a 3D scan of the Kaplan blade.

The other configuration of great importance for EDF is the pipe / cylinder shape, as indicated in Section 1.1.3. Tools are implemented for the generation of pipes, on a flat base plate or on an already existing pipe. The developed tools are parametric scripts, where the inputs are the number of cylinders / pipes, their radius, the associated deposition pattern, the number of beads, the number of layers, their position, etc. Three configurations are presented in Figures 3.5: a cylinder on a flat substrate with a circular deposition pattern, a cylinder on a pipe with a scanning deposition pattern, and finally, multiple cylinders on a pipe. Finally, the association of the different developed tools allows creating more complex geometries, as shown in Figure 3.6 with the PPB.

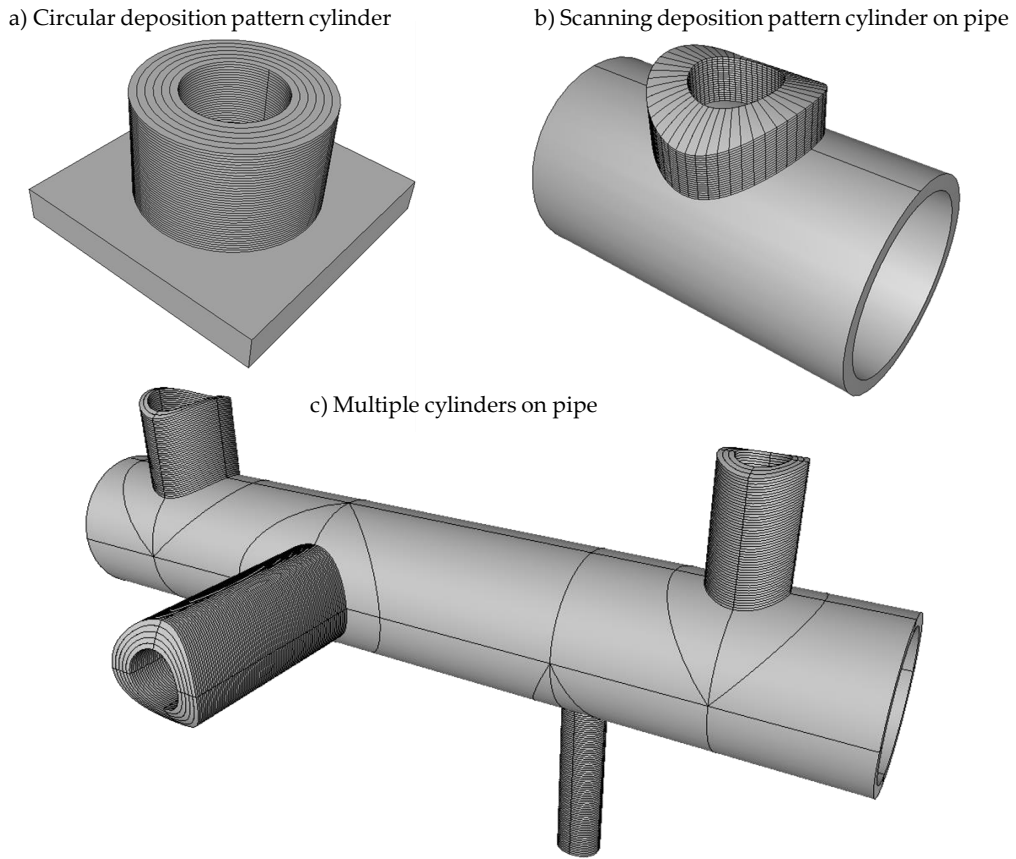


Figure 3.5 – Geometry and mesh generation tools for cylinders: a) Cylinder on a flat substrate with a circular deposition pattern, b) Cylinder on a pipe substrate with a scanning deposition pattern, c) Multiple cylinders on a pipe substrate with a circular deposition pattern.

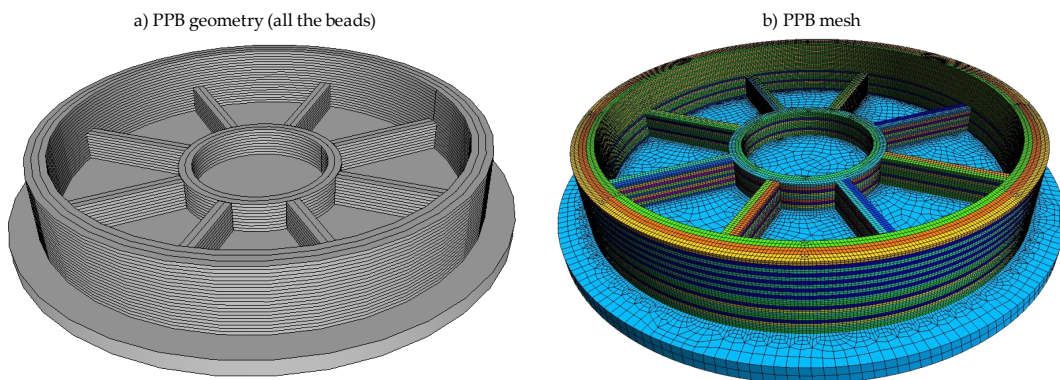


Figure 3.6 – Geometry and mesh generation for the PPB.

3.3 Thermal model

In the light of the conclusions of the previous state of the art presented Chapter 2, the developments and choices made for the implementation of the thermal model are presented in this section. First, the enthalpy formulation (Equation 2.6) is used to consider the latent heat of change of liquid-solid state. The values considered for the conductivity and enthalpy for the 316L SS (identical for parent and weld metal), as well as their evolution with temperature, are listed in Table 3.1.

As previously mentioned, fluid dynamics phenomena inside the molten pool are not modeled. The heat transport phenomena by convection flow (Marangoni effects) in the molten pool are not taken into account. To represent them in a simplified way, one approach is to artificially increase the thermal conductivity with temperature starting from the melting temperature, by a factor that can vary between 2 and 10 depending on the studies [143, 98, 144, 148]. This artificial increase at 1400 °C can be observed in Table 3.1.

Table 3.1 – Evolution of the thermal parameters of 316L SS as a function of temperature: a) The thermal conductivity $\lambda(T)$ ($\text{W}\cdot\text{m}^{-1}\cdot\text{K}^{-1}$), b) The enthalpy $H(T)$ ($\text{J}\cdot\text{m}^{-3}$).

Temperature (°C)	Thermal conductivity $\lambda(T)$ ($\text{W}\cdot\text{m}^{-1}\cdot\text{K}^{-1}$)	Enthalpy $H(T)$ ($\text{J}\cdot\text{m}^{-3}$)
20	0.0147	0.0×10^{-3}
100	0.0158	300.212×10^{-3}
200	0.0172	703.902×10^{-3}
300	0.0186	1127.3295×10^{-3}
400	0.0200	1562.132×10^{-3}
500	0.0211	2004.232×10^{-3}
600	0.0222	2451.282×10^{-3}
700	0.0232	2905.107×10^{-3}
800	0.0241	3373.557×10^{-3}
900	0.0248	3860.257×10^{-3}
1000	0.0255	4357.392×10^{-3}
1200	0.0269	5361.377×10^{-3}
1400	0.0283	_a
1450	_a	6603.346×10^{-3}
1500	_a	8658.636×10^{-3}
1600	_a	9131.044×10^{-3}
1700	_a	9598.790×10^{-3}
1800	_a	1.0062×10^1
2400	0.2830	_b

^a Interpolated value.

^b Linearly extrapolated value.

3.3.1 Equivalent heat source developed: Adaptive Goldak with heat flux correction

■ **Heat source model:** The equivalent heat sources presented in Chapter 2 have each their advantages and drawbacks, depending on the process to be modeled and the shape of melted zone encountered (as illustrated Figure 2.4). Therefore, the equivalent heat source must be carefully selected according

to the configuration studied. The double ellipsoid model proposed by Goldak et al. [110], presented in Equations 2.12, 2.13, and 2.14, is used in this thesis project. It is however important to note that, for configurations with "keyhole" molten pools, often encountered in CMT, conical sources / cylindrical sources or a combination between a double ellipsoid and a conical source can be another interesting alternative.

■ **Generalization of the heat source:** One of the objectives of the current study is to implement the most generic model possible. To this end, a generalized change in the reference frame must accompany the definition of the thermal source. Indeed, the interest of additive manufacturing is the realization of parts with complex trajectories. Moreover, the thermal source, in the case of the Goldak source, is not axisymmetrical, contrary to the half-spherical source or circular surface source. Therefore, the evolution of its orientation according to the welding path of the torch should be considered carefully. The generalized reference frame that follows the thermal source progression is thus defined by taking into account the evolution of the direction of the welding path and the position of the torch, which corresponds to the center of the heat source. Thus, the direction x is always the deposition pattern direction, y is the perpendicular axis along the width direction, and z is the axis in the thickness direction, as shown in Figure 3.9-a.

■ **Heat source flux correction:** Many refinements have been implemented in the models in order to improve the simulations set up. In order to perform mesoscopic scale simulations with larger element sizes compared to welding simulations and given the complex shape of the thermal source selected (the Goldak heat source), it is necessary to ensure the correct energy input at each time step. Therefore, the power provided is controlled to ensure that the right amount of energy is transferred to the part despite the spatial discretization (size of the elements of the finite element mesh) and the time step (which impacts the relative position of the source with regard to the mesh node) as illustrated Figure 3.7.

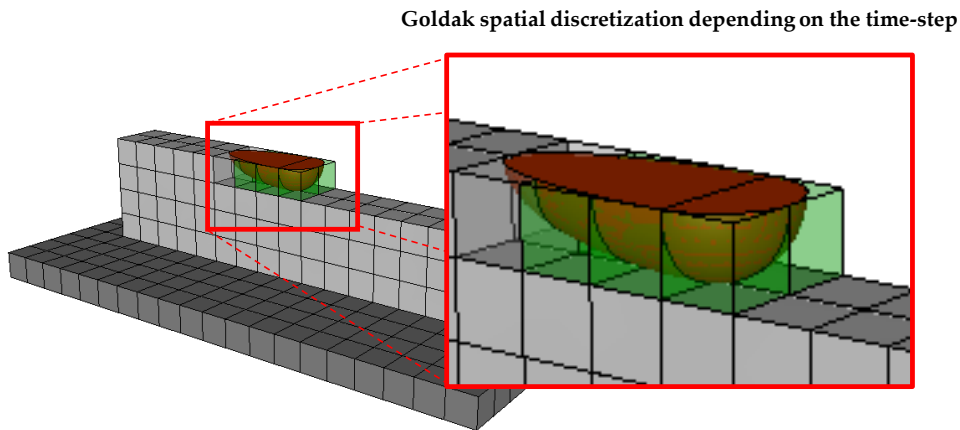


Figure 3.7 – Goldak integral as a function of spatial and temporal discretization.

At each time step, the integral of the heat source is calculated to make sure that the energy supplied is equal to the welding energy, which is ηUI . Figure 3.8-a presents a simple 10 layers test with 4 beads and 4 changes of direction per layer. This test, carried out to study the evolution of the energy supplied,

reveals very clearly issues with the power input.

Indeed, as highlighted in Figure 3.8-b, irregularities in the energy supplied are found. The oscillations are due to the evolution of the relative position of the volume source with respect to the Gauss points of the elements. This implies an oscillation of the integral of the volume source. In addition, it should also be noted that the heat input is not fully respected due to the discretization of the mesh. Very fine refining of the mesh near the source would bring this value closer to the correct energy. For example, Ding et al. [149] also considered that for the use of a gaussian heat source as the Goldak, it is necessary to have a reasonably fine mesh to respect the heat input. Ding et al. [149] proposed a uniformly distributed volumetric heat source model to be insensitive to mesh.

Adapting the efficiency parameter η could compensate for this loss. Nevertheless, this method is not viable for a generalization of the source. Indeed, for a given mesh element size and a given time increment, the selection of an adequate value of the efficiency η can correct the loss due to the discretization. However, if the same simulation is performed with different mesh sizes and time increments, the value of the efficiency used previously would no longer be appropriate. The heat input would thus be dependent on the mesh and the time step, which should be avoided.

To correct this numerical artifact, the integral of the thermal source is calculated for each time step, and a corrective coefficient is applied to the source in order to provide the right amount of heat at each time step and to limit the fluctuations as much as possible:

$$\eta_i = \frac{Q}{\int_{\Omega_i} q_{f,r} dV}. \quad (3.3)$$

The correction of the flux by this factor gives the right energy contribution since we only "modify" the power brought by a numerical efficiency η_i , which is a term that does not depend on space and therefore can be taken out of the integral calculation. This has been validated on simple numerical tests by calculating the integral after correction, which gives the desired results.

For all thermal sources previously presented in Chapter 2 with a gaussian distribution, the edge of the thermal source corresponds to the location where the Gaussian distribution is at 5% of the maximum value of the heat flux. This helps reduce the operations required during the simulations and avoid applying the source on all the nodes of the mesh (with values very close to zero). The loss due to this cut-off of the heat flux distribution is also corrected.

Another phenomenon has been observed in more complex configurations for specific manufacturing steps. Indeed, a part of the heat source may not be applied to the mesh. The heat input is therefore not respected. To remedy this, the calculation of the integral of the source coupled to the corrective coefficient works very well.

■ **Heat source geometric adaptation:** One of the advantages of using the Goldak source is that the distribution of the source allows for a more realistic representation of the welding pool. Nevertheless, in the case of a change in welding path direction (such as corners or half-turns), the welding robot cannot achieve this change of direction without going through zero speed, which is accompanied by a brief localization of the heat input and thus of the welding pool. Therefore, to be more realistic and accurate, a modified Goldak or "morphing" Goldak is implemented. As illustrated in Figure 3.8, when reaching the ends of the beads, the length of the back of the Goldak is corrected so that the Goldak source is fully applied to the mesh. As a consequence, only the rear of the Goldak is modified: a_r . The

"stationary" a_r is defined at the beginning of the simulation. Then, at each step, the distance between the center of the source and the latest direction change location is determined. If this distance is higher than a_r , the Goldak is in its stationary form; otherwise, the a_r is modified. The parameter f_r is adapted as a consequence of the modification of the a_r . This modification does not require the creation and calibration of a new parameter. The other parameters of the source are not modified during the simulation. The comparison between the use of a Goldak and the Adaptive Goldak is presented in Figure 3.8-c. It appears clearly that the local peaks observed at the corners are corrected. The use of the Adaptive Goldak, even before making the flux correction, gives very satisfactory results and is therefore recommended.

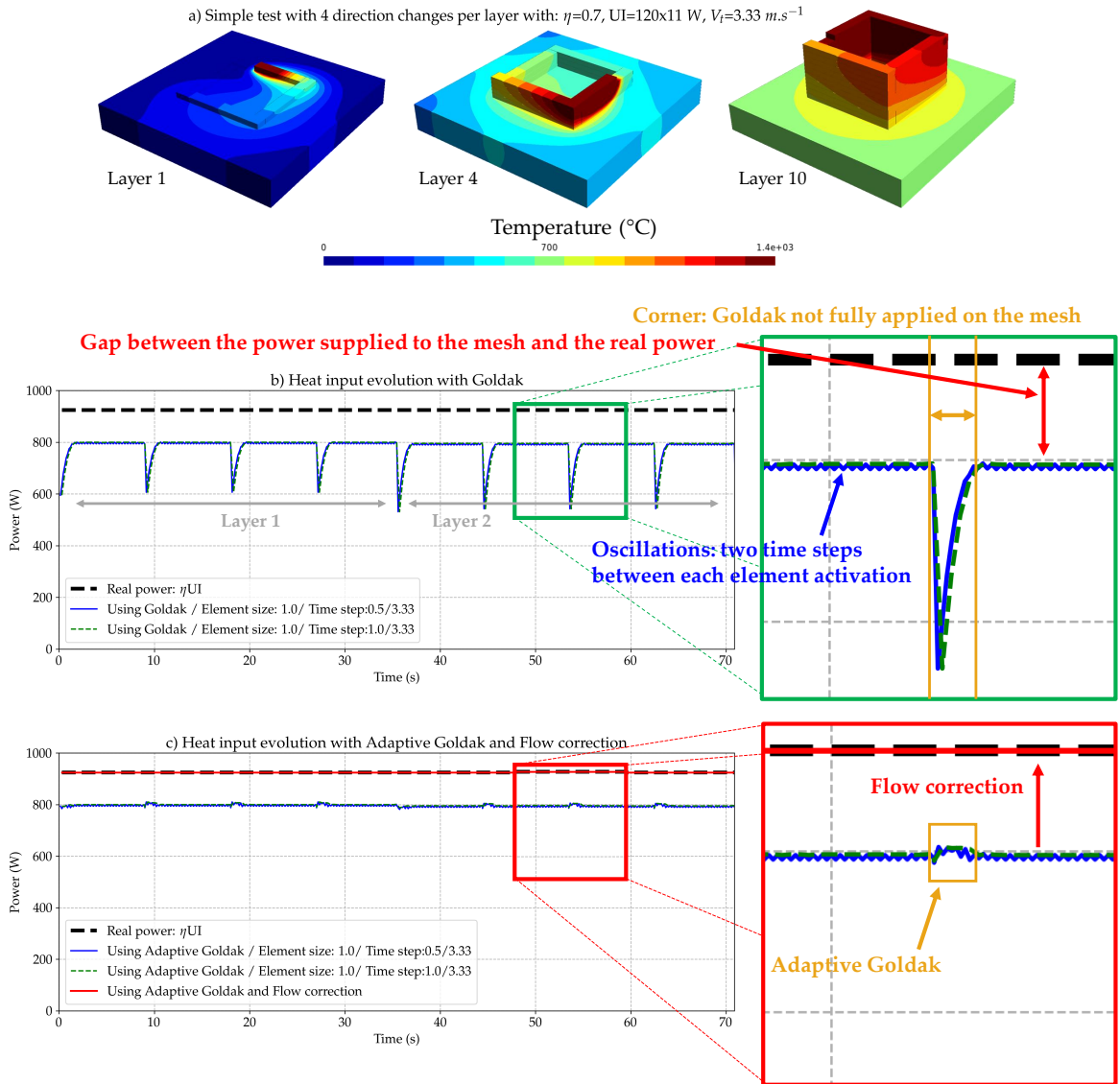


Figure 3.8 – Comparison between the Goldak heat source and the new adaptive Goldak heat source developed.

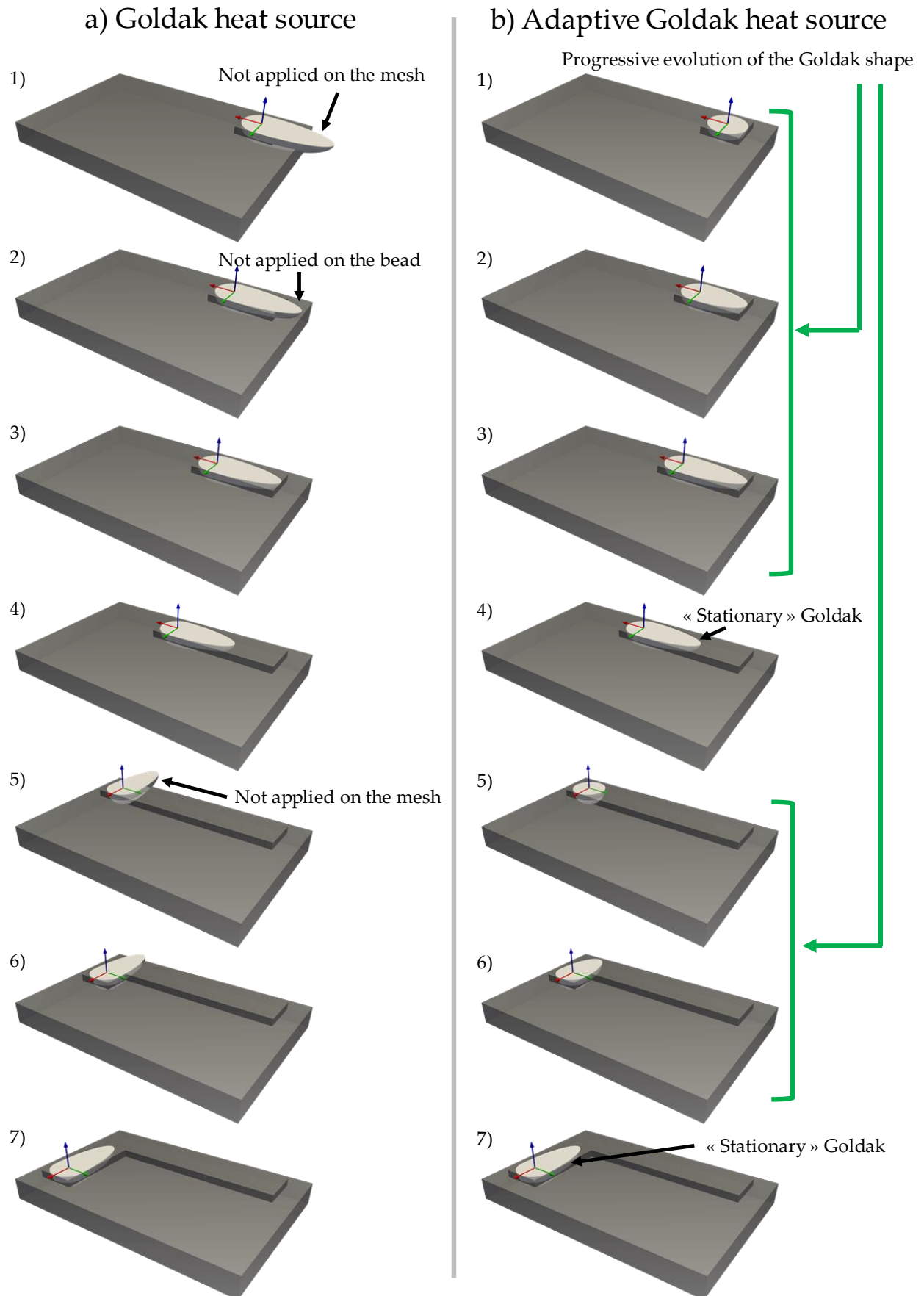


Figure 3.9 – Schematic illustration of the Adaptive Goldak heat source on a simple example.

3.3.2 Boundary conditions

As detailed earlier, most welding and WAAM studies consider the convection and emissivity coefficients to be constant with temperature [127, 61, 150], due to the complexity associated with their measurement. However, for the WAAM process, the tests are much longer than for welding, and the thermal heat accumulation in the manufactured parts is higher, which means that the thermal loss is increasingly influential as the manufacturing process is carried out. Thus, the variation of these parameters with the temperature gradually generates an error that will be progressively propagated during the simulation.

Several approaches for the modeling of the heat losses are presented in Section 2.4.3.2. In this work, the approaches adopted are selected according to the test cases handled: either constant (Equation 3.4) or linear temperature dependant convection and emissivity coefficients, as presented in Equations 3.5 and 3.6 or combined heat losses coefficient (Equations 3.7 and 3.8). The constant heat losses coefficients are defined as follows:

$$h(T) = h_0 \quad \text{and} \quad \varepsilon(T) = \varepsilon_0, \quad (3.4)$$

with h_0 and ε_0 the convection and radiation coefficients, respectively.

For the temperature dependant cases, the following formulation can be proposed:

$$h(T) = h_0 + h_1 \frac{(h_{max} - h_0)}{2000} T, \quad (3.5)$$

$$\varepsilon(T) = \varepsilon_0 + \varepsilon_1 \frac{(\varepsilon_{max} - \varepsilon_0)}{2000} T. \quad (3.6)$$

with h_0 and ε_0 the convection and radiation coefficients at $T = 0^\circ\text{C}$, h_1 and ε_1 parameters between 0 and 1 without unit, and $h_{max} = 120.0$ and $\varepsilon_{max} = 1.0$ respectively the maximum values reachable of $h(T)$ and $\varepsilon(T)$ at a temperature of 2000°C .

Another combined formulation using tanh can also be considered:

$$\begin{aligned} h(T - T_{amb}) + \varepsilon\sigma(T^4 - T_{amb}^4) &= (\varepsilon\sigma(T - T_{amb})(T^2 - T_{amb}^2) + h)(T - T_{amb}) \\ &= f_{loss}(T)(T - T_{amb}) \end{aligned} \quad (3.7)$$

$$f_{loss}(T) = - \left(0.5(c_1 - c_0) \times \tanh \left(\frac{5T}{T_1 - T_0} + \left(2.5 - \left(\frac{5T_1}{T_1 - T_0} \right) \right) \right) \right) + 0.5(c_1 + c_0) \quad (3.8)$$

with c_0 and c_1 two coefficients defining the heat loss coefficient, respectively at T_0 and T_1 .

To illustrate and compare the models, Figure 3.10 represents the values of flux $h(T - T_{amb}) + \varepsilon\sigma(T^4 - T_{amb}^4)$ for temperatures between 0 and 2000°C . For each model, the range presented in the Figure represents the possible values that the model can take on the possible range of variation of these parameters (the ranges of variation are presented in the Appendix D). This shows that all three models are in the same area, and thus possibly relevant. It is apparent that for low temperatures the models are similar, but that at high temperatures there is more variability.

The constant heat losses coefficients modeling is used in the 3rd test case of Chapter 5, which is

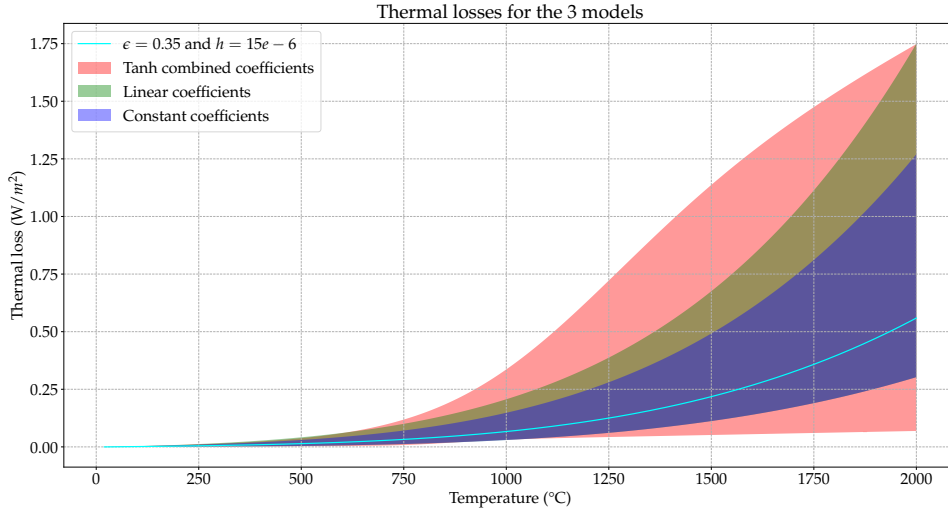


Figure 3.10 – Comparison of the heat losses model (in $\text{W}\cdot\text{mm}^{-2}$): in blue the constant heat coefficients model, in green the linear heat coefficients model, in red the tanh combined model, in cyan the value for $h = 15e - 6$ ($\text{W}\cdot\text{mm}^{-2}\cdot\text{K}^{-1}$) & $\varepsilon = 0.35$ (usually used in literature).

the chapter that focuses on the validation of the model. The linear temperature-dependent heat losses modeling is used for test cases 1 and 2 in this same chapter. Furthermore, a comparative study on the three different (constant, linear, and tanh) approaches is performed in Appendix D on the 2nd test case of Chapter 5. This appendix study focuses on the use of model selection algorithms to get a first idea of the more relevant choice for the modeling of these losses.

In the current work, the clamped zone heat loss is modeled using an increased convection zone (as illustrated in Figure 3.11) such as:

$$q_{cl} = h_{cl}(T - T_{amb}), \quad (3.9)$$

with q_{cl} the heat flux at the clamped zone, h_{cl} ($\text{W}\cdot\text{m}^{-2}\cdot\text{K}^{-1}$) the equivalent convective heat exchange coefficient at the clamped zone, T (K) the temperature, T_{amb} (K) the reference temperature which corresponds to the ambient temperature in general. However, it is important to note that the transfer coefficient is difficult to determine experimentally and requires calibration.

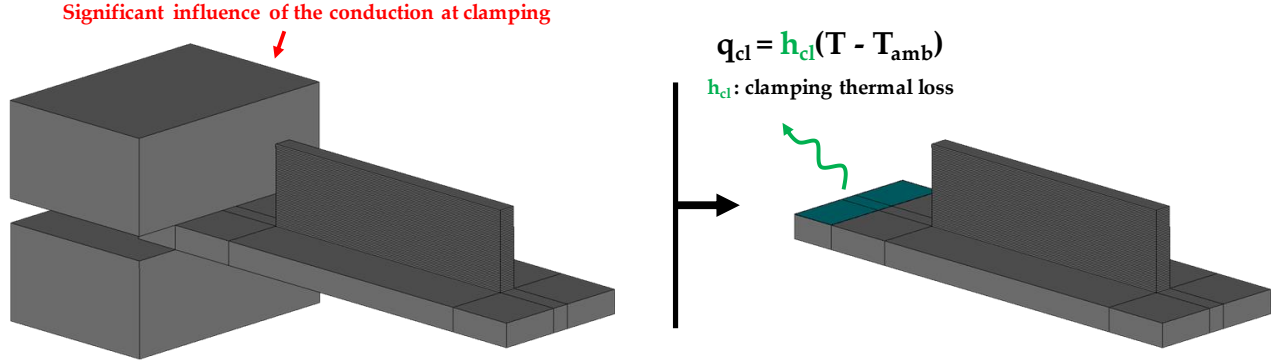


Figure 3.11 – Schematic illustration of the clamping heat loss.

3.3.3 Material deposition

Before the activation of the first elements of the part, the temperature field of the support at the beginning of the simulation is initialized to the ambient temperature T_{amb} , which in the framework of the thesis is equal to 25°C as:

$$T(\underline{x}, 0) = T_{amb} \quad \forall \underline{x} \in \Omega_0. \quad (3.10)$$

As indicated in Section 2.4.3, when activating new elements, an adaptation of the temperature field at the time t_{i-1} must be made to be used as the initial temperature field at the time t_i . First, the thermal field obtained at the previous time step is applied as the initial condition of the previously existing elements. Moreover, new elements are activated at the melting temperature (initial temperature) T_f of the material under study (e.g., about 1400°C for 316L SS) in order to best represent the fact that the material is brought in the liquid state.

$$\left\{ \begin{array}{l} \text{if } \Delta\Omega_i = \emptyset \Rightarrow T(\underline{x}, t_i) = T(\underline{x}, t_{i-1}) \quad \forall (\underline{x}, t) \in \Omega_i \times [0, t_{last}], \\ \text{if } \Delta\Omega_i \neq \emptyset \Rightarrow \begin{cases} T(\underline{x}, t_i) = T(\underline{x}, t_{i-1}) & \forall (\underline{x}, t) \in \Omega_{i-1} \times [0, t_{last}], \\ T(\underline{x}, t_i) = T_f & \forall (\underline{x}, t) \in \Delta\Omega_i \times [0, t_{last}]. \end{cases} \end{array} \right. \quad (3.11)$$

3.3.4 Synthesis of the thermal model parameters

In this section, all the modeling assumptions of the thermal model were described. The parameters considered for the simulations were presented. They can be of different types: process parameters, efficiency, morphological parameters of the source, thermal losses, etc. First, there are manufacturing process parameters:

- d (m), the wire feed diameter,
- U (V), the voltage,
- I (A), the current,
- V_{torch} ($\text{m}\cdot\text{s}^{-1}$), the welding torch speed,
- V_{wire} ($\text{m}\cdot\text{s}^{-1}$), the wire feed speed.

Moreover, the material parameters involved in the thermal model are:

- $\lambda(T)$ ($\text{W.m}^{-1}.\text{K}^{-1}$), the thermal conductivity,
- $H(T)$ (J.m^{-3}), the enthalpy.

The parameters of the equivalent thermal sources are the following:

- a_r and a_f (m), the back and front lengths of the double ellipsoid,
- f_r and f_f , the ratios of the heat flux at the front and the rear of the source,
- b (m), the width of the double ellipsoid,
- c (m), the depth of the double ellipsoid,
- η , the arc efficiency.

Finally, the parameters that govern the thermal losses are:

- h or $h(T)$ ($\text{W.m}^{-2}.\text{K}^{-1}$), the convective coefficient,
- ε or $\varepsilon(T)$, the emissivity of the material,
- h_{cl} ($\text{W.m}^{-2}.\text{K}^{-1}$), the thermal loss coefficient at the clamped zone.

Nevertheless, some of the parameters are either poorly known because they are difficult to access experimentally or unknown because they cannot be measured. Among all the parameters, the process parameters are considered known. Indeed, they are generally known at the beginning of the test. Although there are oscillations of these parameters during the test, the nominal values remain close to those supplied to the robot or generator. As for the material parameters of 316L SS (enthalpy $H(T)$ and conductivity $\lambda(T)$), these parameters are considered accurately characterized based on previous studies. Therefore, the data sets provided by EDF, presented in Table 3.1, are used. The determination of the parameters involved in the source model is crucial, complex, and requires a calibration step using experimental data [43, 144]. The methodology developed to access these parameters will be the aim of the Chapter 4.

This section focuses on the thermal modeling hypothesis as well as on the parameters of the thermal model. First, in order to account for the time delays and the changes of direction of the torch, an equivalent double ellipsoid thermal source with an adaptive shape is proposed. Moreover, in order to make sure that the heat input is constant, accurate, and independent of the time step or spatial discretization throughout the simulation, a flux correction is performed. Linear temperature dependent dissipation coefficients are considered to take into account the heat accumulation in WAAM manufactured part, especially when large dimensions are involved. However, a key issue in the modeling is that some parameters, such as the equivalent heat source parameters, are unknown because they cannot be measured. Therefore, these parameters must be calibrated.

3.3.5 Examples

To illustrate the possible uses of the thermal model, Figures 3.12 and 3.13 present two examples of complex applications of the thermal model on workpieces of interest for EDF. Figure 3.12 presents three different instants of a thermal simulation performed on pipes with two different deposition patterns: scanning (Figure 3.12-a) and circular (Figure 3.12-b). These figures highlight the difference in heat accumulation in the parts and the difference in molten pool size for the two manufacturing strategies. Figure 3.13 presents another example: the thermal simulation of the PPB at a scale of 1:5.

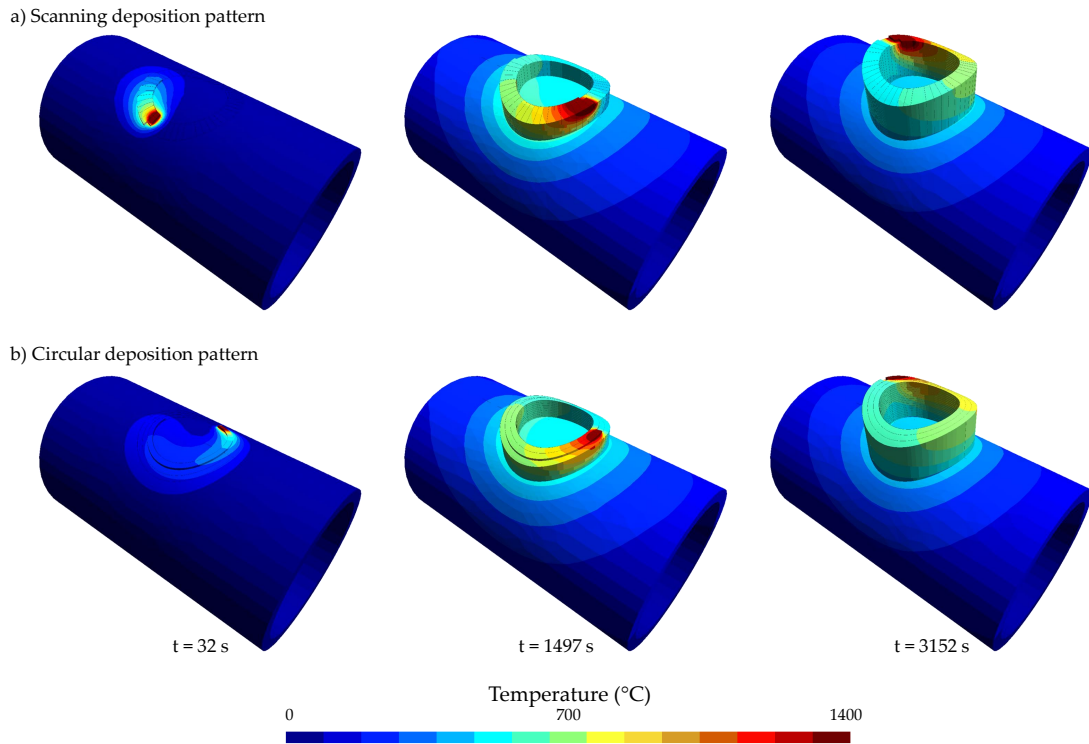


Figure 3.12 – Thermal simulations of two pipes made with different deposition patterns at three instants (32 s, 1497 s and 3152 s): a) Scanning deposition pattern, b) Circular deposition pattern.

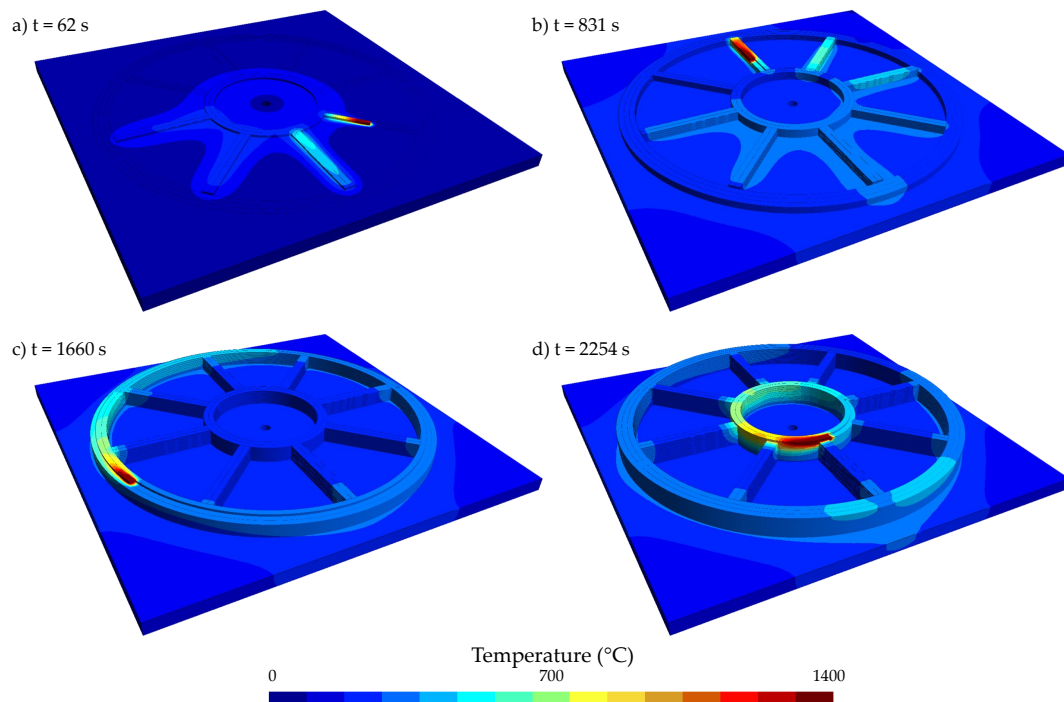


Figure 3.13 – Thermal simulation of the PPB at 1:5 scale at four instants (62 s, 831 s, 1660 s and 2254 s).

3.4 Mechanical model

In Chapter 2, the general formulation of the non-linear and quasi-static mechanical problem was described. This formulation is accompanied by the selection of a constitutive behavior model defined by temperature-dependent parameters. In this PhD work, the weld metal is considered as identical to parent which is a reasonable approximation. Its important to specify that these constitutive behavior models have not been fitted on the same experimental dataset, and potentially do not match the same material.

In this section, the mechanical modeling choices are presented. Indeed, some aspects of the process require particular attention, such as the fact that part of the mesh is in a liquid phase, and that the activation of the elements is made progressively. Like most studies in the thermo-mechanical literature, the assumption of small deformations is used. As mentioned before, according to the small deformation hypothesis, the deformation tensor is decomposed into several parts, which in the present case are the thermal part, the elastic part, and the plastic part:

$$\underline{\underline{\varepsilon}}^{tot} = \underline{\underline{\varepsilon}}^e + \underline{\underline{\varepsilon}}^{th} + \underline{\underline{\varepsilon}}^p \text{ (or } vp) \quad \forall (\underline{x}, t) \in \Omega_i \times [0, t_{last}], \quad (3.12)$$

$$\underline{\underline{\varepsilon}}^{th} = \alpha(T)(T - T_{ref})\underline{\underline{1}} \quad \forall (\underline{x}, t) \in \Omega_i \times [0, t_{last}], \quad (3.13)$$

$$\underline{\underline{\sigma}} = \underline{\underline{\mathcal{C}}} : \underline{\underline{\varepsilon}}^e \quad \forall (\underline{x}, t) \in \Omega_i \times [0, t_{last}]. \quad (3.14)$$

To define ε_e , it is therefore necessary to estimate ε_p .

The material parameters for the elastic behavior (which are Young's modulus, Poisson's ratio and yield strength), as well as the coefficient of thermal expansion, are presented in Table 3.2 for 316L SS.

Table 3.2 – Evolution of Young’s modulus, Poisson ratio, yield strength, and thermal dilation coefficient with temperature.

Temperature (°C)	Young’s modulus (MPa)	Poisson ratio	Thermal dilation coefficient (K ⁻¹)	Yield strength (MPa)
20	197000	0.296	15.9 × 10 ⁻⁶	287.
25	- ^a	0.296	- ^a	- ^a
100	- ^a	0.298	16.25 × 10 ⁻⁶	- ^a
200	184000	0.304	16.70 × 10 ⁻⁶	198.
300	176500	- ^a	17.10 × 10 ⁻⁶	172.
400	168000	0.315	17.40 × 10 ⁻⁶	157.
500	160000	0.320	17.90 × 10 ⁻⁶	152.
600	151500	0.323	18.30 × 10 ⁻⁶	145.
700	142500	0.326	18.50 × 10 ⁻⁶	136.
800	130000	0.330	18.80 × 10 ⁻⁶	127.
900	108000	0.336	19.10 × 10 ⁻⁶	115.
1000	81500	0.339	19.40 × 10 ⁻⁶	79.
1100	20000	0.346	19.60 × 10 ⁻⁶	30.
1200	3000	0.349	19.90 × 10 ⁻⁶	20.
1300	- ^a	0.353	- ^a	- ^a
1390	- ^a	0.353	- ^a	- ^a
1400	501	- ^a	- ^a	20.
1420	- ^a	0.353	20.0 × 10 ⁻⁶	- ^a
1450	- ^a	0.353	20.0 × 10 ⁻⁶	- ^a
3000	501	0.353	20.0 × 10 ⁻⁶	20.

^a Interpolated value.

3.4.1 Plasticity model

As established in Section 2.4.4.2, the modeling of the plastic behavior is one of the most critical points, and more specifically the hardening model. Different constitutive behavior models historically used for welding are available and have been characterized at EDF for the 316L SS. In the context of this thesis, the implementation and calibration of constitutive behavior laws is not an objective. The used models are presented in this section in increasing order of complexity: linear and nonlinear isotropic hardening, kinematic hardening, mixed hardening, Chaboche elastoplastic model, and Chaboche elasto-viscoplastic model.

The deviation operator \underline{s} is defined as:

$$\underline{s} = \underline{\sigma} - \frac{1}{3}Tr(\underline{\sigma})\underline{1}, \quad (3.15)$$

and the equivalent stress of Von Mises is expressed as follows:

$$J_2(\underline{\sigma}) = \sqrt{\frac{3}{2}s_{ij}s_{ij}} = \sqrt{\frac{1}{2}((\sigma_1 - \sigma_2)^2 + (\sigma_2 - \sigma_3)^2 + (\sigma_3 - \sigma_1)^2)}. \quad (3.16)$$

3.4.1.1 Elastoplastic behavior with isotropic hardening

A constitutive behavior law based on isotropic hardening takes into account the increase of the elastic range proportionally to the plastic strain. This way of modeling the hardening does not take into account the Bauschinger effect, since the load surface remains centered in 0. This type of hardening is generally highly suitable in monotonic loading calculations but does not allow a good representation

of cyclic phenomena.

Isotropic hardening can be defined in several ways. It can be chosen linear (called VMIS_ISOT_LINE model on Code_Aster), piecewise linear based on tensile curves (VMIS_ISOT_TRAC model). The definition of isotropic hardening relies on the choice of the expression for the hardening function $R(p)$. Table 3.3 summarizes the equations of the model, where \underline{s} is the deviation operator, $J_2(\underline{\sigma})$ is the equivalent stress (Von Mises), p is the cumulative plastic strain, and $R(p)$ is the isotropic hardening function.

Table 3.3 – Linear & Piecewise linear isotropic hardening elasto-plastic model.

Yield function	$f(\underline{\sigma}, p) = J_2(\underline{\sigma}) - R(p) \leq 0$	(3.17)
Flow function	$\underline{\dot{\varepsilon}}^p = \dot{\lambda} \frac{\partial f}{\partial \underline{\sigma}} = \frac{3}{2} \dot{\lambda} \frac{\underline{s}}{J_2(\underline{\sigma})}$ with $\dot{\lambda} = \dot{p}$	(3.18)
Hardening function	Linear hardening:	
	$R(p) = \frac{EE_T}{E - E_T} p + \sigma_y$	(3.19a)
	Piecewise linear hardening:	
	$R(p) = \frac{\sigma_{i+1} - \sigma_i}{p_{i+1} - p_i} (p - p_i) + \sigma_i$	(3.19b)

In conclusion, there are 2 internal variables for this type of constitutive behavior law: V_1 the cumulative plastic strain ε_{eq}^p and V_2 the plasticity indicator (0 = purely elastic and 1 = plastic).

The VMIS_ISOT_LINE model or bilinear material assumption relies on a linear isotropic hardening function. This function takes as input a hardening coefficient E_T (in MPa). On the other hand, VMIS_ISOT_TRAC model relies on a piecewise linear (or non-linear) isotropic hardening function. This function can be deduced from several stress-strain tensile curves (one for each temperature). Its expression is given in Equation 3.19, where (p_{i+1}, σ_{i+1}) are the points of the stress-strain curves. The parameters of the linear isotropic and piecewise linear hardening laws are presented in Table 3.4 and Table 3.5.

Table 3.4 – Linear isotropic hardening parameter E_T as a function of the temperature.

Temperature (°C)	E_T (MPa)
20	286.
200	212.
400	180.
600	137.
800	139.
1000	70.
1100	35.
1200	16.
1300	10.
1500	10.

Table 3.5 – Piecewise linear isotropic hardening parameter: stress (MPa) depending on temperature (°C) and cumulative plastic strain (%).

Temperature °C	Cumulated plastic strain p					
	0.0%	0.01%	0.05%	0.2%	1%	2%
20	287	315	419	561	1200	1656.5
200	198	231	334	470	1000	1401
300	172	201	307	451	900	1264
400	157	186	294	435	599	820
500	152	179	282	419	550	749
600	145	170	262	387	500	677.5
700	136	161	212	340	400	532
800	127	152	199	294	350	461.5
900	115	137	161	169	180	212.5
1000	79	83	97	100	105	118
1100	30	32	33	34	35	36
1200	20	22	23	24	25	26
1400	20	21	22	23	24	25
3000	20	21	22	23	24	25

3.4.1.2 Elastoplastic behavior with kinematic hardening

Unlike isotropic hardening, kinematic hardening corresponds to a translation of the center of the elastic domain. This type of hardening model allows taking into account the Bauschinger effect but does not represent well the effects of cyclic strengthening (isotropic part of the hardening). It is assumed in kinematic hardening that the initial plasticity surface translates without deforming in the stress space during plastic loading. Linear kinematic hardening is defined by the tensor $\underline{\chi}$, which characterizes the center of the loading surface. In this section, an elastoplastic constitutive behavior with linear kinematic hardening relying on a criterion of the Von Mises type is presented. Table 3.6 summarizes the equations of the model, where C is the Prager coefficient (in MPa) which reflects the isotropic/kinematic part of the hardening, and E_T (in MPa) is the gradient of the tensile curve in the plastic state. The model associated with this type of hardening on Code_Aster is the VMIS_CINE_LINE model.

The parameter of the linear kinematic hardening law is presented in Table 3.7.

In conclusion, there are 7 internal variables for the constitutive behavior laws with kinematic

Table 3.6 – Linear kinematic hardening elasto-plastic model.

Yield function	$f(\underline{\underline{\sigma}}, \underline{\underline{\chi}}) = J_2(\underline{\underline{\sigma}} - \underline{\underline{\chi}}) - \sigma_y \leq 0$	(3.20)
Flow function	$\underline{\underline{\dot{\varepsilon}}}^p = \dot{\lambda} \frac{\partial f}{\partial \underline{\underline{\sigma}}} = \frac{3}{2} \dot{\lambda} \frac{\underline{\underline{\sigma}} - \underline{\underline{\chi}}}{J_2(\underline{\underline{\sigma}} - \underline{\underline{\chi}})}$ with $\dot{\lambda} = \dot{p}$	(3.21)
Hardening function	$\underline{\underline{\chi}} = C \underline{\underline{\varepsilon}}^p = \frac{2}{3} \frac{EE_T}{E - E_T}$	(3.22a)

Table 3.7 – Kinematic hardening constitutive behavior parameters as a function of the temperature (VMIS_CINE_LINE): the Prager coefficient C .

Temperature (°C)	C (MPa)
20	2.4×10^3
700	2.4×10^3
800	2.35×10^3
900	1.5×10^3
1000	0.8×10^3
1100	0.725×10^3
1200	0.150×10^3
1300	0.010×10^3

hardening: $V_{1,\dots,6}$ the 6 components of the kinematic hardening tensor χ and V_7 the plasticity indicator (0: purely elastic and 1: plastic)

3.4.1.3 Elastoplastic behavior with mixed hardening

It has been shown that for simulations with a cyclic loading, in which tensile/compressive stress states can follow each other in each cycle, it is imperative to consider a kinematic part of the hardening. Therefore, in practice, models that combine isotropic and kinematic hardening are used for many metallic materials. This section presents a combined hardening with a kinematic and isotropic linear part. Table 3.8 summarizes the model equations, where $\underline{\underline{\chi}}$ is the kinematic hardening tensor χ , C is the Prager coefficient (in MPa), which reflects the isotropic/kinematic part of the hardening, and E_T (in MPa) is the gradient of the tensile curve in the plastic state.

The parameter of the mixed hardening law is presented in Table 3.9. There are 8 internal variables for the Prager mixed model VMIS_ECMI_LINE: V_1 the cumulative plastic strain ε_{eq}^p , V_2 the plasticity indicator (0 = purely elastic and 1 = plastic), $V_{3,\dots,8}$ the 6 components of the kinematic hardening tensor $\underline{\underline{\chi}}$.

Table 3.8 – Mixed isotropic hardening elasto-plastic model.

Yield function	$f(\underline{\sigma}, \underline{\chi}, R(p)) = J_2(\underline{\sigma} - \underline{\chi}) - R(p) \leq 0$	(3.23)
Flow function	$\underline{\dot{\epsilon}}^p = \dot{\lambda} \frac{\partial f}{\partial \underline{\sigma}} = \frac{3}{2} \dot{\lambda} \frac{\underline{\sigma} - \underline{\chi}}{J_2(\underline{\sigma} - \underline{\chi})}$ with $\dot{\lambda} = \dot{p}$	(3.24)
Hardening function	$\underline{\chi} = C \underline{\epsilon}^p$	(3.25a)
	$R(p) = \frac{EE_T}{E - E_T} p + \sigma_y$ with $E_T < E$	(3.25b)

 Table 3.9 – Mixed hardening constitutive behavior parameters as a function of the temperature (VMIS_ECMI_LINE): the Prager coefficient C .

Temperature (°C)	C (MPa)
20	1.2×10^3
700	1.2×10^3
800	1.17×10^3
900	0.75×10^3
1000	0.4×10^3
1100	3.625×10^2
1200	0.750×10^2
1300	0.50×10^1

3.4.1.4 Elastoplastic & elasto-viscoplastic Chaboche constitutive behavior

The Chaboche type behavior laws are the most complex laws at our disposal. These laws allow taking into account the cyclic behavior of the material, with a nonlinear kinematic hardening tensor, a part of nonlinear isotropic hardening, and the Bauschinger effect. These constitutive behaviors are much more complex to characterize than the laws presented above and thus require more experimental tests. Table 3.6 summarizes the model equations which involve the following quantities:

- $\underline{\chi}_1$ the 1st kinematic hardening tensor,
- $R(p)$ (MPa) defines the isotropic part of the hardening,
- R_0 (MPa) the yield stress without cumulative plastic deformation,
- R_∞ (MPa) the yield stress with infinite cumulative plastic deformation,
- b a parameter that defines the variation of $R(p)$ with respect to p ,
- α_1 is defined with $C_1(p)$ (in MPa),
- $\gamma_1(p)$ the coefficient relating to the kinematic tensor of the material,
- and where b and w are assumed to be positive coefficients.

The VISC_CIN1_CHAB model is the elasto-viscoplastic version of the Chaboche VMIS_CIN1_CHAB constitutive behavior. It is similar to the elasto-plastic version. The addition of viscosity is modeled

Table 3.10 – Chaboche hardening elasto-plastic & elasto-viscoplastic model.

Yield function	$f(\underline{\underline{\sigma}}, \underline{\underline{\chi}}_1, R(p)) = J_2(\underline{\underline{\sigma}} - \underline{\underline{\chi}}_1) - R(p) \leq 0$	(3.26)
	$\dot{\underline{\underline{\epsilon}}}^p = \dot{\lambda} \frac{\partial f}{\partial \underline{\underline{\sigma}}} = \frac{3}{2} \dot{\lambda} \frac{(\underline{\underline{\sigma}} - \underline{\underline{\chi}}_1)}{J_2(\underline{\underline{\sigma}} - \underline{\underline{\chi}}_1)}$	(3.27a)
Flow function	Elasto-plastic: $\dot{p} = \dot{\lambda}$	(3.27b)
	Elasto-viscoplastic: $\dot{p} = \left(\frac{\langle f \rangle}{K} \right)^N$	(3.27c)
	$R(p) = R_\infty + (R_0 - R_\infty)e^{-bp}$	(3.28a)
Hardening function	$\underline{\underline{\chi}}_1 = \frac{2}{3} C_1(p) \alpha_1$	(3.28b)
	$\dot{\alpha}_1 = \dot{\underline{\underline{\epsilon}}}^p - \gamma_1(p) \alpha_1 \dot{p}$	(3.28c)
	$C_1(p) = C_1^\infty (1 + (k - 1)e^{-wp})$	(3.28d)
	$\gamma_1(p) = \gamma_1^0 (a_\infty + (1 - a_\infty)e^{-bp})$	(3.28e)

by replacing the coherence condition presented previously by the equation below using a Norton-type model 3.27c (a special case of Perzyna's flow rule). The notation $\langle f \rangle$ denotes the Macaulay brackets, which correspond to the positive part of f . K and N are two viscosity parameters of the material.

In this work, only the one-variable kinematic laws will be considered (CIN1_CHAB type model). Although the two-variable laws are certainly more precise, the differences they might induce are negligible given all the other assumptions and manipulations carried out in the simulations. Therefore, as a first approximation, it is not necessary to consider them. The parameters of the elasto-plastic Chaboche and elasto-viscoplastic Chaboche constitutive behaviors are presented in Table 3.11 and Table 3.12. The number of internal variables for the Chaboche's constitutive laws is 8: V_1 the cumulative plastic strain p , V_2 the plasticity indicator ($0 =$ purely elastic and $1 =$ plastic), $V_{3,\dots,8}$ the 6 components of the 1st kinematic hardening tensor $\underline{\underline{\chi}}_1$.

Table 3.11 – Elastoplastic Chaboche constitutive behavior parameters as a function of the temperature (VMIS_CIN1_CHAB), $\gamma_1^0 = 727.6$, $b = 2.74$, $k = 1$, $w = 0$, $a_\infty = 0$.

Temperature (°C)	R_0 (MPa)	R_∞ (MPa)	C_1^∞ (MPa)
20	138.	1154.	138.
275	136.	966.	136.
550	92.	818.	92.
750	80.	800.	80.
900	78.	712.	78.
1000	67	139.	67.
1100	10.	25.	10.
1300	5.	6.	5.
1500	2.	2.	2.

 Table 3.12 – Elasto-viscoplastic Chaboche constitutive behavior parameters as a function of the temperature (VISC_CIN1_CHAB), with $k = 1$, $w = 0$, $a_\infty = 1$.

Temperature (°C)	R_0 (MPa)	R_∞ (MPa)	b	K	N	C_1^∞ (MPa)	γ_1^0
20	60.	130.	130.	151.	24.	30.0×10^3	350.
600	10.	80.	80.	150.	12.	20.0×10^3	300.
775	9.2	79.4	79.4	179.	12.8	8.12×10^3	279.
850	2.4	19.8	19.8	298.	7.06	1.324×10^3	154.
1000	1.0	15.8	15.8	192.	5.25	0.2446×10^3	26.3
1150	0.2	0.2	0.2	111.	4.98	0.0×10^3	26.3
1250	0.1	0.1	0.1	70.	4.91	0.0×10^3	26.3

3.4.2 Hardening annealing

In the calculations, the hardening annealing is introduced at high temperatures. This hardening annealing operation consists in modifying the internal variables, such as the cumulated plastic strain and the tensor components that describe the hardening, by multiplying them by a coefficient between 0 and 1 that depends on the temperature. The impact of hardening annealing on stresses is identified as potentially important in the case of austenitic SS. Indeed, previous experimental tests [33] highlight a significant hardening annealing in a temperature range around 600-1000°C. Therefore, in this study, the hardening annealing begins at 600°C, and the annealing is considered total at 1000°C. The evolution of the hardening annealing coefficient with temperature is shown in Figure 3.14. It should be noted that other studies suggest that for the 316L SS, any annealing model should not take effect until 800°C or above on the timescales associated with conditions in the heat affected zone [151, 135].

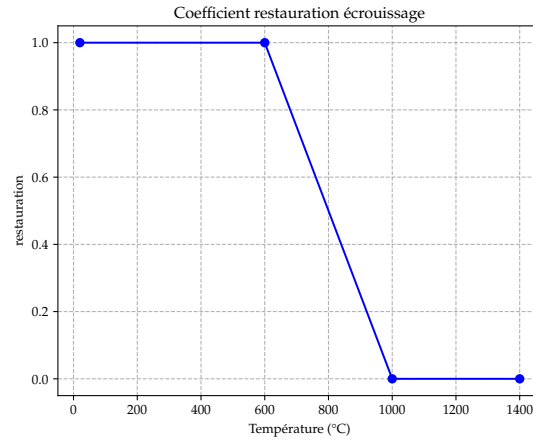


Figure 3.14 – Hardening annealing coefficient as a function of temperature: below 600 °C, no hardening annealing and above 1000 °C complete hardening annealing.

3.4.3 Material deposition

In the context of a mechanical calculation, the fields requiring adaptation are displacements, stresses, and internal variables.

■ **Stress field:** As mentioned earlier, when adding elements to the thermal model, the elements are activated at the melting temperature of the material under study (1400°C for 316L SS) in order to represent the fact that the material is brought in a liquid state. This means that the material is mechanically "virgin". The newly activated elements are therefore stress-free.

■ **State variables field:** In the same way as for the stresses, there is no hardening of the material in the liquid state. Therefore, the associated internal variables V^i are initialized at 0.

■ **Displacement field:** During the mechanical calculation, if the elements are activated in their reference configuration, unrealistic deformations due to the non-accommodation of the deformation of adjacent elements are observed. Therefore, when adding elements, a linear elastic calculation is performed on the new domain by applying the displacement field at the previous time step on all nodes already present as boundary conditions. The calculation is performed with a Poisson's ratio ν very close to 0.5 to be in the quasi-incompressibility state, and thus respect the conservation of the volume of the material deposited. Moreover, a reference temperature equal to the melting temperature is applied to the newly brought elements to calculate the thermal deformations. Indeed, the activated elements represent the material brought in liquid form with a "virgin" deformation beforehand. These elements will then progressively cool down and contract. Therefore, the displacements are initialized between two-time steps as follows:

$$\begin{cases} \text{if } \Delta\Omega_i = \emptyset \Rightarrow \underline{u}^i(\underline{x}) = \underline{u}^{i-1}(\underline{x}) & \forall \underline{x} \in \Omega_i \\ \text{if } \Delta\Omega_i \neq \emptyset \Rightarrow \begin{cases} \underline{u}^i(\underline{x}) = \underline{u}^{i-1}(\underline{x}) & \forall \underline{x} \in \Omega_{i-1} \\ \underline{u}^i(\underline{x}) = \underline{U}^*(\underline{x}) & \forall \underline{x} \in \Delta\Omega_i \end{cases} \end{cases} \quad (3.29)$$

Moreover, the linear elastic calculation needed to obtain an initial state are the following:

$$\begin{cases} \text{div } \underline{\sigma} = 0 & \forall x \in \Omega_i \\ \underline{\sigma} = \lambda \text{tr}(\underline{\varepsilon})I + 2\mu\underline{\varepsilon} \\ \underline{\varepsilon} = \frac{1}{2}(\nabla\underline{u} + \nabla^T\underline{u}) \\ \underline{u}_i = \underline{u}_{i-1} & \forall x \in \Omega_{i-1} \\ \underline{u}_i \cdot \vec{n} = 0 & \forall x \in \Delta\Omega_i \end{cases} \quad (3.30)$$

with:

$$\lambda = \frac{E\nu}{(1+\nu)(1-2\nu)} \quad (3.31)$$

$$\mu = \frac{E}{2(1+\nu)} \quad (3.32)$$

The parameters E and ν are chosen to respect the conservation of the volume of the newly activated elements $\Delta\Omega_i$. For the Young's modulus, it is chosen arbitrarily, for example, the value of the Young's modulus of 316L SS at room temperature, which is 197 000 MPa. The Poisson ratio is set at $0.499 \sim 0.5$. The proposed material deposition method is evaluated in the 1st test case in Chapter 5.

3.4.4 Molten pool mechanical reset

At each time step, the state of stress of the elements above the melting point (in the case of austenitic 316L SS, approximately 1400°C) and the state variables are reinitialized (reset to zero). In fact, since the molten pool is liquid, the notion of mechanical stress does not exist, the history of this zone is reset, and the material returns to a "virgin" mechanical state:

$$\text{if } \Omega_i^{\text{liquid}} \neq \emptyset \Rightarrow \begin{cases} \begin{cases} \underline{\sigma}^i(\underline{x}) = \underline{\sigma}^i(\underline{x}) & \forall \underline{x} \in \Omega_i^{\text{solid}} \\ \underline{\sigma}^i(\underline{x}) = 0 & \forall \underline{x} \in \Omega_i^{\text{liquid}} \end{cases} \\ \begin{cases} V^i(\underline{x}) = V^i(\underline{x}) & \forall \underline{x} \in \Omega_i^{\text{solid}} \\ V^i(\underline{x}) = 0 & \forall \underline{x} \in \Omega_i^{\text{liquid}} \end{cases} \end{cases} \quad (3.33)$$

3.4.5 Reference temperature change

One of the parameters of the models is the reference temperature for the calculation of thermal deformations. For the substrate, this reference temperature is the ambient temperature, taken in this case to be 25 °C. This implies that, at 25 °C, the thermal deformation is equal to zero, and that the deformation increases as the temperature increases.

Regarding the material deposited, the reference temperature of the elements must be different. Indeed, when the elements are "activated", they are activated with an initial temperature of 1400 °C

to represent the fact that they are in the liquid state. They have a "blank" mechanical state in the liquid phase, with zero stress. However, the molten material shrinks as it cools down, and compressive stresses appear. However, if the reference temperature of these elements is taken to be 25 °C, these elements will be subjected to tensile stresses. Therefore, the reference temperature of the deposited elements is set to be the melting temperature (Figure 3.15-a).

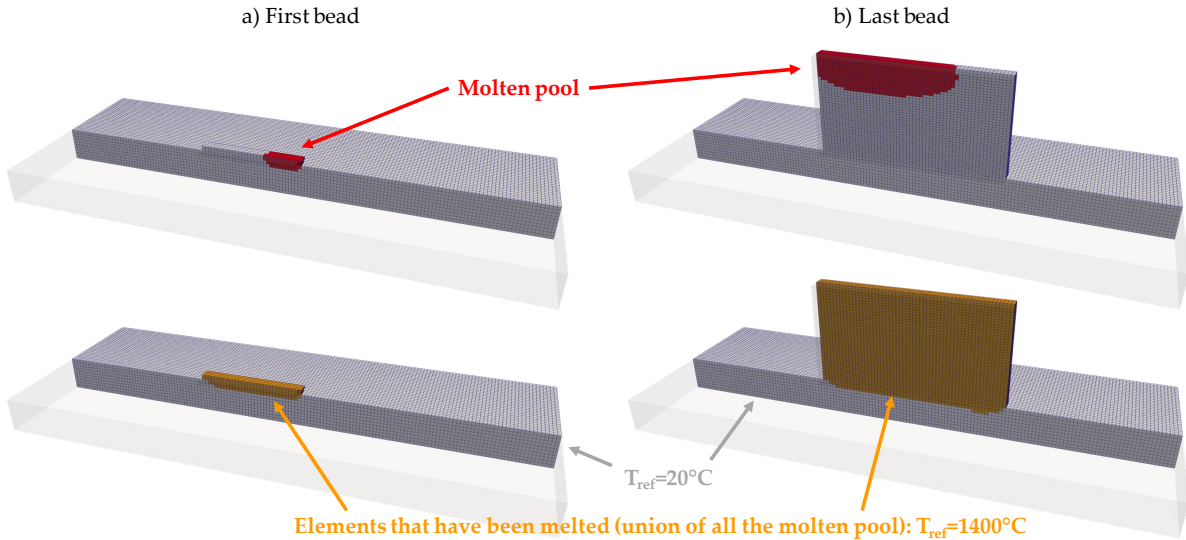


Figure 3.15 – Reference temperature: a) configuration with a reference temperature of 1400 °C on the elements of the deposited material, b) configuration where all the elements that passed the melting temperature threshold have a reference temperature of 1400 °C.

In addition, one more adaptation is made. When elements of the substrate (with a reference temperature of 25 °C) go above the melting point, the mechanical state can also be considered "mechanically blank". Then, during the cooling phase, the material in liquid form becomes solid again by contracting progressively. The new reference temperature for these elements is thus set to be the melting temperature (Figure 3.15-b).

In conclusion, during the manufacturing process, the reference temperature of the elements above the melting temperature is changed. This only concerns the elements of the base plate since the elements deposited are activated with a reference temperature set at the melting temperature. Nevertheless, this manipulation remains to be justified phenomenologically and numerically.

3.4.6 Cut-off temperature

The material's mechanical properties are very weak at very high temperatures close to the melting temperature. These properties, which are close to zero and generally extended by interpolation, can cause oscillations or convergence issues in the area of very high temperatures.

■ **Field "cut-off":** The first method that can be used to solve this issue is to simply manipulate the temperature field by considering a cut-off temperature set at the melting temperature. This means that all temperatures above the melting temperature are considered equal to the melting temperature. This manipulation is not problematic from a mechanical point of view since, above the melting temperature,

the mechanical state of the material is zero.

A lower cut-off temperature can be chosen. This manipulation consists in defining a temperature above which the material is considered sufficiently ductile (or having sufficiently weak properties) to solve the mechanical problem only on this zone of the mesh. The decrease of the material properties at high temperatures coupled to the hardening recovery model used can justify the definition of a cut-off temperature for these properties. This cut-off temperature can be considered as the temperature from which no change in material properties is considered. The study of Tekriwal et al. [152] shows that there is less than 15% error on the residual stresses for cut-off temperatures between 600 °C and the melting temperature. This study has also shown that an overestimation of the stresses can be observed for lower cut-off temperatures. For this method of "field cut-off", the manipulation of the thermal field is thus carried out at each time step.

■ **Mesh "cut-off"**: Another more drastic approach can be undertaken. The non-linear mechanical calculation is performed only on the elements below the cut-off temperature. Thus, if a cut-off temperature of 600 °C is identified as valid, very large numbers of meshes can be removed from the non-linear resolution, in addition to an improvement in convergence. For the elements removed from the non-linear mechanical computation, as for the material input, the stresses and internal variables are reset to zero, and the displacement field is obtained by an elastic calculation. For the "mesh cut-off" method, the elements below the threshold are identified at each time step.

In the following, a simple test case, presented in Figure 3.16, is considered to illustrate this mesh cut-off temperature. The simulated case is a 20 beads wall of 50 mm length deposited with a "Zigzag" pattern. The part is clamped on both sides of the base plate. The thermo-mechanical simulation is carried out for different cut-off temperatures: 700 °C, 800 °C, 900 °C, 1000 °C, 1100 °C, 100 °C, 1300 °C. For each of these values, the error on the stresses is calculated with respect to the reference simulation. The reference simulation is taken to be the simulation with a temperature "field cut-off" of 1400 °C. Figure 3.16 shows for each cut-off temperature, the "mesh cut-off" temperature at the last time steps of the 20th bead, and the Von Mises stress field after cooling of the wall to room temperature. The first finding is that, qualitatively, the cut-off temperatures that seem to give a stress field close to the reference simulation are 1300 °C, 1200 °C, and perhaps 1100 °C. For each cut-off isotherm, the reduction in computation time is also estimated. Figure 3.16 shows the error on the stresses (Von Mises equivalent stress) and the associated time-saving. For a cut-off temperature of 1100 °C, an error of the order of 3.5 MPa is observed on the Von Mises stresses for a reduction in computation time of 14%.

The drawback of the mesh cut-off temperature approach for the mechanical resolution is the fact that its use is not compatible with the material deposition model developed in Section 3.2. This method is therefore used for very long simulations of massive workpieces with low deformations. Indeed, in this case, this method improves the convergence of the calculations and reduces the calculation times without having a significant influence on the deformations. On the contrary, for high deformation simulations, the "mesh cut-off" is not recommended for a good prediction of the workpiece morphology.

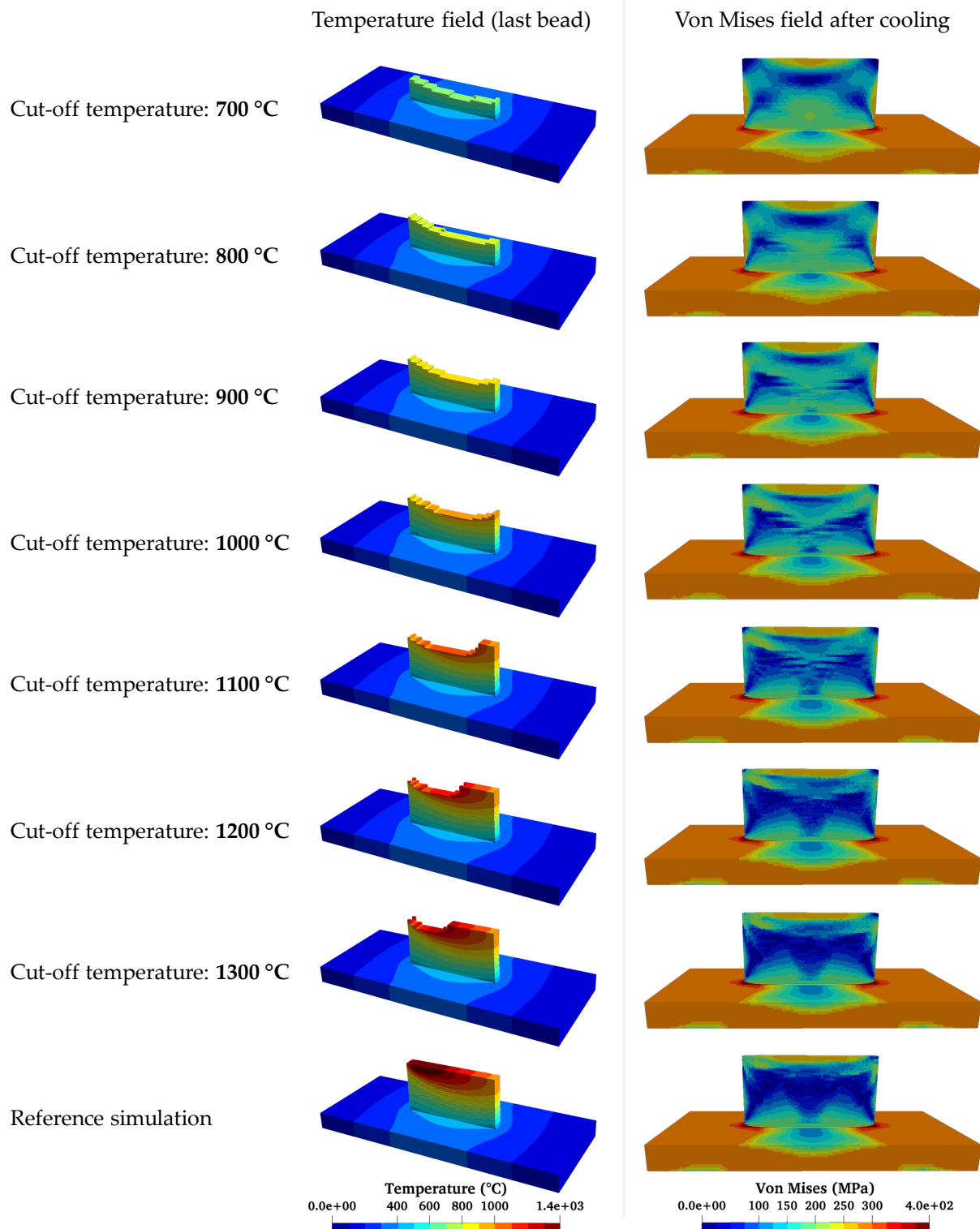


Figure 3.16 – Thermo-mechanical simulations performed using the "mesh cut-off" method for different temperature isotherms: on the left column the temperature field on the cut mesh on which the resolution of the nonlinear mechanical problem is performed, on the right column the residual stress field after complete cooling of the workpiece.

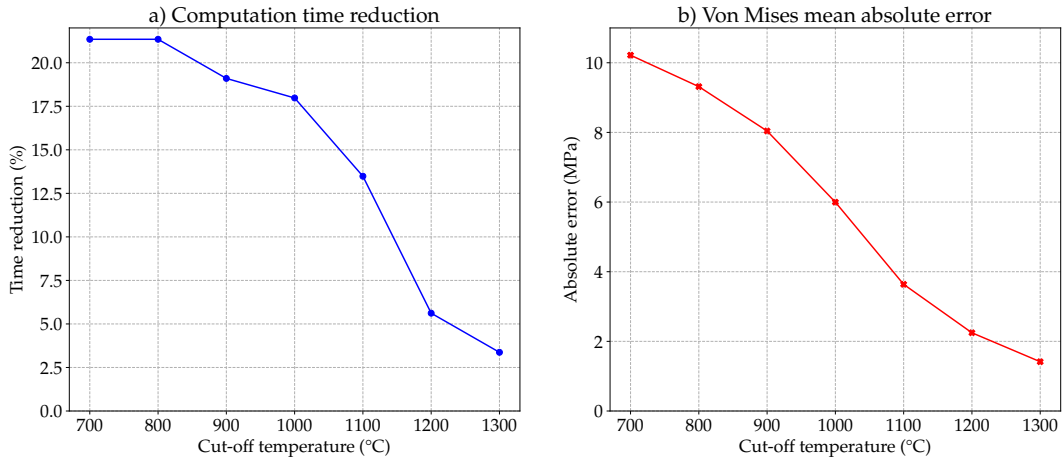


Figure 3.17 – Evolution of the residual stress error (Von Mises mean absolute error) and the reduction of the computational time of the simulations with temperature mesh "cut-off" with respect to the reference simulation presented in Figure 3.16.

3.4.7 Examples

As for the thermal model, to illustrate the possible uses of the mechanical model, Figure 3.18 presents the two pipes application examples presented in Figure 3.12. The Figure represents the Von Mises residual stresses fields after cooling to ambient temperature. As can be qualitatively seen, for the same process parameters, the stress field is not similar for the two different paths. It can be seen that the stresses with a circular deposition pattern are smaller.

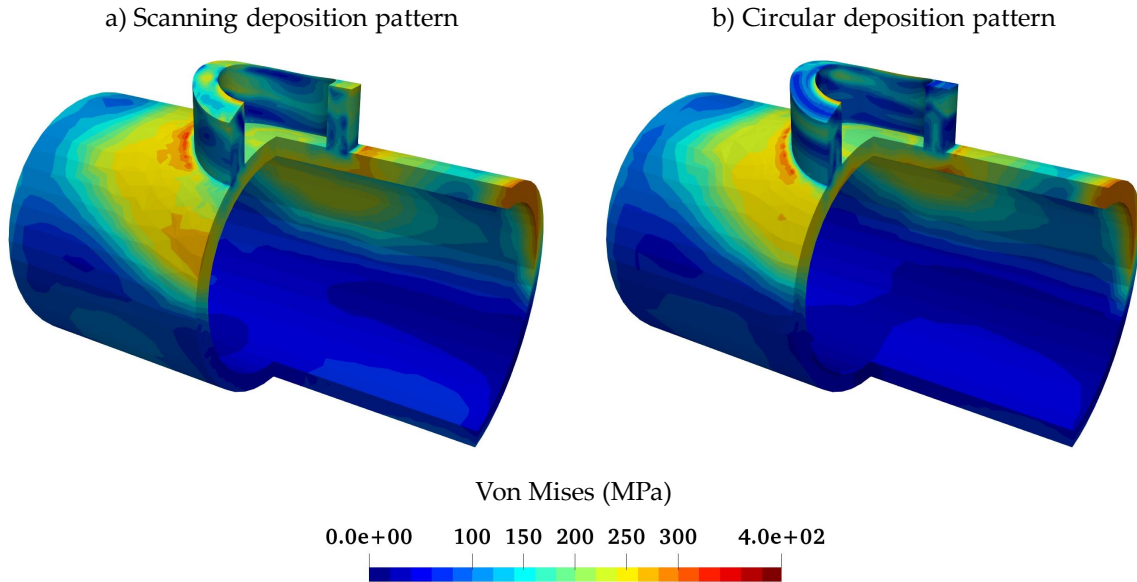


Figure 3.18 – Thermo-mechanical simulations of two pipes made with different deposition patterns after cooling to ambient temperature: a) Scanning deposition pattern, b) Circular deposition pattern.

3.5 Conclusion & perspectives

In the first section of this chapter, the material deposition approach selected is described. The main objective is to implement robust tools that can generate a great variety of geometries and configurations.

In the second section, the modeling hypothesis of the thermal model and all the thermal parameters considered are presented. An equivalent double ellipsoid thermal source with an adaptive shape is proposed. The advantage of such a source is better to understand the time delays and the changes of direction. Moreover, throughout the simulation, a flux correction step is performed to ensure an appropriate heat input that is constant and independent of the time step or of the spatial discretization. For the boundary conditions, an approach with linear temperature-dependent dissipation coefficients is chosen to take into account the heat accumulation in the workpiece during a WAAM fabrication. However, some parameters of the thermal model, such as the equivalent heat source parameters, are unknown because they cannot be measured and need to be optimized. The calibration methodology put in place to adjust these parameters is thoroughly described in Chapter 4.

In the last section of this chapter, the implemented mechanical model is presented. First, the general formulation of the mechanical problem and all the associated equations are described. The different constitutive behaviors of the material and the parameters associated with these models are introduced. The aspects related to the modeling of the process are then described. First, the hardening recovery is taken into account in addition to the material behavior. Moreover, a complete reset of the stress state in the molten pool is performed at each time step. In addition, the reference temperature for the calculation of thermally induced deformation is changed for the elements that have reached the melting temperature. Furthermore, a new methodology for managing the material deposition is proposed based on the computation of an elastic calculation with boundary conditions to take into account the welding torch path. Finally, several approaches of temperature cuts are introduced to simplify the resolution of the mechanical problem, improve the convergence of the calculations, and reduce the computational times.

Chapter 4 presents the methodology for setting up a digital twin of thermal simulations for the calibration of thermal model parameters from experimental data. In Chapter 5, the model associated with the different modeling aspects presented in this chapter will be evaluated through 4 experimental tests. Indeed, the thermo-mechanical should be validated before using it for numerical prediction.

3.6 In a nutshell

Material deposition approach

- Development of a geometry and mesh generation tool (using Salome-Meca) from a manufacturing path file.
- Presentation of the geometric parameters of the beads (derived from the process parameters: wire feed speed, wire feed diameter, welding path and welding torch speed).
- Implementation of the "Quiet element" method for material deposition.

Proposed thermal model

- Use of an enthalpy formulation to take into account the latent heat phenomena of solid/liquid state transition.
- Development of a new equivalent heat source: adaptive Goldak (double ellipsoid) to better manage the complex deposition patterns.
- Monitoring and adjustment of the heat input at each time step.
- Selection of temperature-dependent heat loss coefficients: emissivity $\varepsilon(T)$ and convection $h(T)$.
- Consideration of the thermal dissipation at the clamping location as forced heat loss h_{cl} .

Proposed mechanical model

- Computation of the quasi-static non-linear mechanical problem.
- Presentation of multiple constitutive behaviors:
 - Elasto-plastic behavior with linear and piecewise isotropic hardening,
 - Elasto-plastic behavior with linear kinematic hardening,
 - Elasto-plastic behavior with mixed hardening,
 - Elasto-plastic Chaboche constitutive behavior,
 - Elasto-viscoplastic Chaboche constitutive behavior,
- Development of a material deposition method to take into account the welding path.
- Consideration of hardening annealing & mechanical reset in the molten pool.
- Change in the reference temperature of the elements reaching the melting temperature.
- Proposition of two cut-off temperatures: "field" and "mesh".

Chapter 4

Digital twinning for mesoscopic model calibration

Contents

4.1	Introduction	76
4.2	Problem description	76
4.3	State of the art	77
4.4	Surrogate model approach: Sparse Polynomial Chaos Expansion	78
4.4.1	Theoretical presentation of chaos polynomials	79
4.4.2	Construction steps	81
4.4.3	Sensitivity analysis	84
4.4.4	Conclusion	85
4.5	Bayesian parameter estimation	86
4.5.1	Introduction	86
4.5.2	Bayesian inference	86
4.5.3	Monte Carlo Markov Chain (MCMC) sampling	87
4.5.4	Inverse problem step-by-step instructions	89
4.6	Example for the application of the method	90
4.7	Conclusion & perspectives	92
4.8	In a nutshell	93

4.1 Introduction

In this section, a methodology of digital twinning is developed, which features a novel calibration method for the thermal model meant to simulate heat diffusion during the WAAM process.

The thermal model implemented is presented in Chapter 3. It is now necessary to calibrate and validate it experimentally to ensure its representativeness, reliability, and performance. In this section, a fast calibration method is proposed to allow engineers to tune thermal models from experimental data. Indeed, numerical simulations require the definition and identification of specific parameters for each simulation. These parameters characterize the system under investigation, such as the material conductivity or density and the limiting conditions of the model. Moreover, since the thermal field is used as an input for the metallurgical and the mechanical calculations, it is impossible to correctly account for the stresses, the strains and the microstructure without a reliable thermal modeling. However, one of the major sources of uncertainty of the thermal model comes from the representation and calibration of the heat input. Indeed, for the most part, the parameters of the heat source models are unknown, often not directly measurable, and, if measured, their values may be subject to uncertainties.

This chapter focuses on the determination of the unknown parameters taken as inputs for the thermal models. The general objective of this chapter is to develop a robust methodology of digital twinning using a "standardized" test case to calibrate the thermal model based on the resolution of an bayesian inverse problem. This method allows determining an optimized set of parameters, as well as the probability distribution of thermal parameters, from experimental thermal data, such as thermocouple profiles.

The main points covered in this chapter are therefore:

- **Problem description:** Description of the thermal model parameters calibration methodology using experimental thermal data,
- **Digital twinning:** Implementation of a surrogate model using Sparse Polynomial Chaos Expansion PCE,
- **Parameters calibration:** Resolution of a bayesian inverse problem using MCMC Adaptive Metropolis-Hasting algorithm.

4.2 Problem description

It is necessary to identify the "well-known" parameters, the parameters to be adjusted, and any assumptions that can be made on these parameters. In the context of this study, the parameters related to the process (voltage, current, speed of the torch, etc...), which are parameters provided to the generator or the robot, are considered to be "well-known". Although they can fluctuate very slightly during manufacture, their nominal values remain close to those defined at the start of the manufacturing process. In addition, the materials studied (in the case of this report, 316L SS) are considered to be well characterized by EDF based on several previous studies [33, 153]. Therefore, the physical parameters related to the material, and more particularly, the enthalpy (or the density and the specific heat) and the conductivity (which are temperature dependent) are considered well characterized.

On the other hand, other parameters need to be adjusted. They will be referred to as "unknown" parameters. They can be of different natures. First, some parameters are considered poorly known,

since their measurement is difficult and can be uncertain. This is the case for the thermal loss parameters. Other parameters are not directly measurable since they represent non-physical quantities. This is the case for the morphological parameters of the equivalent thermal source: a_r or a_f , f_r or f_f , b , and c , the efficiency η which is often chosen by an empirical law defined by experts [154, 155], and the thermal transfer coefficient at the clamping h_{cl} . The focus of this section is on the estimation of these "unknown" parameters.

Of all the parameters, the heat input plays the most crucial role in the temperature distribution in a part. Determining the parameters involved in the models of the equivalent thermal sources described in Section 3.3 is not easy. It requires a calibration step on experimental data, such as continuous temperature measurements at various positions within the part (thermocouples, laser pyrometer), the thermal surface field (thermal imaging), the shape of the melted zone or the HAZ (Heat Affected Zone) based on macrographies. In this manuscript, the experimental data used for the calibration are temperature profiles obtained by thermocouples (in Appendices B and F, other approaches are tested). Therefore, when reference is made to the experimental data in this section, it is therefore referred to as thermocouples temperature profiles.

4.3 State of the art

Several approaches exist to identify the various parameters of the thermal model in welding or additive manufacturing. In several studies, they use data sets found in the literature, or do not specify the origin of their parameter values. In most studies, the parameters are defined according to data found in the literature, empirical laws, or without specifying the origin of the parameter values [156, 102, 48, 154, 155]. Another calibration methodology used is the so-called "trial-and-error" approach. For example, a first approach for the determination of the parameters of the Goldak source relies on the shape of the molten pool extracted from macrographs. This approach consists in considering that the dimensions of the molten pool are the parameters: the length, the depth, as well as the width, are used to fix the coefficients a_f , a_r , b , and c of the double ellipsoid (Goldak model) [70]. Nevertheless, this method remains imprecise given that the Goldak source is in no way the molten pool but an equivalent model to represent the interactions between the molten pool and the electric arc. In addition, during WAAM manufacturing, the size of the molten pool fluctuates significantly over time. In the absence of other data, Goldak et al. [110] recommend to consider a_f equal to half of the molten zone depth and a_r equal to double of the depth [101].

Some other studies use the inverse problem approach. For example, Unnikrishnakurup et al. [43] established a multi-physics modeling of a static gas tungsten arc welding (TIG) operation. The authors modeled the heat input with a surface heat source with a Gaussian distribution. Two parameters had to be estimated: the efficiency of the arc and the radius of the source. An inverse problem was carried out in order to calibrate these parameters based on experimental data. Moreover, in their study, Bai et al. [144] presented a new approach to calibrate the input parameters. This approach is based on the solution of the thermal inverse problem using thermal camera images. The parameters of the equivalent heat source a_r , c , and η and of the combined heat transfer coefficient are optimized (the other parameters are fixed). The average layer temperature and the cooling rate are used to compare the results between the thermal images and the simulation. Finally, the validity of this inverse model approach is demonstrated by performing a different experimental test but with similar

process parameters. Fu et al. [157] determined the temperature distribution and the size of the molten pool using an analytical thermal model with a Goldak source for different sets of parameters. From these data, a neural network was set up to predict the equivalent heat source parameters from experimental results. Lastly, in their study, Azar et al. [158] use an analytical model to solve the inverse problem. They showed that the set of parameters obtained after calibration using an analytical model on the shape of the fusion line, can be applied to finite element numerical simulations. This allows them to avoid a very large computational time since the analytical model is not very computationally expensive. Nevertheless, this approach has some limitations. The main one is that the calibration is done on a bead-on-plate configuration, which may not be sufficient for the calibration of the parameters for additive manufacturing, which is a longer process.

In general, an inverse problem can be considered as an optimization problem. This optimization problem consists in minimizing or maximizing a defined cost function. To solve this problem, several numerical methods or types of algorithms exist. The solution of an inverse problem is potentially accompanied by several difficulties. First of all, the data available to solve the problem is of primary interest. A lack of data can lead to an inverse problem that can generate several solutions: several parameter sets can generate the same observations (non-unicity of the solution). In addition, the available data, which in this study are data of experimental origin, have noise. In a second step, the cost function to minimize can have local minima. The optimization method can therefore converge to any of these local minima, and not find the global minimum. Finally, the algorithms for solving the inverse problem require many iterations. At each iteration, the cost function is computed, which means that a numerical simulation of the thermal problem is performed at each iteration. This operation can be very computationally expensive.

To overcome this drawback, a methodology based on Sparse Polynomial Chaos Expansion (PCE) is used in the current work. The advantage of this approach lies in the construction of a digital twin (or surrogate model) for the FEM simulations. Based on this surrogate model, unlike the FEM simulations, it would be possible to have an instantaneous prediction of the temperature field for a set of input parameters. Therefore, the optimization step performed for the determination of a suitable set of parameters from the experimental data, which may require many iterations, will be carried out quickly using the metamodel constructed.

First, a brief presentation of the theory of sparse PCE is given. After that, the surrogate model construction methodology is detailed. Subsequently, the bayesian inverse problem approach is explained, and the MCMC is introduced. Then, the calibration step is presented. Finally, the validation step is described. To this end, in the following, a "generic" methodology to find the set of "unknown" parameters is described, with as objective to minimize the difference between the experimental data available and the predictions obtained by the thermal model.

4.4 Surrogate model approach: Sparse Polynomial Chaos Expansion

Optimization or calibration methods often require a very large number of iterations and, therefore, of simulations. For example, in the configurations presented in this thesis, the FE thermal simulations require several hours of calculation, making direct use of the thermal model unrealistic. Therefore, an alternative to this is the use of a surrogate model.

A surrogate model (metamodel) is a mathematical function approximating the response of a physical numerical model, of negligible computational cost and allowing to predict with a good accuracy new responses. The aim of the surrogate model is to make accurate predictions of some outputs of the original model at a negligible cost. It is built from a sample of results of numerical simulations for different sets of input parameters defined beforehand using a design of experiments. For the construction of the surrogate model, the numerical simulation model can be used as a "black box". To set up the surrogate model, a limited number of simulations of the original numerical model are needed. For a sample of input parameters, finite elements numerical simulations are performed, and quantities of interest are extracted.

The surrogate model is then constructed in order to predict these quantities of interest given a set of input parameters. A well-constructed surrogate model is an accurate approximation of the original model with almost instantaneous predictions. It is thus a perfect alternative if many calls to the original numerical code are needed to extract the defined quantities of interest. This characteristic will be exploited for the resolution of the inverse problem from the observed experimental data. However, it is necessary to evaluate the precision of the surrogate model because parameters estimation will depend on the precision of the approximation. This method has been used in various fields and for various applications [159, 160]: calibration, sensitivity analysis or propagation of uncertainties, etc. Among the disadvantages of this approach is the difficulty to build a good approximation of the model. There are many surrogate model types: polynomial regression, neural networks, kriging also called gaussian process, polynomial chaos expansion, and many others. . . In this report, only PCE will be presented. Indeed, the latter is often quite simple to set up and can be built from a reasonable number of simulations (a few hundred). The purpose of this section is to give a brief theoretical description of Polynomial Chaos Expansion and then apply it to construct a surrogate model [161].

The use of a surrogate model has many advantages. In general, for welding, the simulations are relatively simple, either in terms of simulated physical times or simplified configurations (2D, for example), which are synonymous with low computation times. Therefore, the calibration of the parameters of the models is usually performed by directly running simulations. For the WAAM process, it would also be possible to simulate only a small part of the test, considering or not a simplified configuration. However, unlike multi-pass welding, some parameters can evolve and eventually become more and more influential over time. Therefore, it is necessary to model a large part of the test to capture these effects. The calibration phase will thus be carried out on several beads in the real configuration. Although not very costly individually in terms of calculation time (between several tens of minutes and several hours per simulation), running multiple simulations consecutively becomes considerably costly in terms of computational time if the number of iterations needed to calibrate the model is high.

4.4.1 Theoretical presentation of chaos polynomials

Let p denote the number of parameters that must be identified. The vector \mathcal{X} represents the input parameters of the numerical model. In the case considered here, the quantities extracted from the thermal model to generate the metamodel are vectors representing the temperature evolution in several nodes of the mesh. For vectorial output, the same procedure is performed for each point of the output. To simplify notations, this value \mathcal{Y} is considered as a scalar output.

The PCE is a method that consists in developing an integrable square function based on a orthonormal polynomial basis according to the measures of the inputs [162, 163]. For example, let \mathcal{X} be a set of p independent random variables with a probability density function (PDF) such that:

$$f_{\mathcal{X}}(x) = \prod_{i=1}^p f_{\mathcal{X}_i}(x_i). \quad (4.1)$$

Considering $\mathcal{Y} = \mathcal{M}(\mathcal{X})$ the quantity of interest of the physical numerical model, it is shown that if \mathcal{Y} has a finite variance, it can be expressed as an infinite sum of orthonormal basis functions such that:

$$\mathcal{Y} = \mathcal{M}(\mathcal{X}) = \sum_{\alpha \in \mathbb{N}^p} a_{\alpha} \psi_{\alpha}(\mathcal{X}), \quad (4.2)$$

with $\psi_{\alpha}(\mathcal{X})$, $\alpha \in \mathbb{N}^p$ the polynomial chaos basis: multivariate polynomials orthonormal with respect to the probability density of the parameters, and a_{α} the coefficients to be determined. The construction of the orthonormal polynomial basis is performed in several steps. First, the multivariate polynomial basis is defined as a product of the univariate polynomial of each parameter, where $\alpha = (\alpha_1, \dots, \alpha_p)$ is a multi-index, written as follows:

$$\psi_{\alpha}(x) = \psi_{(\alpha_1, \dots, \alpha_p)}(x) = \prod_{i=1}^p \pi_{\alpha_i}^{(i)}(x_i), \quad (4.3)$$

with the degree of $\|\alpha\|_1 = \sum_{i=1}^p \alpha_i$.

For each input parameter \mathcal{X}_i , a family of univariate orthonormal polynomials is identified with respect to the probability density of the parameters. Indeed, the type of polynomials chosen depends only on the probability density function of the parameters to satisfy the orthonormality condition:

$$\langle \pi_j^{(i)}, \pi_k^{(i)} \rangle = \int \pi_j^{(i)}(x_i) \pi_k^{(i)}(x_i) f_{\mathcal{X}_i}(x_i) dx_i = \delta_{jk}. \quad (4.4)$$

For example, for a parameter with a gaussian distribution, Hermit polynomials are chosen, and for a parameter with a uniform distribution, the Legendre polynomials are selected. Once the basis functions have been identified, the next step is to truncate the polynomial to a limited number of terms. In practice, the truncation strategy selects all the polynomials of degrees less than or equal to a certain degree d . The decomposition is thus defined by:

$$\mathcal{Y} = \mathcal{M}(\mathcal{X}) = \sum_{\alpha \in \mathbb{N}^p} a_{\alpha} \psi_{\alpha}(\mathcal{X}) = \sum_{\{\alpha \in \mathbb{N}^p: \|\alpha\|_1 \leq d\}} a_{\alpha} \psi_{\alpha}(\mathcal{X}) + \varepsilon, \quad (4.5)$$

where ε represents all the terms not considered. The number of terms P , which is a function of the number of variable p and the degree d of truncation, is defined as follows:

$$P = \frac{(p+d)!}{p!d!}. \quad (4.6)$$

Moreover, since α is a multi-index, a strategy for enumeration of the terms of the sum must be chosen. The next step is to define the coefficients a of the polynomial. Consider a set of values taken by the input vector (i.e., an experimental design) and the corresponding model evaluations such as:

- $\{\mathcal{X}^{(j)} \in \mathbb{R}^p, j = 1, \dots, n\}$ the Design Of Experiment (DoE),
- $\{\mathcal{Y}^{(j)} = \mathcal{M}(\mathcal{X}^{(j)}), \mathcal{Y} \in \mathbb{R}^n\}$ the model responses with respect to the DoE.

\mathcal{Y} can be written using the following matrix notation:

$$\mathcal{Y} = \mathcal{M}(\mathcal{X}) = \sum_{\alpha \in \mathbb{N}^p} a_{\alpha} \psi_{\alpha}(\mathcal{X}) = \sum_{\{\alpha \in \mathbb{N}^p: \|\alpha\|_1 \leq d\}} a_{\alpha} \psi_{\alpha}(\mathcal{X}) + \varepsilon = \Psi a + \varepsilon, \quad (4.7)$$

with:

- $\Psi \in \mathbb{R}^{n(P+1)}$ and $\Psi_{ij} = \psi_i(\mathcal{X}^{(j)})$,
- $a \in \mathbb{R}^{P+1}$.

The coefficients a_{α} are then determined by the least-squares method. This minimization problem can be reduced to the resolution of the following linear system:

$$\tilde{a} = \underset{a}{\operatorname{argmin}} \|\mathcal{Y} - \Psi a\|_2 = (\Psi^T \Psi)^{-1} \Psi^T \mathcal{Y}. \quad (4.8)$$

One of the drawbacks of the PCE approach is that the number of coefficients increases significantly with the number of parameters and the order of truncation of the polynomials. The higher the number of coefficients to be determined, the greater the number of evaluations of the model necessary to implement the model: this is referred to as the curse of dimensionality. The approach of Sparse PCE coefficient vectors is determined through sparse regression, which, in addition to a good regression fit, requires the solution to be sparse. In order to construct Sparse PCE, a \mathcal{L}_1 regularization is performed by adding a penalty term (LAR-LASSO) that can significantly reduce the number of coefficients:

$$\tilde{a} = \underset{a}{\operatorname{argmin}} (\|\mathcal{Y} - \Psi a\|_2 + \lambda \|a\|_1). \quad (4.9)$$

4.4.2 Construction steps

To summarize, the general methodology used to elaborate a surrogate model is the following:

Surrogate model methodology

1. Identification of the p parameters to be calibrated and their range of variation,
 2. Generation of a design of experiments of n samples using a sampling method,
 3. Run of numerical thermal simulations for the n sets of parameters generated previously,
 4. Construction of the surrogate model based on the n numerical simulations,
 5. Validation of the surrogate model using cross-validation,
 6. Exploitation of the surrogate model: prediction, sensitivity analysis, calibration ...
-

4.4.2.1 Unknown parameter identification step

All the parameters needed for the thermal simulations are identified and presented in Section 3.3. First, there are manufacturing process parameters:

- d (m), the wire diameter,

- U (V), the voltage,
- I (A), the current,
- V_{torch} (m.s⁻¹), the welding torch speed,
- V_{wire} (m.s⁻¹), the wire feed speed.

Moreover, the material parameters involved in the thermal model are:

- $\lambda(T)$ (W.m⁻¹.K⁻¹), the thermal conductivity,
- $H(T)$ (J.m⁻³), the enthalpy.

The parameters of the equivalent thermal sources (in the general case of the Goldak source) are the following:

- a_r and a_f (m), the back and front lengths of the double ellipsoid,
- f_r and f_f , the ratios of the heat flow at the front and the rear of the source,
- b (m), the width of the double ellipsoid,
- c (m), the depth of the double ellipsoid,
- η , the arc efficiency.

Finally, the parameters that govern the thermal losses are:

- h or $h(T)$ (W.m⁻².K⁻¹), the convective coefficient,
- ε or $\varepsilon(T)$, the emissivity of the material,
- h_{cl} (W.m⁻².K⁻¹), the thermal loss coefficient at the clamped zone.

Among all the parameters, the process parameters are considered known. Indeed, they are generally known at the beginning of the test. Although there are oscillations of these parameters during the test, the nominal values remain close to those supplied to the robot or generator. As for the material parameters of 316L SS (enthalpy $H(T)$ and conductivity $\lambda(T)$), these parameters are considered accurately characterized based on previous studies. The parameters that are likely to be subject to calibration are the parameters of the thermal equivalent heat source and the thermal losses.

4.4.2.2 Design of Experiments (DoE) generation step: Sobol' sequences

The objective of the Design of Experiments (DoE) is to generate parameter sets in a domain of interest and to optimize their distribution in the input parameter space in order to maximize the accuracy of the surrogate model [164]. Several sampling methods exist. The most known is the Monte Carlo (MC) sampling technique, where a random sample of n points is generated from the joint distribution of the input variable. The disadvantage of this method is that it can be inefficient. Indeed, if the number of draws is not sufficient, the distribution of draws may not be balanced, and some intervals within the space get no samples, as illustrated in Figure 4.1-a. More suitable space-filling approaches exist based on criteria like the distance between points or the uniformity, such as the discrepancy. The LHS, for Latin Hypercube Sampling, is an optimized sampling method. The general idea is to spread the n points across all possible values of the input parameter. To do so, the range of each input variable is divided into intervals, and one point is selected for each interval [165, 166]. Finally, the Sobol' sequences are low discrepancy quasi-random sampling methods that fill the space in a highly uniform

manner [167]. As shown in Figure 4.1-b, this method gives way more uniform sample distribution than a Monte Carlo sampling for the same number of draws.

The privileged method in this manuscript is the method of Sobol sequences with low discrepancy. In general, it should be noted that it is recommended to choose a sample size that is a power of 2 for the Sobol sequences to have the most balanced distribution. For this step of generation of the design of experiments, the opensource library dedicated to uncertainty quantification, Openturns [168], partly developed by EDF, is used.

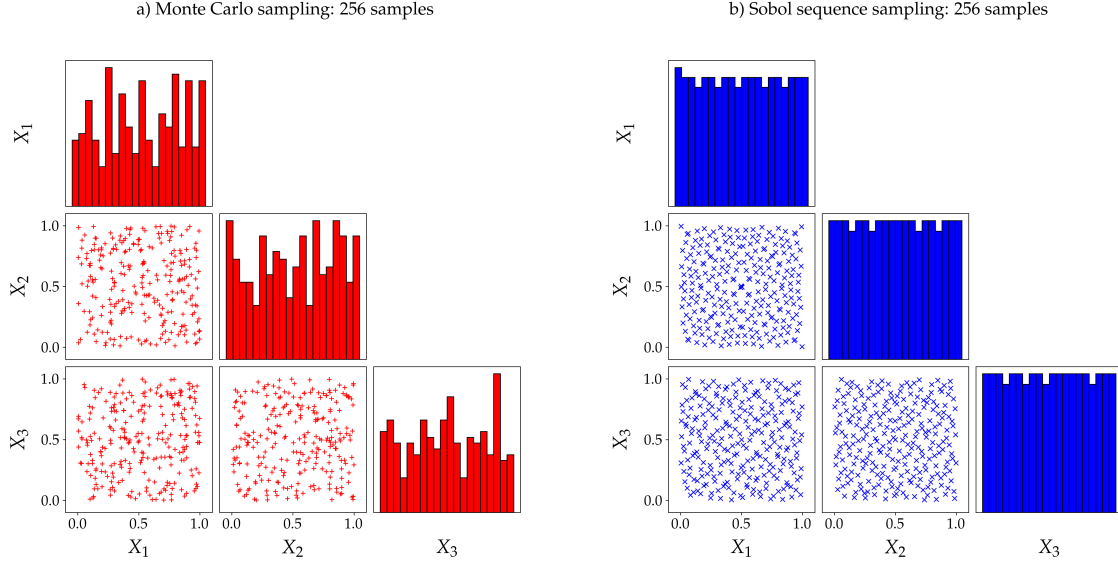


Figure 4.1 – Design Of Experiment examples using Monte Carlo sampling method and the Sobol's sequences. The input parameters \mathcal{X} are independent random variables ($p = 3$) uniformly distributed: $\mathcal{X} = (\mathcal{X}_1, \mathcal{X}_2, \mathcal{X}_3)$, $\mathcal{X}_i \sim \mathcal{U}(0, 1)$, $i = 1, \dots, 3$.

4.4.2.3 Validation step: Cross-validation

Now that the method used to build the substitution model has been described, it is necessary to develop a method to validate the constructed metamodel. To do this, the error estimator R^2 is used:

$$R^2 = 1 - \frac{\sum_{j=1}^n (\mathcal{Y}^{(j)} - \tilde{\mathcal{Y}}^{(j)})^2}{\sum_{j=1}^n (\mathcal{Y}^{(j)} - \bar{\mathcal{Y}}^{(j)})^2}, \quad (4.10)$$

with $\mathcal{Y}^{(j)}$ the dataset (of size n) used for the validation of the metamodel, $\tilde{\mathcal{Y}}^{(j)}$ the predicted value using the metamodel, and $\bar{\mathcal{Y}}^{(j)}$ the mean of the validation dataset. R^2 ranges from 0 to 1 with R^2 equal to 1 when the fitted metamodel predicts perfectly the data.

In general, the metamodel is not built on the whole dataset to keep a subset for the metamodel validation. Indeed, we should not use training data to validate the model to avoid the possible overfitting of the metamodel. Overfitting is the fact that the metamodel fits perfectly to the data used for its construction but gives poor predictions outside these data. Several approaches are possible

to validate the accuracy of a metamodel. The first approach is to divide the dataset to build the metamodel into two sets: a set for learning and a set for validation. 70-80% of the dataset is generally kept for metamodel training. The remaining 20 to 30% will be used to validate the model. However, generally, the dataset is limited. In addition, another disadvantage of this method is that part of the data is "lost" (not used for the construction of the model) in order to validate the model. Moreover, the estimate of the metamodel error is obtained only for limited data. A much more suitable method is the cross-validation method. Multiple types of cross-validation can be distinguished.

The k -folds cross-validation [169, 170] is a "resampling" procedure that has a single parameter called k that refers to the number of groups that a given data sample is to be split into. Then, after a shuffling, the dataset is divided into k smaller sets. The metamodel is built from $k - 1$ sets and validated using the last set. This operation is performed k times at each iteration by validating on a different subset. An estimate of the error is thus obtained for each of the subsets. The final metamodel is finally built using all the data available, and its error is considered to be the average of the k errors of the subset. A significant advantage of this method is that it ensures that all observations in the original data set have a chance to appear in the training set and the test set.

The value of k should be neither too low nor too high. Experience has shown that a value k between 5 and 10 generally estimates the model performance with a low bias and a modest variance [171]. The general procedure of the cross-validation is as follows:

Cross-validation general procedure

1. Shuffle the dataset randomly,
2. Split the dataset into k groups (k between 5 and 10),
3. For each fold:
 - (a) Take the fold as the test dataset,
 - (b) Take the remaining as the training dataset,
 - (c) Fit the model on the training dataset,
 - (d) Evaluate the model on the test dataset,
 - (e) Save the evaluation score R^2 ,
4. Calculate the model evaluation score using all the R^2 ,
5. Construct the final model through training on all the dataset.

Once the metamodel is built and validated, it can be used for many studies. Indeed, in addition to being able to be used as indicated previously to carry out the calibration of parameters, it can also be used to carry out sensitivity studies of the parameters.

4.4.3 Sensitivity analysis

Sensitivity studies allow highlighting the parameters which have the most significant influence on the output of a model. In general, this type of study also requires many calls to the model, hence the interest in metamodels. This quantity can be quantified in different ways, among others, by a variance-based approach based on the Sobol indices [172, 173], which will be used in some studies performed in this thesis.

4.4.3.1 Sobol' indices

The general idea of Sobol' indices is to determine the ratio between the variance of the model outputs explained by a parameter and the total variance of the model [174]. The first order Sobol' index S_i measures the part of the variance of \mathcal{Y} explained by \mathcal{X}_i alone, with \mathcal{Y} a scalar output. The total order Sobol' index ST_i quantifies the part of the variance of \mathcal{Y} that is due to the effect of \mathcal{X}_i and its interactions with all the other input variables. It can also be viewed as the part of the variance of \mathcal{Y} that cannot be explained without \mathcal{X}_i . Other Sobol' order indices exist but are disregarded in this study due to the fact that they are more difficult to interpret. The first order Sobol indices \mathcal{S}_i are expressed as follows:

$$\mathcal{S}_i = \frac{\text{var}[E[\mathcal{Y}|\mathcal{X}_i]]}{\text{var}[\mathcal{Y}]} = \frac{V_i}{\text{var}[\mathcal{Y}]}, \quad (4.11)$$

while the total order Sobol indices \mathcal{S}_{T_i} is:

$$\mathcal{S}_{T_i} = \frac{\text{var}[E[\mathcal{Y}|\mathcal{X}_1, \dots, \mathcal{X}_{i-1}, \mathcal{X}_{i+1}, \dots, \mathcal{X}_p]]}{\text{var}[\mathcal{Y}]} = 1 - \frac{V_{-i}}{\text{var}[\mathcal{Y}]}. \quad (4.12)$$

4.4.3.2 Sobol' indices from PCE

One of the advantages of the PCE surrogate model is that it allows computing the Sobol' indices analytically as a post-processing of the PCE coefficients [175]. The mean $E[\mathcal{Y}]$ and variance $\text{var}[\mathcal{Y}]$ are expressed as follows:

$$E[\mathcal{Y}] = a_0 \quad \text{and} \quad \text{var}[\mathcal{Y}] = \sum_{j=1}^P a_\alpha^2 \quad (4.13)$$

. Moreover, the first and total order Sobol indices are respectively:

$$\mathcal{S}_i = \frac{\sum_{\alpha \in J_i^S} a_\alpha^2}{\sum_{j=1}^P a_\alpha^2} \quad \text{with} \quad J_i^S = \{\alpha = (0, \dots, \alpha_i, \dots, 0) \in J, \alpha_i > 0\}, \quad (4.14)$$

$$\mathcal{S}_{T_i} = \frac{\sum_{\alpha \in J_i^T} a_\alpha^2}{\sum_{j=1}^P a_\alpha^2} \quad \text{with} \quad J_i^T = \{\alpha = (\alpha_1, \dots, \alpha_i, \dots, \alpha_p) \in J, \alpha_i > 0\}. \quad (4.15)$$

4.4.3.3 Aggregated Sobol' indices

If \mathcal{Y} is a multivariate output or a time series, for example with a size m higher than 1, the indices can be aggregated [176] with respect to each output variable. The equations can be written:

$$\mathcal{S}_i^A = \frac{\sum_{k=1}^m \text{var}[E[\mathcal{Y}^k|\mathcal{X}_i]]}{\sum_{k=1}^m \text{var}[\mathcal{Y}^k]} = \frac{\sum_{k=1}^m V_i^k}{\sum_{k=1}^m \text{var}[\mathcal{Y}^k]}, \quad (4.16)$$

$$\mathcal{S}_{T_i}^A = \frac{\sum_{k=1}^m \text{var}[E[\mathcal{Y}^k|\mathcal{X}_1, \dots, \mathcal{X}_{i-1}, \mathcal{X}_{i+1}, \dots, \mathcal{X}_p]]}{\sum_{k=1}^m \text{var}[\mathcal{Y}^k]} = 1 - \frac{\sum_{k=1}^m V_{-i}^k}{\sum_{k=1}^m \text{var}[\mathcal{Y}^k]}. \quad (4.17)$$

4.4.4 Conclusion

In this section, the methodology for building a surrogate model of the numerical model (FE thermal model) is presented. After a brief theoretical introduction, the setting up and the choices of the most

adapted sampling method are discussed in order to build the most accurate surrogate model of the numerical model. The model is then validated by cross-validation.

As mentioned previously, when the output of the model is a vector, the same procedure is performed for each of the points of the output. In other words, a surrogate model is built for each point of the vector. In order to reduce the computation time for large vector outputs, a dimension reduction approach can be considered.

The surrogate models thus allow reducing the calculation time from several hours using numerical models to a few milliseconds. The next section presents the probabilistic parameter calibration method on experimental data using the surrogate model. For the following, the experimental data available for the calibration are considered to be temperature profiles.

4.5 Bayesian parameter estimation

4.5.1 Introduction

This part is devoted to the inverse problem. The general idea of an inverse problem is to estimate the optimal parameter values by knowing the output at a few observation points. It is a challenging problem to find an input that results in the minimum or maximum cost of a given objective function. In our case, as indicated previously, the thermal model parameters are estimated using thermocouple curves at different points. The objective function is the distance between the experimental thermocouple curves and the computed temperature profiles.

To do this, a surrogate model of the thermal model is set up beforehand for this optimization step. The search for optimal solutions requires the use of an optimization algorithm. Several optimization methods exist. Deterministic algorithms explore the search space in a deterministic way, identifying the direction of the optimal value and gradually decreasing the distance between the current point and the optimal value. The most well-known algorithms are the gradient descent algorithm or quasi-Newton algorithms such as BFGS (Broyden - Fletcher - Goldfarb - Shanno) [177], etc. On the other hand, stochastic optimization algorithms randomly explore the parameter space by considering the parameters as random variables.

Within the framework of this study, the parameters to be determined may generate a possible error resulting from the modeling assumptions. In addition, measurement errors on the thermocouple curves (measurement error due to measurement noise and the uncertainty on the position of the thermocouples) can be obtained. Therefore, the bayesian approach has been favored. Indeed, unlike standard calibration methods, where only an optimal value of the parameters is obtained, the Bayesian inverse problem will output a density of possible parameter vectors, in addition to the most probable outcome, which is the sole output of the deterministic calibration approaches mentioned previously.

4.5.2 Bayesian inference

The bayesian approach offers a rigorous framework for estimating parameters from experimental data by integrating the various information available [178]: an estimation of the experimental data variance $\Sigma_{D_{obs}}$ and an a priori estimation of the PDF of the parameters $p(\theta)$ by expertise.

According to the Bayes formula, the Bayesian calibration indicates that the posterior distribution can be obtained from the prior distribution and the likelihood function. Bayesian calibration is based on

the posterior distribution, which characterizes the joint probability distribution of the model parameter and the observed data. According to Bayes' theorem, the conditional probability of θ given D_{obs} is expressed as follows:

$$p(\theta|D_{obs}) = \frac{p(D_{obs}|\theta)p(\theta)}{p(D_{obs})}, \quad (4.18)$$

with:

- $p(\theta|D_{obs})$, the posterior: the probability distribution of the parameters of the model θ given the observed data D_{obs} .
- $p(D_{obs}|\theta)$, the likelihood: the probability distribution of the observed data according to the value of the parameters. It is obtained by assuming that the model measured data D_{obs} are generated and polluted by a gaussian noise ε such as: $D_{obs} = \mathcal{M}(\theta) + \varepsilon$. We then have: $p(D_{obs}|\theta) = \mathcal{N}(\mathcal{M}(\theta), \Sigma_{D_{obs}})$.
- $p(\theta)$, the prior: the a priori knowledge and/or beliefs and expertise on the parameters. The parameters are thus assimilated to random variables described by an a priori probability density. If no knowledge is available on the parameters, the prior can be uniform or with a large variance.
- $p(D_{obs})$, the evidence also called marginal likelihood or prior predictive probability of the experimental data: the probability distribution of the observed experimental data.

All the terms of Bayes' formula can be computed explicitly, except the evidence term $p(D_{obs})$. The posterior can be written as follows:

$$p(\theta|D_{obs}) \propto p(D_{obs}|\theta)p(\theta) = \exp\left(-\frac{1}{2}(D_{obs} - \mathcal{M}(\theta))^T \Sigma_{D_{obs}}^{-1} (D_{obs} - \mathcal{M}(\theta))\right) p(\theta). \quad (4.19)$$

As the posterior distribution $p(\theta|D_{obs})$ cannot be calculated directly but can be only evaluated point-wise, it is necessary to sample the parameter values according to the desired probability density. Therefore, the principle consists in using a method to go through the space of the parameters randomly and preserving only the values of the sets of parameters that seem the most probable.

4.5.3 Monte Carlo Markov Chain (MCMC) sampling

The sampling referred to at the end of the previous section can be carried out using Markov Monte Carlo Chain type algorithms (also called MCMC). The general idea of the MCMC is to gradually build a chain whose resulting distribution converges towards the desired posterior distribution of the "unknown" parameters.

Among the methods based on Markov chains, several algorithms exist, such as the Gibbs algorithm, the Metropolis algorithm, the Metropolis-Hasting algorithm, the Hamiltonian Monte Carlo algorithm, and others. The Metropolis-Hastings and adaptive Metropolis-Hastings are presented in this section. This algorithm uses a Markov chain to go through the parameter space so that the final sample generated agrees with the target probability density: the posterior probability density $p(\theta|D_{obs})$.

The idea of this algorithm is based on a "methodical" sampling methodology based on a strategy of accepting and rejecting a set of parameters. At each iteration, a set of parameters θ_{i+1} is generated from a proposal distribution θ^{prop} . θ^{prop} results from a multivariate gaussian centered on the current

state (the set of parameters θ_i retained at the previous iteration i) such as: $\theta^{prop} \sim \mathcal{N}(\theta_i, \Sigma_{prop})$. The choice of Σ_{prop} is an important aspect. It must be large enough to explore the whole domain without being blocked in a local minimum, but small enough not to have a very low acceptance rate due to the high number of rejects. A good compromise is choosing a variance of the proposal that allows an acceptance rate of the Metropolis-Hasting algorithm of more than 25%. To get rid of the choice of Σ_{prop} , adaptive methods have been proposed in the literature. Among them, Haaris et al. [179] propose to define Σ_{prop} from the covariance matrix of the previously accepted sample [180] such that:

$$\begin{cases} \Sigma_i^{prop} = \Sigma_{prop}^{ini} & \text{if } i < N_{prop}, \\ \Sigma_i^{prop} = \frac{2.4^2}{n} \Sigma_i & \text{with } \Sigma_i = \text{cov}(\theta^0, \dots, \theta^i) \text{ if } i \geq N_{prop}. \end{cases} \quad (4.20)$$

The Metropolis-Hastings algorithm is presented at Algorithm 1.

Algorithm 1 Adaptive Metropolis-Hastings algorithm

Initialization:

$$\theta^0 = (\theta_0^0, \theta_1^0, \dots, \theta_n^0)$$

$$\Sigma_{prop} = \Sigma_{prop}^{ini}$$

$$i = 1$$

while $i \leq N_{mcmc}$ **do**

$$\theta_i^* \sim \mathcal{N}(\theta_{i-1}, \Sigma_i^{prop})$$

$$\alpha = \min\left(1, \frac{P(\theta_i^* | D_{obs})}{P(\theta_{i-1} | D_{obs})}\right) = \min\left(1, \frac{P(D_{obs} | \theta_i^*) P(\theta_i^*)}{P(D_{obs} | \theta_{i-1}) P(\theta_{i-1})}\right)$$

$$u \sim \mathcal{U}(0, 1)$$

if $\alpha \geq u$ **then**

$$\theta_i = \theta_i^*$$

else

$$\theta_i = \theta_{i-1}$$

end if

$$\Sigma_i^{prop} = \frac{2.4^2}{n} \times \text{cov}(\theta_0, \dots, \theta_i)$$

$$i = i + 1$$

end while

To correctly estimate the posterior distribution, many iterations are necessary so that the chain can converge. To ensure the convergence of the chain, it is advisable to use several chains, with different initial values of parameters θ_0 . Moreover, in general, the first iterations are deleted as burn-in. From the obtained posterior distribution, several data can be extracted. In addition to the 95% confidence intervals that can be determined, an optimal parameter set, called the Maximum A Posteriori (MAP), can be identified on the discrete set of samples S such as:

$$\theta_{\text{MAP}} = \underset{\theta_i \in S}{\text{argmax}} p(\theta | D_{obs}). \quad (4.21)$$

Gradient-informed samplers, such as the HMC (Hamiltonian Monte Carlo), which drastically improve the acceptance rate, have been tested [181]. Nevertheless, in the context of the studies carried out in this manuscript, the gain in computation time generated by the increase in the acceptance rate is not sufficient to counterbalance the increase in the computation time of the operations at each iteration of the algorithm. For more complex problems, the use of such algorithms would be of great interest.

4.5.4 Inverse problem step-by-step instructions

In this section, the parameter estimation methodology is presented. In practice, to carry out a bayesian inverse problem, it is preferable to have a first approximation of the maximum a posteriori (MAP), which corresponds to the value of the parameters that have the most significant probability of representing the experimental data. This approximation of the MAP is then used as an initialization for the MCMC. Several steps are then carried out, using the experimental data, the surrogate model, and the thermal model evaluation for each sample of the DOE. In this section, D_{obs} is noted T_{exp} (for experimental temperature).

1st step: Initialisation from sampling

To develop the surrogate model, a sample of n curves associated with n sets of parameters is used. The first optimization by sampling exploration is carried out, corresponding to the minimization of the distance between the n simulation temperature profiles $T_{\mathcal{X}_n}$ that are used to build the surrogate model and the experimental data T_{exp} (temperature profiles from thermocouples). This distance, defined as the quadratic deviation, gives a first approximation of the optimal set of parameters θ_{ini} as follows:

$$\theta_{ini} = \operatorname{argmin}_{\theta \in \mathcal{X}_n} \|T_{\mathcal{X}_n} - T_{exp}\|_2. \quad (4.22)$$

2nd step: Determinist inverse problem - BFGS algorithm

To have a more precise estimation of θ_{ini}^* , the second step of optimization using the gradient descent method is carried out with the quasi-newton BFGS optimization iterative algorithm. This method is based on the definition of a descent direction from the gradient and an approximation of the Hessian matrix. From this direction, a new parameter set is thus obtained. These steps are performed for each iteration, as long as the convergence criterion is not reached (which in this case is a criterion on the gradient). The details of the different steps can be found in the literature [182, 183]. For a simple approach based simply on the deviation from the data, least-squares can be used with θ_{ini} as the initial value of the set of parameters for the descent. :

$$\theta_{ini}^* = \operatorname{argmin}_{\theta \in \mathbb{R}^p} \|\tilde{\mathcal{Y}}(\theta) - T_{exp}\|_2. \quad (4.23)$$

For a more accurate estimation of the map for the MCMC, the objective function to minimize is the function used for bayesian calibration 4.19. The inverse problem to solve can therefore be defined as:

$$\theta_{ini}^* = \operatorname{argmin}_{\theta \in \mathbb{R}^d} -\exp\left(-\frac{1}{2} \left(T_{exp} - \tilde{\mathcal{Y}}(\theta)\right)^T \Sigma_{T_{exp}}^{-1} \left(T_{exp} - \tilde{\mathcal{Y}}(\theta)\right)\right) p(\theta). \quad (4.24)$$

One of the advantages of this approach is that it is very fast since the number of iterations is only the one needed to converge towards a solution (unlike the MCMC algorithm for the approximation of a distribution). Moreover, if only an "optimal" parameter set is needed to perform a "calibrated" simulation, and therefore if there is no interest for the distribution of the parameters or the study of their uncertainties, this step can be sufficient, fast, and efficient. Moreover, to reduce the risk of having a θ_{ini}^* that corresponds to a local minimum, this operation is also performed by taking as random initialization draws of the parameters on the bounds of the parameters. The retained θ_{ini}^* is

the one with the lowest cost function value.

3rd step: Bayesian inverse problem - Adaptive Metropolis–Hastings algorithm

The bayesian calibration is performed using θ_{ini}^* as initialization to the MCMC algorithm. The Adaptive Metropolis-Hasting algorithm is used. For Σ_{prop}^{ini} , it is defined as $(2.5\%)^2$ of the range of each parameter. As for $\Sigma_{T_{exp}}$, it is chosen either according to an a priori knowledge on the errors of the temperature measurements, or by calculating the standard deviation from experimental data. In the studies presented in this manuscript, the number of accepted samples N_{mcmc} is generally set at 500000. A burn-in of the 100000 first samples of the chain is made. With these settings, the run time is usually around 20 to 30 minutes.

4.6 Example for the application of the method

A simple case is performed to illustrate the steps of the methodology proposed in this Chapter. A schematic illustration of all the methodology is also presented in Figure 4.2. The test consists of a 50 mm long wall with 5 beads and a "Zigzag" deposition pattern. The parameters to be calibrated for this example are: a_r, f_r, b, c, η . The data available for the calibration is a temperature history at a specific point. For this illustrative example, this temperature profile is generated numerically and noised to "represent" an experimental profile. The steps, illustrated in Figure 4.2, are the following:

1. A sampling is performed: 256 parameter sets are generated using the low discrepancy Sobol' sequences.
2. Simulations are performed, and temperature profiles at the position of the thermocouples are extracted.
3. The Sparse PCE surrogate model is constructed from the profiles.
4. (Optional) Sensitivity analysis is performed from the surrogate model. Computation of the first-order Sobol indices: the efficiency η is the most influential parameter.
5. Deterministic calibration using BFGS algorithm: have an estimation of the MAP for the initial state of the MCMC.
6. Bayesian calibration using MCMC algorithm: for a given prior, a given variance of the experimental data, and a proposal, the posterior distribution is derived, and a MAP is identified.

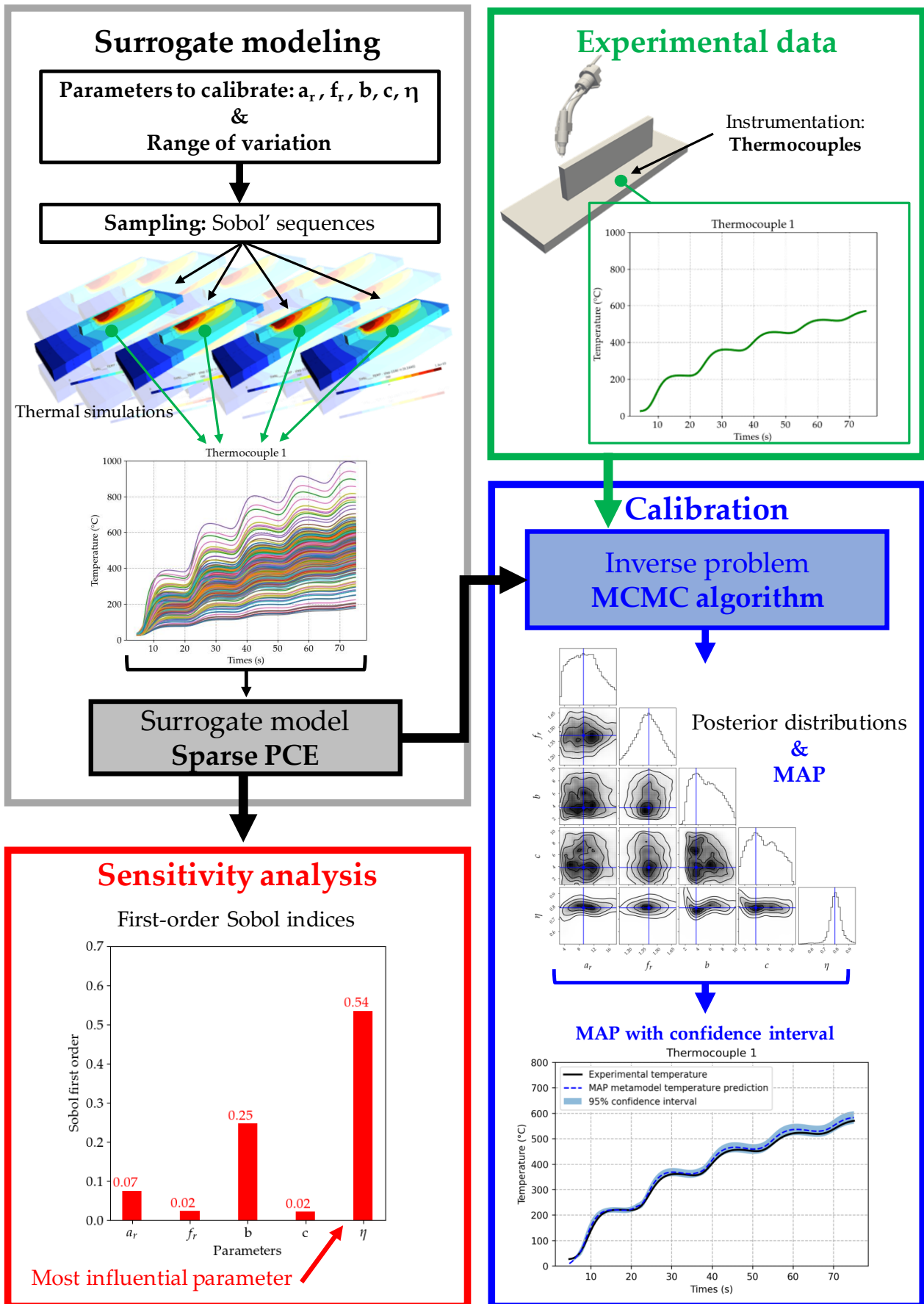


Figure 4.2 – Illustration of the digital twinning Bayesian calibration method.

4.7 Conclusion & perspectives

In this chapter, a methodology for the calibration of the thermal model parameters is presented, relying on a digital twinning approach. First, the parameters to be calibrated are identified. Then, a surrogate model approach based on sparse PCE is considered in order to overcome the issue raised by the calculation time of the numerical simulations, coupled with the very large number of calls to the code needed for the calibration step. Subsequently, the surrogate model implemented is used as an alternative to the numerical simulation model for the resolution of the bayesian inverse problem. The use of MCMC, and more specifically of the Adaptive Metropolis-Hasting algorithm, allows estimating the posterior distribution of the parameters to be calibrated, according to the experimental data available.

As indicated earlier, one of the most important final objectives for this work is to set up a so-called "standardized" calibration test. This test would have a specific configuration, in terms of deposition pattern, cooling time between layers, and any other manufacturing strategies. Once this configuration is chosen and fixed, a single digital twin of this standardized experimental test will be built considering all the process parameters and modeling parameters: power (UI), wire feed speed, torch speed, as well as all the parameters involved in the thermal model, defined previously in Section 3.3.4, which must be calibrated. Once such a digital twin is built, if a new manufacturing process is to be performed and simulated, the preliminary "standardized" calibration test will be performed and instrumented. Then, for the calibration step, the digital twin previously built will be used to minimize the deviation from the experimental data. The power, the wire speed, and the welding speed are considered to be known process parameters, and the objective of the calibration step is to determine the other parameters.

Another advantage of the method used to determine the "unknown" parameters is that it can be transposed to other problems. For the examples presented in this section, only thermocouples data are used for the calibration of the parameters. Nevertheless, the information observed at the level of the thermocouples can sometimes turn out to be unfit for an accurate representation of the thermal behavior in the vicinity of the molten pool. Therefore, in this manuscript, this methodology is also applied, for instance, based on macrograph profiles (fusion lines) in Appendix B, and on residual stress profiles in Appendix F.

4.8 In a nutshell

Thermal inverse problem

- Presentation of a digital twinning method for the bayesian calibration of the thermal model parameters.
- Construction of a surrogate model from simulations from the FE thermal model using Sparse Polynomial Chaos Expansion.
- Use of the surrogate model to conduct parameter sensitivity analysis.
- Use of Monte Carlo Markov Chain approach (Adaptive Metropolis Hasting algorithm) to estimate the posterior distribution of the researched parameters.
- Most important final objective: set up a so-called "standardized" test to be carried out for a fast calibration of the thermal parameters.

Chapter 5

Validation cases and numerical results

Contents

5.1	Introduction	95
5.2	1st use case: high displacement "Zigzag" wall test case	96
5.2.1	Introduction and objectives	96
5.2.2	Description of the experimental setup	96
5.2.3	Thermal model parameters calibration	98
5.2.4	Numerical results	100
5.2.5	Conclusion of the study	104
5.3	2nd use case: "Zigzag" & "Raster" walls	106
5.3.1	Introduction and objectives	106
5.3.2	Description of the experimental setup	106
5.3.3	Thermal model parameters calibration	111
5.3.4	Numerical results	114
5.3.5	Conclusion of the study	126
5.4	3rd use case: NET Network consortium Task Group 9 (TG9)	127
5.4.1	Introduction and objectives	127
5.4.2	Description of the experimental setup	127
5.4.3	Thermal model parameters calibration	131
5.4.4	Numerical results	133
5.4.5	Conclusion of the study	142
5.5	4th use case: AFH block with cooling devices and idle time	145
5.5.1	Introduction and objectives	145
5.5.2	Description of the experimental setup	146
5.5.3	Thermal model parameters calibration	149
5.5.4	Numerical results	153
5.5.5	Conclusion of the study	157
5.6	Thermal parameters sensitivity analysis	158
5.7	Conclusion & perspectives	160
5.8	In a nutshell	162

5.1 Introduction

The previous chapters presented the methodology developed for the simulations of the WAAM process. The associated modeling choices selected, as well as the different developments and contributions made were also described. Nevertheless, it is essential to confront the models with application cases to validate these choices. Therefore, in this chapter, the accuracy and reliability of the models are tested by comparing numerical results with experimental validation tests.

As part of this thesis project, four experimental studies allow for the comparison of the numerical models to experimental data. Two of them were made in the "Laboratoire de Soudage et de Fabrication Additive" at EDF Research and Development Lab in Chatou, PRISME Department, one was performed at the AFH WAAM installation at Air Liquide Research and Development Lab, and finally, one experimental study was carried out during the PhD thesis of Cambon et al. [70, 100] as part of the NET network [132] in which EDF participates. These experimental studies allow validating the calibration methodology and its adaptability to different cases: parameters to be identified, welding processes (GTAW and CMT), etc.

In the following sections, each one of the four studies is described in two steps. In the first part of each section, the experimental study carried out and the instrumentation used are presented in detail. The experimental data acquired are also presented and analyzed. In the second part of each section, the calibration of the parameters for each test is performed using the developed methodology based on the resolution of a bayesian inverse problem using thermal data described in Section 3.3. After describing the simulations, a comparison between the experimental data and the numerical results is carried out and discussed. Thereafter, once the models are calibrated, the numerical simulations are confronted with several types of experimental data. Indeed, these four test cases have been chosen among others because of their complementarity, in order to demonstrate and make sure of the transposability of the models. In addition, each test allows comparing a specific aspect of the models: the material deposition method, the temperature, the size of the molten pool, the residual displacement, and the residual stress measurements throughout the manufacture.

5.2 1st use case: high displacement "Zigzag" wall test case

5.2.1 Introduction and objectives

The first use case considered here is a test case with displacements of high magnitudes. This test is used for the validation of the thermo-mechanical model using the residual displacement field in the part, as well as the methodology of the activation elements method, presented in Section 3.2.1.

5.2.2 Description of the experimental setup

5.2.2.1 Process parameters

This test consists in manufacturing a 32 beads height and 100 mm long wall on a base plate clamped at one end. Figure 5.1 shows the dimensions of the test case setup. The wall is made by successively stacking the 32 beads in a back and forth path, also called a "Zigzag", continuously without turning off the electric arc. These tests are carried out with a *Panasonic* six-axis robot equipped with a *ValkWelding* GTAW welding torch with 10 L min^{-1} 100% Argon shielding. The wire feed is made of 316L austenitic SS, with a diameter of 0.8 mm, and the plate is also made of 316L SS. The process parameters used for this test are the following: an arc voltage of 10 V, an arc current of 100 A, a welding torch speed of 2.33 mm s^{-1} , and a wire speed feed of 25 mm s^{-1} . The test is carried out with the AVC (for "Arc Voltage Control") mode, which consists in an automatic adjusting the height of the welding torch to maintain a constant arc voltage [184]. Although there is a height adjustment, the welding torch path in the two other directions remains unchanged. Such an option is an asset when manufacturing a part with strong deformations as in the present case with a thin base plate. It is the effect of this option on the shape of the wall after fabrication that will allow the evaluation of the element activation method. Table 5.1 summarizes the process parameters associated with the high displacement experimental test:

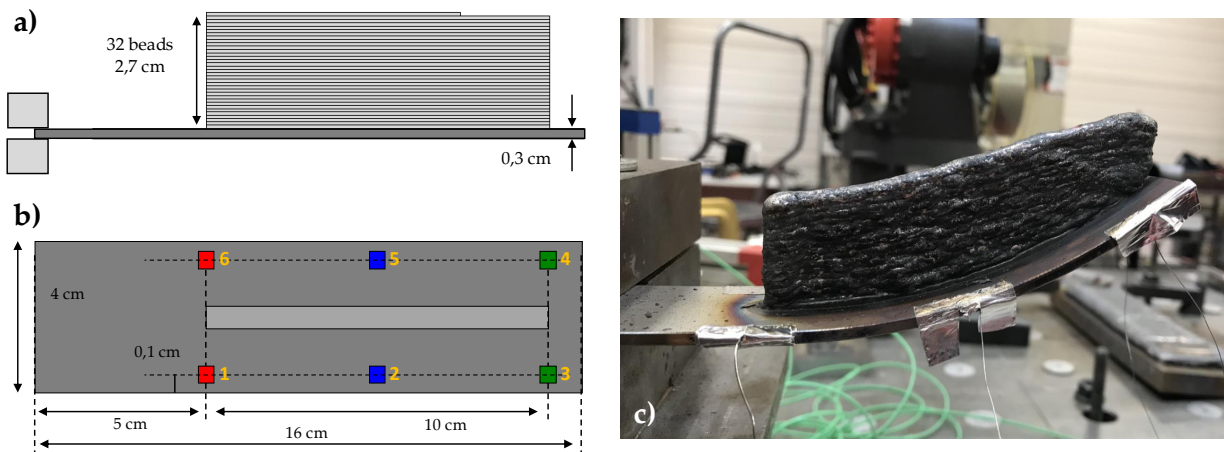


Figure 5.1 – Illustration of the 1st test case: a) Schematic illustration of the wall, b) Thermocouples locations, c) The final part.

Table 5.1 – Process parameters used for the 1st test case.

Welding parameter	Value
Process type	GTAW
Voltage U (V)	10.0
Intensity I (A)	100.0
Travel speed V_s (m s^{-1})	0.00233
Maximal stroke rate (m min^{-1})	1.5

5.2.2.2 Instrumentations

■ **Thermocouples:** The temperature is measured at different points on the base plate using commercial type K thermocouples with a diameter of 0.5 mm with semi-rigid metal sheaths. The high-density thermocouple spring-terminal connectivity module from *National Instruments* NI 9213 coupled with the *LabVIEW* software is used. The error of a thermocouple acquisition depends on the type of thermocouple, the accuracy of the thermocouple, the temperature measured. For K type thermocouple temperature measurements, the accuracy is under $\pm 0.25^\circ\text{C}$ (maximum errors) for temperatures between -200°C and 1300°C (not to be mistaken with the accuracy of the thermocouple itself). Concerning the uncertainty of measurement related to thermocouples, it is usually around $\pm 2.2^\circ\text{C}$ for type K thermocouples.

Six type K thermocouples are placed on the base plate as shown in Figure 5.1, symmetrically (3 on each side to validate the acquisitions), with a continuous measurement range between 0°C and 1100°C and a sampling frequency of 50 Hz (Figure 5.2). The thermocouples are fixed to the base plate with aluminum tape. Only thermocouples n°1, 2, 3, 4, and 5, which seem to be the least disturbed, are kept for the study.

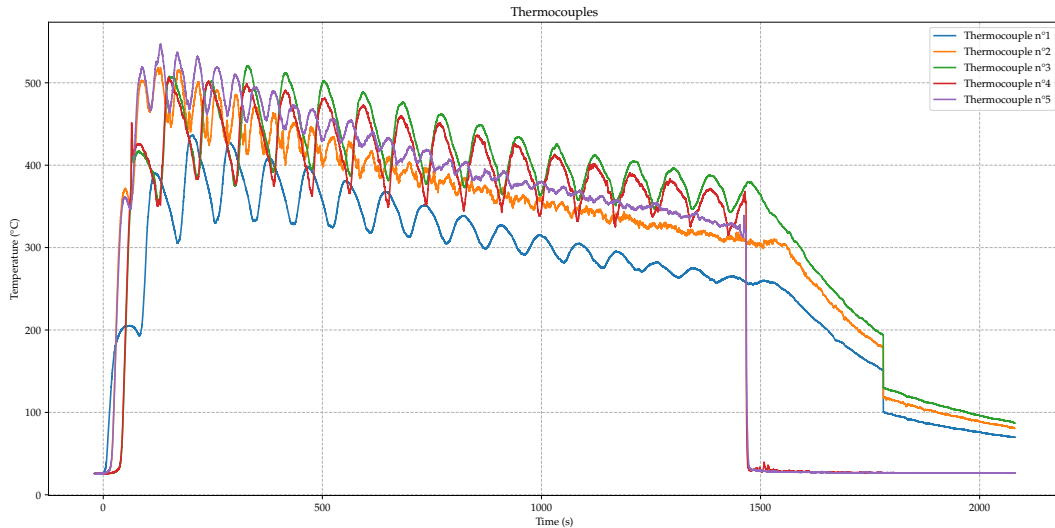


Figure 5.2 – Temperature profiles during the 32 beads wall use case using type K thermocouples

■ **3D scan:** After the fabrication process, the part is scanned to study the displacements of the part

(Figure 5.3). The 3D scan used is a Handyscan Black Elite Edition of the *Creaform*. The acquisition and post-processing softwares *VXelements* and *VXmodel* (Creaform Inc; Canada; www.creaform3d.com) are used. The scans are performed with an accuracy of 0.1 mm. The image of the part after manufacture, as well as the 3D scan of the part, are shown in Figure 5.3.

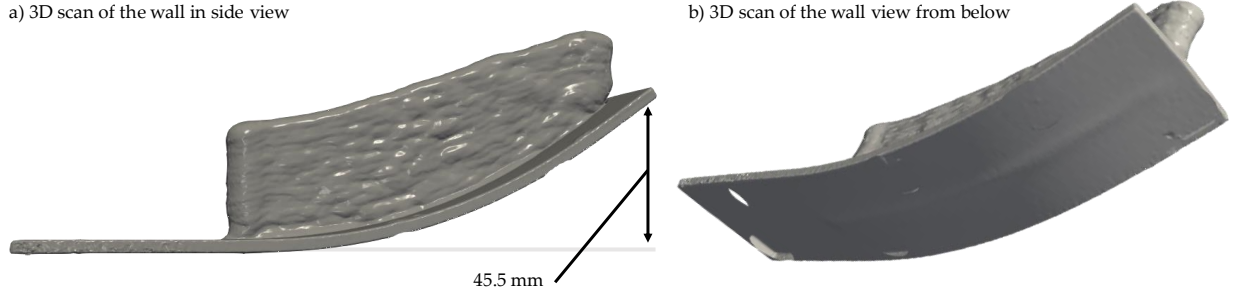


Figure 5.3 – 3D scan of the 32 beads wall use case, and free end displacement measurement.

For the calibration and validation of the model, the generation of the mesh for the simulations is required. Using the procedure presented in Section 3.2.2.1 and considering the process parameters presented in Table 5.1, the height and width of the beads are evaluated at 1mm and 4mm. The generated mesh consists of about 7000 hexahedral elements. For the calibration, the linear elements mesh is used (about 10000 nodes). For the results presented in the numerical results in Section 5.2.3, the same mesh as for the model calibration and validation is used, but quadratic elements are preferred for the thermo-mechanical simulations (about 36000 nodes). Previous tests have shown that thermal simulations with linear or quadratic elements give similar results.

5.2.3 Thermal model parameters calibration

In this section, the methodology presented in Chapter 4 is applied to calibrate the thermal model parameters using the experimental data presented previously. First, the surrogate model based on the PCE is constructed, then the inverse problem is performed. For this first use case, eight parameters are to be identified. To constitute the database needed to build the surrogate model, a DOE is set up. The following distributions of the parameters are first identified:

Table 5.2 – Parameters to be calibrated, with the sampling distribution for the PCE surrogate model training and the prior distribution for the MCMC algorithm calibration step.

Parameters	Sampling distribution	Prior distribution
a_r (mm)	$\sim \mathcal{U}(3.0, 18.0)$	$\sim \mathcal{N}(8.0, (7.0)^2)$
f_r	$\sim \mathcal{U}(1.10, 1.70)$	$\sim \mathcal{N}(1.4, (0.25)^2)$
c (mm)	$\sim \mathcal{U}(1.0, 10.0)$	$\sim \mathcal{N}(5.0, (3.0)^2)$
η	$\sim \mathcal{U}(0.50, 0.95)$	$\sim \mathcal{N}(0.75, (0.4)^2)$
ε_0	$\sim \mathcal{U}(0.20, 0.80)$	$\sim \mathcal{N}(0.35, (0.25)^2)$
ε_1	$\sim \mathcal{U}(0.0, 1.0)$	$\sim \mathcal{N}(0.5, (0.4)^2)$
h_0 (W.mm ⁻² .K ⁻¹)	$\sim \mathcal{U}(2.5 \times 10^{-6}, 80.0 \times 10^{-6})$	$\sim \mathcal{N}(15.0 \times 10^{-6}, (25.0 \times 10^{-6})^2)$
h_1	$\sim \mathcal{U}(0.0, 1.0)$	$\sim \mathcal{N}(0.5, (0.4)^2)$

In this study, the width of the heat source is imposed at the width of the bead. This assumption is made because in the configuration of the wall, increasing the width would mean applying the source outside the mesh, which would not have much influence, and on the contrary, could be in conflict with other parameters such as the efficiency η . Moreover, in this test, the thermal dissipation at the clamped area is not taken into account due to the small contact zone. These assumptions are made to simplify the inverse problem and not have too many parameters to identify compared to the amount of experimental data available. For the Goldak parameters, the order of magnitude of the variation of these parameters is chosen based on expertise and all the possible values taken in the studies of the literature. Regarding the efficiency η , historically, the expertise shows that, for the processes used in welding and WAAM, it is generally between 0.6 and 0.9. This justifies the choice of the distribution presented above. Concerning the thermal dissipation parameters, the literature shows that the emissivity coefficient ε is between 0.2 and 0.8 and that the convection h is often around 10.0×10^{-6} (W.mm⁻².K⁻¹).

To constitute the database to build the surrogate model, 512 draws are made. For the design of the experiment, Sobol sequences with low discrepancies are preferred because of the high number of parameters. The simulations are performed with a time step of 0.5 second and are run on 8 CPUs. The computation time of each thermal simulation takes about 1 hour of computation. Before building the surrogate model, the results of the simulations are post-processed. The temperature profiles at the experimental thermocouple points are extracted from the results of the 512 thermal simulations. The surrogate model of the temperature profiles is built. Using only the temperature profiles simplifies the surrogate model, its complexity, and thus increases its accuracy. The error of the implemented surrogate model is estimated to be around 3%.

The MCMC is run using the surrogate model of the first 300 seconds of the computed temperature profiles and the associated thermocouple experimental data. The variance of the observation $\Sigma_{D_{obs}}$ issued for the likelihood calculation chosen is 12.6² (°C). This value is obtained by a calculation of the standard deviation of the temperature profiles from the symmetrically disposed thermocouple pairs 2 – 5 en 3 – 4. For the prior distributions, gaussian distributions are used to take into account the knowledge of some parameters, or help identify an optimized value despite a low impact of a parameter. The prior distributions used are presented in Table 5.2.

The posterior distributions obtained are made up of 500000 accepted draws, with an acceptance rate of approximately 44%. The first 100000 draws are burn-in. Indeed, it is considered that the first draws are not necessarily relevant if the starting point of the chain is not close to the searched area. The accepted samples from the MCMC algorithm are displayed on a grid in which the diagonals show the 1-dimensional posteriors and the lower-left half shows the pairwise projections (Figure 5.4). From the distributions of each parameter, the maximum a posteriori (also called the MAP) is identified. The MAP corresponds to the most probable value of the parameters. This set of parameters is represented in blue in Figure 5.4 and Table 5.3.

Table 5.3 – Identified MAP from the thermal inverse problem.

Parameters	a_r	f_r	c	η	ε_0	ε_1	h_0	h_1
MAP	9.85	1.36	5.22	0.594	0.316	0.566	1.46e-05	0.617

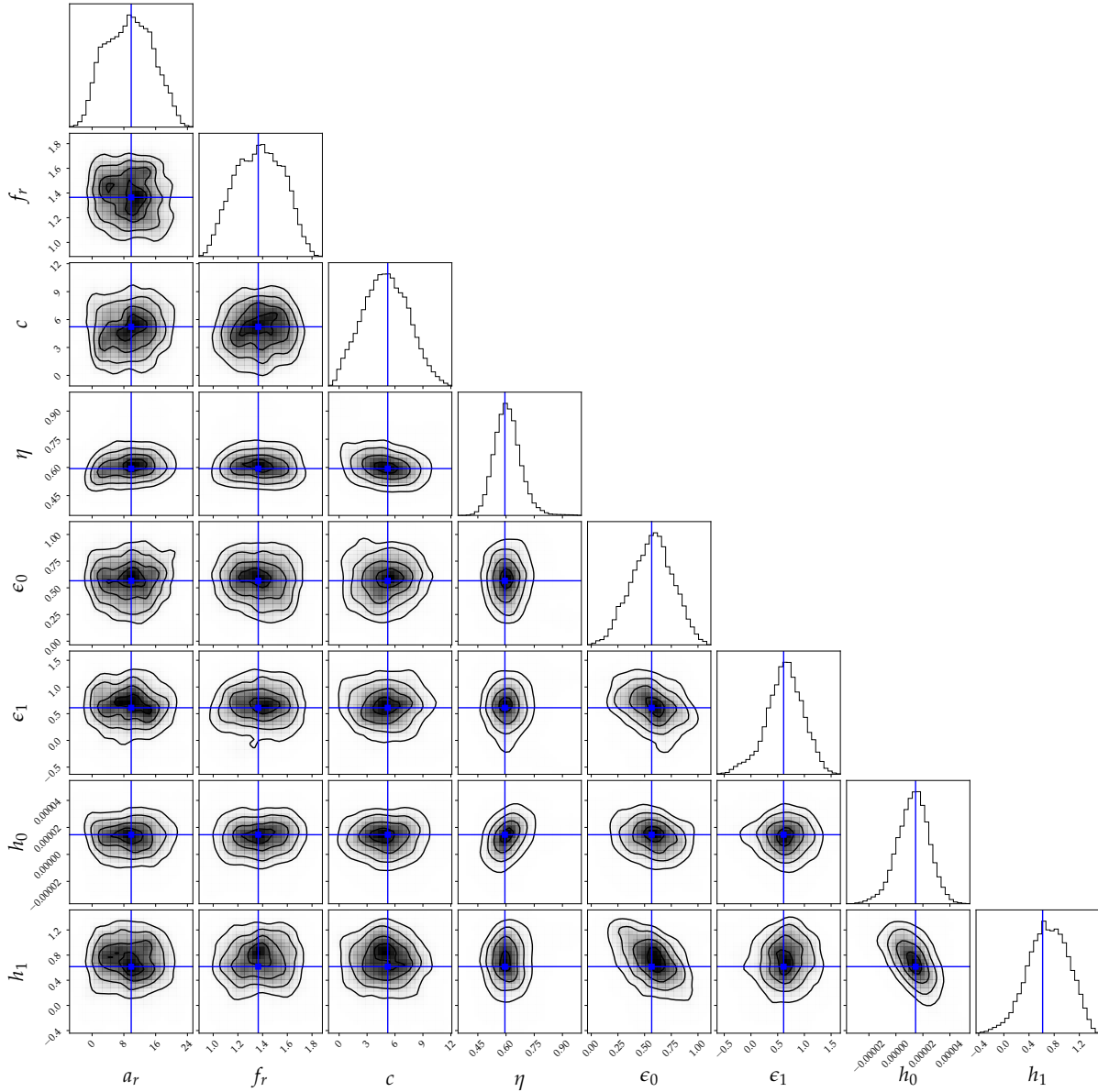


Figure 5.4 – Corner plot of the posterior distribution resulting from the calibration step. The MAP is represented in blue.

5.2.4 Numerical results

The thermo-mechanical simulations are performed using the MAP of the probability distribution obtained for the parameters using the surrogate model. The simulation is run on a quadratic element mesh and with the same time step of 0.5 second. The computation time of each of the simulations presented in this section is on average 48 hours. The simulations are performed using a piecewise linear isotropic hardening constitutive behavior (VMIS_ISOT_TRAC model in Code_Aster).

5.2.4.1 Material deposition method

In this section, the objective is to test the proposed material deposition strategy introduced in Section 3.2. To do so, three different types of deposition strategies are simulated.

In the first configuration, no manipulation is performed on the material input. The displacement field used as an initial state is only extended to zero on the non-contributing elements. As shown in Figure 5.5, by performing the simulation with this material input methodology, the wall has a very non-physical profile. Nevertheless, this result could be expected since the base plate deforms significantly, but each displacement of the input material is initialized to zero. However, it is essential to point out that the numerical result found for the displacement of the base plate is satisfactory, with a predicted deflection of 46 mm, while the deflection observed experimentally is of 45.5 mm.

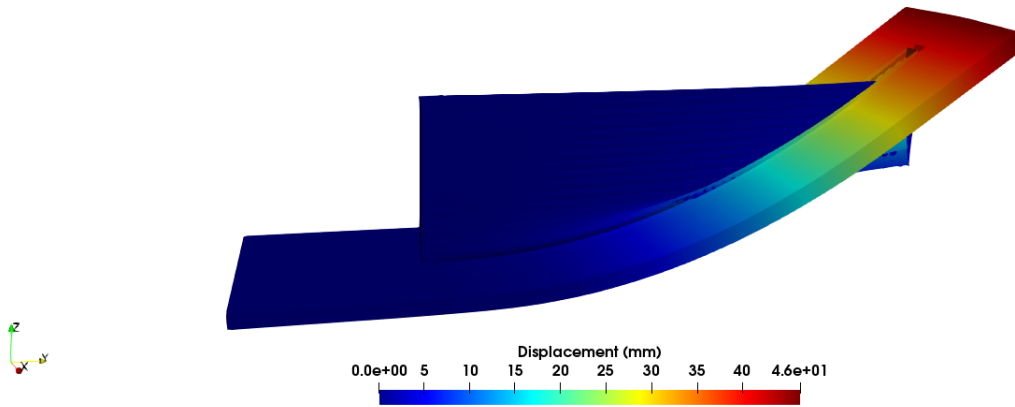


Figure 5.5 – Displacement field for the 32 beads wall, using the VMIS_ISOT_TRAC model, without the linear elastic computation at the activation of the elements.

A second method is implemented to investigate the effect of the base plate deflection on the initial state of the material input. An elastic calculation is performed at each addition of new elements, as presented in Equation 3.33. During this intermediate elastic calculation, the previous displacement field is applied as a Dirichlet boundary condition so that the nodes without displacement adapt accordingly. Moreover, to keep the volume of the contributed elements and avoid any contraction of the elements, a Poisson ratio of 0.5 (or very close to 0.5, for example, 0.499) is used. The result presented is shown in Figure 5.6. A first finding is that the geometry of the wall has evolved and has gradually adapted to the deformation of the base plate. Moreover, the base plate deflection estimation is still very satisfactory, with a prediction of 46mm, as for the first deposition strategy considered.

Finally, for the third configuration, an elastic calculation is performed at each addition of new elements as for the case presented previously. Moreover, an additional Dirichlet boundary condition is considered on the newly activated nodes to block the component of their position over the welding direction at the welding torch position. The shape of the wall is very satisfactory and very close to the shape observed experimentally. Indeed, the collapse at the right corner of the wall, which is caused by the welding torch AVC mode, is well observed. The material activation approach, with elastic calculation with the additional Dirichlet boundary condition on the nodes according to the path of the welding torch, seems to represent the process well. However, a more pronounced collapse can be seen

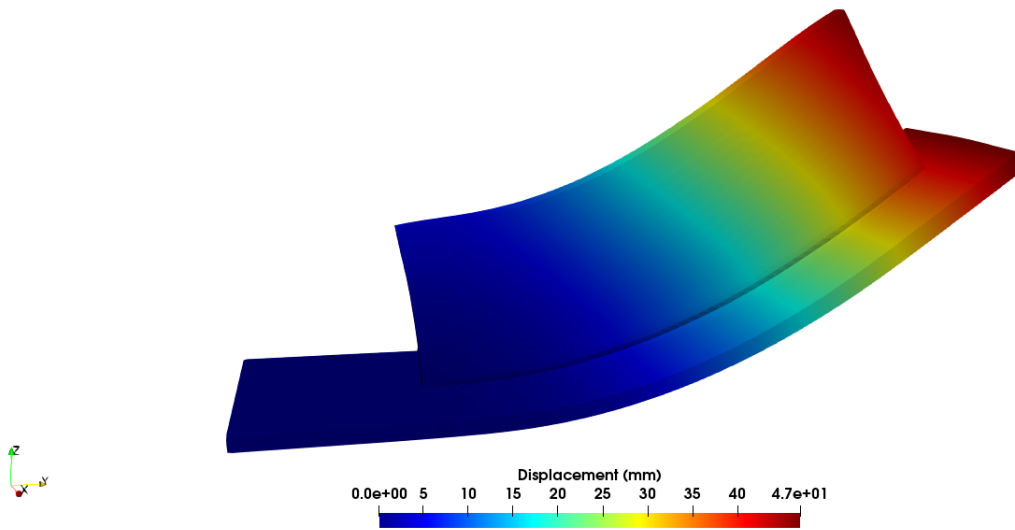


Figure 5.6 – Displacement field for the 32 beads wall, using the VMIS_ISOT_TRAC model, with the linear elastic computation at the activation of the elements.

on the 3D scan. This is probably due to the heat accumulation on the edge which makes the molten pool larger, combined with the fact that the right edge of the wall is tilted on that side of the wall which accentuates the flow of molten metal. As for the two previous deposition strategies, the result of the base plate deflection is still very satisfactory, with a prediction of 46mm (Figure 5.7).

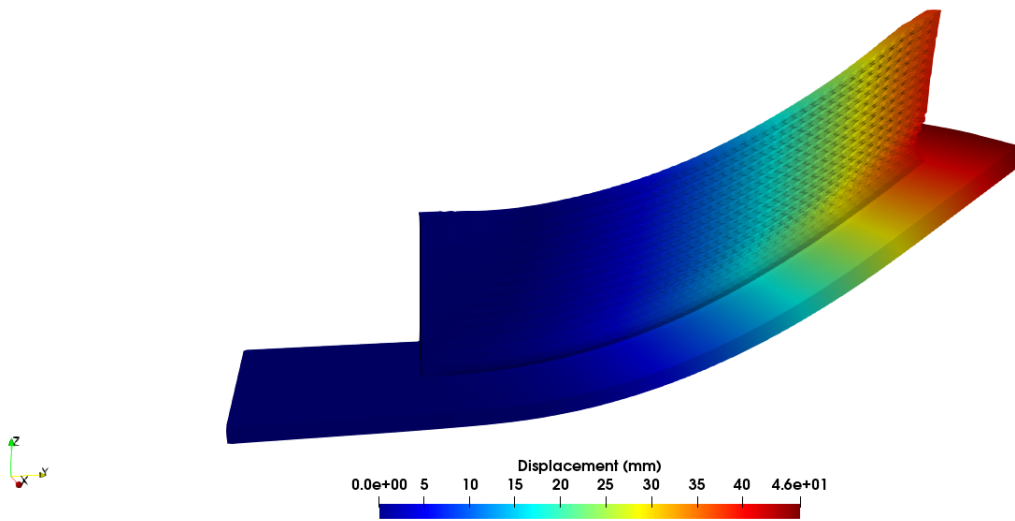


Figure 5.7 – Displacement field for the 32 beads wall, using the VMIS_ISOT_TRAC model, with the linear elastic computation when activating the elements and with a boundary condition representing the welding torch position.

To conclude this section, Figure 5.7 highlights that the third configuration is the most faithful to the final morphology of the part. Moreover, this step is not very time-consuming since there were no significant differences in the total computation time of the simulation. Nevertheless, what is interesting

to point out is that the deposition strategy has no "noticeable" influence on the displacement field of the base plate. Therefore, it is essential to use the third deposition strategy on configurations that are likely to be highly deformed if the final geometry of the component needs to be predicted. However, for a study where only the displacements of the base plate are studied, a calculation without optimization of the deposition strategy may be sufficient.

It is also apparent from Figure 5.7 that the right end of the wall is extremely collapsed. This collapse is caused by the flow of the molten pool under the influence of gravity. As for the simulation with the linear elastic computation when activating the elements and with a boundary condition representing the welding torch position at each element activation, the final shape of the experimentally manufactured wall is tilted, which causes the wall to gradually collapse on this extremity due to gravity and heat accumulation on the extremities because of the "Zigzag" deposition pattern.

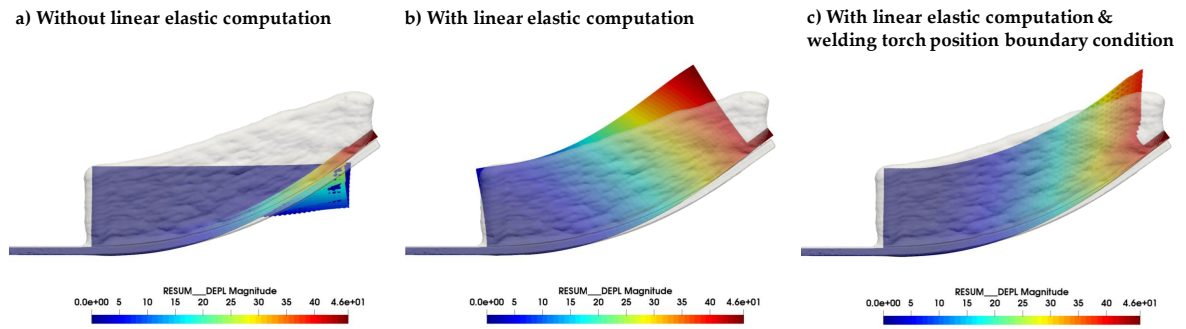


Figure 5.8 – Material deposition methodology.

5.2.4.2 Benchmark of constitutive behavior models

As previously mentioned, the simulations used for the material deposition strategy study are performed with the VMIS_ISOT_TRAC model. Although this model gives a reasonable estimate of the final deformation of the part, or more specifically of the base plate deflection, it is interesting to have its estimate for all the constitutive behavior models presented in Section 3.4. In Figure 5.9 are shown the results for the VMIS_ISOT_TRAC model with and without hardening annealing, and for VISC_CIN1_CHAB. In general, they provide satisfactory results on the estimation of the base plate deflection, between 41 mm and 47 mm. Additionally, by studying the fields of the different workpieces, one can observe the impact of the hardening annealing on the stress field, having lower stresses with the hardening annealing taken into account. Furthermore, with the hardening annealing, a higher displacement is observed, closer to the one observed experimentally. This may be due to the fact that the structure is less hardened, which allows it to deform more. As for the VISC_CIN1_CHAB behaviour, an even weaker field is observed overall. There are two reasons for this. The Chaboche models are in general more suitable for cyclic loading, whereas the VMIS_ISOT_TRAC model may overestimate them (piecewise linear isotropic hardening). The second reason may be the presence of viscous effects.

In order to investigate deeper the mechanical behaviors and have a better idea of the accuracy of the results according to the mechanical constitutive behaviors used, it would be interesting to study

the residual stress profiles. Indeed, in order to complete this study and further validate the results, it would be interesting to have experimental stress measurements. Such experimental measurements are not available for the current study case. Nonetheless, the validation of the models by comparison with residual stresses is presented in Section 5.4 on another test case carried out in the framework of a european consortium: the NET network.

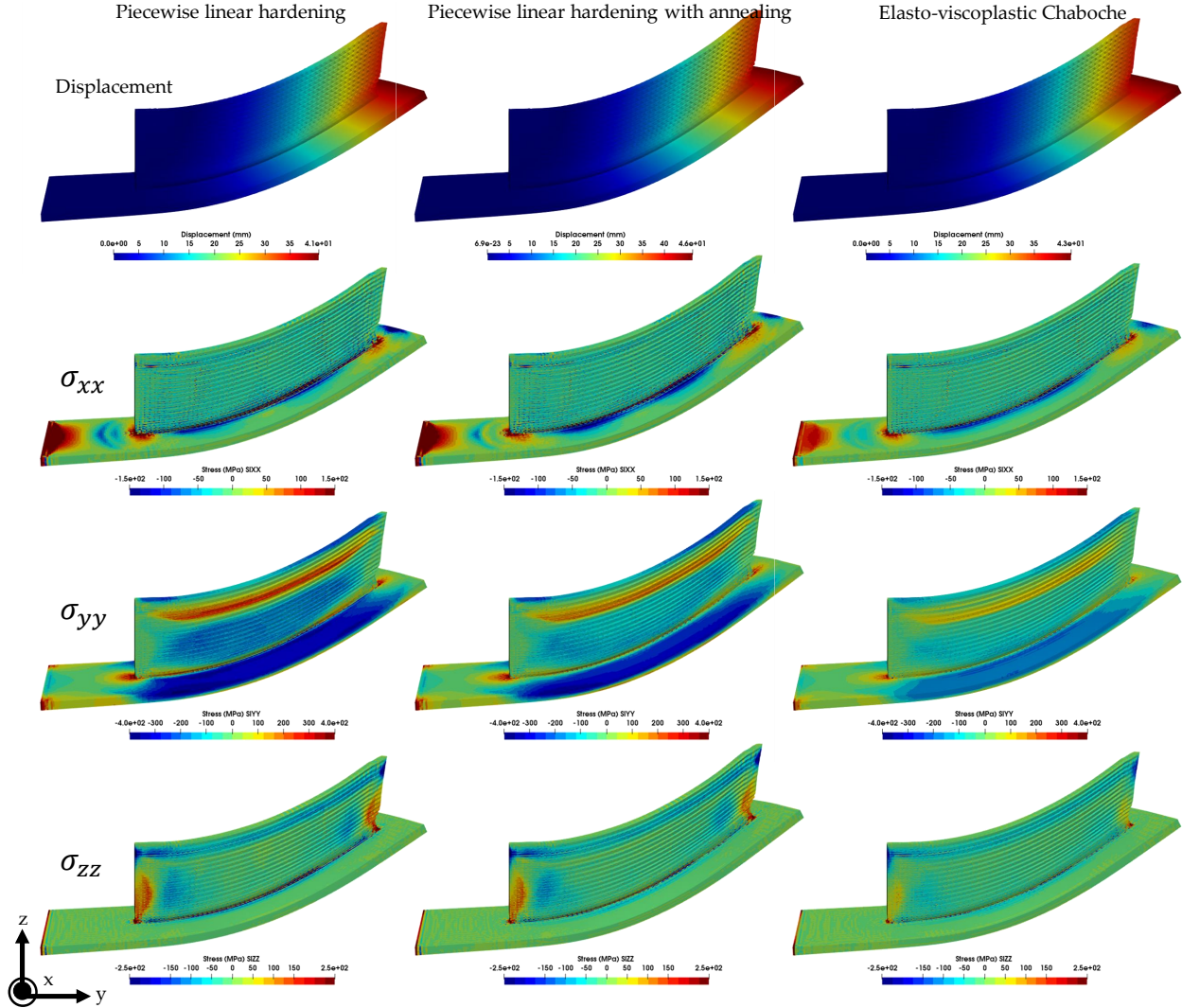


Figure 5.9 – Benchmark of constitutive behavior models for the "Zigzag" test case.

5.2.5 Conclusion of the study

The experimental test described in this section consisted of a 32 beads wall deposited on a base plate clamped at one side. A surrogate model of the thermal model has first been set up. Using this metamodel, the thermal model parameters have been calibrated by solving a bayesian inverse problem on thermocouple data. The posterior distributions obtained allowed identifying a MAP. This MAP has then been used to run the thermo-mechanical model and further validate the choice of parameters on other experimental data.

A study has then been carried out to investigate the effect of the material activation method.

A very promising strategy has been identified, based on an elastic calculation when activating new elements, coupled with boundary conditions consisting in blocking the displacements of the nodes over the welding torch path (Section 3.4). Moreover, simulations have been run for different constitutive behavior models available in Code_Aster. Again, the results seem to be very satisfactory.

5.3 2nd use case: "Zigzag" & "Raster" walls

5.3.1 Introduction and objectives

The second test campaign consists in the manufacturing of two walls. The two walls are performed using the same process parameters but with different deposition patterns. The main objective of these tests is to apply the methodology developed for the calibration of the parameters of the thermal source and the coefficients of thermal losses (emissivity and convection), relying on the instrumentation set up. Subsequently, the aim is to validate the thermal model, the mechanical model, and the associated modeling hypotheses, as well as to study the influence of the deposition strategy on the residual state and on the morphology of the part. Indeed, after the calibration of the thermal model parameters, the thermo-mechanical model can be validated based on the comparison of the experimental data with the numerical simulation results. The used data are thermocouple profiles, size evolution of the molten pool, or the evolution of the displacements measured during the test. Compared to the 1st study, the tests are performed on deposition patterns, using the same process parameters (but different from the 1st test case), and are better instrumented.

5.3.2 Description of the experimental setup

5.3.2.1 Process parameters

The two instrumented tests are two walls carried out with different deposition strategies: "Zigzag" and "Raster" (Figure 5.10).

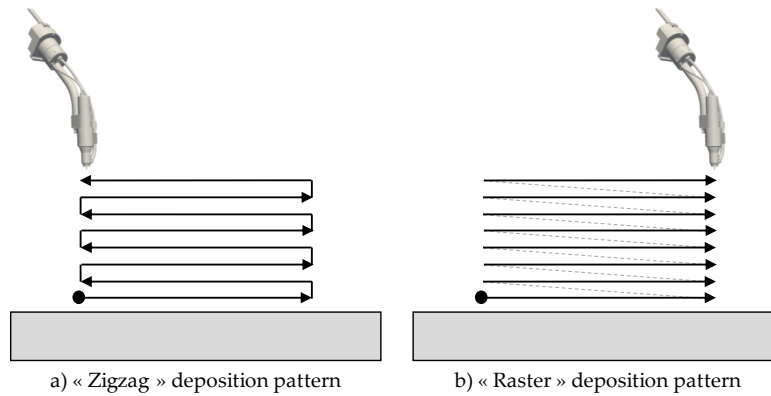


Figure 5.10 – Schematic illustration of the "Zigzag" and "Raster" deposition pattern.

These tests consist in manufacturing single-bead walls of 50 beads height and 120 mm length on a base plate clamped at one end. The plate is 200 mm long, 60 mm wide, and has a thickness of 10 mm. This test is carried out in the same installation as the study presented in Section 5.2: a *Panasonic* six-axis robot equipped with a *ValkWelding* GTAW welding torch with 10 L min⁻¹ 100% Argon shielding. The feed wire is made of 316L SS, with a diameter of 0.8 mm, and the base plate is also made of 316L SS. The process parameters used for this test are the following: an arc voltage of 11 V, an arc intensity of 120 A, a torch speed of 3.33 mm s⁻¹, and a wire feed speed of 25 mm s⁻¹. The tests are carried out with the AVC mode. The "Zigzag" test is performed continuously without switching off the arc, unlike

the "Raster" test which starts each new bead at the same position. To move back to this position, the welding robot takes 5.45 seconds. This time is considered as a cooling time between the wall layers for the "Raster" test. Table 5.4 summarizes the process parameters associated with the two experimental tests:

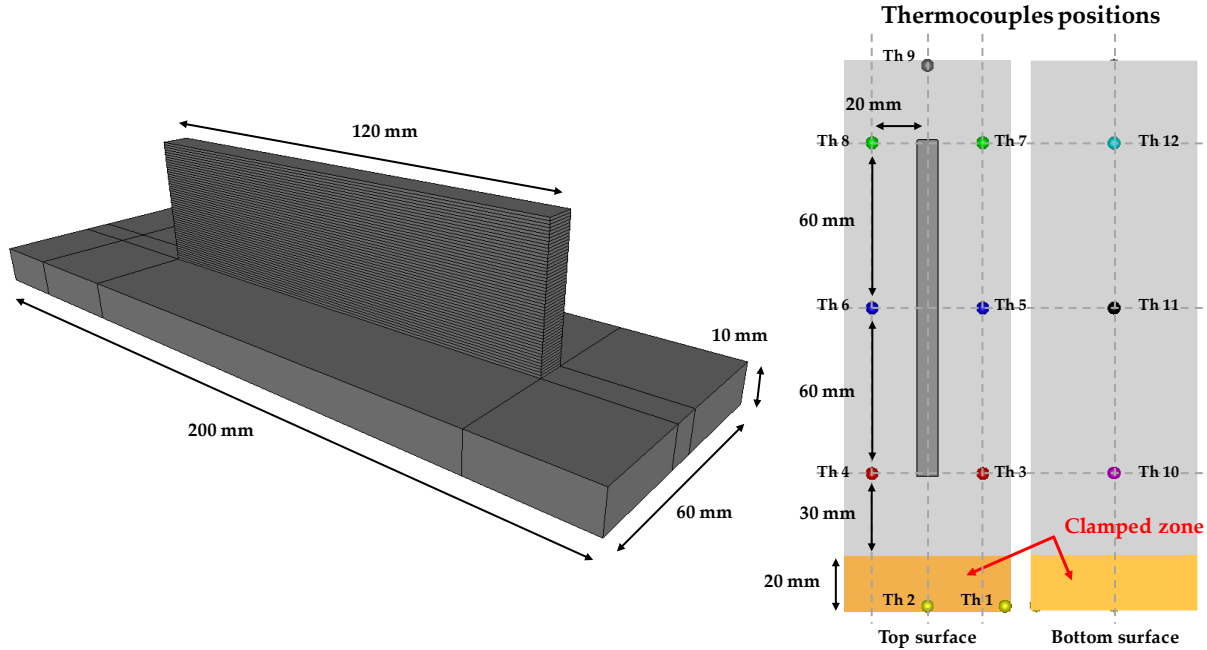


Figure 5.11 – "Zigzag" and "Raster" experimental test cases presentation.

Table 5.4 – Process parameters used for the 50 beads "Zigzag" and "Raster" walls.

Welding parameter	Value
Process type	GTAW
Voltage U (V)	11.0
Intensity I (A)	120.0
Travel speed V_s (m s^{-1})	0.00333
Wire feed rate (m min^{-1})	1.5

5.3.2.2 Instrumentation

The instrumentation for these two experimental tests is presented in this section. The instrumentation of the two tests is the same.

■ **Thermocouples:** The temperature is measured during the tests at different positions on the base plate. 12 type K thermocouples are placed on the base plate, as indicated in Figure 5.11. The thermocouples 1&2 are commercial type K thermocouples (same as the 1st use case) fixed with aluminum tape at the clamping. The thermocouples 3 to 12 were crafted at EDF and micro-welded with a ceramic coating on the micro-weld to protect the thermocouples from measurement noise caused by the electric arc. These thermocouples have a diameter of 0.20 mm with a ceramic sheath. Some of them are

positioned symmetrically with respect to the wall in order to validate the acquisitions. This is the case for the thermocouple pairs 3 – 4, 5 – 6, and 7 – 8. The thermocouples have a continuous temperature measurement range between 0 °C and 1100 °C and an acquisition frequency of 50 Hz. The *National Instruments* NI 9213 spring-terminal connectivity module presented before is also used.

The thermocouple curves are used for the calibration step of the thermal model parameters. As highlighted by the thermocouple data of the "Zigzag" test represented in Figure 5.15, there are strong disturbances at certain times. These disturbances correspond to the damage of the thermocouples during the test. A pre-processing operation of the data is necessary to keep only the representative parts of the curves.

■ **Thermal imaging:** The temperature field of the wall is also recorded throughout the tests. The thermal camera used for the non-intrusive temperature measurement is a *FLIR* (www.flir.fr) Orion SC7500-BB system which is an infrared multispectral imager (8 filters) with an image resolution of 320×256 pixels (Figure 5.12).



Figure 5.12 – Thermal camera *FLIR* Orion SC7500-BB.

A robust methodology for the calibration of thermal images has been implemented by Boutin et al. [185] as part of his PhD work at EDF. The *FLIR* camera is an infrared camera equipped with an 8-position filter wheel that splits the scene signal into several spectral bands. The filter wheel mechanism can be used in both fixed and rotating modes. When used in an 8-filter mode, the maximum frequency per filter is 50 Hz. It is possible to increase the frequency by reducing the resolution size. Moreover, the lack of knowledge of the material's emissivity is the main problem in thermography. Therefore, the development of measurement methods to liberate from the knowledge of emissivity is necessary. The *FLIR* camera can be used both in monochromatic mode (needing the knowledge of emissivity) and bichromatic mode (which allows overcoming the knowledge of emissivity). Bichromatic pyrometry is based on the simultaneous measurement of two luminances at two different wavelengths. The ratio of these luminances shows the ratio of emissivities at both wavelengths. Measuring temperature without contact requires relating the camera's luminance levels to the luminance received at the detectors. This conversion must be done for each filter and for each integration time. When the flux included in the spectral range associated with the filters reaches a pixel, it is converted into a Digital Level (DL), proportional to the energy received. Therefore, the calibration of the thermal camera is made by bringing a black reference body (with a known emissivity equal to 1) at different temperatures. From the calibration on the black body, the camera can perform several measurements parallel to the flux emitted on the range of temperature programmed. Thus, the curves are then combined into a

single file to calibrate a range of temperature depending on the exposure time and the filter used. The calculation of the temperature at each pixel of the image is made from the ratio of luminances using Planck's law and Wien's approximation:

$$\frac{L_1}{L_2} = \left(\frac{\lambda_1}{\lambda_2}\right)^{-5} \frac{\varepsilon_{\lambda_1} \exp\left(\frac{C_2}{\lambda_2 T}\right)}{\varepsilon_{\lambda_2} \exp\left(\frac{C_2}{\lambda_1 T}\right)} \quad (5.1)$$

The temperature can thus be expressed as follows (by considering the assumption of a gray body where the ratio of emissivities is simplified):

$$T = \frac{C_2(\lambda_1 - \lambda_2)}{\lambda_1 \lambda_2} \frac{1}{\ln\left(\frac{L_1 \lambda_1^5}{L_2 \lambda_2^5}\right)} \quad (5.2)$$

To calculate the temperature in each of the pixels, the ratio of luminances is expressed as the ratio of DL multiplied by a calibration factor k :

$$T = \frac{C_2(\lambda_1 - \lambda_2)}{\lambda_1 \lambda_2} \frac{1}{\ln\left(k \frac{DL_1 \lambda_1^5}{DL_2 \lambda_2^5}\right)} \quad (5.3)$$

■ **Stereo-correlation:** In order to use these tests to validate the simulations on mechanical quantities, stereo-correlation cameras are used to continuously measure the displacement of the plate during the WAAM manufacturing process. To do this, the base plates are first painted with a matte black coating, on which white projections are randomly deposited (also called speckles) (Figure 5.13). These white projections act as markers and thus enable the extraction of the evolution of the displacement profile and the deflection of the base plate during the tests. The cameras used are *Pike F-421* with high-resolution images of 2048×2048 pixels and high frame rates. The calibration and acquisition steps are performed using the *VIC-SNAP* and *VIC-3D* software suite (www.correlatedsolutions.com).

The stereo-correlation images must be processed to be compared with the experimental data. However, the images are very complicated to post-process. Indeed, the very bright electric arc creates a saturation of the image at the position of the welding torch. Therefore, only the results of the wall base plate deflection are used in order to extract reliable data that can be compared to the simulation results. To compare the experimental data and the simulations, an *ImageJ* [186] tracking plugin named *TrackMate* [187] is used to track and extract the path of a given marker during the test and the cooling step. Figure 5.13 describes the procedure and shows the displacement profiles obtained.

■ **3D scan:** Finally, as for the 1st test case, after fabrication, the two walls are scanned (Figure 5.14) with the Handyscan Black Elite Edition of the *Creaform*. The *VXelements* and *VXmodel* acquisition and post-processing softwares are used. The scans are performed with an accuracy of 0.1 mm. These scans can allow for precise comparison of the simulated residual displacements with the experimental data measured. The scans are also be used in Chapter 7.

From the process parameters presented in Table 5.4, the height and width of the beads are evaluated at 0.67 mm and 7.5 mm. The generated mesh is made of about 24000 hexahedral elements. For the calibration, the linear (8-nodes) elements mesh is used (about 32000 nodes). For the results presented in the numerical results section, the same mesh is used but quadratic (20-nodes) elements are preferred

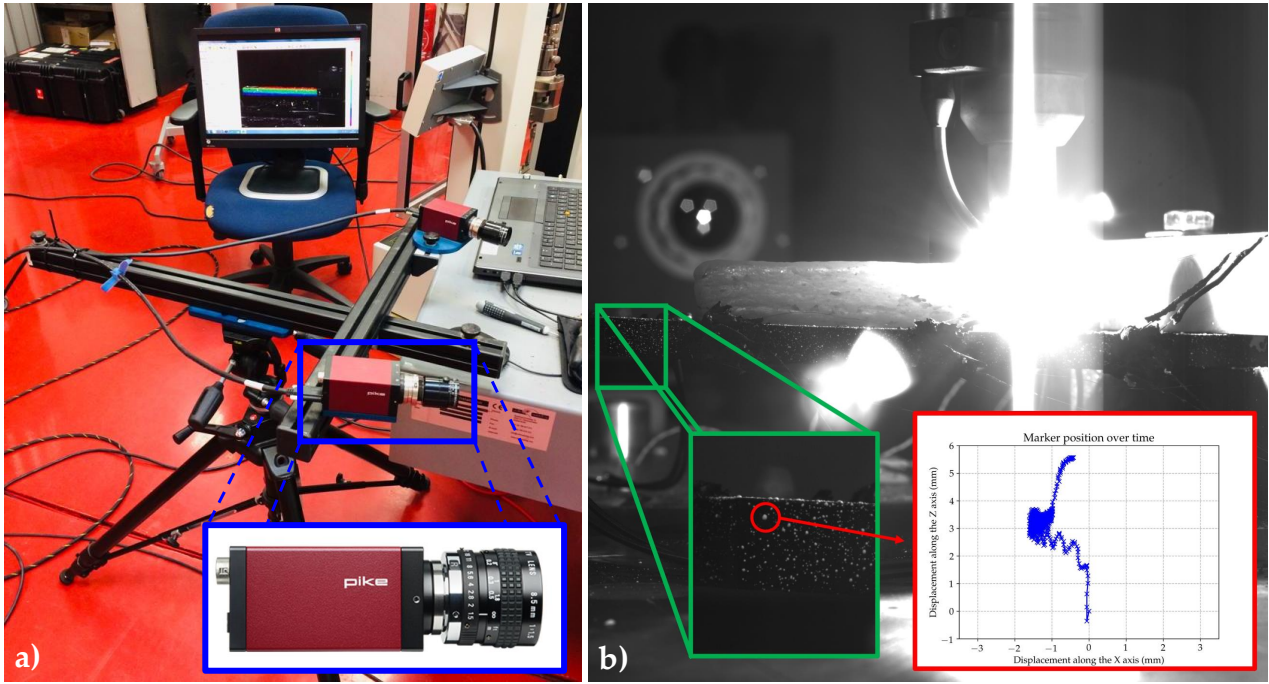


Figure 5.13 – a) Stereo-correlation device, b) Displacement measurement of a marker during the "Zigzag" wall test case



Figure 5.14 – 3D scan of the "Zigzag" and "Raster" 50 beads walls

for the thermo-mechanical simulations (about 115000 nodes).

5.3.3 Thermal model parameters calibration

This section focuses on the calibration of the thermal model parameters using the thermocouple data presented earlier. The calibration is performed in three steps. In the first step, only the thermocouple data of the "Zigzag" test are used for the calibration. Then, the same study is performed using the data from the "Raster" test. Finally, both tests are used to perform the calibration. The objective of this three-step study is to ensure that the calibration performed on one experiment is transposable to the other experiment, which has similar process parameters but a different deposition pattern. In addition, only the first 20 beads are used for the calibration. This allows firstly to shorten the calibration time and validate the calibration on the complete thermocouple data of the tests, particularly on the beads not taken into account for the calibration. The methodology presented in Section 4, and used for the calibration of the parameters in the 1st test case, is applied for the current use case.

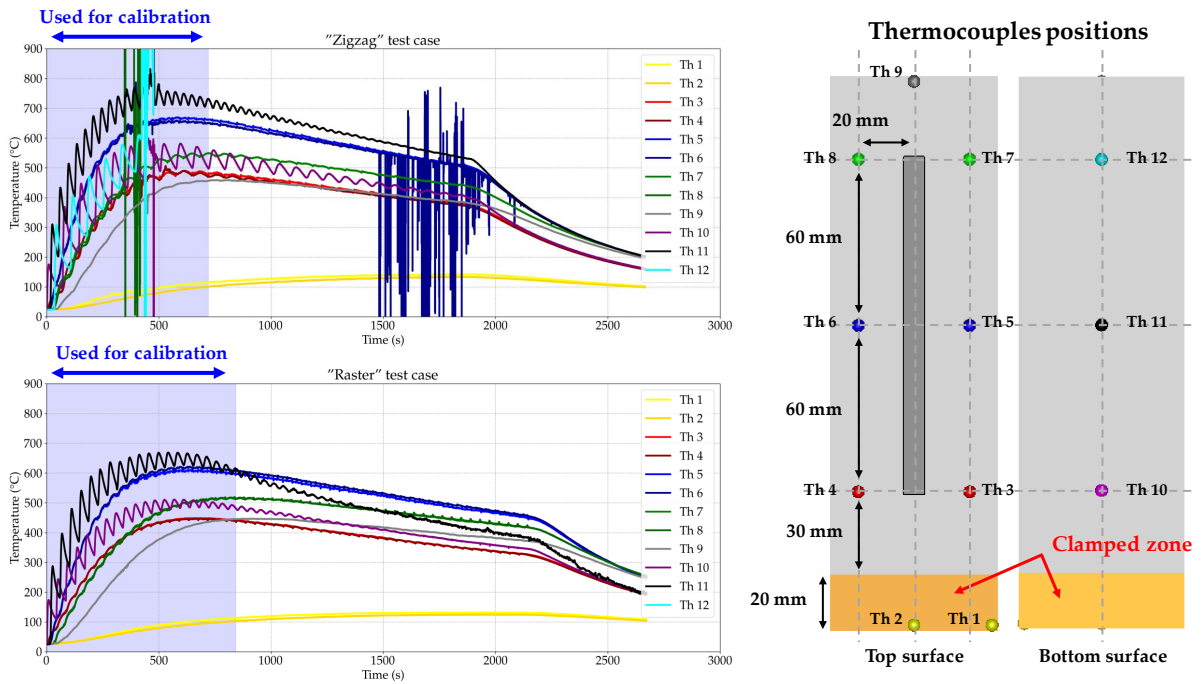


Figure 5.15 – Thermocouple curves of the "Zigzag" and "Raster" 50 beads walls, and the experimental data used for the calibration step.

For these tests, nine parameters are to be identified. In order to constitute the database to build the metamodel, a design of experiments is set up to generate the sets of parameters. As for the 1st study, the width of the heat source is imposed at the width of the bead because of the wall configuration for these tests. The thermal losses coefficients are considered linearly temperature-dependent, using ε_0 , ε_1 , h_0 , and h_1 (see Section 3.3.2 for more details). The newly added parameter is the thermal dissipation at the clamped area, which is included in this study. The distributions selected for these parameters are chosen based on the same expertise and studies as presented in Section 5.2. For the thermal dissipation at the clamped area, the range is chosen between 0, which means no convection, and 300.0×10^{-6} ($\text{W}\cdot\text{mm}^{-2}\cdot\text{K}^{-1}$), which is between the air and water forced convection. The distributions of the nine parameters are presented in Table 5.5.

Table 5.5 – Parameters to be calibrated, with the sampling distribution for the PCE surrogate model training and the prior distribution for the MCMC algorithm calibration step.

Parameters	Sampling distribution	Prior distribution
a_r (mm)	$\sim \mathcal{U}(3.0, 18.0)$	$\sim \mathcal{N}(8.0, (7.0)^2)$
f_r	$\sim \mathcal{U}(1.10, 1.70)$	$\sim \mathcal{N}(1.4, (0.25)^2)$
c (mm)	$\sim \mathcal{U}(1.0, 10.0)$	$\sim \mathcal{N}(5.0, (3.0)^2)$
η	$\sim \mathcal{U}(0.50, 0.95)$	$\sim \mathcal{N}(0.75, (0.4)^2)$
ε_0	$\sim \mathcal{U}(0.20, 0.80)$	$\sim \mathcal{N}(0.35, (0.15)^2)$
ε_1	$\sim \mathcal{U}(0.0, 1.0)$	$\sim \mathcal{N}(0.5, (0.4)^2)$
h_0 (W.mm ⁻² .K ⁻¹)	$\sim \mathcal{U}(0.0 \times 10^{-6}, 30.0 \times 10^{-6})$	$\sim \mathcal{N}(15.0 \times 10^{-6}, (15.0 \times 10^{-6})^2)$
h_1	$\sim \mathcal{U}(0.0, 1.0)$	$\sim \mathcal{N}(0.5, (0.4)^2)$
h_{cl} (W.mm ⁻² .K ⁻¹)	$\sim \mathcal{U}(0.0 \times 10^{-6}, 300.0 \times 10^{-6})$	$\sim \mathcal{N}(150.0 \times 10^{-6}, (100.0 \times 10^{-6})^2)$

From these distributions, the design of experiments is constructed using the low discrepancy Sobol sequences. 512 parameter samples have been generated, and the 512 associated simulations have been performed. The modeling of the experimental test is performed using the procedure described in Section 4. The clamping of the base plate has not been modeled, but it is represented by a clamped condition that has been applied to the nodes on the surface. The calibration was performed on the first 20 simulated beads. This allows reducing the computation time necessary to perform the 512 "*Zigzag*" and "*Raster*" simulations while having a simulation long enough to observe the influence of the thermal dissipation parameters (convection and radiation) and the effect of the heat loss at the clamp. Indeed, preliminary studies in the framework of this thesis project have shown that the influence of these phenomena is complicated to observe for the first beads. It is necessary to wait until the component accumulates enough heat. A certain number of beads is thus necessary for the calibration of the models. The time needed for each thermal simulation is about 3 hours, on 8 CPUs. Nevertheless, one of the significant advantages is that the simulations do not depend on each other. Therefore, they can be performed simultaneously in parallel on a computing cluster. With the calculation resources available at EDF, 512 simulations could be carried out in a day.

To simplify the surrogate model to be implemented, the entire temperature field is not taken into account. The temperature profiles during the fabrication of the first 20 beads at the thermocouple points are extracted for each of the 512 simulations. For each simulation, the thermocouple curves are then concatenated so that the output of the surrogate model is an estimate of the temperature curves at the points of all the experimental thermocouples. This dramatically simplifies the construction of the surrogate model, its complexity, and thus increases its accuracy. To validate the surrogate model, cross-validation is used. The sample of 512 simulations is thus subdivided into 10 subsets, and for each subset, the error is determined. The error of the implemented surrogate model is estimated to be around 2%, which is a very satisfactory result. The execution time of the surrogate model to achieve a prediction is about ten milliseconds.

The MCMC is then run using the surrogate model of the computed temperature profiles for the first 20 beads and the associated thermocouple experimental data. As for the 1st study, the variance of the observation $\Sigma_{D_{obs}}$ issued for the likelihood calculation is calculated from the symmetrically disposed thermocouple pairs, and a value of 8.0² (°C) is found. For the prior distributions, the gaussian distributions used are presented in Table 5.5.

The posterior distributions obtained are made up of 500000 accepted draws, with an acceptance

rate of approximately 35% for the three calibrations. The first 100000 draws are burn-in. For each of the three calibrations, the MAP is identified from the distributions of each parameter. The three MAPs are designated θ_z^* , θ_r^* , and $\theta_{z\&r}^*$, respectively for the calibration using the "Zigzag" test, using the "Raster", and both tests. The results are summarized in Table 5.6. All the distributions can also be studied. For example, the results of the "Zigzag" & "Raster" are presented in Figure 5.16 that display the accepted samples on a grid in which the diagonals show the 1-dimensional posteriors and the lower-left half shows the pairwise projections. The corner plots resulting from the calibration step of the "Zigzag" and for the calibration step of the "Raster" are presented in Appendix A.1.

Table 5.6 – Identified MAP for each 3 thermal inverse problems.

Parameters	a_r	f_r	c	η	ε_0	ε_1	h_0	h_1	h_{cl}
"Zigzag" MAP	16.1	1.49	4.99	0.748	0.332	0.339	1.22e-05	0.191	8.07e-05
"Raster" MAP	13.1	1.37	5.35	0.747	0.342	0.486	7.81e-06	0.313	1.51e-04
"Zigzag" & "Raster" MAP	13.8	1.38	5.01	0.754	0.316	0.276	1.33e-05	0.255	1.27e-04

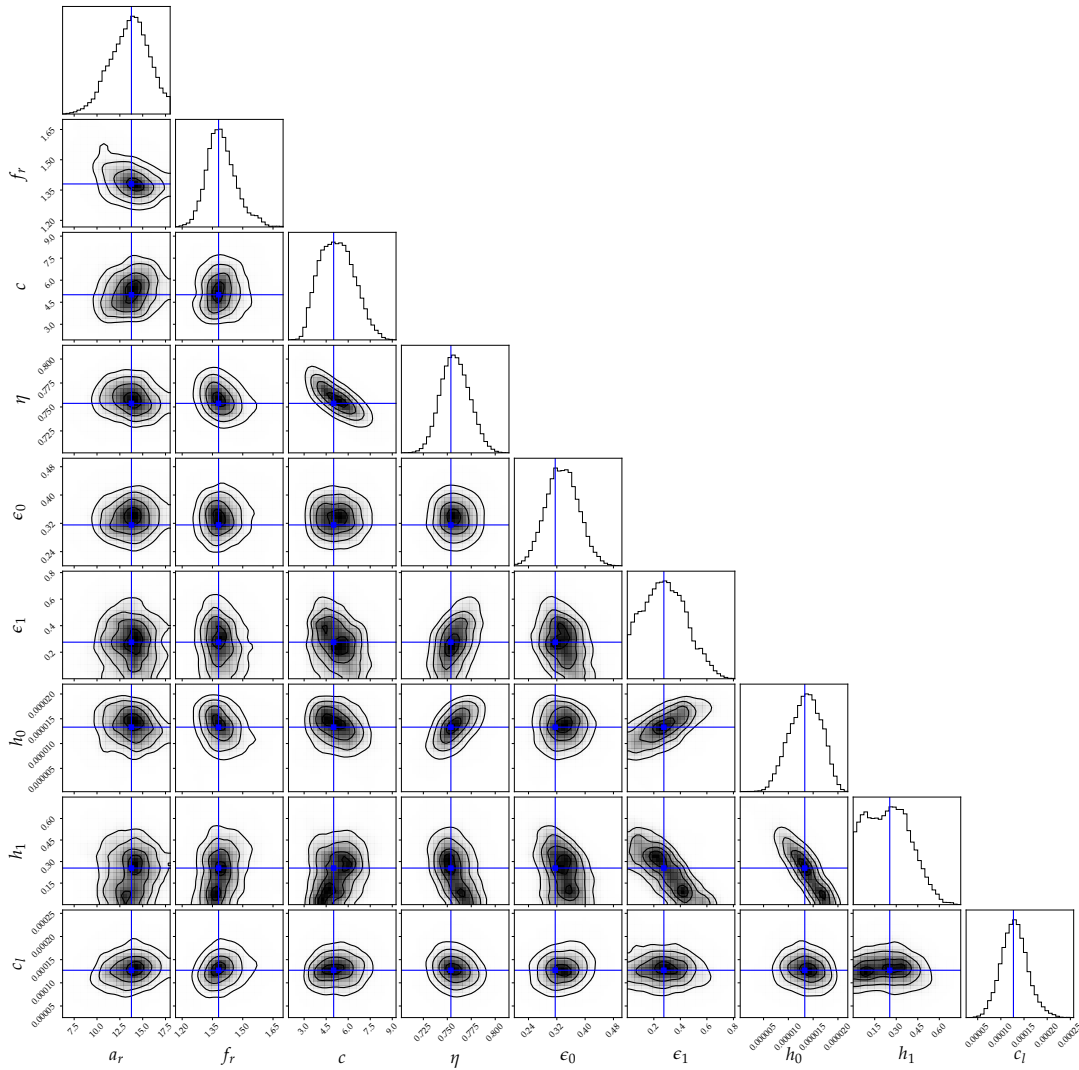


Figure 5.16 – Corner plot of the posterior distribution resulting from the calibration step of the "Zigzag" & "Raster" tests cases. The MAP $\theta_{z\&r}^*$ is represented in blue.

5.3.4 Numerical results

The posterior distributions and the MAPs were identified in the previous section. In the following, the comparison of the 3 optimal parameters set is performed. In addition, the models are compared with the other available experimental data (thermocouples, infrared (IR) thermal imaging, stereo-correlation) to validate the thermo-mechanical model and the parameter set acquired through calibration. For the results presented in this section, the thermo-mechanical simulation are performed using a quadratic element mesh. The simulations are performed using a piecewise linear isotropic hardening constitutive behavior (VMIS_ISOT_TRAC model in Code_Aster) with hardening annealing. It should be noted that the value of the yield strength of the substrates (at ambient temperature) given by the manufacturer is higher than the "standard" yield strength of 316L SS (around 340 MPa). This may be due to transformations on the substrate that result in hardening in the material. The yield strength used for the simulation is modified for these tests (2nd test case). A data set was found in the literature whose value at ambient temperature is close to the value given by the manufacturer. The yield strength taken into account for this section is presented in Table 5.7.

Table 5.7 – Evolution of the yield strength with temperature [188].

Temperature (°C)	20	200	300	400	500	600	700	800	900	1000	1100	1200	1400	3000
σ_y (MPa)	324	310	302	295	284	278	254	156	72	36	22	20	20	20

It should be noted that another approach exist. In general, the normalised yield strength is a broadly invariant function of temperature for 316L SS ($\sigma_y(T)/\sigma_y(T_{room})$), and to use this normalised variation, scaled by the actual measured yield strength for the actual component taken from the material certificate.

5.3.4.1 Thermal model results

■ **Temperature profiles:** Previously, three MAPs are estimated from three thermal inverse problems: "*Zigzag*" inverse problem, "*Raster*" inverse problem, and "*Zigzag*" & "*Raster*" inverse problem. Since the calibration steps were done using a surrogate model, it is necessary to ensure that the numerical simulations associated are well representative of the thermocouple curves. To achieve this thermal validation, and also to study the different MAPs, the "*Zigzag*" and "*Raster*" thermocouples data of the full tests are compared with the computed temperature profiles for each MAP.

The "*Zigzag*" and "*Raster*" simulations are performed for the 3 parameter sets. Figures 5.17 and 5.18 show the results curves for the 3 parameter sets (in red, green, and blue) and the thermocouple curves for the whole test and the cooling step. First of all, the trends of the curves are very satisfactory. Indeed, the experimental and simulated temperature profiles are very similar, even in the zone that is not used for the calibration. The thermocouples with the greatest difference are thermocouples 1 and 2. This difference can be explained by the simplified modeling selected for the conduction (forced convection) to simulate the thermal dissipation at the embedding. Nevertheless, the main interest of these thermocouples lies in the estimation of a thermal transfer at the embedded zone, so this discrepancy is not problematic. For the other thermocouple data, a good match is observed. The curves obtained with the θ_z^* give the best results, with an average relative error of 4.44% (10.26 °C).

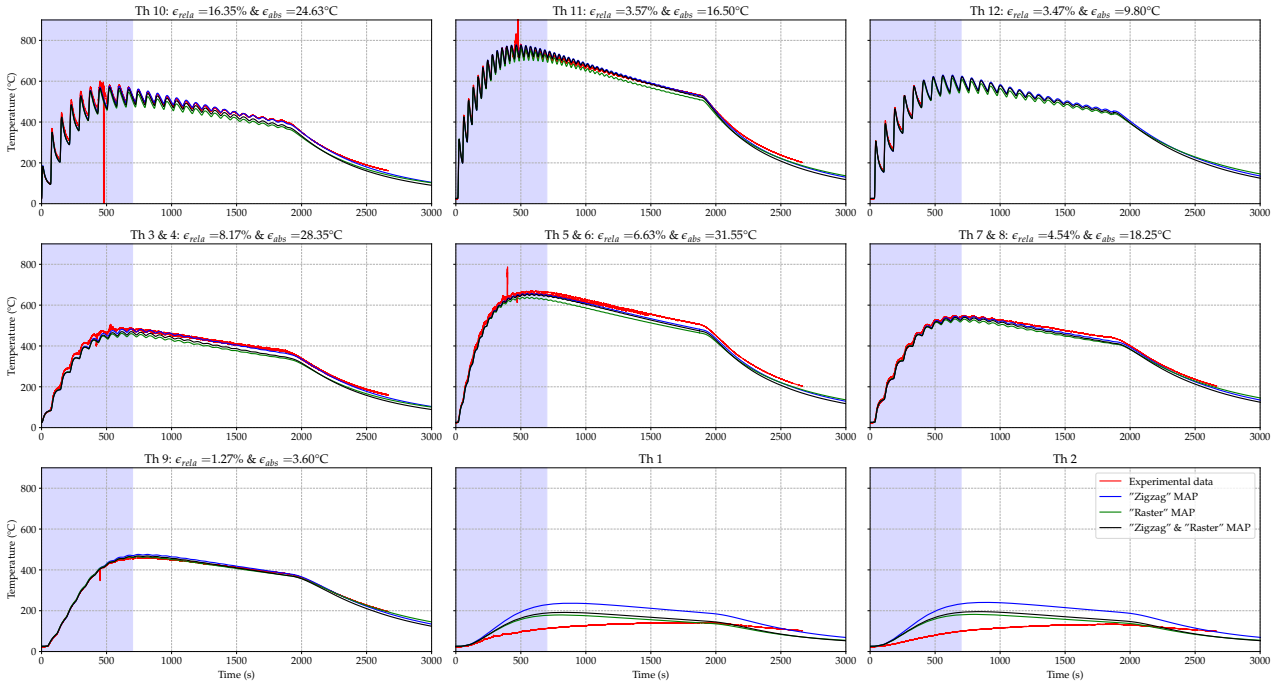


Figure 5.17 – Comparison of the thermocouples profiles of the "Zigzag" wall test with the temperature profiles for the 3 MAP: in red the experimental data, in blue the computed thermal profiles for the calibration on the "Zigzag" test, in green the computed thermal profiles for the calibration on the "Raster" test, and in black computed thermal profiles for the calibration on both tests.

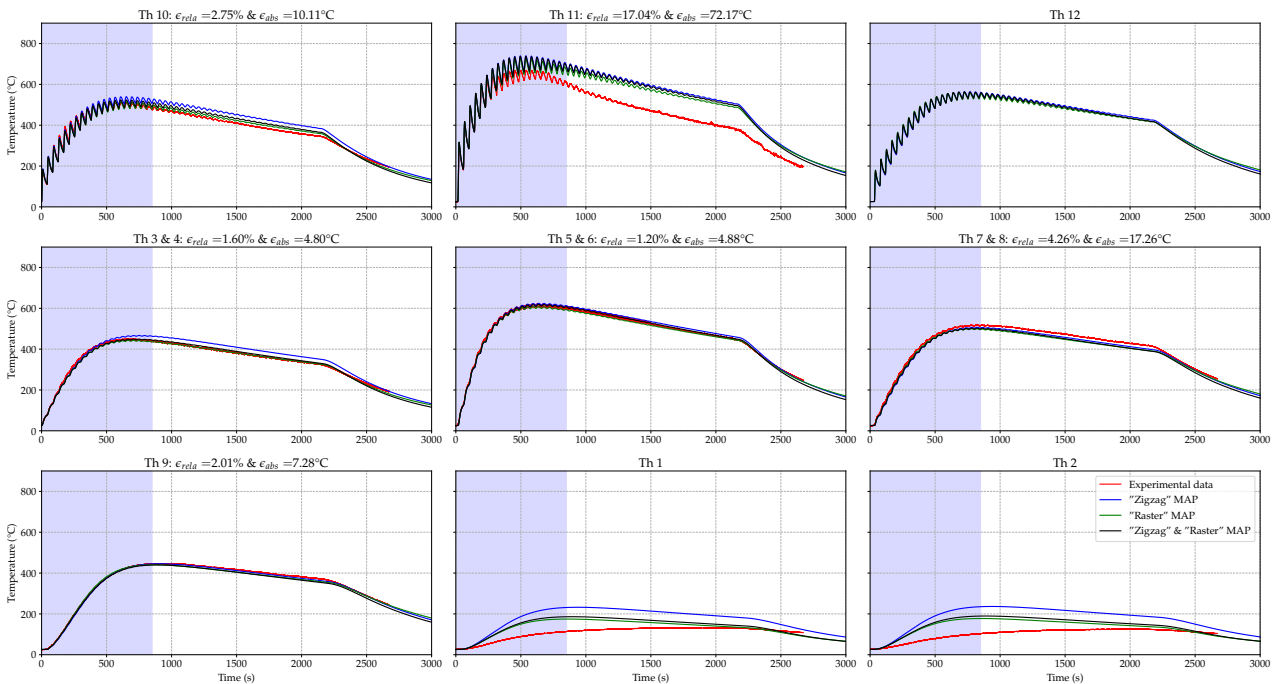


Figure 5.18 – Comparison of the thermocouples profiles of the "Raster" wall test with the temperature profiles for the 3 MAP: in red the experimental data, in blue the computed thermal profiles for the calibration on the "Zigzag" test, in green the computed thermal profiles for the calibration on the "Raster" test, and in black computed thermal profiles for the calibration on both tests.

Moreover, it is important to highlight that the prediction of temperatures using θ_r^* gives very similar results to the experimental data, with an average relative error of 6.67% (20.22 °C). Finally, the estimates using $\theta_{z\&r}^*$ are also very satisfactory, with an error of about 6.50% (16.90 °C), which, not surprisingly, is in between the error obtained with θ_z^* and θ_r^* .

For the "*Raster*" test, the same conclusions as for the "*Zigzag*" are reached. There is an excellent estimation of the thermocouples profiles, with an error of 4.81% (19.42 °C) for the simulation with θ_r^* , an error of 6.65% (26.89 °C) for θ_r^* , and of 5.75% (23.11 °C) for $\theta_{z\&r}^*$. Moreover, the results for thermocouple 11 are quite different from the numerical estimates. This deviation starts to appear before the first 20 beads and is obtained for the 3 MAPs. This deviation may come from a phenomenon not taken into account in the simulations. However, since this thermocouple is located under the fusion line, it is also highly probable that this deviation is caused by a slight detachment or damage of the thermocouple during the test. Otherwise, this phenomenon could also be explained by the different morphology of the "*Raster*" wall and the mesh used for the simulation.

The simulations on the two experiments demonstrated excellent results. Moreover, the simulations performed with the various MAPs have shown that the calibrated parameters of one experiment can be applied to another experimental test with the same process parameters but a different configuration. For all the following studies, the optimal parameter set used is the one resulting from the thermal inverse problem using "*Zigzag*" & "*Raster*": $\theta_{z\&r}^*$.

■ **Molten pool size evolution:** From the simulations, the molten pool sizes are extracted throughout the test at each time step. To do this, at each time step, the melting temperature isotherm is identified (at 1400 °C). A "bounding box" is built from the melting temperature isotherm to extract the length, width, and thickness. These quantities correspond respectively to the molten pool length, width, and depth. For both tests, the experimental measurements are originated from the IR camera images.

For the "*Zigzag*" wall test, the length of the molten pool is measured at each bead in the center of the wall and the cusp is extracted from the thermal camera images. Indeed, there is an oscillation in the size of the molten pool, which is very elongated in the center of the wall and very localized but deeper on the ends. The experimentally measured length is shown in blue in Figure 5.19. The simulation allows extracting the evolution of the molten pool length during the manufacturing of the "*Zigzag*" wall, which is represented in red on the same Figure 5.19. The experimental data and the computed estimations correspond very strongly. Indeed, the numerical curves accurately predict the size of the molten pool while capturing its general gradual evolution during the test. Moreover, the estimated and measured orders of magnitude are very similar.

For the "*Raster*" test, the molten pool length is measured at the middle of each bead (Figure 5.20). As for the "*Zigzag*" test, the results obtained are very satisfactory. The estimation of the molten pool length is very accurate, and its general evolution during the test is well captured.

■ **Inter-layer temperature evolution:** One of the quantities of interest in the control of welding and additive manufacturing parts is the inter-layer or inter-bead temperature. Therefore, the temperature of the elements below the next bead to be deposited is extracted from the simulations. The same quantity of interest is extracted from the thermal images.

Figures 5.21 and 5.22 show the numerical and the experimental inter-layer temperatures, for the

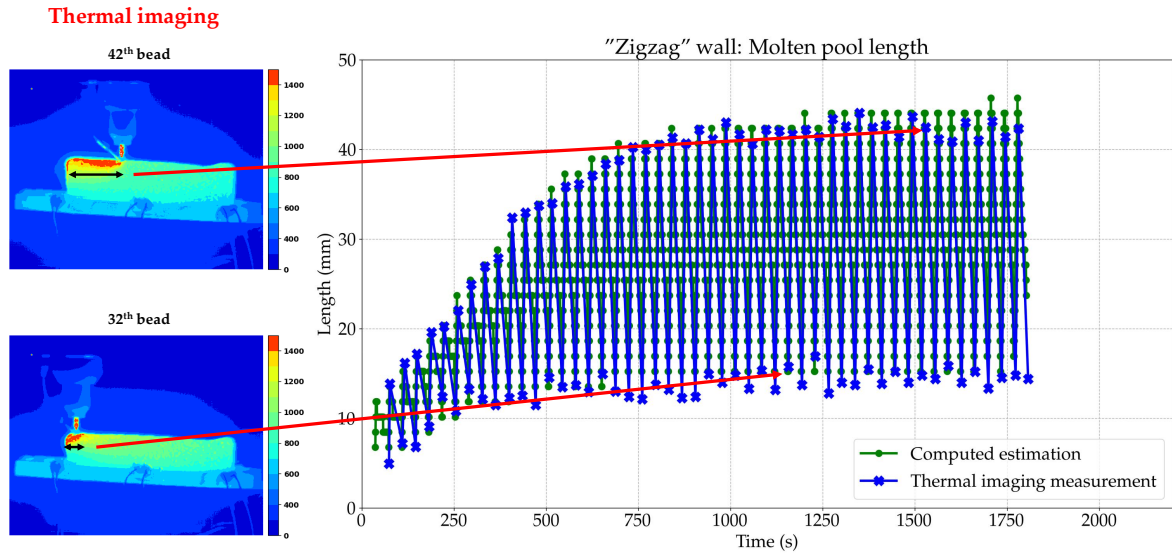


Figure 5.19 – Evolution of the molten pool length during the 50 beads "Zigzag" wall test: in red the computed estimation, and in blue, the experimental measurements.

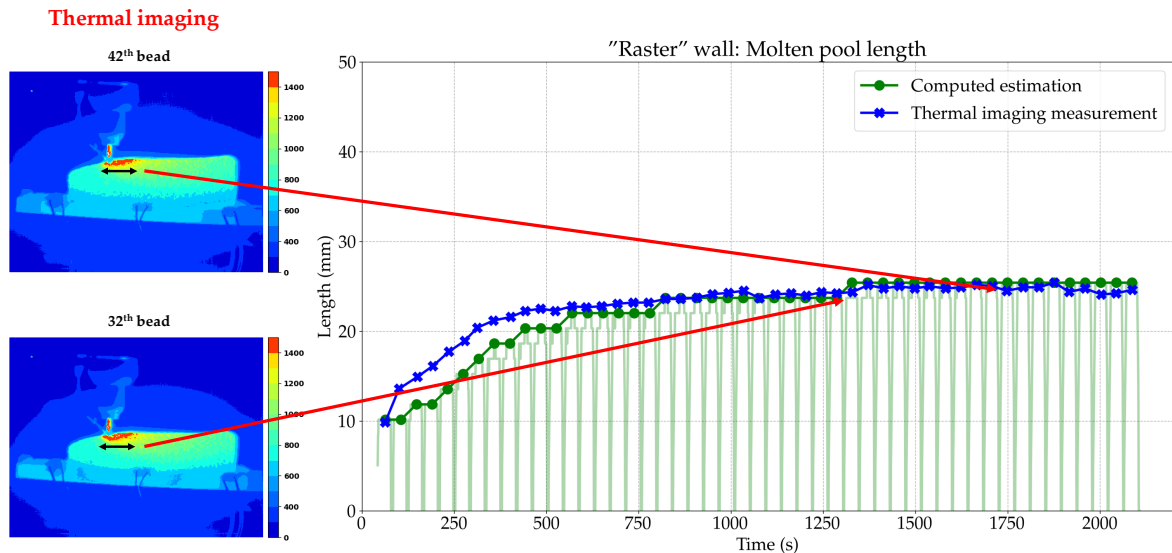


Figure 5.20 – Evolution of the molten pool length during the 50 beads "Raster" wall test: in red the computed estimation, and in blue, the experimental measurements.

"Zigzag" and the "Raster" respectively. The blue curve represents the inter-layer temperatures measured from the thermal camera, and the red the numerical predictions. The results show a very good match between the numerical predictions and the experimental data for both tests. For the "Zigzag" test, the inter-layer temperatures converge progressively and stabilize towards the 1700°C since the beginning of the new bead is above the end of the previous bead, and thus of the molten zone. On the contrary, for the "Raster" wall, the new bead deposition starts on the other end of the bead, making the inter-layer temperature much lower than for the "Zigzag" wall: it converges progressively towards 700-800°C. These orders of magnitude are very well predicted by the simulation, with a good general trend of the evolution of the curves. The inter-layer temperature results are therefore very satisfactory.

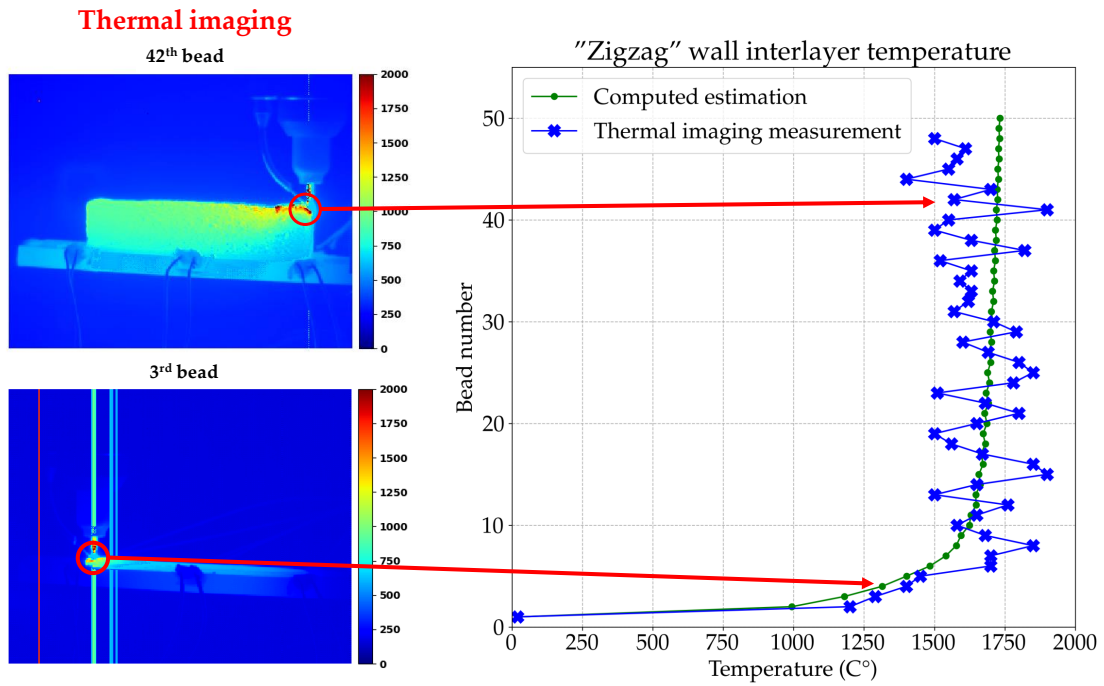


Figure 5.21 – Evolution of the inter-layer temperature of the "Zigzag" wall.

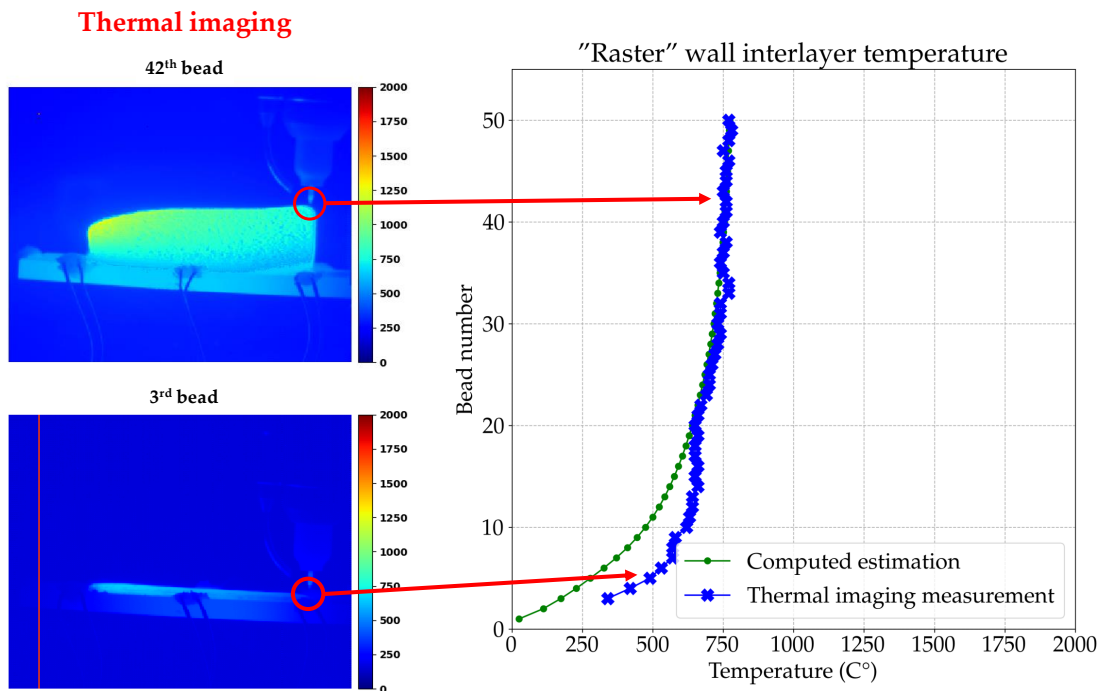


Figure 5.22 – Evolution of the inter-layer temperature of the "Raster" wall.

5.3.4.2 Free end displacement evolution

During the calibration of the thermal model, a probability distribution is obtained for each parameter. The MAP is determined from these posterior probability distributions. Figure 5.23 shows the displacement field after cooling for the "Zigzag" and "Raster" test with the MAP parameter set: $\theta_{z\&r}^*$.

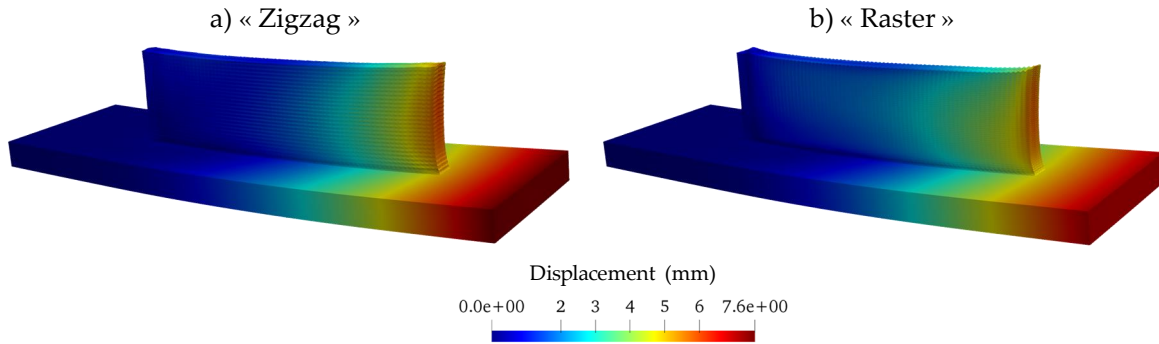


Figure 5.23 – Displacement field of the "Zigzag" and "Raster".

In order to study the influence of the variation of the thermal parameters on the mechanical model, 20 sets of parameters among the 400000 draws accepted during the MCMC are selected randomly. Then, the associated 20 thermo-mechanical simulations are performed in order to have a first propagation of uncertainty. Figures 5.24 and 5.25 represent the profile of the simulation with the MAP of the parameters, as well as the 95% confidence interval deduced from the 20 simulations for the "Zigzag" and the "Raster". In blue are represented the experimental displacement profiles obtained from the stereo-correlation data.

The numerical profiles of the "Zigzag" test have a very similar trend as the experimental profile. The displacement oscillations are of the same "shape": there are in phase with amplitudes of the same order of magnitude. For the first 20 beads, the numerical results and the experimental profile are very close, to the point that the experimental profile is within the 95% confidence interval of the numerical curves. However, from the middle of the test, a progressive overestimation of the displacement is observed until the end of the test. This phenomenon can have multiple causes. One of them is that the yield strength considered may not be perfectly adapted to the material. It is also possible that the other parameters of the constitutive law are not perfectly adapted for long-duration tests. Indeed, the behavior law used was calibrated for welding operations. For the WAAM process, the manufacturing time is much longer, the cycles are more numerous, and the component temperature is higher. These last two points can also be at the origin of the divergence. The behavior law used is of the isotropic piecewise linear hardening model with hardening annealing. Since the cycles are rather numerous, a hardening model more adapted to the cyclic phenomena might be more relevant. Therefore, the use of an elasto-viscoplastic type law could be judicious. Moreover, the manufactured wall continuously accumulates heat, increasing viscous phenomena and thermal creep.

For the "Raster" test (Figure 5.25), the same findings and conclusions as the ones for the "Zigzag" test are made. The numerical curves and the experimental profile trends are very similar, with oscillations well in phase. The results are overall very satisfactory. The same phenomenon of overestimation of the displacement is observed starting from the middle of the test. However, it seems slightly weaker than for the "Zigzag" test. This may be consistent with the hypothesis that heat accumulation in the part is one of the leading causes of this slight divergence. Indeed, the experimental data and curves presented above highlight the fact that the "Raster" accumulates less heat than the "Zigzag" due to

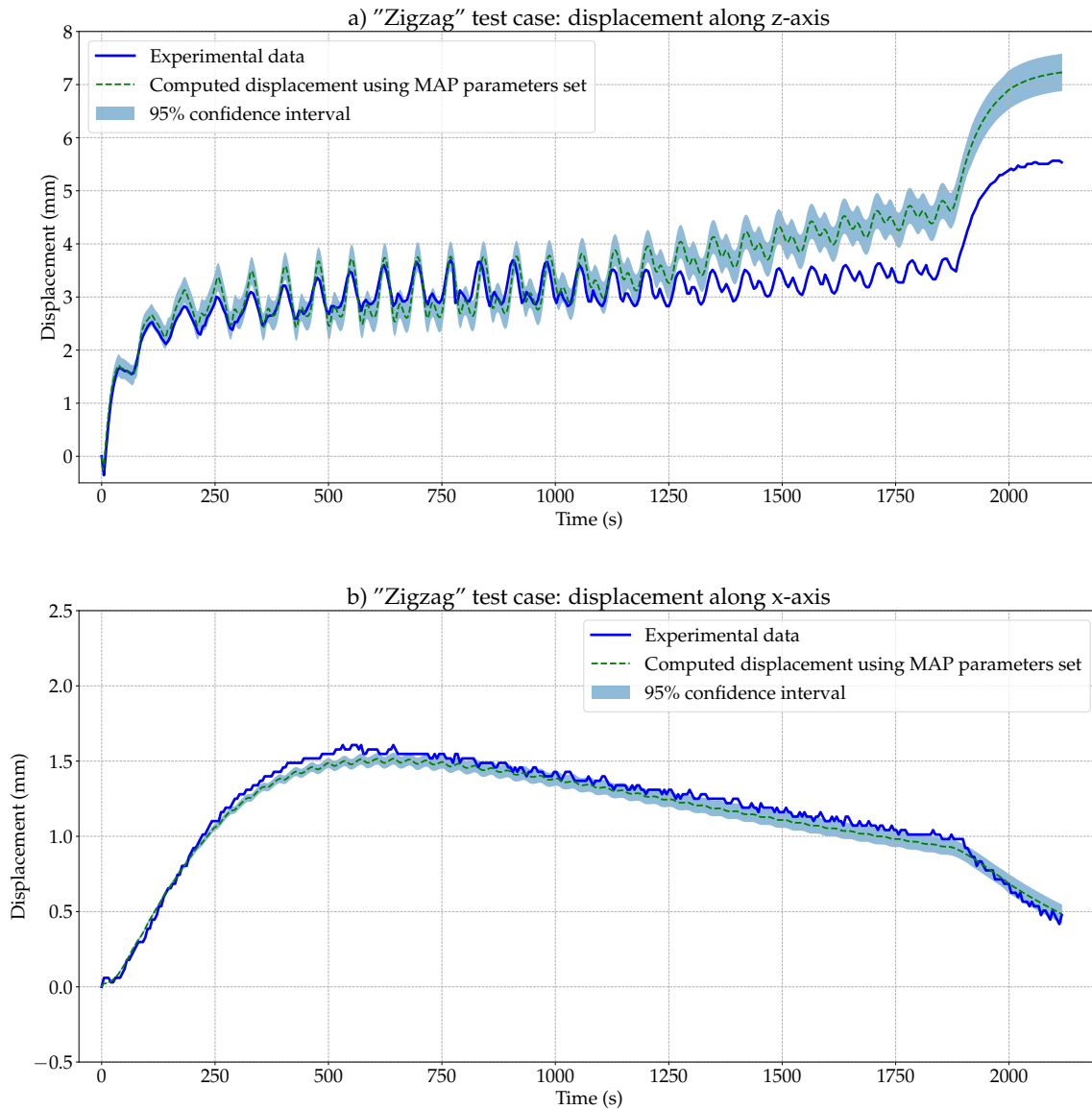


Figure 5.24 – Experimental (in blue) and computed (in green) deflection profiles evolution of the "Zigzag" wall: a) Displacement along the z-axis, b) Displacement along the x-axis.

the deposition strategy and the 6 seconds of cooling between the beads.

These results open up many possibilities for future work. First, it would be interesting to perform a similar test with a cooling strategy, considering, for instance, an idle time between the beads. Such a test will allow investigating if the divergence phenomenon comes from the heat accumulation in the part. In addition, it would be interesting to perform this test on a virgin hardening state base plate to use the available elasto-viscoplastic constitutive behavior.

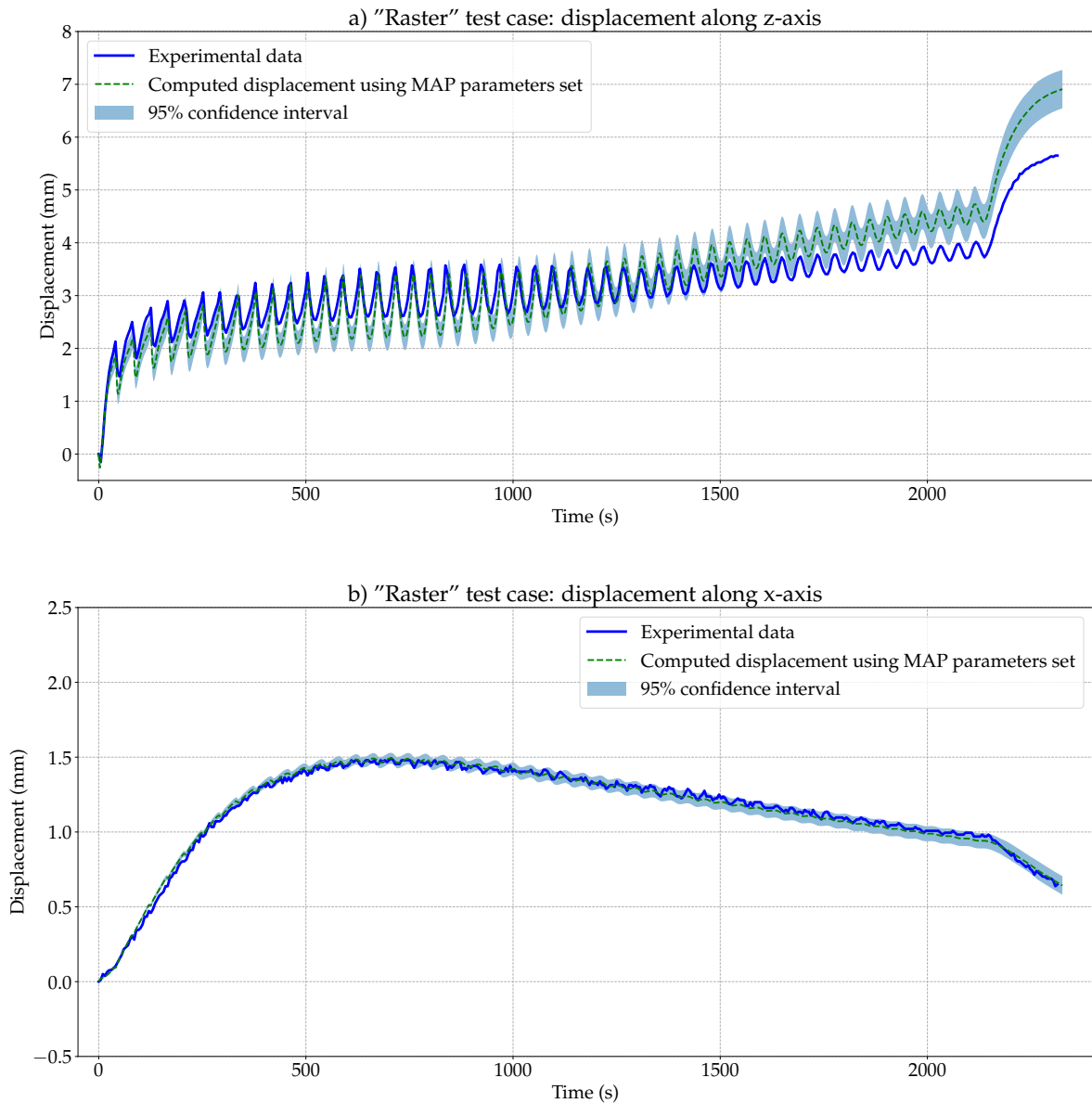


Figure 5.25 – Experimental (in blue) and computed (in green) deflection profiles evolution of the "Raster" wall: a) Displacement along the z-axis, b) Displacement along the x-axis.

5.3.4.3 Residual stresses

Figures 5.26 and 5.27 show the stress fields for the "Zigzag" and "Raster" test for the MAP $\theta_{z&r}^*$. The general finding that emerges is that the stress fields seem very similar for both tests, despite the difference in manufacturing path. It is highlighted that stresses in the welding direction are predominant, which is an observation that is consistent with that observed for welding. In addition, a concentration of contraction is observed at the geometric singularities, which is quite obvious. Due to the action of the input material (the wall), the base plate is subjected to bending stresses, which

explains the tension/compression stress profile. A more symmetrical stress distribution of the residual stresses is observed for the "*Zigzag*" case than for the "*Raster*" case. This is in agreement with the unidirectional aspect of the "*Raster*" and the alternating aspect of the "*Zigzag*". This highlights the effect of the deposition pattern.

Figure 5.28 presents the uncertainty propagation study of the thermal parameters on the stress fields. The standard deviation field of each component of the stress tensor (σ_{xx} , σ_{yy} , σ_{zz} , σ_{xy} , σ_{xz} , σ_{yz}) is built from the 20 thermo-mechanical simulations of each test as shown in Figure 5.28 (for the σ_{xx} , σ_{yy} and σ_{zz} components). The average standard deviations for each stress tensor component and each test are shown in Table 5.8. To get a better idea of the distribution of standard deviations, a histogram of all the concatenated standard deviation of each component and for each node is shown for both tests in Figure 5.28. The histograms show that the standard deviations are localized towards the small values, with a mean of 4.5MPa for the "*Zigzag*" and 5.1MPa for the "*Raster*", and a median of 3.0MPa for the "*Zigzag*" and 3.2MPa for the "*Raster*".

Table 5.8 – Mean standard deviation of the residual stress fields of the 3 stress components σ_{xx} , σ_{yy} , and σ_{zz} for the two tests (MPa).

Stress tensor component (MPa)	" <i>Zigzag</i> "	" <i>Raster</i> "
σ_{xx}	3.3	4.7
σ_{yy}	4.4	5.4
σ_{zz}	1.2	1.7

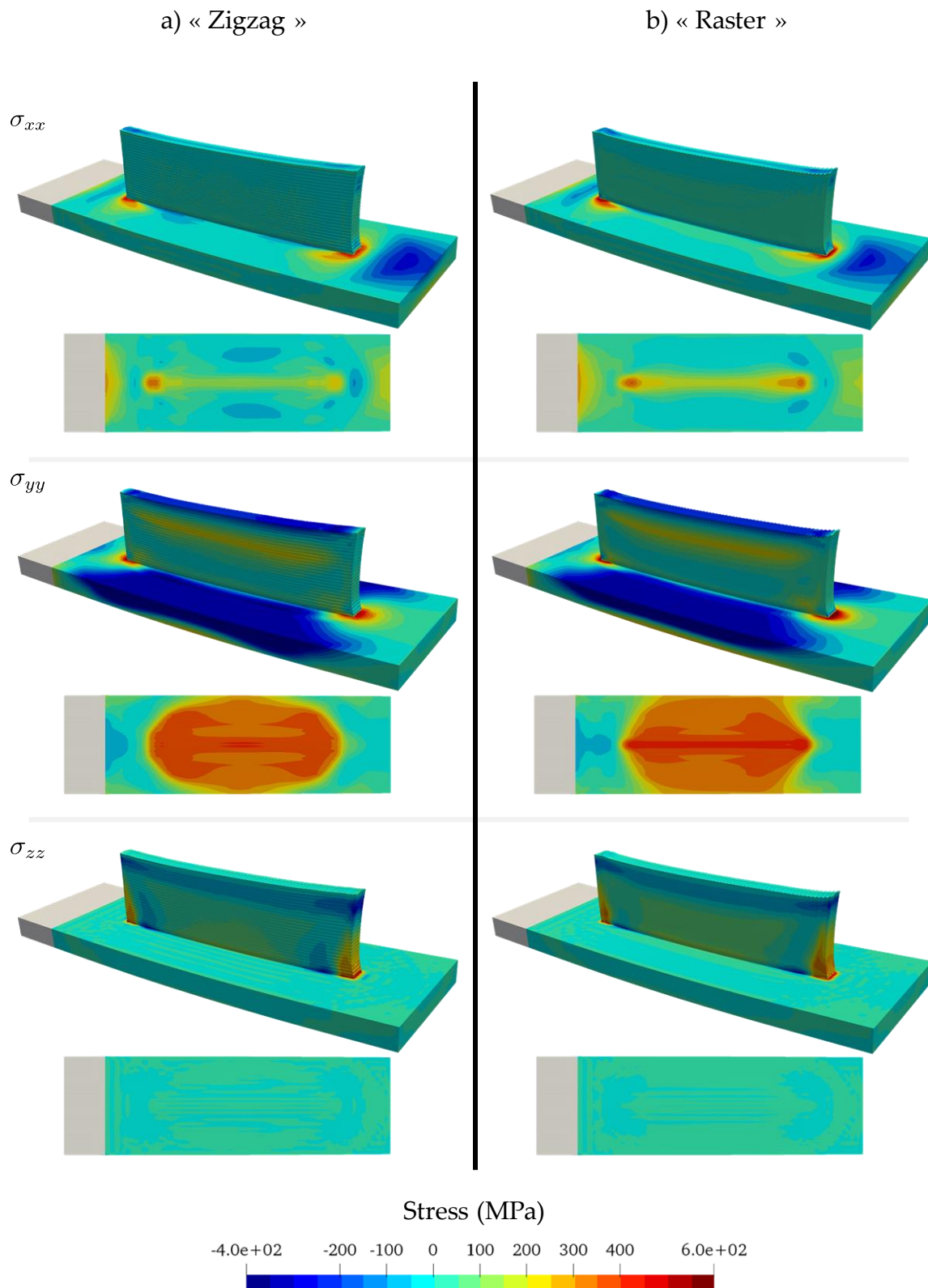


Figure 5.26 – Residual stress fields of the 3 stress components σ_{xx} , σ_{yy} , and σ_{zz} for the two tests: a) "Zigzag", b) "Raster".

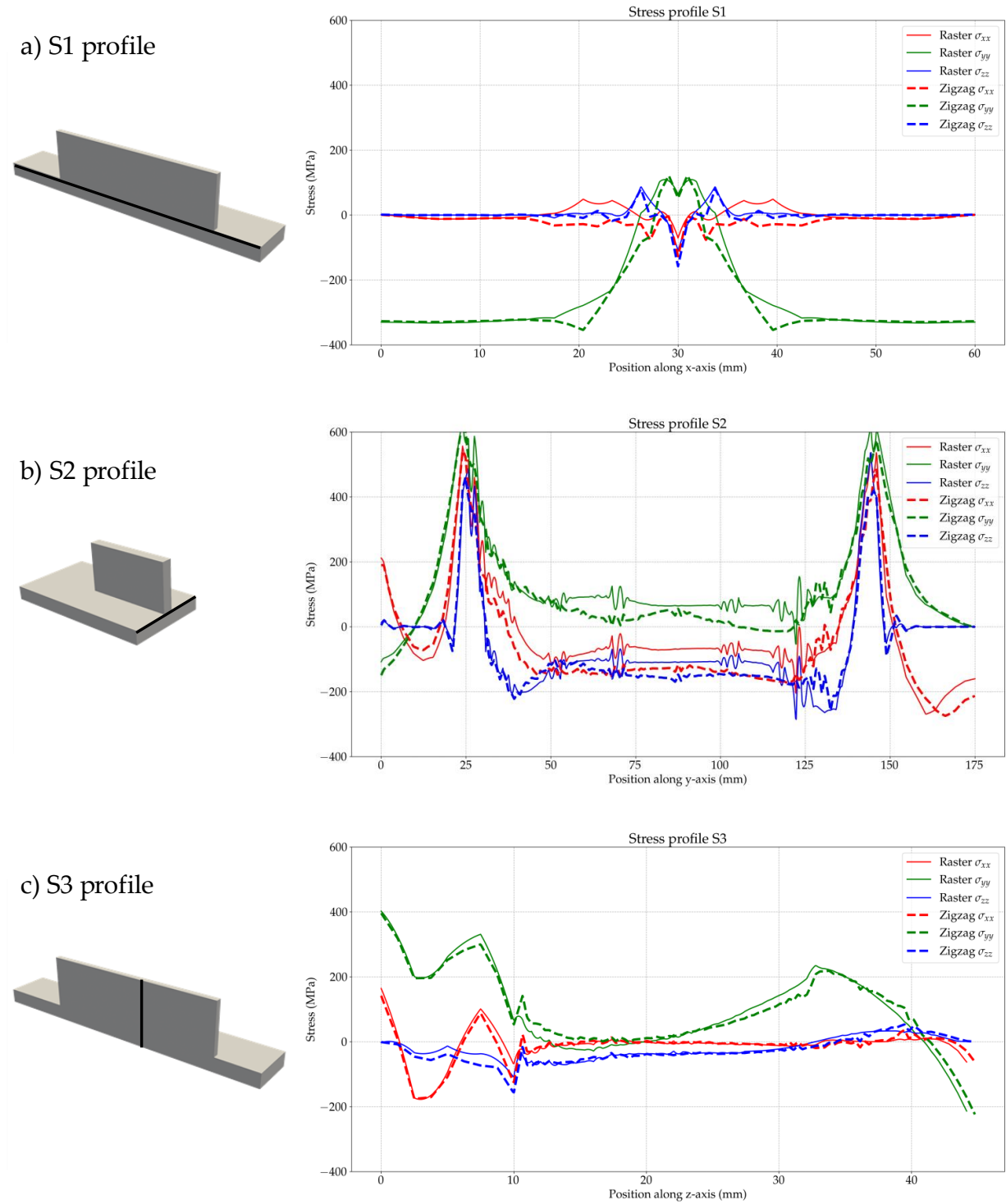


Figure 5.27 – Residual stress profiles of the 3 stress components σ_{xx} , σ_{yy} , and σ_{zz} for the two tests on 3 sections: a) "Zigzag", b) "Raster".

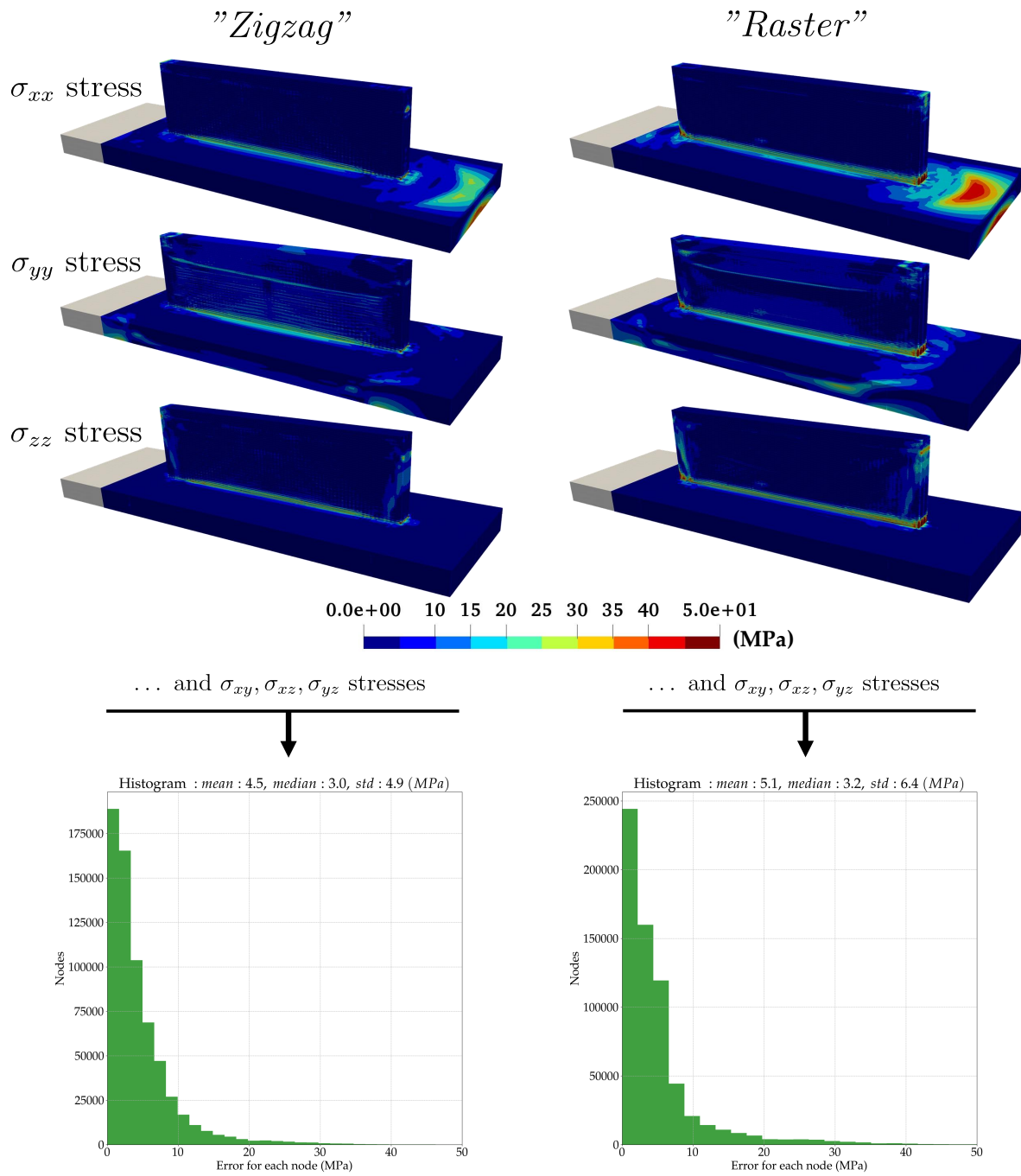


Figure 5.28 – Standard deviation of the residual stress fields of the 3 stress components σ_{xx} , σ_{yy} , and σ_{zz} for the two tests: a) "Zigzag", b) "Raster".

5.3.5 Conclusion of the study

This study consists in the conduction and the analysis of two well-instrumented tests. The two experiments are performed with similar process parameters, but with different path or shape configurations. The purpose of such a study is to see if the calibration of the thermal model parameters on a test can be used for another test with the same process parameters. The results showed that this is possible and once again demonstrated the performance of the methodology used to solve the thermal inverse problem. Moreover, in this study, the models are validated on multiple physical quantities. In addition to the thermal validation using thermocouple data, the thermal model showed high performance in estimating the length of the molten pool, which is found in good agreement with the molten pool measured by the thermal camera. Moreover, the simulation allows a very good estimation of the inter-layer temperature trend, which is defined in this section as the temperature of the part below the starting point of the deposit of a new bead. In conclusion, despite a calibration step performed only with thermocouple data, the prediction of the molten pool length and inter-layer temperature is very satisfactory.

The second step of validation concerned the mechanical model. As indicated in the section, the constitutive behavior law used is a piecewise linear isotropic hardening model, whose yield stress is adapted due to the fact that the base plate was originally hardened. The results of the mechanical model are compared with the displacement profiles of the free extremity of the base plate obtained using stereo correlation. For this comparison, several mechanical simulations are performed, with draws from the posterior parameter distributions. In this way, a first propagation of uncertainty from the thermal parameters to the mechanical predictions is made. The results seem very satisfactory and open several perspectives for the choice of the constitutive behavior.

This experimental test has been used in other studies which are presented in Appendices [A.2](#), [C](#), and [D](#). Initially, a complementary test at the two walls was carried out to validate the calibration step: a cylinder. In Appendix [A.2](#), the thermal results of the cylinder for the calibrated parameters are presented. Appendix [C](#) covers a thermal sensitivity study of this test at the scale of the "Zigzag" wall, not just at the point of thermocouples. Finally, a model selection study to identify which heat dissipation model is most suitable is presented in Appendix [D](#).

5.4 3rd use case: NET Network consortium Task Group 9 (TG9)

5.4.1 Introduction and objectives

The experiments presented in this section compares models and experimental measurements on residual stresses. The experimental tests were carried out at the University of Montpellier in the framework of the European Network on NET program (Neutron Techniques Standardisation for Structural Integrity). This experimental test case is named TG9 for Task Group 9.

The interest of these tests is that they were very well-instrumented from a mechanical point of view, with continuous measurement of the displacement of the free end of the base plate during the tests, and with residual stress measurements carried out on several profiles at the end of the test. In this section, these data are compared to the computed results obtained using the thermo-mechanical model implemented. Moreover, this comparison is carried out considering all the available constitutive behaviors presented in Chapter 4, with and without hardening annealing. Its again important to specify that these models have not been fitted on the same experimental dataset, and potentially do not match the same material. Thus, the objective is not to perform a sensitivity analysis on the hardening modeling approach, by to have a first discussion on the constitutive behavior models associated with the available parameter sets for the WAAM residual stresses prediction.

The main objectives of this section are the following:

- Modeling and calibration on an experimental test case with another welding process: GMAW with CMT transfer mode,
- Comparison of the stresses experimentally measured and predicted by the simulations for different constitutive behaviors and modeling of hardening.

All residual stress measurements were performed by the Task Group 9 (TG9) in the European Network on Neutron Techniques Standardisation for Structural Integrity (NET) [132].

5.4.2 Description of the experimental setup

The experimental study is carried out on the WAAM Pro 3D additive manufacturing platform of the IUT of Nîmes. The arc welding equipment used is GMAW with CMT transfer mode. The GMAW-CMT welding torch is mounted on a *Kuka KR 16* 6-axis robot. This experimental study consists of two experiments. Both tests are performed in the same configurations and with the same process parameters. The difference between the two tests is that one of them is a single-bead, while the other consists of 5 beads. They are called respectively in this manuscript the "single-bead" and the "five-beads" tests. The following description is the description of the test "five-beads", but it can also apply to the "single-bead" test, the only difference being that there is a unique bead.

The "five-beads" experimental case TG9 consisted of a superposition of five 100 mm long weld beads. The beads are deposited with alternating welding direction ("*Zigzag*" deposition strategy) as shown in Figure 5.29. The base plate used is a rectangular plate of 124 mm long, 50 mm height, and 6 mm thickness. The part is fixed on one end with a screw. The other end of the plate is free in order to study the evolution of the displacement. The beads deposited are centered on the base plate. The material used for the base plate and the filler material is 316L SS. The shielding gas is composed of 98% Argon and 2% CO₂. The process parameters are chosen in such a way as to obtain a bead of

good appearance and dimensions. The diameter of the 316L SS wire feed is 1.2 mm, and the flow rate of the material input is fixed at 14 L/min. The workpiece-nozzle distance is set at 15 mm. The process parameters are adapted for optimal manufacturing. During the deposition of the first layer, the energy and the speed of wire feed are higher than for the other four following layers. In addition, an idle time of 35 s is established between each bead. Furthermore, at the beginning of each bead, there is a dwelling time during which the torch is held in position for 0.5 second. This ignition step is deemed necessary to stabilize the arc and the molten pool. Table 5.9 summarizes the process parameters associated with the TG9 experimental test:

Table 5.9 – Process parameters used for the TG9 test case.

Welding parameter	First layer	Other layers
Process type	CMT	CMT
Voltage U (V)	13.0	13.0
Intensity I (A)	107.0	86.0
Travel speed V_s (m s^{-1})	0.007	0.007
Maximal stroke rate (m min^{-1})	3.2	2.5
Idle time (s)	15	15
Dwelling time (s)	0.5	0.5

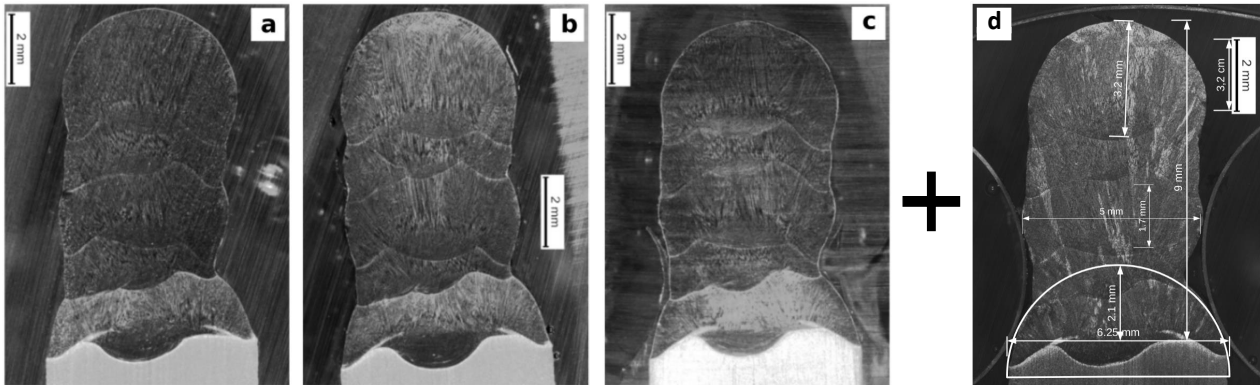


Figure 5.29 – Macrograph of the "five-beads" test at different sections. Images from the PhD thesis of Cambon et al. [100].

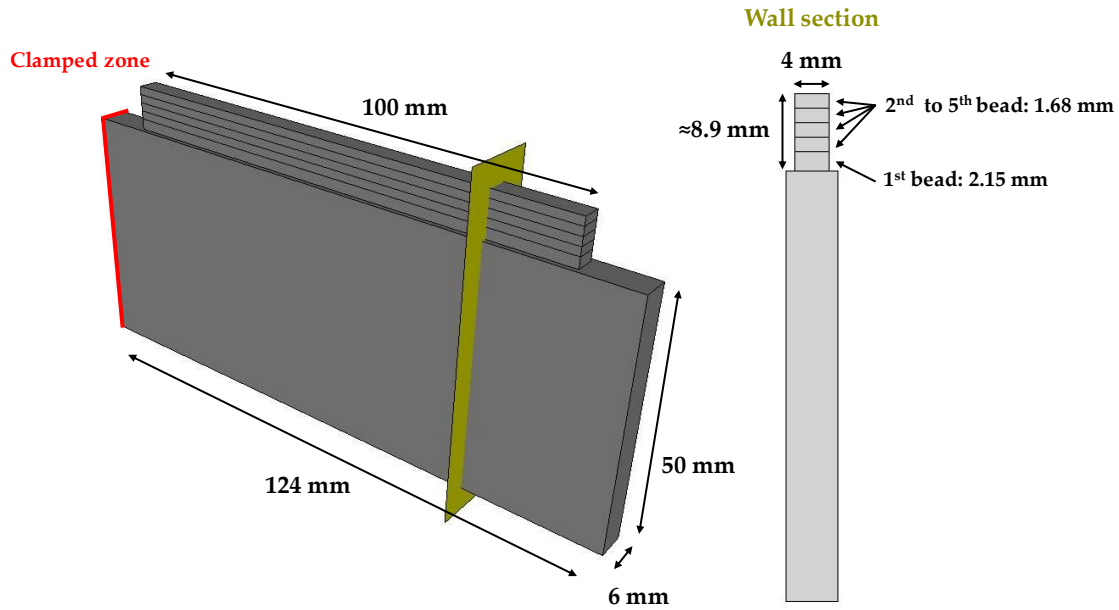


Figure 5.30 – TG9 "five-beads" full test: wall dimensions.

5.4.2.1 Instrumentation

Several physical quantities are measured during the manufacturing process: the voltage, the current, the temperature using thermocouples, the size of the molten pool, and the displacement at the free end of the base plate. Other analyses are also carried out a posteriori once the manufactured part had completely cooled down to ambient temperature: the morphology of the deposits is investigated by macrography analysis, the metallurgical analysis is performed using Electron Back Scattered Diffraction (EBSD), and the residual stresses are measured using a neutron diffractometer. In this study, only some of these data will be considered. For more information, one can refer to the work of Cambon et al. [70, 100] which presents these tests in a clear and detailed way.

■ **Thermocouples:** For the "five-beads" test, the temperature is measured at four points using 0.5 mm diameter type K thermocouples during the manufacturing process and the subsequent cooling step to room temperature. The acquisition rate is 20 Hz during 2500 s. The thermocouples are positioned in-depth in the base plate. They are inserted in holes of a diameter equal to 1 mm and a depth of about 1 mm, and are fixed on the bottom of the hole using metallic glue. The positions of the thermocouples are shown in Figure 5.31.

■ **Displacement evolution:** The vertical displacement of the free edge of the sample is recorded during the deposition and the beginning of the cooling step using a profilometer with an acquisition rate of 0.2 Hz during 800 s for both the "single-bead" and the "five-beads" tests. The used profilometer is a laser line profile sensor Micro-Epsilon ScanControl LLT 26xx-25. The evolution of the displacement along the z-axis over time is obtained by averaging the points of the measured profile for each measurement time. The profilometer is located under the base plate free end, as represented in Figure 5.32 with a blue arrow.

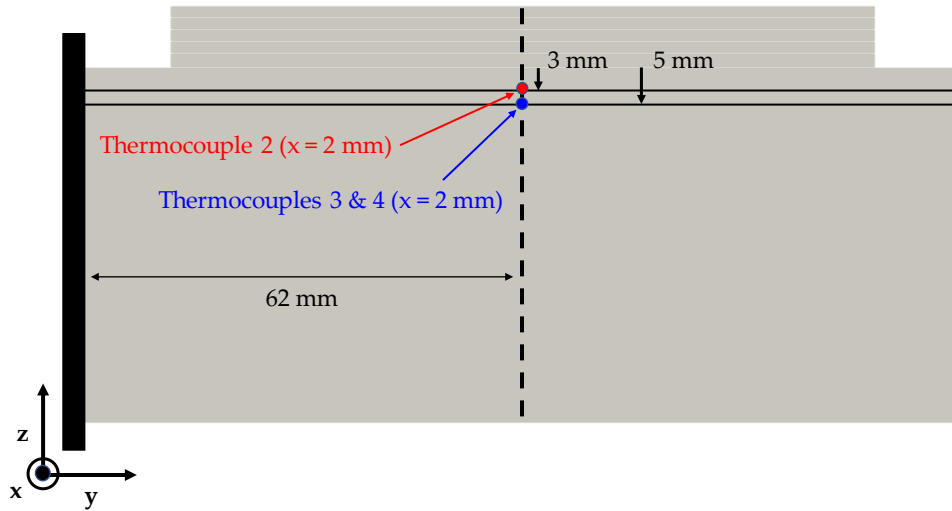


Figure 5.31 – TG9 "five-bead" test: thermocouples locations.

■ **Residual stresses:** After the manufacturing and the cooling steps of the TG9 component, the residual stresses in different directions are measured for both the "single-bead" and the "five-beads" tests. The measurement campaign was conducted by Dr. Robert Wimporoy in the "Helmholtz-Zentrum Berlin für Materialien und Energie" as part of the NET network consortium (Neutron Techniques Standardization for Structural Integrity), and more specifically in Task Group 10, which focuses on additive manufacturing topics. This task group uses a nuclear reactor as a continuous neutron source. The measurements for the analysis of strains and residual stresses are performed with the E3 diffractometer on the BER II research reactor [189]. The residual stresses are estimated from the measured strains using Hooke's law with the assumption of plane stresses, which is justified by the configuration of the test (small thickness compared to the other dimensions). The method of characterization of stresses by diffraction is based on the estimation of the lattice strain from the inter-atomic distance. The latter is obtained from the diffraction angles using Bragg's law [190]. For the "single-bead" test, the stress measurements are carried out on four profiles S1, S2, S3, and S4, as shown in Figure 5.32-a. For the "five-beads" test, the stress measurements are taken according to the single profile S5 shown in Figure 5.32-b. The different experimental stress profiles are presented in Figures 5.39, 5.40, 5.41, 5.42, 5.43, 5.44, 5.45, 5.46, 5.48, and 5.49 in the comparative study of numerical and experimental results.

From the process parameters presented in Table 5.9, the height and width of the 1st beads are evaluated at 2.15mm and 4mm, and the others at 1.68mm and 4mm, as shown in Figure 5.30. The generated mesh for the full "five-beads" test (also used for the "single-bead" test) is made of about 42000 hexahedral elements. For the calibration, the linear elements mesh is used (about 51000 nodes). For the results of the numerical results section, the same mesh but with quadratic elements is preferred for the thermo-mechanical simulations (about 200000 nodes).

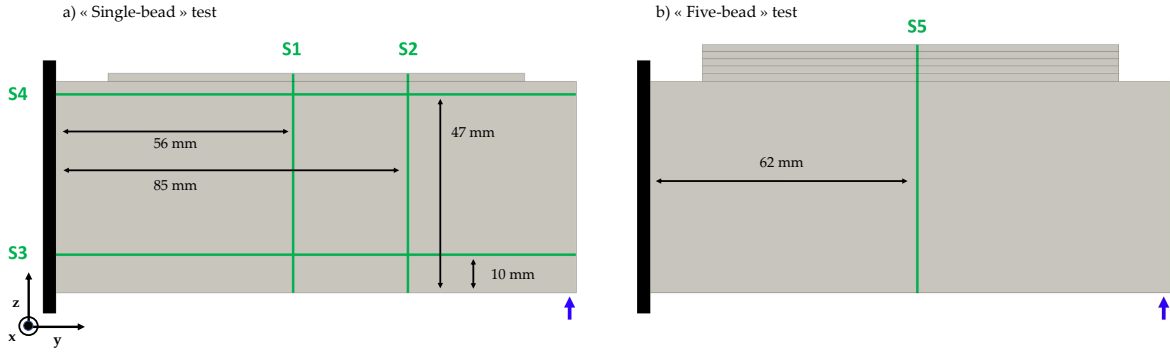


Figure 5.32 – a) TG9 nominal "single-bead" test: residual stress measurement profiles S1, S2, S3 and S4 are shown in green, and the displacement measurement location during the test is indicated with the blue arrow, b) TG9 full "five-beads" test: residual stress measurement profile S5 are shown in green, and the displacement measurement location during the test is indicated with the blue arrow.

5.4.3 Thermal model parameters calibration

The calibration step is performed on the complete experimental "five-beads" test. The duration of the experimental test simulated is 500 seconds. For this test case, eight parameters are to be identified. Unlike the two previous studies (wall configurations), the width of the heat source is not imposed at the width of the part. The thermal losses coefficients are considered constant and not temperature-dependent, simply using ε and h . Indeed, as the test has a quite short duration, and since there is only a little heat accumulation, it does not seem necessary to take into account a possible dependence of these parameters on temperature. The thermal dissipation at the clamped zone is also included in this study. The distributions of these parameters are chosen based on the same expertise and studies as those presented in Section 5.3. The DOE distributions of the eight parameters are presented in Table 5.10.

Table 5.10 – Parameters to be calibrated, with the sampling distribution for the PCE surrogate model training and the prior distribution for the MCMC algorithm calibration step.

3 rd test case: Parameters	Sampling distribution	Prior distribution
a_r (mm)	$\sim \mathcal{U}(3.0, 18.0)$	$\sim \mathcal{N}(8.0, (7.0)^2)$
f_r	$\sim \mathcal{U}(1.10, 1.70)$	$\sim \mathcal{N}(1.4, (0.25)^2)$
b (mm)	$\sim \mathcal{U}(1.0, 10.0)$	$\sim \mathcal{N}(5.0, (3.0)^2)$
c (mm)	$\sim \mathcal{U}(1.0, 10.0)$	$\sim \mathcal{N}(5.0, (3.0)^2)$
η	$\sim \mathcal{U}(0.50, 0.95)$	$\sim \mathcal{N}(0.75, (0.4)^2)$
ε	$\sim \mathcal{U}(0.20, 0.80)$	$\sim \mathcal{N}(0.35, (0.15)^2)$
h (W.mm ⁻² .K ⁻¹)	$\sim \mathcal{U}(0.0 \times 10^{-6}, 30.0 \times 10^{-6})$	$\sim \mathcal{N}(15.0 \times 10^{-6}, (15.0 \times 10^{-6})^2)$
h_{cl} (W.mm ⁻² .K ⁻¹)	$\sim \mathcal{U}(0.0 \times 10^{-6}, 300.0 \times 10^{-6})$	$\sim \mathcal{N}(150.0 \times 10^{-6}, (100.0 \times 10^{-6})^2)$

From these distributions, the design of experiments is constructed using the Sobol sequences with low discrepancy. 512 parameter samples have been generated, and the 512 associated simulations have been performed. The modeling of the experimental test is performed using the procedure described in Section 4. The mesh generated consists of 23112 hexahedral linear elements (29750 nodes in total). The calibration was performed on the five simulated beads with a cooling stage. The duration of each

thermal simulation is about 1 hour, on 8 CPUs.

To construct the surrogate model, the temperature evolution at the thermocouple points during the manufacturing of the first 20 beads are extracted for each of the 512 simulations. The thermocouple curves are then concatenated for each simulation so that the output of the surrogate model is an estimate of the temperature curves at the points of all the experimental thermocouples. The error of the implemented surrogate model is estimated to be around 1.5%, which is a very satisfactory result (Figures 5.33 and 5.34). The execution time of the surrogate model to achieve a prediction is about ten milliseconds.

For the MCMC, as for the 1st study, the variance of the observation $\Sigma_{D_{obs}}$ issued for the likelihood calculation is calculated from the symmetrically disposed thermocouple pairs 3-4: 8.0^2 ($^{\circ}\text{C}$). For the prior distributions, the gaussian distributions used are presented in Table 5.10.

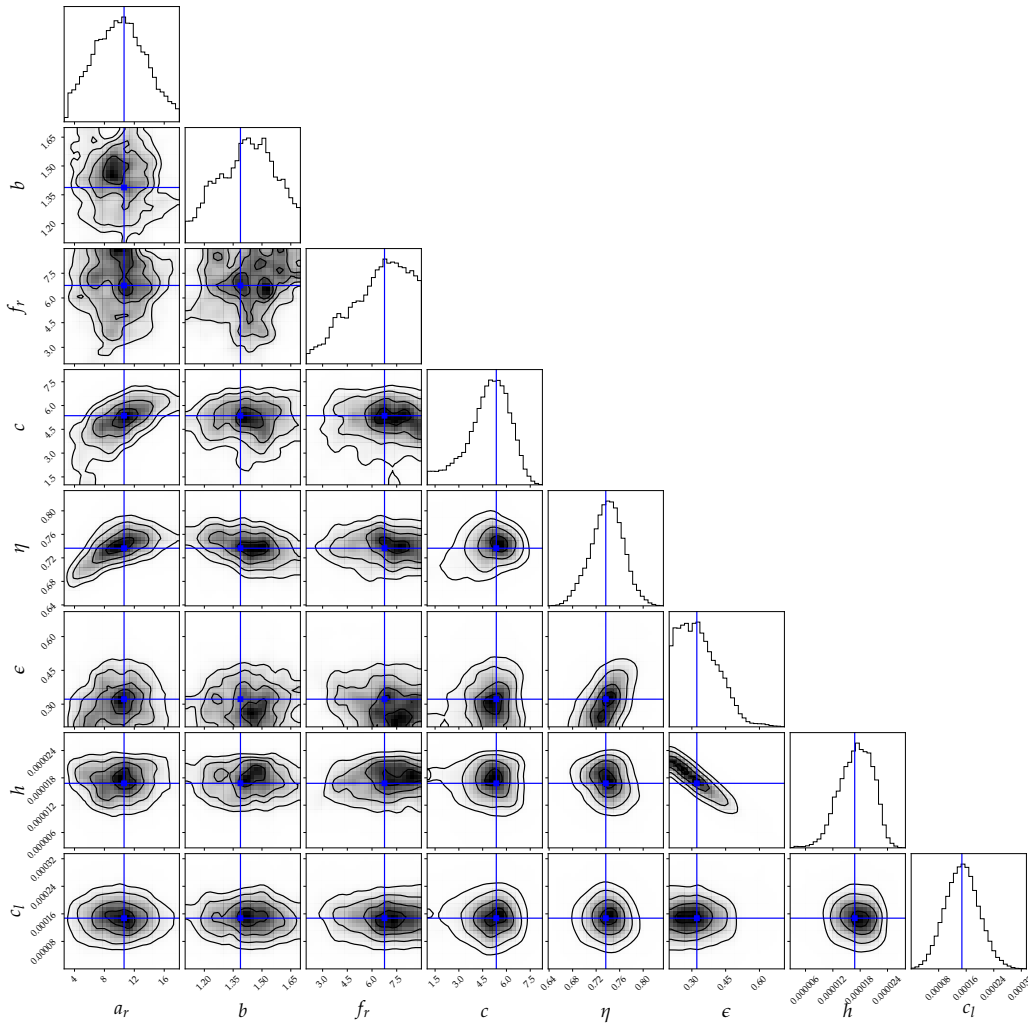


Figure 5.33 – Corner plot of the posterior distribution resulting from the calibration step of the TG9 test case. The MAP is represented in blue.

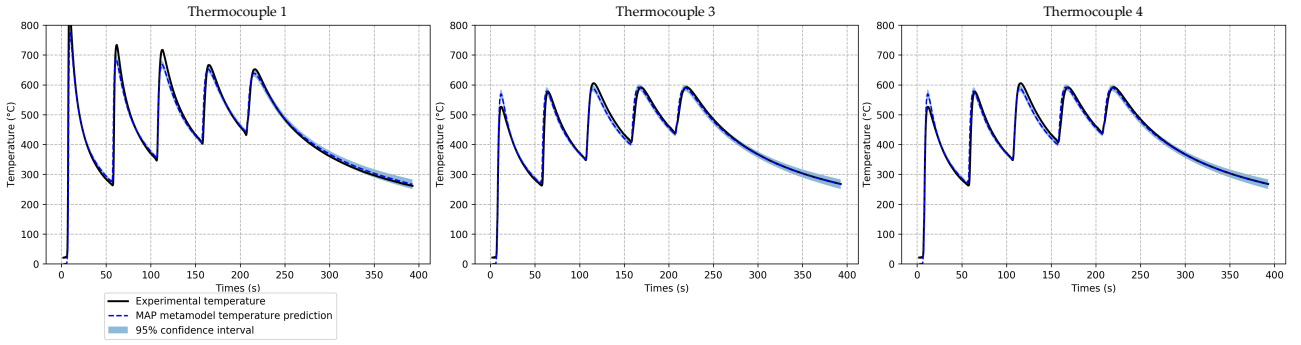


Figure 5.34 – In black the experimental data, in blue the surrogate model estimation using the MAP, with the 95% confidence interval.

Table 5.11 – Identified MAP for the TG9 test case.

Parameters	a_r	f_r	b	c	η	ε	h	h_{cl}
MAP	1.06e+01	1.39e+00	6.76e+00	5.36e+00	7.36e-01	3.22e-01	1.68e-05	1.47e-04

5.4.4 Numerical results

In the first part of this section, a thermal validation is first carried out by comparing the thermocouple data with the numerical simulation thermal profiles using the MAP parameter set. The second part of this section focuses on the validation of the mechanical model. The residual stress and displacement data (free end displacement evolution) experimentally acquired for the TG9 "single-bead" and "five-beads" TG9 test are compared with the thermo-mechanical simulations for all the available constitutive laws presented in this manuscript, with and without hardening annealing. Such a study is made in order to validate the thermo-mechanical model and to discuss the constitutive laws and the hardening modeling choices.

5.4.4.1 Thermal results for the full "five-beads" test

This subsection focuses on the thermal validation of the model (after calibration) on the "single-bead" test and the full "five-beads" test that was partly used for calibration. As for the previous studies, the calibration step allowed finding the MAP of the distribution of the parameters and showed an excellent correspondence with the surrogate model. The complete thermal simulation must now be compared to the thermocouple data to validate this parameter set. Figures 5.35 and 5.36, on which the numerical and experimental curves are compared, show a very good correspondence. Indeed, absolute errors of 9.5°C and 15.5°C are respectively found for thermocouple 2 and thermocouples 3 – 4, which are very satisfactory.

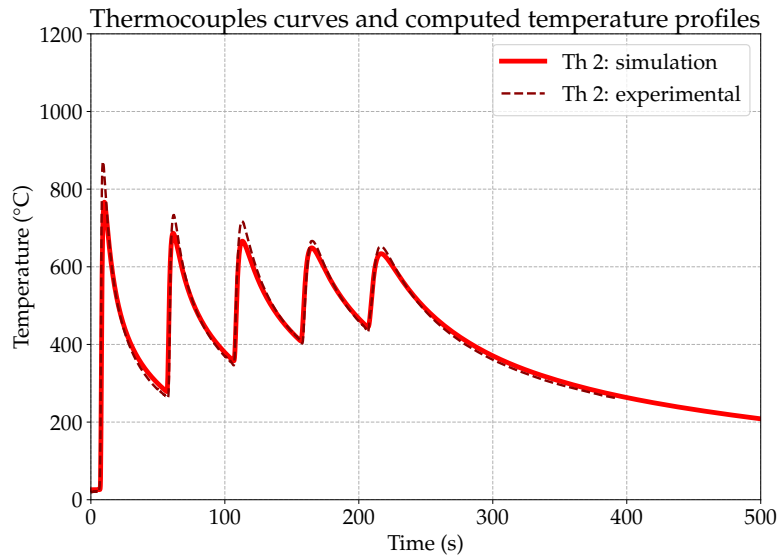


Figure 5.35 – Comparison of computed and experimental temperature profiles of the thermocouple 2.

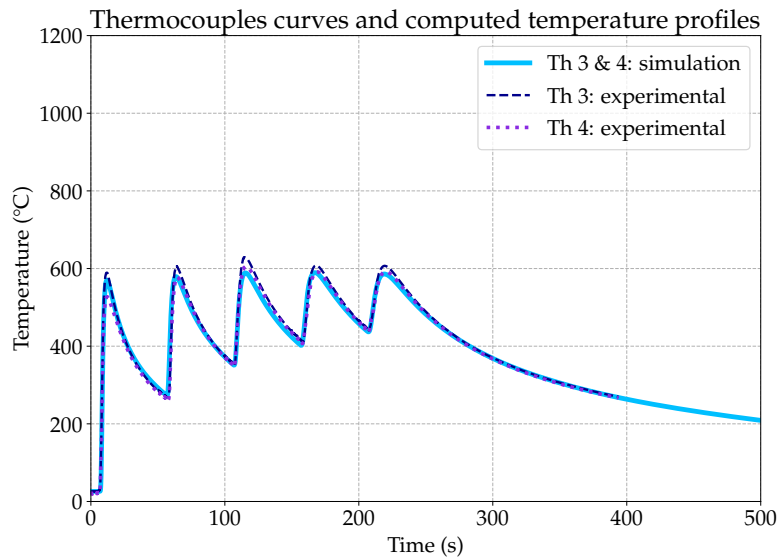


Figure 5.36 – Comparison of computed and experimental temperature profiles of the thermocouples 3-4.

5.4.4.2 Mechanical results

In this section, the experimental mechanical data are compared for all available and defined behavior laws for the welding simulation performed at EDF to evaluate the developed numerical model and to have a first impression of the most suitable constitutive behavior models. The constitutive laws used in this section are all the ones presented in Section 3.4: the elasto-plastic constitutive laws VMIS_ISOT_LINE, VMIS_ISOT_TRAC, VMIS_CINE_LINE, VMIS_ECFI_LINE, VMIS_CIN1_CHAB both with and without hardening annealing, and the elasto-viscoplastic constitutive law VISC_CIN1_CHAB

without hardening annealing. The use of hardening annealing is noted as "Anneal" in the following figures. The experimental data are extracted from 2 experimental tests: the first test focuses only on the first bead followed by the cooling step. The second one takes into account the complete test, i.e., the carrying out of the "five-beads", followed by the cooling step (Figure 5.37).

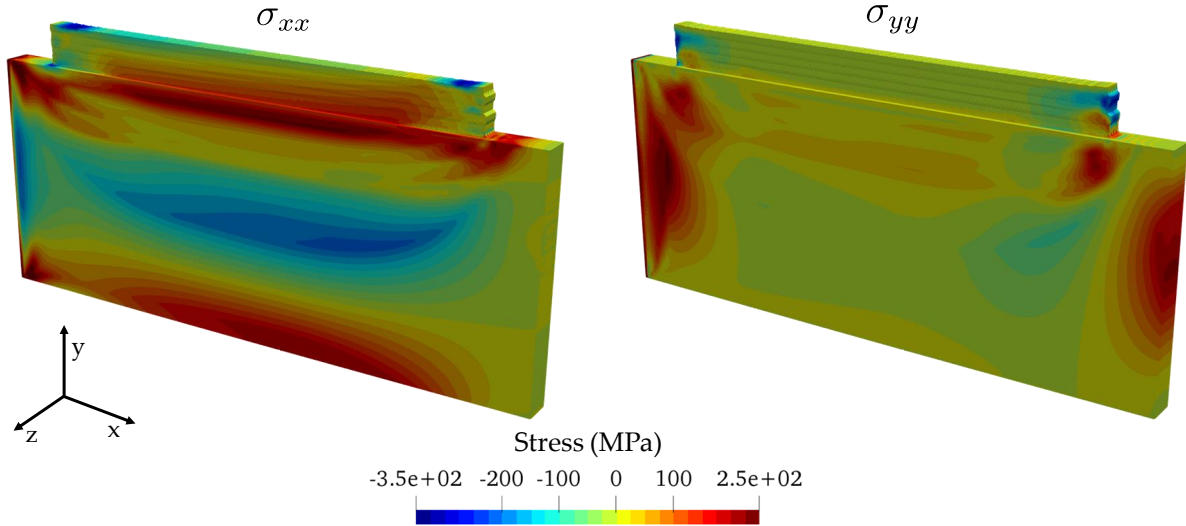


Figure 5.37 – "Five-beads" test residual stress fields using the VMIS_CINE_LINE behavior model with hardening annealing.

■ **"Single-bead" test - Free end displacement evolution:** The evolution of the deflection at the free end is measured experimentally using a laser sensor for the "single-bead" experimental test during the manufacturing and the post-fabrication cooling step. In Figure 5.38 are compared the experimental and numerical profiles: in blue is represented the experimental curve and the continuous curves are the numerical predictions, each corresponding to a different behavior law. Figure 5.38 shows that the trend of the numerical curves and the experimental curve are very close, with displacement amplitudes of the same order of magnitude. Moreover, the residual displacement, i.e., at the end of the manufacturing process, stabilizes at about 0.6 mm after returning to room temperature. The curves highlight that the kinematic hardening VMIS_CINE_LINE behavior provides the best estimates, with an absolute error of 0.033 mm. The results are also very good for the kinematic hardening VMIS_CINE_LINE with hardening annealing and the mixed hardening VMIS_ECMI_LINE law without and with the hardening annealing. The worst estimate is obtained for the behavior law VMIS_CIN1_CHAB with an absolute error of about 0.27 mm. Nevertheless, it is important to note that for a large number of the behavior laws considered, the results are very satisfactory.

■ **"Single-bead" test - Residual stresses:** In Figures 5.39, 5.40, 5.41, and 5.42 are represented the longitudinal residual stresses along the z-axis and the transverse residual stresses obtained by neutron diffraction strain measurements, respectively. The experimental measurement points are represented in blue. The continuous curves are the numerical profiles obtained for all the behavior laws available for welding simulations. The first finding is that the longitudinal stress curves of the profiles S1 and

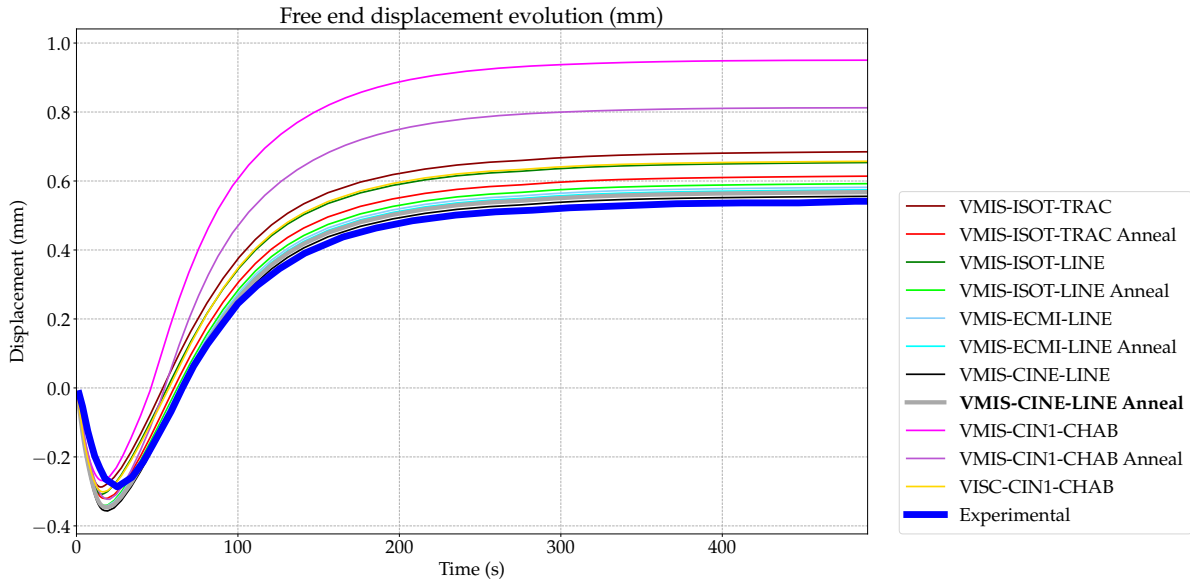


Figure 5.38 – Evolution of the free end displacement along the z-axis during the complete TG9 nominal "single-bead" test. In blue, the experimental measurements, and in solid line the numerical predictions for different constitutive behaviors.

S2 presented have an "S" profile very characteristic of the residual stress curves usually measured for welding operations [191]. On the experimental stress profile, three loading zones are identified. A first tensile zone is obtained in the lower part of the specimen. The material deposited and the zone below it are also in tension. The curves extracted from numerical simulations very well respect this trend. Moreover, the orders of magnitude of the numerical and experimental values seem to match well. The experimental profiles of the transverse stresses of the sections S1 and S2 are very close to zero, with some variations at the HAZ (Heat Affected Zone). The corresponding numerical predictions seem to be in adequacy with the experimental curves.

Figures 5.43 and 5.44 show the curves of the stress measurements according to the profile S3. The first finding is that there is little difference between the numerical curves using the different behavioral laws and the experimental curve, either for the longitudinal or the transverse stress profiles. Moreover, the trend of the numerical results coincides with the experimental profile, with a slight underestimation of the longitudinal stresses. The curves show that the Chaboche elasto-plastic constitutive behavior (VMIS-CIN1-CHAB model) provides the best estimates, with an absolute error of 10.7 MPa. For the transverse stresses, given the strong similarity of the numerical profiles, studying the average error on all the laws is more interesting than identifying the more fitting one. The average error for the transverse stresses is 9.14 MPa.

Still with regard to the residual stresses for the "single-bead" test, the stress measurements according to the profile S4 are presented in Figures 5.45 and 5.46. The first finding is that the stress state is rather constant for both longitudinal and transverse stresses (around 225 MPa for longitudinal stresses and 0 MPa for transverse stresses). The general trend is similar between the numerical and experimental profiles. For longitudinal stresses, the use of the piecewise linear isotropic hardening behavior (VMIS_ISOT_TRAC model) seems to be the most suitable, with an absolute error of 13.6

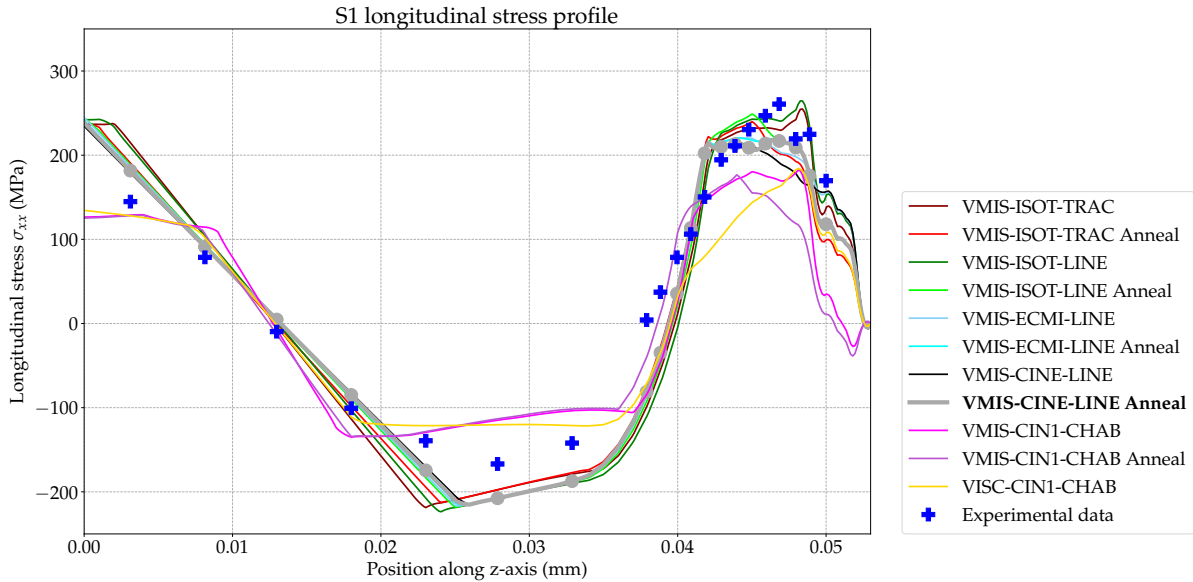


Figure 5.39 – Longitudinal stress profile on the S1 section for the TG9 "single-bead" test: in blue the experimental measurements, in solid line the numerical predictions for different constitutive behaviors, and in bold, the curve closest to the experimental data.

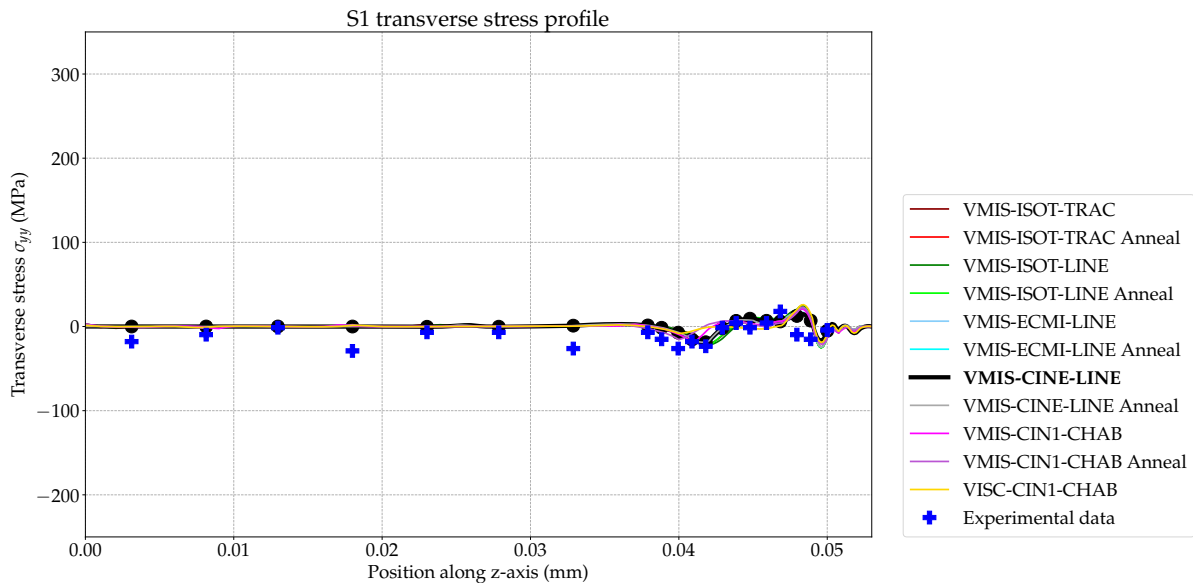


Figure 5.40 – Transverse stress profile on the S1 section for the TG9 "single-bead" test: in blue the experimental measurements, in solid line the numerical predictions for different constitutive behaviors, and in bold, the curve closest to the experimental data.

MPa. The linear isotropic hardening behavior also provides good results, as well as the kinematic or the mixed hardening with hardening annealing. On the contrary, the Chaboche constitutive behavior (VMIS_CIN1_CHAB model) with the hardening annealing seems to give, once again, the most distant profile, with an absolute error of 105 MPa. Concerning the transverse stresses, the numerical profiles are very similar, with an average error in comparison with the experimental profile of 18.8 MPa.

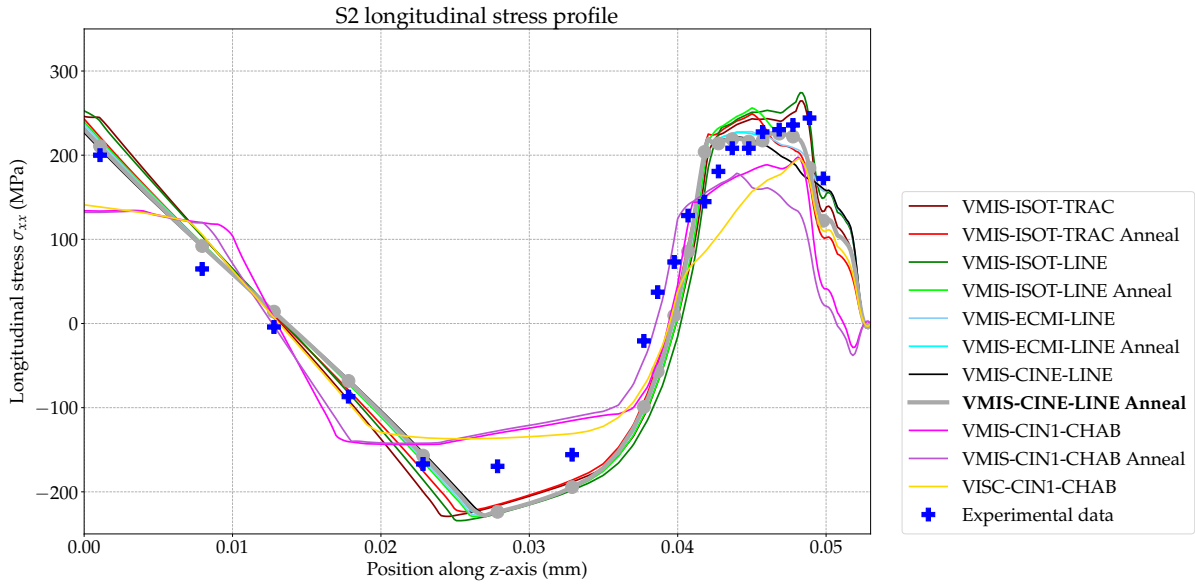


Figure 5.41 – Longitudinal stress profile on the S2 section for the TG9 "single-bead" test: in blue, the experimental measurements, in solid line, the numerical predictions for different constitutive behaviors and in bold the curve closest to the experimental data.

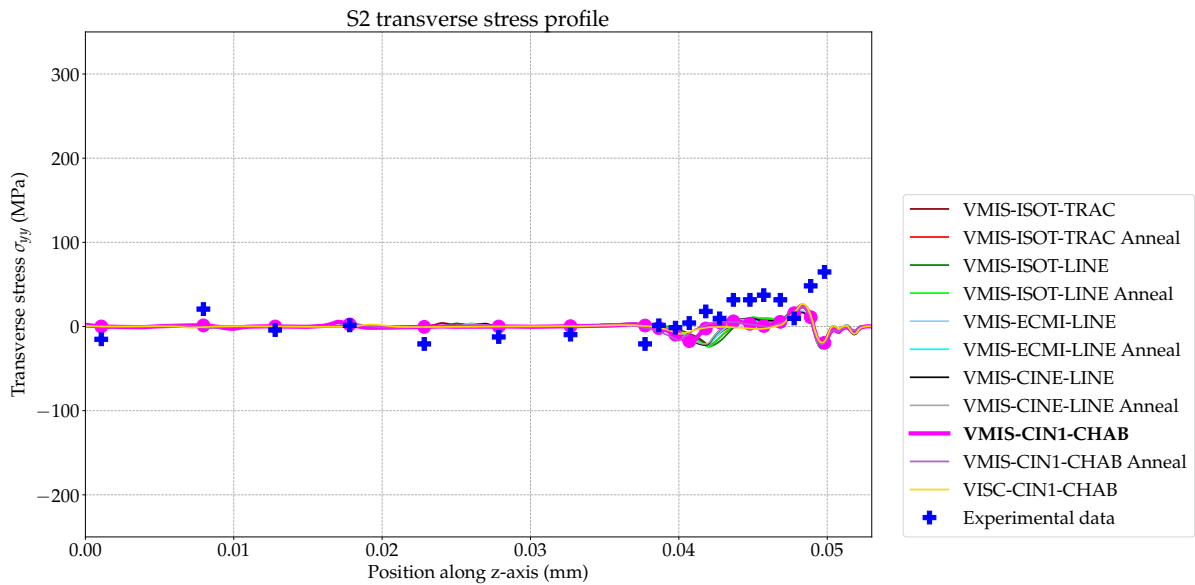


Figure 5.42 – Transverse stress profile on the S2 section for the TG9 "single-bead" test: in blue, the experimental measurements, in solid line, the numerical predictions for different constitutive behaviors, and in bold the curve closest to the experimental data.

To conclude on the residual stresses for the "single-bead" test, the numerical results are very satisfactory. Indeed, similar trends are observed for all characterized stress profiles, both longitudinal and transverse. If the error is calculated on all the stress profiles, the behavior law for which the error is the lowest is the kinematic hardening **VMIS_CINE_LINE** with hardening annealing, with an average absolute error of 23.1 MPa. Moreover, all the constitutive laws considered seem to give predictions of

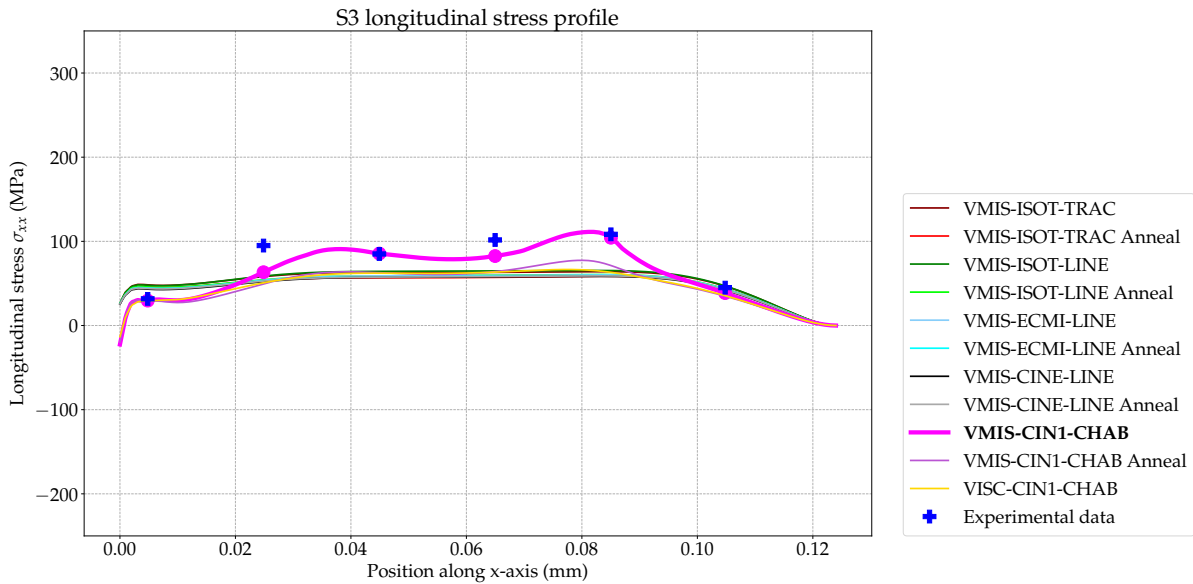


Figure 5.43 – Longitudinal stress profile on the S3 section for the TG9 "single-bead" test: in blue, the experimental measurements, and in solid line, the numerical predictions for different constitutive behaviors. In bold is represented the curve closest to the experimental data.

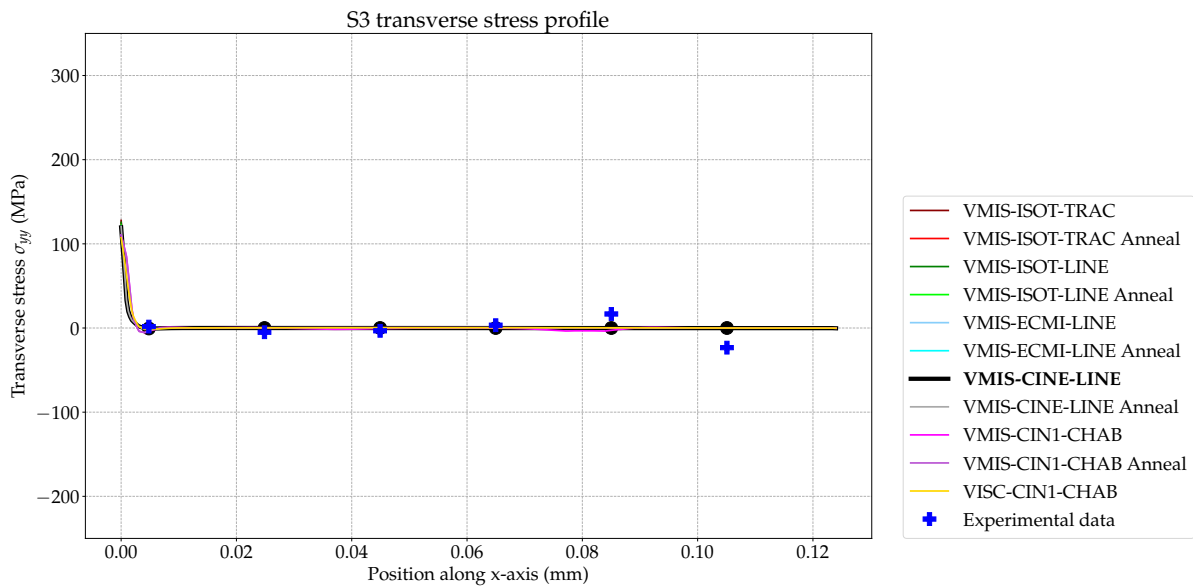


Figure 5.44 – Transverse stress profile on the S3 section for the TG9 "single-bead" test: in blue, the experimental measurements, and in solid line, the numerical predictions for different constitutive behaviors. In bold is represented the curve closest to the experimental data.

high quality with the exception of the Chaboche laws.

■ **"Five-beads" test - Free end displacement evolution:** The evolution of the deflection at the free end is measured experimentally with a laser sensor. In Figure 5.47, the experimental curve is shown in blue, along with the error interval obtained from the dispersion of the measurements. This

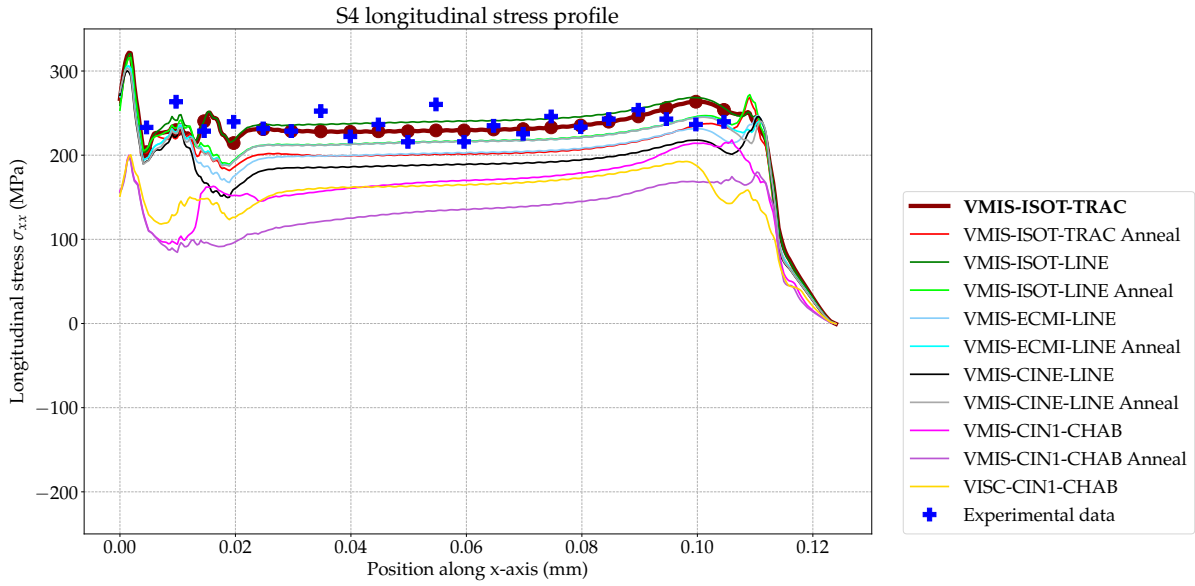


Figure 5.45 – Longitudinal stress profile on the S4 section for the TG9 "single-bead" test: in blue, the experimental measurements, and in solid line, the numerical predictions for different constitutive behaviors. In bold is represented the curve closest to the experimental data.

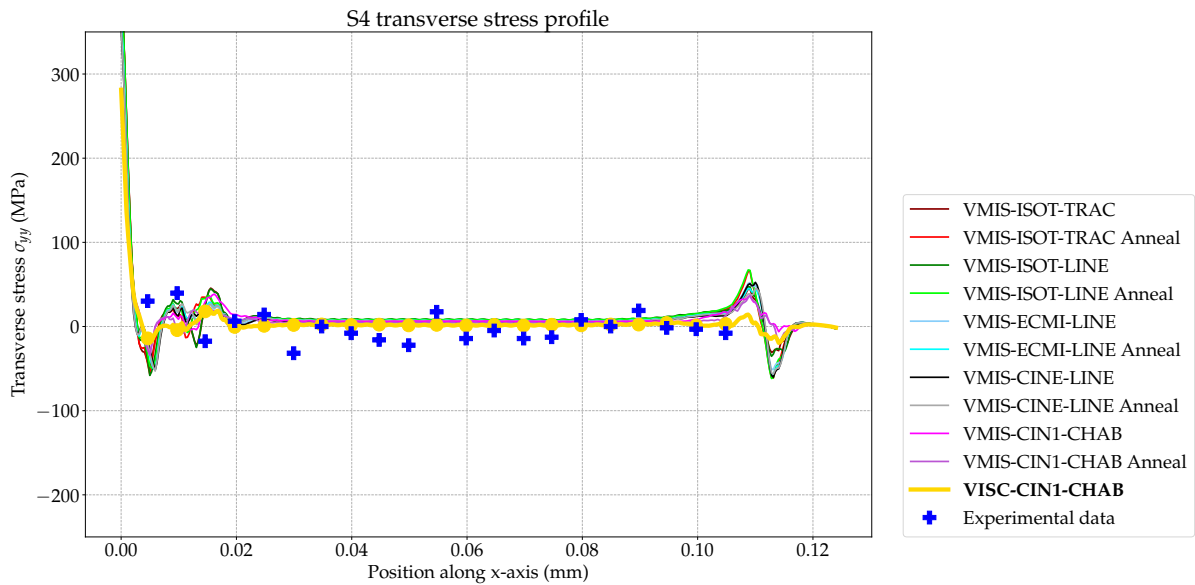


Figure 5.46 – Transverse stress profile on the S4 section for the TG9 "single-bead" test: in blue, the experimental measurements, and in solid line, the numerical predictions for different constitutive behaviors. In bold is represented the curve closest to the experimental data.

Figure shows that the residual displacement stabilizes at about 0.5 mm at the end of the fabrication, after returning to room temperature. The other curves in this Figure correspond to the estimates made using the different behavior laws. At first, it can be observed that the general trend of the numerical curves is in agreement with the experimental curve, with a good correspondence between the displacement peaks. The constitutive law that seems to give the most satisfactory results is

the isotropic hardening (VMIS_ISOT_LINE model) with an absolute error of about 0.052mm. The mixed hardening model with or without hardening annealing also gives very good estimates with errors of about 0.06mm. Nevertheless, one behavior seems much less suitable than the others: the Chaboche VMIS_CIN1_CHAB model. The results obtained and presented are thus, on the whole, very satisfactory.

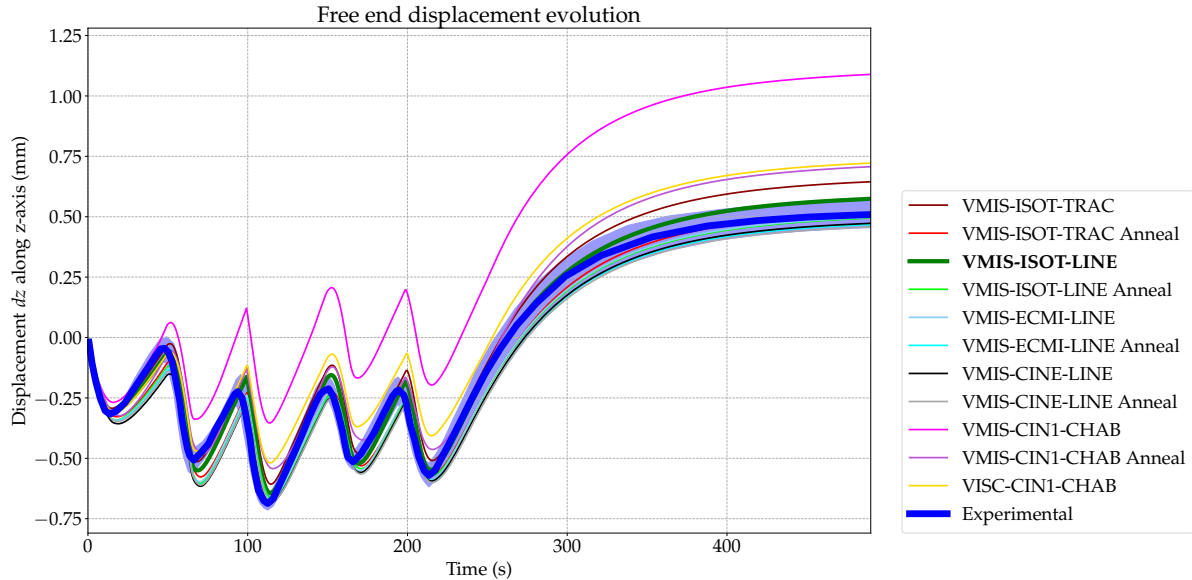


Figure 5.47 – Evolution of the free end displacement along the z-axis during the complete TG9 test (5 beads). In blue are represented the experimental measurements, and in solid line, the numerical predictions for different constitutive behaviors.

■ **"Five-beads" test - Residual stresses:** As for the "single-bead" test presented above, the longitudinal and transverse residual stresses along the z-axis experimentally obtained by neutron diffraction are represented in Figures 5.48 and 5.49, respectively. The first finding is that the experimental stress trend (tension, compression) coincides with the longitudinal stress profiles. Moreover, the transverse stresses are very close to zero. For the longitudinal stresses, the numerical results and the experimental measurements are in very good agreement. Indeed, the maximum values of the different curves are very close, and the trends are very similar. For the estimation of the longitudinal stresses, the kinematic VMIS_CINE_LINE model or mixed hardening VMIS_ECMI_LINE model seems to be the most suitable, with an average absolute error of 13.5 MPa. On the contrary, the elasto-plastic Chaboche constitutive behaviors with hardening annealing (VMIS_CIN1_CHAB) have the largest deviation from the experimental data. For the transverse stresses, the numerical curves are relatively close to the experimental curves. As for the "single-bead" test, it is not particularly relevant to identify a specific law and the average error for all laws combined is 10.5 MPa. Combining longitudinal and transverse stress data, the kinematic or mixed hardening constitutive laws provides the best prediction.

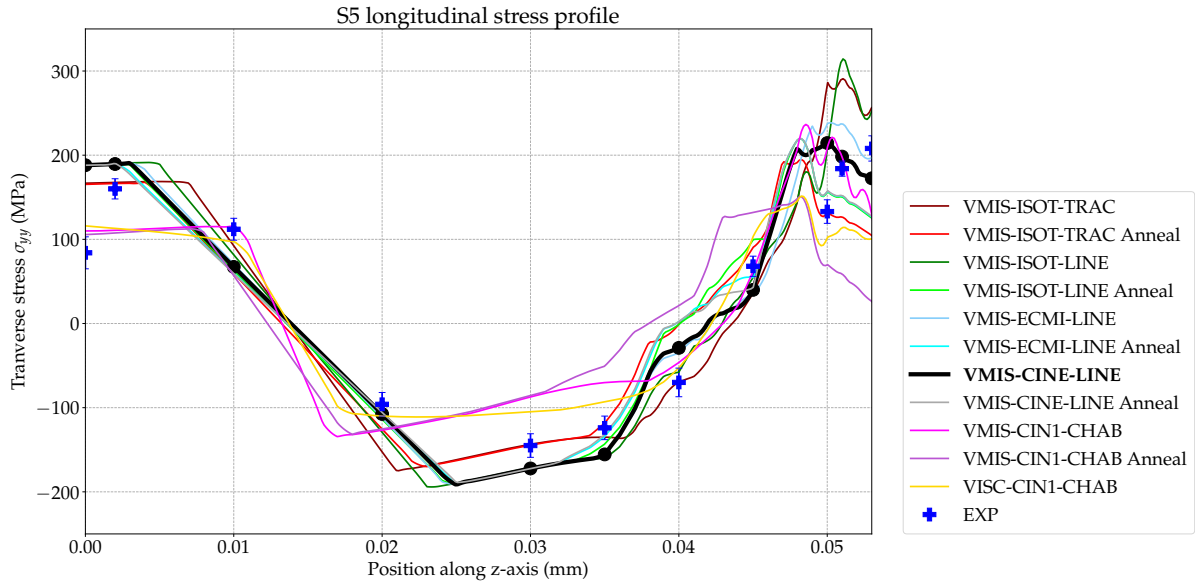


Figure 5.48 – Longitudinal stress profile on the S5 section for the TG9 "five-beads" full test. In blue are represented the experimental measurements, and in solid line, the numerical predictions for different constitutive behaviors. In bold is shown the curve closest to the experimental data.

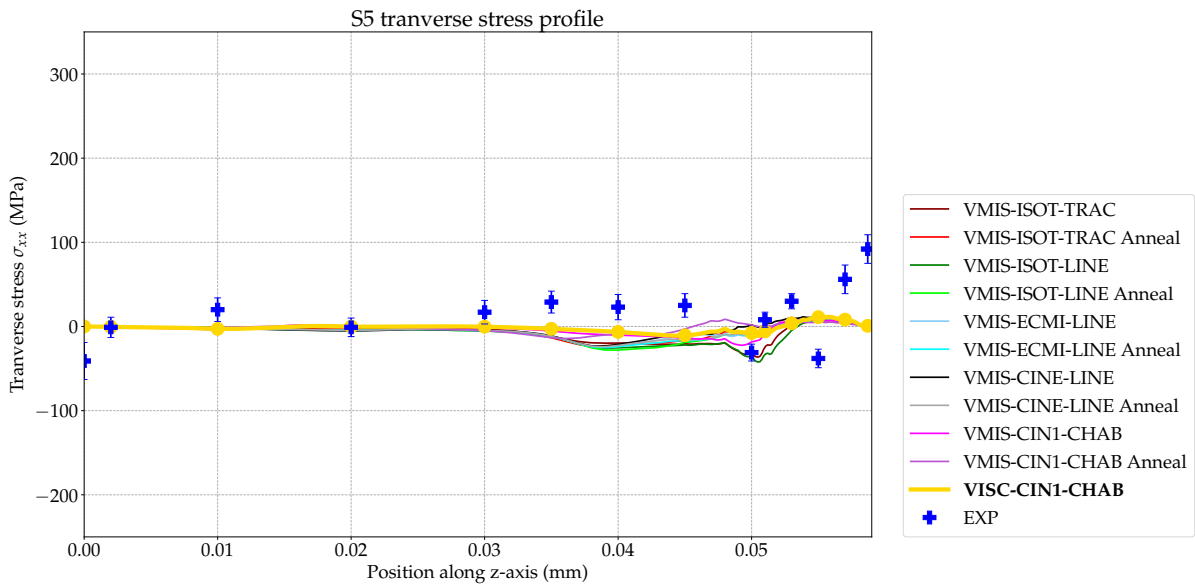


Figure 5.49 – Transverse stress profile on the S5 section for the TG9 "five-bead" full test. In blue are represented the experimental measurements, and in solid line, the numerical predictions for different constitutive behaviors. In bold is shown the curve closest to the experimental data.

5.4.5 Conclusion of the study

The objective of this test is to perform a complementary validation of the mechanical model. After a thorough and accurate calibration of the thermal parameters on the complete test and a validation on the "single-bead", the mechanical simulations are carried out.

The numerical and experimental deflection profiles of the support are found in good agreement, both in terms of trend and numerical values. The constitutive behavior which gives the best estimate, given the parameters considered, is the kinematic or Prager mixed hardening models (with and without hardening annealing), both for the "single-bead" and the "five-beads" tests.

Regarding the residual stresses, the experimental measurements and the numerical predictions on the two previous tests ("single-bead" and "five-beads") show good correspondence. Indeed, the previous discussions have highlighted the similarity of the profiles and orders of magnitude. For both the "single-bead" and "five-beads" tests, the kinematic hardening model is identified as the more suitable behavior.

Since the tests are performed under the same conditions and with the same process parameters, an optimal behavior model can be identified using all available data. The most appropriate seem to be the kinematic or Prager mixed hardening models with or without the hardening annealing. Although this behavior has the lowest error, several other behaviors seem to also provide very accurate results, with a slightly higher error. It is the case, for instance, of the linear or piecewise linear isotropic hardening models. However, this choice should be taken with caution, given the small number of beads in the test. Indeed, a higher number of beads could possibly accentuate the possible discrepancy between the stress predictions and the experimental curves. The impact of hardening annealing is not strongly visible. This is most likely due to the fact that, for both tests, there is not much cycling and the duration of the test is short, and thus has little heat build-up. Moreover, the results show that the simplest constitutive behaviors, coupled with the material behaviors used, give better results than the Chaboche hardening models.

Most welding studies on 316L SS show a different ranking of material models and agree with the fact that mixed hardening models (mainly Chaboche) are the most accurate when correctly fitted to relevant data. The predicted through-wall profile for the Chaboche models (VMIS_CIN1_CHAB and VISC_CIN1_CHAB) suggests that their yield strength is too low, since they show evidence of yielding on the back face. However, if the models were fitted on different experimental test cases with different configurations and loading, then they may deviate for this reason. Therefore, it is important, if hardening models are to be compared, that they are fitted to similar, representative, tensile and isothermal cyclic data, and compared first for the quality and nature of their representation of both monotonic and isothermal cyclic data before using in a welding simulation. Otherwise, there is no guarantee that deviations between models in the welding simulation are not due to either being fitted to different material heats, or due to quirks of the fit. The figures presented in Appendix E show that the monotonic response to a tensile test is clearly different between the Chaboche models and the others. This could be explained by the fact that the tests are made of a few beads (1 and 5), which makes the cyclic behavior have little influence and may be the Chaboche models used were fitted to the saturated cyclic response, inducing the too low monotonic yield strength observed.

To conclude, for the two tests presented above, the numerical results correspond well to the experimentally observed trends. Figure 5.50 summarises the results of the experimental stress profiles of the two tests and the numerical results for the model VMIS_CINE_LINE which gives the closest profiles.

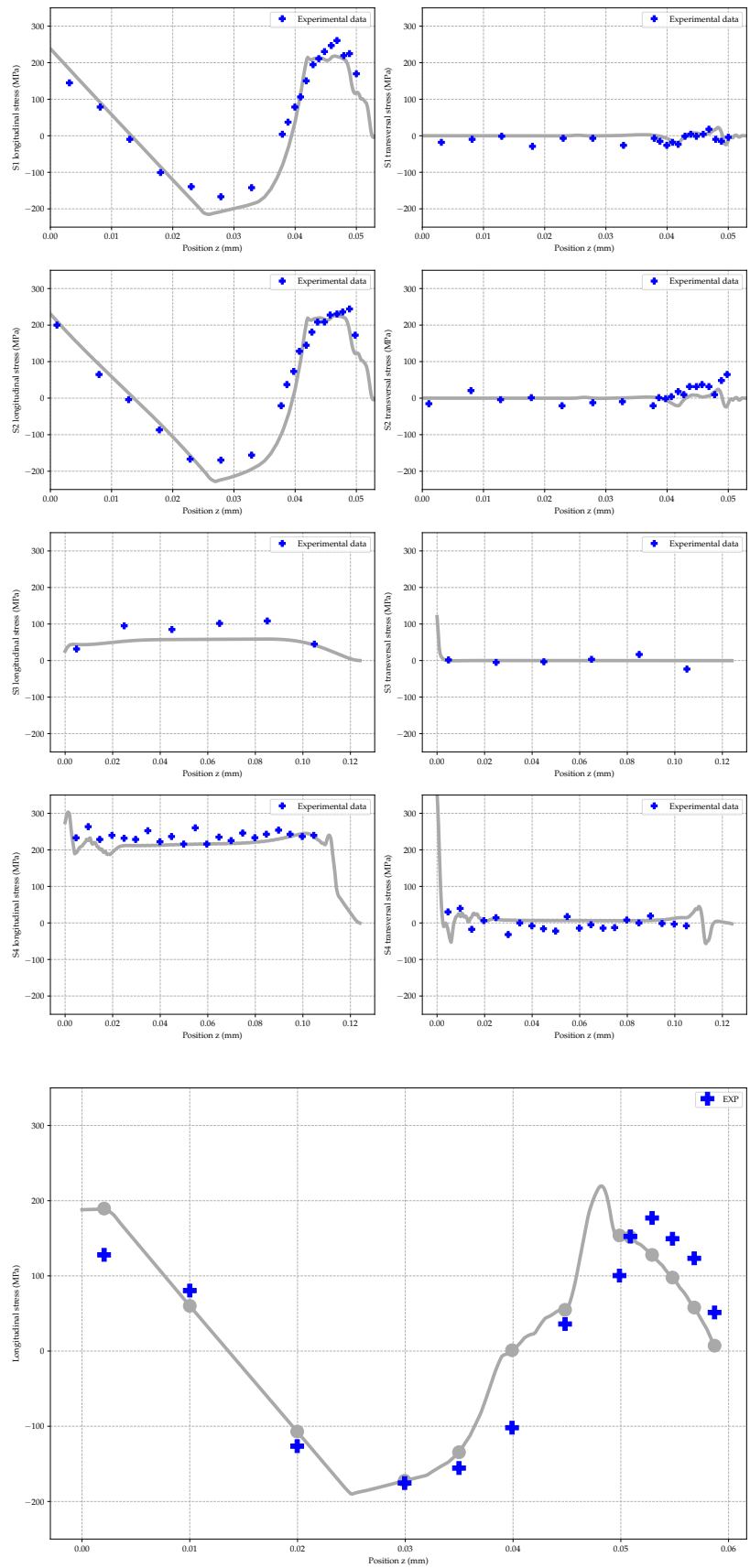


Figure 5.50 – Comparison of residual stress measurements and computational results for the material behavior that gives the closest results, using the kinematic hardening model VMIS_CINE_LINE with hardening annealing on the "single-bead" and the "five-beads" tests.

5.5 4th use case: AFH block with cooling devices and idle time

5.5.1 Introduction and objectives

Among the most important quantities of interest when controlling multipass and WAAM welding operations are the inter-layer temperatures and the idle time between two successive layers. Selecting a cooling strategy is particularly important to control the manufacture of a component and ensure an appropriate residual state. The first possible strategy is a time-controlled inter-layer cooling, i.e., an idle time between the layers or a different idle time per layer defined beforehand. The second possible strategy is a temperature-controlled inter-layer cooling for which a cooling criterion is defined. This means that, as long as the temperature is higher than this criterion, the cooling of the part continues. However, these quantities remain difficult to measure and control, especially in the case of a component with several hundred layers. In fact, before carrying out production, it is not easy to predict the inter-layer temperature reached for a specific cooling time for each layer, and vice versa, the cooling time needed to respect a target inter-layer temperature. In general, they are chosen by experimental expertise.

Numerical simulations allow for the prediction of these quantities of interest. Thus, an adequate cooling time per layer can be provided at the end of the calculation, in addition to the thermal field and the other quantities of interest.

It is necessary to define the target inter-layer temperature beforehand. This quantity can be defined differently. Therefore, in this study, numerical tools have been implemented in the simulations to extract the different quantities usually considered. For each layer k , the thermal simulations return the average temperature of the nodes of the current layer k , the maximum temperature, but also the average of the temperatures of the group of nodes below the first elements of the layer $k + 1$. Figure 5.51 schematizes these quantities of interest.

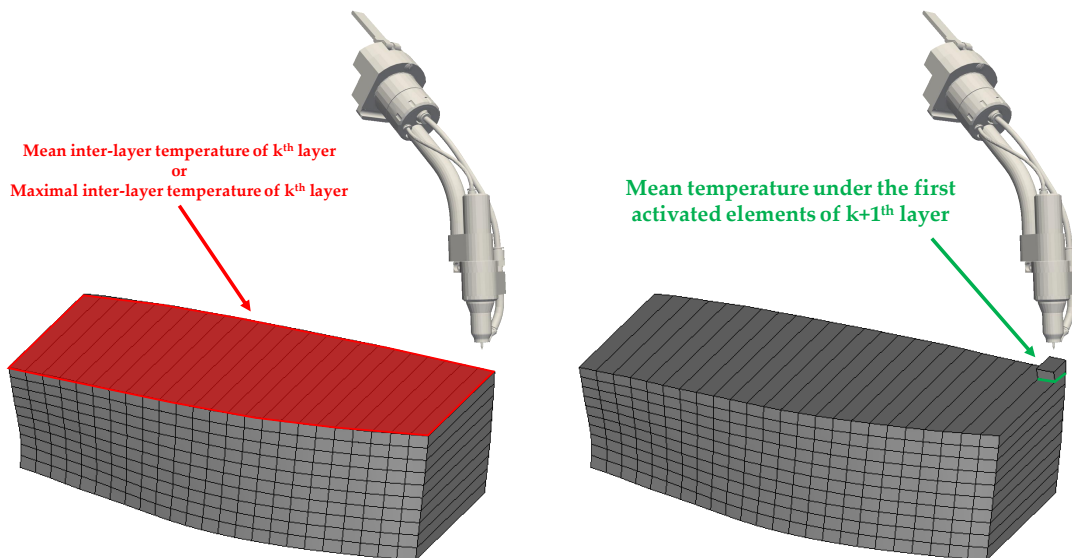


Figure 5.51 – Schematic illustration of the inter-layer temperature.

In order to study the inter-layer temperatures and cooling times between two successive layers, this section will focus on specific tests performed within the AFH consortium. Indeed, various experimental test campaigns have been carried out within the framework of AFH to explore the process parameters and their relationships for several kinds of materials, including austenitic 316L SS. One of the objectives of these test campaigns is to set up a "repeatability test" to ensure the reproducibility of the tests and good control of the manufacturing process. To do so, one specific test configuration on a block has been selected to be implemented four times. However, the control of the inter-layer temperature has been identified as a major obstacle, preventing the carrying out of these "repeatability tests" in the exact same conditions. Indeed, this implies real-time experimental measurements of the inter-layer temperature, which makes manufacturing automation difficult. Moreover, one of the requirements of AFH for the "repeatability test" is to ensure that it will be conducted in less than a day.

The general objective of this fourth study is to determine the cooling duration needed to respect a target inter-layer temperature that allows the tests to be carried out in less than a day. All this aims to ensure proper planning, automation, and repeatability of the experimental conditions of the tests.

This section presents the implementation of an instrumented experimental test carried out within the framework of the AFH consortium, with as objective the calibration of the "repeatability test". The "calibration test" is selected very similar to the "repeatability test": it has the same process parameters, manufacturing configuration and cooling devices.

The "calibration test" is carried out in two steps. The first part of the test consists in fabricating the first nine layers of the block, with a cooling time of approximately 8 minutes between two successive layers.

After depositing the first nine layers, the part is cooled in the open air to room temperature. During the second part of the test, nine other layers are deposited in the same configuration and process parameters. However, during this second step, the coolers are removed, and the inter-layer cooling time is significantly reduced down to 1 minute.

The advantage of having carried out this test in two parts is the simplicity of the calibration step of the numerical simulations. Indeed, for the test without cooling devices (step 2), the temperature accumulation in the component is higher, which allows for a more precise calibration of the thermal source and of the "natural" heat dissipation. After the calibration of the thermal source, the first part of the test is used to calibrate the cooling device around the welding torch and the base plate cooling by pressurized air.

The objectives of this section are:

- Carrying out of the experimental test and the modeling of a block using the CMT process with cooling devices and an idle time between layers,
- Two-step calibration of the parameters,
- Prediction of the idle time for different inter-layer temperature criteria.

5.5.2 Description of the experimental setup

5.5.2.1 Process parameters

The "calibration test" consists of a block using a 316L austenitic SS filler wire of 1 mm diameter. The base plate is also made of 316L SS and is 450 mm length, 80 mm width, and 20 mm thick. The

chosen wire feed speed is 8 m min^{-1} , and the torch speed is 1 m min^{-1} . Regarding the thermal power parameters, the programmed voltage is 22.40 V, and the programmed current is 153.00 A. The block defined for the test is 150 mm long and 40 mm wide. The chosen deposition strategy for this experiment is a "Zigzag" with alternating directions from layer to layer, as shown in Figure 5.52.

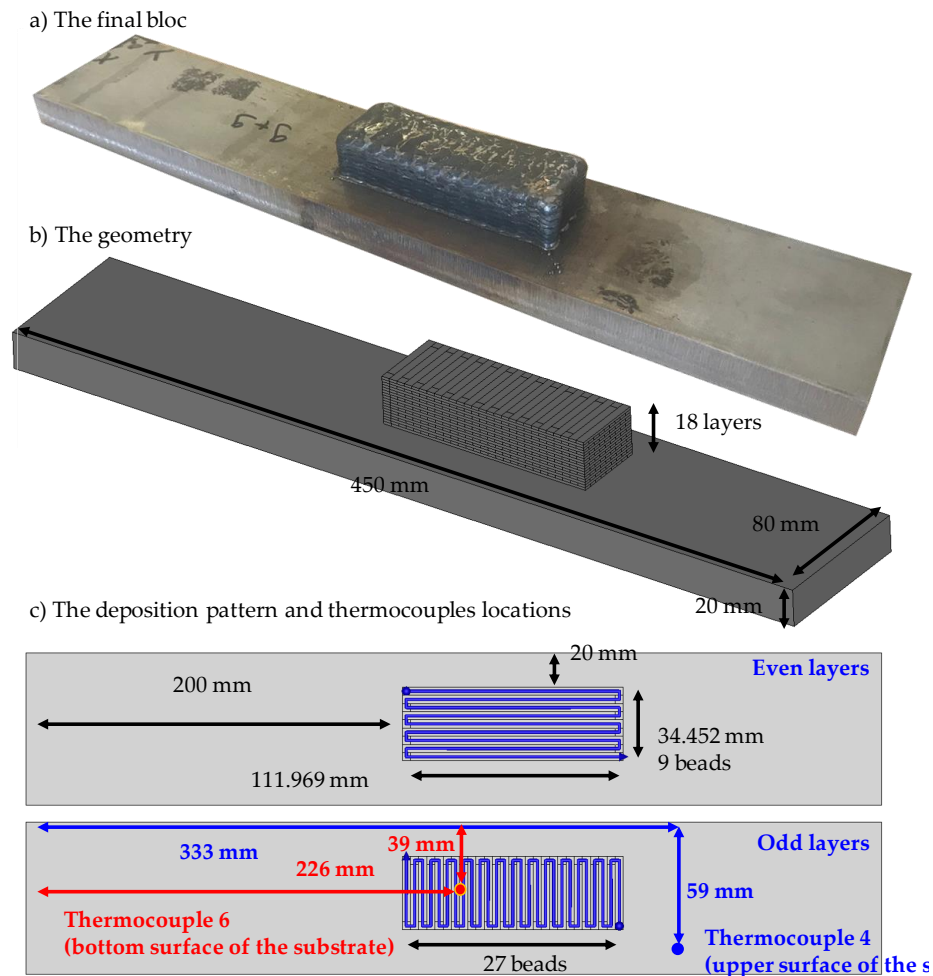


Figure 5.52 – Calibration bloc test, with the associated deposition strategy.

An optimized cooling strategy comprising several devices is used for this test. First, to accentuate the thermal dissipation of the part produced by the base plate and thus to reduce the temperatures during manufacture, the base plate is cooled by compressed air. To do so, the base plate is lifted to introduce a tube underneath drilled randomly in many locations. This tube passes high-pressure compressed air which increases the convection at the bottom surface.

In addition, in order to accentuate the cooling during the test and to increase the shielding at the level of the molten pool and of the last layer, a cylinder device of 8 cm diameter is placed around the torch. The use of such a device was chosen following numerous tests carried out within the AFH consortium since it demonstrated a significant improvement in the quality of the beads. The cooling devices are illustrated in Figure 5.53.

Finally, as indicated previously, a cooling time between layers is applied. For the first nine layers, it is of 8 minutes, after which the block is cooled down to room temperature. For the other nine beads,

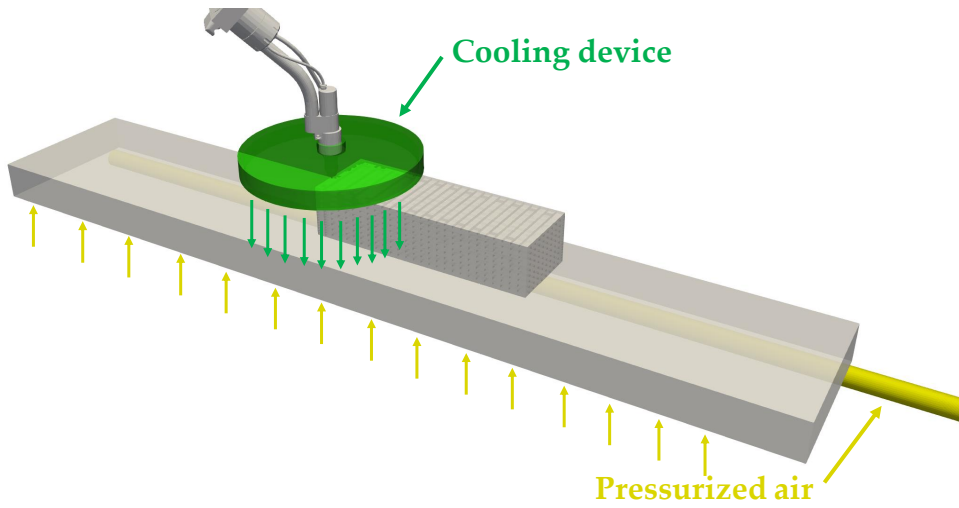


Figure 5.53 – Schematic illustration of the used cooling devices: in green cylinder device around the welding torch, and in yellow high-pressure compressed air on the base plate.

the cooling is of 1 minute between beads. Table 5.12 summarizes the process parameters associated with the experimental tests:

Table 5.12 – Process parameters used for the AFH block test case.

Welding parameter	1 st to 9 th layers	10 th to 18 th layers
Process type	CMT	CMT
Voltage U (V)	22.40	22.40
Intensity I (A)	153.00	153.00
Travel speed V_s (m/s)	0.01667	0.01667
Maximal stroke rate (m/min)	8.0	8.0
Torch cooling device (L min^{-1})	10	10
Idle time between layer (min)	8	1

From Table 5.12 and based on the deposition pattern presented Figure 5.52, the height and width of the 1st beads are evaluated at 1.46mm and 4.31mm. The generated mesh is made of about 180000 linear volume elements (tetrahedrons and pyramids) and about 50000 nodes.

5.5.2.2 Instrumentation: Thermocouples

This test is instrumented in order to allow for the calibration of the models. Seven type K thermocouples are positioned as shown in Figure 5.54. The seven thermocouples are micro-welded. Three thermocouples are on the surface and are thus subjected to forced cooling near the block. For this test case, only thermocouple data are used. Among the seven thermocouples, several were damaged or detached. For the calibration step, only two of them are used. Figure 5.54 shows the segments of the thermocouple curves used for the calibration step.

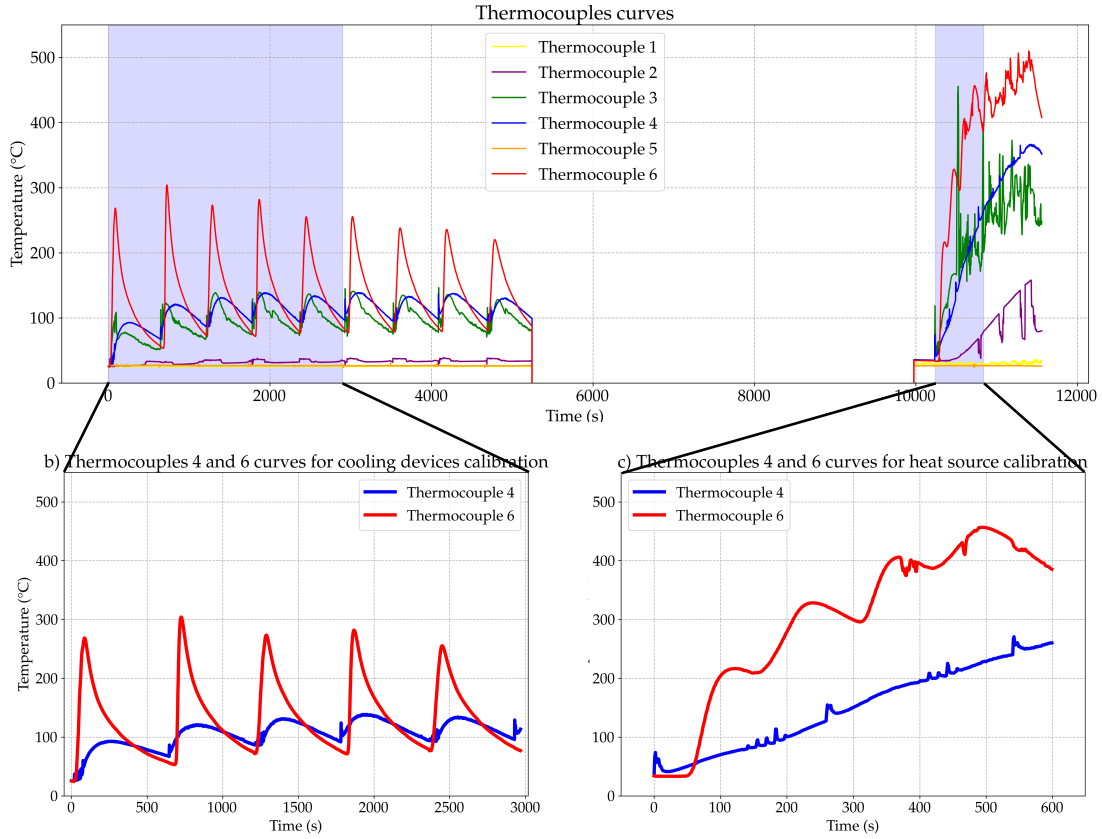


Figure 5.54 – a) Thermocouples during all the duration of the "calibration test", b) Part of the thermocouple data selected for the calibration of the cooling parameters, c) Part of the thermocouple data selected for the calibration without cooling devices.

5.5.3 Thermal model parameters calibration

In contrast to the previous studies, the calibration step is performed in two steps. In the first step, the last 9 layers of the test are used to calibrate the parameters of the thermal source, as well as the emissivity and the radiation coefficients of the material. After fixing the source parameters, the forced heat dissipation parameters are calibrated. Given the objectives of these tests, some modeling choices are made. Indeed, since the main aim of the test is to determine the cooling time between layers, it is not necessary to have a very high accuracy of the shape of the thermal source and the local thermal gradients at the molten pool. The most important aspect in this test is rather the overall thermal aspect of the component. Therefore, the first assumption made is that the equivalent source is a semi-spherical source, so a Goldak for which the length, the width, and the depth are equal. This simplification allows going from four parameters for the shape of the source to only one. In addition to the number of parameters, this simplification facilitates the calibration since the thermocouples are relatively far from the molten pool.

The emissivity and convection parameters of the material are considered constant for this study. For the modeling of forced cooling, two coefficients are introduced. A forced convection is applied on the bottom surface of the base plate with a constant coefficient h_{plate} to be calibrated to represent the compressed air. For the cooling device around the welding torch, a forced convection is applied with a

coefficient h_{torch} to be calibrated on a surface mesh group that moves along the manufacturing path, and that has a diameter of 8 cm (which is the diameter of the device).

5.5.3.1 10th to 18th layer calibration step

First, 4 parameters are to be identified and calibrated using a surrogate model. To constitute the database needed to build the metamodel, a design of experiments must be set up. The distribution of these parameters is chosen based on the same expertise as the previous studies of this chapter. The distributions of the parameters are presented in Table 5.13.

Table 5.13 – Parameters to be calibrated, with the sampling distribution for the PCE surrogate model training and the prior distribution for the MCMC algorithm calibration step.

4 th test case: Parameters	Sampling distribution	Prior distribution
r (mm)	$\sim \mathcal{U}(2.5, 12.0)$	$\sim \mathcal{N}(7.0, (4.0)^2)$
η	$\sim \mathcal{U}(0.50, 0.95)$	$\sim \mathcal{N}(0.75, (0.4)^2)$
ε	$\sim \mathcal{U}(0.20, 0.80)$	$\sim \mathcal{N}(0.35, (0.25)^2)$
h (W.mm ⁻² .K ⁻¹)	$\sim \mathcal{U}(0.0 \times 10^{-6}, 30.0 \times 10^{-6})$	$\sim \mathcal{N}(10.0 \times 10^{-6}, (15.0 \times 10^{-6})^2)$

From these distributions, 256 parameter samples have been generated using the Sobol sequences with low discrepancy. The mesh, generated from the developed mesh generation tools, consists of 150000 (tetrahedrons and pyramids) linear elements (35000 nodes in total). As mentioned previously, the calibration is performed on the 10th to 14th simulated beads. The simulations are performed simultaneously in parallel on a computing cluster. The time for each thermal simulation is about 3 hours, on 8 CPUs. The surrogate model is build using Sparse PCE, with a degree of 4, and a hyperbolic enumeration strategy. The error by cross-validation of the implemented surrogate model is estimated to be around 5%, which is a very satisfactory result. For the MCMC, the variance of the observation $\Sigma_{D_{obs}}$ issued for the likelihood calculation chosen is 12.0² (°C). For the prior distributions, the gaussian distributions used are presented in Table 5.13.

The resulting distributions are presented in Figure 5.55 for the 4 parameters. From these distributions, the MAP is identified in blue in Figure 5.55 and presented in Table 5.14. The confrontation of the experimental profiles with the profiles of the metamodel using the MAP is represented in Figure 5.56. The prediction at the MAP level seems very satisfactory. Indeed, the experimental curves are very close to the predictions with an error of around 5.5 %, and are included in the confidence interval of 95%.

Table 5.14 – Identified MAP of the 10th to 18th layer of the calibration bloc test case.

Parameters	r	η	ε	h
MAP	7.19e+00	8.44e-01	5.07e-01	1.57e-05

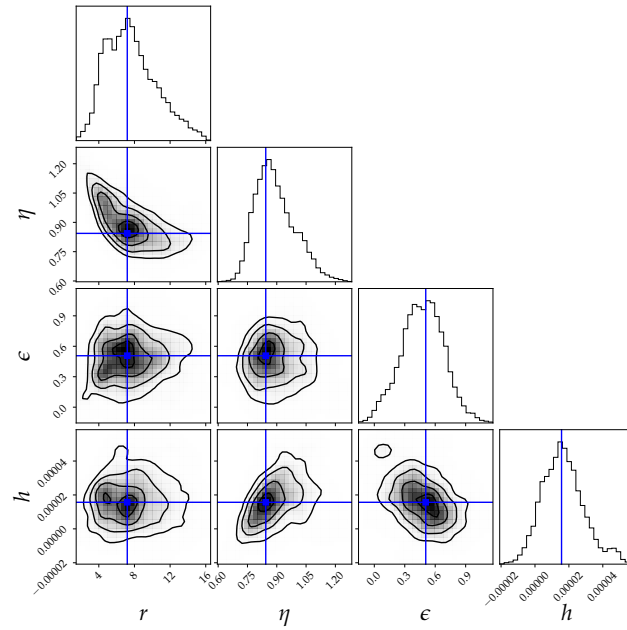


Figure 5.55 – Corner plot of the posterior distribution resulting from the calibration step of the 10th to 18th layer of the calibration bloc test case. The MAP is represented in blue.

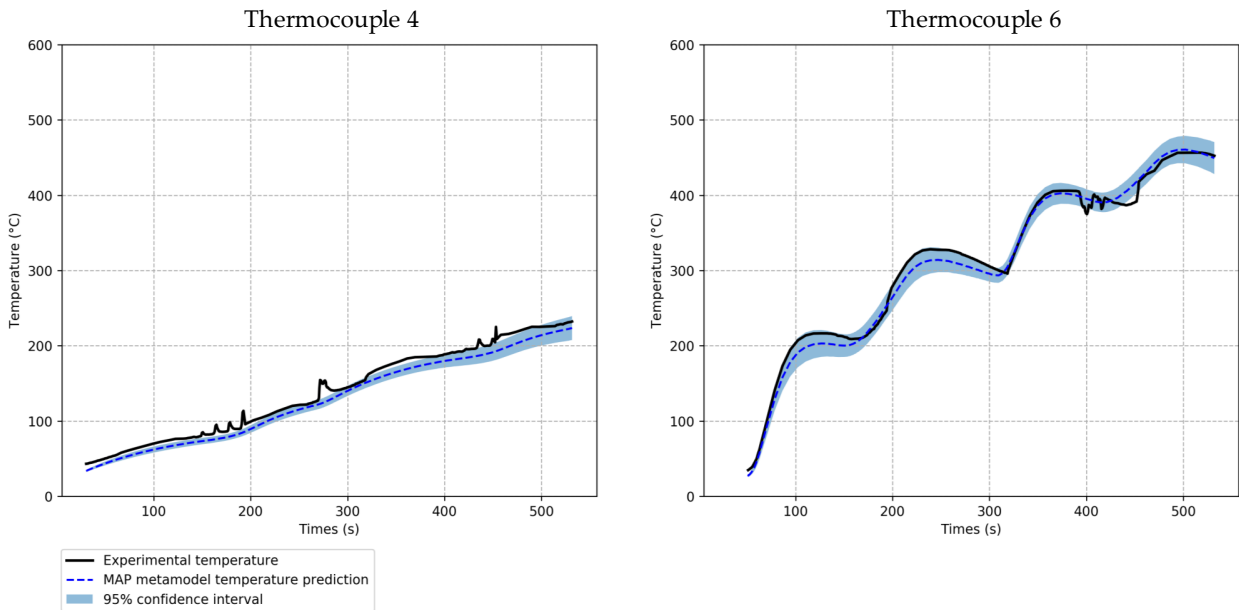


Figure 5.56 – Results of the calibration step: in black, the experimental data used for the calibration, in blue and dotted line, the curve predicted by the surrogate model using the MAP, and in light blue the 95% confidence interval of the posterior distribution.

5.5.3.2 1th to 9th layer calibration step

For the second calibration step, only the two forced cooling parameters are calibrated h_{plate} and h_{torch} . As previously, the Sobol sequences are used to generate the design of experiments from the distributions

presented in Table 5.15.

Table 5.15 – Parameters to be calibrated, with the sampling distribution for the PCE surrogate model training and the prior distribution for the MCMC algorithm calibration step.

4 th test case: Parameters	Sampling distribution	Prior distribution
h_{plate} ($\text{W}\cdot\text{mm}^{-2}\cdot\text{K}^{-1}$)	$\sim \mathcal{U}(0.0 \times 10^{-6}, 500.0 \times 10^{-6})$	$\sim \mathcal{N}(200.0 \times 10^{-6}, (500.0 \times 10^{-6})^2)$
h_{torch} ($\text{W}\cdot\text{mm}^{-2}\cdot\text{K}^{-1}$)	$\sim \mathcal{U}(0.0 \times 10^{-6}, 500.0 \times 10^{-6})$	$\sim \mathcal{N}(200.0 \times 10^{-6}, (500.0 \times 10^{-6})^2)$

Only 64 simulations are performed this time, using the same mesh. The Sparse PCE is constructed with a degree of 4 and using a hyperbolic enumeration strategy. The error by cross-validation is around 3%, which is very satisfactory. For the MCMC, the variance of the observation $\Sigma_{D_{obs}}$ chosen is 12.0^2 ($^{\circ}\text{C}$) as previously. For the prior distributions, the gaussian distributions used are presented in Table 5.15.

In the same way as for the first calibration step, the posterior distribution is presented in Figure 5.57 for the 2 parameters. The MAP is identified in blue in Figure 5.57 and presented in Table 5.16. Moreover, Figure 5.58 shows the experimental curves and the curves of the metamodel with the MAP. Once again, the prediction using the MAP parameter set seems very satisfactory with an error of 6.5 %, and the experimental results are included in the confidence interval of 95%.

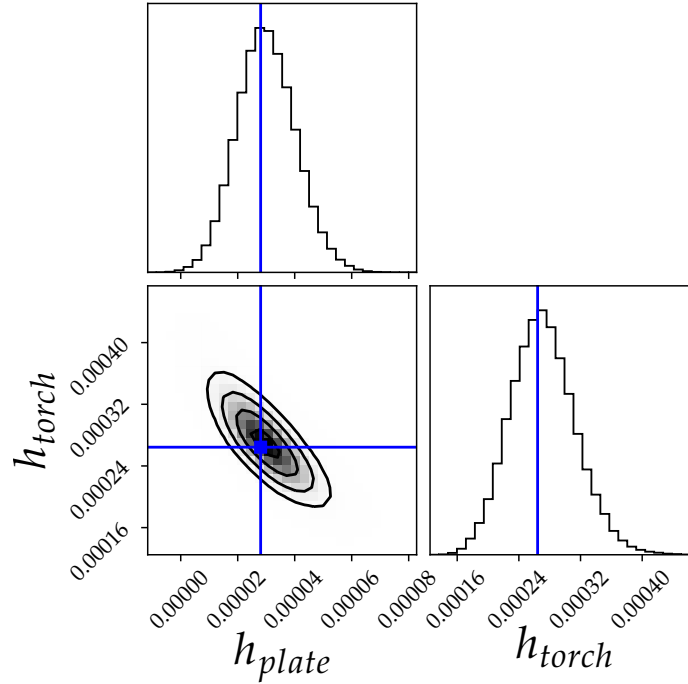


Figure 5.57 – Corner plot of the posterior distribution resulting from the calibration step of the 10th to 18th layer of the calibration bloc test case. The MAP is represented in blue.

Table 5.16 – Identified MAP of the 1st to 9th layer of the calibration bloc test case.

Parameters	h_{plate}	h_{torch}
MAP	2.80e-05	2.64e-04

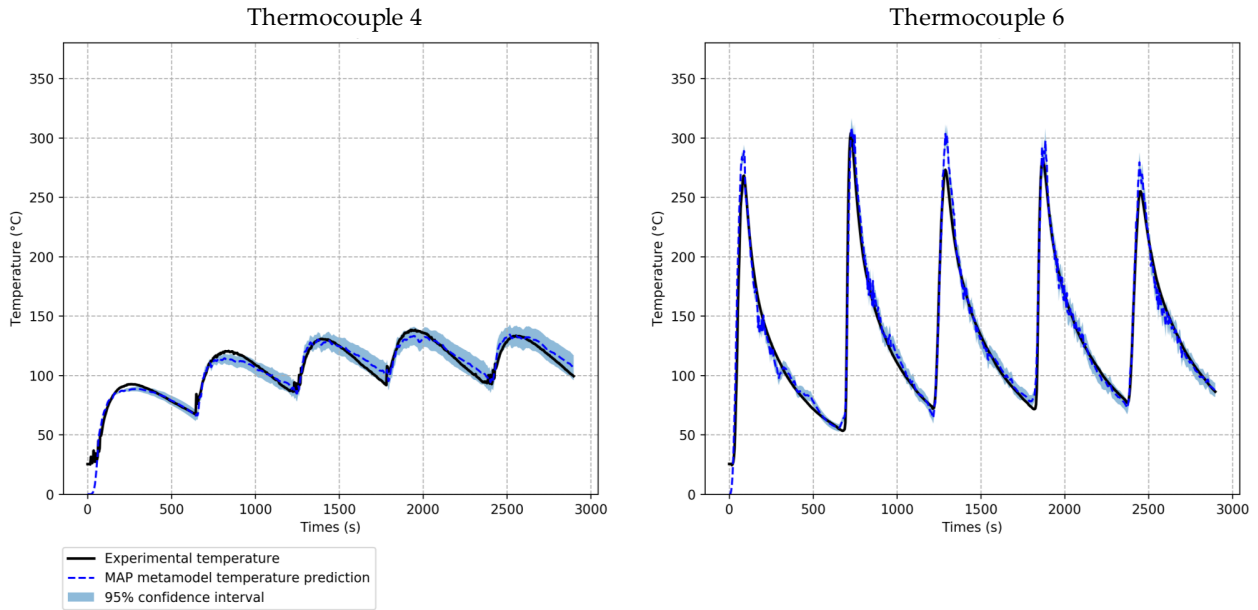


Figure 5.58 – Results of the calibration step: in black, the experimental data used for the calibration, in blue and dotted line, the curve predicted by the surrogate model using the MAP, and in light blue the 95% confidence interval of the posterior distribution.

5.5.4 Numerical results

5.5.4.1 Thermal results

The thermal simulation of the "repeatability block" calibration test is performed using the MAP parameter set. The temperature curves at the thermocouple points, presented in Figures 5.59 and 5.60, show very good similarity with the experimental thermocouples over the entire "calibration test". The average error is of 5.0 °C for the first step of the test with the cooling devices, and, for the second step without cooling, of 12.9 °C.

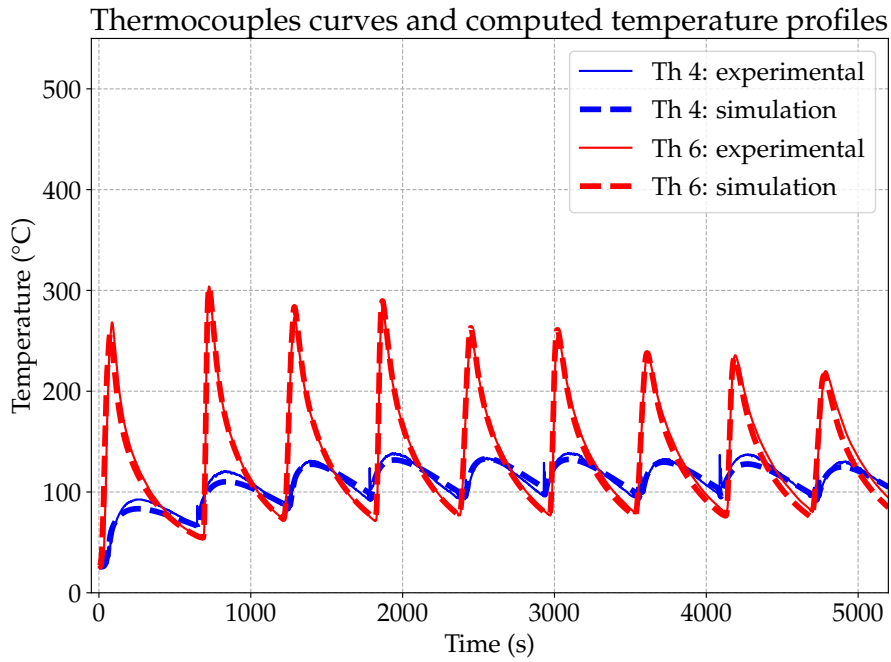


Figure 5.59 – Comparison of computed and experimental temperature curves for the first 9th layers (manufacturing with cooling devices).

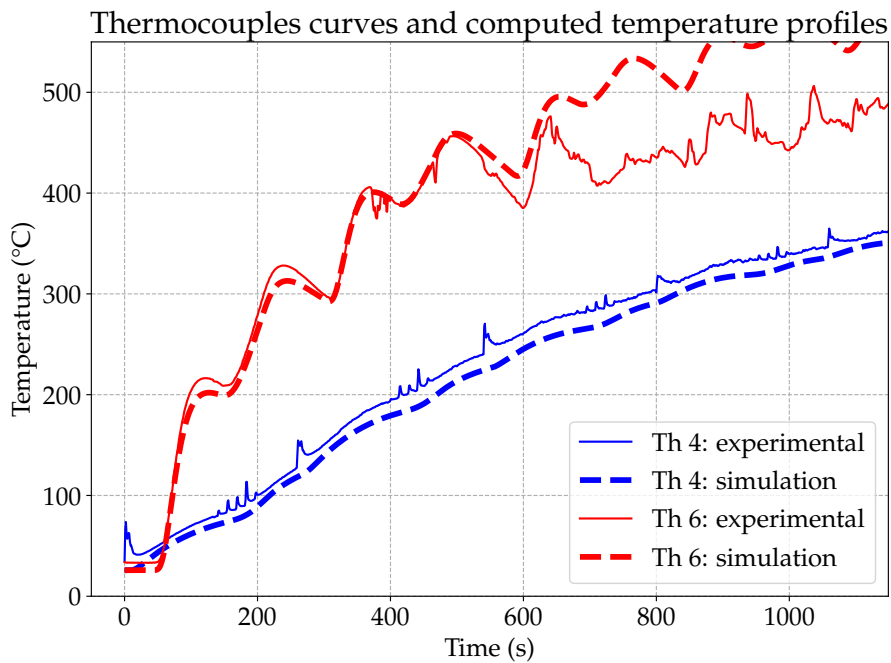


Figure 5.60 – Comparison of computed and experimental temperature curves for the last 9th layers (manufacturing without cooling devices).

5.5.4.2 Idle-time prediction for the "repeatability block"

The initial objective of this 4th test case is to estimate the cooling time necessary between each layer to respect a target temperature control criterion between each layer for the "repeatability test", while keeping a test duration under 24 hours. Moreover, the prediction of the cooling time allows to estimate the total duration of the test and eventually adapt and automate the test. In the previous sections, the thermal model parameters are calibrated and validated for the "calibration test". As mentioned earlier, the process parameters are the same for the "calibration test" and the "repeatability test", only the trajectories are different. Therefore, the parameter sets defined can be used for the simulation of the "repeatability block" test. The deposition pattern of the "repeatability test" is presented in Figure 5.61.

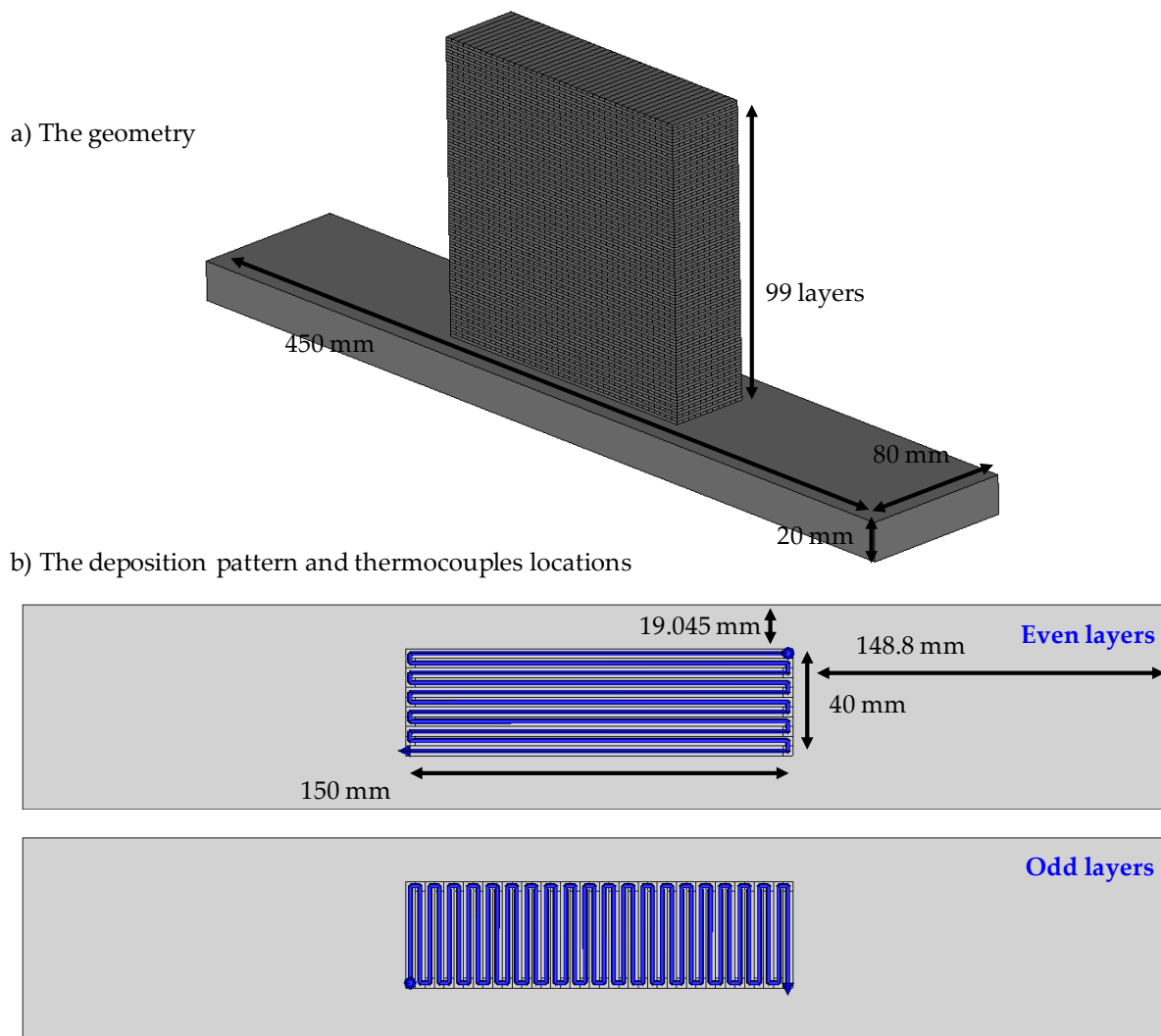


Figure 5.61 – 100 layers "repeatability block" deposition pattern

The simulations are performed by applying an inter-layer temperature to be respected between each layer. The tested temperatures are 40°C, 80°C, 100°C, 150°C, 200°C and 250°C. The first 20th layers are simulated, and the results are presented in Figure 5.62.

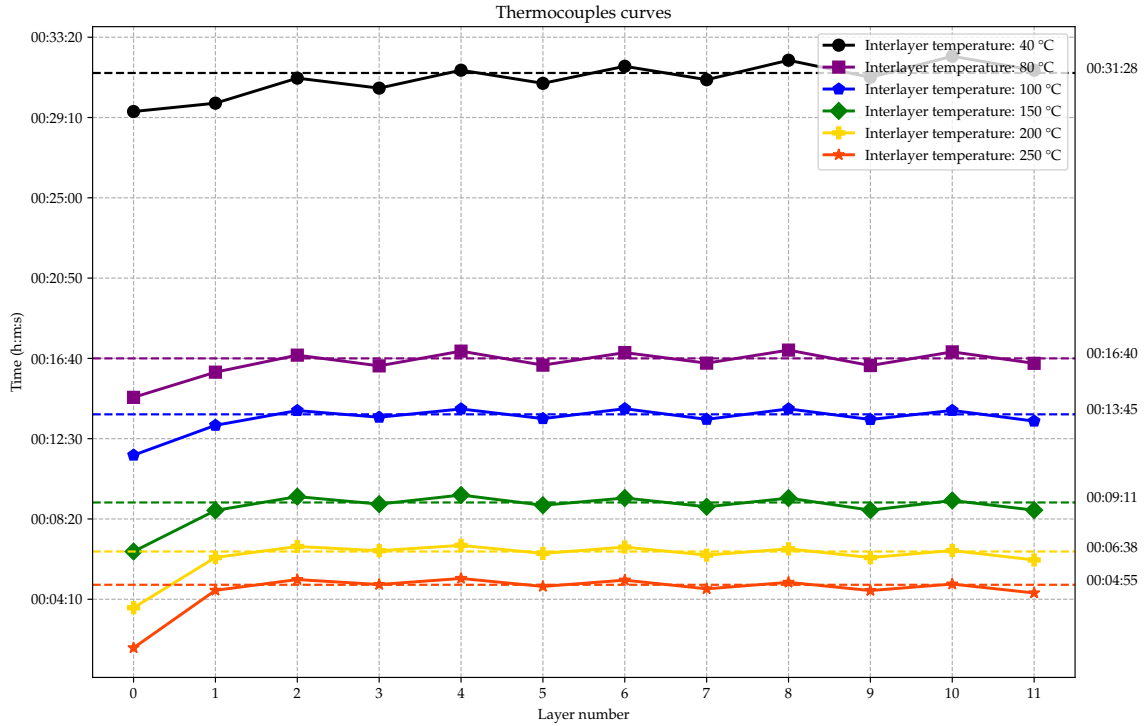


Figure 5.62 – Inter-layer cooling time required for different inter-layer temperatures criteria (12th first layers).

The first finding is that, around the end of the fourth layer and for each temperature criterion, the necessary cooling time per layer converges and seems to stabilize toward an asymptote value. Moreover, on each curve, there are oscillations of the cooling value from one layer to another. These oscillations are due to the trajectory difference between the even and odd layers.

Figure 5.62 shows that the required cooling time evolves exponentially as a function of the inter-layer temperature criterion to be respected. If the cooling time is considered stabilized and to have converged, it is possible to automate the manufacturing of the block. Moreover, the total manufacturing time of the block can be estimated. The manufacturing time of a layer is approximately 100 s. Table 5.17 shows the manufacturing time of a 99-layer "repeatability block" for the different inter-layer temperatures.

Table 5.17 – Estimation of the manufacturing time according to the inter-layer temperature to be respected.

Inter-layer temperature criteria (°C)	Estimated manufacturing time of a 100 layers bloc
250	0 day, 10 hours, 47 minutes and 37 seconds
200	0 day, 13 hours, 36 minutes and 53 seconds
150	0 day, 17 hours, 46 minutes and 14 seconds
100	1 day, 1 hour, 14 minutes and 28 seconds
80	1 day, 5 hours, 59 minutes and 0 seconds
40	2 days, 6 hours, 10 minutes and 28 seconds

Table 5.17 thus allows concluding that, if the test must be performed in less than one day, and in order to ensure maximum repeatability of the test and have perfect control of the inter-layer temperature, inter-layer temperatures of either 250°C, 200°C, or 150°C can be considered. Based on this study, future "repeatability block" fabrication tests will be designed to validate these fabrication times.

5.5.5 Conclusion of the study

In this study, the objective was to predict the cooling time between each layer to respect a specific inter-layer temperature, which will then allow estimating the associated total manufacturing time. In this perspective, a simplified test is set up to perform the calibration step of the thermal model parameters. The test is carried out in two stages to allow for a two-step calibration. Indeed, the objective was to increase the influence of the source parameters in the second part of the test to better identify the influence of the cooling parameters in the first part of the test. Once the parameters are calibrated, the validation step performed on the first part of the test shows a very good match.

Subsequently, the cooling time required per layer for different inter-layer temperatures is estimated on the real configuration of the "repeatability block" on the first 20 layers. The total manufacturing time for each configuration is thus determined. Based on these results, one can conclude that, in order to manufacture one repeatability test block in less than a day, the lowest and most constraining inter-layer temperature that can be used is 150°C.

Finally, this test also highlights the validity of the thermal models for a complex configuration such as a block with changes of trajectory at each layer and many changes of torch direction. Moreover, the results obtained are satisfactory even though a different process is used (the CMT process instead of the GTAW process), as well as another welding robot.

5.6 Thermal parameters sensitivity analysis

In this section, the sensitivity indices of the thermal model parameter sets are investigated for the four studies presented. From the surrogate models set up for the calibrations, the first-order Sobol indices are determined. They are presented in Figures 5.63.

The first observation is that the most influential parameters are the efficiency and the parameters of heat dissipation by convection and radiation. The morphological parameters of the equivalent heat source are in general not very influential, except for the AFH test, where the heat source is defined by only one parameter. This may be due to the fact that the source is defined by only one morphological parameter set (rather than 4), or to the more complex welding path of the part which may accentuate the importance of the only one parameter defining the shape of the heat source.

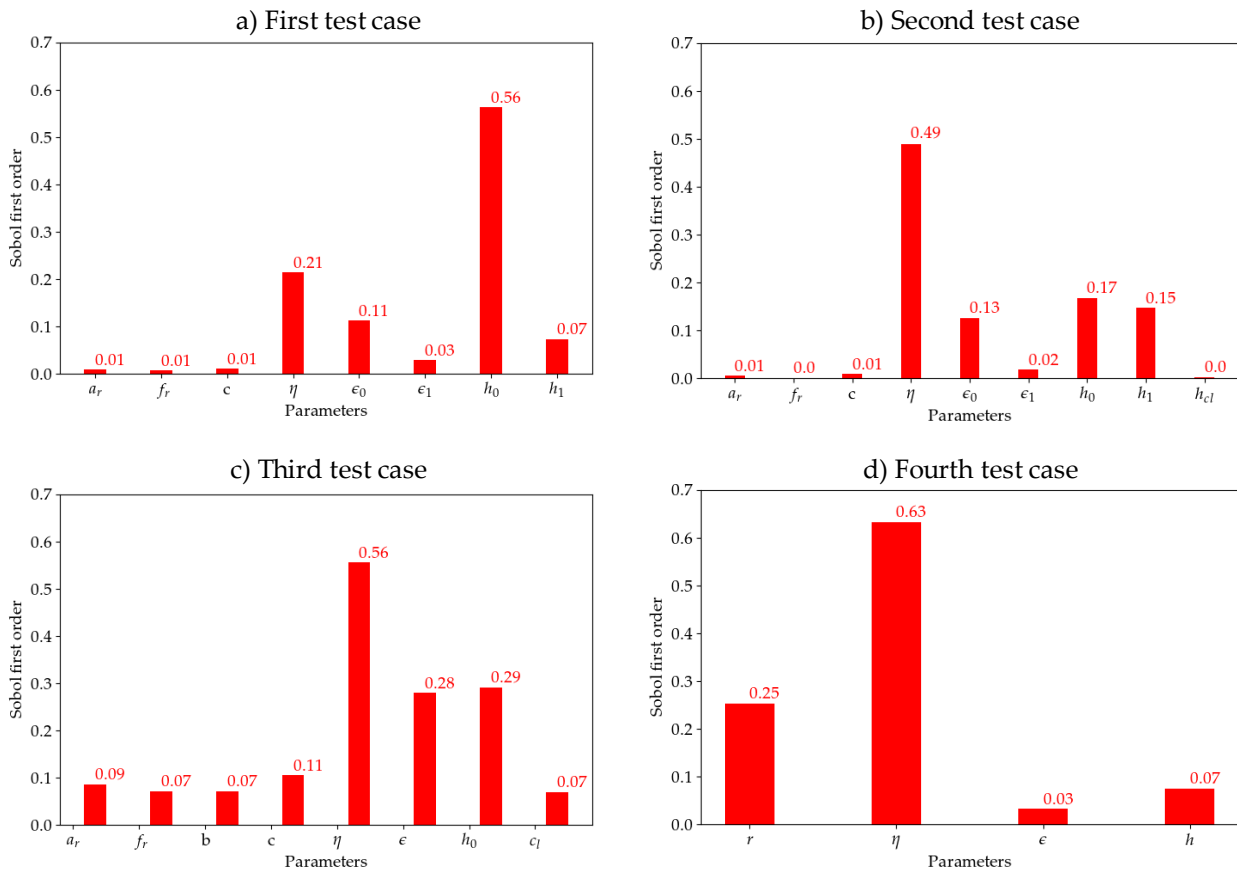


Figure 5.63 – Thermal parameters sensitivity analysis results (first-order Sobol indices) of the four test cases presented previously: a) 1st test case, b) 2nd test case, c) 3rd test case, d) 4th test case.

This means that, at the thermocouple locations, the parameters defining the heat fluxes are prioritized over the parameters defining the equivalent heat source distribution. To get a good estimate of the thermal field "away" from the molten pool, a good estimate of the efficiency and thermal dissipations can give satisfactory results. This is not surprising, as thermocouples are normally positioned far enough from an arc weld pool that the heat source shape only has second order effects: the temperature rise is driven almost wholly by the efficiency once the power, speed and path are fixed.

A further study is carried out in Appendix F on the calibration of the parameters sets of the thermal

model from the residual stresses on the 3rd case study. The Sobol indices obtained by this study show that the influence of the parameters on the residual stresses is different. Figure 5.64 shows that, as in the sensitivity analysis using the temperature profiles, the efficiency is the most influential parameter. However, the heat losses coefficients have little influence, while the depth and length of the heat source are influential. The distribution of the heat source is therefore important for the correct estimation of the residual stresses.

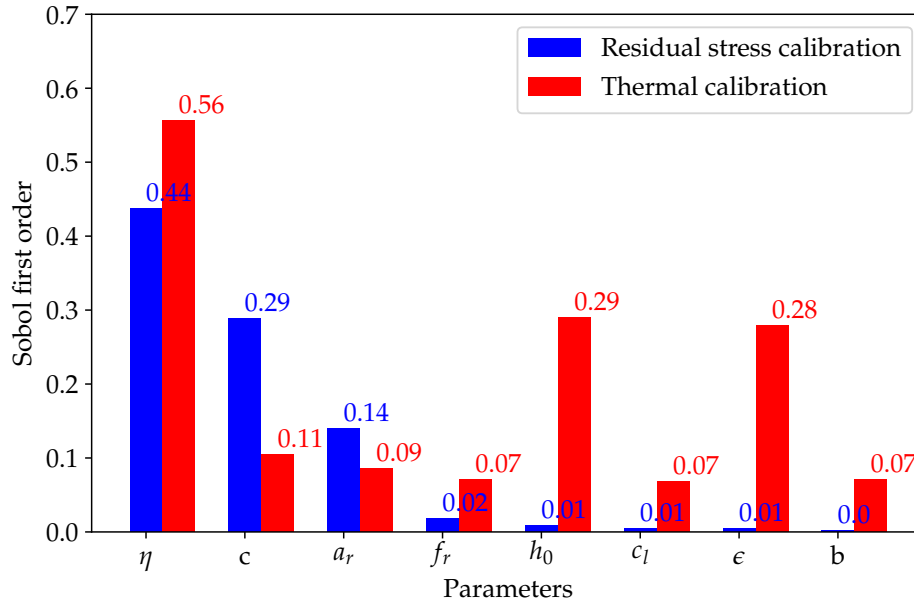


Figure 5.64 – Comparison of aggregated first-order Sobol indices obtained from the calibration using residual stress data (blue) and from the calibration using temperature data at thermocouple points (red). The parameters are ranked in descending order according to the aggregated first-order Sobol indices using residual stress data.

In the end, this study shows that to have a good global thermal field, the parameters of the efficiency and the heat losses coefficients are very important and more influential than the morphological parameters of the heat source. However, for the prediction of residual stresses where local thermal gradients are important, the thermal source parameters gain in influence, while the heat losses coefficients have less impact. However, the efficiency is still the most influential parameter in general.

5.7 Conclusion & perspectives

In this chapter, the results of the mesoscopic thermo-mechanical model proposed are compared with four instrumented experimental studies. The four tests are carried out for different manufacturing configurations: type of process (GTAW or CMT), process parameters, deposition patterns.

For each test case, the first step consists of building a surrogate model of the test. The calibration of the thermal parameters is then performed using this metamodel based on thermocouple data. For the four tests, the results obtained with the calibrated model show very good agreement with experimental data of various nature (thermal or mechanical), thus highlighting the reliability and robustness of the methodology for various manufacturing configurations.

Each test validated the models on specific points:

- In the 1st test, the material input method is tested for a case with large displacements. The results show that the material activation method is able to take into account the path of the robot during the activation of the elements. The resulting shape is found in agreement with that observed experimentally.
- In the 2nd study, two experimental wall tests were carried out with two different deposition strategies. These tests, very well-instrumented thermally, have shown that the calibrations on one test allow the prediction on the other test. Subsequently, the simulations show a very good match in terms of predicting the evolution of the size of the molten pool and the inter-layer temperature obtained by thermal imaging, thus allowing the calibration step on the thermocouples to be validated. Finally, a comparison of the evolution of the displacement of the base plate free end shows a good match between the numerical predictions and the experimental measurements.
- The 3rd study is carried out within the framework of the NET network consortium and aims at measuring the residual stresses for single and multiple bead tests. In this study, the stress profiles measured by neutron diffraction are compared to the numerical profiles carried out for all the constitutive behavior models presented in Section 3.4, with and without hardening annealing. Overall, the numerical results are in good agreement with the experiments. This study shows that the most suitable models are the kinematic hardening and mixed hardening models with and without hardening annealing. The Chaboche models, on the other hand, give the most distant results.
- The test presented in the 4th study is set up in order to optimize the performance of an experimental test within the framework of the AFH consortium, called the "repeatability block". A representative block test is carried out in two steps to calibrate better the heat source and the heat losses coefficients representing the two cooling devices involved. The calibrated model provided suitable results with respect to the experimental data. The simulation of the complete "repeatability block" carried out with the optimized parameter set show that if the block test has to be carried out in one day, as required by AFH, the inter-layer temperature to be respected is 150 °C or more.

The simulations carried out in this chapter show that the mesoscopic model used is highly efficient. Nevertheless, they have highlighted the following fact: thermo-mechanical simulations are costly in terms of calculation time. They are therefore difficult to apply to industrial-scale workpiece simulations, while still having reasonable computation times. This is the subject of the next part of this manuscript.

In the next two chapters, two methods of reducing the computation time are explored. In Chapter 6, the macro-deposition method is studied, optimized, and discussed for the estimation of residual stresses and displacements. A combined approach of macro-deposition and mesoscopic simulations is also proposed: the "local meso-resolution" method.

A method is proposed to predict inherent strains from the thermal behavior of a workpiece in Chapter 7. A deep learning model is built to predict the part morphology from a thermal simulation.

5.8 In a nutshell

Validation cases and numerical results

- Application of the calibration method on 4 case studies with four different configurations (process type, process parameters, deposition pattern), and with various parameters to be validated (equivalent heat source, heat losses coefficients: convection, radiation, clamping or cooling devices).
- Validation of the calibration on experimental thermal quantities:
 - Thermocouples temperature profiles,
 - Molten pool length measured from thermal imaging,
 - Inter-layer temperature measured from thermal imaging.
- Validation of the thermo-mechanical models on experimental mechanical quantities:
 - Displacement (residual or evolution over time),
 - Residual stresses with a study on the influence of the material models with and without hardening annealing.

Part II

Computationally efficient approaches

Chapter 6

Macro-deposition & local meso-resolution methods

Contents

6.1	Introduction	165
6.2	Description of the macro-deposition method	166
6.2.1	Main concepts behind macro-deposition	166
6.2.2	Problematic	167
6.3	Calibration of the macro-deposition method	167
6.3.1	Introduction	167
6.3.2	Presentation of the study cases	168
6.3.3	1 st case study: " <i>Raster</i> " using TIG process	171
6.3.4	2 nd case study: " <i>Raster</i> " using CMT process	174
6.3.5	3 rd case study: " <i>Zigzag</i> " using TIG process	177
6.3.6	4 th case study: " <i>Raster</i> " using TIG process	179
6.3.7	5 th case study: Kaplan blade representative bloc using TIG process	181
6.3.8	Conclusion on the five study cases	183
6.3.9	Perspectives and possible applications for macro-deposition	184
6.4	Mixed approach: macro-deposition with "local meso-resolution"	187
6.4.1	Overview of the "local meso-resolution" approach	187
6.4.2	Application to the 5 th case study	187
6.5	Conclusion & perspectives	190
6.6	In a nutshell	192

6.1 Introduction

Modeling is an effective tool to investigate, better control, and optimize the WAAM manufacturing process, as well as to make predictions. However, one of the main issues raised by the simulation of WAAM manufactured parts at the industrial scale is the computational time. For AM fabricated large components with complex geometries containing many thousand beads, a complete simulation of all the beads is not feasible from a resource and computation time point of view. Indeed, in addition to the size of the mesh that becomes larger as the size of the component to be modeled increases, the simulations include many iterations of non-linear thermal and mechanical calculations and many operations. These operations are of various natures: the manipulations on the mesh for the progressive activation of the meshes, the adjustment of the contributed energy, as well as the possible post-processings during the simulation.

Therefore, specific modeling strategies are necessary to reduce the computational time while maintaining accurate predictions in order to apply the developed tools to industrial problems. Various simplified approaches exist in the literature for the simulation of multi-pass welding, as presented in the literature review performed in Chapter 2. In this chapter and the following chapter, similar approaches are developed and explored to significantly reduce the computational time in the framework of the thermo-mechanical model proposed and implemented in the previous chapters.

The current chapter investigates the simplified method based on macro-deposition in order to simulate the WAAM process for the prediction of the residual stress field. This method is based on a simplification of the material and energy input modeling strategies. It thus relies on new modeling parameters that need to be optimized. One of the main original features of this work is that these new numerical parameters are directly optimized.

Moreover, a second originality of this study is that the results obtained with the macro-deposition method are confronted with the numerical simulations presented in Chapters 3, 4 and 5. Indeed, in Chapter 5, the models developed have demonstrated their performances to predict mechanical quantities, which is the main objective of the current study. Moreover, taking the thermo-mechanical models developed in the previous chapters as references helps avoid performing additional experimental tests. In this chapter, these thermo-mechanical simulations are referred to as "reference simulations".

Finally, in this chapter, a new simplified method is also proposed. It consists in going one step further and combining macro-deposition with meso-scale fully resolved solutions in regions of interest. This method is referred to as "local meso-resolution".

Therefore, the main points covered in this chapter are:

- Development and implementation of a macro-deposition method to accurately predict the residual stresses or displacements fields of the thermo-mechanical simulation while significantly reducing the computation time.
- Calibration and validation of the method by comparing the results to "reference simulations".
- Development and implementation of a hybrid method (local meso-resolution) combining the macro-deposition method and the reference thermo-mechanical simulations.
- Validation of the local meso-resolution method by comparing the results to "reference simulations".

6.2 Description of the macro-deposition method

6.2.1 Main concepts behind macro-deposition

The general description of the macro-deposition method can be found in Chapter 2. In this section, the modeling parameters of the method investigated in this chapter are briefly presented [76].

■ **Material deposition:** In the following, the parameter characterizing the material deposition is the percentage (or fraction) of the layer deposited at once f_{l_d} , also called layer fraction. The parameter l_d (m) is related to the distance covered by the welding torch inside each layer fraction such as:

$$f_{l_d} = \frac{l_d}{l_{full}}, \quad (6.1)$$

where l_{full} (m) is related to the distance covered by the welding torch for the full layer.

The layer fraction is also associated with the time t_d (s) needed for the welding torch to cover the layer fraction:

$$t_d = \frac{l_d}{v_t}. \quad (6.2)$$

■ **Energy input:** Rather than modeling the moving equivalent heat source, each layer fraction is entirely heated. In this study, a uniform volumetric power flux can be defined in different ways. The simplest way is to apply a uniform volumetric flux on the macro deposit, with V_d (m³) the layer fraction volume:

$$q_{l_d}(x, y, z) = \frac{\eta UI}{V_d}. \quad (6.3)$$

If the manufacturing time of the activated macro-deposit is t_d , the total energy to be supplied is $\eta UI \times t_d$. Figure 6.1 is a schematic representation of the macro-deposition approach.

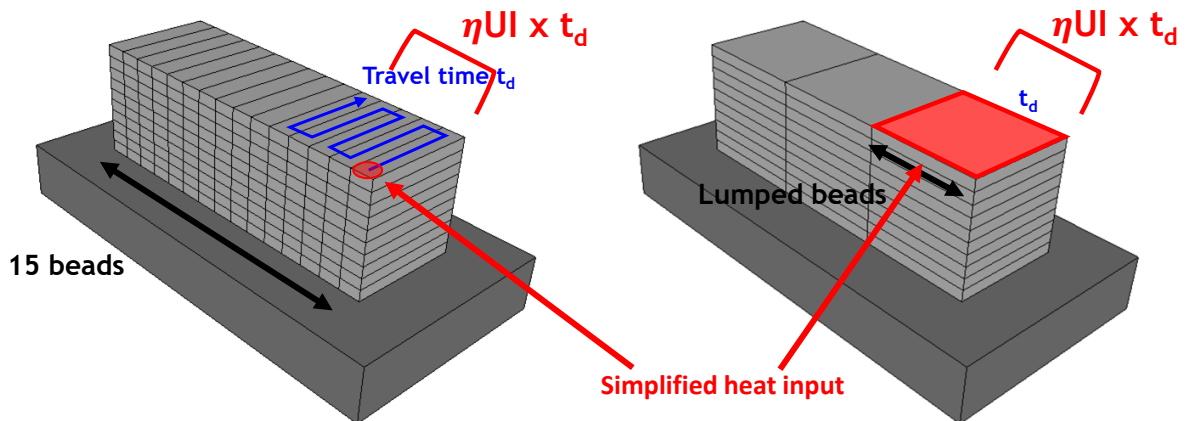


Figure 6.1 – Schematic representation of the macro-deposition approach: the mesoscopic approach on the left, and the corresponding macro-deposition approach on the right.

As presented in Chapter 2, the manufacturing time t_d can be divided in two terms: t_d^{heat} , the heating time during which the layer fraction is heated, and $t_d^{cool} = t_d - t_d^{heat}$, the cooling time after the heating step. The value selected for the heating time parameter is crucial since it has an influence on the temperature of the part (especially on the local maximum temperature reached), and thus on the mechanical residual state.

6.2.2 Problematic

The macro-deposition method requires the adjustment of two parameters: the layer fraction deposited simultaneously f_{l_d} , and the heat input time fraction applied to each macro-deposit: $f_{t_d^{heat}} = t_d^{heat}/t_d$. The choice of the values of these parameters is not trivial. In general, they are defined empirically or by progressive adaptation of the "trial-and-error" type. Therefore, in this study, the influence of the choice of these two parameters is investigated. For the selection of the two parameters, a set of "mechanical indicators" that correspond to the main quantities of interest is defined for the calibration step of the simplified simulations with respect to the reference simulations. This is to ensure the excellent reproducibility of the results. Indeed, the criteria that ensure a good fit can vary according to the objective of the calculation.

Within the framework of this thesis, all the other operations carried out on the reference simulations (Chapters 3 and 4) are also carried out in this model: change of the reference temperature, cut-off temperature, hardening annealing, management of the material input, etc. The piecewise isotropic hardening is used (VMIS_ISOT_TRAC).

6.3 Calibration of the macro-deposition method

6.3.1 Introduction

In this study, the selection of the simplified model parameters will be carried out by determining the parameter set minimizing the deviation from the reference numerical simulations while reducing the calculation time. Numerous numerical simulations are thus carried out with the objective of covering the whole range of possible configurations in order to build a response surface of the error with respect to the reference simulations. A set of "mechanical indicators" corresponding to the main quantities of interest needs to be defined beforehand to calculate the error. The error criteria considered are presented in Tables 6.1 and 6.2.

For the study presented in this section, the error results considered are those using the Von-Mises equivalent stress criterion and the displacement field error criterion. However, in the framework of this PhD thesis, studies were performed using the different criteria listed and showed similar results.

Table 6.1 – Stress field error criteria.

Maximum principal stress at each node

$$\varepsilon_{\sigma_{max}} = \frac{1}{|\Omega|} \int_{\Omega} \|\sigma_{max}(\underline{x}) - \sigma_{max}^{ref}(\underline{x})\|_2 d\underline{x} \quad \text{with} \quad \sigma_{max} = \max(\sigma_1, \sigma_2, \sigma_3) \quad (6.4)$$

Von-Mises equivalent stress

$$\varepsilon_{\sigma_{eq}} = \frac{1}{|\Omega|} \int_{\Omega} \|\sigma_{eq}(\underline{x}) - \sigma_{eq}^{ref}(\underline{x})\|_2 d\underline{x} \quad (6.5)$$

Frobenius norm

$$\varepsilon_{\sigma_F} = \frac{1}{|\Omega|} \int_{\Omega} \|\underline{\sigma}(\underline{x}) - \underline{\sigma}^{ref}(\underline{x})\|_F d\underline{x} \quad \text{with} \quad \|\sigma\|_F = \sqrt{\sum_{\substack{1 \leq i \leq 3 \\ 1 \leq j \leq 3}} |\sigma_{ij}|^2} \quad (6.6)$$

Table 6.2 – Displacement field error criteria.

Maximum displacement component of the displacement field

$$\varepsilon_{u_{max}} = u_{max} - u_{max}^{ref} \quad (6.7)$$

Displacement field

$$\varepsilon_u = \frac{1}{|\Omega|} \int_{\Omega} \|\underline{u}(\underline{x}) - \underline{u}^{ref}(\underline{x})\|_2 d\underline{x} \quad (6.8)$$

6.3.2 Presentation of the study cases

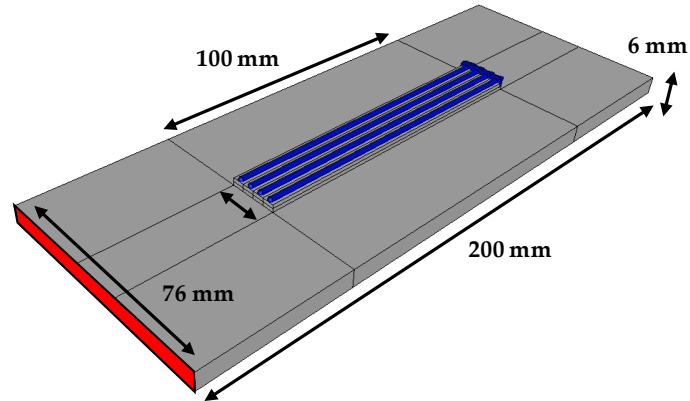
To better understand the influence of macro-deposition modeling points, five simple cases are set up. The four first ones are presented in Figure 6.2. The same methodology as for the setting up of the surrogate models in Section 4 is used to construct error response surfaces as a function of the macro-deposition parameters. The surrogates models constructed in this study rely on kriging, also called Gaussian Process (GP) [192].

The two parameters identified are the fraction of the layer deposited f_{l_d} and the fraction of heat input $f_{t_{heat}}$ on the macro-deposits. A design of experiments on these two parameters is first generated. Then, the associated macro-deposition simulations are performed. In addition, the corresponding reference thermo-mechanical simulation is performed. The errors on the displacement and the stresses associated with each macro-deposition simulation are calculated with respect to the reference simulation. These response surfaces are used both to select the optimal configurations to perform the simulation and to find a possible correlation between all the response surfaces.

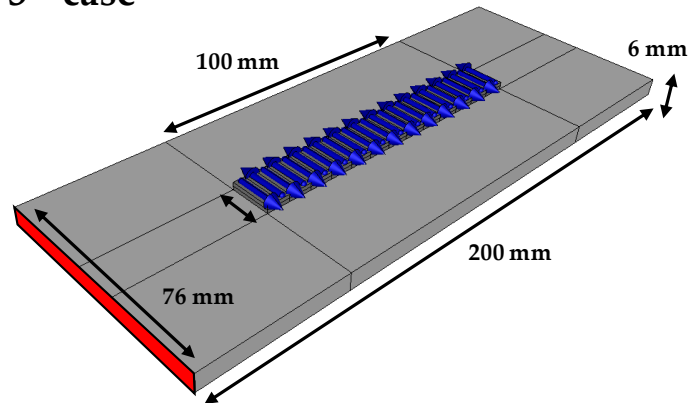
For each study case presented in this section, the reference and simplified thermo-mechanical simulations are performed using quadratic elements to have the most accurate results. In addition, the mesh size used for both simulations is the same for each case study. This allows for a more accurate

comparison of the results on the whole mesh without any projection step. Finally, all the comparisons are carried out on the final state of the component, after the cooling of the component to room temperature.

a) 1st and 2nd case



b) 3rd case



c) 4th case

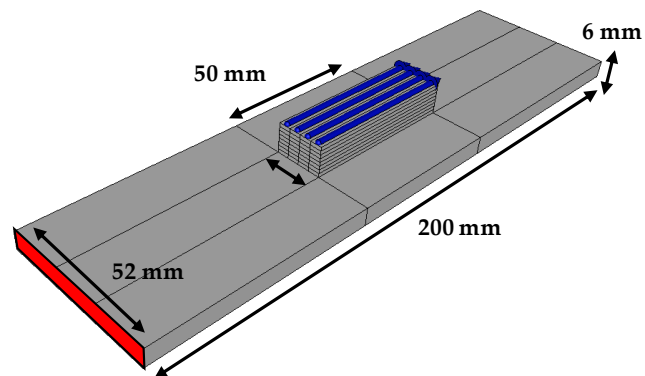


Figure 6.2 – Presentation of the geometry and the deposition pattern of the first 4 study cases: a) 1st and 2nd 2 layers full "Raster" study case, b) 3rd 2 layers "Zigzag" study case, c) 4th 8 layers full "Raster" study case.

The results of each test case (described in the following sections) are presented in Figures 6.5, 6.6,

6.8, 6.9, 6.11, 6.12, 6.14, and 6.15. These Figures are subdivided in 4. The sub-Figure "a" presents the 3D response surface obtained by kriging from the different sets of parameters. In sub-Figure "b" is represented this same response surface (error on the stresses or the displacements depending on the figures considered) with a "threshold" value. This threshold value represents the maximum accepted error level. A response surface predicting the percentage of computation time (and not the error) for the same sets of parameters is shown on the sub-Figure "c". Finally, the sub-Figure "d" presents the response surface of the calculation time on the domain where the error (on the stresses or the displacements) is lower than the defined "threshold" value. The objective is to identify the set of parameters that takes the least amount of computing time with respect to a specified tolerance (threshold value: maximum accepted error). The optimal parameter sets are then obtained for stresses and displacements (θ_{displ} and θ_{stress}) and compared for each test. The procedure is described in detail for the first case. The other studies are performed using the same methodology.

6.3.3 1st case study: "Raster" using TIG process

For the 1st case study represented in Figure 6.2-a, 2 layers of 4 beads each are deposited using the TIG process on a base plate clamped at one end. The manufacturing deposition pattern is the "Raster". For this case, the parameters used for the simulation are the manufacturing parameters of the 2nd test case of the Chapter 5: $U = 11.0$ V, $I = 120.0$ A, $v_{torch} = 0.00333$ m s⁻¹. The same parameters for the thermal source and thermal dissipations are used. The reference thermo-mechanical simulation is performed in about 38 hours.

For the design of experiments used for the macro-deposition simulations, the parameter of the layer fraction f_{l_d} is discrete: $[1/4, 1/2, 1]$. These values are chosen in order to study configurations where the volume of beads is similar. Indeed, as illustrated in Figure 6.3, the layer is constituted of 4 beads. Therefore, the deposition is either performed bead by bead, 2 beads by 2 beads or 4 beads at once. As for the heat input, the draw is made based on a uniform distribution, between the percentage corresponding to the travelling time of the heat source, which corresponds to $f_{t_d}^{heat}$ (Figure 6.4), and 1.0, which corresponds to a heat input distributed over a the full layer such as: $\mathcal{U} \left(\frac{2a_f}{V_t} \left(\frac{l_{full} f_{l_d}}{V_t} \right)^{-1}, \frac{l_{full} f_{l_d}}{V_t} \left(\frac{l_{full} f_{l_d}}{V_t} \right)^{-1} \right)$. Fractions are used to scale the values of the parameters since it is simpler to construct a response surface using fractions as shown in Figure 6.4.

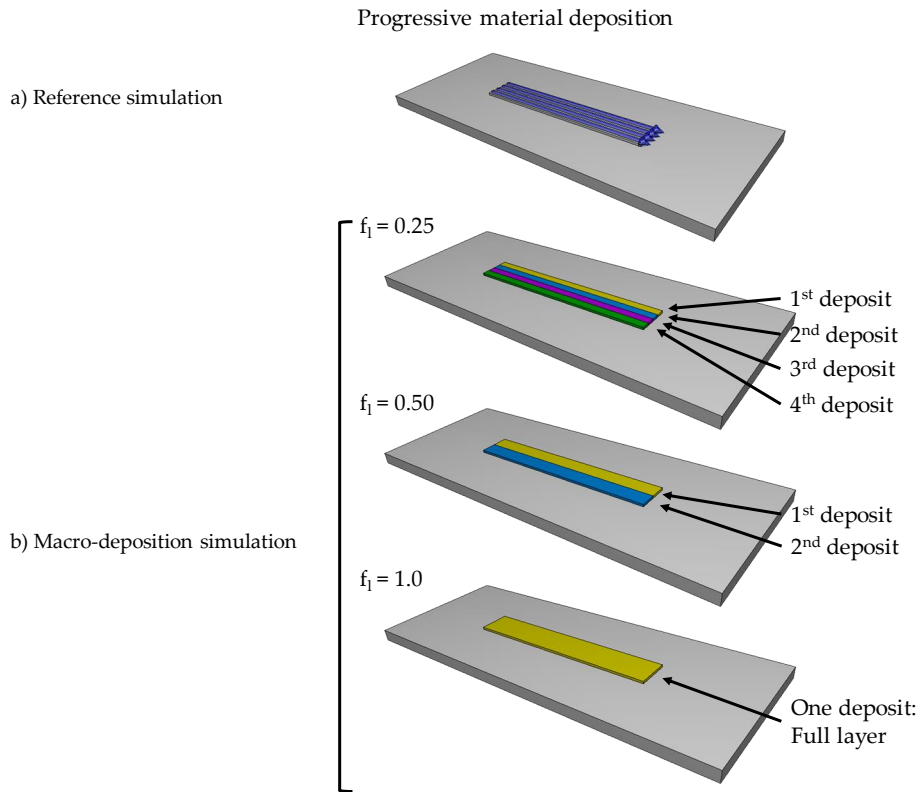


Figure 6.3 – Illustration of the management of the material deposition in macro-deposition method for the 1st use case.

The response surfaces of the displacement error are obtained with a R^2 of 0.944. Figure 6.5 presents the results for the displacement error study. Figures 6.5-a and 6.5-b highlight a very particular trend

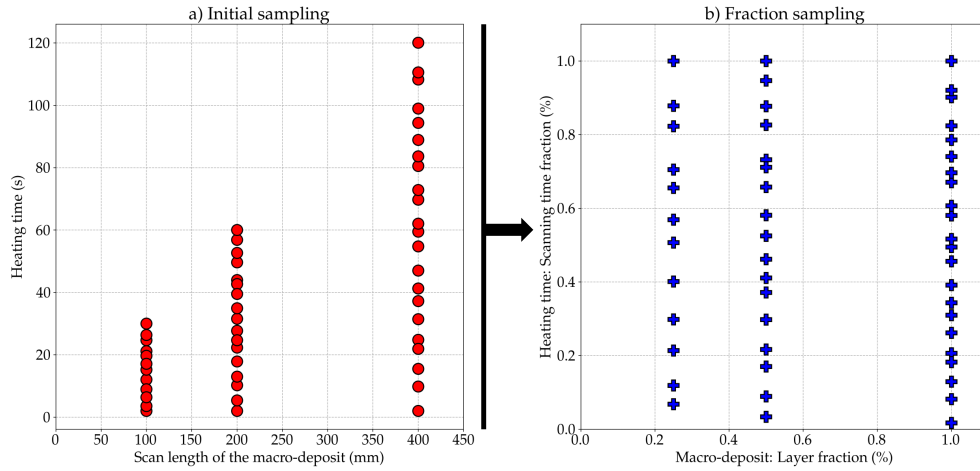


Figure 6.4 – Sampling presentation for the parametric study of the macro-deposition method for the test case 1: a) Sampling using l_d and t_d^{heat} , b) Sampling using the fraction parameter f_{l_d} and $f_{t_d^{heat}}$.

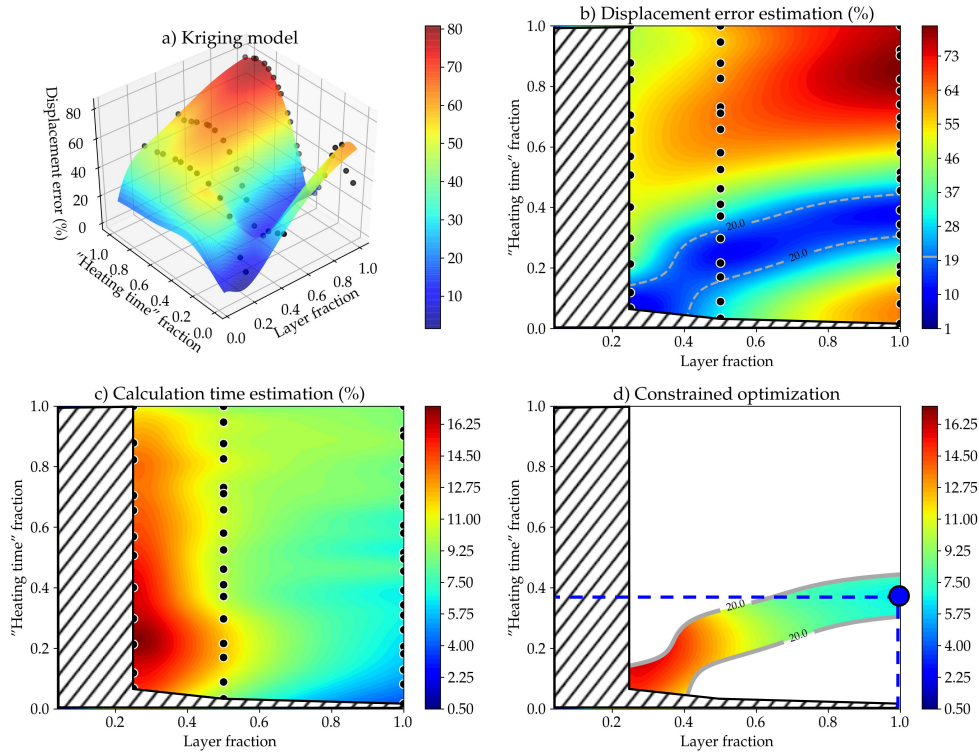


Figure 6.5 – Macro-deposition displacement prediction for the 1st case study: a) 3D displacement error response surface, b) Response surface of the displacement error with a "threshold" value (maximum error accepted), c) Response surface predicting the computation time of the macro-deposition simulation as a percentage of reference simulation computation time, d) Response surface of the calculation time on the domain where the error on the displacements is lower than the defined "threshold" value and the associated computation time for the "optimal" parameter set.

of the displacement error. A preferential zone is found in Figure 6.5-b, and a threshold contour at 20%

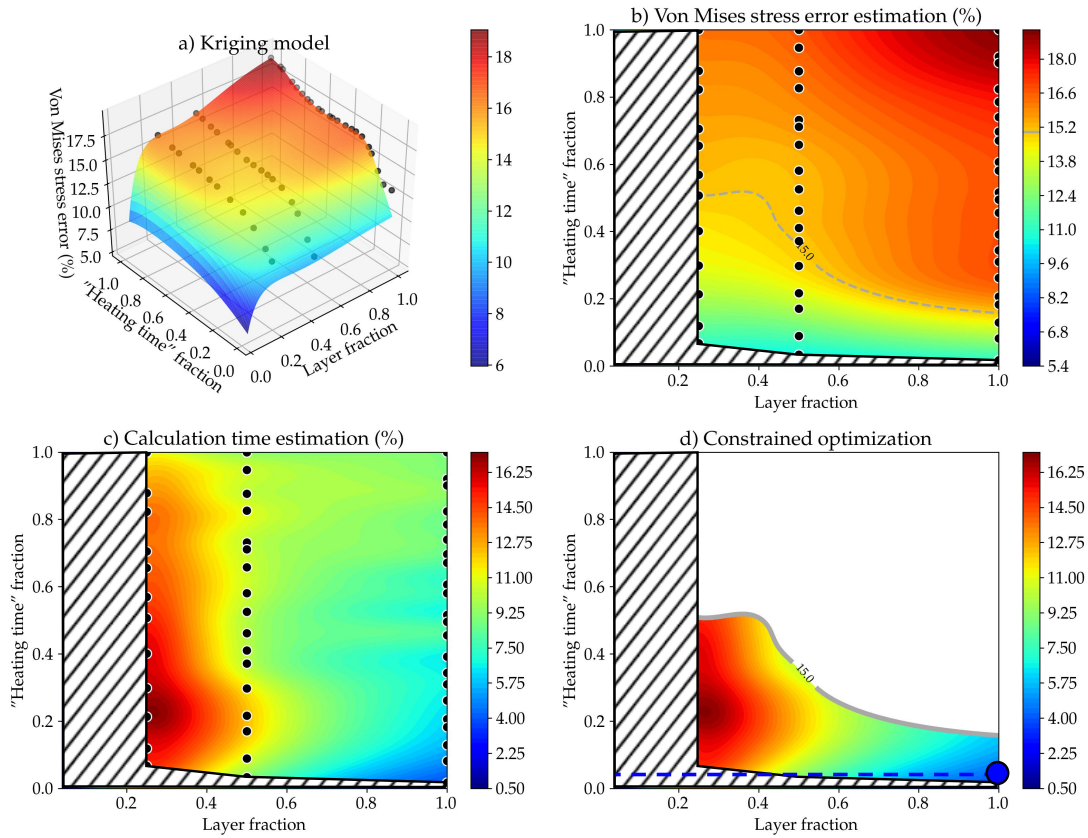


Figure 6.6 – Macro-deposition stress prediction for the 1st case study.

error (chosen arbitrarily) is represented. From this contour, the parameter set that allows the fastest simulation is identified: $\theta_{displ} = (f_{l_d} = 1.0, f_{t_d}^{heat} = 0.34)$ (Figure 6.5-d). According to the predictions, this parameter set allows to have an estimation of the displacements with an error of about 12.2% with a decrease in computation time of 93.5%.

Regarding the errors on the stress, the results are presented in Figure 6.6. The response surface has a R^2 of 0.937. The first finding is that the response surface of the error in stress is different than that in displacement. For a tolerance of 15% error in stress, the "optimal" parameter set identified is: $\theta_{stress} = (f_{l_d} = 1.0, f_{t_d}^{heat} = 0.017)$. This parameter set allows having an estimation of the stresses with an error of about 11.4% with a reduction of the computation time of 96.2%.

In Table 6.3, the equivalence of the optimal parameter sets in meters and in seconds are presented for the displacement and stress configurations. It is noteworthy that the trends of the error response surfaces for the stresses and displacements are not similar. In conclusion, this first test case shows that optimal configurations for the prediction of stresses and displacements exist, with a significant reduction of the computation time. Nevertheless, these optimal configurations are not the same.

As a verification step, the macro-deposit simulations with the optimal parameter sets are performed, with the aim of investigating the similarities with the reference simulation. Figure 6.7 highlights that, for θ_{displ} , the displacement field is very similar to the field of the reference simulation, but that the stress field is different but still rather reasonable. For θ_{stress} , the stress field obtained is very close to the reference field. Yet, the displacement of the base plate end is overestimated.

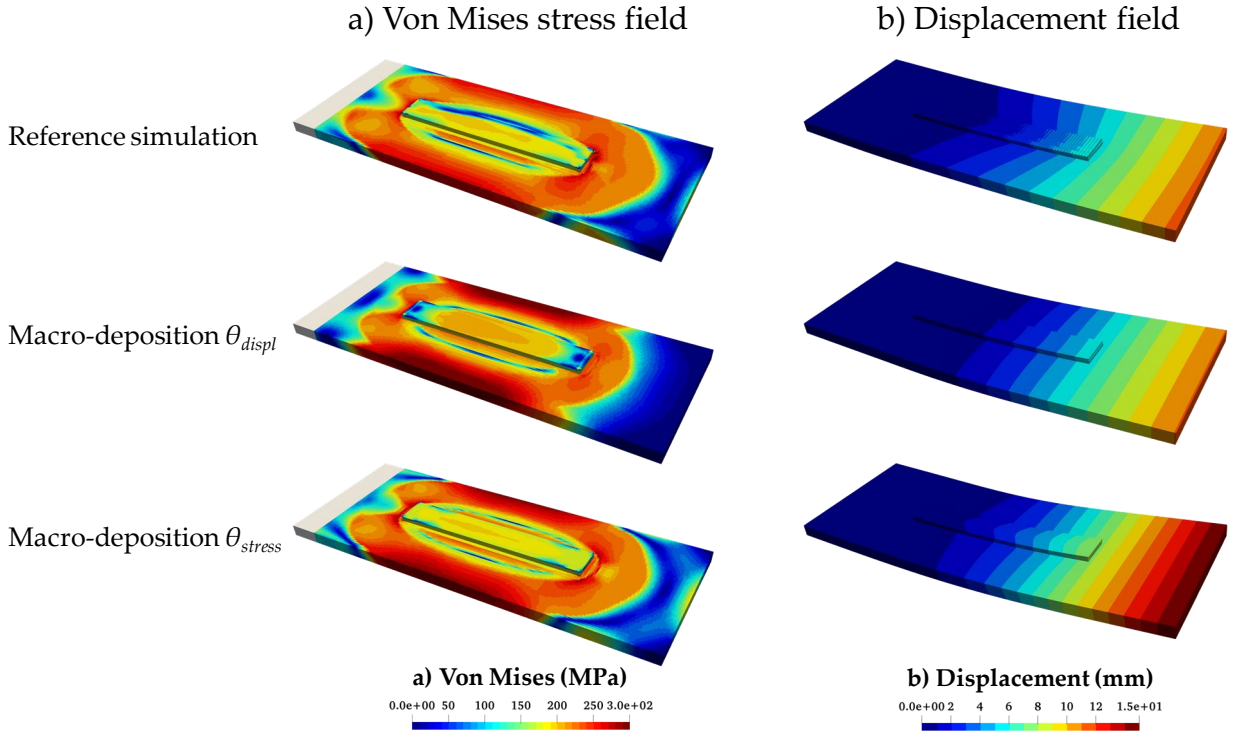


Figure 6.7 – 1st test case results of the reference and macro-deposition simulations for the optimal displacement and stress configurations θ_{displ} and θ_{stress} : a) Von Mises stress field, b) Displacement field.

Table 6.3 – Macro-deposition calibration results summary for the 1st case study.

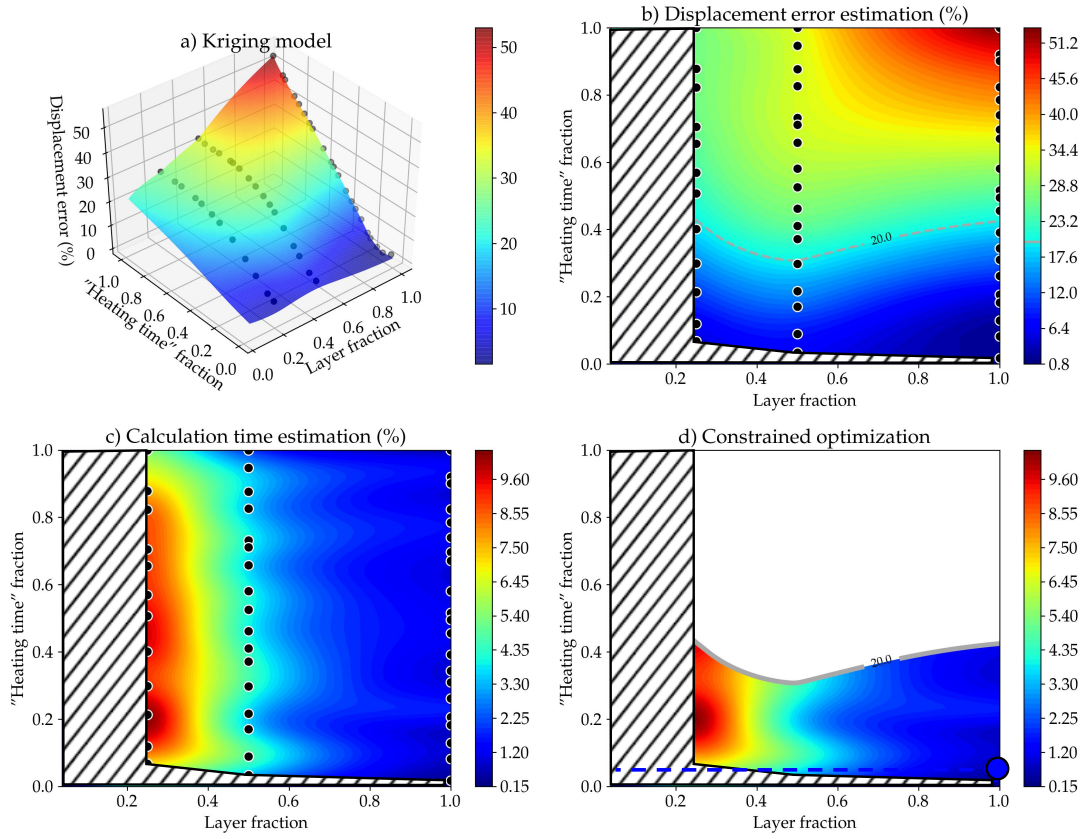
Configuration	f_{l_d} (fraction)	$f_{t_d^{heat}}$ (fraction)	l_d (mm)	t_d^{heat} (s)
Displacement	1.0	0.34	400	40.8
Stress	1.0	0.017	400	2.04

6.3.4 2nd case study: "Raster" using CMT process

The 2nd case study is performed on a similar configuration as the 1st case study but with process parameters corresponding to the CMT process in order to determine if the trends evolve according to the process parameters. For the design of experiments of the macro-deposition simulations, the same approach as for the TIG process is used. The reference thermo-mechanical simulation is performed in about 44 hours.

The response surface of the displacement error is obtained with a R^2 of 0.998. The results on the displacement error are shown in Figure 6.8. A preferential zone is shown by Figure 6.8-b, and the threshold contour at 20% error is represented. From this contour, the parameter set that allows the fastest simulation is identified for: $\theta_{displ} = (f_{l_d} = 1.0, f_{t_d^{heat}} = 0.0169)$. According to the predictions, this parameter set allows having an estimation of the displacements with an error of about 4.18% with a decrease of the computation time of 99.2%.

The results of the stress error study are presented in Figure 6.9. The response surface of the error is obtained with a R^2 of 0.973. Again, the first finding is that the response surface of the stress errors


 Figure 6.8 – Macro-deposition displacement prediction for the 2nd case study.

is different than the displacement one. For a tolerance of 15% of error in stresses, the "optimal" parameter set identified is: $\theta_{stress} = (f_{l_d} = 1.0, f_{t_d}^{heat} = 0.0169)$. This parameter set allows for an estimation of the stresses with an error of about 3.87% with a reduction of the computation time of 99.2%.

Unlike for the 1st study, even though the error response surfaces for stresses and displacements are not similar, the identified optimal parameter sets are the same (Table 6.4). Moreover, the optimal parameter set allows for a significant reduction of the computation time. Finally, Figure 6.10 highlights that, for $\theta_{displ} = \theta_{stress}$, the displacement and the stress fields are very similar to the fields of the reference simulation.

 Table 6.4 – Macro-deposition calibration results summary for the 2nd case study.

Configuration	f_{l_d} (fraction)	$f_{t_d}^{heat}$ (fraction)	l_d (mm)	t_d^{heat} (s)
Displacement	1.0	0.017	400	~ 0.5
Stress	1.0	0.017	400	~ 0.5

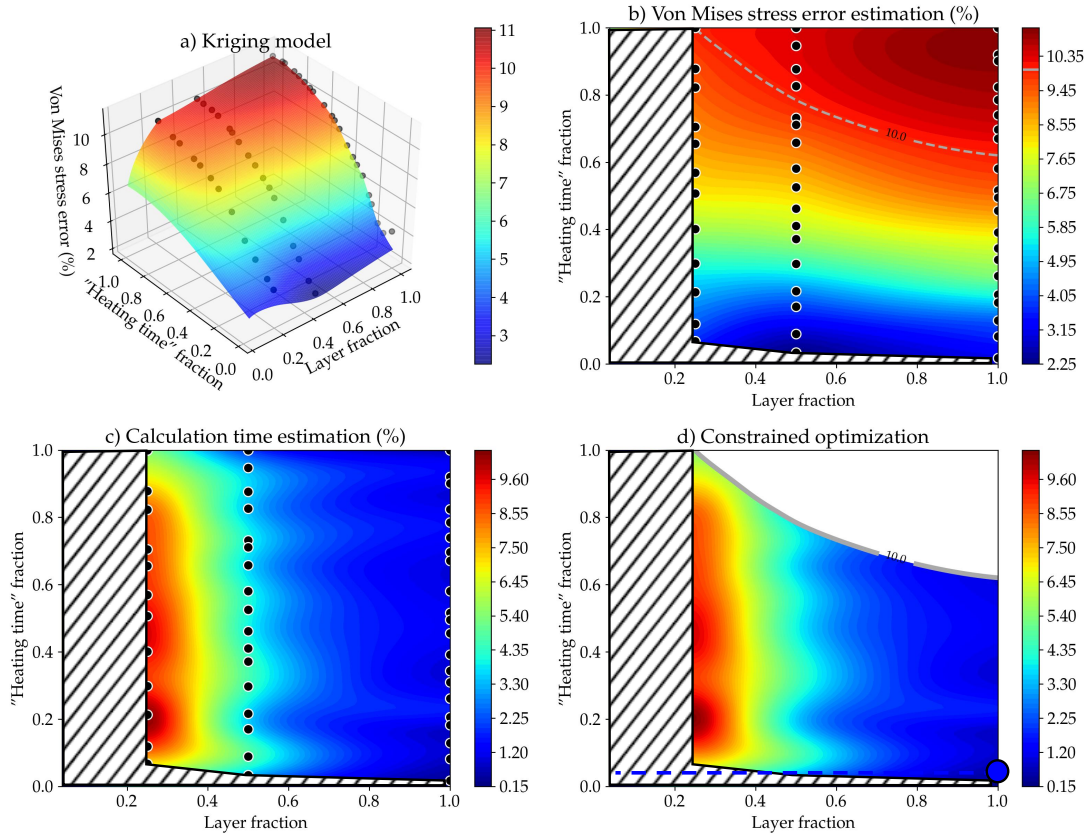


Figure 6.9 – Macro-deposition stress prediction for the 2nd case study.

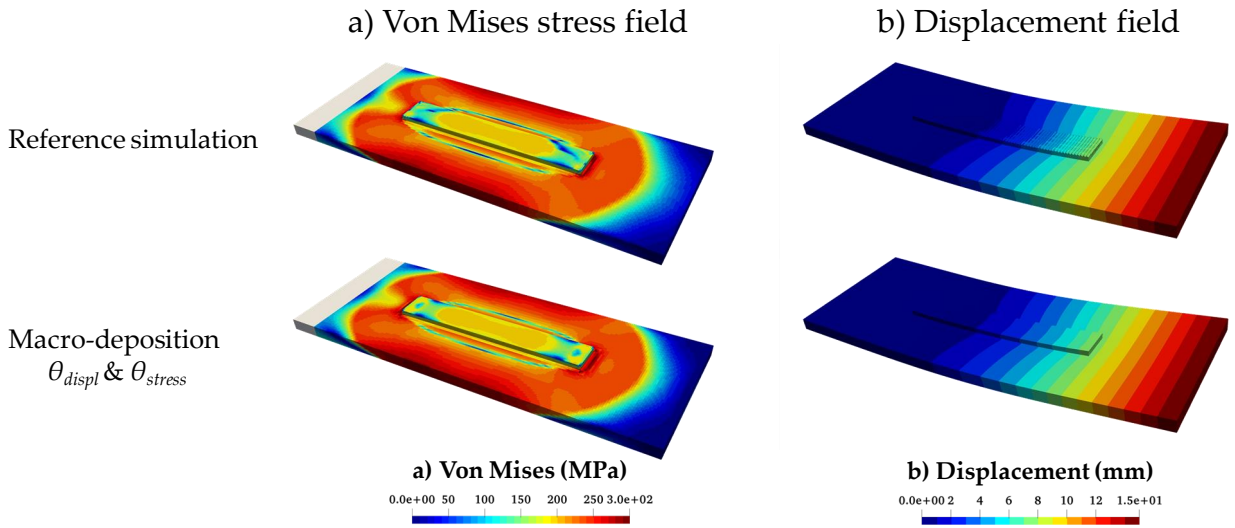


Figure 6.10 – 2nd test case results of the reference and macro-deposition simulations for the optimal displacement and stress configurations θ_{displ} and θ_{stress} : a) Von Mises stress field, b) Displacement field.

6.3.5 3rd case study: "Zigzag" using TIG process

The 3rd case study consists in the manufacturing of the same geometry and with the same process parameters as the 1st case study, but with a different manufacturing path: "Zigzag" in the transverse direction. The objective is to investigate the influence of the manufacturing path on the response surfaces. The layer fraction f_{l_d} parameter is discrete: $f_{l_d} \sim [1/26, 2/26, 4/26, 7/26, 13/26, 26/26]$. For the heat input, as for the 1st case study, the sampling is performed considering a uniform distribution between the percentage corresponding to the travel time of the heat source and 1.0. The reference thermo-mechanical simulation is performed in about 37 hours.

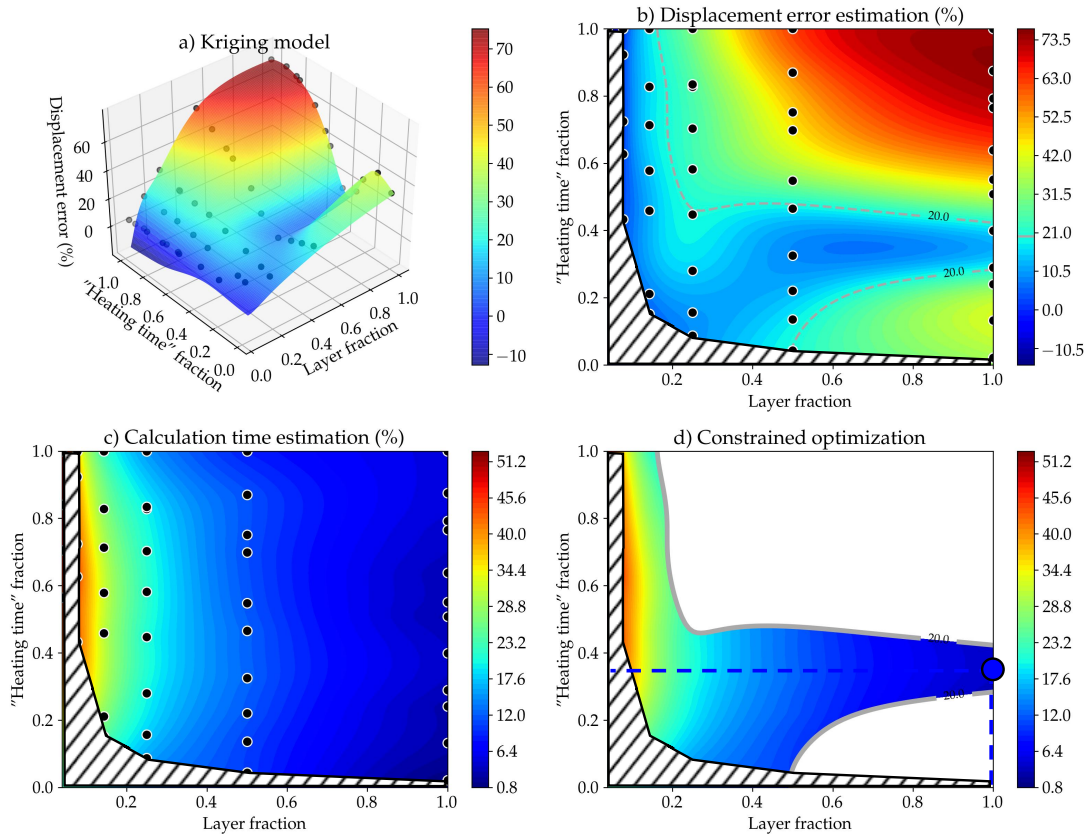


Figure 6.11 – Macro-deposition displacement prediction for the 3rd case study..

Figures 6.11 and 6.12 highlights that the trend of the response surface of the error in displacement and stress are very similar to those of the 1st test case. Therefore, the deposition pattern seems to have little effect on the choice of the two macro-deposit parameters. Moreover, the identified optimal parameter sets are similar between the two case studies. Indeed, the parameter set that allows the fastest simulation is $\theta_{displ} = (f_{l_d} = 1.0, f_{t_d}^{heat} = 0.345)$ for a good estimation of the displacements and $\theta_{stress} = (f_{l_d} = 1.0, f_{t_d}^{heat} = 0.022)$ for the stresses. Table 6.5 summarizes the macro-deposition calibration results. These parameter sets allow having an estimation of the displacements with an error of about 14.3% with a decrease of the computation time of 94%, and of the stresses with an error of about 14.2% with a decrease of the computation time of 97.0%.

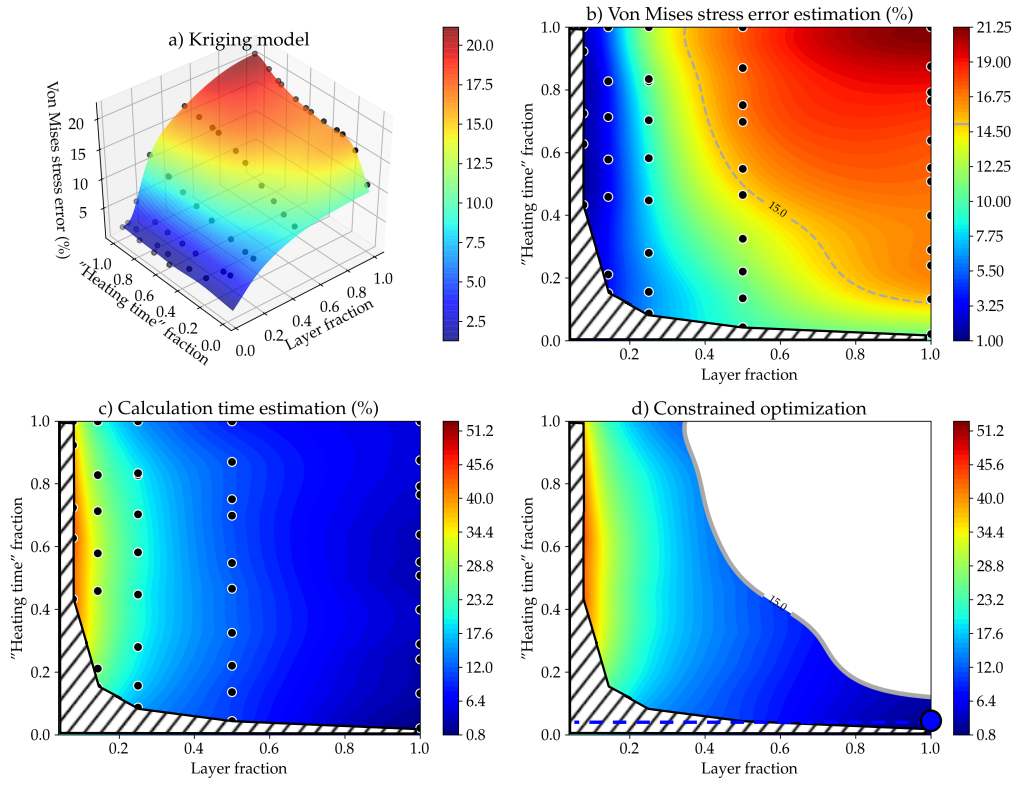


Figure 6.12 – Macro-deposition stress prediction for the 3rd case study.

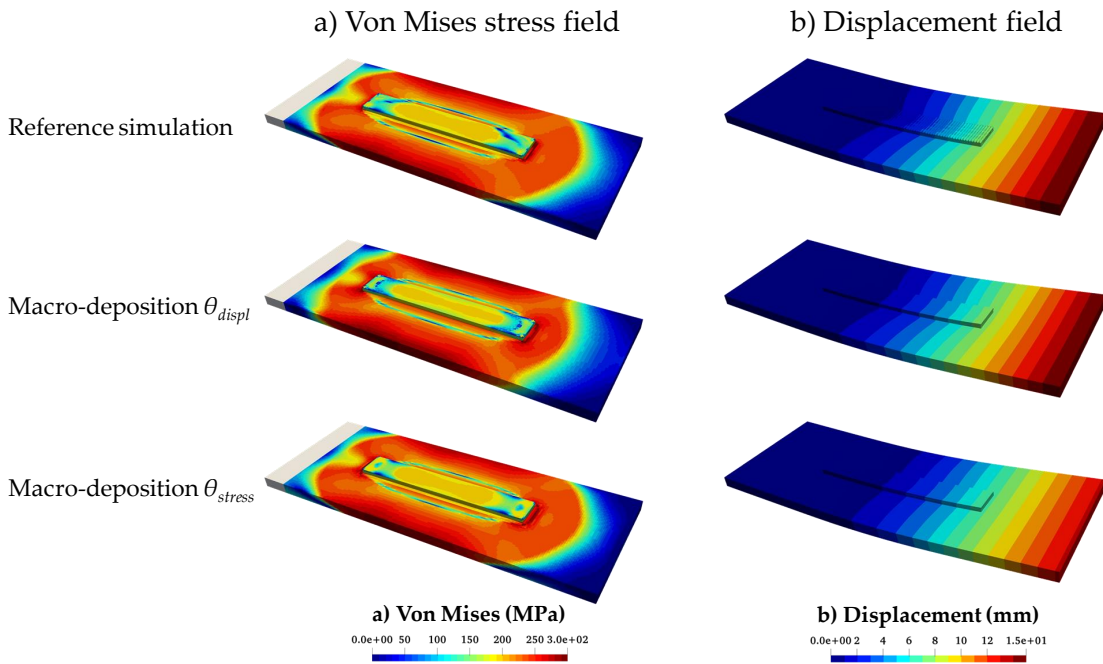


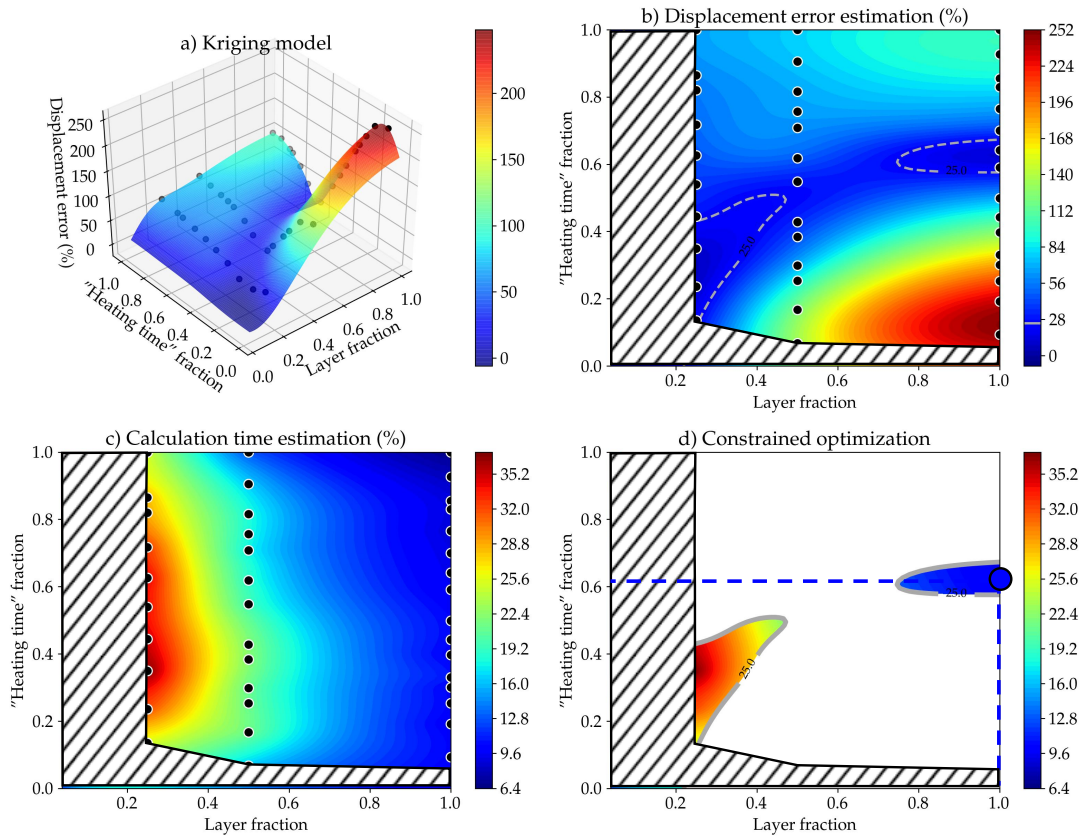
Figure 6.13 – 3rd test case results of the reference and macro-deposition simulations for the optimal displacement and stress configurations θ_{displ} and θ_{stress} : a) Von Mises stress field, b) Displacement field.

Table 6.5 – Summary of the 3rd case study macro-deposition calibration results.

Configuration	f_{l_d} (fraction)	$f_{t_d^{heat}}$ (fraction)	l_d (mm)	t_d^{heat} (s)
Displacement	1.0	0.345	312	32.3
Stress	1.0	0.022	312	2.06

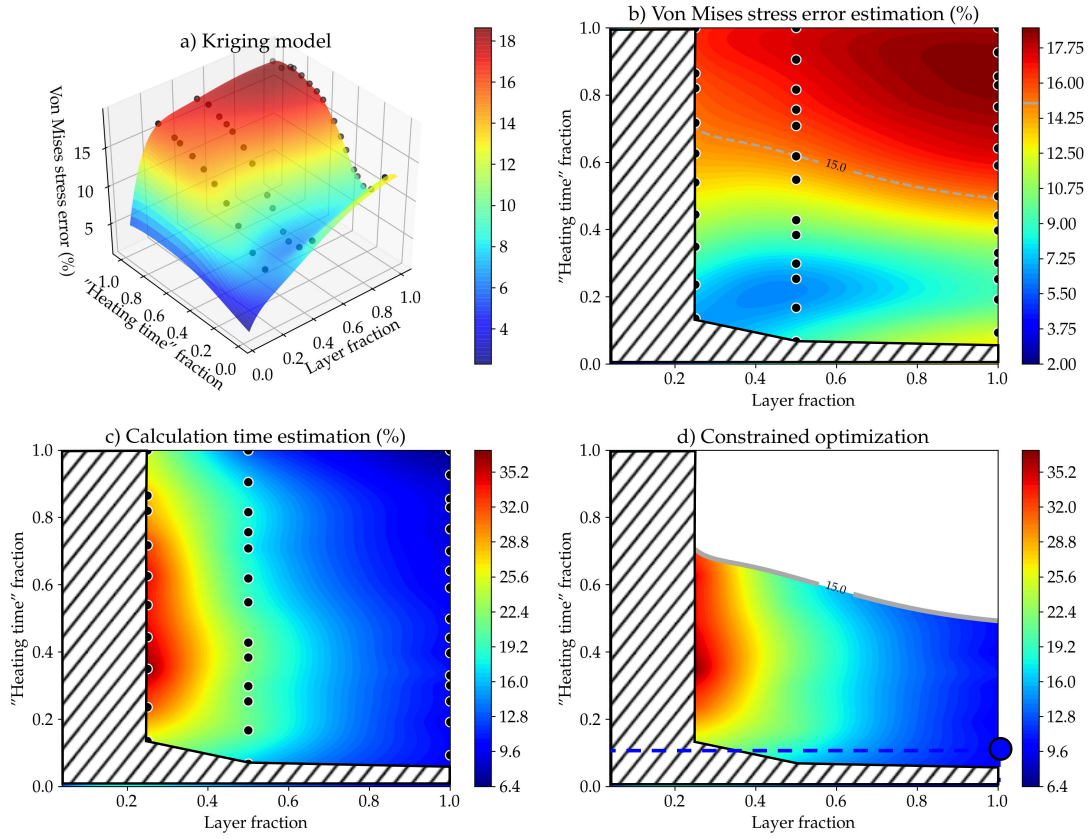
6.3.6 4th case study: "Raster" using TIG process

The 4th case study consists in the superposition of 8 layers, composed each one of 4 50-mm length beads, with a "Raster" manufacturing pattern. This configuration strongly resembles the configuration of the 1st test case, but with layers two-times shorter and more layers. In addition, a different base plate is used. The objective of this study is to investigate the effect of the layer dimensions and numbers on the value of the macro-deposition optimal parameters. All the dimensions involved in this test are shown in Figure 6.2. The reference thermo-mechanical simulation is performed in about 53 hours.

Figure 6.14 – Macro-deposition displacement prediction for the 4th case study .

The response surfaces of the displacement and stress errors are obtained with R^2 of respectively 0.985 and 0.997 (Figures 6.14 and 6.15). The optimal parameter sets are $f_{l_d} = 1.0$, $f_{t_d^{heat}} = 0.67$ and $f_{l_d} = 1.0$, $f_{t_d^{heat}} = 0.034$, respectively for the displacements and the stresses. The corresponding reductions in computation times and computation errors are 91% and 22.04% for the displacements, and 90% and 12.3% for the stresses.

As shown in Figure 6.16, for θ_{displ} , the displacement field is very similar to the field of the reference simulation, while the stress field is slightly different, as for all the previous study cases. Moreover,


 Figure 6.15 – Macro-deposition stress prediction for the 4th case study.

for θ_{stress} , the displacement of the base plate end is strongly overestimated, whereas a very satisfying prediction is obtained for the stress.

The overall trend is quite similar to that of the study cases 1 and 3 (which are the other two study cases with the same process parameters). However, for the displacements, the optimal area is not located at the same position on the response surface (Figure 6.14). Table 6.6 shows nonetheless that, although the optimal parameter set is different when the parameters are considered as fractions, when they are denormalized, the orders of magnitude are very similar to those of the study cases 1 and 3 (Tables 6.3 & 6.5). Therefore, despite the fact that each layer is two times smaller than for the 1st test case and that there are four times more layers, the absolute value of t_d^{heat} found for the three cases are very close:

- Displacement: $t_d^{heat1} = 40.8s$, $t_d^{heat3} = 32.3s$, $t_d^{heat4} = 40.2s$,
- Stress: $t_d^{heat1} = 2.04s$, $t_d^{heat3} = 2.04s$, $t_d^{heat4} = 2.04s$.

 Table 6.6 – Macro-deposition calibration results summary for the 4th case study.

Configuration	f_{l_d} (fraction)	$f_{t_d^{heat}}$ (fraction)	l_d (mm)	t_d^{heat} (s)
Displacement	1.0	0.67	200	40.2
Stress	1.0	0.034	200	2.04

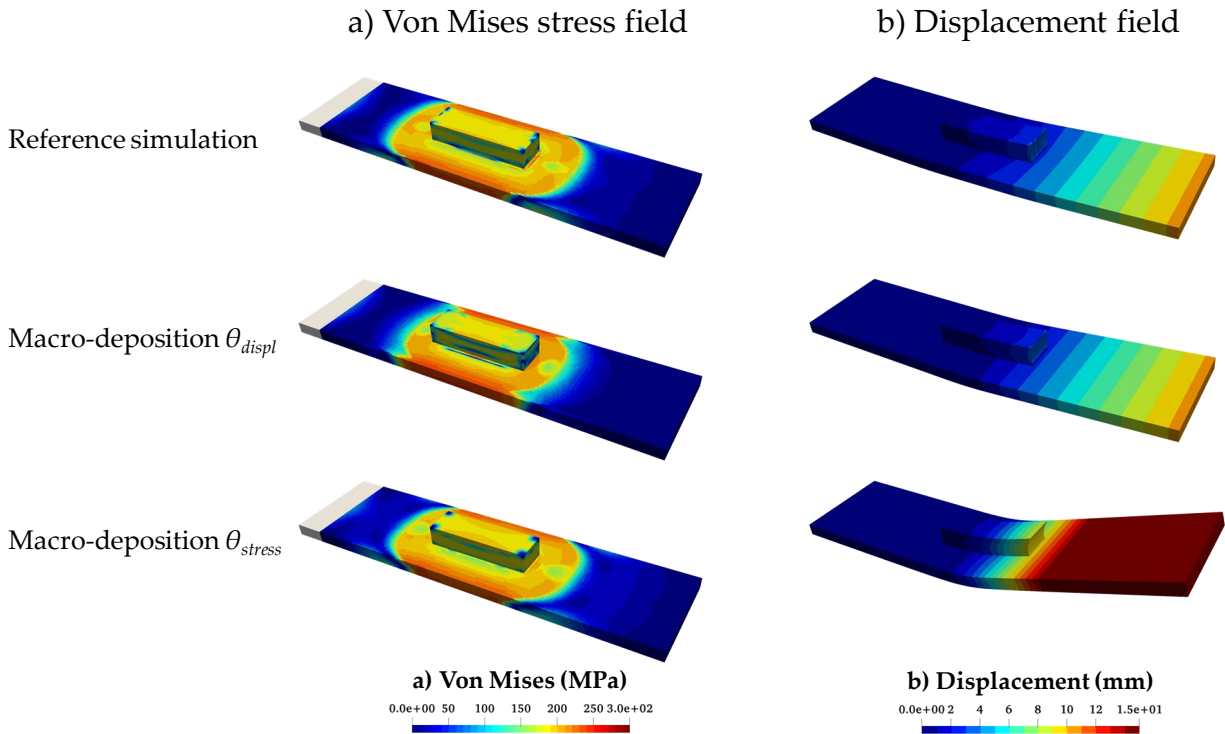


Figure 6.16 – 4th test case results of the reference and macro-deposition simulations for the optimal displacement and stress configurations θ_{displ} and θ_{stress} : a) Von Mises stress field, b) Displacement field.

6.3.7 5th case study: Kaplan blade representative bloc using TIG process

The 5th test case selected is a real component: a Kaplan blade, which is a component of interest to EDF in the hydraulic domain. For this case, the same welding process parameters as in studies 1, 3, and 4 are used with the exception of the wire feed speed ($v_{wire} = 1.5 \text{ m min}^{-1}$). The bead shapes are therefore different due to the change in the wire speed, but also due to the deposition pattern of the blade, with a spacing between the beads different than for the other studies (4.0 mm for the previous studies vs 3.5mm for the blade).

Given the computational cost of the reference simulations, this study is performed only on 8 layers. Each layer is composed of 54 beads, as shown in Figure 6.17-a. The deposition pattern of the blade is simplified, in order to have macro-deposits of similar lengths for the study as represented in Figure 6.17-b. It takes about 32 days to perform the baseline thermo-mechanical simulation.

The optimal configuration identified for the stresses is ($f_{l_d} = 1.0, f_{t_d}^{heat} = 0.0061$) (Figure 6.18), which is associated with an error of 5.45% and a reduction in computation time of 96.8% (about 1 day). Again, this highlights the fact that a good estimation of the stresses is possible for very short heat input times.

For the displacements, the optimal parameter set identified is ($f_{l_d} = 1.0, f_{t_d}^{heat} = 0.095$) (Figure 6.19). The denormalized equivalent of the heat input is $t_d^{heat} = 31.6 \text{ s}$ (Table 6.7), which is surprisingly similar to those found for the 1st, 3rd and 4th study cases. This test, again, leads to the conclusion that for a given combination of welding process parameters, an optimal configuration for the macro-

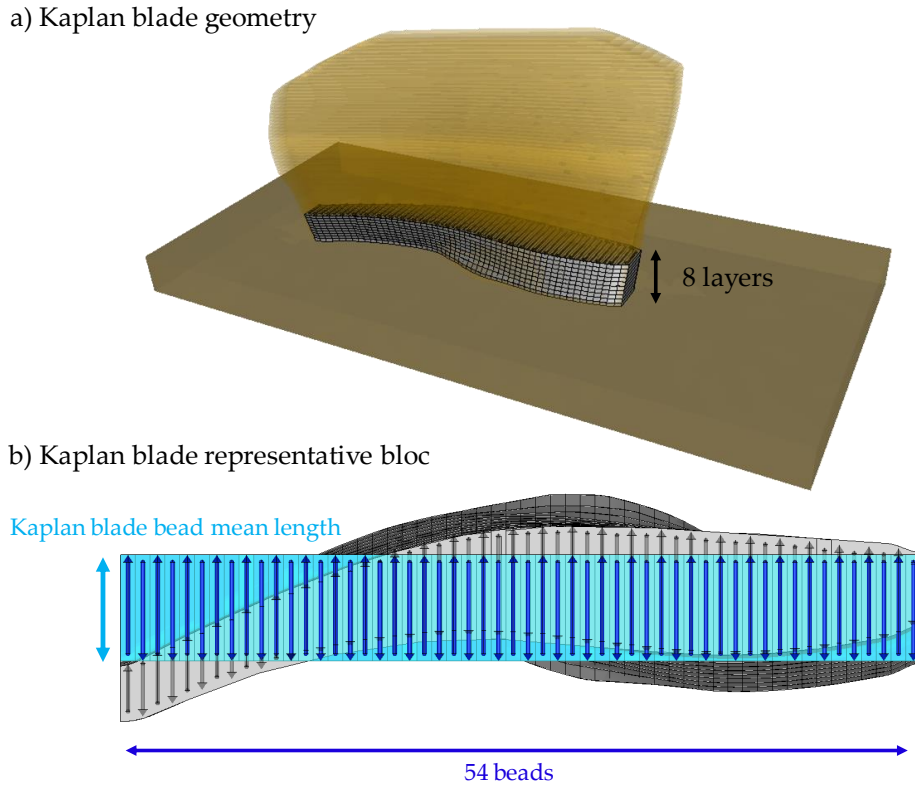


Figure 6.17 – The Kaplan blade geometry and the representative bloc: a) In orange the full Kaplan blade and in gray the 8 first layers, b) In gray the 8th layer deposition pattern and in blue the simplified deposition pattern for the 5th test case.

deposition method can be identified, even for a more complex geometry of the part.

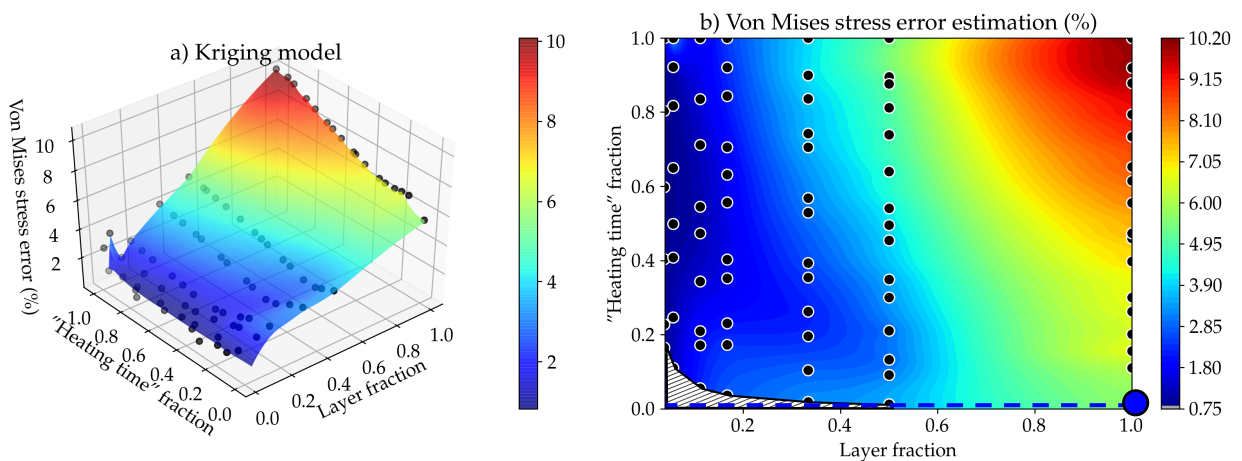


Figure 6.18 – Macro-deposition stress prediction for the 5th case study: a) 3D stress error response surface, b) Response surface of the stress error.

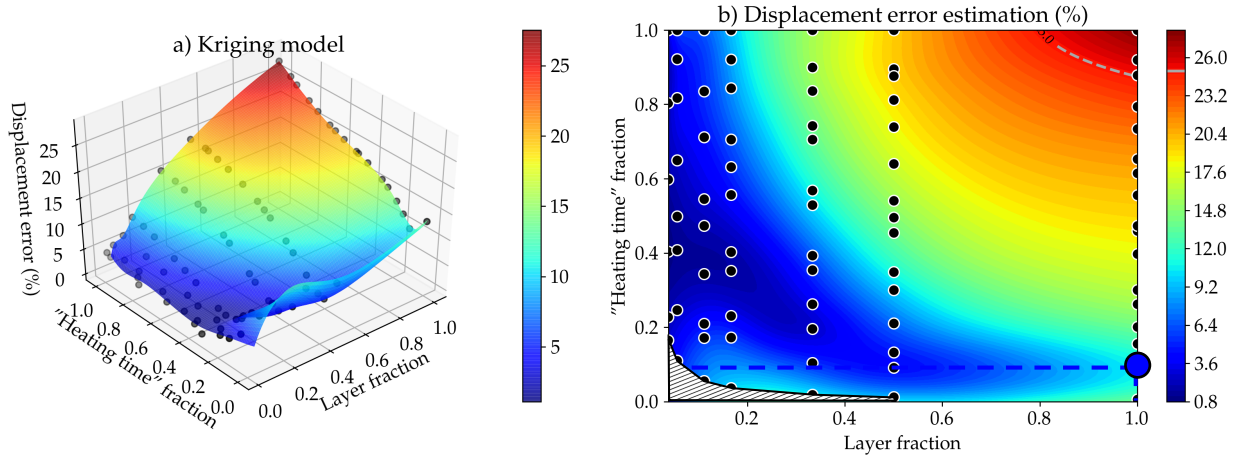


Figure 6.19 – Macro-deposition displacement prediction for the 5th case study: a) 3D displacement error response surface, b) Response surface of the displacement error.

Table 6.7 – Macro-deposition calibration results summary for the 5th case study.

Configuration	f_{l_d} (fraction)	$f_{t_d^{heat}}$ (fraction)	l_d (mm)	t_d^{heat} (s)
Displacement	1.0	0.095	1107	31.6
Stress	1.0	0.0061	1107	2.04

6.3.8 Conclusion on the five study cases

The five study cases have highlighted several important points.

- First, these studies have proven the existence of optimal configurations for the implementation of the macro-deposition method to predict either stresses or displacements. The optimal parameter sets to reduce the computational times identified for a given tolerance are always with a layer fraction at 100% (layer-by-layer deposition). Moreover, the optimal parameter sets determined for stresses and displacements do not coincide, except for the 2nd study case using the CMT process.
- The optimal configurations for stress predictions are always found to correspond to very short heat input durations t_d^{heat} around 2.0 s for the TIG study cases and 0.5 s for the CMT test case. These values correspond to the time during which each node of the part is subjected to the heat source in the "reference" simulations. This feature can be explained by the fact that it is necessary to reach the high temperatures typical of the WAAM and welding processes for a good stress prediction.
- For the displacement predictions, except for the 2nd study case using the CMT process, a more distributed heat input than that for stress is preferred. A trend seems to appear for the cases with similar process parameters (here TIG), even though the trajectories, number of layers, or layer lengths are different (cases 1, 3, and 4). Indeed, the optimal absolute values obtained for the heat input are very close when considering the denormalized parameters: $t_d^{heat1} = 40.8s$, $t_d^{heat3} = 32.3s$, $t_d^{heat4} = 40.2s$. Nevertheless, establishing a global behavior of the optimal parameter sets for displacement predictions using other process parameters requires further investigation.

- Indeed, for the 2nd study case, the optimal configurations for stress and displacement coincide. A very short heat input is found necessary to have a good prediction for both the stresses and the displacements. This can possibly be due to the fact that for the CMT parameterization considered, the linear welding energy is 2 to 3 times lower than for the TIG parameterization used which means that the total heat input is consequently less important.
- Moreover, for all the study cases considered, a layer-by-layer input with a total distribution of heat input time is the worst configuration for stresses and displacements. Therefore, selecting a fraction of the heat input is crucial for a layer-by-layer approach.

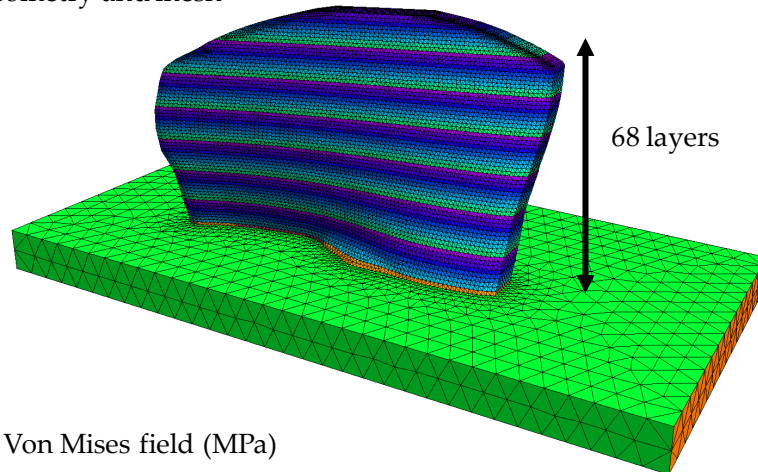
To conclude on these five study cases, the macro-deposition method is very satisfactory since it allows having precise estimates of the stresses or displacements with a reduction of the calculation time up to 95%. However, unlike for stress fields estimation, it is necessary to carry out a parametric study beforehand to know which modeling parameter to use for the macro-deposition if an estimation of displacements is desired.

6.3.9 Perspectives and possible applications for macro-deposition

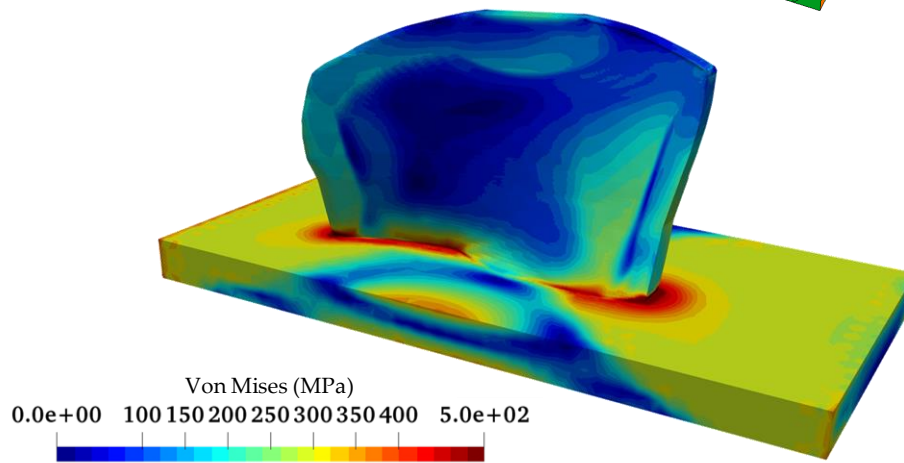
Figures 6.20 and 6.21 show calculations performed by macro-deposition on real parts. In Figure 6.20 is presented the macro-deposition simulation performed on a whole Kaplan Blade. The part has been performed at EDF using the TIG process and the process parameters of test cases 1, 3, 4, and 5. The simulation is performed layer by layer with the parameter sets previously identified for stress prediction: layer per layer and $t_d^{heat} = 40.0s$ approximately. Such a simulation in mesoscopic thermo-mechanics is not currently possible due to its computational cost. However, the macro-deposition simulation is performed in one week, which is quite reasonable.

The second example is the 1:5 scale PPB clamped in its center presented in Figure 6.21. This test was performed using the CMT process. To carry out this simulation, the parameters used for the macro-deposition simulation are those identified in the 2nd case study, and the deposition is performed layer by layer. A first and qualitative finding is that, although only 10 of the 20 layers are simulated, the displacements found for the base plate are about 15 mm (leading to little or no evolution for the other layers due to the displacement of the base plate, and the distance between the layers and the base plate), while experimentally the displacement observed is about 14-15 mm. Although this study needs a much more detailed and in-depth validation, the first results seem very promising and pave the way to the simulation of larger and much more complex parts.

a) Kaplan blade geometry and mesh



b) Residual stress: Von Mises field (MPa)



c) Experimental test



Figure 6.20 – Kaplan blade macro-deposition simulation: a) Kaplan blade mesh with the 68 layers, b) Von Mises residual stress field after cooling to ambient temperature.

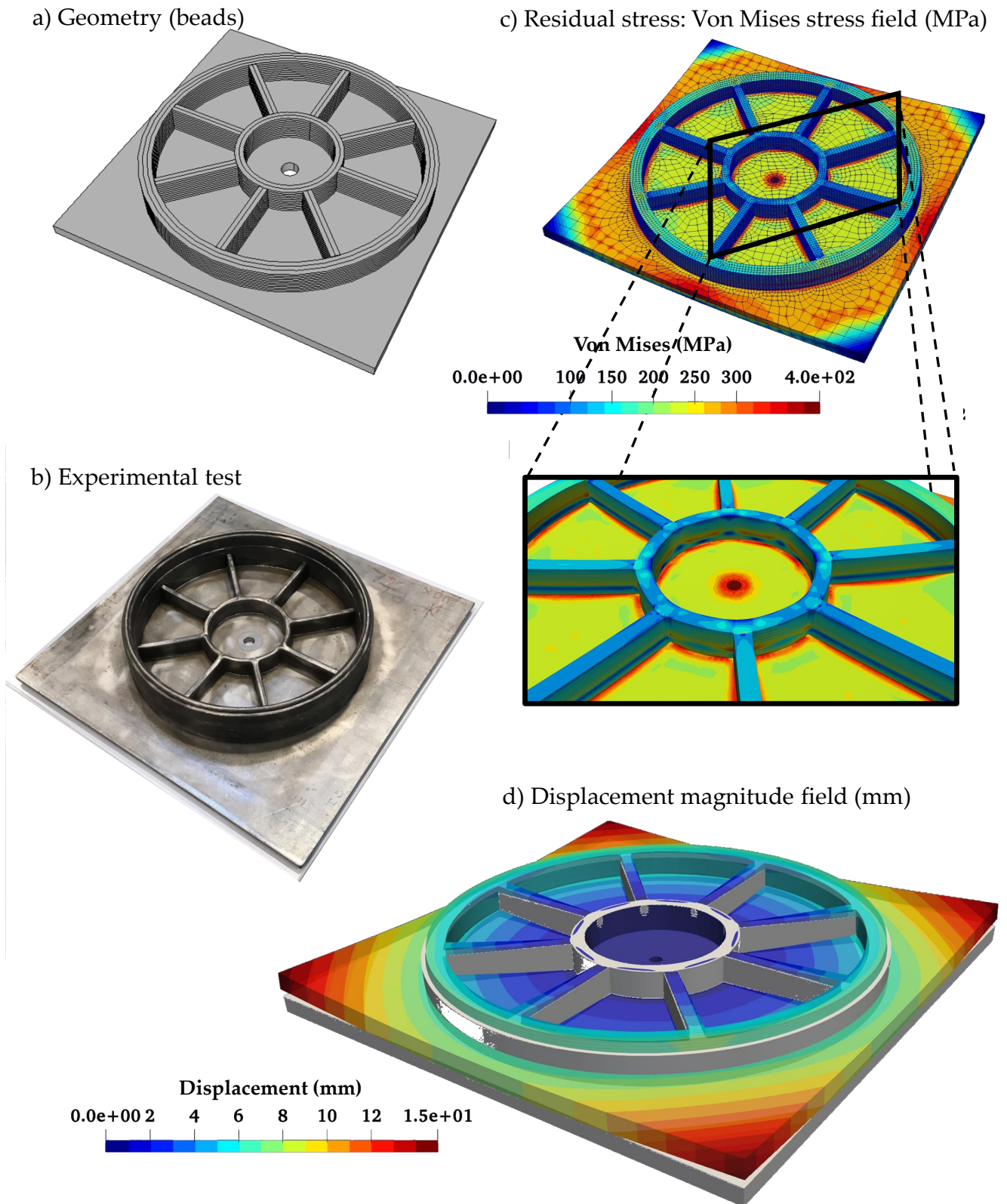


Figure 6.21 – PPB macro-deposition simulation: a) Geometry of the 10 first layer of the PPB, b) Experimental test, c) Von Mises residual stress field, d) Magnitude displacement field.

6.4 Mixed approach: macro-deposition with "local meso-resolution"

6.4.1 Overview of the "local meso-resolution" approach

The previous section highlights the relevance of the macro-deposition method. Although this method seems to be suitable to predict the global behavior of the component, the local accuracy of the component behavior is however not ensured.

In this section, an alternative approach is proposed, based on a combination of the macro-deposition method and the structural zoom. The general idea behind the structural zoom is the following (see Chapter 2 for more details). In the zone of interest of the mesh, the simulation is carried out in a "fine" way by using the standard thermo-mechanical model with a progressive deposition of the material and an equivalent thermal source. In the other zones, the macro-deposition approach layer by layer is used.

6.4.2 Application to the 5th case study

To illustrate and present the results obtained using this method, the 5th case study is selected (Kaplan blade). This case contains 54 beads per layer and 8 layers, which corresponds to 432 beads in total. The middle 12 beads for each layer are considered to be the beads of interest, as shown in Figure 6.22. On the other parts of the block, each layer is deposited at once. For the macro-deposition, the optimal parameters found in Section 6.3.7 are used.

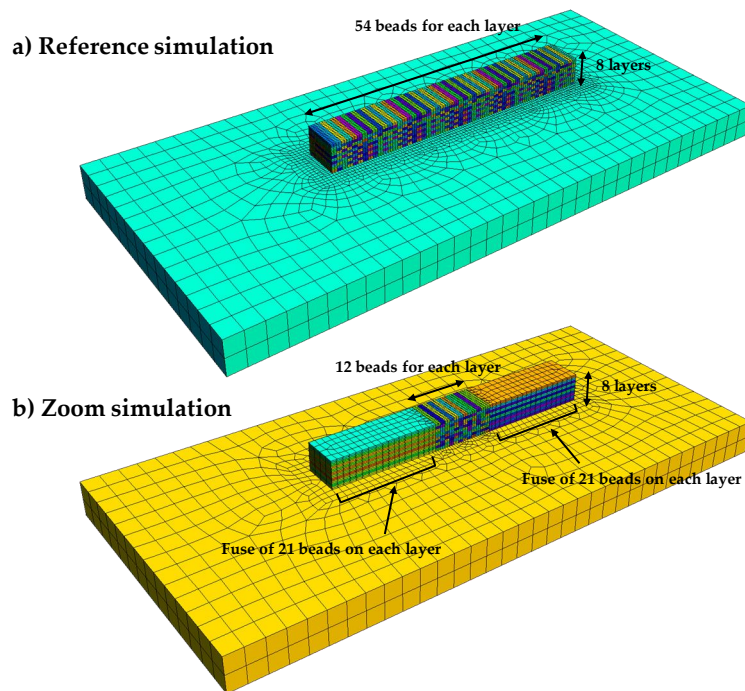
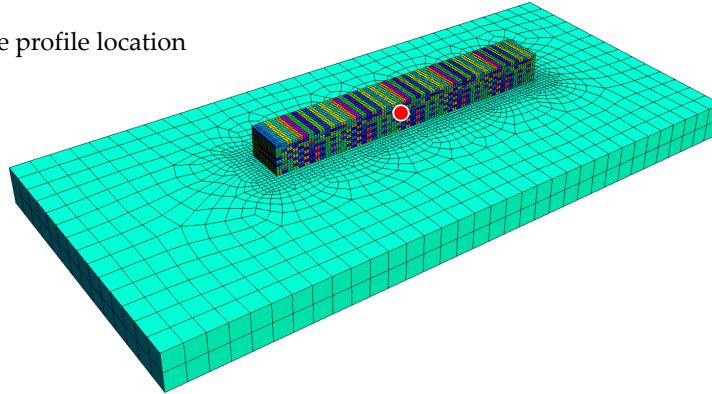


Figure 6.22 – Illustration of the mixed approach macro-deposition / local zoom for the block of the 5th study case: a) reference configuration, b) configuration with macro-deposition and full thermo-mechanical simulation on 12 beads of each layer in the middle of the block.

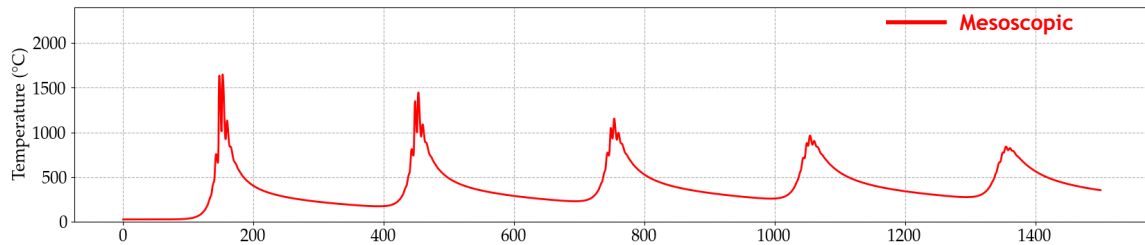
As shown in Figure 6.23, the local fine simulation allows for an accurate thermal simulation. This implies that, although the modeling and the heat input are simplified on the other zones, very good

thermal field estimates are obtained. Therefore, it is possible to perform detailed studies on the zone of interest: thermal gradients, cooling rate, numerical macrography, metallurgical calculations, residual stresses, or the evolution of the hardening.

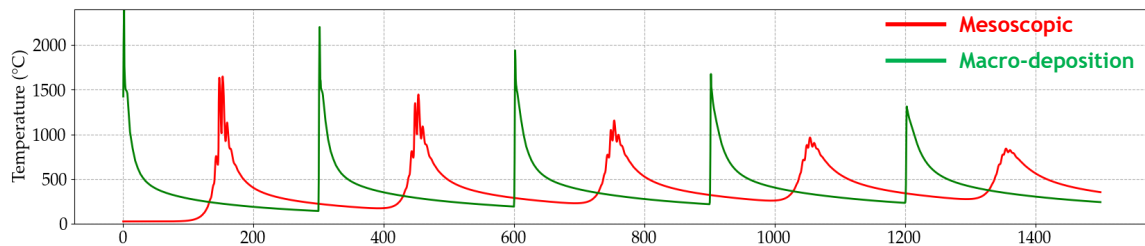
a) Mesh and temperature profile location



b) Temperature profile using the mesoscopic model



c) Temperature profile using the macroscopic model



d) Temperature profile using the local meso-resolution model

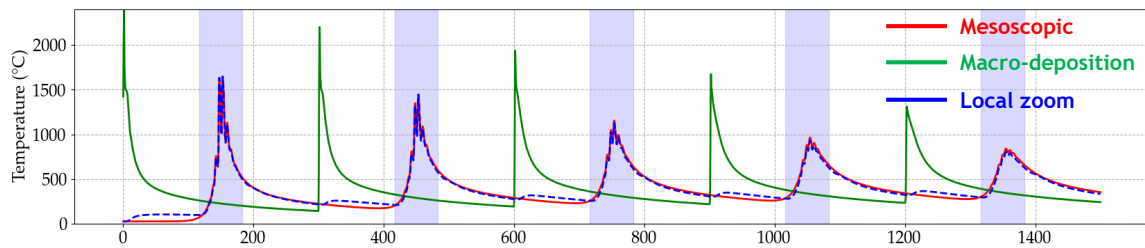
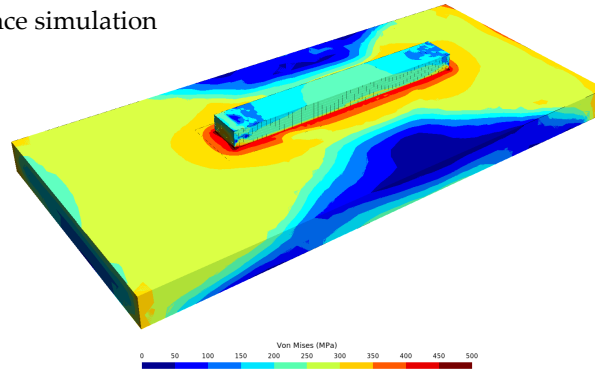


Figure 6.23 – 5th Case study: Evolution of the temperature profile at the same location: a) Mesh and in red the point location, b) Mesoscopic approach in red, c) Macro-deposition approach in green, d) Local meso-resolution approach in blue, with the zones highlighted in blue correspond to the mesoscopic local focus.

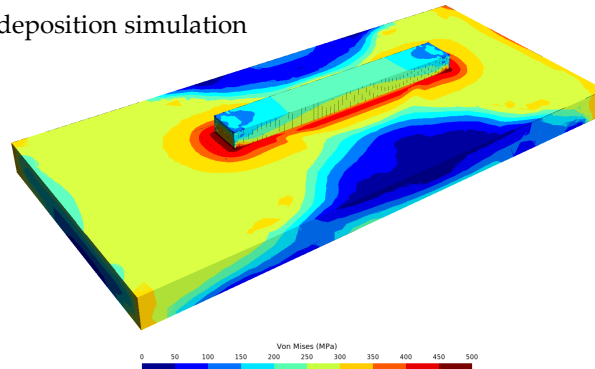
In Figure 6.24, the equivalent Von-Mises stress fields for the reference simulation and the simulation with the local zoom are shown. The results seem very satisfactory, with an average relative error of about 2.5%, and an absolute error of about 8 MPa over the whole domain (block and base plate). On

the block part, the average relative error is about 5.5%, and an absolute error of about 14.7 MPa is found. From a general point of view, there does not seem to be any problematic discontinuity in the stresses. Moreover, the gain in computational time is of 87.5% (from 32 days to 4 days).

a) Reference simulation



b) Macro deposition simulation



c) Zoom simulation

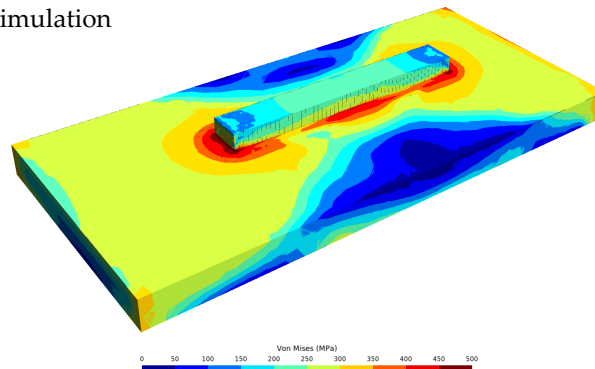


Figure 6.24 – 5th Case study: Von-Mises equivalent stress field: a) Reference thermo-mechanical simulation, b) Macro-deposition, c) Macro-deposition and local meso-resolution.

In conclusion, the combined method of macro-deposition and structural zoom seems to provide a very good prediction of the stresses for a significant gain in computation time, and thus opens the way towards simulations with large and complex parts.

6.5 Conclusion & perspectives

In this section, the macro-deposition method is explored. A study is carried out to investigate and find the optimal values of the two parameters of the method: the layer fraction brought f_{ld} , and the heating time fraction contribution $f_{t^{heat}}$. The 5 test cases have revealed several aspects. First of all, the optimal parameter sets for stress and displacement prediction are not similar. Moreover, the preliminary tests presented show that for a given process parameter set (U, I, v_t) , the optimal parameters identified are transposable to other test configurations (deposition pattern or part geometry).

For the prediction of the stress field, a layer-by-layer configuration with a very short heat input fraction is to be favored. This is most certainly due to the fact that it is necessary to have temperatures representative of the welding operations to get adequate residual stresses. For the displacements, it appears that a heat input over a longer duration is more suitable. Nevertheless, a deeper understanding of such a phenomenon requires further studies. For instance, it would be interesting to explore more the process parameter range to validate or not the hypothesis that an optimal configuration for the displacements can be identified for a given process parameter set, and thus transposable to other more complex geometrical and path configurations with the same process parameter set.

The macro-deposition method has thus proven to be successful at reducing computational times while maintaining accurate predictions of target mechanical quantities (displacements or stresses), opening the way to the simulation of usually very high computational cost configurations (large and/or complex parts) in reasonable times with good precision.

A perspective of the method would be to improve the heat input. Rather than using a uniform heat input, another method, which seems very efficient, is to apply a thermal source with a distribution that corresponds to the integral of the distribution of the equivalent thermal source used in the reference models. This integral is made according to the fabrication path of the "macro-deposited" beads. This integration of the Goldak can for example, be defined for 2 points along x-axis such as:

$$\begin{aligned}
 q_{ld}(x, y, z) &= \int_{x_0}^{x_1} q(x, y, z) dx \\
 &= \frac{3\eta UI}{|x_1 - x_0|bc\pi} \exp\left(\frac{-3y^2}{b^2} + \frac{-3z^2}{c^2}\right) \left(\operatorname{erf}\left(\frac{\sqrt{3}(x - x_1)}{a}\right) - \operatorname{erf}\left(\frac{\sqrt{3}(x - x_0)}{a}\right) \right). \quad (6.9)
 \end{aligned}$$

For a more complex torch path, the integral along the whole path can be computed as the sum of the integrals for each fragment of the deposition pattern. This approach is relevant for a good distribution of the heat input.

The combined method of macro-deposition and structural zoom has been applied to the 5th test case and seems to provide a very good prediction of the stresses for a significant gain in computation time, thus opening the way to several very promising perspectives. First, the "local meso-resolution" method can be used to calibrate the macro-deposition method on more complex configurations. Indeed, if a test requires a prior calibration of the macro-deposition parameters on a specific configuration, a "local meso-resolution" can be used as a reference calculation. An iterative optimization can thus be considered: (1) Perform the "local meso-resolution" with a parameter set for the macro-deposits chosen arbitrarily thanks to the a priori knowledge, (2) Find the optimal parameter set thanks to

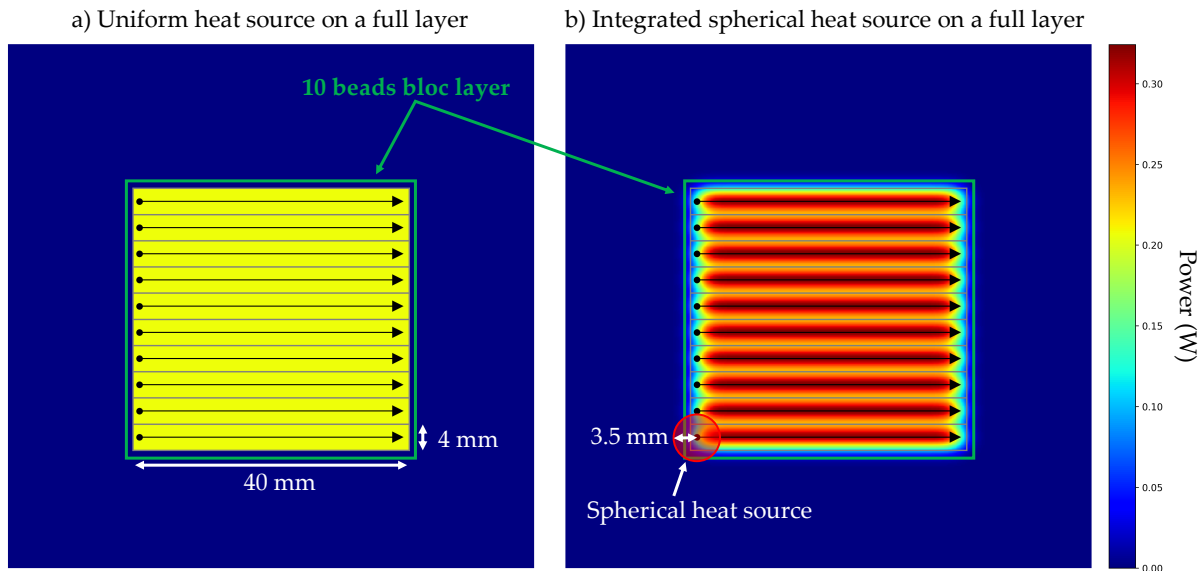


Figure 6.25 – Goldak integration along welding torch path: a) Uniform heat source on a full layer, b) Integrated spherical heat source on a full layer.

the focus zone, (3) Adapt the macro-deposit parameters to the boundary conditions and repeat the simulation. These steps can be performed a few times until the value of the optimal macro-deposition parameter set is reached. The second possibility offered by the "local meso-resolution" is to study precisely sensitive areas, either identified by expertise, experiments, or macro-deposition simulations. After the identification of these sensitive areas, a customized study can be considered without having to simulate the entire part. This would allow studying with precision the evolution of the hardening, to predict the hardness, or even to achieve local metallurgical calculations in specific zone of very large parts.

6.6 In a nutshell

Macro-deposition method & "local meso-resolution" method

- Implementation and evaluation of the macro-deposition method.
- Calibration of the macro-deposition on multiple study cases.
- For stress fields prediction: very short heat input time t_d^{heat} , corresponding to the duration needed for the torch to cover the Goldak heat source length $2 \times a_f$.
- For displacement fields prediction: a general trend appears given a process parameter set. More investigation is needed to come to a more definite conclusion.
- For a defined synergy of process parameters, an optimum that can be transposed to other tests seems to be identified.
- New method proposed: mesoscopic simulation on a "local meso-resolution", coupled with macro-deposition on the other areas of the part:
 - Reference mesoscopic thermo-mechanical simulation on a specific zone of the part,
 - Use of macro-deposition to have relevant thermo-mechanical boundary conditions.

Chapter 7

Data-driven inherent strain prediction

Contents

7.1	Introduction	194
7.2	Inherent strain field calibration step	195
7.2.1	Problem description	195
7.2.2	Inherent strain field results	196
7.3	Inherent strain prediction by Deep Learning	200
7.3.1	Introduction	200
7.3.2	MultiLayer Perceptron (MLP) using prior feature extraction: Isothermal values	201
7.3.3	Full temperature profiles: Convolutional Neural Network (CNN)	204
7.3.4	Full temperature profiles: Recurrent Neural Network (RNN)	205
7.3.5	Discussion on the use of Deep Learning to investigate inherent strains	207
7.4	Conclusion & perspectives	208
7.4.1	Conclusion	208
7.4.2	Perspectives: residual stress prediction by inherent strain	209
7.5	In a nutshell	210

7.1 Introduction

In order to better control the surface finish and to have a suitable part shape, several studies in the literature investigate the shape of the beads. For example, in the study of Jiang et al. [102], the workpiece morphology is investigated for different linear energy. In their study, thermal simulations are also performed in order to understand the interaction between the temperature field and the workpiece morphology. Other studies [45, 193] showed that the geometry of the beads evolves during the WAAM manufacturing process, mainly due to the fluid phenomena that occur during manufacture (fluid flows in the molten pool, for example). Therefore, in order to control the shape of the WAAM manufactured parts and ensure their morphological integrity for possible machining after manufacturing, it is essential to be able to predict the shape of the parts after manufacturing. Figure 7.1 illustrates a practical example. In blue is shown the geometry of a blade built from the manufacturing path (using the tools developed in Section 3.2), and in grey is represented the 3D scan of a manufactured blade. On the edges of the blade, a difference in the shapes is observed.

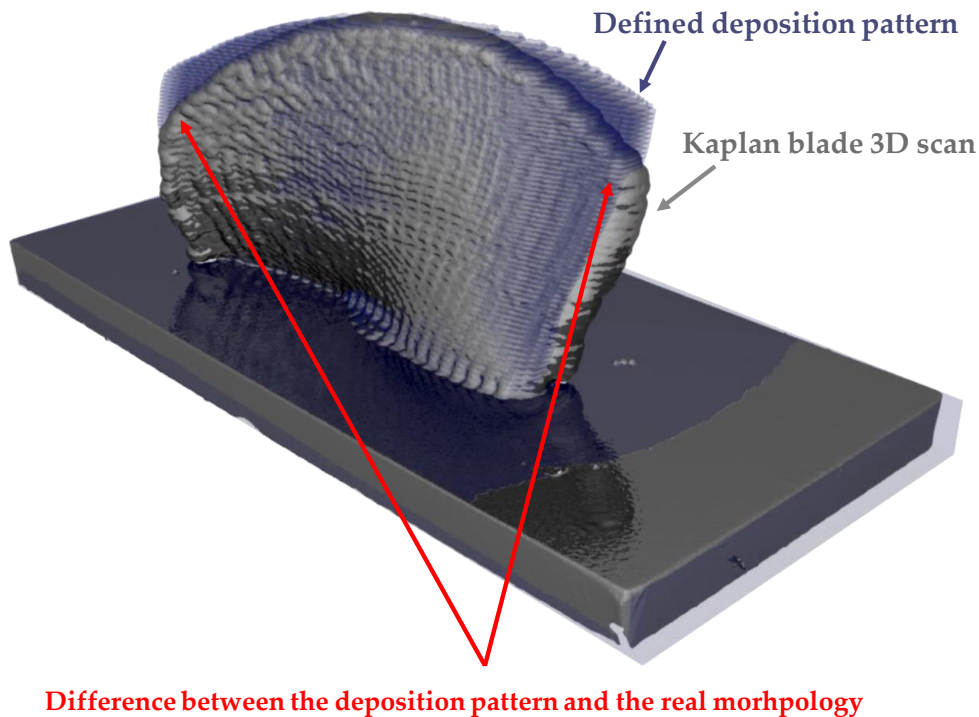


Figure 7.1 – Comparison of the "ideal" geometry of the Kaplan blade resulting from the manufacturing paths and the 3D scan of the Kaplan blade after manufacturing.

This type of defect can also be observed on the two walls presented in Section 5.3, that are manufactured in the same conditions and using the same parameters but have two different shapes. This highlights the existence of other physical mechanisms that are not taken into account in the simulations performed (multi-scale and multi-physics aspects). Indeed, to be able to simulate the manufacturing of large components, the simulations within the framework of this PhD thesis are carried out at a mesoscopic or macroscopic scale, and the phenomena present in the electric arc, molten pool, and material input are thus not modeled. As a consequence, the shape of the beads is not predicted by the

simulation but is defined beforehand during the construction of the mesh of the studied part.

Therefore, a feature must be added to the current thermo-mechanical model to be able to accurately predict the deformations of the parts in order to guarantee the morphological integrity of the parts while preserving reasonable computational times.

The objective of this section is therefore to implement a model allowing for the prediction of the inherent strain field, and thus of the residual shape of the part produced. This study will focus on the two "similar" tests presented above. The model developed in this section is constructed using 3D scans of experimentally manufactured parts and has as final objective the prediction of the deformation field based on the temperature field obtained by mesoscopic thermal simulation. Indeed, the assumption is made here that the deformation depends only on the temperature.

This study is divided into two parts that aim to:

- **Set up a mathematical model to estimate an inherent strain field** that allows the transition from the initial mesh (used for the mesoscopic simulation) to the 3D scan.
- **Develop robust data assimilation algorithms to predict the inherent strain field** from the temperature field obtained using thermal mesoscopic simulation.

These algorithms are developed on python, using the open-source differential equation solving environment *Fenics* [194]. All the work and predictions in this study are also made to be easily transferable to Code_Aster. The work presented in this chapter and in Appendix G was conducted by Nicolas Pistenon within the framework of an internship involving EDF, the *Centre des Matériaux des Mines Paristech*, and the AFH consortium.

7.2 Inherent strain field calibration step

7.2.1 Problem description

As stated previously, the first objective is to succeed in making the link between the numerical mesh and the two 3D scans of the WAAM manufactured walls selected for this study. Therefore, this first part focuses on setting up a calibration algorithm between the 3D scan and the mesh. This means that the mesh must be deformed to match the 3D scan. This calibration has thus three constraints:

- **A good reconstruction of the object:** The mesh must fit the 3D scan as well as possible. Therefore, it is necessary to define the distance between the two objects: the mesh and the 3D scan. It is also necessary to choose the degree of precision of the fit. Indeed, one must avoid capturing the measurement errors of the 3D scan. Moreover, the surface roughness of the manufactured parts is not always relevant to take into account,
- **A good quality of the deformed mesh after calibration:** Indeed, having a good mesh quality is very important during finite element simulations in order to have accurate simulations, good stability of the solutions, as well as a good convergence of the calculations,
- **A realistic deformation field:** The strain field identified must be able to be explained physically a posteriori. In particular, too large discontinuities between two adjacent mesh elements must be avoided.

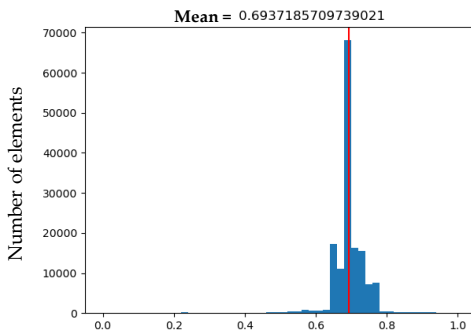
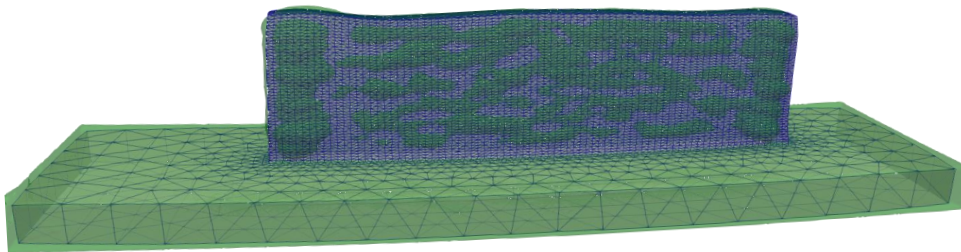
The calibration algorithm implemented to fit a mesh on a 3D scan is briefly presented in the following. A more detailed description can be found in Appendix G. The objective is to deform an initial point cloud (the mesh), also called *template*, towards a *target* point cloud (the 3D scan). The general idea of the developed algorithm is to start by having a very stiff mesh, and then by decreasing the stiffness of the mesh to approximate as well as possible the local deformations. Moreover, a term is used to penalize the distance between the *template* and the *target*, based on the two-by-two association of the points of the two objects. The problem is approached by considering local associations of points. This is done by searching for the closest points in the *target* for each point of the *template* in order to approach the "true" solution of the problem.

This algorithm is built to extract the inherent strain field to be applied on the mesh to obtain the real geometry, which in the case of this section, is the 3D scan of the part. The extracted inherent strain field will be the basis of the next section and will allow the construction of a prediction model of the inherent strain based on the thermal history of the part.

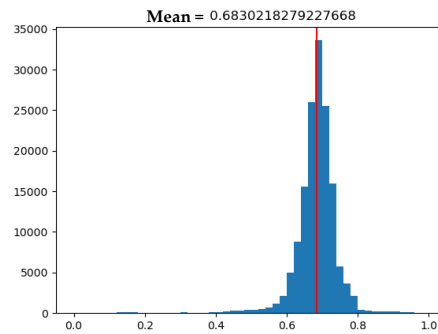
7.2.2 Inherent strain field results

Figures 7.2 and 7.3 present the deformed meshes for the "Zigzag" and "Raster" walls using the calibration algorithm presented in the previous section and in A.1 with an accuracy of 0.25 mm. Figures 7.2 and 7.3 also confront the associated quality of the meshes after the calibration step with the initial mesh quality for both tests. The histograms show that there is no significant degradation of the quality.

a) Deformed mesh obtained for the « Zigzag » wall



b) Quality of the initial mesh



c) Quality of the deformed mesh

Figure 7.2 – a) Deformed mesh obtained for the "Zigzag" wall using the calibration algorithm, b) Quality of the initial mesh, c) "Zigzag" wall mesh quality evolution.

a) Deformed mesh obtained for the « Raster » wall

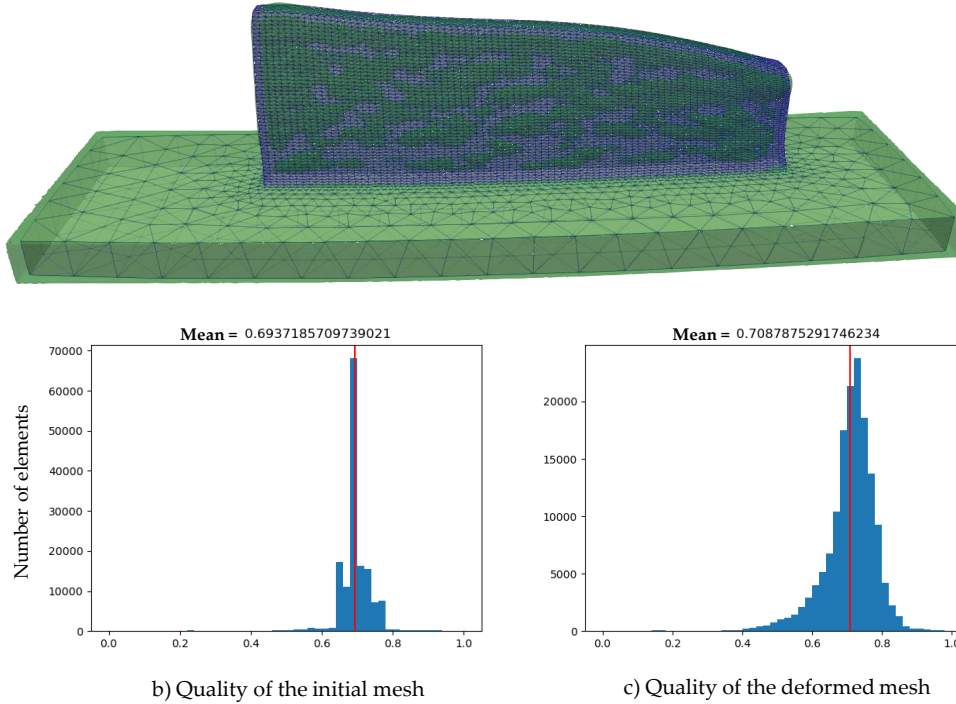


Figure 7.3 – a) Deformed mesh obtained for the "Raster" wall using the calibration algorithm, b) Quality of the initial mesh, c) "Raster" wall mesh quality evolution.

Figures 7.4-a and 7.4-b show the resulting pre-deformation field for the "Zigzag" wall and "Raster" wall, respectively. For the "Raster", the collapse observed on the 3D scan is reflected by a compression of the elements of the right edge and an expansion of the left edge of the wall (ε_{zz}^*). Moreover, the strain tensor component ε_{xx}^* highlights the surface roughness of the structure resulting from the manufacturing process. The "Zigzag" is quite different compared to the "Raster" case. First, the deformation amplitudes along the z -axis are much lower, revealing less pronounced subsidence. Moreover, concerning the strain field components ε_{yy}^* and ε_{zz}^* , a symmetrical behavior of the fields between the left and the right is observed, with respect to the (z, x) plane and passing through the center of the structure along the y axis (Figure 7.4-b). This can be associated with the wall construction strategy, which also follows this symmetry pattern.

The inherent strain fields of the two experiments are thus estimated. Before proceeding to the construction of a model from these inherent strains, the possible origins of such a difference in shapes of the two workpieces are investigated in the following.

During the WAAM manufacturing process, several types of defects can be generated. The major groups of defects are the following: cracks which are caused by a high-stress state, cavities due to the aggregation of gas bubbles in the molten pool, solid particles of different nature generated from the filler material, volume defects located at the interfaces between the beads also referred to as lack of fusion and penetration, shape defects...

In the current case, the type of defects investigated are shape defects, also called geometrical

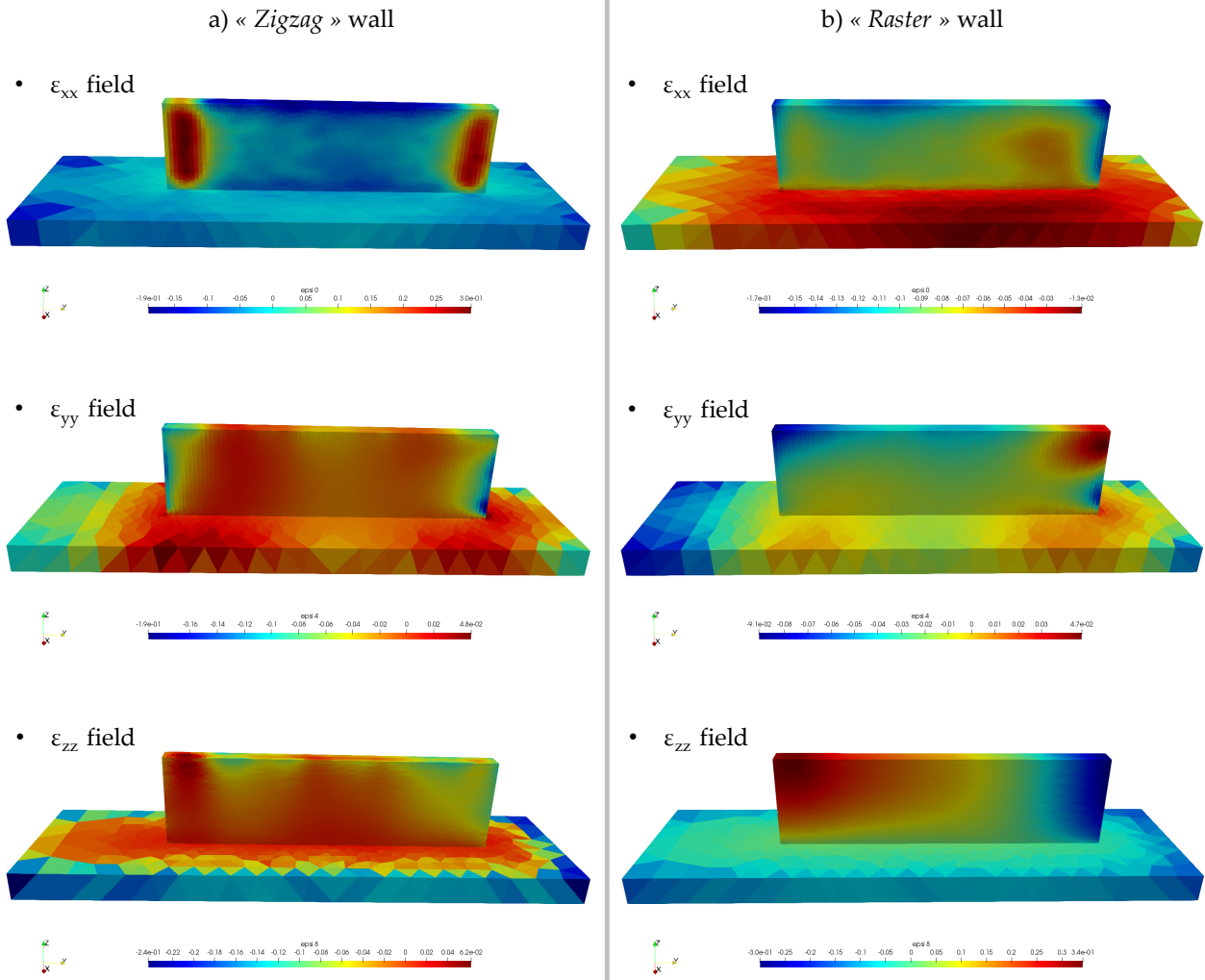


Figure 7.4 – Deformed mesh obtained for the "Zigzag" & "Raster" wall using the calibration algorithm.

defects. In addition to the deformations of mechanical origins of the solid (that can be obtained by the mesoscopic or macroscopic scale models), two mechanisms seem to come into play during the wall manufacturing to provide an explanation regarding the difference in shape between the "Raster" and "Zigzag" walls.

First, a pronounced correlation can be observed between the inter-layer temperature distribution (presented in Section 5.5) and the possible collapse of the wall. This can be explained by the fact that the beads sag progressively as the deposited material is added. Indeed, the base plate temperature is low at first, and the filler metal solidifies quickly and does not propagate. Gradually, the more heat the part accumulates, the larger the molten pool. Due to gravity, this causes the filler metal to flow and sag more easily. The collapse of the parts can even be observed in the case of an excess of heat due either to a too-significant energy contribution (unsuitable operating parameters) or to the accumulation of heat in the manufactured part. Figure 7.5 represents "inter-element" temperature fields, which is the average temperature of the neighbor nodes of a newly activated element. The fields show that for "Zigzag" (Figure 7.5-a), the elements on the ends of the wall are activated in alternate

layers on elements above the melting temperature ($> 1400\text{ }^{\circ}\text{C}$). For the "*Raster*" (Figure 7.5-b), the elements at the start of a new layer are activated on elements that have cooled down, and then on elements that are around $900\text{ }^{\circ}\text{C}$ (never on elements that have exceeded the melting temperature). What is interesting to highlight is that these fields are in accordance with the geometry of the walls after fabrication.

Moreover, looking a little closer at the "*Raster*" test, another mechanism seems to be involved: the convective movements within the molten pool. As shown in several studies [42], in the molten pool, the velocity field seems to highlight the backward projection of the metal. In a continuous test such as the "*Zigzag*" wall, when the direction of welding is reversed for each layer, the variation of the deposit height is filled from one layer to another. In the case of arc extinction tests such as the "*Raster*", it becomes significant, especially since it increases as the test progresses.

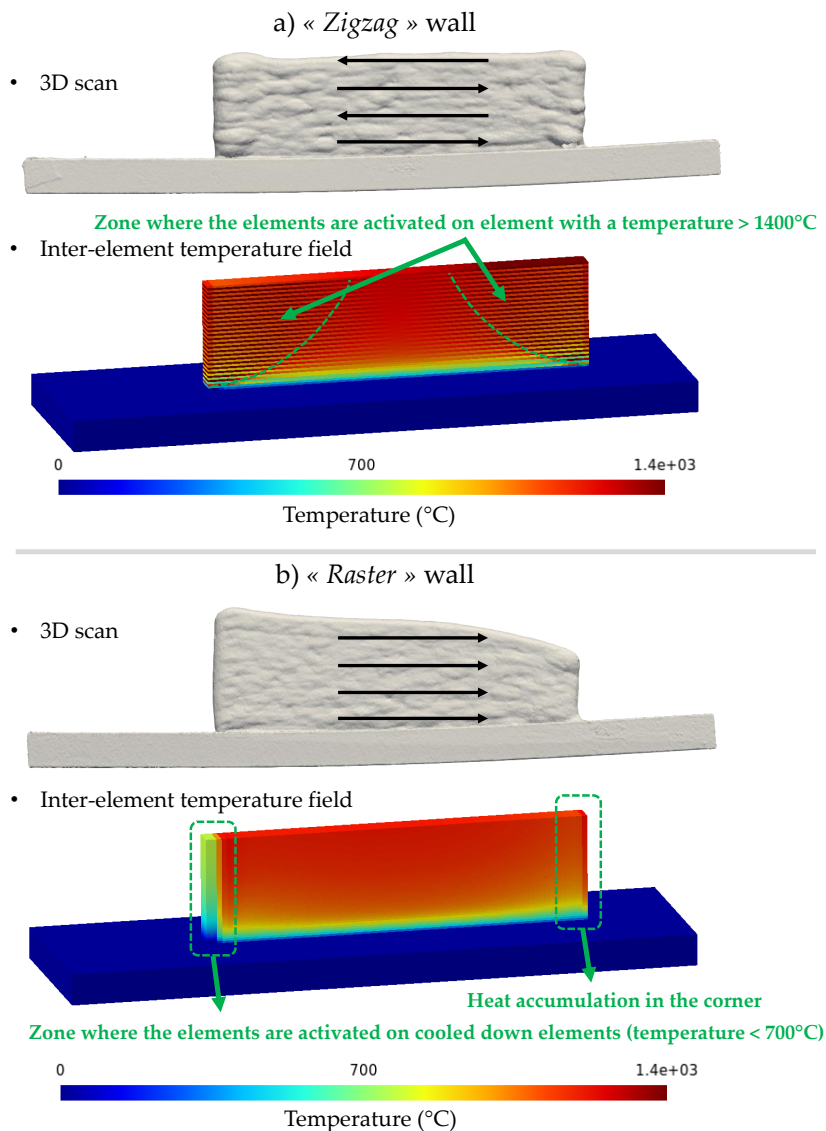


Figure 7.5 – Relationship between the inter-layer temperatures at each element activation and the resulting wall shape.

This discussion on the origin of the difference in shapes between the "*Raster*" and the "*Zigzag*" walls supports the relevance of the strategy considered in this chapter based on the assumption that the inherent strain field can be predicted from the thermal history of each node of the part.

7.3 Inherent strain prediction by Deep Learning

The objective of this section is to set up a model that predicts the inherent strain field in order to determine the shape of the part after manufacturing. In this section, the model is computed using Neural Networks. This model is intended to take into account all the physics that leads to the deformation of the part during the process. This section focuses mainly on the results obtained using the different Neural Networks investigated. A deeper description of Neural Networks can be found in Appendix H.

7.3.1 Introduction

For this study, the assumption is made that the geometrical deformations come from the thermal history of the part during the manufacturing process. Indeed, the "*Zigzag*" reaches much higher temperatures than the "*Raster*" as illustrated by Figure 7.6. This Figure shows the temperature evolution at a point of the wall for the two manufacturing strategies. The resulting "*Zigzag*" wall is more slumped. This can be explained by the fact that a metal with a low initial temperature quickly solidifies. However, the part accumulates heat during the manufacturing process, thus making the molten pool larger. The melted material in the molten pool flows more easily under the action of gravity. The model to be set up must thus take as input the temperature evolution of a point of the mesh to predict the deformation field at this point.

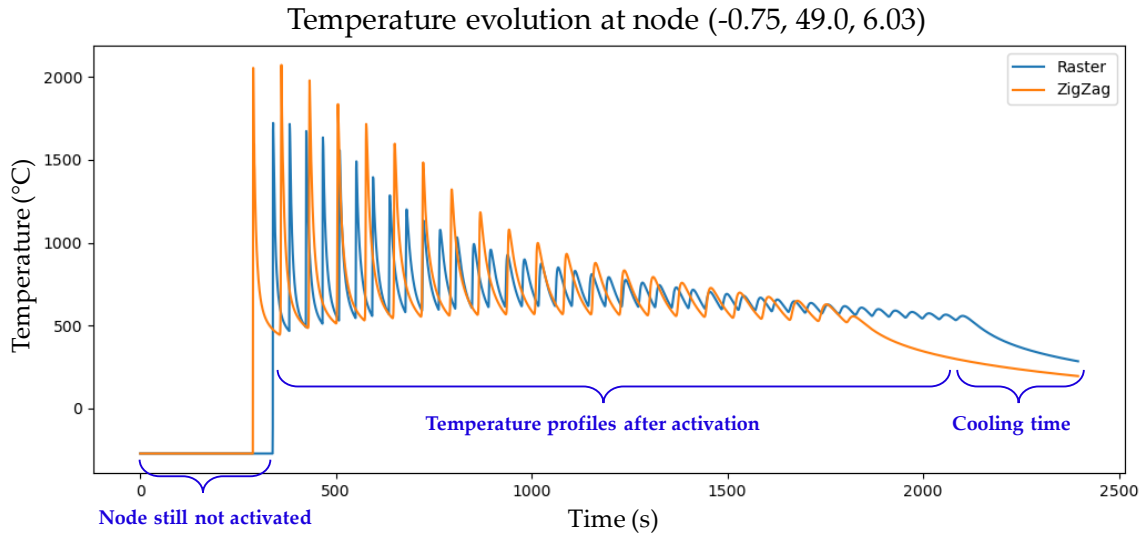


Figure 7.6 – Computed temperature profiles at the $(x = -0.75, y = 49.0, z = 6.03)$ coordinate point for the "*Raster*" and "*Zigzag*" walls.

In this section, different neural network models are presented to predict the deformation field from the temperature field during the manufacturing process. A deformation tensor has theoretically 9

components, among which 6 are different due to the symmetry of the tensor. However, in general, these deformations are almost equal to zero. Moreover, in the context of inherent strains, Buggati et al. [195] showed that only the three diagonal terms are the most important. Thus, in the models developed, for each node of the mesh, there are:

- as input, an evolution of the temperature with time,
- as output, three inherent strains components (pre-deformation) corresponding to ε_{xx}^* , ε_{yy}^* and ε_{zz}^* .

The input is thus composed of a series of thousands of values for each node of the mesh. Two approaches are presented in this section. The first one has as objective to synthesize in a few values the temperature curve. These values are then used as inputs to a neural network. The second one aims at using other neural architectures directly on the whole temperature curve.

For each model, different cases are studied. These study cases are essentially based on the definition of the training data. The training data is the set of data (temperature curves and deformation field values) that is used to build the model. The test data are not used in the training phase and are therefore values that the network had never seen before during the training. The study cases considered are:

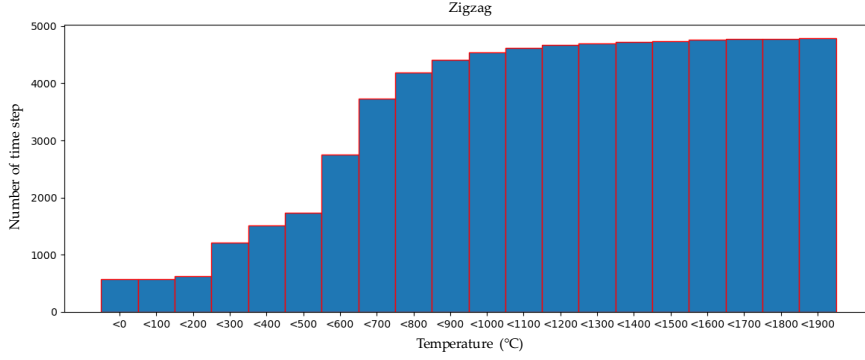
1. **1st study case - "Raster"**: using only the "Raster" in the training phase. In this case, about 8% of the test nodes are randomly selected for learning. There are two test sets: (i) the set of other nodes of the "Raster", and (ii) the set of all the nodes of the "Zigzag". The first set (i) allows studying the quality of the reproduction because the temperature profiles of the training set are very close to the curves of the test set. The second set (ii) allows studying the quality of the prediction on a different configuration. Indeed, it is interesting to study the results of the model learned from the "Raster" on the "Zigzag" data,
2. **2nd study case - "Zigzag"**: using only 8% of the test nodes of the "Zigzag" in the learning phase, for similar motives as for the previous point,
3. **3rd study case - "Raster" & "Zigzag"**: using both the "Raster" and the "Zigzag" in the learning phase. In this case, all the nodes are mixed, and 8% of all the nodes are considered for the training step.

7.3.2 MultiLayer Perceptron (MLP) using prior feature extraction: Isothermal values

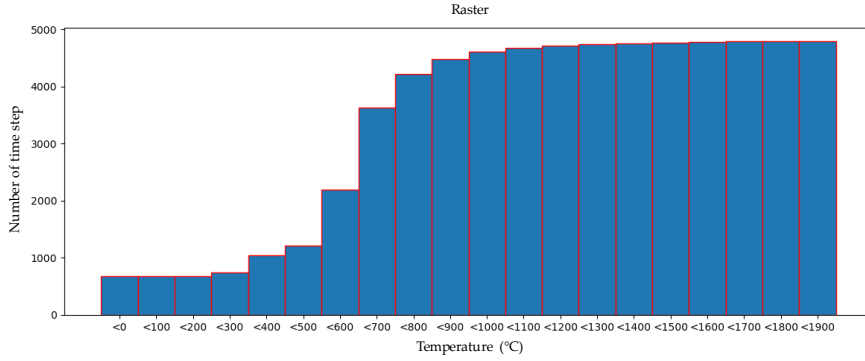
7.3.2.1 Model description

As mentioned earlier, the assumption that only the temperature influences the deformations is made. For the first model implemented, the thermal history of each point is simplified by 20 values: the time spent under isothermal temperature level.

In the following, the 2000th node, located at $(x = -0.75, y = 49., z = 6.03)$, is taken as example to investigate the temperature evolution in the "Raster" and "Zigzag" cases. The two histograms in Figure 7.7 represent the time spent under each threshold temperature for the two wall cases. The temperature profiles could thus all be synthesized into 20 values which are the inputs of the neural network. Several distributions of neurons are tested, but the selected one is: 3 layers with 140 neurons on each hidden layer (Appendix H.1).



(a) "Zigzag" wall - Histogram of the isothermal values at the 2000th node.



(b) "Raster" wall - Histogram of the isothermal values at the 2000th node.

Figure 7.7 – Histogram of the time spent under each temperature for node located at $(x = -0.75, y = 49., z = 6.03)$

7.3.2.2 Results

Table 7.1 presents the numerical results of the built models. For the 1st study case, the test set corresponds to the nodes of the "Raster" that are not in the training set. The same methodology is used for the 2nd study case with the "Zigzag" test. Two criteria are used to calculate errors of the models: the mean of the absolute differences between the theoretical and predicted values and the median of the relative errors between the theoretical and predicted values.

Table 7.1 – Numerical results of the deformation prediction using isothermal values model

Study	Train		Error					
	Mean abs.	Median rela.	Test		"Raster"		"Zigzag"	
			Mean abs.	Median rela.	Mean abs.	Median rela.	Mean abs.	Median rela.
1	$2.3e-3$	2.3%	$2.9e-3$	2.6%	$2.9e-3$	2.6%	$2.0e-1$	5.3e2%
2	$1.8e-3$	4.9%	$2.4e-3$	5.7%	$2.8e-1$	3.7e2%	$2.3e-3$	5.6%
3	$3.7e-3$	5.2%	$4.0e-3$	5.5%	$3.5e-3$	3.2%	$4.4e-3$	1.0e1%

Based on the results presented in Table 7.1, it can be concluded that the neural network implemented succeeded in approximating the training set with a reasonable accuracy evaluated at 10^{-3} .

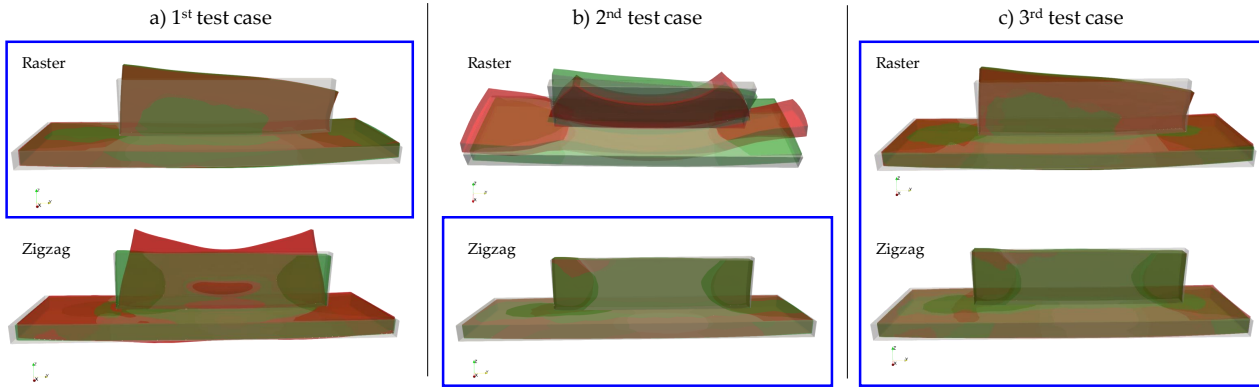


Figure 7.8 – Deformation with the isotherm model. In red: the predicted deformation, In green: the theoretical deformation, In grey: the initial mesh, In blue: the test used for training.

Indeed, as also shown by the median located between 2 and 5%, the average order of magnitude of the theoretical values for the *"Raster"* is $4.1 \cdot 10^{-2}$ and for the *"Zigzag"* $2.0 \cdot 10^{-2}$, which is thus 10 times higher than the precision obtained on the training set.

In the 1st study case, the accuracy obtained for the test set containing the rest of the nodes of the *"Raster"* is similar to that of the training set, which shows that a correlation between the temperature of the *"Raster"* and the deformation field has been identified. Figure 7.8-a compares the deformation obtained with the field predicted by the model in the first case of study. This corroborates the previous numerical results. However, as shown in Table 7.1, errors higher than the average error values are obtained for the *"Zigzag"* nodes, which is not acceptable. Moreover, the deformation results represented in Figure 7.8-a show that the model developed in the 1st study case is not generalizable to the *"Zigzag"* test. The deformations obtained do not respect the orders of magnitude of the expected deformations, as well as the collapsing trend for the wall. However, the wall base plate is well approximated, which shows that the correlation found in the *"Raster"* test for the base plate is also verified in the *"Zigzag"* test.

In the 2nd study case, the *"Zigzag"* as a whole is well predicted by this model, as shown in Figure 7.8-b. However, as in the 1st study case, the generalization to the *"Raster"* is poor, as shown in Figure 7.8-b. Moreover, a good approximation of the base plate is not obtained, contrary to the 1st case, where the generalization had worked for this specific point.

In the 3rd study case, the training set is made of both 8% of the *"Raster"* data and 8% of the *"Zigzag"* data. The predictions obtained are found very close to the theoretical values. A correlation has been found for the two configurations. The induced distortions are represented in Figure 7.8-c.

In conclusion, these results, particularly those for 1st study, show that the temperature data considered as input correlate well with the deformation field for a similar deposition pattern. However, the poor generalizations from the *"Raster"* to the *"Zigzag"* (or vice versa) tend to show that other phenomena participate to the deformation. In particular, the notion of temperature-time history has been lost in this synthesis, but this history can be of primary importance in the prediction of the pre-deformation.

7.3.3 Full temperature profiles: Convolutional Neural Network (CNN)

In the previous section, the temperature profiles are simplified into a couple of parameters in order to construct a neural network relying only on these reduced data to predict the deformation field. The limitations found for this first approach allowed highlighting that a thorough description of the temperature evolution with time may be essential. Different information extracted from the temperature curves can be useful to predict the inherent strains field, such as the number of temperature oscillations above a specific temperature level, the maximum temperature reached, or the time to go down definitively under a temperature plateau. Instead of defining all this upstream of the network, some neurons are used directly to extract the relevant information from the temperature curves.

Convolution filters are widely used in image classification because they allow correlating the information in the neighborhood of a pixel at various scales. On a curve representing the time evolution of a quantity, this aspect is an asset to identify trends and characteristics of the curve, justifying their use in this study (Appendix H.2).

7.3.3.1 Model description

The structure of the proposed neural network is briefly presented in the following. A more detailed description of the different elements of the Neural Networks can be found in Appendix G. The stride is set to 1, and the padding is set in such a way as to obtain the same output time serie size as the input. The pooling kernels are all equal in size to the kernel of the previous convolutional layer. Figure 7.9 shows the structure of the network used: it is composed of 3 hidden layers systematically made of a set of filters and a max pooling. A last 1-filter convolution layer is used at the end to obtain a single column vector. Then, there is a hidden layer made of the same number of neurons as the number of values in the column vector of the convolution output. The output layer is made of three neurons. Multiple models using filter cores of different sizes are performed. The set with (3, 1, 6, 1) as kernels present the most accurate results.

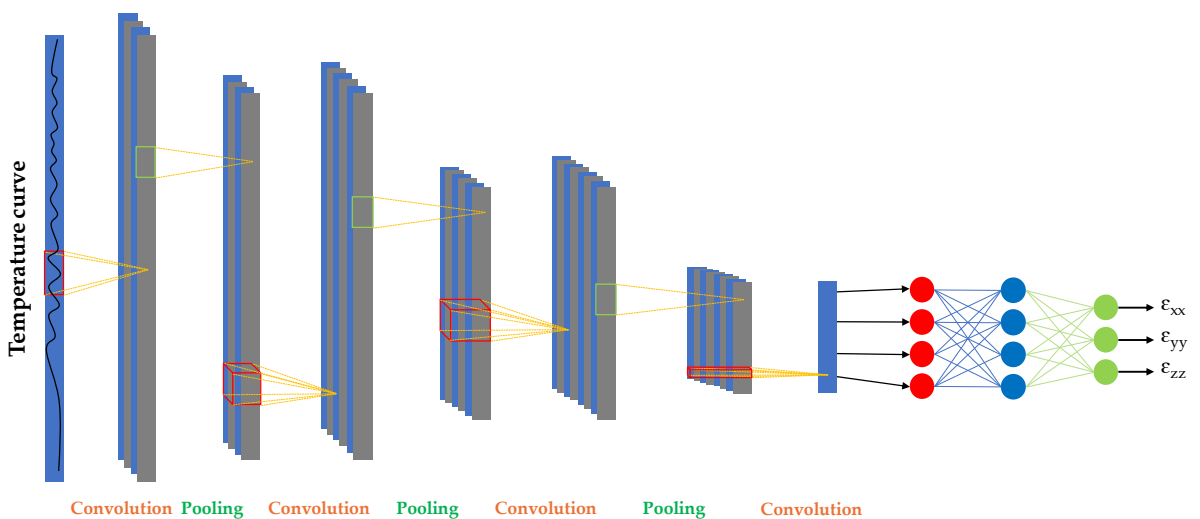


Figure 7.9 – Neural network structure for the convolutional model.

7.3.3.2 Results

Table 7.2 presents the numerical results for different sets of hyperparameters.

Table 7.2 – Numerical results of the deformation prediction using CNN

Study	Train		Error					
	Mean abs.	Median rela.	Test		"Raster"		"Zigzag"	
			Mean abs.	Median rela.	Mean abs.	Median rela.	Mean abs.	Median rela.
1	$2.2e-3$	2.0%	$3.1e-3$	2.7%	$3.0e-3$	2.6%	$7.7e-2$	2.5e2%
2	$1.9e-3$	4.7%	$2.7e-3$	6.2%	$8.2e-1$	7.3e2%	$2.6e-3$	6.1%
3	$2.0e-3$	2.8%	$2.9e-3$	4.0%	$2.9e-3$	2.3%	$2.7e-3$	6.7%

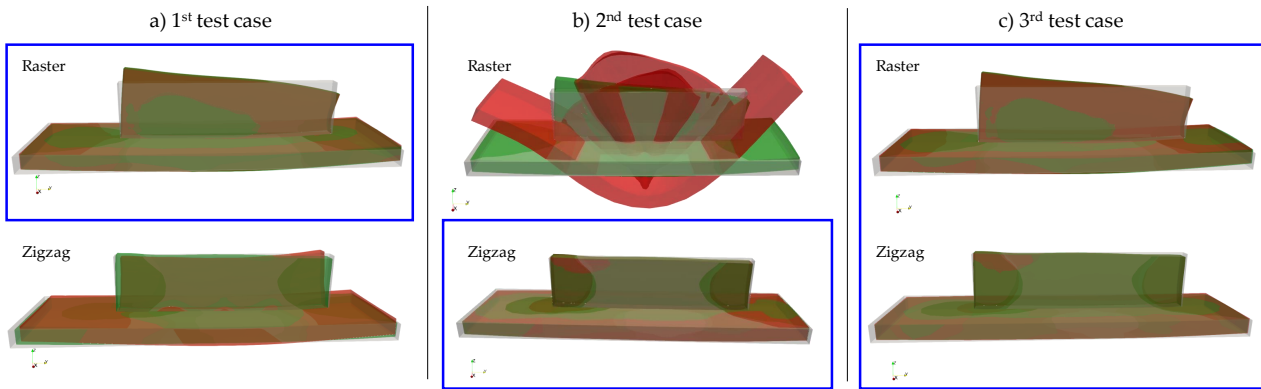


Figure 7.10 – Deformation with the isotherm model. In red: the predicted deformation, in green: the theoretical deformation, in grey: the initial mesh, In blue: the test used for training.

For all three study cases, the neural model approximated the training set with reasonable accuracy on the order of 10^{-3} (median relative error of 2 – 5%). The accuracy achieved with this structure is of the same order as those obtained with isotherms in Table 7.1, slightly better.

As for the previous test cases, a very good estimation is obtained for the test from which are extracted the 8% of data used as the training set (Figure 7.10). The results are very satisfactory and show a relative median error of about 2.6% for the "Raster", 6.1% for the "Zigzag", and 4.5% for both tests. Nevertheless, the generalization from one test to the other is still unsatisfactory (Figure 7.10). These models are, however, more accurate than the model with isotherms presented in Table 7.1.

Nonetheless, it is possible to consider the time series used as input differently by remembering relevant information as the time series are read. It is this type of model that is introduced in the next section.

7.3.4 Full temperature profiles: Recurrent Neural Network (RNN)

7.3.4.1 Model description

Figure 7.11 displays the structure of the final network used. It consists of two recurrent hidden layers and one layer with three output neurons. The first hidden layer has in this example 8 LSTM (for Long Short-Term Memory) in parallel. Each LSTM produces a time series output. So there are 8 time series

in the output of the first hidden layer. In the second hidden layer, there are 3 LSTM. Each one takes as input a time series of dimension 8 and performs as first operation a scalar product. Concerning the output of the second hidden layer, for each LSTM, only the last value of the produced series is kept. In other words, as stated earlier, for a time series of size T , an LSTM produces a time series of the same size T . Here, for each of the three time series (one for each LSTM of the layer), only the last value is kept for the rest of the network. Thus, in practice, the output of the second hidden layer is a column vector with three values. A dense layer of three neurons then links these three values together (Appendix H.3).

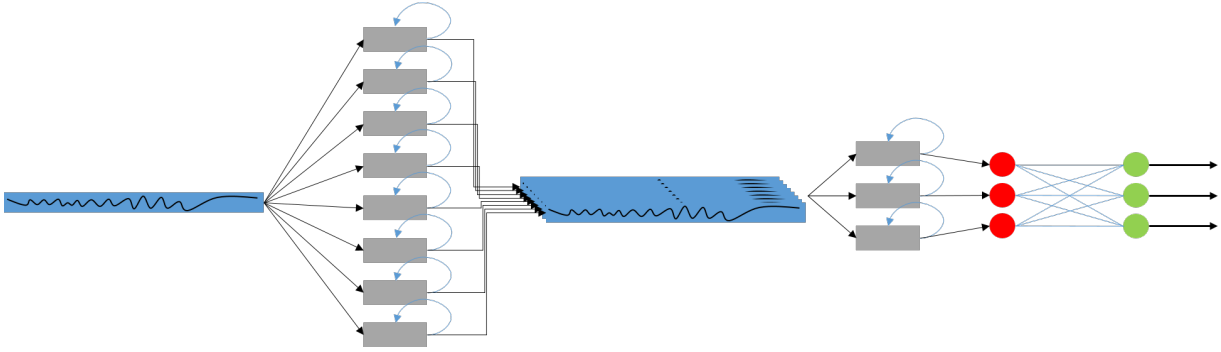


Figure 7.11 – Neural network structure for the recurrent model.

7.3.4.2 Results

Table 7.3 presents the numerical results for different sets of hyperparameters. The hyperparameters are respectively: the sampling performed on the time series, the number of LSTM in the first hidden layer, and the number of LSTM in the second hidden layer.

Table 7.3 – Numerical results of the deformation prediction using Recurrent Neural Network model.

Study	Error							
	Train		Test		"Raster"		"Zigzag"	
	Mean abs.	Median rela.	Mean abs.	Median rela.	Mean abs.	Median rela.	Mean abs.	Median rela.
1	$2.8e-3$	2.7%	$3.0e-3$	2.8%	$3.0e-3$	2.8%	$9.0e-2$	$3.0e2\%$
2	$4.3e-3$	1.1e1%	$1.8e-2$	3.3e1%	$1.4e-1$	2.0e2%	$9.7e-3$	1.6%
3	$4.2e-3$	6.8%	$4.3e-3$	6.9%	$4.8e-3$	5.0%	$1.6e-2$	3.7e1%

In the tests performed on this model, another hyperparameter is added. It corresponds to the sampling done on the time series. Indeed, networks with LSTM take much more time to train and run due to the more complex structure of the network. Thus, to gain in speed, it was decided to sample the time series by taking a temperature value every 25 values (a value on 10 has also been tested).

In all three cases, the neural model approximated the training set with an accuracy of about 10^{-3} (Figure 7.12). The accuracy obtained is lower than for the previous models. This can partly be explained by the fact that it is more difficult to make a recurrent network converge.

The results on this model do not allow us to establish that recurrent neural networks are the most appropriate to deal with this problem. However, these results must be qualified with the number of

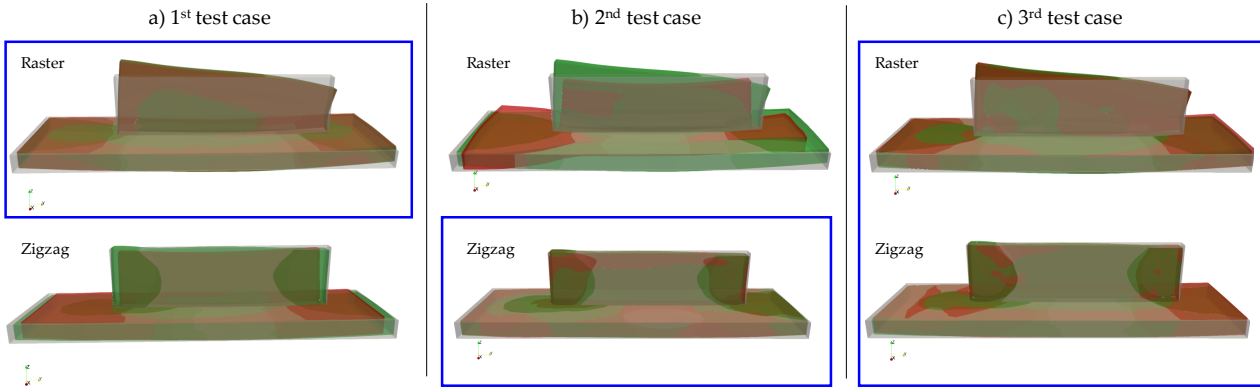


Figure 7.12 – Deformation with the isotherm model. In red: the predicted deformation, In green: the theoretical deformation, In grey: the initial mesh, In blue: the test used for training.

parameters used for each model and the depth of the network used. Table 7.4 summarizes the number of parameters and hidden layers of each model. It should be noted that the recurrent model has significantly less parameters than the other two, as shown in Table 7.4. The numerical results appear more encouraging for the recurrent model, in the light of this information. A test has been made with a similar number of parameters, comparing the results of the test case 1 between the (7, 7, 7, 1) set of the convolutional model and the (12, 3) sets of the recurrent model. This last model presents much better numerical results and a more faithful description of the "Raster".

Table 7.4 – Parameters sets comparisons of the different models.

Model used	hyperparameter set	Number of hidden layers	Number of parameters
MLP	140,140,140	3	42 843
CNN	3,1,6,1	5	71 888
RNN	25,12,3	2	936

7.3.5 Discussion on the use of Deep Learning to investigate inherent strains

In this section, different models for the prediction of the deformation field from the temperature field have been introduced. These models have shown a strong correlation between the temperatures reached during manufacturing and the parts shape for a given deposition strategy. This highlights that the thermal history is fundamental data for understanding the induced deformations. The tests revealed that training the models on only one of the two tests was not sufficient the model training. But the results obtained with the models trained on the two tests give satisfactory results.

However, the developed models still need to be further improved. For instance, the recurrent model, as pointed out by Table 7.4, must be enriched by increasing the number of LSTM on the hidden layers, or even by adding a new layer to increase depth and complexity.

Other avenues are also to be explored to refine the results and identify the influencing characteristics. First, a tool can be developed to identify what is essential in a time series for the convolution neural network. To do this, the regression problem can be reformulated into a classification problem by discretizing the image space, enabling the use, for example, of the class activation map [196, 197].

Moreover, the nodes of the mesh have been treated here independently from each other. However, spatial information can also be relevant for deformations. For example, considering the temperature variability in the area around a node can be pertinent.

Nonetheless, the lack of independent testing has strongly limited the neural network structures to be explored. For instance, in order to verify the predictions of the optimized models, a new trial is needed to qualify the accuracy obtained. Moreover, the training performed is based on the same part geometry: a wall. There is no guarantee that the model learned can be generalized to other structures such as blades, spades, or blocks. The results presented in this section seem very promising, but further experimental testing is needed to improve model learning and validation.

7.4 Conclusion & perspectives

7.4.1 Conclusion

The prediction of the final shape of a part is essential to ensure its integrity. In general, the phenomena occurring in the molten pool coupled with the influence of gravity are at the origin of the geometrical deviations of the workpieces. These phenomena are not taken into account in the mesoscopic simulations performed in this PhD thesis. In this chapter, a methodology is set up to assimilate the geometrical data of WAAM manufactured experimental part. Starting from a 3D scan of the part, a deformation field is determined based on a calibration algorithm. This field is then used as a basis to feed neural network models. These models aim to predict the deformation fields, thus allowing correcting the predicted shapes by numerical simulations. The assumption is made that the inherent strains are due to the thermal history of the part.

The calibration algorithm established follows a principle of de-rigidification of the regularizing constraints. Iteratively, the deformed solid, initially considered arbitrarily rigid, is relaxed in order first to approach the global deformations (translations, global rotations), and then localize more and more the difference between the scan and the mesh. This algorithm was built to diffuse the deformations as much as possible in order to get closer to a physically realistic deformation field. One of the main limitations of this algorithm is the non-guaranteed preservation of the volume of the solid between the initial mesh and the deformed mesh. For this, several approaches can be explored, such as adding a term to minimize the volume difference during the process. Another method would be to do a post-processing after each iteration to "enlarge" or "shrink" the mesh in a homogeneous way to have a conservation of the volume.

The different assimilation neural network models implemented to predict the deformation field from the temperature field have allowed highlighting the correlation between these two fields. These models showed a strong correlation between the temperature history during the process and the deformation fields for a given deposition strategy, supporting the assumption made on the link between the deformation fields and the temperature fields. However, mainly because of the lack of test data with only two trials available, the models could not be validated for new configurations. Having new and diversified experimental cases is fundamental to exploring these approaches more deeply.

7.4.2 Perspectives: residual stress prediction by inherent strain

The work presented focuses on the prediction of inherent strains in order to determine the component shape after manufacturing. However, for the prediction of stresses by inherent strain, only plastic deformations are required, whereas, in the work presented in this chapter, the total deformation field is considered. To investigate this point, two studies can be undertaken in the future. The first one consists in using the same methodology as in Section 7.3 to build a model that predicts plastic deformations from the transient thermal field. Given that mesoscopic models are considered accurate, they can be used to perform a large number of simulations with different process parameters, geometries, and paths. The latter can be carefully selected to generate many plastic deformation fields that will serve as a basis to train neural networks. Such a model would allow, from a thermal simulation, predicting the plastic deformation field and the residual stress field by a linear elastic simulation with a pre-deformation field.

Moreover, another perspective of this work is to use the calibration algorithm presented in the first section to estimate plastic deformation fields of a part with no significant hydrodynamic deformation, as in multi-pass welding, for example, in order to predict residual stresses.

Finally, the prediction models could be used simultaneously with a "simple" thermal simulation. The plastic deformation prediction model could be implemented based on numerical simulation. Then, a model for predicting the deformations of a hydrodynamic origin only could be set up by using deformation fields of experimental origin from which the plastic deformation field estimated by mesoscopic simulations are subtracted. The implementation of these two models would allow first to estimate the residual stress field, and then to predict the shape of the part. Such a model would make possible the prediction and study of the impact of the deposition pattern, the process parameters, and the welding speed on the shape of the part. Moreover, this tool could also be used to optimize the parameters during the manufacturing process. For example, it can be used to control the inter-layer temperature of the part or the heat input (variation of the intensity and speed of the torch). Finally, such numerical tools may help optimize the manufacturing process beforehand.

7.5 In a nutshell

Data-driven inherent strain prediction

- Implementation of a mathematical model to estimate an inherent strain field that allows the transition from the initial mesh to the 3D scan.
- Development of robust data assimilation algorithms (neural network) to predict the inherent strain field from the temperature field (FE thermal model).
- Three neural network architectures were tested. The results show the need to have a training set representative of the configuration to predict.
- Currently the CNN model gives the best results but the RNN model seems more promising.

Chapter 8

Conclusion

Contents

8.1	Mesoscopic thermo-mechanical model	212
8.2	Digital twinning assisted calibration	214
8.3	Computationally efficient approaches	216
8.4	Final words	218

The objective of this thesis work was the prediction of the thermo-mechanical residual state for WAAM manufactured parts made of austenitic 316L steel. This work focused on the numerical simulation of the WAAM process at the mesoscopic and macroscopic scales using the finite element code Code_Aster [12] developed by EDF. Indeed, the long term objective of this project is to apply the developed model to the simulation of large industrial components used in the energy production plants of EDF. A precise investigation of each modeling aspect was carried out in order to carefully propose modeling choices, and understand their consequences and limitations, as well as the influence of the various parameters involved. In addition, all the tools and models implemented in this thesis have been developed in order to be transposable to the wide variety of configurations offered by additive manufacturing (various deposition strategies, application of an idle time between layers and a final cooling time, post-processing of numerous simulations. . .).

This PhD thesis is articulated around 4 main axes.

First, since the models must provide results in reasonable times on industrial scale parts, meso-scale modeling is favored. The physical phenomena involved in the molten pool and the electric arc are thus not taken into account. Therefore, a simplification of the modeling of the material and the thermal input is performed. Due to the fact austenitic stainless steel 316L does not undergo metallurgical changes, the model implemented is a thermo-mechanical model. Moreover, the thermal and the mechanical simulations are performed sequentially, given the poor coupling found between the thermal and mechanical calculations. The implementation of the thermal and mechanical models is described in Chapter 3.

Because of this sequential strategy, the second axis of the manuscript focused on the calibration of the thermal model (Chapter 4). To this end, an innovative methodology based on the resolution of the probabilistic inverse problem, associated with the implementation of a digital twin for each simulated test, is proposed.

The third aspect presented in this manuscript is the validation of the thermo-mechanical mesoscopic model and the associated calibration methodology on thermal and mechanical experimental data obtained during different instrumented tests (Chapter 5). The models developed provided very satisfactory results with respect to these various experimental data.

Despite the simplifications made in the mesoscopic scale model, the simulations are still very complex and costly in computation time, due to the many iterations of the non-linear thermal and mechanical calculations and the many operations performed (mesh manipulation, energy adjustment. . .). The prediction of the thermo-mechanical properties of an industrial scale part of several tens of kilograms thus seems to be unfeasible at the present time at this scale of modeling. Therefore, the last axis presented in this manuscript deals with the implementation of methods to reduce the computation time. Chapter II deals with the optimization and validation of the macro-deposition method for the prediction of stress and displacement fields. Finally, in the last chapter, an innovative exploratory study is proposed to predict the inherent strains by data assimilation (based on the 3D scan of manufactured parts) using Deep Learning models.

8.1 Mesoscopic thermo-mechanical model

■ **Main Contributions:** A mesoscopic thermo-mechanical model capable of estimating the distribution of temperature, residual stresses and distortions during the manufacturing process of a

WAAM manufactured part has been implemented. An equivalent thermal source is used to represent the interaction between the arc and the molten pool. The material input is modeled with the inactive element method. The work done in this thesis has greatly improved the understanding of different aspects of the thermal modeling. A new thermal source based on the double ellipsoid Goldak volume source is developed in order to manage better the paths encountered during manufacturing. Indeed, the source adapts geometrically to have a more suitable behavior during changes in path direction. Associated with the thermal source developed, the control and correction of the heat flow is applied to provide the exact heat input. Indeed, due to the spatial and temporal discretization of the thermal problem, the heat input is not fully provided. To avoid wrongly correcting this numerical artefact during the calibration of the model, for example by determining a higher η efficiency (which is a "physical" parameter), the thermal contribution is integrated on the mesh and adjusted.

This mesoscopic model proposed allows predicting many quantities of interest (temperature profile, molten pool size, inter-layer temperature, displacement evolution, and residual stress profile). Some of the predicted quantities have been used for the validation step of the model, based on several instrumented experimental studies. Indeed, as the models were developed to be robust and adaptable, they can be applied to many different configurations in terms of process parameters, geometries of the parts, and deposition strategies.

■ **Perspectives:** For future work, it would be interesting to perform a validation of the mechanical model using constitutive behavior models fitted on the same experimental dataset, to better compare the relevance of the hardening model used. It would also be interesting to validate the proposed model on other measurable quantities such as the cooling rate, the numerical macrographs (Figure 8.1), the hardness field (which can be estimated from the plastic deformation by using empirical models [56]). The possibility to predict these quantities have been implemented in the models. It would also be interesting to perform validation tests on other materials. Indeed, the architecture of the models allows for the transposition to other materials, including with metallurgical phase transformation, provided that the material parameters are available: the thermal parameters, the mechanical parameters, the TRC diagram if there are metallurgical transformations, and the constitutive behavior law.

Another possible prospect of this work is the prediction of the microstructure. Indeed, one of the crucial points is the control of the microstructure obtained by additive manufacturing, which is very variable depending on the path, the process parameters, or the cooling strategies. The residual microstructure (grain size or grain orientation) can thus generate an anisotropy in the mechanical behavior of the part [198]. It would be interesting, for example, to be able to couple the thermal simulations to CAFE (Cellular Automaton Finite Element) type algorithms. Indeed, these algorithms allow for the prediction of the evolution of the grain size [51]. Another approach, simpler and easier to implement, would be to use a Hall-Petch type model [199] to predict an equivalent grain size diameter, to take into account a possible variation of the yield strength, which is of major importance for the accurate estimation of the mechanical residual state.

As the results presented in this manuscript are very promising, the developed numerical tools could be used to help in the set up of future experimental trials, as in the study performed in Chapter 5 that aimed at identifying a suitable cooling time. The prediction of the different

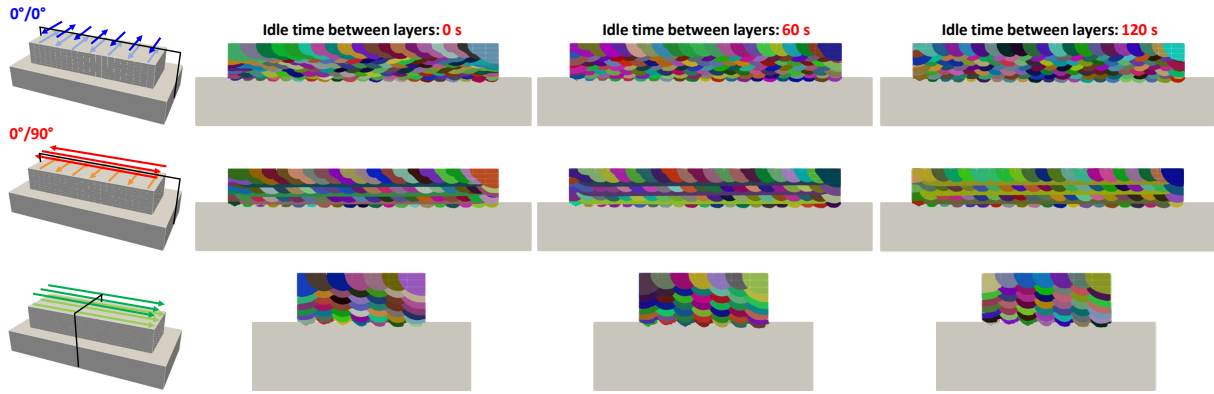


Figure 8.1 – Deformed mesh obtained for the "Raster" wall using the calibration algorithm.

quantities of interest specified above could thus be used to identify parameters sets that would be considered for the design and the optimization of the fabrications beforehand. Moreover, they would also give access to quantities of interest difficult to measure on complex parts.

The computation time of such a model is relatively large, as indicated in Chapter 5. A first approach could be the development of some steps and operations in the source code of Code_Aster, which would greatly reduce the computational cost of some of the intermediate steps performed. Indeed, the management of the progressive contribution of the elements is very costly step, which can go up to 30% of the total calculation time for large meshes. This is due to the successive and numerous creation and suppression of several groups of meshes during the simulation. Integrating these functionalities in Code_Aster could strongly reduce the cost of these manipulations. Another possibility would be the coupling with the MedCoupling library tool to manipulate meshes and fields (developed among others by EDF).

8.2 Digital twinning assisted calibration

■ **Main Contributions:** A robust calibration method is implemented for the calibration of the unknown parameters of the thermal model. The method is based on the solution of an inverse Bayesian problem using the numerical twin of a numerical test. Since the solution of an inverse problem often requires many calls to the numerical model (sequentially), the construction of a numerical twin from a reasonable number of simulations allows reducing the computation time greatly. Moreover, in the long term, one of the objectives of the method set up is to define a standardized test for the calibration of new parts. The numerical twin of this standardized test would be built once and used in each calibration step. In this thesis, the substitution models are built using the Polynomial Chaos Expansion approach. For the design of experiments, the Sobol sequences are applied. Once the digital twin is constructed, it is used for the calibration step using Monte Carlo Markov Chain algorithms in order to obtain the probability distribution of the parameters to be identified, given the available experimental data.

The models implemented and the calibration methodology put in place are then validated using four instrumented experimental tests. For these four tests, thermocouple curves are used to cali-

brate the unknown parameter sets. The thermal results are found very satisfactory in the different cases investigated. For instance, the second case study has shown that the calibrated parameter set is transposable to a different manufacturing configuration with a different deposition pattern. Moreover, the 4th case study has demonstrated that the methodology developed can be deployed for a CMT manufactured block with a complex deposition strategy and cooling devices. After the calibration of the parameters sets from the thermocouple data, other experimental data are compared to the simulation results to validate the models implemented for the four test cases. The comparisons performed on the size of the molten pool, the inter-layer temperature, and the displacement or the residual stresses showed a very strong correspondence, showing the accuracy and robustness of the developed models.

■ **Perspectives:** One of the most promising perspectives would be to help define a simple standardized test to be performed before each new manufacturing. This would allow building a single twin of this standardized case. The model construction step would thus be carried out once. After that, only the calibration step will have to be achieved for each new manufacturing. In order to build the most suitable test, a preliminary study may be to define the more relevant tests, as well as the optimal instrumentation. The work presented in Appendices C and D can provide first guidelines for the construction of such a test.

Moreover, it would be interesting to validate some modeling choices based on model selection, considering, for instance, the thermal losses as shown in Appendix D. Indeed, because of the great variety of possible models of equivalent thermal sources, model selection studies could be envisaged in order to have a hierarchy of the relevance of the models to the experimental data. This would allow identifying the most suitable modeling hypotheses for the different configurations investigated.

Furthermore, another prospect of this PhD thesis is to study the different types of tests, with different configurations and durations to help carry out spatial sensitivity studies as indicated in Appendix C. This would enable the identification of the areas in which the parameters are the most influential. These points of maximum sensitivity correspond to the locations where the temperature in the whole part is the most sensitive to each parameter. Coupled with this study, another possible prospect would be to calibrate the models on other types of data than thermocouples, such as the size of the melted zone (as presented in Appendix B). The objective would be to identify the best instrumentation and experimental measurements to be carried out to calibrate the models. Indeed, such information can be very rich compared to a thermocouple measurement, which is generally done far from the fusion line. In particular, this would allow instrumenting standardized tests with optimal yet limited instrumentation that is easily applicable in an industrial environment.

Finally, a deeper investigation of the influence of the process parameters on target mechanical quantities can also be of high interest. Indeed, if the mechanical quantities are the priority, it is important to know which parameters are the most relevant and which parameters can be defined empirically. To this end, once the uncertainties on the thermal parameters are calibrated during the resolution of the Bayesian inverse problem on the thermal simulations, their uncertainty can be propagated in the subsequent mechanical calculation in order to evaluate their influence on the variability of the output of the mechanical model (deformations, stresses, etc.).

All these studies can be carried out to help with the design of a very optimal standardized test and with the selection of the most suitable modeling choices.

8.3 Computationally efficient approaches

■ **Main Contributions:** Two investigative studies are carried out on simplified methods for the reduction of computation times.

First, although commonly used, the macro-deposition method depends on modeling parameters that are usually chosen empirically. The first part of the study focused on the calibration of the method for the prediction of two quantities of interest (residual stresses and displacements), using as reference the corresponding mesoscopic thermo-mechanical simulation. Then, kriging error response surfaces are constructed, and a constrained optimization phase is used to extract the optimum modeling parameters to minimize the prediction error. Several conclusions are reached. The main one is that the optimal numerical parameter sets are not similar for the prediction of residual stresses and displacements. Indeed, in a layer-by-layer configuration, a short heat input gives a good prediction of residual stresses, whereas displacements are obtained for more spread-out heat input. It also appears that for the same process parameter set (U, I, v_t, \dots), an optimal configuration can be identified and transposed to other deposition paths and geometries. These results are very promising.

Moreover, a new and innovative approach is proposed, based on the coupling of the macro-deposition method with a region of interest on which the mesoscopic thermo-mechanical simulation is performed.

The last study of this manuscript focuses on the implementation of a shape prediction model of a workpiece by data assimilation. In the context of an internship, a mesh calibration method is implemented to identify a field of inherent strain to fit the mesh on 3D scans. Subsequently, a model is proposed to predict inherent strains from the thermal history of a part by deep learning algorithms. The preliminary results are rather promising. However, the results obtained are not sufficient to identify whether a neural model is relevant to be transposed from a given manufacturing configuration to another. Indeed, the lack of independent experiments has limited the structures to be explored. Nevertheless, this study opens several perspectives.

■ **Perspectives:** In order to have a deeper understanding of the influence of the modeling parameters of the macro-deposition method, new validation steps are required considering idle times between layers, new process parameters, or other configurations such as pipes. A validation on larger cases is also to be done. Moreover, it would be interesting to test the difference between macro-deposition with uniform heat input and with a more complex distribution, as proposed and presented in Section 6.5.

Finally, the macro-deposition of a group of layers (rather than layer-by-layer, or of a fraction of layer) can be carried out to estimate the maximum number of layers deposited at once that allows having a good estimation of the residual stresses. This type of approach is, for instance, used for the LBM FE simulation, but needs to be validated for welding / WAAM processes.

The local focus method is very promising since its use would allow precise numerical studies on areas of interest. Indeed, although the macro-deposition simulation is satisfactory from a residual

stress prediction point of view, the local and accurate thermal field prediction is not satisfactory. This means that studies on temperature prediction, hot spots, numerical macrographs, and local cooling rates cannot be performed accurately.

It would also be interesting to vary the layer fraction according to the zones to be studied during the simulation. For example, several layers can be brought at the beginning, then the number of layers brought may be progressively decreased until reaching a one-by-one deposition. After that, the portions of layers deposited can be incrementally smaller until getting to the area of interest where the complete mesoscopic simulation is performed.

This method of local focus would deserve a more thorough validation on an industrial case, such as the Kaplan blade. To do so, the blade can, for instance, be manufactured with two zones of interest, one in the first layer and another one further in the manufacturing. The associated experimental test can be carried out with a focus on the same zones of interest in order to validate the method and show the real contribution on the quantities of interest at the level of the zones of focus.

For the inherent strains, other approaches are also to be explored to refine the results and identify the influencing features. As pointed out in Chapter 7, the recurrent model should be enriched by increasing the number of LSTM on the hidden layers, or even adding a new one to gain depth and complexity. First, for convolution neural networks, tools can be used to identify better the areas of interest in the time series for the prediction. To do this, it may be sufficient to reformulate the regression problem into a classification problem by discretizing the image space, for example, and to use the "class activation map" [196, 197]. Furthermore, taking into account spatial information (the temperature variability in the area around a node such as a spatial temperature gradient) can also be relevant for deformations.

Two novel studies can be considered. First, prediction models for plastic deformation of numerical origin could be implemented. Considering that the simulations are validated, many simulations can be performed on different manufacturing configurations and different process parameter sets. The same methodology could be used to build a plastic deformation prediction model from the thermal history. From a simple thermal calculation, a prediction of the residual stress state could be made by performing an elastic calculation with an imposed pre-deformation.

The second possible study would be to predict the inherent strain that only results from the non modeled physics: hydrodynamic phenomena in the molten pool that generate geometrical artifacts such as local subsidence. Thus, as for the study carried out in Chapter 7, it would be interesting to carry out the same study but not to build a model from the total strain but from the total strain from which the plastic strain is subtracted. This would allow predicting only the deformations that do not generate stresses. Such a model would predict the potential areas of collapse and the defects due to an accumulation of too much temperature.

These two models would allow obtaining an inherent strain to calculate residual stresses and mechanical deformations of a workpiece from a thermal simulation, but also predicting a second inherent strain from which the morphological aspects of the workpiece are determined (deformations not inducing the generation of stresses).

8.4 Final words

In this thesis, a thermo-mechanical model for the simulation of the WAAM process at the mesoscopic scale is implemented. Associated with this model, a methodology for the probabilistic calibration of the thermal model parameters is developed, using the numerical twin of a mesoscopic simulated test. The validation of the mesoscopic model and the calibration method for different manufacturing configurations was successfully performed based on several experimental tests. The next step was to accelerate the computational times in order to allow for the simulation of large industrial parts. Therefore, after the validation of the mesoscopic models, these models were used to explore and optimize the modeling parameters of the simplified macro-deposition method. Moreover, the last study of this thesis focused on implementing of a data assimilation inherent strain prediction model for the rapid prediction of the residual shape of manufactured parts from their thermal history.

All the tools and models developed in this thesis have been developed with a view to being transposable to the wide variety of configurations offered by additive manufacturing (meshes, deposition patterns, application of an idle time between layers and final cooling time, numerous simulation post-processing, etc.). A point of honor is made on the implementation of the models for them to be reliable, robust, and efficient.

The developed models and calibration methodologies can now be deployed to a large variety of industrial cases for better control of the WAAM process and its application in an industrial context.

Bibliography

- [1] LE Murr, SA Quinones, SM Gaytan, MI Lopez, A Rodela, EY Martinez, DH Hernandez, E Martinez, F Medina, and RB Wicker. Microstructure and mechanical behavior of ti-6al-4v produced by rapid-layer manufacturing, for biomedical applications. *Journal of the mechanical behavior of biomedical materials*, 2(1):20–32, 2009.
- [2] Neugebauer Keller, Fa Neugebauer, H Xu, and V Ploshikhin. Thermo-mechanical simulation of additive layer manufacturing of titanium aerospace structures. In *LightMAT Conference*, volume 3, 2013.
- [3] Ana Vafadar, Ferdinando Guzzomi, Alexander Rassau, and Kevin Hayward. Advances in metal additive manufacturing: a review of common processes, industrial applications, and current challenges. *Applied Sciences*, 11(3):1213, 2021.
- [4] Osama Abdulhameed, Abdulrahman Al-Ahmari, Wadea Ameen, and Syed Hammad Mian. Additive manufacturing: Challenges, trends, and applications. *Advances in Mechanical Engineering*, 11(2):1687814018822880, 2019.
- [5] Davoud Jafari, Tom H.J. Vaneker, and Ian Gibson. Wire and arc additive manufacturing: Opportunities and challenges to control the quality and accuracy of manufactured parts. *Materials & Design*, 202:109471, 2021.
- [6] Gianni Campatelli, Giuseppe Venturini, Niccolò Grossi, Francesco Baffa, Antonio Scippa, and Kazuo Yamazaki. Design and testing of a waam retrofit kit for repairing operations on a milling machine. *Machines*, 9(12):322, 2021.
- [7] Wanwan Jin, Chaoqun Zhang, Shuoya Jin, Yingtao Tian, Daniel Wellmann, and Wen Liu. Wire arc additive manufacturing of stainless steels: a review. *Applied sciences*, 10(5):1563, 2020.
- [8] Nadhira Nasir, Mohammad Khairul Azhar Abdul Razab, Sarizam Mamat, and Iqbal Ahmad. Review on welding residual stress. 11:6166–6175, 05 2016.
- [9] Mayank Chaurasia and Manoj Kumar Sinha. Investigations on process parameters of wire arc additive manufacturing (waam): A review. *Advances in Manufacturing and Industrial Engineering*, pages 845–853, 2021.
- [10] Faezeh Hosseinpour and H. Hajihosseini. Importance of simulation in manufacturing. 51, 01 2009.
- [11] Yuan Zhong, Lars-Erik Rännar, Leifeng Liu, Andrey Koptuyug, S. Wikman, Jon Olsén, Daqing Cui, and Z. Shen. Additive manufacturing of 316l stainless steel by electron beam melting for nuclear fusion applications. *Journal of Nuclear Materials*, 486:234–245, 01 2017.

- [12] Electricité de France. Finite element *code_aster*, analysis of structures and thermomechanics for studies and research, 1989–2021.
- [13] Kaufui V Wong and Aldo Hernandez. A review of additive manufacturing. *International scholarly research notices*, 2012, 2012.
- [14] William E Frazier. Metal additive manufacturing: a review. *Journal of Materials Engineering and performance*, 23(6):1917–1928, 2014.
- [15] S Sun, Milan Brandt, and MJLAM Easton. Powder bed fusion processes: An overview. *Laser Additive Manufacturing*, pages 55–77, 2017.
- [16] Swee Leong Sing, Jia An, Wai Yee Yeong, and Florencia Edith Wiria. Laser and electron-beam powder-bed additive manufacturing of metallic implants: A review on processes, materials and designs. *Journal of Orthopaedic Research*, 34(3):369–385, 2016.
- [17] Jean-Pierre Kruth, X Wang, Tahar Laoui, and Ludo Froyen. Lasers and materials in selective laser sintering. *Assembly Automation*, 2003.
- [18] Gideon N Levy, Ralf Schindel, and Jean-Pierre Kruth. Rapid manufacturing and rapid tooling with layer manufacturing (lm) technologies, state of the art and future perspectives. *CIRP annals*, 52(2):589–609, 2003.
- [19] C Körner. Additive manufacturing of metallic components by selective electron beam melting—a review. *International Materials Reviews*, 61(5):361–377, 2016.
- [20] Wadea Ameen, Atef M Ghaleb, Moath Alatefi, Hisham Alkhalefah, and Abdulrahman Alahmari. An overview of selective laser sintering and melting research using bibliometric indicators. *Virtual and Physical Prototyping*, 13(4):282–291, 2018.
- [21] Lawrence E Murr, Sara M Gaytan, Diana A Ramirez, Edwin Martinez, Jennifer Hernandez, Krista N Amato, Patrick W Shindo, Francisco R Medina, and Ryan B Wicker. Metal fabrication by additive manufacturing using laser and electron beam melting technologies. *Journal of Materials Science & Technology*, 28(1):1–14, 2012.
- [22] Adrita Dass and Atieh Moridi. State of the art in directed energy deposition: From additive manufacturing to materials design. *Coatings*, 9:418, 06 2019.
- [23] Adrita Dass and Atieh Moridi. State of the art in directed energy deposition: From additive manufacturing to materials design. *Coatings*, 9(7):418, 2019.
- [24] R Rumman, DA Lewis, JY Hascoet, and JS Quinton. Laser metal deposition and wire arc additive manufacturing of materials: An overview. *Archives of Metallurgy and Materials*, pages 467–473, 2019.
- [25] Amir Baghdadchi, Vahid A Hosseini, Maria Asuncion Valiente Bermejo, Björn Axelsson, Ebrahim Harati, Mats Högström, and Leif Karlsson. Wire laser metal deposition additive manufacturing of duplex stainless steel components—development of a systematic methodology. *Materials*, 14(23):7170, 2021.
- [26] Bintao Wu, Zengxi Pan, Donghong Ding, Dominic Cuiuri, Huijun Li, Jing Xu, and John Norrish. A review of the wire arc additive manufacturing of metals: properties, defects and quality improvement. *Journal of Manufacturing Processes*, 35:127–139, 2018.

-
- [27] Damien Borel. *Étude numérique et expérimentale des transferts thermiques dans un plasma d'arc: Application au soudage à l'arc TIG*. PhD thesis, Rouen, 2013.
- [28] 4 popular types of welding procedures. <https://www.lincolntech.edu/news/skilled-trades/welding-technology/types-of-welding-procedures>.
- [29] Alexandre Benoit. *Développement du soudage MIG CMT pour la réparation de pièces aéronautiques. Application aux pièces en alliage base aluminium 6061*. Theses, Université Paris Sud - Paris XI, December 2012.
- [30] Emilie Le Guen. *Etude du procédé de soudage hybride laser/MAG : Caractérisation de la géométrie et de l'hydrodynamique du bain de fusion et développement d'un modèle 3D thermique*. Theses, Université de Bretagne Sud, November 2010.
- [31] Melih Cemal KUŞHAN, Özgür POYRAZ, Yağız UZUNONAT, and ORAK Sezan. Systematical review on the numerical simulations of laser powder bed additive manufacturing. *Sigma Journal of Engineering and Natural Sciences*, 36(4):1197–1214, 2018.
- [32] Manabu Tanaka and JJ Lowke. Predictions of weld pool profiles using plasma physics. *Journal of Physics D: Applied Physics*, 40(1):R1, 2006.
- [33] Lionel Depradeux. Simulation numérique du soudage, acier 316l, validation sur cas tests de complexité croissante, 2004.
- [34] Z Hu, R Kovacevic, and M Labudovic. Experimental and numerical modeling of buckling instability of laser sheet forming. *International Journal of Machine Tools and Manufacture*, 42(13):1427–1439, 2002.
- [35] Shekhar Srivastava, Rajiv Kumar Garg, Vishal S Sharma, and Anish Sachdeva. Measurement and mitigation of residual stress in wire-arc additive manufacturing: A review of macro-scale continuum modelling approach. *Archives of Computational Methods in Engineering*, 28(5):3491–3515, 2021.
- [36] Yassine Saadlaoui, Eric Feulvarch, Alexandre Delache, Jean-Baptiste Leblond, and Jean-Michel Bergheau. A new strategy for the numerical modeling of a weld pool. *Comptes Rendus Mécanique*, 346(11):999–1017, 2018.
- [37] S. Cadiou, M. Courtois, M. Carin, W. Berckmans, and P. Le Masson. Heat transfer, fluid flow and electromagnetic model of droplets generation and melt pool behaviour for wire arc additive manufacturing. *International Journal of Heat and Mass Transfer*, 148:119102, 2020.
- [38] Yosuke Ogino and Yoshinori Hirata. Numerical simulation of metal transfer in argon gas-shielded gmaw. *Welding in the World*, 59(4):465–473, 2015.
- [39] HG Fan and R Kovacevic. A unified model of transport phenomena in gas metal arc welding including electrode, arc plasma and molten pool. *Journal of Physics D: Applied Physics*, 37(18):2531, 2004.
- [40] S. Cadiou, M. Courtois, M. Carin, W. Berckmans, and P. Le masson. 3d heat transfer, fluid flow and electromagnetic model for cold metal transfer wire arc additive manufacturing (cmt-waam). *Additive Manufacturing*, 36:101541, 2020.
- [41] Yosuke Ogino, Yoshinori Hirata, and Anthony B Murphy. Numerical simulation of gmaw process using ar and an ar-co2 gas mixture. *Welding in the World*, 60(2):345–353, 2016.
-

- [42] Xiangman Zhou, Haiou Zhang, Guilan Wang, and Xingwang Bai. Three-dimensional numerical simulation of arc and metal transport in arc welding based additive manufacturing. *International Journal of Heat and Mass Transfer*, 103:521–537, 2016.
- [43] Sreedhar Unnikrishnakurup, Sébastien Rouquette, Fabien Soulié, and Gilles Fras. Estimation of heat flux parameters during static gas tungsten arc welding spot under argon shielding. *International Journal of Thermal Sciences*, 114:205 – 212, 2017.
- [44] Xingwang Bai, Paul Colegrove, Jialuo Ding, Xiangman Zhou, Chenglei Diao, Philippe Bridgeman, Jan roman Hönnige, Haiou Zhang, and Stewart Williams. Numerical analysis of heat transfer and fluid flow in multilayer deposition of paw-based wire and arc additive manufacturing. *International Journal of Heat and Mass Transfer*, 124:504 – 516, 2018.
- [45] Y Ogino, S Asai, and Y Hirata. Numerical simulation of waam process by a gmaw weld pool model. *Welding in the World*, 62:393–401, 2018.
- [46] Kohei Oyama, Spyros Diplas, Mohammed M’hamdi, Anette E Gunnæs, and Amin S Azar. Heat source management in wire-arc additive manufacturing process for al-mg and al-si alloys. *Additive Manufacturing*, 26:180 – 192, 2019.
- [47] Rakesh Goyal, Eric Johnson, Mohamad El-Zein, J Goldak, M Coulombe, and S Tchernov. A model equation for the convection coefficient for thermal analysis of welded structures. 06 2008.
- [48] Tomasz Kik. Heat source models in numerical simulations of laser welding. *Materials*, 13(11), 2020.
- [49] Jerzy Winczek. The influence of the heat source model selection on mapping of heat affected zones during surfacing by welding. *Journal of Applied Mathematics and Computational Mechanics*, 15:167–178, 1 2016.
- [50] Filippo Montevicchi, Giuseppe Venturini, Niccolò Grossi, Antonio Scippa, and Gianni Campatelli. Idle time selection for wire-arc additive manufacturing: A finite element-based technique. *Additive Manufacturing*, 21:479 – 486, 2018.
- [51] A Zinoviev, O Zinovieva, V Ploshikhin, V Romanova, and R Balokhonov. Evolution of grain structure during laser additive manufacturing. simulation by a cellular automata method. *Materials & Design*, 106:321–329, 2016.
- [52] Guillaume Marion, Georges Cailletaud, Christophe Colin, and Matthieu Maziere. A finite element model for the simulation of direct metal deposition. In *International Congress on Applications of Lasers & Electro-Optics*, volume 2014, pages 834–841. Laser Institute of America, 2014.
- [53] Ondrej Muránsky, MC Smith, PJ Bendeich, TM Holden, V Luzin, RV Martins, and L Edwards. Comprehensive numerical analysis of a three-pass bead-in-slot weld and its critical validation using neutron and synchrotron diffraction residual stress measurements. *International Journal of Solids and Structures*, 49(9):1045–1062, 2012.
- [54] Lionel Depradeux and Frédérique Rossillon. A time saving method to compute multi-pass weld residual stresses. In *Pressure Vessels and Piping Conference*, volume 55713, page V06BT06A063. American Society of Mechanical Engineers, 2013.
- [55] O. Muránsky, C.J. Hamelin, M.C. Smith, P.J. Bendeich, and L. Edwards. The effect of plasticity theory on predicted residual stress fields in numerical weld analyses. *Computational Materials Science*, 54:125–134, 2012.

-
- [56] O. Muránsky, C.J. Hamelin, V.I. Patel, V. Luzin, and C. Braham. The influence of constitutive material models on accumulated plastic strain in finite element weld analyses. *International Journal of Solids and Structures*, 69-70:518–530, 2015.
- [57] Lionel Depradeux and Rémi Coquard. Influence of viscoplasticity, hardening, and annealing effects during the welding of a three-pass slot weld (net-tg4 round robin). *International Journal of Pressure Vessels and Piping*, 164, 04 2017.
- [58] L Mouelle, Francis Praud, Georges Chatzigeorgiou, Fodil Meraghni, J Serri, and E Fleury. Thermally-activated hardening recovery of thermo-elasto-plastic metals during annealing: Constitutive modeling for the simulation of welding process. *Mechanics of Materials*, 140:103218, 2020.
- [59] Zhuqing Wang, Erik Denlinger, Panagiotis Michaleris, Alexandru D Stoica, Dong Ma, and Allison M Beese. Residual stress mapping in inconel 625 fabricated through additive manufacturing: Method for neutron diffraction measurements to validate thermomechanical model predictions. *Materials & Design*, 113:169–177, 2017.
- [60] Qianru Wu, Tuhin Mukherjee, Changmeng Liu, Jiping Lu, and Tarasankar DebRoy. Residual stresses and distortion in the patterned printing of titanium and nickel alloys. *Additive Manufacturing*, 29:100808, 2019.
- [61] Rameez Israr, J Buhl, L Elze, and M Bambach. Simulation of different path strategies for wire-arc additive manufacturing with lagrangian finite element methods chair of mechanical design and manufacturing. 1 2019.
- [62] Huihui Zhao, Guangjun Zhang, Ziqiang Yin, and Lin Wu. Three-dimensional finite element analysis of thermal stress in single-pass multi-layer weld-based rapid prototyping. *Journal of Materials Processing Technology*, 212:276–285, 1 2012.
- [63] Xuan Liang, Lin Cheng, Qian Chen, Qingcheng Yang, and Albert C To. A modified method for estimating inherent strains from detailed process simulation for fast residual distortion prediction of single-walled structures fabricated by directed energy deposition. *Additive Manufacturing*, 23:471–486, 2018.
- [64] K Ren, Y Chew, JYH Fuh, YF Zhang, and GJ Bi. Thermo-mechanical analyses for optimized path planning in laser aided additive manufacturing processes. *Materials & Design*, 162:80–93, 2019.
- [65] Michele Chiumenti, Miguel Cervera, Alessandro Salmi, Carlos Agelet de Saracibar, Narges Dialami, and Kazumi Matsui. Finite element modeling of multi-pass welding and shaped metal deposition processes. *Computer Methods in Applied Mechanics and Engineering*, 199:2343 – 2359, 2010.
- [66] Xiaolong Wang and Aimin Wang. Finite element analysis of clamping form in wire and arc additive manufacturing. *2017 7th International Conference on Modeling, Simulation, and Applied Optimization (ICMSAO)*, pages 1–5, 2017.
- [67] Yangyang Lei and Rong Li. Finite element analysis and experimental validation of thermal behavior for thin-walled parts in gmaw-based additive manufacturing with various substrate preheating temperatures. *Applied Thermal Engineering*, 126, 07 2017.
-

- [68] Kazuo Ogawa, Dean Deng, Shoichi Kiyoshima, Nobuyoshi Yanagida, and Koichi Saito. Investigations on welding residual stresses in penetration nozzles by means of 3d thermal elastic plastic fem and experiment. *Computational materials science*, 45(4):1031–1042, 2009.
- [69] L Depradeux F Rossillon. A methodology for a simplified thermo-mechanical welding simulation in an engineering framework. 2011.
- [70] Camille Cambon, Sebastien Rouquette, Issam Bendaoud, Cyril Bordreuil, R. Wimpory, and Fabien Soulié. Thermo-mechanical simulation of overlaid layers made with wire + arc additive manufacturing and gmaw-cold metal transfer. *Welding in the World*, 64, 07 2020.
- [71] Stefan Kollmannsberger, Ali Özcan, Massimo Carraturo, Nils Zander, and Ernst Rank. A hierarchical computational model for moving thermal loads and phase changes with applications to selective laser melting. *Computers & Mathematics with Applications*, 75(5):1483–1497, 2018.
- [72] Shiyam Jayanath and Ajit Achuthan. A computationally efficient finite element framework to simulate additive manufacturing processes. *Journal of Manufacturing Science and Engineering*, 140, 1 2018. 041009.
- [73] Hui Huang, Yao Zhao, and Hua Yuan. Finite element simulation of multi-pass welding process with rezoning technique. *Quarterly Journal of the Japan Welding Society*, 29(3):95s–99s, 2011.
- [74] Filippo Monteverchi, Giuseppe Venturini, Niccolò Grossi, Antonio Scippa, and Gianni Campatelli. Finite element mesh coarsening for effective distortion prediction in wire arc additive manufacturing. *Additive Manufacturing*, 18:145 – 155, 2017.
- [75] Richard Martukanitz, Pan Michaleris, Todd Palmer, Tarasankar DebRoy, Zi-Kui Liu, Richard Otis, Tae Wook Heo, and Long-Qing Chen. Toward an integrated computational system for describing the additive manufacturing process for metallic materials. *Additive Manufacturing*, 1-4:52 – 63, 2014. Inaugural Issue.
- [76] Yancheng Zhang, Gildas Guillemot, Marc Bernacki, and Michel Bellet. Macroscopic thermal finite element modeling of additive metal manufacturing by selective laser melting process. *Computer Methods in Applied Mechanics and Engineering*, 331:514–535, 2018.
- [77] Andreas Malmelöv, Andreas Lundbäck, and Lars-Erik Lindgren. History reduction by lumping for time-efficient simulation of additive manufacturing. *Metals*, 10(1), 2020.
- [78] Abhilash Kiran, Josef Hodek, Jaroslav Vavřík, Miroslav Urbánek, and Jan Džugan. Numerical simulation development and computational optimization for directed energy deposition additive manufacturing process. *Materials*, 13:2666, 06 2020.
- [79] Michael F Zaeh and Gregor Branner. Investigations on residual stresses and deformations in selective laser melting. *Production Engineering*, 4(1):35–45, 2010.
- [80] L Papadakis, A Loizou, J Risse, and J Schrage. Numerical computation of component shape distortion manufactured by selective laser melting. *Procedia Cirp*, 18:90–95, 2014.
- [81] Yukio Ueda, Keiji Fukuda, and Masayuki Tanigawa. New measuring method of three dimensional residual stresses based on theory of inherent strain (welding mechanics, strength & design). *Transactions of JWRI*, 8(2):249–256, 1979.
- [82] Michael R Hill and Drew V Nelson. The inherent strain method for residual stress determination and its application to a long welded joint. *ASME-PUBLICATIONS-PVP*, 318:343–352, 1995.

-
- [83] Qiukai Lu, Erwan Beauguesne, and Tadeusz Liszka. Enhancements to the inherent strain method for additive manufacturing analysis. *International Journal for Multiscale Computational Engineering*, 17(1), 2019.
- [84] Thoufeili Taufek, Yupiter HP Manurung, Stephan Lüder, Marcel Graf, and Farrahshaida Mohd Salleh. Distortion analysis of slm product of ss316l using inherent strain method. In *IOP Conference Series: Materials Science and Engineering*, volume 834, page 012011. IOP Publishing, 2020.
- [85] Iñaki Setien, Michele Chiumenti, Sjoerd van der Veen, Maria San Sebastian, Fermín Garcíandía, and Alberto Echeverría. Empirical methodology to determine inherent strains in additive manufacturing. *Computers & Mathematics with Applications*, 78(7):2282–2295, 2019.
- [86] Xuan Liang, Qian Chen, Lin Cheng, Qingcheng Yang, and Albert To. A modified inherent strain method for fast prediction of residual deformation in additive manufacturing of metal parts. In *2017 International Solid Freeform Fabrication Symposium*. University of Texas at Austin, 2017.
- [87] Xuan Liang, Qian Chen, Lin Cheng, Devlin Hayduke, and Albert C To. Modified inherent strain method for efficient prediction of residual deformation in direct metal laser sintered components. *Computational Mechanics*, 64(6):1719–1733, 2019.
- [88] Akira Maekawa, Atsushi Kawahara, Hisashi Serizawa, and Hidekazu Murakawa. Fast three-dimensional multipass welding simulation using an iterative substructure method. *Journal of Materials Processing Technology*, 215:30–41, 2015.
- [89] C Li, CH Fu, YB Guo, and FZ Fang. A multiscale modeling approach for fast prediction of part distortion in selective laser melting. *Journal of materials processing technology*, 229:703–712, 2016.
- [90] Michael Gouge and Pan Michaleris. *Thermo-mechanical modeling of additive manufacturing*. Butterworth-Heinemann, 2017.
- [91] Stanley Osher and James A Sethian. Fronts propagating with curvature-dependent speed: Algorithms based on hamilton-jacobi formulations. *Journal of computational physics*, 79(1):12–49, 1988.
- [92] Stephen Cadiou. *Modélisation magnéto-thermohydraulique de procédés de fabrication additive arc-fil (WAAM)*. Theses, Université de Bretagne Sud, December 2019.
- [93] J. Hu and H.L. Tsai. Heat and mass transfer in gas metal arc welding. part i: The arc. *International Journal of Heat and Mass Transfer*, 50(5):833–846, 2007.
- [94] Marcel Graf, Andre Hälsig, Kevin Höfer, Birgit Awiszus, and Peter Mayr. Thermo-mechanical modelling of wire-arc additive manufacturing (waam) of semi-finished products. *Metals*, 8:1009, 1 2018.
- [95] Panagiotis Michaleris. Modeling metal deposition in heat transfer analyses of additive manufacturing processes. *Finite Elements in Analysis and Design*, 86:51 – 60, 2014.
- [96] Tuan Dinh Trong. *Modèles hyper-réduits pour la simulation simplifiée du soudage en substitut de calcul hors d’atteinte*. Theses, Université Paris sciences et lettres, September 2018.
- [97] Patrice Peyre, Morgan Dal, Sebastien Pouzet, and Olivier Castelnau. Simplified numerical model for the laser metal deposition additive manufacturing process. *Journal of Laser Applications*, 29:22304, 1 2017.
-

- [98] Arnaud Longuet, Christophe Colin, Patrice Peyre, Stéphane Quilici, and Georges Cailletaud. Modélisation de la fabrication directe de pièces par projection laser : application au ti-6al-4v. 01 2006.
- [99] J Ding, P Colegrove, J Mehnen, S Ganguly, P M Sequeira Almeida, F Wang, and S Williams. Thermo-mechanical analysis of wire and arc additive layer manufacturing process on large multi-layer parts. *Computational Materials Science*, 50:3315 – 3322, 2011.
- [100] Camille Cambon. *Étude thermomécanique du procédé de fabrication métallique arc-fil : approche numérique et expérimentale*. Theses, Université Montpellier, May 2021.
- [101] Mohammed Akram Chergui. *Evaluation et optimisation des stratégies de dépôt en fabrication additive arc-fil basée sur la simulation*. PhD thesis, Université Grenoble Alpes, 2021.
- [102] Fengchun Jiang, Laibo Sun, Ruisheng Huang, Hui Jiang, Guangyong Bai, Xiaopeng Qi, Chuanming Liu, Yan Su, Chunhuan Guo, and Jiandong Wang. Effects of heat input on morphology of thin-wall components fabricated by wire and arc additive manufacturing. *Advanced Engineering Materials*, 23(4):2001443, 2021.
- [103] M Abid and M Siddique. Numerical simulation to study the effect of tack welds and root gap on welding deformations and residual stresses of a pipe-flange joint. *International Journal of Pressure Vessels and Piping*, 82:860 – 871, 2005.
- [104] Haiou, Wang Guilian Bai Xingwang, and Zhang. Modeling of the moving induction heating used as secondary heat source in weld-based additive manufacturing. *The International Journal of Advanced Manufacturing Technology*, 77:717–727, 3 2015.
- [105] L-E Lindgren. Numerical modelling of welding. *Computer methods in applied mechanics and engineering*, 195(48-49):6710–6736, 2006.
- [106] John A Goldak and Mehdi Akhlaghi. *Computational welding mechanics*. Springer Science & Business Media, 2005.
- [107] John N. Dupont and Arnold R. Marder. Thermal efficiency of arc welding processes. *Welding Journal*, 74, 1995.
- [108] Rosenthal D. Mathematical theory of heat distribution during welding and cutting. *Welding Journal*, pages 220–234, 1941.
- [109] Eagar T.W and Tsai N.S. Temperature fields produced by traveling distributed heat sources. *Welding Journal*, 62:346–355, 1983.
- [110] John Goldak, Aditya Chakravarti, and Malcolm Bibby. A new finite element model for welding heat sources. *Metallurgical Transactions B*, 15:299–305, 1984.
- [111] JN Dupont and AR Marder. Thermal efficiency of arc welding processes. *Weld Res Suppl*, pages 406–416, 1995.
- [112] Jazeel Rahman Chukkan, M. Vasudevan, S. Muthukumaran, R. Ravi Kumar, and N. Chandrasekhar. Simulation of laser butt welding of aisi 316l stainless steel sheet using various heat sources and experimental validation. *Journal of Materials Processing Technology*, 219:48–59, 2015.
- [113] Shuwan Cui, Shuwen Pang, Dangqing Pang, Qin Zhang, and Zhiqing Zhang. Numerical simulation and experimental investigation on 2205 duplex stainless steel k-tig welded joint. *Metals*, 11(8), 2021.

-
- [114] Michele Chiumenti, Miguel Cervera, Narges Dialami, Bin Wu, L Jinwei, and C Agelet de Saracibar. Numerical modeling of the electron beam welding and its experimental validation. *Finite Elements in Analysis and Design*, 121:118–133, 2016.
- [115] C.S. Wu, H.G. Wang, and Y.M. Zhang. A new heat source model for keyhole plasma arc welding in fem analysis of the temperature profile. *Welding Journal (Miami, Fla)*, 85:284–s, 12 2006.
- [116] Peizhi Li, Yu Fan, Chonghao Zhang, Zhiyuan Zhu, Wenteng Tian, and Anmin Liu. Research on heat source model and weld profile for fiber laser welding of a304 stainless steel thin sheet. *Advances in Materials Science and Engineering*, 2018:1–12, 04 2018.
- [117] Yan Li, Yan-Hui Feng, Xin-Xin Zhang, and Chuan-Song Wu. An improved simulation of heat transfer and fluid flow in plasma arc welding with modified heat source model. *International Journal of Thermal Sciences*, 64:93–104, 2013.
- [118] Anoop K. Unni and M. Vasudevan. Determination of heat source model for simulating full penetration laser welding of 316 L stainless steel by computational fluid dynamics. *Materials Today: Proceedings*, 45:4465–4471, 2021. Second International Conference on Aspects of Materials Science and Engineering (ICAMSE 2021).
- [119] Junqiang Wang, Jianmin Han, Joseph Domblesky, Zhiyong Yang, Yingxin Zhao, and Qiang Zhang. Development of a new combined heat source model for welding based on a polynomial curve fit of the experimental fusion line. *The International Journal of Advanced Manufacturing Technology*, 87, 11 2016.
- [120] Jialuo Ding. Thermo-mechanical analysis of wire and arc additive manufacturing process. 2012.
- [121] Fionn Dunne and Nik Petrinic. *Introduction to computational plasticity*. OUP Oxford, 2005.
- [122] Chin-Hyung Lee and Kyong-Ho Chang. Finite element simulation of the residual stresses in high strength carbon steel butt weld incorporating solid-state phase transformation. *Computational materials science*, 46(4):1014–1022, 2009.
- [123] Keval Prajadhama, Yupiter Manurung, Zaidi Minggu, Fetisia Pengadau, Marcel Graf, Andre Hälsig, Tom-Eric Adams, and Hui Leng Choo. Development of bead modelling for distortion analysis induced by wire arc additive manufacturing using fem and experiment. *MATEC Web of Conferences*, 269:5003, 1 2019.
- [124] Jun-feng Hu, Jian-guo Yang, Hong-yuan Fang, Guang-min Li, Yong Zhang, and Xin Wan. Temperature, stress and microstructure in 10Ni5CrMoV steel plate during air–arc cutting process. *Computational materials science*, 38(4):631–641, 2007.
- [125] Ondrej Muránsky, Cory J Hamelin, MC Smith, Philip J Bendeich, and Lyndon Edwards. The effect of plasticity theory on predicted residual stress fields in numerical weld analyses. *Computational Materials Science*, 54:125–134, 2012.
- [126] Charles O Frederick and PJ Armstrong. A mathematical representation of the multiaxial bauschinger effect. *Materials at High Temperatures*, 24(1):1–26, 2007.
- [127] Philippe Gilles, Walid El-Ahmar, and Jean-François Jullien. Robustness analyses of numerical simulation of fusion welding net-tg1 application: “single weld-bead-on-plate”. *International Journal of Pressure Vessels and Piping*, 86(1):3–12, 2009. The NeT Residual Stress Measurement and Modelling Round Robin on a Single Weld Bead-on-Plate Specimen.
-

- [128] William Prager. A new method of analyzing stresses and strains in work-hardening plastic solids. 1956.
- [129] Jean Lemaitre and Jean-Louis Chaboche. *Mechanics of solid materials*. Cambridge university press, 1994.
- [130] Jean-Louis Chaboche. Constitutive equations for cyclic plasticity and cyclic viscoplasticity. *International journal of plasticity*, 5(3):247–302, 1989.
- [131] *A Study of the Effect of Hardening Model in the Prediction of Welding Residual Stress*, volume Volume 6: Materials and Fabrication, Parts A and B of *Pressure Vessels and Piping Conference*, 07 2012.
- [132] C Ohms, RV Martins, O Uca, AG Youtsos, PJ Bouchard, M Smith, M Keavey, Steve K Bate, Philippe Gilles, RC Wimpory, et al. The european network on neutron techniques standardization for structural integrity (net). In *ASME Pressure Vessels and Piping Conference*, volume 48296, pages 625–637, 2008.
- [133] MC Smith, AC Smith, R Wimpory, and C Ohms. A review of the net task group 1 residual stress measurement and analysis round robin on a single weld bead-on-plate specimen. *International Journal of Pressure Vessels and Piping*, 120:93–140, 2014.
- [134] Mike C Smith and Ann C Smith. Advances in weld residual stress prediction: A review of the net tg4 simulation round robin part 1, thermal analyses. *International Journal of Pressure Vessels and Piping*, 164:109–129, 2018.
- [135] Mike C Smith and Ann C Smith. Advances in weld residual stress prediction: A review of the net tg4 simulation round robins part 2, mechanical analyses. *International Journal of Pressure Vessels and Piping*, 164:130–165, 2018.
- [136] Philippe Gilles, Walid El-Ahmar, and Jean-François Jullien. Robustness analyses of numerical simulation of fusion welding net-tg1 application: “single weld-bead-on-plate”. *International Journal of Pressure Vessels and Piping*, 86(1):3–12, 2009.
- [137] JJ Xu, Philippe Gilles, YG Duan, and C Yu. Temperature and residual stress simulations of the net single-bead-on-plate specimen using sysweld. *International Journal of Pressure Vessels and Piping*, 99:51–60, 2012.
- [138] Dieter Radaj. *Heat effects of welding: temperature field, residual stress, distortion*. Springer Science & Business Media, 2012.
- [139] M.C. Smith and A.C. Smith. Net bead-on-plate round robin: Comparison of residual stress predictions and measurements. *International Journal of Pressure Vessels and Piping*, 86(1):79–95, 2009. The NeT Residual Stress Measurement and Modelling Round Robin on a Single Weld Bead-on-Plate Specimen.
- [140] M.C. Smith, P.J. Bouchard, M. Turski, L. Edwards, and R.J. Dennis. Accurate prediction of residual stress in stainless steel welds. *Computational Materials Science*, 54:312–328, 2012.
- [141] J.J. Xu, P. Gilles, Y.G. Duan, and C. Yu. Temperature and residual stress simulations of the net single-bead-on-plate specimen using sysweld. *International Journal of Pressure Vessels and Piping*, 99-100:51–60, 2012.

-
- [142] Josselin Delmas and Aimery Assire. Salome-meca : une plate-forme au service de la simulation mécanique. 05 2009.
- [143] Víctor D Fachinotti, Alberto Cardona, Bernd Baufeld, and Omer Van der Biest. Finite-element modelling of heat transfer in shaped metal deposition and experimental validation. *Acta materialia*, 60(19):6621–6630, 2012.
- [144] Haiou, Wang Guilun Bai Xingwang, and Zhang. Improving prediction accuracy of thermal analysis for weld-based additive manufacturing by calibrating input parameters using ir imaging. *The International Journal of Advanced Manufacturing Technology*, 69:1087–1095, 11 2013.
- [145] P Sreeraj and T Kannan. Modelling and prediction of stainless steel clad bead geometry deposited by gmaw using regression and artificial neural network models. *Advances in Mechanical Engineering*, 4:237379, 2012.
- [146] Jun Xiong, Guangjun Zhang, Jianwen Hu, and Lin Wu. Bead geometry prediction for robotic gmaw-based rapid manufacturing through a neural network and a second-order regression analysis. *Journal of Intelligent Manufacturing*, 25(1):157–163, 2014.
- [147] Guillaume Marion. *Modélisation de procédés de fabrication directe de pièces aéronautique et spatiales en TA6V par projection et fusion sélective d’un lit de poudre par laser : Approche thermique, métallurgique et mécanique*. PhD thesis, 10 2016.
- [148] Boštjan Taljat, B Radhakrishnan, and T Zacharia. Numerical analysis of gta welding process with emphasis on post-solidification phase transformation effects on residual stresses. *Materials Science and Engineering: A*, 246(1-2):45–54, 1998.
- [149] Donghong Ding, Shimin Zhang, Qinghua Lu, Zengxi Pan, Huijun Li, and Kai Wang. The well-distributed volumetric heat source model for numerical simulation of wire arc additive manufacturing process. *Materials Today Communications*, 27:102430, 2021.
- [150] Filippo Montevicchi, Giuseppe Venturini, Antonio Scippa, and Gianni Campatelli. Finite element modelling of wire-arc-additive-manufacturing process. *Procedia CIRP*, 55:109 – 114, 2016. 5th CIRP Global Web Conference - Research and Innovation for Future Production (CIRPe 2016).
- [151] MC Smith, PJ Bouchard, Mark Turski, Lyndon Edwards, and RJ Dennis. Accurate prediction of residual stress in stainless steel welds. *Computational Materials Science*, 54:312–328, 2012.
- [152] P Tekriwal and J Mazumder. Transient and residual thermal strain-stress analysis of gmaw. *Journal of Engineering Materials and Technology*, pages 113–336, 1991.
- [153] Giai Tran Van. *Détermination d’un critère de fissuration à chaud par liquation en fonction de la teneur en bore et de sa localisation pour l’acier inoxydable austénitique 316L*. Theses, Université de Bretagne Sud, December 2018.
- [154] M. R. Bosworth. Effective heat input in pulsed current gas metal arc welding with solid wire electrodes. *Welding Journal*, 70, 1991.
- [155] N Ppe, Stephan Egerland, P Colegrove, David Yapp, A Leonhartsberger, and Americo Scotti. Measuring the process efficiency of controlled gas metal arc welding processes. *Science and Technology of Welding & Joining*, 16:412–417, 07 2011.
- [156] Rong Li, Jun Xiong, and Yangyang Lei. Investigation on thermal stress evolution induced by wire and arc additive manufacturing for circular thin-walled parts. *Journal of Manufacturing Processes*, 40:59–67, 2019.

- [157] Guangming Fu, Jijun Gu, Marcelo Igor Lourenco, Menglan Duan, and Segen F Estefen. Parameter determination of double-ellipsoidal heat source model and its application in the multi-pass welding process. *Ships and Offshore Structures*, 10:204–217, 2015.
- [158] Amin S Azar, Sigmund K Ås, and Odd M Akselsen. Determination of welding heat source parameters from actual bead shape. *Computational materials science*, 54:176–182, 2012.
- [159] Noura Fajraoui. *Analyse de sensibilité globale et polynômes de chaos pour l'estimation des paramètres : application aux transferts en milieu poreux*. Theses, Université de Strasbourg, January 2014.
- [160] Nabil El Moçayd. La décomposition en polynôme du chaos pour l'amélioration de l'assimilation de données ensembliste en hydraulique fluviale. March 2017.
- [161] Géraud Blatman. *Chaos polynomial creux et adaptatif pour la propagation d'incertitudes et l'analyse de sensibilité*. Theses, Université Blaise Pascal - Clermont-Ferrand II, October 2009.
- [162] Norbert Wiener. The homogeneous chaos. *American Journal of Mathematics*, 60(4):897–936, 1938.
- [163] R. H. Cameron and W. T. Martin. The orthogonal development of non-linear functionals in series of fourier-hermite functionals. *Annals of Mathematics*, 48(2):385–392, 1947.
- [164] Thomas J. Santner, Brian J. Williams, and William I. Notz. The design and analysis of computer experiments. 2003.
- [165] M. D. McKay, R. J. Beckman, and W. J. Conover. A comparison of three methods for selecting values of input variables in the analysis of output from a computer code. *Technometrics*, 21(2):239–245, 1979.
- [166] Ronald Iman, Jon Helton, and James Campbell. An approach to sensitivity analysis of computer models: Part i—introduction, input variable selection and preliminary variable assessment. *J Qual Technol*, 13:174–183, 07 1981.
- [167] Paul Bratley and Bennett L Fox. Algorithm 659: Implementing sobol's quasirandom sequence generator. *ACM Transactions on Mathematical Software (TOMS)*, 14(1):88–100, 1988.
- [168] Michaël Baudin, Anne Dutfoy, Bertrand Iooss, and Anne-Laure Popelin. Open turns: An industrial software for uncertainty quantification in simulation, 2015.
- [169] Markus Ojala and Gemma C. Garriga. Permutation tests for studying classifier performance. *Journal of Machine Learning Research*, 11(62):1833–1863, 2010.
- [170] Sebastian Raschka. Model evaluation, model selection, and algorithm selection in machine learning, 2020.
- [171] Fariha Sohail, Muhammed Sohail, and Javid Shabbir. An introduction to statistical learning with applications in r: by Gareth James, Daniela Witten, Trevor Hastie, and Robert Tibshirani, New York, Springer Science and Business Media, 2013, 41.98, isbn: 978-1-4614-7137-7. *Statistical Theory and Related Fields*, pages 1–1, 09 2021.
- [172] Andrea Saltelli. Making best use of model evaluations to compute sensitivity indices. *Computer Physics Communications*, 145(2):280–297, 2002.

-
- [173] Andrea Saltelli, Paola Annoni, Ivano Azzini, Francesca Campolongo, Marco Ratto, and Stefano Tarantola. Variance based sensitivity analysis of model output. design and estimator for the total sensitivity index. *Computer Physics Communications*, 181(2):259–270, 2010.
- [174] I.M Sobol. Global sensitivity indices for nonlinear mathematical models and their monte carlo estimates. *Mathematics and Computers in Simulation*, 55(1):271–280, 2001. The Second IMACS Seminar on Monte Carlo Methods.
- [175] Bruno Sudret. Global sensitivity analysis using polynomial chaos expansion. *Reliability Engineering & System Safety*, 93:964–979, 07 2008.
- [176] Fabrice Gamboa, Alexandre Janon, Thierry Klein, and Agnès Lagnoux. Sensitivity analysis for multidimensional and functional outputs. *Electronic Journal of Statistics*, 8(1):575 – 603, 2014.
- [177] J. Nocedal and S. Wright. *Numerical Optimization*. Springer Series in Operations Research and Financial Engineering. Springer New York, 2006.
- [178] Erwin Jeremiah, Scott Sisson, Lucy Marshall, Rajeshwar Mehrotra, and Ashish Sharma. Bayesian calibration and uncertainty analysis of hydrological models: A comparison of adaptive metropolis and sequential monte carlo samplers. *Water Resources Research*, 47(7), 2011.
- [179] Heikki Haario, Eero Saksman, and Johanna Tamminen. An adaptive metropolis algorithm. *Bernoulli*, pages 223–242, 2001.
- [180] Dan Lu, Daniel Ricciuto, Anthony Walker, Cosmin Safta, and William Munger. Bayesian calibration of terrestrial ecosystem models: a study of advanced markov chain monte carlo methods. *Biogeosciences*, 14(18):4295–4314, 2017.
- [181] Simon Duane, Anthony D Kennedy, Brian J Pendleton, and Duncan Roweth. Hybrid monte carlo. *Physics letters B*, 195(2):216–222, 1987.
- [182] Michel Kern. Problèmes inverses : aspects numériques. Lecture, September 2002.
- [183] Jorge Nocedal and Stephen J Wright. *Numerical optimization*. Springer, 1999.
- [184] Reginald Crawford, George Cook, Alvin Strauss, and Daniel Hartman. Adaptive voltage control of gas tungsten arc welding. *Int. J. Modelling, Identification and Control Int. J. Modelling, Identification and Control*, 1:133–139, 01 2006.
- [185] Théo Boutin. *Analyse des plages de températures des filtres bichromatiques et monochromatique - Caméra FLIR*. Technical report, EDF, July 2020.
- [186] Caroline A Schneider, Wayne S Rasband, and Kevin W Eliceiri. Nih image to imagej: 25 years of image analysis. *Nat Meth*, 9(7):671–675, July 2012.
- [187] Jean-Yves Tinevez, Nick Perry, Johannes Schindelin, Genevieve M. Hoopes, Gregory D. Reynolds, Emmanuel Laplantine, Sebastian Y. Bednarek, Spencer L. Shorte, and Kevin W. Eliceiri. Trackmate: An open and extensible platform for single-particle tracking. *Methods*, 115:80–90, 2017. Image Processing for Biologists.
- [188] Per Lindström. *Improved CWM platform for modelling welding procedures and their effects on structural behaviour*. PhD thesis, University West, 2015.
- [189] Mirko Boin and R. Wimpory. E3: Residual stress neutron diffractometer at ber ii. *Journal of large-scale research facilities JLSRF*, 2, 12 2016.
-

- [190] Vasileios Akrivos, Robert C. Wimpory, Michael Hofmann, Beverly Stewart, Ondrej Muransky, Mike C. Smith, and John Bouchard. Neutron diffraction measurements of weld residual stresses in three-pass slot weld (Alloy 600/82) and assessment of the measurement uncertainty. *Journal of Applied Crystallography*, 53(5):1181–1194, Oct 2020.
- [191] A De and T DebRoy. A perspective on residual stresses in welding. *Science and Technology of Welding and Joining*, 16(3):204–208, 2011.
- [192] CE Rasmussen. Gaussian processes in machine learning. pages 63–71, 01 2004.
- [193] Tiago A Rodrigues, V Duarte, Julian A Avila, Telmo G Santos, RM Miranda, and JP Oliveira. Wire and arc additive manufacturing of hsla steel: Effect of thermal cycles on microstructure and mechanical properties. *Additive Manufacturing*, 27:440–450, 2019.
- [194] Martin S. Alnæs, Jan Blechta, Johan Hake, August Johansson, Benjamin Kehlet, Anders Logg, Chris Richardson, Johannes Ring, Marie E. Rognes, and Garth N. Wells. The fenics project version 1.5. *Archive of Numerical Software*, 3(100), 2015.
- [195] Matteo Bugatti and Quirico Semeraro. Limitations of the inherent strain method in simulating powder bed fusion processes. *Additive Manufacturing*, 23:329–346, 2018.
- [196] Bolei Zhou, Aditya Khosla, Agata Lapedriza, Aude Oliva, and Antonio Torralba. Learning deep features for discriminative localization. In *Proceedings of the IEEE Conference on Computer Vision and Pattern Recognition (CVPR)*, June 2016.
- [197] Ramprasaath R. Selvaraju, Abhishek Das, Ramakrishna Vedantam, Michael Cogswell, Devi Parikh, and Dhruv Batra. Grad-cam: Why did you say that? visual explanations from deep networks via gradient-based localization. *CoRR*, abs/1610.02391, 2016.
- [198] Tim FW van Nuland, JAW van Dommelen, and Marc GD Geers. Microstructural modeling of anisotropic plasticity in large scale additively manufactured 316l stainless steel. *Mechanics of Materials*, 153:103664, 2021.
- [199] Yung-Chien Huang, Che-Hsuan Su, Shyi-Kaan Wu, and Chieh Lin. A study on the hall–petch relationship and grain growth kinetics in fcc-structured high/medium entropy alloys. *Entropy*, 21(3):297, 2019.
- [200] Olivier Asserin, Alexandre Loredon, Matthieu Petelet, and Bertrand Iooss. Global sensitivity analysis in welding simulations—what are the material data you really need? *Finite elements in analysis and design*, 47(9):1004–1016, 2011.
- [201] Satish K Velaga and A Ravisankar. Finite element based parametric study on the characterization of weld process moving heat source parameters in austenitic stainless steel. *International Journal of Pressure Vessels and Piping*, 157:63–73, 2017.
- [202] Mikael Sunnåker, Alberto Giovanni Busetto, Elina Numminen, Jukka Corander, Matthieu Foll, and Christophe Dessimoz. Approximate bayesian computation. *PLoS computational biology*, 9(1):e1002803, 2013.
- [203] Katalin Csilléry, Michael GB Blum, Oscar E Gaggiotti, and Olivier François. Approximate bayesian computation (abc) in practice. *Trends in ecology & evolution*, 25(7):410–418, 2010.
- [204] Brian Amberg, Sami Romdhani, and Thomas Vetter. Optimal step nonrigid icp algorithms for surface registration. 06 2007.

- [205] Yuxin Yao, Bailin Deng, Weiwei Xu, and Juyong Zhang. Quasi-newton solver for robust non-rigid registration, 2020.
- [206] Andriy Myronenko, Xubo Song, Miguel A Carreira-Perpinán, et al. Non-rigid point set registration: Coherent point drift. *Advances in neural information processing systems*, 19:1009, 2007.
- [207] Federico Girosi, Michael Jones, and Tomaso Poggio. Priors, stabilizers and basis functions: from regularization to radial, tensor and additive splines, 1993.
- [208] G. K. L. Tam, Z. Cheng, Y. Lai, F. C. Langbein, Y. Liu, D. Marshall, R. R. Martin, X. Sun, and P. L. Rosin. Registration of 3d point clouds and meshes: A survey from rigid to nonrigid. *IEEE Transactions on Visualization and Computer Graphics*, 19(7):1199–1217, 2013.
- [209] Documentation Fenics Project. Hyperelasticity.
- [210] G. Cybenko. Approximation by superpositions of a sigmoidal function. 2(4):303–314.
- [211] Richard Liaw, Eric Liang, Robert Nishihara, Philipp Moritz, Joseph E. Gonzalez, and Ion Stoica. Tune: A research platform for distributed model selection and training. *CoRR*, abs/1807.05118, 2018.
- [212] J. Rapin and O. Teytaud. Nevergrad - A gradient-free optimization platform. <https://GitHub.com/FacebookResearch/Nevergrad>, 2018.
- [213] Wikipedia contributors. Sobel operator — Wikipedia, the free encyclopedia. https://en.wikipedia.org/w/index.php?title=Sobel_operator&oldid=1036063258, 2021.
- [214] Asifullah Khan, Anabia Sohail, Umme Zahoor, and Aqsa Saeed Qureshi. A survey of the recent architectures of deep convolutional neural networks. *Artificial Intelligence Review*, 53(8):5455–5516, 12 2020.
- [215] John F. Kolen and Stefan C. Kremer. *Gradient Flow in Recurrent Nets: The Difficulty of Learning LongTerm Dependencies*, pages 237–243. 2001.

Appendix A

Additional data from the 2nd test case of Chapter 5

A.1 Calibration steps of the "Zigzag" and of the "Raster"

■ "Zigzag" wall:

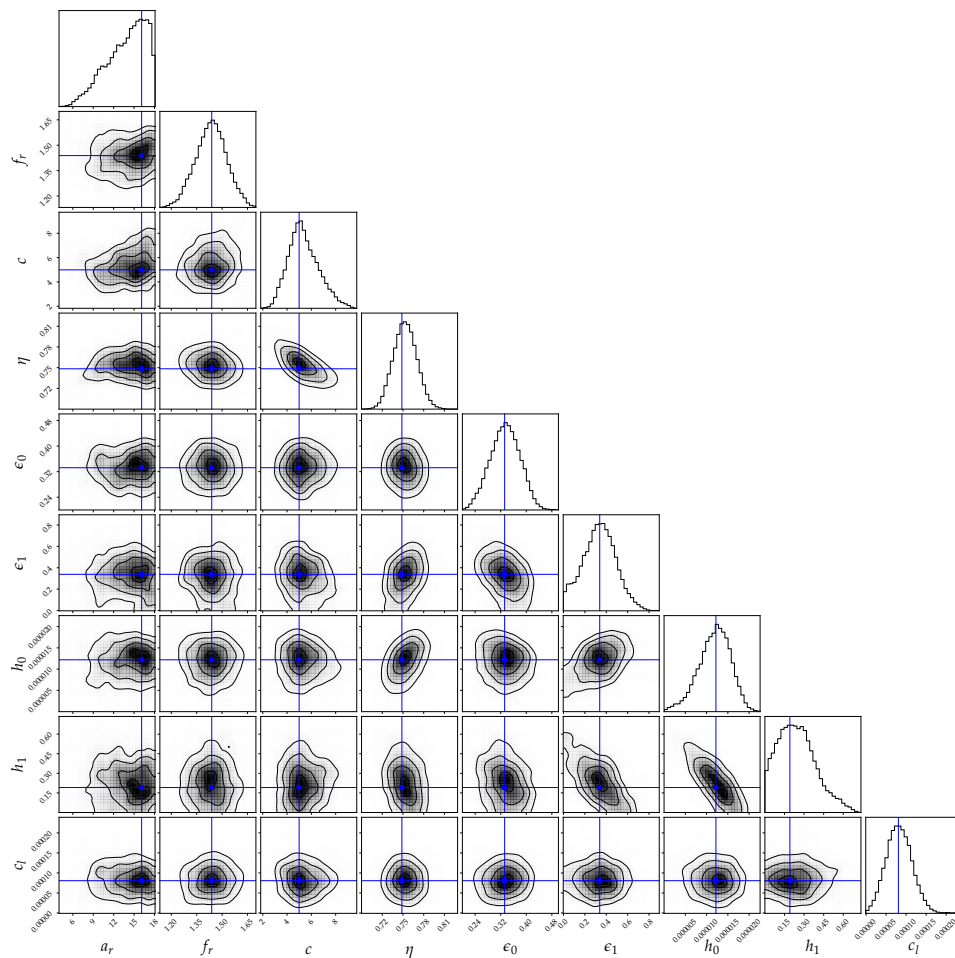


Figure A.1 – Corner plot of the posterior distribution resulting from the calibration step of the "Zigzag" test case. The MAP θ_z^* is represented in blue.

■ "Raster" wall:

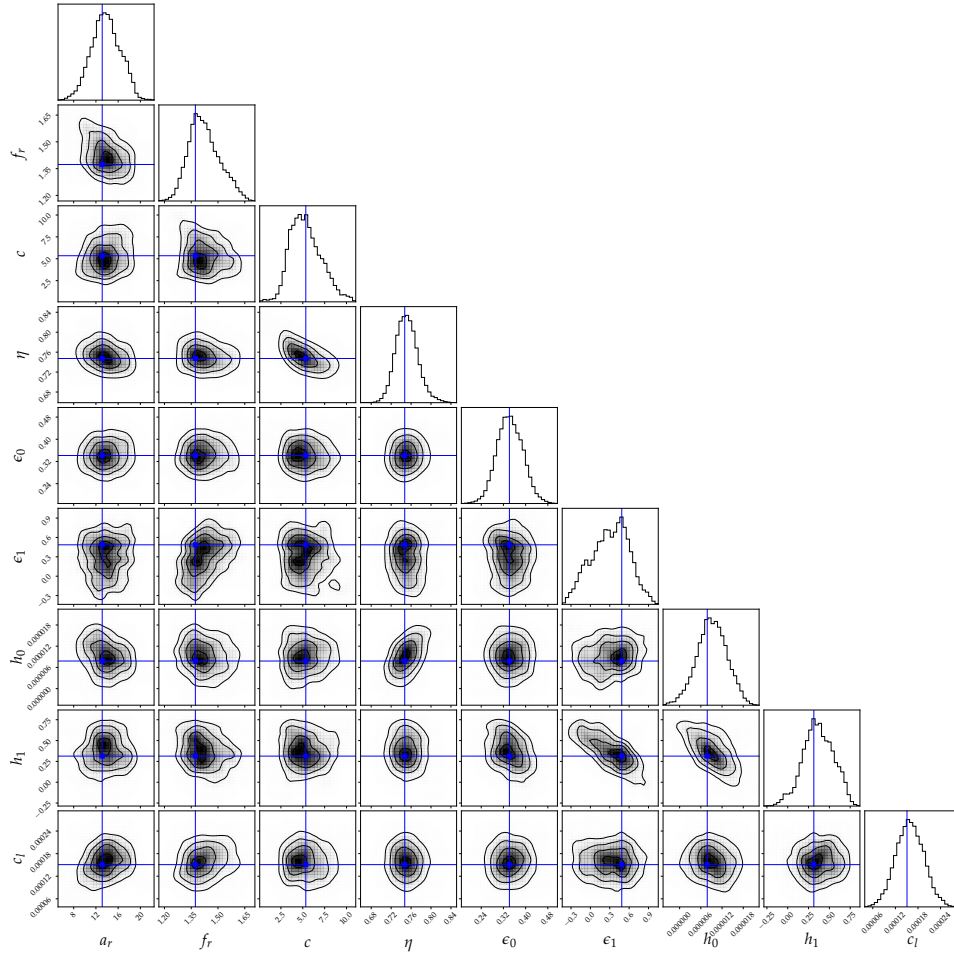


Figure A.2 – Corner plot of the posterior distribution resulting from the calibration step of the "Raster" test case. The MAP θ_r^* is represented in blue.

A.2 Validation of the thermal model calibration methodology on a cylinder

The objective of this appendix is the investigation of the generalization of the optimal set of parameters found for a given part geometry to another one performed with the same experimental test configuration (process parameters and material). To do so, an experimental test is performed with the same process parameters as the two walls described in Section 5.3, but on a more complex configuration. The test consists of an 80 beads cylinder with a diameter of 60 mm. The cylinder is fabricated on a square base plate of side length and thickness of 10 mm, clamped at two ends, as shown in Figure A.3. It is important to note that the clamping of the cylinder and the two walls are different since it is not the same contact surface nor the same clamp material.

In contrast to the study presented in Section 5.3, the numerical simulation of the cylinder is performed without calibration with the experimental data of this test, but with the parameter set obtained after calibration on the "Zigzag" test. The comparison between the experimental data and

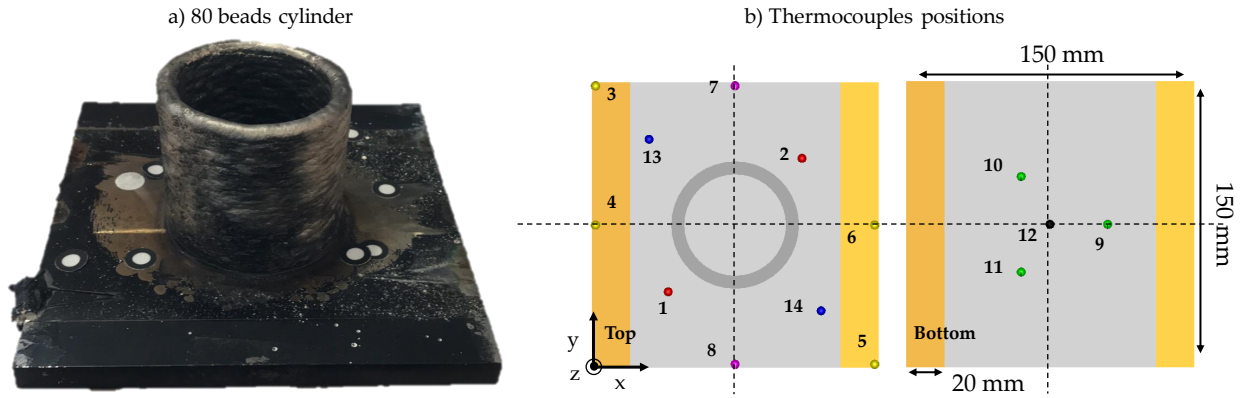


Figure A.3 – Cylinder experimental test.

Table A.1 – Thermocouples locations.

Thermocouple	x (mm)	y (mm)	z (mm)
1	40	40	10
2	110	110	10
3	2	148	10
4	2	75	10
5	148	2	10
6	148	75	10
7	75	148	10
8	75	2	10
9	105	75	0
10	60	101	0
11	60	49	0
12	75	75	0
13	120	30	10
14	30	120	10

the simulation for the first 25 beads is presented in Figure A.5. Only an adaptation of the thermal heat loss at the clamped zone parameter set at the clamping is carried out since the cylinder clamping conditions were different from the wall. The error between the thermocouple curves and the numerical prediction is between 1 and 7%, which is very satisfactory. It is thus shown that, for the same parameter set, after calibration on a given part geometry (wall), the simulations can be predictive for another more complex part geometry (cylinder). Nonetheless, it would have been interesting to have the same clamping boundary conditions to be absolutely sure of the transposition of the parameter set. For future work, other part geometries can be considered, for example with juxtaposed beads (block for instance).

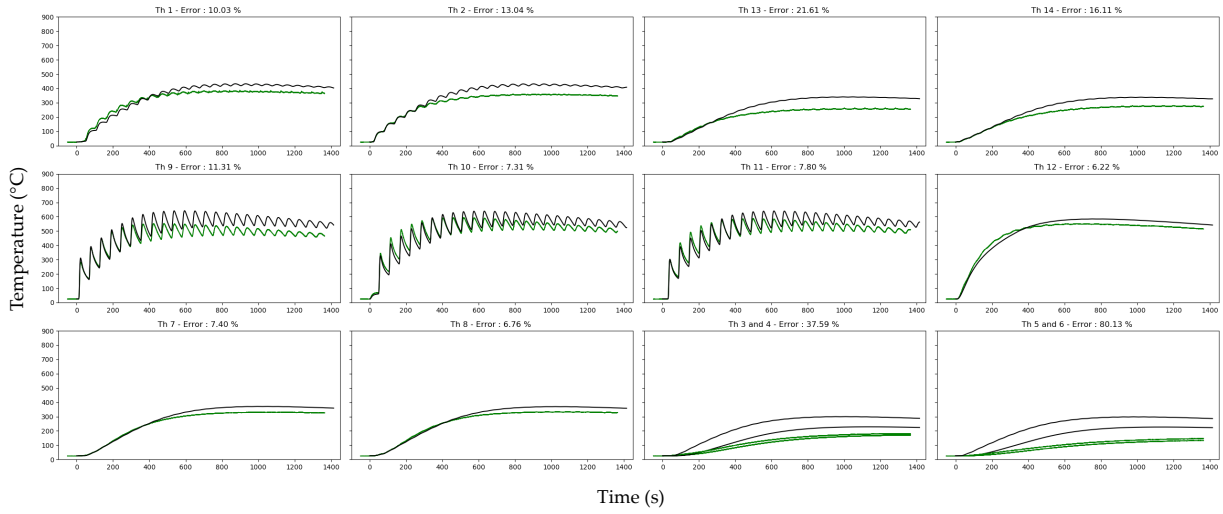


Figure A.4 – Validation of the temperature profiles for the thermocouples of the cylinder test on the first 25 beads with the parameters $\theta_{z&r}^*$.

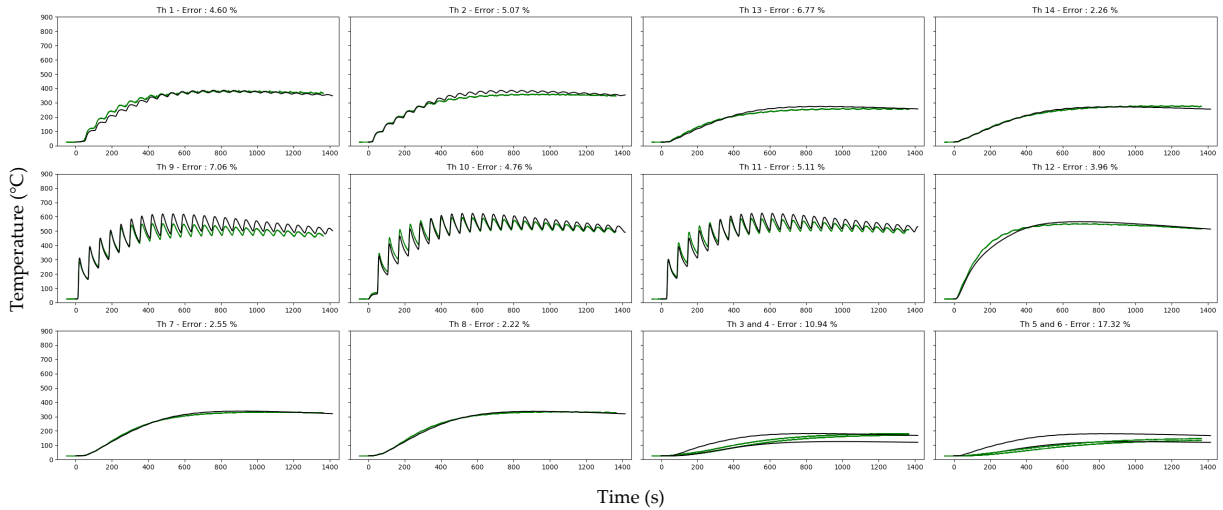


Figure A.5 – Validation of the temperature profiles for the thermocouples of the cylinder test on the first 25 beads with the parameters $\theta_{z&r}^*$ and an adaptation of $h_{cl} = 200$ ($\text{W}\cdot\text{m}^{-2}\cdot\text{K}^{-1}$).

Appendix B

Extra study: Inverse problem using macrographies

One of the benefits of the inverse problem method developed in Chapter 4 is that it can be extended to other types of experimental data, provided that the experimental data are available and that the same quantities of interest can be extracted from the simulations. For instance, this method can be easily transposed to melted zone profiles, Heat Affected Zone (HAZ) profiles, or even residual stress profiles. Below, a simple example presents the parameter set calibration procedure developed on melted zone profiles in the case of a fusion line.

The example shown in Figure B.1 consists of a single 120 mm long fusion line. Figure B.1-a represents the "maximum" temperature field reached by each node during the test. The 1400°C isotherm in this field thus corresponds to the area that was melted during the test.

As shown in Figure B.1-b, by taking a slice of this field, a numerical macrograph is obtained. It is thus possible to extract the molten zone profile (in green) or HAZ. Following the methodology presented in Chapter 4, a first example of calibration on molten zone profile is presented. 256 simulations are performed by varying the parameters of the equivalent heat source, a_r, f_r, b, c, η , in the ranges shown in Table 5.10 using Sobol sequence DOE. As for all the case studies presented in the manuscript, a surrogate model by PCE is built from the macrography profiles (Figure B.1-c). Finally, a calibration step is performed using the surrogate model. In the absence of experimental data from this test, an artificial numerical profile is generated, which serves as an "experimental" profile on which the surrogate model is calibrated (in red in Figure B.1-d). After the calibration step, the generated parameter set gives the molten zone profile presented in blue in Figure B.1-d. This example shows very promising results for future calibrations.

The advantage of performing calibration on other types of data is to "add" information that is not present in the considered experimental data. Indeed, some parameters may seem to be less influential in the case of calibration using thermocouple data, which measures the temperature quite "far" from the molten pool. The information observed at the thermocouple location may thus be insufficient to represent the temperature around the molten pool accurately. Therefore, considering the shape of the molten pool in the calibration allows adding local thermal information, which can eventually help in the better calibration of some parameters. The use of several types of experimental measurements in future work may provide a much more accurate calibration of the simulations.

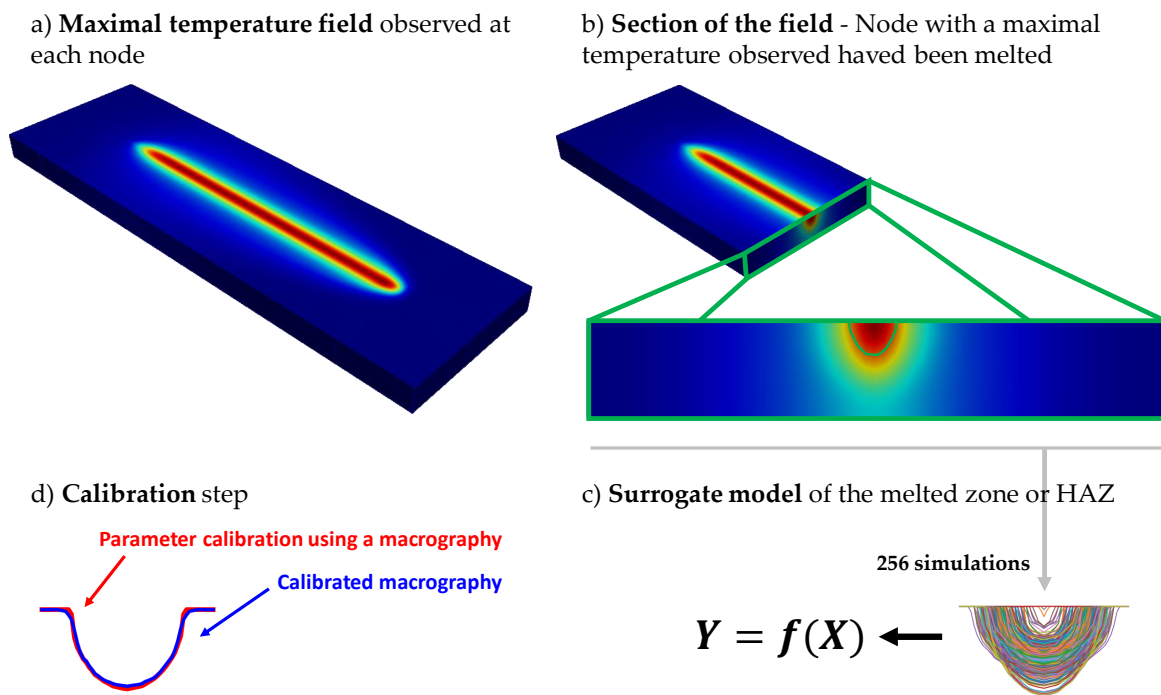


Figure B.1 – Example of calibration of the thermal source on a molten zone profile.

Appendix C

Extra study: Sensitivity analysis

Several studies in the literature focus on the sensitivity of the model parameters. For example, Asserin et al. [200] performed a sensitivity analysis on material properties. Velaga et al. [201] studied the influence of the radius of an equivalent surface source on the shape of the molten pool. The authors determined that the molten pool is further apart and shallower as the radius increases. Moreover, since the source used is gaussian, the larger the r , the smaller the maximum temperature reached.

One of the significant advantages of using Polynomial Chaos Expansion is the explicit computation of Sobol indices. Sobol indices provide the areas of the relevance of the parameters, their evolution in time, and their global influence. In this appendix, a sensitivity study is performed for the two walls presented in Section 5.3. This sensitivity study does not only consider the data used for the calibration. Indeed, 512 simulations are performed in this section. Moreover, the entire top surface of the wall base plate is used. This sensitivity study is carried out considering three approaches.

For the first approach, the temperature profile is extracted at each mesh node on the upper face. For each node, a surrogate model is built considering the following parameters: a_r , f_r , b , c , η , ε_0 , ε_1 , h_0 , h_1 , and h_{cl} . From the surrogate models built on each node, the associated Sobol indices are extracted for different time steps of the temperature curves (1 time step out of 5 to reduce the computational costs). A spatial and temporal field is thus obtained for each parameter. Figures C.1 and C.3 respectively represent the first-order Sobol indices field at three different instants for the "Zigzag" test and the "Raster" test: at 24 s, at 348 s, and at 708 s.

Several conclusions can be drawn from these fields. First of all, the Goldak parameters (a_r , f_r , b , c) are not very influential during the manufacturing process. On the contrary, the efficiency η is highly influential, and its influence decreases progressively on the base plate as the part is being manufactured. This can be explained by the fact that, as the manufacturing progresses, the source "moves away" from the base plate. Regarding the parameters describing the thermal dissipation by convection and emissivity (ε_0 , ε_1 , h_0 , h_1), their influence increases on the base plate as the part is being produced. This observation is consistent with the analysis performed in Section 5.3 stating that one of the particularities of the WAAM process is that the influence of the thermal dissipations increases during the manufacturing process due to the accumulation of heat during the manufacturing process.

The second approach considered for this sensitivity study is the calculation of the aggregated Sobol indices according to time for each node: there is thus only one aggregated value of the Sobol indices

per parameter set for each node. The Sobol indices fields are represented in Figures C.2 and C.4 for the "Zigzag" and the "Raster", respectively. These fields allow studying the overall distribution of the parameter sets sensitivities on the upper surface of the base plate. These figures clearly show that the most influential parameters are the efficiency and the thermal dissipation coefficients.

Finally, the third approach consists in aggregating of the Sobol indices of all the nodes together. A global estimate of the most influential parameters is thus obtained. As for the two previous approaches, the efficiency is the most influential parameter by far.

Moreover, it seems that the morphological parameters of the equivalent heat source are not very influential. Multiple reasons can justify this. The first is that the morphological parameters may not influence the top surface of the base plate. However, a study on the whole volume could increase the sensitivity index of these parameters. Moreover, this might also be due to the discretization of the mesh, which may not be fine enough to see a significant influence of these parameters, but sufficient to provide very good thermal predictions. Finally, these parameters may not significantly influence the temperature field. However, they might have an impact on other quantities of interest (for instance, target mechanical properties).

The parameters describing the thermal dissipation by convection and radiation appear to be influential. Moreover, the first-order parameters (ε_0 , h_0) are superior to the second-order parameters (ε_1 , h_1). This means that it may not be necessary to use a time-dependent description for the dissipations, and that constant values may be sufficient. A more detailed study could be carried out to validate this hypothesis. The approximate Bayesian Computation (ABC) approaches described in Appendix D can for instance be considered to estimate which of thermal dissipation models has the highest probability of representing experimental data.

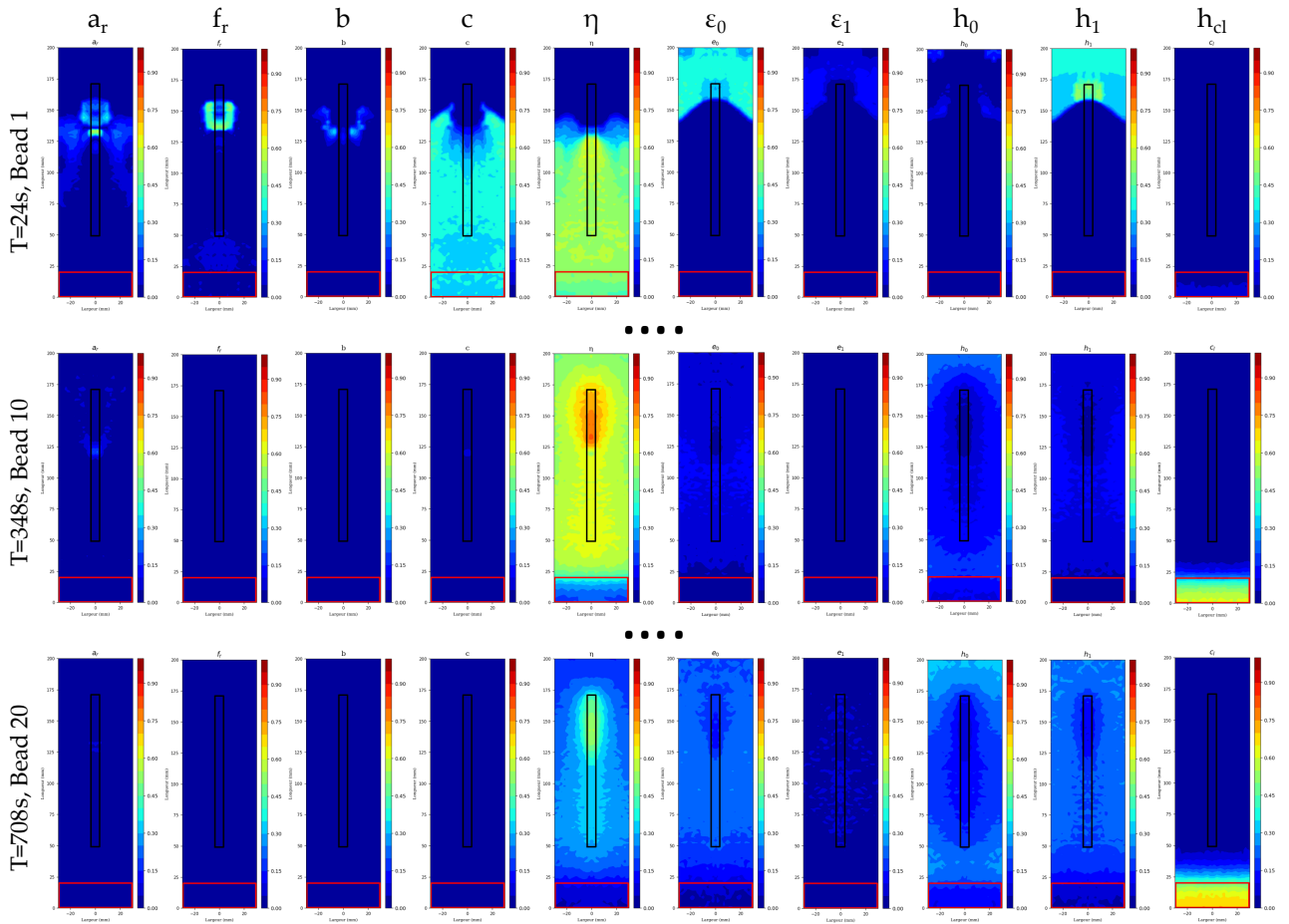


Figure C.1 – "Zigzag" test case: Sensitivity analysis field

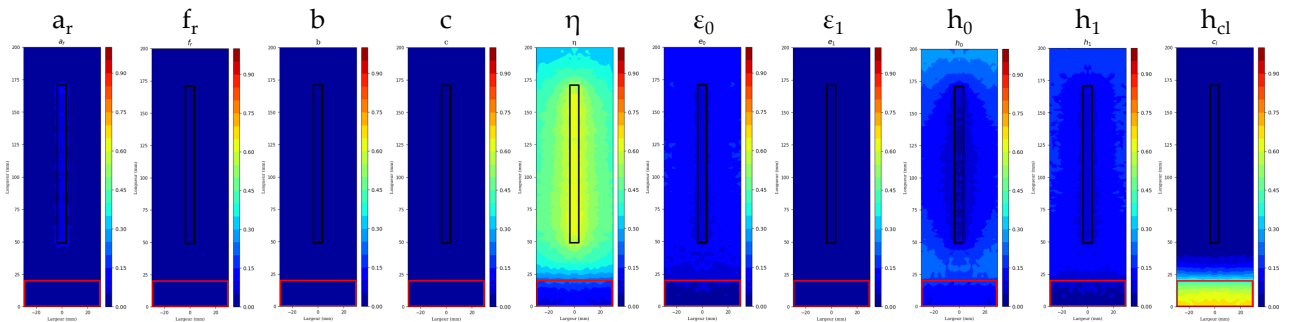


Figure C.2 – "Zigzag" test case: Sensitivity analysis field aggregated on time

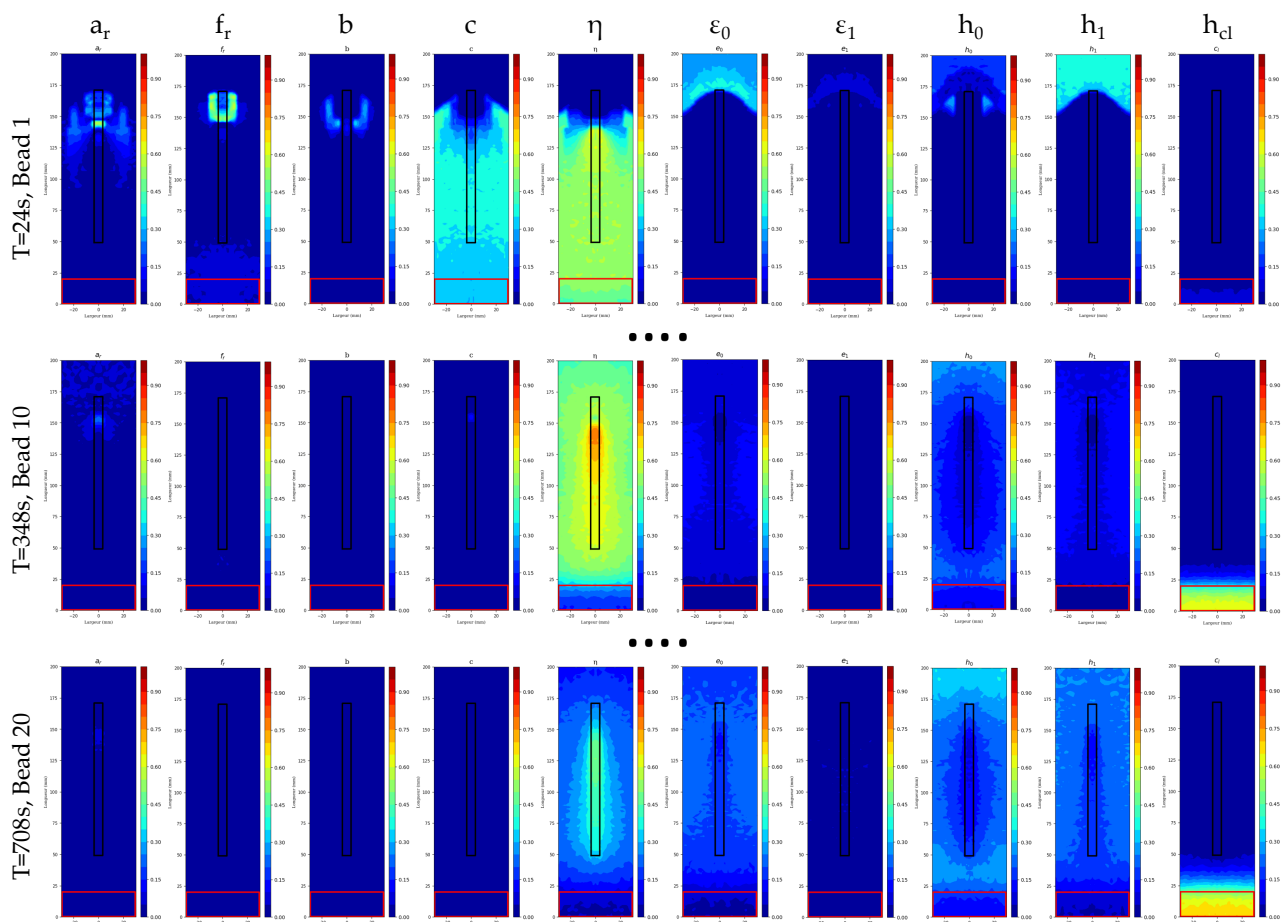


Figure C.3 – "Raster" test case: Sensitivity analysis field

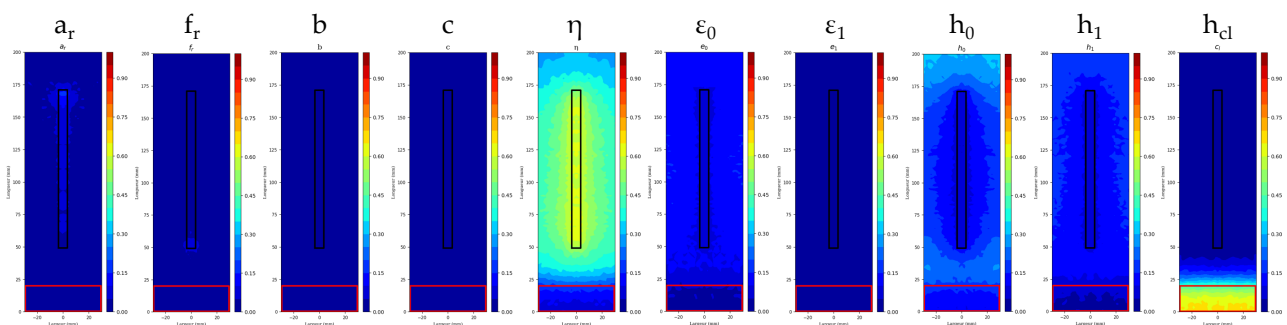


Figure C.4 – "Raster" test case: Sensitivity analysis field aggregated on time

Appendix D

Extra study: Thermal dissipation model selection

D.1 Presentation of the study

In this section, a preliminary model selection study is performed. As indicated in Section 2.4.3.2, several approaches to modeling heat losses are possible. In this Appendix, the three proposed modelings of the thermal dissipation presented below are compared.

Model selection consists in choosing a model from a set of candidate models, which seems to be the most suitable given the data. The best model is the one with the highest probability of representing the experimental data at disposal. To do this, the Approximate Bayesian Computation approach (ABC) [202, 203] is used.

Approximate Bayesian Computation (ABC) is a method in the field of Bayesian inference which is used to estimate the posterior distributions of the model parameters and the estimation of the parameters, in the same way as the MCMC introduced in Chapter 4, but also to make model selection [202].

In contrast to the adaptive Metropolis-Hasting algorithm, the draw rejection algorithm for the ABC is simpler. The major difference lies in the fact that the successive draws do not depend on the previous point. The steps of the rejection algorithm are the following: (1) the proposal is drawn on the prior distribution of the parameters. (2) The model is estimated for each draw. (3) If the estimate $\mathcal{Y}(\theta)$ is too far from the experimental observations D_{obs} , the draw is rejected; otherwise, it is accepted. In this study, a norm L_2 is used to compute this distance and ε_{ABC} the tolerance for the acceptance or not of a draw such that:

$$\|\mathcal{Y}(\theta) - D_{obs}\|_2 \leq \varepsilon_{ABC}. \quad (\text{D.1})$$

As for the MCMC, the result of such an algorithm is an approximation of the posterior distribution of the parameters. Nevertheless, the acceptance rates are the result used for the ranking of the models. Thus, for a similar tolerance ε_{ABC} , the fact that a model has a higher acceptance rate than the other candidate models means that it has a higher probability of generating predictions close to the experimental data. Moreover, for candidate models with similar predictive power, the "simplest" model is the most likely to be the best choice. Indeed, the higher the dimension of the problem, the

lower the probability of generating a run whose distance from the experimental data is small. It should also be kept in mind that the estimate obtained gives an indication of the model that seems to most easily approximate the experimental data at hand. Although these methods are dependent on the priority given as input, it is very interesting to have a first estimation of which model seems the most relevant.

D.2 Models & Results

After this short presentation of the principle of the ABC approach, the case studied is presented. For this study, the experimental test that is used for this study is the "Zigzag" test presented in the 2nd case study. The three types of thermal dissipation modeling are:

■ Constant heat losses coefficients:

$$h(T) = h_0 \quad \text{with} \quad \varepsilon(T) = \varepsilon_0. \quad (\text{D.2})$$

■ Linearly temperature-dependent heat losses coefficients:

$$h(T) = h_0 + h_1 \frac{(120.0 - h_0)}{2000} T, \quad (\text{D.3})$$

$$\varepsilon(T) = \varepsilon_0 + \varepsilon_1 \frac{(1 - \varepsilon_0)}{2000} T. \quad (\text{D.4})$$

■ Combined temperature-dependent heat losses coefficients:

$$\begin{aligned} h(T - T_{amb}) + \varepsilon\sigma(T^4 - T_{amb}^4) &= (\varepsilon\sigma(T - T_{amb})(T^2 - T_{amb}^2) + h)(T - T_{amb}) \\ &= f_{loss}(T)(T - T_{amb}) \end{aligned} \quad (\text{D.5})$$

$$f_{loss}(T) = \left(0.5(c_1 - c_0) \times \tanh\left(\frac{5T}{T_1 - T_0} + \left(2.5 - \left(\frac{5T_1}{T_1 - T_0}\right)\right)\right) + 0.5(c_1 + c_0) \right) \quad (\text{D.6})$$

Assuming nothing is known about the parameters, a uniform prior for each parameter is employed for the surrogate model training and the ABC step. The intervals are presented in Table D.1, D.2, and D.3.

Table D.1 – Parameters range for the 1st model.

Parameters	a_r	f_r	b	c	η	ε	h	h_{cl}
Variation	[3.0,18.0]	[1.10,1.7]	[3.0,9.0]	[1.0,10.0]	[0.50,0.95]	[0.2,0.8]	[0.0e-6,30.0e-6]	[0.0e-6,300.0e-6]

Table D.2 – Parameters range for the 2nd model.

Parameters	a_r	f_r	b	c	η	ε_0	ε_1	h_0	h_1	h_{cl}
Variation	[3.0,18.0]	[1.10,1.7]	[3.0,9.0]	[1.0,10.0]	[0.50,0.95]	[0.2,0.8]	[0.0,1.0]	[0.0e-6,30.0e-6]	[0.0,1.0]	[0.0e-6,300.0e-6]

As for the WAAM algorithm, a number of samples are generated from the prior distribution and the associated estimation using the surrogate model are performed. Each estimation is compared to

Table D.3 – Parameters range for the 3rd model.

Parameters	a_r	f_r	b	c	η	c_0	c_1	T_0	T_1	h_{cl}
Variation	[3.0,18.0]	[1.10,1.7]	[3.0,9.0]	[1.0,10.0]	[0.50,0.95]	[5.5e-6,3.5e-5]	[3.5e-5,9.0e-4]	[50,500]	[1200,2200]	[0.0e-6,300.0e-6]

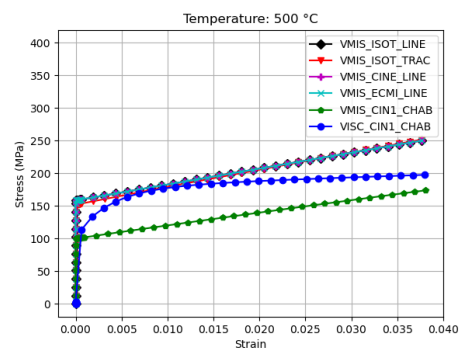
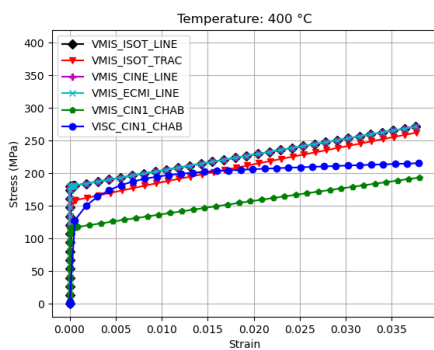
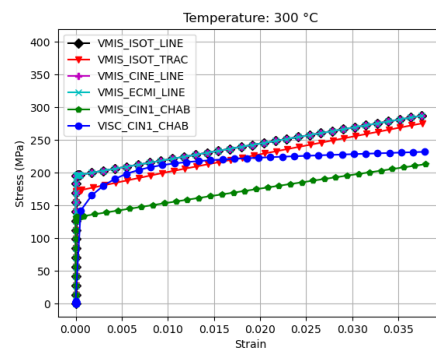
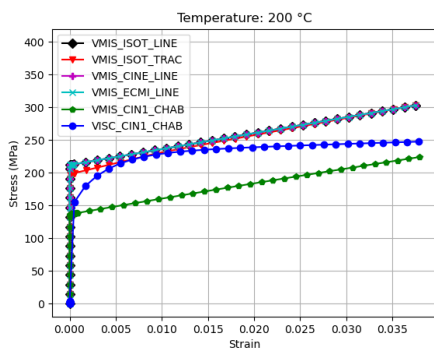
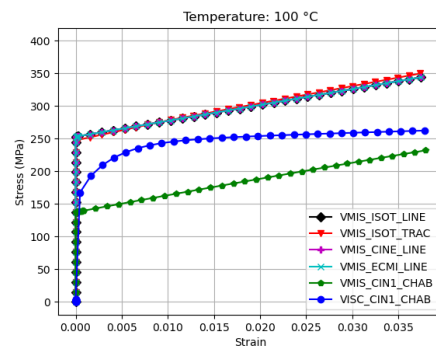
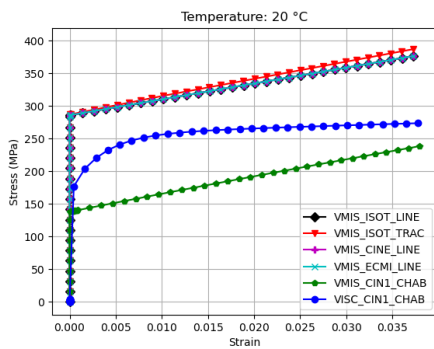
the experimental data, and if the distance is smaller than or equal to the defined error, the parameter set is accepted. These steps are performed using multiple models: the constant-coefficient thermal losses surrogate model, the linearly temperature-dependent thermal losses surrogate model and the "*tanh*" temperature-dependent thermal losses surrogate model. For each surrogate model, the resulting acceptance ratio is computed. The models are thus classified by the resulting acceptance rate with the model, with the highest acceptance rate being the one that has the highest probability of representing the experimental data. The acceptance rates for each of the three surrogate models are presented in Table D.4. These results highlight the fact that the model that seems to be best suited for representing thermocouple data is the model with constant convection and radiation coefficients, and the worst is the "*tanh*". This observation is very interesting since the best fitting model is the simplest one. Moreover, these observations coincide with the observation in Appendix C, which shows that the first-order heat dissipation parameters are the most influential and that the other two do not seem to be very influential.

Table D.4 – ABC results: Acceptance rate for the 3 models.

Model	1 st : Constant coefficients	2 nd : Linear coefficients	3 rd : Combined coefficient
Acceptance rate	23%	15%	8%

Appendix E

Constitutive behavior models monotonic response to a tensile loading



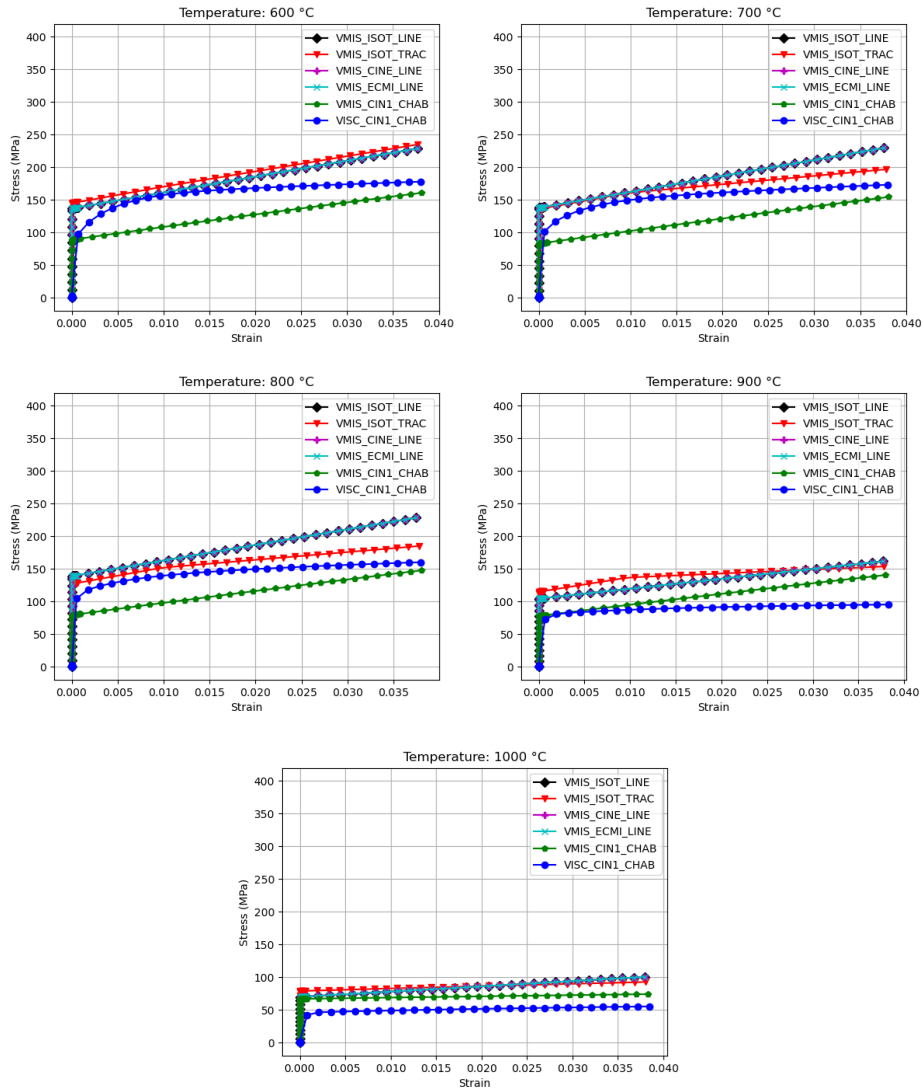


Figure E.1 – Constitutive behavior models monotonic response to a tensile loading for multiple temperatures: 20°C, 100°C, 200°C, 300°C, 400°C, 500°C, 600°C, 700°C, 800°C, 900°C, 1000°C.

Appendix F

Extra study: Thermal model calibration using stress experimental data

The single-bead test of the third study presented in Section 5.4 is instrumented by X-ray diffraction on 4 profiles. The 8 associated residual stress curves are thus obtained. These experimental data provide a wealth of information that can be used in several ways. One idea is to perform the calibration step of the thermal model parameters on these residual stress profiles. Such a study would allow comparing the posterior distributions to those obtained by the calibration of the temperature curves. Moreover, as explained in Appendix C, the construction of the associated surrogate models allows performing a sensitivity analysis of the thermal parameters to study their influence on the residual stress profiles.

The 512 simulations associated with the same DOE presented in Appendix C are performed. For this purpose, the model VMIS_ECMI_LINE is used since it seems to give satisfactory results (Section 5.4 for more details). For the calibration step and the associated surrogate model, the 8 experimental and numerical residual stress profiles are concatenated to obtain the longitudinal and transverse residual stresses on the 4 measured profiles. Figures F.1 and F.2 represent the shape of the data.

The surrogate model is constructed using Sparse PCE, as presented in Chapter 4. The R^2 obtained is 0.94. As a first step, a sensitivity study is performed using the trained surrogate model. The aggregated Sobol indices are determined and presented in Figure F.4. The results highlight that the most influential parameters are the source length a_r and depth c and the efficiency η . Interestingly, length and depth were not among the influential parameters in the thermal sensitivity analysis (Appendix C). On the other hand, efficiency is the most influential parameter, as for the previous sensitivity analysis study. A global sensitivity analysis on the whole mesh could be performed to compare the influences of the parameters on the thermal and mechanical target properties. The calibration step is done using the same DOE as for the thermal calibration. The results show a good estimation of the stress as shown in Figure F.5.

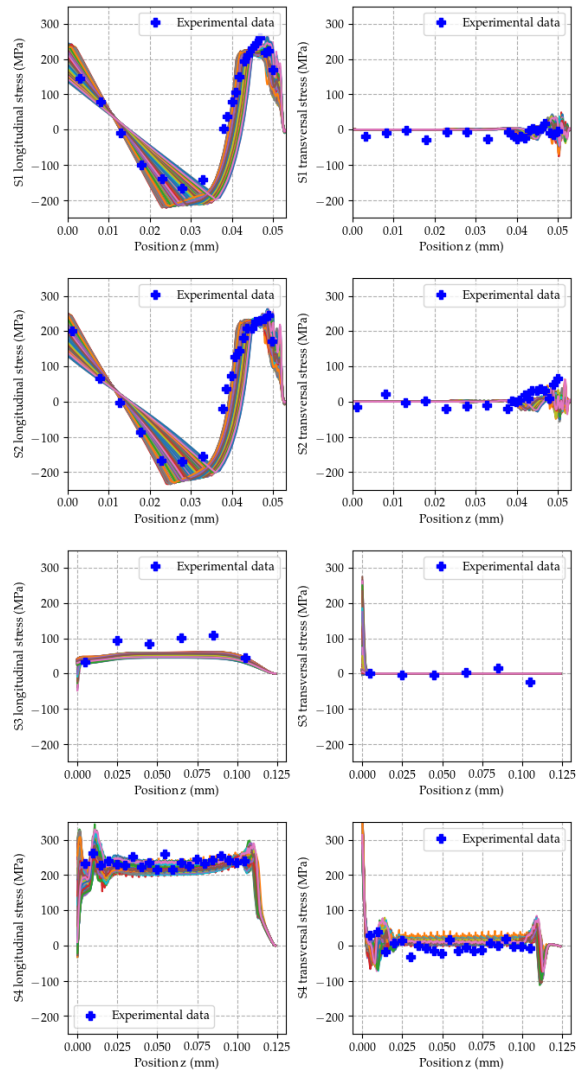


Figure F.1 – All the experimental data with the 512 stress curves used for the metamodel construction

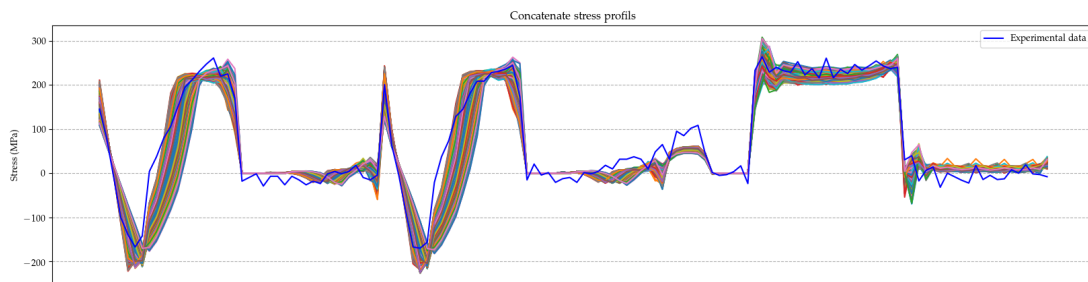


Figure F.2 – All the concatenate experimental data with the 512 stress curves concatenate used for the metamodel construction

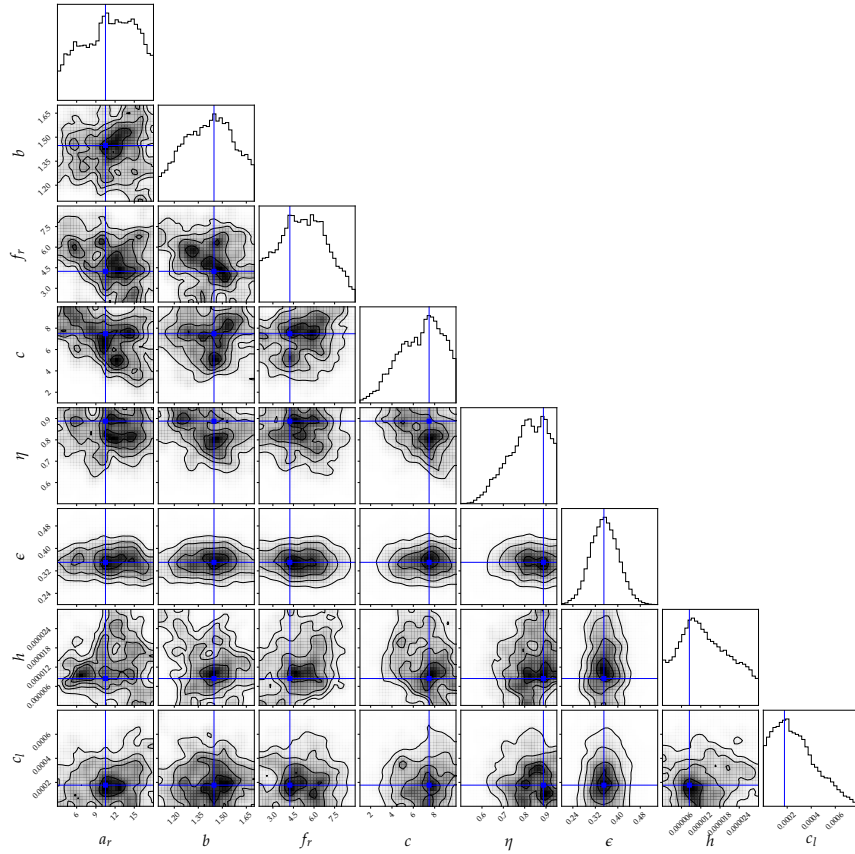


Figure F.3 – Corner plot of the posterior distribution resulting from the calibration step.

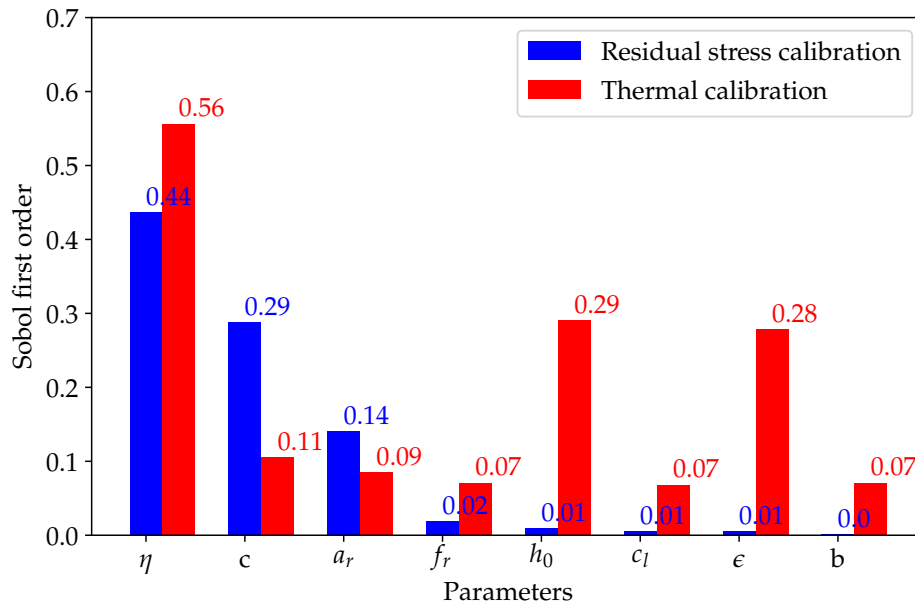


Figure F.4 – Comparison of aggregated first-order Sobol indices obtained from the calibration using residual stress data (blue) and from the calibration using temperature data at thermocouple points (red). The parameters are ranked in descending order according to the aggregated first-order Sobol indices using residual stress data.

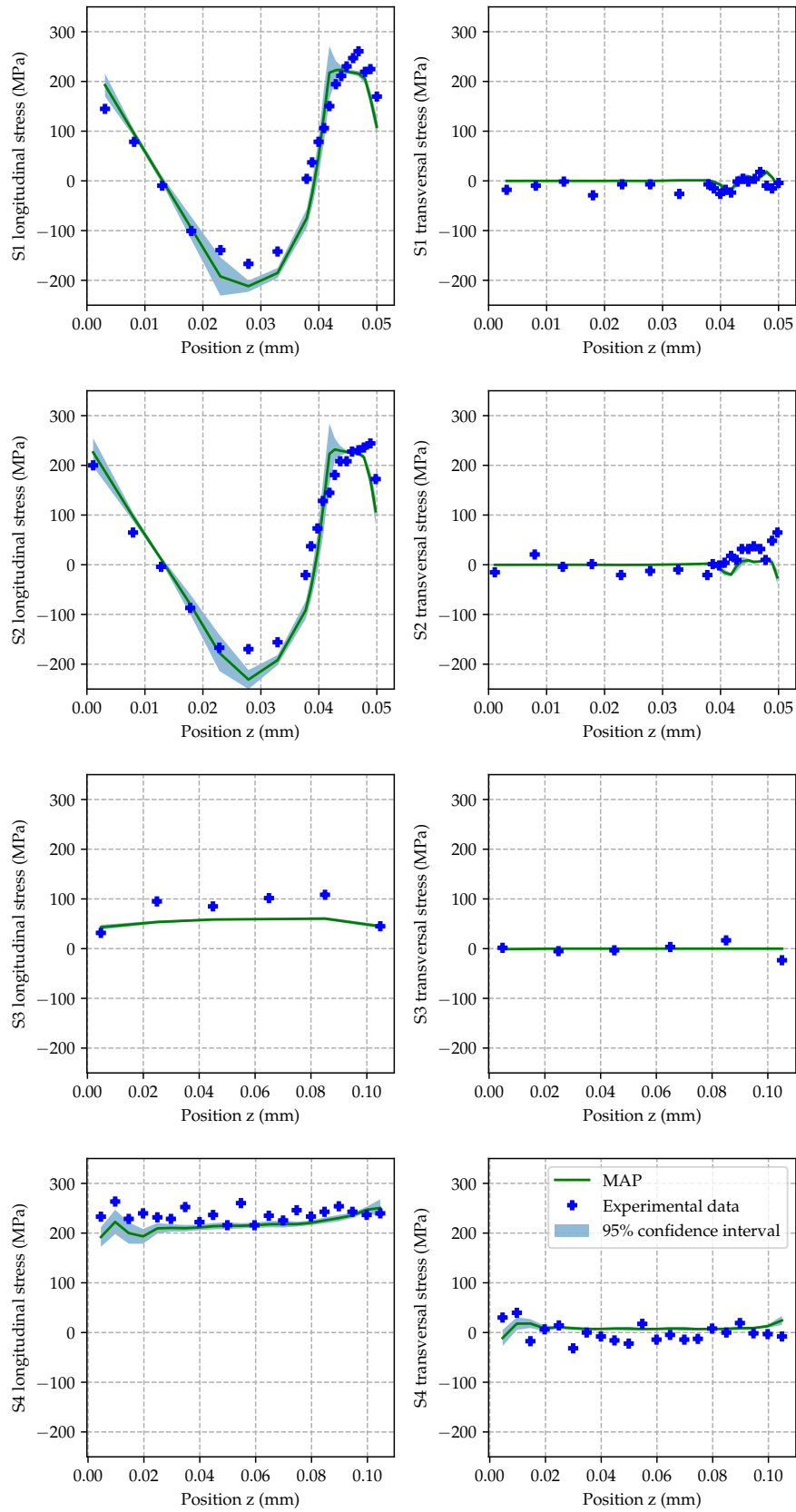


Figure F.5 – Experimental and MAP metamodel estimation with the confidence interval

Appendix G

Data-driven inherent strain field calibration method

G.1 Introduction

G.1.1 Overview of the problem

As it stated previously, the first objective is to succeed in making the link between the numerical mesh and the two 3D scans of the WAAM manufactured walls. Therefore, this first part focuses on setting up a calibration algorithm between the 3D scan and the mesh. This means that the mesh must be deformed to match the 3D scan. This calibration has thus three constraints:

- A good reconstruction of the object. Indeed, the mesh must fit the 3D scan as well as possible. Therefore, it is necessary to define the distance between the two objects: the mesh and the 3D scan. It is also necessary to choose the degree of precision of the fit. Indeed, it is necessary to avoid capturing the measurement errors of the 3D scan. Moreover, the surface roughness of the manufactured parts is not always relevant to take into account,
- The quality of the deformed mesh after calibration. Indeed, having a good quality mesh is very important during finite element simulations for the calculations to be carried out with good accuracy, for a good stability of the solutions, but also for a good convergence of the calculations,
- A realistic deformation field. The search field must, afterward, be able to be explained physically. In particular, too large discontinuities between two adjacent mesh elements must be avoided.

The 3D scan can be considered as a point cloud. Several methods aim to deform an initial point cloud, also called *template*, towards a *target* point cloud. Amberg et al. [204] define the problem as the sum of three terms: one term aiming at reducing the distance between the *template* and the *target*, another one aiming at having an ensemble motion between the points of the *template* by putting springs between the neighboring points, and a last term that gathers an a priori knowledge of the relationship between the *template* and the *target*. More precisely, in the case where we know a priori that specific points of the *template* and the *target* must be brought closer, the last term allows associating them. The developed algorithm has a "reduce stiffness" structure: the idea is to start by having a very stiff mesh, and then by decreasing the force of the springs in order to have a less and less stiff mesh to approximate as well as possible the local deformations. Moreover, the term to penalize the distance

between the *template* and the *target* is based on the two-by-two association of points of these two objects. However, the determination of this association is not feasible a priori because of the very large dimension of the solution space. Thus, the problem is approached by considering local associations of points. This is done by searching for the closest points in the *target* for each point of the *template* in order to approach the "true" solution of the problem.

Yao et al. [205] propose a similar approach, but that differs regarding several points. First, in order to decrease the algorithmic complexity of the problem, the authors introduce a *template* extraction. Indeed, they only consider a part of the points of the *template*. Moreover, in order to move the others, they consider a neighborhood for each point and apply an affine transformation to move the points not included in the extraction. Finally, the authors seek to decrease the number of deformation discontinuities between neighboring points by introducing an approximation of the L_0 norm.

Another method is to have a probabilistic point of view, as developed in the article by Myronenko et al. [206]. For this approach, the displaced points are considered to be the realization of 3-dimensional centroids of equally-weighted gaussians with equal isotropic covariance matrices. Moreover, unlike the two previous methods, the association of points between the *target* and the *template* is not sought. The minimization of the distance is done by comparing the distance of all the points of the *template* with all the points of the *target*. Finally, in order to have an ensemble motion, a regularization term is added to tend to penalize discontinuous motions. For this, the authors introduced a high-pass filter in order to minimize the oscillations in the deformation field [207].

The solution of the Scholkopf et al. problem [206] goes through an expectation-maximization algorithm whose objective is to find the maximum of likelihood while using the basics of the annealing principle by starting to have a strongly randomized search that reduces in time to explore the most promising regions found during diversification.

There are many other variants to these three methods which are compared in the study of Tam et al. [208]. However, most of the methods only concern point clouds that try to approximate point clouds, or point clouds with edges, that try to approximate point clouds. From a mesh point of view, for the *template*, the problem is poorly explored. Moreover, in this study, the objective is to wedge the nodes of the edge of the mesh to a point cloud, and the points inside the mesh must be able to follow the motion, which is much less explored in the literature.

In the following, now that the problem has been defined, methods of calibration between a mesh and a point cloud will be explored. This study is based on the work of Amberg et al. [204], which is widely used in the literature.

G.1.2 Proposed model

The initial mesh (the *template*) is denoted $\Omega = \{\nu, \varepsilon\}$. It is composed of N vertices ν and M edges ε . An edge $\mathcal{E} \in \varepsilon$ is defined as a linear function of $[0, 1]$ in \mathbb{R}^3 connecting two nodes of the mesh. The vertices on the boundary of the mesh are called skin summits or skin nodes, $\tau = \{x \in \mathbb{R}^3; x \in \partial\Omega \cap \nu\}$. This set is a discrete set of \mathbb{R}^3 points of cardinal N_{skin} . The target π is a cloud of points of \mathbb{R}^3 . Denoting $X \in \mathbb{R}^{N \times 3}$ the position of the vertices in the initial mesh, the positions of all nodes $x \in \mathbb{R}^{N \times 3}$ of the deformed mesh searched for are written as:

$$x = U + X, \tag{G.1}$$

with $U \in \mathbb{R}^{N \times 3}$ the displacement of each vertex of the mesh. The displacement U corresponds to the minimum of the energy $E(U)$:

$$E(U) = E_{data}(U) + E_{reg}(U) = E_{data}(U) + \alpha E_{jump}(U) + \gamma E_{solid}(U). \quad (\text{G.2})$$

This problem is based on the definition of two terms:

- The data deviation term E_{data} aims at minimizing the distance between the skin vertices of the mesh and the target point cloud (Section G.2),
- The regularization term E_{reg} which aims to have an internal movement of the vertices of the mesh. It must allow respecting the various criteria mentioned in Section G.3.

G.2 Data deviation term

The data deviation term E_{data} is intended to minimize the distance between the skin vertices and the target point cloud. This energy term is therefore written:

$$E_{data} = \frac{1}{2} \sum_{x_i \in \tau} k_i \text{dist}(x_i, \pi)^2 \quad (\text{G.3})$$

The distance between the node x_i and the point cloud is denoted $\text{dist}(x_i, \tau)$. To define such a distance, correspondence must be established between the skin nodes of the mesh and the points of the target. The coefficient k_i corresponds to the stiffness to be put on the spring associated with the node x_i . Since the objective is to define a surface force on the whole skin of the mesh, this stiffness is set to be proportional to the area $|\Omega_i|$ of the surface element. This element corresponds to the set of triangles of the mesh (located on the skin of the mesh), of which one of the vertices is x_i . The set of vertices of these triangles is thus constituted by all the skin nodes that are connected by an edge to the node x_i , a set noted here by abuse of notation Ω_i such as $\Omega_i = \{x \in \tau; \exists \mathcal{E} \in \varepsilon / \mathcal{E}(0) = x_i, \mathcal{E}(1) = x\}$. Thus, the stiffness k_i associated with the node x_i is defined as:

$$k_i = k_i^* |\Omega_i|, \quad (\text{G.4})$$

with k_i^* a multiplier coefficient chosen constant and equal to 1 for all nodes.

Nevertheless, defining the distance between the node x_i and the point cloud is necessary. There are several methods to define it depending on the problem considered. For example, Amberg et al. [204] define a $\mathcal{A}x_i$ match for the x_i node as the point of the target closest to x_i . This is a mesh-to-target approach. Nevertheless, this definition leads to some complications. Indeed, the case of study here corresponds to the case where the point cloud contains many more points than those in the skin of the mesh. For example, in the example case represented in Figure G.1, some pairings are not satisfactory to best represent the target.

The target is a rectangle with a greater length than the skin of the initial mesh. In Figure G.1, only the skin of the mesh is represented, but it is understood that the mesh is a solid that also has interior nodes. In this case, it is easy to see that the correspondences represented by the red binders do not allow having a deformed mesh which tends towards a good representation of the point cloud: target points are not "seen" in such a configuration.

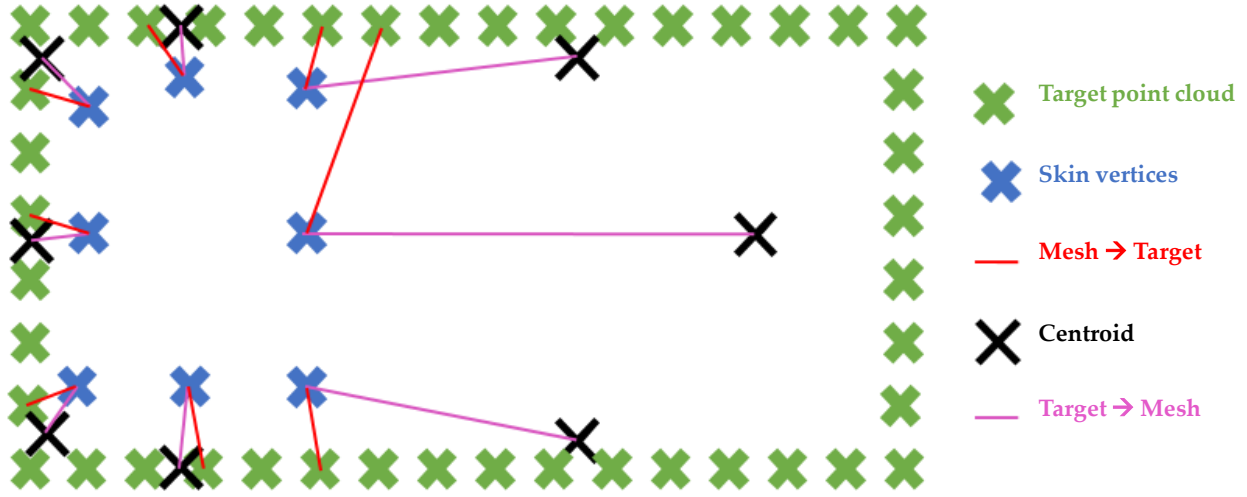


Figure G.1 – Diagram illustrating the choice of correspondence between the skin of the mesh and the target: in green the points of the target point cloud, in blue the skin nodes of the mesh, in red the correspondences following the mesh-to-target strategy, in black the centroids associated with the target-to-mesh method, in purple the correspondences of the target-to-mesh method.

Thus, in order to have a good representation of the target point cloud, it is better to have an inverse approach going from the target to the skin nodes. Moreover, in order to avoid disparities in the number of target points associated with each skin node, for instance, if a skin node has only one target point while another skin node has many, the targets are constructed as centroids associated with each skin node of the mesh. This is schematically shown in Figure G.1 with purple binders and black centroids. This way, the whole target point cloud is reached.

To define this correspondence, the application \mathcal{B} , which gives the skin node of the mesh that is closest to the point y of the point cloud is considered:

$$\forall y \in \pi, \mathcal{B}y = \operatorname{argmin}_{x \in \tau} \|y - x\|_2. \quad (\text{G.5})$$

The match for the skin node x is constructed as the centroid of all target points closest to x . Therefore:

$$\forall x \in \tau, \mathcal{A}x = \begin{cases} \frac{1}{\#\mathcal{B}^{-1}x} \sum_{z \in \mathcal{B}^{-1}x} z & \text{if } \mathcal{B}^{-1}x \neq \emptyset \\ \operatorname{argmin}_{y \in \pi} \|x - y\|_2 & \text{else.} \end{cases} \quad (\text{G.6})$$

In the case where $\mathcal{B}^{-1}x = \emptyset$, the correspondence is forced by searching for the closest point in the point cloud for a skin node. This allows overcoming the few cases where the point cloud implies, for example, a strong contraction of the mesh.

In this configuration, the distance term penalizes the normal distance term as much as the tangential distance term. Nevertheless, it is preferable to have a "slip" of the mesh skin on the target point cloud. This "slip" means that tangential movements with respect to the wall surface are allowed, so they are not penalized. For example, in a 2D case like on the diagram G.1, the blue points must not be

penalized by transverse movements according to the vector \vec{t} . Moreover, these points must move more freely in this direction to minimize the regularization term as much as possible, which corresponds to decreasing the deformation field's discontinuities. This will penalize the normal distance between the skin vertices and the point cloud. For a skin node x_i , the set of skin triangles where x_i is one of the vertices is denoted \mathbf{T}_i . A skin triangle, \mathbf{t} is a triangle of the Ω mesh such that the set of points that compose it belongs to $\partial\Omega$. For each skin triangle \mathbf{t} , its normal \vec{n}_t is defined as unitary and outgoing from Ω . Thus, the normal \vec{n}_i of the skin node x_i is defined as the average of the normals of the skin triangles of \mathbf{T}_i :

$$\vec{n}_i = \frac{1}{\#\mathbf{T}_i} \sum_{\mathbf{t} \in \mathbf{T}_i} \vec{n}_t. \quad (\text{G.7})$$

This allows defining for all nodes the notion of average. It corresponds to our intuition for relatively thin meshes where the changes in normal direction between neighboring skin triangles are small. However, there are geometric areas where such a definition does not correspond to what is desired to be approximated. This is the case, for instance, on the corners of the wall where this definition consists in averaging two very distant directions. In such cases, this definition of normal is less justified and can lead to a very irregular deformation behavior. This is why, for these borderline cases, the penalty is made on the whole distance with all its components without distinction between normal and tangential components. Nevertheless, in order to simplify the notations, in the following, the notation \vec{n}_i will be used for the different cases, but it will be understood that this vector is not normal, but, for example, a simple unit vector in the same direction as $x_i - \mathcal{A}x_i$. The energy to be minimized can then be written as follows:

$$E_{data}(U) = \frac{1}{2} \sum_{x_i \in \tau} k_i \|(x_i - \mathcal{A}x_i) \cdot \vec{n}_i\|_2^2. \quad (\text{G.8})$$

In this problem, the displacement U which leads to a minimization of the energy $E(U)$ is to be found. Indeed, the term $\mathcal{A}x_i = \mathcal{A}(U_i + X_i)$ is an unknown of the problem. Amberg et al. [204] propose to solve this by iterating local correspondences in a fixed point problem. For this, a fixed point problem is introduced, where starting from $U^{[0]} = 0$, $(\mathcal{A}x_i^{[j]})_{i \in \llbracket 1, N_{skin} \rrbracket}$ is used to determine $U^{[j+1]}$ so that:

$$\begin{cases} x^{[j+1]} &= U^{[j+1]} + X \\ U^{[j+1]} &\text{minimize } \tilde{E}^{[j+1]}(U) = \tilde{E}_{data}^{[j+1]}(U) + E_{reg}(U) \end{cases}, \quad (\text{G.9})$$

where $\tilde{E}_{data}^{[j+1]}$ is defined as a variation of the data deviation energy of the equation G.8:

$$\tilde{E}_{data}^{[j+1]} = \frac{1}{2} \sum_{x_i \in \tau} k_i \left\| (x_i - \mathcal{A}x_i^{[j]}) \cdot \vec{n}_i \right\|_2^2, \quad (\text{G.10})$$

with $x_i = U_i + X_i$ for all $i \in \tau$. Thus, in Equation G.10, $\mathcal{A}x_i^{(j)}$ is completely known and independent of U . The fixed point consists in finding a state where the new assignment $(\mathcal{A}x_i^{[j+1]})_{i \in \llbracket 1, N_{skin} \rrbracket}$ associated to $x^{[j+1]}$ is the same as the previous one $(\mathcal{A}x_i^{[j]})_{i \in \llbracket 1, N_{skin} \rrbracket}$.

G.3 Regularization term

The regularization term allows the whole structure to deform in accordance with the constraints imposed on the skin of the mesh while ensuring a good quality of the mesh. For this purpose, two energy terms are used. They are presented in this section.

G.3.1 Jump model

The idea is to minimize the jumps of deformations from one element to another directly without minimizing the values of the deformation fields. Thus, high values of deformations are possible. The first regularization, E_{jump} , aims at penalizing the discontinuities in the deformation field by penalizing the discontinuities in the displacement gradient.

In the Galerkin method, the solution $u \in H^1(\Omega)$ is approximated by a function U_h of a finite-dimensional subspace V_h . This function is then formed by a linear combination of the shape functions in the finite element case \mathbb{P}_1 . Finally, the discontinuities of the gradient are defined as the difference on the boundary between two elements T^+ and T^- :

$$[[\nabla U_h]] = (\nabla U_h^+ - \nabla U_h^-) \cdot \vec{n}, \quad (\text{G.11})$$

with \vec{n} the normal vector oriented from T^+ to T^- as represented in Figure G.2, and with U_h^+ and U_h^- the functions defined on T^+ and T^- respectively. The quantity E_{reg} must then be minimized:

$$E_{reg}(U_h) = \frac{1}{2} \sum_{e \in \varepsilon_h^{int}} \int_e [[\nabla U_h]] \cdot [[\nabla U_h]] dS \quad (\text{G.12})$$

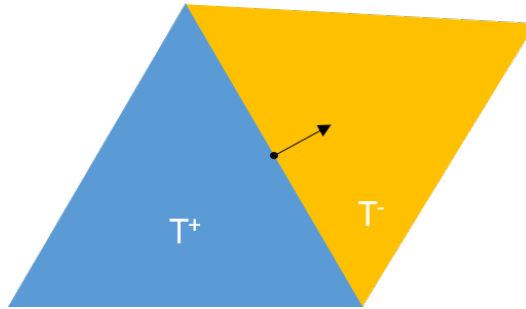


Figure G.2 – Orientation of the normal between two elements T^+ and T^- for the definition of the gradient jump.

G.3.2 Neo-Hook term

Another term, E_{solid} , is also taken into account. This extension guarantees a good quality of the mesh and prevents elements from degenerating. Indeed, there is no way to control or guarantee that a mesh element does not degenerate. However, this type of case can happen for configurations where the point cloud and the mesh are distant. For this, a constitutive behavior law of large deformations called hyperelasticity is used [209]. Finally, the potential energy is decomposed, in a general way, in three terms:

$$E_{solid}(u) = \int_{\Omega} \psi(u) dx - \int_{\Omega} B \cdot u dx - \int_{\partial\Omega} T \cdot u ds, \quad (\text{G.13})$$

where B represents the volumetric forces and T the forces on the boundary (surface forces). In the calibration case, these forces are introduced via the energies $E_{jump}(U)$ and $E_{data}(U)$, so $B = 0$ and $T = 0$. The energy density of a compressible solid is given by:

$$\psi(u) = \frac{\mu}{2}(I_c - 3) - \mu \ln(J) + \frac{\lambda}{2} \ln(J)^2, \quad (\text{G.14})$$

with λ and μ the Lamé coefficients, and I_c, J two invariants.

G.4 Overview of the method

For a fixed skin node-to-target cloud correspondence, i.e., for a fixed j , the problem is written:

$$\begin{cases} \text{Find } U \text{ by minimizing } \tilde{E}^{[j]}(U) \\ \tilde{E}^{[j]}(U) = \tilde{E}_{data}^{[j]}(U) + E_{reg}(U) = \tilde{E}_{data}^{[j]}(U) + \alpha E_{jump}(U) + \gamma E_{solid}(U) \end{cases} \quad (\text{G.15})$$

This is a non-linear problem because of the expression of $\psi(u)$. To solve it, Newton's method is used. Newton's iterations are noted with the index n . The developed mathematical model uses two convergence loops. The first one consists of a fixed point algorithm to find the local correspondences, due to the first energy term $\tilde{E}_{data}^{[j]}(U)$. The second convergence loop is nested in the first one due to the last added term from the large deformation theory. Finally, a third level is added to these loops. This one comes from the "jump" regularization term $\alpha E_{jump}(U)$. It consists of starting by having a rigid motion wedge and gradually reducing the rigidity of the structure to have motions less and less constrained by a solid rigidity. The structure must first be globally wedged. Then, the approximation of the two structures needs to be progressively refined. This is done to reach the optimal correspondences without falling into a total deconstruction of the structure. Considering initially a very rigid solid, which is then relaxed over time, makes it possible to guide the structure towards behaviors that would avoid this type of deformation. The implementation of this loop consists in making the coefficient α of the system in Equation (G.15) evolve with time. Indeed, at first, this coefficient makes regularization predominant with high values of α , then it decreases iteratively once the solution is stabilized, i.e. once the fixed point problem on the local correspondences has converged. The structure of the algorithm is shown below:

Calibration algorithm

Parameters :

- $\bar{\alpha} := \{\alpha_1, \dots, \alpha_r\}$, $\forall j, \alpha_j > \alpha_{j+1}$: stiffening coefficient in the system (G.15),
 - γ : coefficient before the Neo-Hook term of the system (G.15),
 - ε_{erreur} : setting accuracy,
 - ε : convergence of the fixed point and Newton's method.
-

Algorithm :

- Initialize $U^{[0]} \leftarrow 0$ and $Error \leftarrow +\infty$
- For each stiffness values $\alpha \in \bar{\alpha}$ and while $Erreur > \varepsilon_{erreur}$
 - While $\|U^{[j-1]} - U^{[j]}\| \geq \varepsilon$
 - Initialize $U^{[j](0)} \leftarrow U^{[j-1]}$
 - Find the local correspondences between $(x_i^{[j-1]} = U_i^{[j-1]} + X_i)_i$ and the target point cloud
 - While $\|U^{[j](n-1)} - U^{[j](n)}\| \geq \varepsilon$
 - Find ΔU^n
 - Update the displacement $U^{[j](n)} = U^{[j](n-1)} + \Delta U^n$
 - Compute the error ($Error$) between the centroids and the skin nodes of the mesh from the last local match found

There is no theoretical assurance of having a stabilized solution for the local correspondences. In particular, it has been observed numerically that specific configurations between the point cloud and the skin nodes can lead to an oscillating solution at the level of the local correspondences. A node can alternately change target centroids without asymptotic stabilization. Thus, the convergence condition of the fixed point problem of local correspondences is coupled to a condition of a maximum number of iteration j .

Moreover, knowing that there are three nested loops, the convergence of Newton's method is not required. Indeed, it is assumed that the total solution stabilizes under the effect of the two other convergence loops of the problem. Thus, the convergence condition of Newton's problem at j fixed is coupled to a time condition, with a much shorter maximum time than in the previous condition, i.e., the maximum number of iterations over n at j fixed is much smaller than the maximum number of iterations of the fixed point problem.

Appendix H

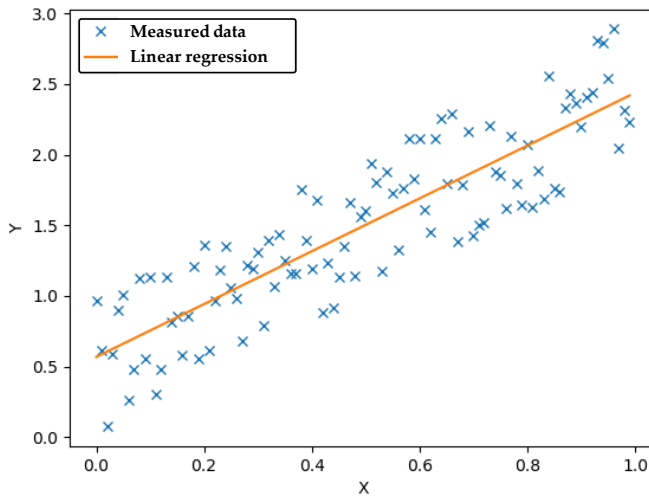
Neural network architectures

H.1 MLP model description

In this part, the functioning of a neural network is briefly presented, starting with the definition of a neuron, followed then by their association to form more complex models. Finally, the difference between the hyperparameters and the parameters of a model is explained.

A neural network model is a regression model between input and output data. It is an extension of linear regression, which consists in finding the line that most effectively explains the output data $(y_i)_{i \in \llbracket 1, M \rrbracket}$ knowing the input data $(x_i)_{i \in \llbracket 1, M \rrbracket}$ (see Figure H.1-a). In this case, one is looking for the

a) Example of linear regression



b) Neuron with N inputs and 1 output

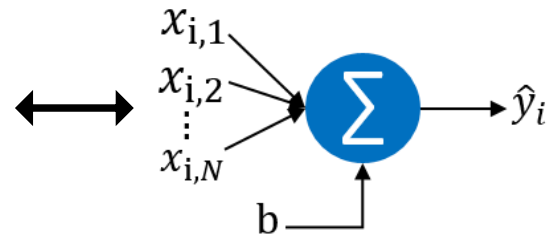


Figure H.1 – a) Example of linear regression, b) Neuron with N inputs and 1 output.

parameters (a, b) of the line, which minimize the difference between the prediction $\tilde{y}_i = ax_i + b$ and the theoretical value y_i . If the explanatory variable is of multiple dimensions and not simply a scalar, $x_i \in \mathbb{R}^N$, there are $N + 1$ parameters to determine: $a = (a_1, \dots, a_N), b \in \mathbb{R}$. The prediction \tilde{y}_i is thus the scalar product:

$$\tilde{y}_i = \langle a, x_i \rangle + b = a^T x_i + b = \sum_{j=1}^N a_j x_{i,j} + b \quad \text{with} \quad x_i = (x_{i,j}) \in \mathbb{R}^N. \quad (\text{H.1})$$

This model then looks for the parameters (a, b) which minimize the difference between the predictions $(\tilde{y}_i)_{i \in \llbracket 1, M \rrbracket}$ and the theoretical values $(y_i)_{i \in \llbracket 1, M \rrbracket}$. This operation corresponds to a single-layer neural network with N inputs and 1 output, as in Figure H.1-b. The b parameter is called the bias. In order for the neural network to learn and perform complex tasks, this scalar product is completed by a function usually non-linear called activation function. Indeed, without an activation function, a neural network is essentially a linear regression model. The activation functions have several fundamental characteristics. First, they are non-linear, which implies that a neural network with 2 layers can be considered as a universal approximator [210]. Moreover, they must be semi-differentiable since the search for the optimal parameters (a, b) is done by gradient descent.

There are many activation functions among which:

- Sigmoid: $\phi(x) = \frac{1}{1+e^{-x}}$,
- Hyperbolic tangent: $\phi(x) = \tanh(x)$,
- Relu: $\phi(x) = \max(0, x)$,
- Elu: $\phi(x) = x\mathbf{1}_{x \geq 0} + x(e^x - 1)\mathbf{1}_{x < 0}$.

The Sigmoid ϕ activation function is typically applied after the previous scalar product as it can be seen in the diagram presented in Figure H.2. This gives the input-output relation:

$$\tilde{y}_i = \phi\left(\sum_{j=1}^N a_j x_{i,j} + b\right) \quad (\text{H.2})$$

Complex models can be built by having several neurons in parallel, i.e., all neurons take the same

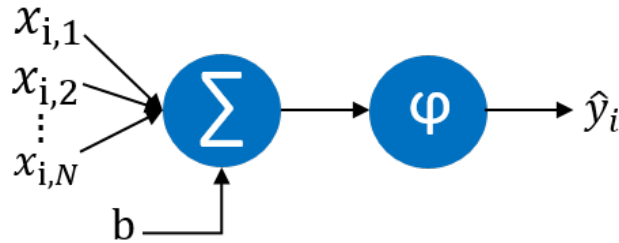


Figure H.2 – Schematic of a N input and 1 output neuron with the ϕ activation function.

inputs $(x_{i,j})_{j \in \llbracket 1, M \rrbracket}$, or in series, i.e., the outputs of a layer can become the inputs of the next layer. The layers of a neuron network can be divided into three classes: the input layer, the hidden layers, and the output layer. The input layer contains the input features. The hidden layers consist of neurons that perform various computations on the input features. The output layer produces the results for the input features considered. To obtain K outputs, it is necessary to put K neurons in parallel on this last layer. The diagram in Figure H.3 shows a network with 4 explanatory input values, 2 hidden layers with respectively 3 and 5 neurons in parallel, and 1 output layer with 2 predicted outputs. In a neural network, a distinction must be made between the hyperparameters and the parameters of the model. The hyperparameters govern the structure of the network while the parameters correspond to what directly allows predicting the output values. The parameters are all the values of the network that must be optimized and that are learned in the learning phase. In the previous example shown in Figure

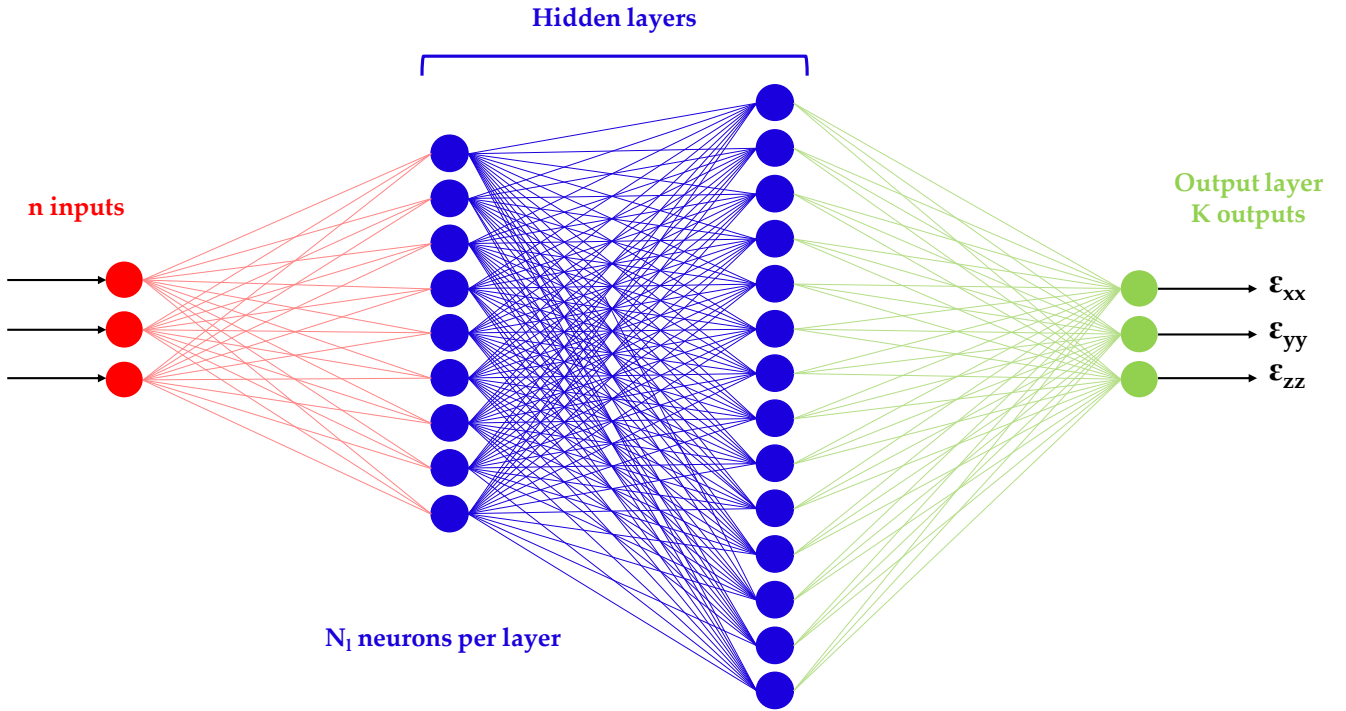


Figure H.3 – Example of a neural network with 3 inputs, 2 hidden layers with respectively 9 and 14 neurons, and 1 layer of 3 outputs.

H.3, they are all the coefficients (a, b) of all the neurons. On the other hand, the hyperparameters of the model are:

- the number of hidden layers,
- the total number of neurons in the hidden layers,
- the distribution of neurons in the layers,
- the learning rate.

The learning rate is the coefficient multiplying the gradient in the gradient descent. A value that is too high can lead to unstable learning that fails to converge. On the other hand, a learning rate that is too small implies slow learning and the possibility of being trapped more easily in the local minima. The choice of these hyperparameters is not obvious and represents an important step for the implementation of the model [211, 212].

H.2 CNN model description

Convolution consists in applying a filter (also called kernel) to an image to extract certain characteristics. To do so, a scalar product is performed, which in this case is the sum of the products term by term of two matrices. One matrix is a part of the image, and the other one is a matrix of parameters to be optimized according to the features sought. The output is then an image highlighting the features of an image as shown in Figure H.4-a (example of a convolution with a Sobel filter [213]).

Starting from the top left corner, the scalar products are performed from left to right, then from top to bottom. The output image is, in this case, smaller than the input image. This shift of one notch to

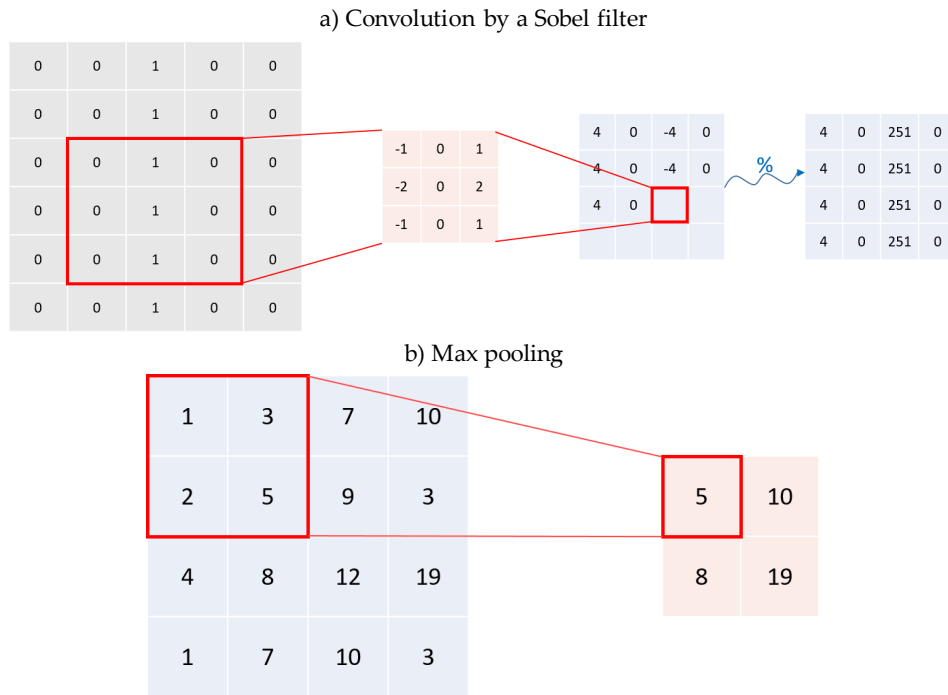


Figure H.4 – a) Illustration of a convolution by a Sobel filter, b) Illustration of max pooling.

the right is a hyperparameter to set for the filter. This hyperparameter is called the stride. Moreover, the desired size of the output image can be different. In this case, it is possible to consider fictitious 0 pixels all around the image. By adjusting the number of fictive columns and lines considered with the size of the filter, it is possible to have an output image of the same size as the input image. These types of considerations will be made thereafter to control, as well as possible, how the size of the data evolves. This hyperparameter is called the padding.

A neural layer can consist of several filters in parallel, i.e., each filter is applied on the same input image. In this case, the output of the convolutional layer is a set of images that are grouped together to form an image of dimension 3, with a depth corresponding to the number of filters applied. The convolution of an image of dimension 3 is done in the same way as before except that the filter is a matrix of dimension 3.

Following a convolutional layer, a dimension reduction is often applied. This dimension reduction is based on the fact that the information around a pixel is very often redundant. Only one value per block can be kept. In general, the maximum intensity is kept. This operation is called max pooling (figure H.4-b). Typically, in a convolutional network, the convolution layers are put in series with a max pooling layer [214].

Convolutions on time series have a similar principle as for images, except that the X direction (along the lines of the image) is only made of one element. Thus, the convolution kernels are column vectors (in the present case with a depth of 1) or column vectors with depth (i.e., of size $K \times 1 \times N$ with K the size of the kernel and N the considered depth). In the convolution neural network considered, there are various types of hyperparameters:

- the number of convolutional layers,

- for each layer, the number of filters in parallel,
- for each filter,
 - the size of the kernel,
 - the size of the stride,
 - the padding: the addition of 0 outside the image to obtain or not an output image of the same size as the input.
- the size of the pooling kernel after each convolutional layer.

H.3 RNN model description

A Recurrent Neural Network RNN is a type of neural network that uses previous outputs as additional inputs, allowing information to be stored within the network. They are perfectly suited for processing sequential data. Let $(x^t)_{t \in \llbracket 0, T \rrbracket}$ be a time series. Then the output \tilde{y}^{t+1} of the network depends on x^{t+1} of the network depends on x^{t+1} but also on the previous inputs:

$$\tilde{y}^{t+1} = f(x^{t+1}, (x^0, \dots, x^t)) \quad (\text{H.3})$$

This can be represented as on Figure H.5. The network used for each term of the sequence is the same. The parameters of the network are thus identical for each term of the time series.

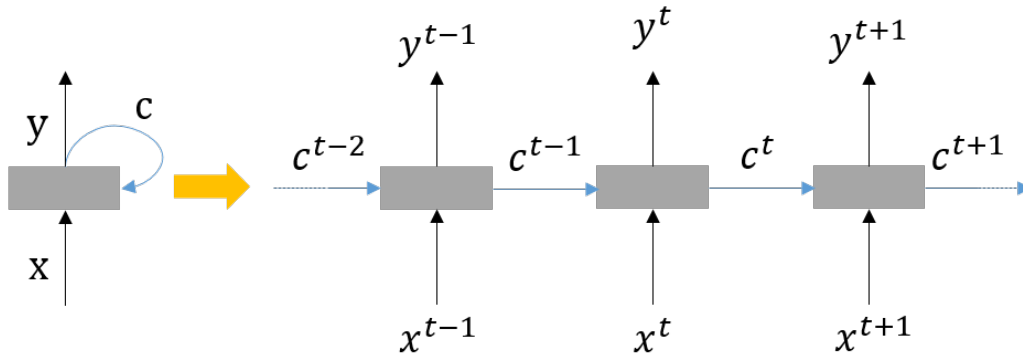


Figure H.5 – Schematic illustration of a recurrent network.

The problem with these network structures is the difficulty of solving the minimization problem during the training phase. Taking distant events into account is not possible due to the problem of gradient vanishing [215]. Indeed, chain derivatives are used in the backpropagation of the gradient to evaluate the derivative of the error according to the weights of the network, thus taking into account distant events. These chain derivatives are equivalent to the product of a large number of derivatives. This product decreases exponentially as the number of derivatives considered increase. For example, to study the influence of the x^{t-k} term on the \tilde{y}^t output, one must consider the product:

$$\frac{\partial h_t}{\partial h_{t-1}} \frac{\partial h_{t-1}}{\partial h_{t-2}} \cdots \frac{\partial h_{t-(k+1)}}{\partial h_{t-k}}$$

where h_i is the output of the hidden layer for the input term x^i . However, for standard activation functions and weights (i.e., values in the interval $[-1, 1]$), this product tends quickly towards 0. For

this reason, another approach is proposed: the *Long Short term Memory* (LSTM) which corresponds to a controlled memory cell with four inputs and one output, which are used in this section but are not detailed.

RÉSUMÉ

Un modèle thermo-mécanique mésoscopique du procédé de fabrication additive WAAM est implémenté à l'aide du code éléments finis Code_Aster développé par EDF. Les simulations sont réalisées pour différentes géométries et avec différentes stratégies de dépôt. L'implémentation du modèle nécessite la détermination de paramètres d'entrée qui ne peuvent pas être mesurés ou caractérisés directement, tels que les paramètres de la source thermique. Afin de calibrer le modèle mis en place, des essais expérimentaux sont réalisés et instrumentés en utilisant différents équipements: thermocouples, imagerie thermique et scan 3D. Pour calibrer le modèle thermique sur les données expérimentales, une méthodologie de calibration des paramètres par résolution d'un problème inverse bayésien basée sur une approche de métamodèle est mise en place. Les résultats numériques sont ensuite validés par comparaison à des données expérimentales sur plusieurs cas d'étude. Une bonne correspondance entre les résultats numériques et les résultats expérimentaux a été établie. Après la validation des modèles, différentes approches macroscopiques sont explorées pour réduire le temps de calcul pour la simulation de grands composants.

Ce travail s'inscrit dans le cadre du consortium de fabrication additive francilien "Additive Factory Hub" (AFH) impliquant des industriels et laboratoires académiques.

MOTS CLÉS

Fabrication additive par dépôt-fil - Simulation éléments finis thermo-mécanique - Problème inverse bayésien - Jumeau numérique - Approche macroscopique

ABSTRACT

The proposed research work consists in setting up, calibrating and validating a model to simulate the WAAM process, aiming to predict residual stresses and distortions on 316 stainless steel industrial parts. A mesoscopic thermo-mechanical model is implemented using the finite element code Code_Aster. Simulations are carried out for various geometries and deposition strategies. The model requires the determination of input parameters, such as the parameters of the heat source, that can not be directly measured or characterized. In order to calibrate the model, instrumented experimental tests are conducted, using thermocouples, thermal imaging and 3D scan. A bayesian calibration based on a surrogate model approach is performed in order to fit the parameters of the thermal model. The finite element results are then compared to multiple test cases experimental data, and showed good agreement. Finally, different approaches are considered to reduce the calculation time for the simulation of large components.

This work is part of the additive manufacturing platform "Additive Factory Hub" (AFH) involving French manufacturers and academics.

KEYWORDS

Wire arc additive manufacturing - Thermo-mechanical FE simulation - Bayesian inverse problem - Digital twinning - Computationally efficient approach